

INTERACTIONS BETWEEN FREEZE LINING AND SLAG BATH IN ILMENITE SMELTING

by

Johannes Hendrik Zietsman

Submitted in partial fulfilment of the requirements for the degree

Philosophiae Doctor (Metallurgical Engineering)

in the

Faculty of Engineering, Built Environment and Information  
Technology

University of Pretoria

30 April 2004

To my Father in Heaven, who created it all, made this work possible and gave me the ability and strength to carry it through. I give to Thee all the glory, all the honour, and all the praise.

To Ennes, a wonderful father and friend. I am privileged to have shared but a small part of your life. The example you set changed me, and will keep doing so until we meet again.

**ABSTRACT**

INTERACTIONS BETWEEN FREEZE LINING AND SLAG BATH  
IN ILMENITE SMELTING

by Johannes Hendrik Zietsman

Supervisor: Professor P. Chris Pistorius  
Department of Materials Science and Metallurgical Engineering

Philosophiae Doctor (Metallurgical Engineering)

**Key words:**

Ilmenite smelting, mathematical modelling, process modelling, heat transfer, DC furnace, freeze lining, slag bath, titania slag.

This study focused on the dynamic behaviour of the freeze lining and slag bath, and the interactions between these components in an ilmenite-smelting furnace process. The purpose of the work was to gain a better understanding of these issues and to ultimately contribute to an improved understanding of the ilmenite-smelting process in its entirety, and to future improvements in the design, operation and control of these processes.

A mathematical model of the freeze lining and furnace sidewall was developed. This model was used in isolation for focused characterisation of the dynamic behaviour and interactions of the freeze lining and slag bath. The influences of net power input and slag composition were studied and various aspects of the freeze lining and slag bath were considered. These aspects included freeze lining thickness, temperature distribution through the freeze lining and furnace sidewall, composition distribution through the freeze lining, slag bath temperature and slag bath composition. The thermal response of thermocouples installed in the furnace sidewall to changing conditions on the inside of the furnace was also investigated.

A mathematical model of the crust that forms on the slag bath surface was developed. This model was not used in isolation, and was only incorporated into a complete model of the process.

A mathematical model of the entire ilmenite-smelting furnace process was constructed. This model incorporated the two models mentioned above and was able to describe the metal bath, slag bath, furnace atmosphere, freeze lining, furnace sidewall and the crust that is sometimes present on top of the slag bath. The model was used to study the influence of changes in operational parameters on the slag bath and freeze lining. The operational parameters that were studied included electrical power and reductant feed rate, both relative to ilmenite feed rate. The influence of severe operational errors and furnace down time were also investigated. Operational errors included loss of all feed while maintain electrical power input, and loss of reductant feed while maintaining power input and ilmenite feed.

The above-mentioned studies were conducted by executing numerous experiments with two of the mathematical models. The experimental results were processed into sets of graphs displaying variations in the aspects that were considered. Many valuable insights resulted from the interpretation of these results.

One specific aspect that formed part of the scope of this work was the origin of the compositional invariance of the slag close to the stoichiometric  $M_3O_5$  composition. This invariance was studied and a mechanism was proposed that explains the observed behaviour. The proposed mechanism created some questions about other mechanisms in the process. These mechanisms were also considered and elaborated on.

The models and results produced in this study provide valuable insights into the behaviour of the ilmenite-smelting process. It also represents a useful foundation for future modelling work, and finally, it presents numerous opportunities for organisations operating ilmenite-smelting furnaces to improve their understanding and even the performance of their processes.

## SAMEVATTING

### INTERAKSIES TUSSEN VRIESVOERING EN SLAKBAD IN ILMENIETSMELTING

deur Johannes Hendrik Zietsman

Studieleier: Professor P. Chris Pistorius  
Departement van Materiaalkunde en Metallurgiese Ingenieurswese

Philosophiae Doctor (Metallurgiese Ingenieurswese)

#### **Sleutelwoorde:**

Ilmenietsmelting, wiskundige modellering, prosesmodellering, hitteoordrag, DC oond, vriesvoering, slakbad, titania slak.

Hierdie studie het gefokus op die dinamiese gedrag van die vriesvoering en slakbad en op die interaksies tussen hierdie komponente van 'n ilmenietsmeltproses. Die oogmerk van die werk was om 'n beter begrip van hierdie sake te verkry en om by te dra tot 'n breër begrip van die ilmenietsmeltproses in sy geheel, en tot toekomstige verbetering in die ontwerp, bedryf en beheer van hierdie prosesse.

'n Wiskundige model van die vriesvoering en die oondmuur is ontwikkel. Hierdie model is in isolasie gebruik om die dinamiese gedrag en interaksies van die vriesvoering en slakbad gefokus te karakteriseer. Die invloede van netto kraginset en slaksamestelling is bestudeer en verskeie aspekte van die vriesvoering en slakbad is beskou. Hierdie aspekte het vriesvoeringdikte, temperatuurverspreiding deur die vriesvoering en oondmuur, samestellingverspreiding deur die vriesvoering, slakbad temperatuur en slakbad samestelling ingesluit. Die termiese reaksie van termokoppels in die oondmuur op veranderende toestande in die oond is ook ondersoek.

'n Wiskundige model van die kors wat op die slakbad oppervlak vorm is ontwikkel. Hierdie model is nie in isolasie gebruik nie. Dit is slegs ingesluit as deel van 'n groter model wat die proses in sy geheel beskryf het.

'n Wiskundige model van die totale ilmenietsmeltproses is ontwikkel. Hierdie model het die twee bogenoemde modelle ingesluit en kon die metaalbad, slakbad, oondatmosfeer, vriesvoering, oondmuur en die kors, wat van tyd tot tyd op die slakbad teenwoordig, is beskryf. Die model is gebruik om die invloed van veranderinge in bedryfsparameters op die slakbad en vriesvoering te ondersoek. Die bedryfsparameters het elektriese kraginset en reduktant voertempo ingesluit, beide relatief tot ilmeniet voertempo. Die invloed van ernstige bedryfsfoute en oond aftyd is ook bestudeer. Bedryfsfoute het ingesluit die verlies van alle materiaalvoer terwyl elektriese kraginset onveranderd bly, en die verlies van reduktantvoer terwyl elektriese kraginset en ilmenietvoer onveranderd bly.

Die bogenoemde studies het die uitvoering van talryke eksperimente met twee van die wiskundige modelle behels. Die eksperimentele resultate is verwerk tot 'n stel grafieke vir elke eksperiment wat variasies in die aspekte wat beskou is aantoon. Die interpretasie van hierdie resultate het gelei tot waardevolle insig.

'n Spesifieke saak wat deel was van die bestek van hierdie werk was die oorsprong van die onveranderlikheid van die slaksamestelling naby die  $M_3O_5$  samestelling. Hierdie onveranderlikheid is ondersoek en 'n meganisme is voorgestel wat die waargenome gedrag verklaar. Die voorgestelde meganisme het vrae laat ontstaan oor ander meganismes in die proses. Hierdie meganismes is ook beskou en bespreek.

Die modelle en resultate wat voortgevloei het uit hierdie studie gee waardevolle nuwe insig in die gedrag van die ilmenietsmeltproses. Dit verskaf ook 'n nuttige platform vir toekomstige modelleringswerk, en skep talryke geleenheid vir organisasies wat ilmenietsmelters bedryf om hul begrip van die prosesse en selfs die prestasie van die hul prosesse te verbeter.

## TABLE OF CONTENTS

ABSTRACT.....	III
SAMEVATTING.....	V
TABLE OF CONTENTS.....	VII
LIST OF FIGURES .....	XV
LIST OF TABLES .....	XVIII
ACKNOWLEDGMENTS .....	XIX
CHAPTER 1 INTRODUCTION.....	1
1.1 INDUSTRY BACKGROUND.....	1
1.1.1 Minerals .....	2
1.1.2 Hard Rock Mineral Processing.....	2
1.1.3 Mineral Sands Processing .....	3
1.1.4 Ilmenite Smelting.....	3
1.1.5 Synthetic Rutile Production.....	5
1.1.6 Sulphate Process Pigment Production.....	7
1.1.7 Chloride Process Pigment Production .....	7
1.1.8 Titanium Metal Production .....	8
1.1.9 Importance of Ilmenite Smelting .....	9
1.2 OVERVIEW OF CURRENT WORK.....	9
1.2.1 Objectives.....	9
1.2.2 Impetus for Study .....	10
1.2.3 Approach.....	12
1.3 ORGANISATION OF CURRENT TEXT.....	12
CHAPTER 2 ILMENITE SMELTING PROCESS OVERVIEW.....	13
2.1 OPERATIONAL OVERVIEW.....	13
2.2 FURNACE CONTROL.....	14
2.3 FURNACE VESSEL .....	15
2.3.1 Hearth .....	15
2.3.2 Sidewalls.....	16
2.3.3 Roof.....	16
2.3.4 Tap holes .....	16
2.4 PROCESS INPUTS .....	16
2.4.1 Ilmenite .....	16
2.4.2 Reductant .....	17
2.4.3 Graphite Electrodes.....	17
2.4.4 Refractory Material .....	17
2.4.5 Water.....	18

2.4.6 Air .....	18
2.4.7 Energy.....	18
<b>2.5 PROCESS OUTPUTS.....</b>	<b>18</b>
2.5.1 Titania Slag.....	18
2.5.2 Pig Iron .....	19
2.5.3 Off-gas.....	19
2.5.4 Dust and Fumes .....	19
2.5.5 Energy.....	19
<b>2.6 PROPERTIES OF TITANIA SLAG .....</b>	<b>19</b>
2.6.1 Thermodynamic Data .....	19
2.6.2 Liquidus and Solidus Temperatures and Solidification Behaviour.....	22
2.6.3 Heat Capacity .....	25
2.6.4 Viscosity .....	26
2.6.5 Thermal Conductivity.....	26
2.6.6 Compositional Invariance .....	26
<b>CHAPTER 3 A 1D MODEL OF THE FREEZE LINING AND FURNACE WALL.....</b>	<b>27</b>
<b>3.1 IDENTIFICATION.....</b>	<b>27</b>
<b>3.2 PROBLEM DEFINITION .....</b>	<b>27</b>
<b>3.3 SYSTEM DESCRIPTION.....</b>	<b>27</b>
3.3.1 System geometry.....	28
<b>3.4 KEY PHENOMENA.....</b>	<b>28</b>
3.4.1 Heat Transfer .....	28
3.4.2 Mass Transfer .....	31
3.4.3 Momentum Transfer.....	31
3.4.4 Chemical Reaction .....	32
3.4.5 Mechanical Effects .....	33
3.4.6 Summary of Key Phenomena .....	33
<b>3.5 APPROACH AND MODEL COMPLEXITY.....</b>	<b>34</b>
3.5.1 Modelling of Heat Transfer.....	34
3.5.2 Modelling of Chemical Reaction.....	35
<b>3.6 MODEL FORMULATION .....</b>	<b>35</b>
3.6.1 Assumptions.....	35
3.6.2 Simplifications.....	39
3.6.3 Material Definitions .....	39
3.6.4 Model Structure.....	42
3.6.5 Heat Transfer .....	43
3.6.6 Slag Solidification and Melting.....	48
<b>3.7 MODEL SOLUTION.....</b>	<b>48</b>
3.7.1 Flow Sheet.....	48
3.7.2 Initial Conditions.....	50
3.7.3 Solution .....	51
<b>3.8 MODEL VALIDATION .....</b>	<b>52</b>
3.8.1 Purpose .....	52
3.8.2 Objectives .....	52
3.8.3 Methodology .....	53
3.8.4 Validation Experiments .....	54



---

3.8.5 Validation Results .....	55
<b>3.9 COMPARISON WITH ACTUAL DATA .....</b>	<b>62</b>
<b>CHAPTER 4 A 1D MODEL OF SOLIDIFICATION ON THE SLAG BATH SURFACE.....</b>	<b>63</b>
<b>4.1 IDENTIFICATION.....</b>	<b>63</b>
<b>4.2 PROBLEM DEFINITION .....</b>	<b>63</b>
<b>4.3 SYSTEM DESCRIPTION.....</b>	<b>63</b>
4.3.1 System Geometry .....	64
<b>4.4 KEY PHENOMENA.....</b>	<b>64</b>
4.4.1 Heat Transfer .....	65
4.4.2 Mass Transfer .....	67
4.4.3 Momentum Transfer .....	67
4.4.4 Chemical Reaction .....	68
4.4.5 Summary of Key Phenomena .....	68
<b>4.5 APPROACH AND MODEL COMPLEXITY .....</b>	<b>69</b>
4.5.1 Modelling of Heat Transfer.....	69
4.5.2 Modelling of Chemical Reaction.....	70
<b>4.6 MODEL FORMULATION .....</b>	<b>70</b>
4.6.1 Assumptions.....	70
4.6.2 Simplifications.....	71
4.6.3 Material Definitions .....	71
4.6.4 Model Structure .....	72
4.6.5 Heat Transfer .....	73
4.6.6 Slag Solidification and Melting .....	76
<b>4.7 MODEL SOLUTION .....</b>	<b>76</b>
4.7.1 Flow Sheet .....	76
4.7.2 Initial Conditions .....	78
4.7.3 Solution .....	78
<b>4.8 MODEL VALIDATION .....</b>	<b>79</b>
4.8.1 Purpose .....	79
4.8.2 Objectives .....	79
4.8.3 Methodology .....	80
4.8.4 Validation Experiments .....	82
4.8.5 Validation Results.....	83
<b>4.9 COMPARISON WITH ACTUAL DATA .....</b>	<b>88</b>
<b>CHAPTER 5 A DYNAMIC MODEL OF THE ENTIRE ILMENITE-SMELTING FURNACE PROCESS .....</b>	<b>89</b>
<b>5.1 IDENTIFICATION.....</b>	<b>89</b>
<b>5.2 PROBLEM DEFINITION .....</b>	<b>89</b>
<b>5.3 SYSTEM DESCRIPTION.....</b>	<b>90</b>
5.3.1 Dimensions.....	90

---

<b>5.4 KEY PHENOMENA</b> .....	<b>91</b>
5.4.1 Heat Transfer .....	91
5.4.2 Mass Transfer .....	94
5.4.3 Momentum Transfer.....	99
5.4.4 Chemical Reaction .....	103
5.4.5 Mechanical Effects .....	108
5.4.6 Summary of Key Phenomena .....	109
<b>5.5 APPROACH AND MODEL COMPLEXITY</b> .....	<b>110</b>
<b>5.6 MODEL FORMULATION</b> .....	<b>110</b>
5.6.1 Assumptions.....	110
5.6.2 Simplifications.....	113
5.6.3 Material Definitions .....	113
5.6.4 Model Structure.....	115
5.6.5 From Model Structure to Process Model.....	119
5.6.6 Sub-models to Calculate Heat Losses.....	121
5.6.7 Sub-models to Calculate Product Flow Rates.....	124
5.6.8 Sub-models to Calculate Mass Transfer Rates to Phase Boundaries .....	125
<b>5.7 MODEL SOLUTION</b> .....	<b>133</b>
5.7.1 Initial Conditions .....	134
5.7.2 Solution .....	134
<b>5.8 MODEL VALIDATION</b> .....	<b>134</b>
5.8.1 Purpose .....	134
5.8.2 Objectives .....	134
5.8.3 Methodology .....	135
5.8.4 Validation Experiments .....	135
5.8.5 Validation Results.....	135
<b>5.9 COMPARISON WITH ACTUAL DATA</b> .....	<b>136</b>
<b>CHAPTER 6 THE DYNAMIC RESPONSE OF A FREEZE-LINING TO STEP CHANGES IN INPUT HEAT FLOW RATE</b> .....	<b>137</b>
<b>6.1 EXPERIMENTAL SETUP</b> .....	<b>137</b>
<b>6.2 EXPERIMENTS</b> .....	<b>137</b>
<b>6.3 EXPERIMENTAL RESULTS</b> .....	<b>139</b>
6.3.1 Experiment 6.1 .....	144
6.3.2 Experiment 6.2 .....	145
6.3.3 Experiment 6.3 .....	146
6.3.4 Experiment 6.4 .....	147
6.3.5 Experiment 6.5 .....	148
6.3.6 Experiment 6.6 .....	149
6.3.7 Experiment 6.7 .....	150
6.3.8 Experiment 6.8 .....	151
6.3.9 Experiment 6.9 .....	152
6.3.10 Experiment 6.10 .....	153
6.3.11 Experiment 6.11 .....	154
6.3.12 Experiment 6.12 .....	155
6.3.13 Experiment 6.13 .....	156
6.3.14 Experiment 6.14 .....	157
6.3.15 Experiment 6.15 .....	158
6.3.16 Experiment 6.16 .....	159

6.3.17 Experiment 6.17 .....	160
6.3.18 Experiment 6.18 .....	161
6.3.19 Experiment 6.19 .....	162
6.3.20 Experiment 6.20 .....	163
6.3.21 Experiment 6.21 .....	164
6.3.22 Experiment 6.22 .....	165
6.3.23 Experiment 6.23 .....	166
6.3.24 Experiment 6.24 .....	167
6.3.25 Experiment 6.25 .....	168
6.3.26 Experiment 6.26 .....	169
<b>6.4 DISCUSSION .....</b>	<b>170</b>
6.4.1 Freeze Lining Thickness .....	170
6.4.2 Thermal Response of Freeze Lining and Furnace Wall .....	170
6.4.3 Slag Bath Composition .....	172
6.4.4 Slag Bath Temperature .....	174
6.4.5 Freeze Lining Composition.....	174
 <b>CHAPTER 7 THE DYNAMIC RESPONSE OF A FREEZE-LINING TO CHANGES IN SLAG BATH COMPOSITION .....</b>	 <b>176</b>
<b>7.1 EXPERIMENTAL SETUP .....</b>	<b>176</b>
<b>7.2 EXPERIMENTS.....</b>	<b>178</b>
<b>7.3 EXPERIMENTAL RESULTS.....</b>	<b>179</b>
7.3.1 Experiment 7.1 .....	181
7.3.2 Experiment 7.2 .....	182
7.3.3 Experiment 7.3 .....	183
7.3.4 Experiment 7.4 .....	184
7.3.5 Experiment 7.5 .....	185
7.3.6 Experiment 7.6 .....	186
7.3.7 Experiment 7.7 .....	187
7.3.8 Experiment 7.8 .....	188
7.3.9 Experiment 7.9 .....	189
7.3.10 Experiment 7.10 .....	190
7.3.11 Experiment 7.11 .....	191
7.3.12 Experiment 7.12 .....	192
7.3.13 Experiment 7.13 .....	193
7.3.14 Experiment 7.14 .....	194
7.3.15 Experiment 7.15 .....	195
7.3.16 Experiment 7.16 .....	196
7.3.17 Experiment 7.17 .....	197
7.3.18 Experiment 7.18 .....	198
7.3.19 Experiment 7.19 .....	199
7.3.20 Experiment 7.20 .....	200
7.3.21 Experiment 7.21 .....	201
7.3.22 Experiment 7.22 .....	202
7.3.23 Experiment 7.23 .....	203
7.3.24 Experiment 7.24 .....	204
7.3.25 Experiment 7.25 .....	205
7.3.26 Experiment 7.26 .....	206
7.3.27 Experiment 7.27 .....	207
7.3.28 Experiment 7.28 .....	208
7.3.29 Experiment 7.29 .....	209
7.3.30 Experiment 7.30 .....	210
<b>7.4 DISCUSSION .....</b>	<b>211</b>

7.4.1 Freeze Lining Thickness .....	211
7.4.2 Thermal Response of Freeze Lining and Furnace Wall .....	212
7.4.3 Slag Bath Composition .....	212
7.4.4 Slag Bath Temperature .....	213
7.4.5 Freeze Lining Composition.....	213
<b>CHAPTER 8 THE DYNAMIC PROCESS RESPONSE TO STEP CHANGES IN FURNACE OPERATING PARAMETERS.....</b>	<b>214</b>
<b>8.1 EXPERIMENTAL SETUP .....</b>	<b>214</b>
<b>8.2 EXPERIMENTS.....</b>	<b>215</b>
<b>8.3 EXPERIMENTAL RESULTS .....</b>	<b>216</b>
8.3.1 Experiment 8.1 .....	219
8.3.2 Experiment 8.2 .....	221
8.3.3 Experiment 8.3 .....	223
8.3.4 Experiment 8.4 .....	225
8.3.5 Experiment 8.5 .....	227
8.3.6 Experiment 8.6 .....	229
8.3.7 Experiment 8.7 .....	231
8.3.8 Experiment 8.8 .....	233
8.3.9 Experiment 8.9 .....	235
8.3.10 Experiment 8.10 .....	237
8.3.11 Experiment 8.11 .....	239
8.3.12 Experiment 8.12 .....	241
8.3.13 Experiment 8.13 .....	243
8.3.14 Experiment 8.14 .....	245
8.3.15 Experiment 8.15 .....	247
8.3.16 Experiment 8.16 .....	249
8.3.17 Experiment 8.17 .....	251
8.3.18 Experiment 8.18 .....	253
8.3.19 Experiment 8.19 .....	255
8.3.20 Experiment 8.20 .....	257
<b>8.4 DISCUSSION .....</b>	<b>259</b>
<b>8.5 THE IMPACT OF SEVERE OPERATIONAL ERRORS .....</b>	<b>259</b>
8.5.1 Freeze Lining Thickness.....	259
8.5.2 Freeze Lining Composition.....	260
8.5.3 Thermal Response of Freeze Lining and Furnace Wall .....	260
8.5.4 Slag Bath Temperature .....	260
8.5.5 Slag Bath Composition .....	261
8.5.6 Metal Bath Composition .....	262
8.5.7 Off-gas Composition .....	262
8.5.8 Reactor Power .....	262
8.5.9 Heat Losses .....	262
<b>8.6 INDEPENDENT ADJUSTMENT OF REDUCTANT AND ENERGY INPUTS .....</b>	<b>263</b>
8.6.1 Freeze Lining Thickness.....	263
8.6.2 Freeze Lining Composition.....	263
8.6.3 Thermal Response of Freeze Lining and Furnace Wall .....	264
8.6.4 Crust Thickness.....	264
8.6.5 Crust Composition .....	264
8.6.6 Slag Bath Temperature .....	264
8.6.7 Slag Bath Composition .....	265
8.6.8 Metal Bath Composition .....	265
8.6.9 Off-gas Composition .....	266

8.6.10 Reactor Power .....	267
8.6.11 Heat Losses .....	268
<b>8.7 APPROPRIATELY COMBINED ADJUSTMENT OF REDUCTANT AND ENERGY INPUTS .....</b>	<b>268</b>
8.7.1 Freeze Lining Thickness .....	268
8.7.2 Freeze Lining Composition.....	269
8.7.3 Thermal Response of Freeze Lining and Furnace Wall .....	269
8.7.4 Slag Bath Temperature .....	269
8.7.5 Slag Bath Composition .....	270
8.7.6 Metal Bath Composition .....	270
8.7.7 Off-Gas Composition.....	271
8.7.8 Reactor Power .....	271
8.7.9 Heat Losses.....	272
<b>CHAPTER 9 THE DYNAMIC PROCESS RESPONSE TO SOLIDIFICATION AND MELTING OF THE FREEZE LINING AND CRUST .....</b>	<b>273</b>
<b>9.1 EXPERIMENTAL SETUP .....</b>	<b>273</b>
<b>9.2 EXPERIMENTS.....</b>	<b>273</b>
<b>9.3 EXPERIMENTAL RESULTS.....</b>	<b>274</b>
9.3.1 Experiment 9.1 .....	275
9.3.2 Experiment 9.2 .....	277
9.3.3 Experiment 9.3 .....	279
9.3.4 Experiment 9.4 .....	281
<b>9.4 DISCUSSION .....</b>	<b>283</b>
9.4.1 Freeze Lining Thickness .....	283
9.4.2 Freeze Lining Composition.....	283
9.4.3 Thermal Response of Freeze Lining and Furnace Wall .....	283
9.4.4 Crust Thickness.....	284
9.4.5 Crust Composition .....	284
9.4.6 Slag Bath Temperature .....	285
9.4.7 Slag Bath Composition .....	285
<b>CHAPTER 10 COMPOSITIONAL INVARIANCE OF HIGH-TITANIA SLAG.....</b>	<b>286</b>
<b>10.1 THE RELATIONSHIP BETWEEN FeO AND Ti<sub>2</sub>O<sub>3</sub>.....</b>	<b>286</b>
<b>10.2 REACTION EQUILIBRIUM AS A POSSIBLE MECHANISM.....</b>	<b>288</b>
10.2.1 Arguments For.....	288
10.2.2 Arguments Against .....	288
<b>10.3 KINETIC EFFECTS AS A POSSIBLE MECHANISM.....</b>	<b>288</b>
10.3.1 Arguments For.....	288
10.3.2 Arguments Against .....	289
<b>10.4 EUTECTIC GROOVE PHASE EQUILIBRIUM AS A POSSIBLE MECHANISM.....</b>	<b>289</b>
10.4.1 Arguments For.....	289
10.4.2 Arguments Against .....	289
<b>10.5 A NEW MECHANISM PROPOSED.....</b>	<b>290</b>
10.5.1 Requirements .....	290
10.5.2 Background Information .....	290
10.5.3 A Step-by-Step Batch Experiment .....	293

10.5.4 Description.....	294
<b>10.6 A REFLECTION ON REDUCTION MECHANISMS .....</b>	<b>297</b>
10.6.1 Reactions in the Bulk Slag and on the Slag Bath Surface .....	297
10.6.2 Reactions at the Interface between the Slag and Metal Baths .....	297
10.6.3 Reactions in the Turbulent Zone underneath the Electrode .....	297
<b>CHAPTER 11 CONCLUSION .....</b>	<b>299</b>
<b>11.1 OBJECTIVES AND APPROACH .....</b>	<b>299</b>
<b>11.2 CONTRIBUTION OF THIS WORK.....</b>	<b>299</b>
11.2.1 Process Models .....	299
11.2.2 Interactions between Freeze Lining and Slag Bath.....	300
11.2.3 Process Mechanisms .....	300
11.2.4 The Nature of Thermocouple Signals.....	301
<b>11.3 OPPORTUNITIES FOR FUTURE WORK .....</b>	<b>301</b>
11.3.1 Model Improvements .....	301
11.3.2 Model Applications .....	302
<b>BIBLIOGRAPHY.....</b>	<b>304</b>
<b>APPENDIX A – MATERIAL PROPERTIES .....</b>	<b>307</b>
<b>APPENDIX B – MODEL ELEMENT DESCRIPTIONS.....</b>	<b>308</b>

Number	Page
Figure 1 – Process routes in the Ti/TiO <sub>2</sub> industry. (Kahn, 1984; Stanaway 1994)	1
Figure 2 – Main process steps in a mineral sands operation. (Kahn, 1984)	3
Figure 3 – Main process steps in ilmenite smelting operations.	4
Figure 4 – The Kerr–McGee synthetic rutile process (Kahn, 1984).	6
Figure 5 – The Becher synthetic rutile process (Kahn, 1984).	7
Figure 6 – Main steps in the chloride process for pigment production (Kahn, 1984).	8
Figure 7 – Simplified process flow of closed-loop titanium sponge production (Kahn, 1984).	9
Figure 8 – Schematic representation of an ilmenite–smelting furnace (Pistorius, 1999).	13
Figure 9 – Constant–FeO binary sections through the TiO <sub>2</sub> –FeO–Ti <sub>2</sub> O <sub>3</sub> ternary phase diagram.	21
Figure 10 – Liquidus diagram for the TiO <sub>2</sub> –FeTiO <sub>3</sub> –Ti <sub>2</sub> O <sub>3</sub> system including Magnéli phases.	23
Figure 11 – Liquidus diagram for the TiO <sub>2</sub> –FeTiO <sub>3</sub> –Ti <sub>2</sub> O <sub>3</sub> system excluding Magnéli phases	23
Figure 12 – Solidus diagram for the TiO <sub>2</sub> –FeTiO <sub>3</sub> –Ti <sub>2</sub> O <sub>3</sub> system including Magnéli phases.	24
Figure 13 – Solidus diagram for the TiO <sub>2</sub> –FeTiO <sub>3</sub> –Ti <sub>2</sub> O <sub>3</sub> system excluding Magnéli phases	24
Figure 14 – Liquid slag composition trajectories during solidification.	25
Figure 15 – Temperature vs. enthalpy curves for three different slag compositions.	26
Figure 16 – Schematic representation of the freeze lining and wall region of the furnace.	28
Figure 17 – One-dimensional representation of the region being modelled.	42
Figure 18 – Flow sheet of a simple process model incorporating the FLC model.	49
Figure 19 – Schematic representation of steps in the FLC model solution procedure.	52
Figure 20 – Analytically calculated steady state freeze lining thickness vs. heat flow rate.	53
Figure 21 – Analytically calculated steady state temperature profiles.	53
Figure 22 – Validation experiment 3.1 results for a heat flow rate of 300 kW (the 300kW Base Condition).	56
Figure 23 – Validation experiment 3.1 results for a heat flow rate of 250 kW.	56
Figure 24 – Validation experiment 3.1 results for a heat flow rate of 350 kW.	56
Figure 25 – Validation experiment 3.2 results for a heat flow rate of 300 kW (the 300kW Base Condition).	57
Figure 26 – Validation experiment 3.2 results for a heat flow rate of 250 kW.	57
Figure 27 – Validation experiment 3.2 results for a heat flow rate of 350 kW.	57
Figure 28 – Validation experiment 3.3 results for a heat flow rate of 300 kW (the 300kW Base Condition).	58
Figure 29 – Validation experiment 3.3 results for a heat flow rate of 250 kW.	58
Figure 30 – Validation experiment 3.3 results for a heat flow rate of 350 kW.	58
Figure 31 – Validation experiment 3.4 results for a heat flow rate of 300 kW (the 300kW Base Condition).	59
Figure 32 – Validation experiment 3.4 results for a heat flow rate of 250 kW.	59
Figure 33 – Validation experiment 3.4 results for a heat flow rate of 350 kW.	59
Figure 34 – Validation experiment 3.5 results for a heat flow rate of 300 kW.	60
Figure 35 – Validation experiment 3.6 results for a heat flow rate of 300 kW (the 300kW Base Condition).	61
Figure 36 – Validation experiment 3.6 results for a heat flow rate of 250 kW.	61
Figure 37 – Validation experiment 3.6 results for a heat flow rate of 350 kW.	61
Figure 38 – Schematic representation of the slag bath and crust region of the furnace.	64
Figure 39 – Representation of the finite-difference model used to describe the crust.	72
Figure 40 – Flow sheet of a simple process model incorporating the SBCC model.	76
Figure 41 – Schematic representation of steps in the SBCC model solution procedure.	79
Figure 42 – Analytically calculated steady state crust thickness vs. heat loss rate from slag surface.	80
Figure 43 – Analytically calculated steady state temperature profiles in the crust layer.	81
Figure 44 – Validation experiment 4.1 results for a heat input of 1000 kW.	84
Figure 45 – Validation experiment 4.1 results for a heat input of 2000 kW.	84
Figure 46 – Validation experiment 4.2 results for a heat input of 1000 kW.	85
Figure 47 – Validation experiment 4.2 results for a heat input of 2000 kW.	85
Figure 48 – Validation experiment 4.3 results for a heat input of 500 kW.	86
Figure 49 – Validation experiment 4.3 results for a heat input of 1000 kW.	86
Figure 50 – Validation experiment 4.4 results for a heat input of 500 kW.	87
Figure 51 – Validation experiment 4.4 results for a heat input of 1000 kW.	87
Figure 52 – Schematic of the furnace and process as described by the ISFP model.	90
Figure 53 – Dimensions in meters of the furnace configuration used in CHAPTER 5.	91
Figure 54 – Heat transfer phenomena in an ilmenite–smelting furnace.	91
Figure 55 – Bulk mass flow phenomena in an ilmenite–smelting furnace.	95
Figure 56 – Solubility limits of carbon in liquid iron as functions of temperature. (FactSage 5.2)	98

---

Figure 57 – Flow patterns in a 30 kA, 270 V arc. (Stenkvist and Bowman, 1987)	103
Figure 58 – Flow sheet of ISFP model.	116
Figure 59 – Compositional invariance of ilmenite smelter slags close to $M_3O_5$ composition.	126
Figure 60 – Experiment 6.1 results.	144
Figure 61 – Experiment 6.2 results.	145
Figure 62 – Experiment 6.3 results.	146
Figure 63 – Experiment 6.4 results.	147
Figure 64 – Experiment 6.5 results.	148
Figure 65 – Experiment 6.6 results.	149
Figure 66 – Experiment 6.7 results.	150
Figure 67 – Experiment 6.8 results.	151
Figure 68 – Experiment 6.9 results.	152
Figure 69 – Experiment 6.10 results.	153
Figure 70 – Experiment 6.11 results.	154
Figure 71 – Experiment 6.12 results.	155
Figure 72 – Experiment 6.13 results.	156
Figure 73 – Experiment 6.14 results.	157
Figure 74 – Experiment 6.15 results.	158
Figure 75 – Experiment 6.16 results.	159
Figure 76 – Experiment 6.17 results.	160
Figure 77 – Experiment 6.18 results.	161
Figure 78 – Experiment 6.19 results.	162
Figure 79 – Experiment 6.20 results.	163
Figure 80 – Experiment 6.21 results.	164
Figure 81 – Experiment 6.22 results.	165
Figure 82 – Experiment 6.23 results.	166
Figure 83 – Experiment 6.24 results.	167
Figure 84 – Experiment 6.25 results.	168
Figure 85 – Experiment 6.26 results.	169
Figure 86 – Change in freeze lining thickness as a function of net input heat flow rate.	170
Figure 87 – Influence of net input heat flow rate on time lag in thermal response inside the brick wall.	171
Figure 88 – Temperature profile in the freeze lining after 1 hour.	172
Figure 89 – Flow sheet of the model used for CHAPTER 7 experiments.	176
Figure 90 – New slag compositions used in CHAPTER 7 experiments.	179
Figure 91 – Experiment 7.1 results.	181
Figure 92 – Experiment 7.2 results.	182
Figure 93 – Experiment 7.3 results.	183
Figure 94 – Experiment 7.4 results.	184
Figure 95 – Experiment 7.5 results.	185
Figure 96 – Experiment 7.6 results.	186
Figure 97 – Experiment 7.7 results.	187
Figure 98 – Experiment 7.8 results.	188
Figure 99 – Experiment 7.9 results.	189
Figure 100 – Experiment 7.10 results.	190
Figure 101 – Experiment 7.11 results.	191
Figure 102 – Experiment 7.12 results.	192
Figure 103 – Experiment 7.13 results.	193
Figure 104 – Experiment 7.14 results.	194
Figure 105 – Experiment 7.15 results.	195
Figure 106 – Experiment 7.16 results.	196
Figure 107 – Experiment 7.17 results.	197
Figure 108 – Experiment 7.18 results.	198
Figure 109 – Experiment 7.19 results.	199
Figure 110 – Experiment 7.20 results.	200
Figure 111 – Experiment 7.21 results.	201
Figure 112 – Experiment 7.22 results.	202
Figure 113 – Experiment 7.23 results.	203
Figure 114 – Experiment 7.24 results.	204
Figure 115 – Experiment 7.25 results.	205

---



---

Figure 116 – Experiment 7.26 results.	206
Figure 117 – Experiment 7.27 results.	207
Figure 118 – Experiment 7.28 results.	208
Figure 119 – Experiment 7.29 results.	209
Figure 120 – Experiment 7.30 results.	210
Figure 121 – Experiment 8.1 results.	220
Figure 122 – Experiment 8.2 results.	222
Figure 123 – Experiment 8.3 results.	224
Figure 124 – Experiment 8.4 results.	226
Figure 125 – Experiment 8.5 results.	228
Figure 126 – Experiment 8.6 results.	230
Figure 127 – Experiment 8.7 results.	232
Figure 128 – Experiment 8.8 results.	234
Figure 129 – Experiment 8.9 results.	236
Figure 130 – Experiment 8.10 results.	238
Figure 131 – Experiment 8.11 results.	240
Figure 132 – Experiment 8.12 results.	242
Figure 133 – Experiment 8.13 results.	244
Figure 134 – Experiment 8.14 results.	246
Figure 135 – Experiment 8.15 results.	248
Figure 136 – Experiment 8.16 results.	250
Figure 137 – Experiment 8.17 results.	252
Figure 138 – Experiment 8.18 results.	254
Figure 139 – Experiment 8.19 results.	256
Figure 140 – Experiment 8.20 results.	258
Figure 141 – Graph (h) of experiments 8.1 (a) and 8.2 (b) superimposed on the liquidus diagram.	261
Figure 142 – Chapter 8 subset 2 change in freeze lining thickness.	263
Figure 143 – Slag bath composition change relative to initial composition.	265
Figure 144 – Metal bath composition change relative to initial composition.	266
Figure 145 – Changes in reactor power values relative to initial steady state.	267
Figure 146 – Chapter 8 subsets 3 and 4 change in freeze lining thickness.	269
Figure 147 – Chapter 8 subsets 3 and 4 change in slag bath temperature relative to initial steady state.	269
Figure 148 – Chapter 8 subsets 3 and 4 change in slag bath composition relative to initial steady state.	270
Figure 149 – Chapter 8 subset 3 and 4 change in metal bath composition relative to initial steady state.	271
Figure 150 – Chapter 8 subsets 3 and 4 changes in reactor power values relative to initial steady state.	272
Figure 151 – Experiment 9.1 results.	276
Figure 152 – Experiment 9.2 results.	278
Figure 153 – Experiment 9.3 results.	280
Figure 154 – Experiment 9.4 results.	282
Figure 155 – Influence of downtime duration and electrical power on freeze lining thickness.	283
Figure 156 – Chapter 9 summary of crust thickness variation.	284
Figure 157 – Chapter 9 summary of variation in slag bath temperature.	285
Figure 158 – Compositional relationships in industrial high-titania slags.	286
Figure 159 – The relationship between FeO and Ti <sub>2</sub> O <sub>3</sub> in industrial high-titania slags.	287
Figure 160 – Slag composition according to reduction reactions at equilibrium.	291
Figure 161 – The influence of solidification on slag composition.	291
Figure 162 – Ternary view on compositions of industrial slags.	293
Figure 163 – Composition points resulting from the hypothetical step-by-step batch experiment.	293
Figure 164 – Illustration of mechanism proposed to cause the observed compositional invariance.	295

---

## LIST OF TABLES

Number	Page
Table 1 – TiO <sub>2</sub> feedstock composition. (Stanaway, 1994)	1
Table 2 – Summary of key phenomena for the FLC model.	34
Table 3 – List of symbols used in CHAPTER 3 heat transfer formulation.	45
Table 4 – Summary of key phenomena for the SBCC model.	69
Table 5 – List of symbols used in CHAPTER 4 heat transfer formulation.	74
Table 6 – Summary of key phenomena for the ISFP model.	110
Table 7 – Description of energy modules used in the ISFP model.	116
Table 8 – Description of energy flow streams used in the ISFP model.	117
Table 9 – Description of material modules used in the ISFP model.	118
Table 10 – Description of material flow streams used in the ISFP model.	119
Table 11 – Variables and parameters of the HeatLoss1Rate sub-model of the ISFP model.	122
Table 12 – Variables and parameters of the HeatLoss2Rate sub-model of the ISFP model.	123
Table 13 – Variables and parameters of the SlagTapFlow sub-model of the ISFP model.	124
Table 14 – Variables and parameters of the MetalTapFlow sub-model of the ISFP model.	125
Table 15 – Variables and parameters of the Reactor2Flow sub-model of the ISFP model.	128
Table 16 – Variables and parameters of the Reactor3Flow sub-model of the ISFP model.	130
Table 17 – Variables and parameters of the Reactor4Flow sub-model of the ISFP model.	131
Table 18 – Variables and parameters of the FreezeLiningFlow sub-model of the ISFP model.	132
Table 19 – Variables and parameters of the CrustFlow sub-model of the ISFP model.	133
Table 20 – Values of parameters of sub-models of the ISFP model.	136
Table 21 – List of experiments conducted for CHAPTER 6.	139
Table 22 – List of experiments conducted for CHAPTER 7.	178
Table 23 – List of experiments conducted for CHAPTER 8.	215
Table 24 – List of experiments conducted for CHAPTER 9.	273
Table 25 – Physical properties of molten iron and molten high-titania slag.	296

## ACKNOWLEDGMENTS

Many people influenced me before the inception of this project and while I was working on it. Several of them are certain to continue enriching my life beyond the completion of this work. However, reaching this milestone provides a valuable and fitting opportunity to reflect on what is past, and recognise the people who contributed to my thoughts, words and acts through that of their own. At the end of this journey it is with great fondness and gratitude that I remember them, and the parts they played.

My parents were there from the beginning. I will not try to capture in words the sacrifices and investments that parents make for their children. I thank you for your prayers, support, encouragement and interest. Mother, I thank you for your willingness to listen, your eagerness to offer your time when Marinda and I did not have enough, and for your unfailing belief in me.

My 'other' parents, Ennes and Andriëtte... You were there to support Marinda and me whenever we needed you. You shared in my excitement, my frustration, my disappointments and my elation as if these were your own. You were always there with confirmation and encouragement when I needed it. I am deeply thankful for this.

Mariëtte, as usual you were able to add something different to the mix. Your often unconventional perspective, sharp sense of humour and candidness are much appreciated. I am also thankful for your empathy during those times when the load felt slightly heavier than I thought I could carry.

There were many other family members who so regularly showed interest and encouragement. Thank you for letting me know that I was in your thoughts, and that you cared.

In my final undergraduate year I became convinced that the objective of doing graduate studies that I had set for myself, was not possible. This conviction was quickly reversed through a few conversations with Professor Rian Dippenaar. Thank you, Rian, for opening doors for me when I desperately needed it.

During my time at Iscor Heavy Minerals I was privileged to have worked with two exceptional individuals: Dr. Willem van Niekerk and Matie von Wielligh. Willem, thank you for your mentorship and for the trust you put in me. Matie, thank you for your interest in the work my colleagues and I were doing, and for your support. Thank you both for the opportunities that you created for me, and for your examples of passion and excellence.

My association with ilmenite smelting resulted in a special friendship with Geoff and Sue Randall. I still remember and profit from the challenging and insightful discussions that I had with you, Geoff. Thank you for helping me to keep my feet on the ground. Thank you, Sue, for your love and encouragement.

Dr. Klaus Hack from GTT assisted me with the thermochemical data files required for this project. Thank you for your assistance, Klaus.

Quinn Reynolds assisted me with the calculation of heat transfer rates in the freeboard of the furnace. Thank you for your quick response to my questions and for your interest in the work.

My colleagues at Ex Mente had to endure the ebbs and flows of my emotions during the time of this work. Thank you for the continued interest you showed. I am also grateful to the company and my business partner Johann Kruger for the financial support.

I had interesting and insightful discussions with the personnel at Ticor South Africa. My association with that company also resulted in valuable exposure and experience. I am grateful both to the company and to the people that I worked with there.

My supervisor, Professor Chris Pistorius, journeyed with me through this project for a considerable time. I am grateful for the opportunity I had to work with you, Chris. Thank you for your guidance, support and, perhaps most of all, your patience.

My daughter Andria had to endure many a consequence of my working late nights and weekends. Thank you for this, Andria, and for always lifting my spirit with your laughter and energy.

Finally I want to thank the person who felt the impact of this work as much as I did: my dear wife Marinda. Thank you for your dedication, your never-ending love, your forbearance, and the tremendous support you gave me.

## CHAPTER 1 INTRODUCTION

The purpose of this first chapter is to introduce the reader to the work conducted during this project. It also aims to provide the reader with some perspective by describing the industry to which the current work is relevant.

### 1.1 INDUSTRY BACKGROUND

The ilmenite smelting process that is the focus of this project is a stage in the production routes of the Ti/TiO<sub>2</sub> industry focussed on the upgrading of titanium dioxide containing minerals to either titanium dioxide pigment or titanium metal. No up-to-date quantitative information (capacities, prices, growth rates, etc.) on this industry was available for inclusion in this text. For this reason the industry and the various process stages and materials are only described qualitatively here.

Figure 1 shows the position of the ilmenite smelting process on a map of process routes found in the Ti/TiO<sub>2</sub> industry (Kahn, 1984; Stanaway, 1994). The dotted lines in Figure 1 indicate routes of intermediate products that are uncertain. It is very possible that these routes may be in use, as will be explained later, but this was not verified. The ranges of TiO<sub>2</sub> content of the various minerals and intermediate products are listed in Table 1 (Stanaway, 1994).

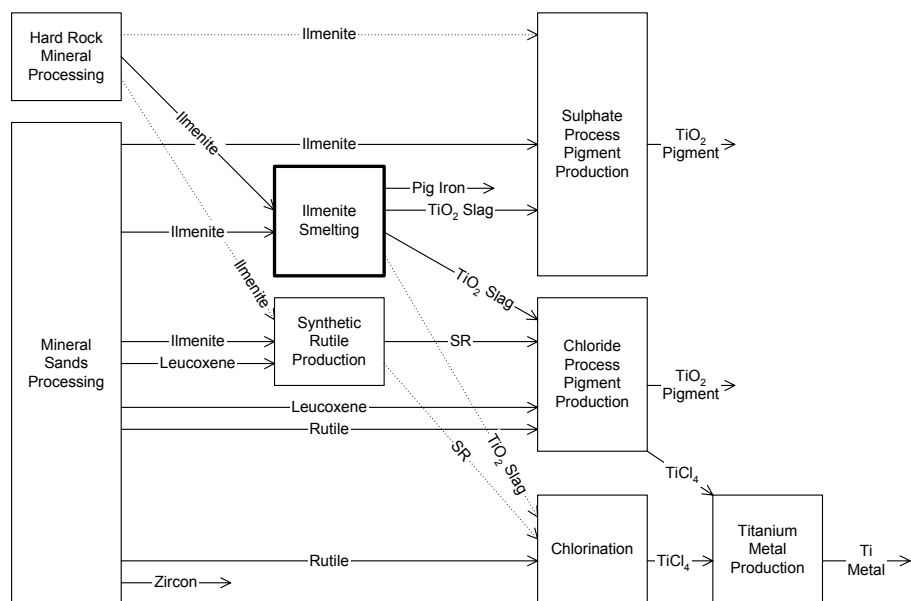


Figure 1 - Process routes in the Ti/TiO<sub>2</sub> industry. (Kahn, 1984; Stanaway 1994)

Material	TiO <sub>2</sub> Content
Ilmenite	37 - 54%
Leucoxene	55 - 65%
Rutile	95%
TiO <sub>2</sub> slag	75 - 85%
Synthetic Rutile (SR)	90 - 93%

Table 1 - TiO<sub>2</sub> feedstock composition. (Stanaway, 1994)

The minerals and process stages indicated on Figure 1 are described in more detail below. These descriptions only serve to introduce the reader to the industrial context of this project, and do not aim to provide complete details of the materials and processes.

### 1.1.1 Minerals

The minerals indicated on Figure 1 (rutile, leucoxene, ilmenite and zircon) are often found together in sand-type mineral deposits and are collectively referred to as 'heavy minerals'. Ilmenite is also found in hard rock deposits where the other heavy minerals are present to a lesser degree or not at all.

#### a. Rutile

As indicated by Table 1, rutile (nominally  $\text{TiO}_2$ ) contains the highest level of  $\text{TiO}_2$  of all the heavy minerals. It is the feedstock of choice for chloride pigment production (and most probably for titanium metal production via chlorination also) because of its bulk density, low iron content and low impurity content (Stanaway, 1994). The sulphate pigment producers do not use rutile because it is insoluble in sulphuric acid (Stanaway, 1994).

#### b. Leucoxene

Leucoxene (also referred to as leucoxenised ilmenite) is ilmenite that had been naturally upgraded to a higher  $\text{TiO}_2$  content as a result of iron that had been leached out by ground water. It is a feedstock used by the chloride pigment producers, but since there are rutile crystals in the grains, the sulphate pigment producers do not favour it. Leucoxene is also used for synthetic rutile production.

#### c. Ilmenite

The  $\text{TiO}_2$  content of ilmenite (nominally  $\text{FeTiO}_3$ ) can vary over a wide range as is indicated in Table 1. Weathering can concentrate  $\text{TiO}_2$  in ilmenite in the same way that leucoxene is formed from ilmenite. Significant levels of impurities (MgO, CaO,  $\text{SiO}_2$ , MnO, etc.) in the mineral can yield ilmenite with  $\text{TiO}_2$  content lower than the 52.6% in pure stoichiometric ilmenite.

As indicated by Figure 1, ilmenite is the most widely used natural mineral in the Ti/ $\text{TiO}_2$  industry. It can be upgraded to feedstock for pigment production by either smelting or synthetic rutile production. In addition, sulphate pigment producers are able to use ilmenite directly for pigment production. This is however not preferred because of the increased levels of waste material produced.

#### d. Zircon

Zircon (nominally  $\text{ZrSiO}_4$ ) is the only product from mineral sands processing that does not contain titanium. It is used in the ceramic tile industry for the manufacture of coatings, and in the refractory materials industry as a component in refractory bricks.

### 1.1.2 Hard Rock Mineral Processing

Hard rock mineral processing is used in cases where ilmenite occurs in hard rock deposits and not in the form of mineral sands. This type of processing is used in Canada and Norway to concentrate hard rock ilmenite. In both cases the ilmenite product is smelted to produce pig iron and high-titania slag. The

purpose of this mineral processing stage is therefore to provide an ilmenite concentrate that can be upgraded to a suitable feedstock for pigment production.

### 1.1.3 Mineral Sands Processing

The mineral sands processing stage in Figure 1 is common to most process routes leading from ore to pigment or metal. This stage yields up to four products, depending on the ore body. These products are the four minerals discussed above. The purpose of this stage (within the context of the Ti/TiO<sub>2</sub> industry) is to produce rutile concentrate for direct use in chloride pigment production, to produce leucoxene either for direct use in chloride pigment production or in synthetic rutile production, and to produce ilmenite that can be upgraded to be a suitable feedstock for pigment production (both sulphate and chloride routes).

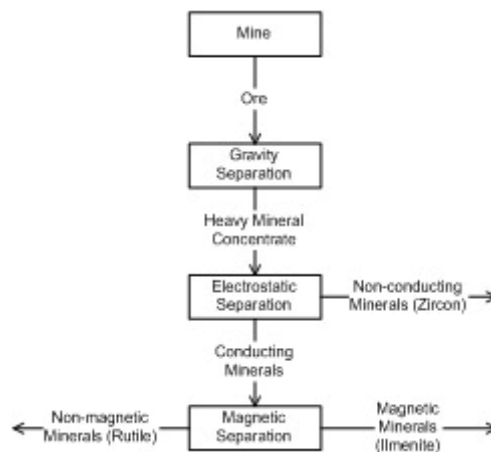


Figure 2 – Main process steps in a mineral sands operation. (Kahn, 1984)

Figure 2 shows a simplified process flow of a mineral sands processing operation. Mining can be done by dredging or hydraulic methods. The ore is then gravity separated by, for example, spirals to yield a heavy mineral concentrate that can be beneficiated further. Electrostatic and magnetic separation are used to extract the valuable minerals from the concentrate.

### 1.1.4 Ilmenite Smelting

The ilmenite smelting stage shown in Figure 1 and, more specifically, the ilmenite smelting furnace, is the focus of the current work. The stage is outlined briefly here and the ilmenite smelting furnace process is discussed in more detail in CHAPTER 2.

The purpose of this stage is to upgrade ilmenite to a suitable feedstock for sulphate and chloride pigment producers. Figure 3 shows the main steps to be found in various ilmenite smelting operations. Ilmenite can be brought into the furnace via the following three routes:

- Feed ilmenite received from the mineral processing plant directly into the furnace at ambient temperature. Most ilmenite smelters (Richards Bay Minerals, Namakwa Sands, and Ticor South Africa) utilise this route. It is not sure whether the Tinfos operation in Norway is able to feed ilmenite directly into their furnace.

- Pre-heat ilmenite before feeding it into the furnace. This is an additional route found in newer ilmenite smelters (Namakwa Sands, Tidor South Africa). The chemical energy in the off-gas from the smelting furnace is utilised to reduce the consumption of electrical energy and graphite electrodes.
- Pre-reduce ilmenite before feeding it into the furnace. This route is used by the Tinfos operation in Norway (Rosenqvist, 1992). Ilmenite is first pelletised with bentonite as binder, and then prereduced in a rotary kiln with coal at temperatures of around 1150 °C (Rosenqvist, 1992). The pre-reduction product, with a degree of metallisation (of iron) of around 70%, is then fed into the smelting furnace.

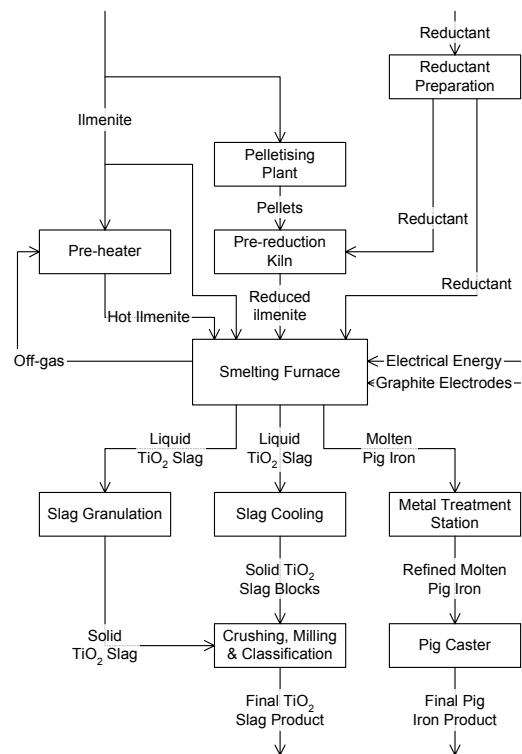


Figure 3 – Main process steps in ilmenite smelting operations.

The smelting furnace itself can be configured in the following ways:

- Rectangular six-in-line AC (alternating current) electric arc furnaces are used by Quebec Iron and Titanium Corporation (QIT) at Sorel in Canada, and by Richards Bay Minerals (RBM) at Richards Bay in South Africa.

As the name suggests, these furnaces operate with six electrodes. Pre-baked graphite electrodes are used. Ilmenite and reductant are fed into the furnace through a multitude of feed ports in the furnace roof.

- A circular AC electric arc furnace is used by Tinfos at Tyssedal in Norway.

This furnace has three self-baking Söderberg electrodes and a number of feed ports are also used to feed pre-reduced ilmenite and coal into the furnace.

- Circular DC (direct current) electric arc furnaces are used by Namakwa Sands (NS) at Vredenburg in South Africa, and by Tidor South Africa (TSA) at Empangeni in South Africa.



These furnaces operate with a single hollow pre-baked graphite electrode. Ilmenite (cold or pre-heated) and reductant are fed into the furnace via the hollow electrode.

The off-gas from the smelting furnaces is usually rich in chemical energy (being mainly CO) and can be used for various heating applications on the site. As stated earlier, the newer smelting plants tend to use this gas to pre-heat the ilmenite and save on their electricity and electrode bills.

After tapping, the metal product from the furnace (typically liquid iron with 2% carbon) is first treated to increase the carbon content and reduce the sulphur content. Some alloy additions may also be done depending on the specification of the particular client. The purified high-carbon metal is then cast into pigs and subsequently shipped.

More than one option is available to handle the slag product tapped from the furnace. The most conventional of these is pouring the slag into pots and letting it cool down in block form. These blocks are then crushed, milled and classified into the desired size fractions required by pigment producer clients. An alternative is to granulate the slag as it exits from the furnace. This option is attractive in that it saves capital cost of crushers, mills and classifiers, and it rules out the need for a block yard for cooling large slag blocks.

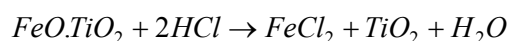
### 1.1.5 Synthetic Rutile Production

The synthetic rutile production stage indicated on Figure 1 has much the same purpose as the ilmenite smelting stage. It aims to upgrade ilmenite and leucoxene to feedstock that is suitable, specifically, for the chloride route of pigment production. The iron in the feed materials is generally not recovered and is turned to waste. This is in contrast with ilmenite smelting that extracts the iron as pig iron that is a valuable by-product for the business and places less strain on the environment.

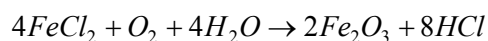
A large number of synthetic rutile production processes exist (Columbia Southern, Murso, Laporte, Benelite, Kerr-McGee, Ishihara, and Becher) (Kahn, 1984). These processes can be classified as involving either partial reduction of iron or total reduction of iron. One partial reduction and one total reduction example are discussed below.

#### a. Kerr-McGee process

The Kerr-McGee process is shown in Figure 4. It involves partial reduction of ilmenite in a rotary kiln. The kiln is operated under oxygen deficient conditions. The iron in the ilmenite is reduced to the ferrous (2+) state. The reduced ilmenite is batch leached in digesters with an 18 to 20% hydrochloric solution. During leaching the iron is dissolved as ferrous chloride ( $FeCl_2$ ) while the  $TiO_2$  remains as porous solid particles according to the following chemical reaction (Kahn, 1984):



The spent leach liquor and solid particles are separated and the liquid sent to an acid regeneration plant. The acid regeneration proceeds as follows (Kahn, 1984):



The separated solids are washed to clean it from chlorides and acid, and then calcined to produce the final synthetic rutile product. (Kahn, 1984)

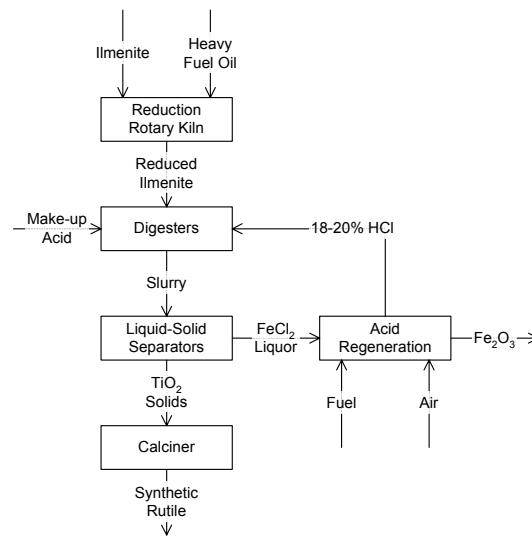
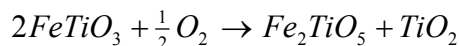


Figure 4 - The Kerr-McGee synthetic rutile process (Kahn, 1984).

#### b. Becher process

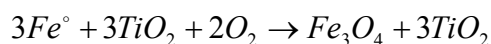
The Becher process utilises complete reduction of iron in ilmenite to produce synthetic rutile. This process is shown in Figure 5.

In the first step of the process, ilmenite is oxidised at around 1000 °C to transform the ilmenite phase to a combination of rutile and pseudobrookite as follows (Kahn, 1984):



The oxidation causes cracking and lattice expansion that are beneficial to the overall kinetics in the following reduction step. In the reduction step coal is added to the oxidised ilmenite at around 1200 °C to convert all iron to the metallic state. The excess coal char exiting from the reduction kiln is separated from the reduced ilmenite by magnetic separation after cooling.

The reduced ilmenite is fed into an aerator together with water, some ammonium chloride as catalyst, and large volumes of air. The main reaction taking place in the aerator is as follows (Kahn, 1984):



The iron oxide precipitates as a slime that is separated from the  $TiO_2$  particles by using hydro cyclones. The solids are calcined to produce the final synthetic rutile product. (Kahn, 1984)

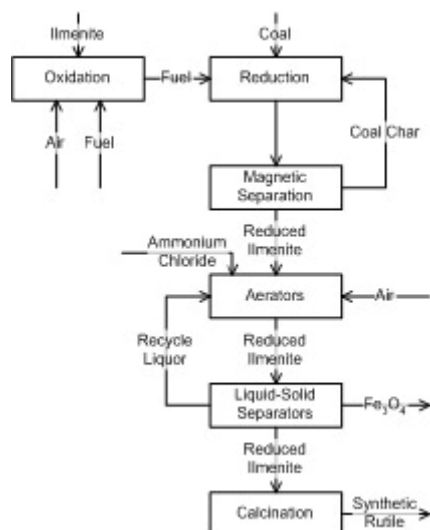


Figure 5 – The Becher synthetic rutile process (Kahn, 1984).

### 1.1.6 Sulphate Process Pigment Production

As indicated on Figure 1,  $TiO_2$  pigment and titanium metal are the final products. The sulphate process of pigment production is one process that can be used to convert  $TiO_2$  feedstock to pigment. The preferred raw materials for the sulphate process are high-titania slag and some ilmenites. Leucoxene, rutile and synthetic rutile are not used because of  $TiO_2$  being present in the form of a rutile phase that is insoluble in sulphuric acid (Stanaway, 1994). Even slags with very high  $TiO_2$  content can cause problems because the fraction of  $TiO_2$  present as rutile increases with total  $TiO_2$  content.

The slag or ilmenite is dissolved in sulphuric acid according to the following reaction (Stanaway, 1994):

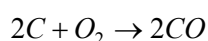


Iron sulphate is removed as solid copperas along with other undissolved solids. Following this, the titanyl sulphate is hydrolysed to hydrated  $TiO_2$  from which  $TiO_2$  is precipitated as either rutile or anatase. The final pigment product is produced after purifying, filtering, calcining and milling of the precipitate. (Stanaway, 1994)

### 1.1.7 Chloride Process Pigment Production

The chloride process for pigment production is the newer alternative to the sulphate process. A major advantage of the chloride process is the reduced amount of waste generated and therefore smaller environmental impact. The main steps of this process are shown in Figure 6.

The feed material (rutile, synthetic rutile, high-titania slag) is fed into the fluid bed chlorinator together with chlorine and petroleum coke. The following reactions take place in the chlorinator at its operating temperature of around 900 °C (Stanaway, 1994):





The product gas from the chlorinator contains excess  $\text{Cl}_2$ ,  $\text{TiCl}_4$ ,  $\text{CO}$ ,  $\text{CO}_2$  and other chlorides. The impurity chlorides ( $\text{AlCl}_3$ ,  $\text{SiCl}_4$ ,  $\text{COCl}_2$ ,  $\text{SnCl}_4$ ,  $\text{VOCl}_3$ , etc.) are removed from the  $\text{TiCl}_4$  by selective distillation (Kahn, 1984). The final purified  $\text{TiCl}_4$  is converted to  $\text{TiO}_2$  by the following reaction (Stanaway, 1994):

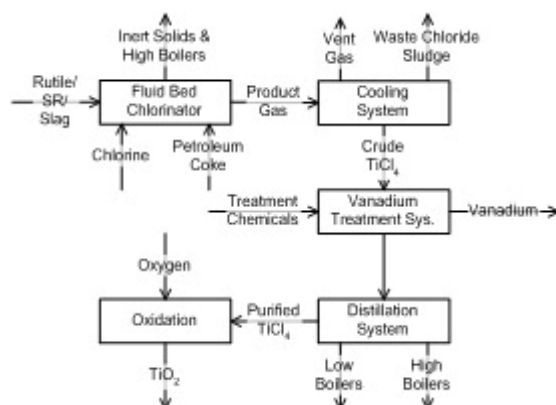
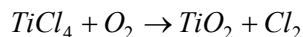


Figure 6 – Main steps in the chloride process for pigment production (Kahn, 1984).

Of specific relevance to ilmenite smelting and this project is the “Inert Solids & High Boilers” output stream from the fluid bed chlorinator indicated in Figure 6. This stream includes high-boiling-point chlorides such as  $\text{CaCl}_2$  and  $\text{MgCl}_2$  that exist as liquids at chlorinator operating conditions. These species tend to build up in the bed, making it necessary to purge it before the bed is defluidised (Kahn 1984). Such purging actions are a cost penalty to the operation both because of the waste generated and because of the production loss (Stanaway, 1994).

Poor control over freeze lining thickness in an ilmenite smelting furnace can result in refractory wear and increased levels of  $\text{MgO}$  in the slag. This directly contributes to the amount of high-boiling-point species in the chlorinator.

### 1.1.8 Titanium Metal Production

The process of titanium metal production is closely related to the chloride process of pigment production. The reason is that the final stage of titanium metal production also makes use of  $\text{TiCl}_4$  for conversion to the sponge metal product. (Kahn, 1984)

Due to this significant similarity, some titanium metal producers simply buy  $\text{TiCl}_4$  from chloride process pigment producers. This is indicated on Figure 1. If a titanium metal producer chooses not to do this, he has to use his own  $\text{TiCl}_4$  production facility that would look identical to the one shown in Figure 6. The only difference is then the conversion of  $\text{TiCl}_4$  to titanium metal rather than to  $\text{TiO}_2$ . A simplified closed-loop titanium sponge production flow sheet is shown in Figure 7. The details of  $\text{TiCl}_4$  production have been omitted here.

This seems to be a very attractive process route because chlorine and magnesium are recycled. The conversion of  $TiCl_4$  to titanium metal occurs according to the following chemical reaction (Kahn, 1984):

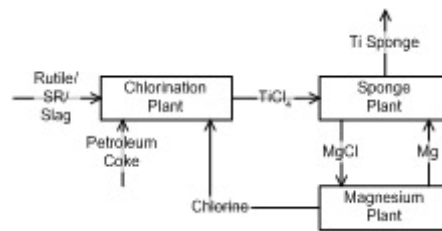
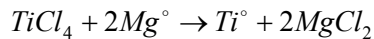
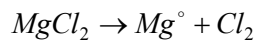


Figure 7 – Simplified process flow of closed-loop titanium sponge production (Kahn, 1984).

The magnesium plant regenerates magnesium and chlorine as follows (Kahn, 1984):



### 1.1.9 Importance of Ilmenite Smelting

To conclude this overview of the Ti/TiO<sub>2</sub> industry, the focus is drawn back to ilmenite smelting. The important role of ilmenite smelting is illustrated by the volumes of feedstock that it provides to pigment producers. In 1994, high-titania slag represented just over 50% of the mass of feedstock provided to pigment producers (Stanaway, 1994). Stanaway's text only refers to the ilmenite smelters operated by QIT, RBM and Tinfos. Today another two smelters, those of Namakwa Sands and Ticor South Africa, are in operation and another is being planned for the Southern African region. It is therefore likely that the fraction of total pigment feedstock provided by ilmenite smelters may have increased in the past nine years. This is however not confirmed.

The importance of ilmenite smelting in the Ti/TiO<sub>2</sub> industry can therefore not be ignored. It also appears likely that this route of upgrading minerals to suitable feedstock for the pigment industry will grow relative to synthetic rutile production due to the impact that waste materials from synthetic rutile processes have on the environment.

## 1.2 OVERVIEW OF CURRENT WORK

Before discussing the current work, an introduction to the ilmenite smelting furnace process is in order. Such an introduction is provided in CHAPTER 2. If the reader is unfamiliar with the process, it is suggested that this chapter is read before continuing here.

### 1.2.1 Objectives

The main objective of this project is to study the dynamic interactions between the freeze lining and slag bath of ilmenite smelting furnaces. The objectives are set out more specifically as follows:

- Study and characterise the time dependent change in
  - freeze lining thickness,

- freeze lining temperature distribution, and
  - freeze lining composition distribution
- in response to
- changes in net power input into the slag bath,
  - changes in slag bath composition, and
  - changes in operating set points such as specific energy and reductant inputs.
- Study and characterise the time dependent change in
    - slag bath temperature, and
    - slag bath composition
- in response to
- changes in net power input into the slag bath,
  - changes in freeze lining thickness, and
  - changes in operating set points such as specific energy and reductant inputs.
- Study and characterise the influence of slag solidification and melting in the furnace on the composition of liquid slag in the slag bath.

The following influences on the freeze lining are considered of secondary importance within the context of this study and are either treated in very simplified ways, or ignored completely:

- The amounts of liquid metal and liquid slag in the furnace,
- the influence of metal and slag taps, and
- the influence of furnace down-time.

### 1.2.2 Impetus for Study

A number of factors make the freeze lining in an ilmenite smelting furnace particularly important. Firstly, no known refractory material can withstand the chemical attack of highly corrosive liquid titania slag. Secondly, the cost involved in replacing a furnace lining (including cost of the refractory material, labour associated with installation, and lost production time) is expensive (Elstad et. al., 2003) and ilmenite smelting businesses are reliant on furnace linings lasting for up to 10 years.

Poor control of the furnace freeze lining can result in rapid deterioration of the furnace refractory lining. This could ultimately lead to the furnace burning through, and more certainly to early replacement of the refractory lining.

The state of the freeze lining cannot be determined by any direct means, except when the furnace had been switched off and emptied. Even in these circumstances much of the freeze lining would have decrepitated and fallen off the wall by the time the furnace is cold enough to examine. The freeze lining state parameter of primary importance to furnace operation and control is thickness. Also of interest are the distribution of chemical and phase composition, and the distribution of temperature through the lining.

Because no direct measures are available, indirect means are used to infer the state of the freeze lining. Thermocouples installed in the furnace refractory lining on the level of the freeze lining are used to infer thickness. These thermocouples are usually installed a significant distance away from the refractory lining

hot face due to the apparent risks of installing thermocouples deep into the lining. The distance of the thermocouple away from the refractory lining hot face and the thickness of the freeze lining add to the total distance between the thermocouple and the point of interest, the interface between the freeze lining and the liquid slag bath.

This distance together with the thermal conductivity and heat capacity of the freeze lining and refractory lining materials has an important influence on the thermocouple signal. It determines the lag between the time when a change in conditions at the freeze lining hot face takes place, and the time when the influence of the changed conditions is detected in the thermocouple signal. This lag is typically in the order of hours. Because the thermocouple signal is used to control the freeze lining thickness, this lag results in dead time in the control problem, making it a much more difficult problem to solve. These signals are also used for monitoring the state of the refractory lining over periods of months and years. Having reliable and interpretable signals for this purpose is another important issue to consider when deciding on the positions at which the thermocouples are installed.

A better understanding of the dynamic response of the freeze lining to changing conditions in the slag bath can contribute in a number of ways to the improved operation and control of an ilmenite smelting furnace:

1. The influence of thermocouple position relative to the refractory lining hot face on the controllability of freeze lining thickness can be quantified. In this way modification of existing thermocouple installations or new installations can be justified responsibly. Modified and new installations can contribute directly to improved freeze lining control and refractory lining monitoring.
2. Knowledge of the dynamic behaviour of the freeze lining can be used directly in the design and development of controllers that can possibly be used for closed-loop control of freeze lining thickness. Implementation of such a controller can result in higher furnace throughput and extended life of the refractory lining. Throughput can be increased by running safely with a thinner freeze lining and by controlling the furnace energy balance in such a way that slag foaming is avoided.
3. Knowledge of the influence of solidification and melting at the freeze lining hot face on the slag bath can be used in the design and development of a more complete slag chemistry control strategy that takes this influence into account. Implementation of such a strategy can result in tighter control over slag chemistry and improved overall process efficiency. Efficiency will improve when slag chemistry is tightly controlled around the set point because excessively high  $\text{TiO}_2$  content in the slag and associated high temperature conditions, resulting in increased heat losses and increased probability of slag foaming, will be avoided.

In addition to the direct contributions to furnace operation and control, the results of this study will contribute to the already existing and growing body of knowledge about ilmenite smelting. It will perhaps contribute a small piece to the puzzle regarding the compositional invariance of ilmenite smelting slag close to the  $\text{M}_3\text{O}_5$  composition. It will also add to the current understanding of freeze lining behaviour, and possibly provide new options for improving furnace control and operation. The added knowledge can be used in future work to improve the process and, perhaps to a lesser degree, to better understand and improve other similar processes.

### 1.2.3 Approach

The approach of this project is purely one of mathematical modelling. The regions of interest in the ilmenite smelting furnace are modelled to such a degree of detail as is required to achieve the objectives of the study. Because of this, numerous assumptions and simplifications are made to arrive at manageable modelling problems that can serve a purpose in the current work.

As a combination of heat transfer and chemical reactions determine the behaviour of the freeze lining and of the furnace as a whole, the modelling technique applied focuses on these aspects. Because it is believed that a detailed description of momentum transfer and therefore fluid flow in the furnace will not add significantly to the value of the models at this stage, momentum transfer is not incorporated into the models except for some simplifications and assumptions in this regard.

## 1.3 ORGANISATION OF CURRENT TEXT

The remainder of the current text is organised as follows:

- CHAPTER 2 is dedicated to describing the ilmenite smelting process and relevant prior work done on the process.
- CHAPTER 3 describes the details of a one-dimensional heat transfer and chemical reaction model of the freeze lining and furnace wall that is used for modelling the dynamic behaviour of the freeze lining.
- CHAPTER 4 describes the details of a mathematical model similar to the one in CHAPTER 3 that is used for modelling formation and melting of the crust on top of the slag bath.
- CHAPTER 5 describes the details of a mathematical model of the entire ilmenite smelting furnace process. This model incorporates the models described in CHAPTER 3 and CHAPTER 4 into a formulation describing the slag bath, metal bath, furnace atmosphere and all relevant chemical reactions.
- CHAPTER 6, CHAPTER 7, CHAPTER 8 and CHAPTER 9 provide details and results of experiments focussed on studying the dynamic behaviour of the freeze lining and slag bath in response to various influences. The work described in these chapters is the main focus of this project.
- CHAPTER 10 provides a focussed discussion of the observed compositional invariance of high-titania slags close to the stoichiometric  $M_3O_5$  composition. A mechanism by which this invariance can be explained is presented here.
- CHAPTER 11 is the concluding chapter that contains summarising statements about the work and results obtained.



## CHAPTER 2 ILMENITE SMELTING PROCESS OVERVIEW

The purpose of this chapter is to introduce the reader to various aspects regarding the ilmenite smelting process. It also combines information from a number of literature resources to provide a consolidated body of data and information on which the work of this study is based.

Although more than one type of furnace design is in industrial use for ilmenite smelting, the current work focuses on a DC furnace like those operated by Namakwa Sands and Ticor South Africa. A schematic of such a furnace is shown in Figure 8.

Because of the secrecy surrounding ilmenite smelting technology (Rosenqvist, 1992) and the resulting lack of published information, the descriptions provided here are for the most part qualitative. Even though this is the case, these descriptions should serve well to introduce a reader that is unfamiliar with the process.

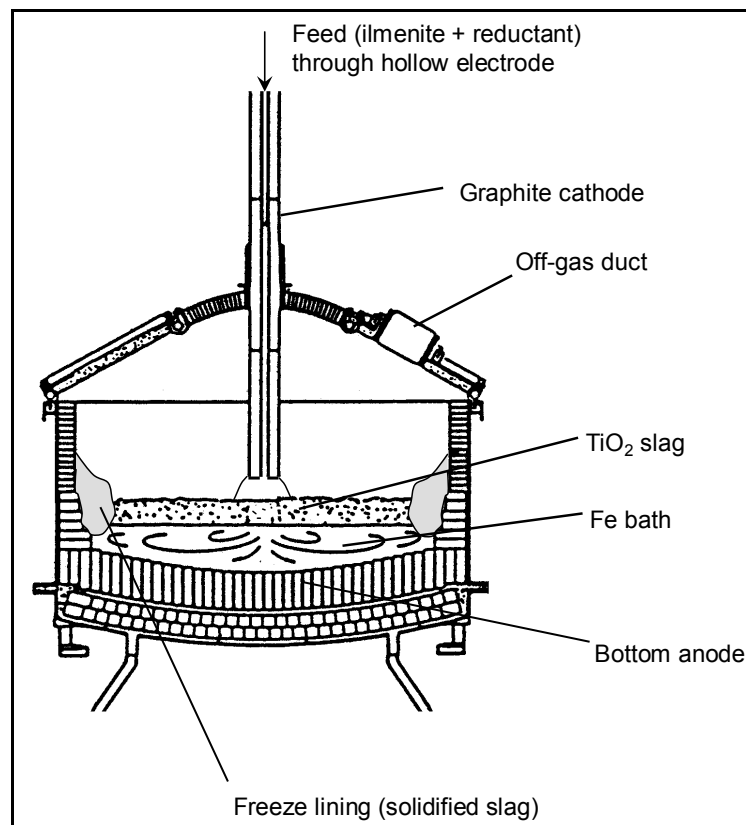


Figure 8 – Schematic representation of an ilmenite-smelting furnace (Pistorius, 1999).

### 2.1 OPERATIONAL OVERVIEW

The process is operated semi-continuously. Ilmenite, reductant and electrical energy are discharged into the furnace as continuously as possible. The operation is only stopped for adding electrodes, planned and unplanned maintenance, and for process-related incidents like severe slag foaming. Off-gas is extracted from the furnace continuously, while slag and metal are tapped separately in batches.

Ilmenite and reductant enter the furnace through a single hollow graphite electrode that extends down into the furnace through the centre of the furnace roof. Since the electrode is consumed as it delivers energy, it

acts as an additional carbon source. Energy is discharged into the furnace via an open arc between the tip of the electrode and the bath. The only other inputs into the process include air drawn in during periods of negative furnace pressure, and water when leaks are present in the furnace roof, off-gas duct or other water-cooled elements.

Ilmenite is expected to melt quickly as it travels through the arc and into the slag bath. This is due to its relatively low melting point of 1397 °C (FactSage 5.2) and its small particle size of between 100 and 1000 µm. As reductant particles are heated up in the arc and slag bath, these particles devolatilise and possibly break up due to thermal shock. Reduction reactions are expected to take place at the interface between liquid slag and reductant particles. The products of these reactions include gas (primarily CO), slag (enriched in TiO<sub>2</sub> and Ti<sub>2</sub>O<sub>3</sub>) and iron metal. Some reduction reactions also occur at the interface between the slag and metal bath because of the high carbon content (around 2%) of the metal bath. The products of these reactions are the same as for reduction with reductant particles.

Because of the density difference between metal and slag (metal being denser than slag), metal collects at the bottom of the furnace as a metal bath and slag on top of it as a slag bath. Small metal droplets are present in the slag bath due to the reduction reactions taking place there, but these droplets continuously find their way down to the metal bath or are reabsorbed into the slag. Gas bubbles forming in the slag bath due to reduction reactions rise up through the slag bath and escape into the furnace freeboard.

Metal is extracted from the furnace through a metal tap hole and slag through a slag tap hole. The slag tap hole is situated at a different angular position than the metal tap hole, and higher in the furnace wall than the metal tap hole. This is because the slag bath is floating on top of the metal bath. Off-gas, fumes and dust that continuously rise up into the furnace freeboard are extracted by the off-gas system through a duct installed in the furnace roof.

The off-gas system is operated in such a way that a slight positive pressure is maintained in the furnace freeboard. This is done to prevent air from being drawn into the furnace. Air consumes carbon and oxidises slag, resulting in reduced reductant efficiencies and electrode wear.

## 2.2 FURNACE CONTROL

The operational personnel and control systems of an ilmenite smelting furnace have the following two primary control objectives:

- Maintain a safe freeze lining thickness to ensure protection of the furnace refractory lining against chemical attack by liquid slag.
- Produce slag with a titanium dioxide content that is within the provided chemical composition specification.

The controlled variables from these objectives are:

- Furnace sidewall temperature  
Sidewall temperature is used as an indirect indication of freeze lining thickness because the state of the freeze lining cannot be measured directly.

- Slag  $\text{TiO}_2$  content

Chemical analyses of tapped slag are used as a measure of this controlled variable.

The manipulated variables used to effect control of the controlled variables are:

- Specific energy input (kWh/ton ilmenite)
- Specific reductant input (ton reductant/ton ilmenite)

Since both manipulated variables have an influence on both controlled variables, the control problem is of the multiple-input-multiple-output (MIMO) type. This together with the dead time associated with measurement of both controlled variables, makes this an interesting control problem that is difficult to solve. It has been reported that the two manipulated variables cannot be changed independently (Pistorius, 1999). This is due to a balance between the enthalpy of the reduction reaction and the enthalpy required to keep the slag at or just above its liquidus temperature. This relationship between the two manipulated variables can be used to simplify the control problem to some degree.

## 2.3 FURNACE VESSEL

The furnace vessel is shown in Figure 8. It is used to contain the metallurgical process of ilmenite smelting.

The vessel is divided into the following four parts for discussion here:

- Hearth
- Sidewalls
- Roof
- Tap holes

### 2.3.1 Hearth

The hearth of a DC furnace has two roles. The first is to act as the floor of the furnace, containing the metal bath present directly above. The second is to provide the anode connection of the DC electrical circuit.

To contain the hot liquid metal, multiple layers of refractory brick are contained in a steel shell. The bricks are precision manufactured and installed to ensure that no metal will penetrate the lining and burn through after the lining has been heated up and the bricks have completed thermal expansion.

The hearth bricks are usually chosen to have high thermal conductivity, similar to the sidewalls. Air cooling or water cooling is used to extract heat from the outer surface of the hearth and cool it down. Thermocouples are installed in the hearth to generate temperature signals for monitoring the hearth's condition.

The anode connection of the DC electrical circuit can be integrated into the hearth through a number of anode designs. Examples include fins or concentric metal rings built into the anode, metal pins, metal billets and a conductive hearth. The last design is the only one where the contact between the metal bath and the anode is not metal, but rather through electrically conductive refractory brick.

### 2.3.2 Sidewalls

The sidewalls of an ilmenite-smelting furnace also have a dual purpose. Firstly, similar to the hearth, it must contain the metal and slag baths and the furnace freeboard. Secondly, the sidewalls must extract heat from the slag bath at a high enough rate to establish and maintain a freeze lining of solidified slag on the wall.

The sidewalls are constructed from refractory brick, a steel shell and often a layer of ramming material that is inserted between the bricks and shell to prevent air gaps and ensure good thermal contact. This is especially important on the level of the slag bath where heat extraction is critical.

To further ensure adequate heat extraction on the slag bath level, refractory brick with high conductivity and high density is chosen and water cooling is applied on the outside of the steel shell.

Thermocouples are installed at various vertical, angular and radial positions in the sidewalls. Signals from these instruments are used to monitor the condition of the sidewall refractory lining, and as an indirect measure of freeze lining thickness.

### 2.3.3 Roof

The roof of the furnace acts as a lid, closing the furnace so that no gas, fumes or dust escapes other than through the off-gas duct. Because the slag bath surface is fluid and at temperatures of between 1650 and 1750 °C, heat is radiated to the furnace roof at high rates. For this reason the roof is water cooled.

One or more inspection ports are usually installed into the roof to enable operational personnel to do visual inspections of the furnace interior.

### 2.3.4 Tap holes

Tap holes are installed into the furnace sidewalls. One or two metal tap holes are installed on the level of the metal bath, and another one or two slag tap holes are installed at a higher elevation on the level of the slag bath. The tap holes assemblies usually include water cooling aimed at preventing overheating and excessive wear of the refractory lining in the region of the tap holes.

Opening a tap hole is usually done by drilling into the wall up to a specific depth and then using an oxygen lance to burn through to the bath (Noda, 1965). It is closed with a clay plug that is pushed into the hole with a clay gun.

## 2.4 PROCESS INPUTS

### 2.4.1 Ilmenite

Ilmenite is the primary input material into the furnace since the purpose of the process is to upgrade ilmenite to a product of higher TiO<sub>2</sub> content. Both DC ilmenite-smelting furnace operations (Namakwa Sands and Ticor South Africa) utilise sand-type ilmenite as feedstock. The particle size of this ilmenite is usually less than 1000 µm.

The major phase in the ilmenite feed is, of course, ilmenite (nominally FeTiO<sub>3</sub>). Depending on the ore body, some FeO could have been weathered out to leave some rutile (nominally TiO<sub>2</sub>) or pseudorutile (Fe<sub>2</sub>Ti<sub>3</sub>O<sub>9</sub>)

(Nell, 1999). It is also possible that the ilmenite feed could have been roasted to increase the magnetic susceptibility of ilmenite grains over that of unwanted impurities such as chromium-bearing spinel (nominally  $\text{FeCr}_2\text{O}_4$ ) and garnet ( $(\text{Fe}^{2+}, \text{Mg}, \text{Mn}, \text{Ca})_3(\text{Al}, \text{Fe}^{3+})_2\text{Si}_3\text{O}_{12}$ ) (Nell, 1999). Such roasting is usually oxidising and could result in some of the ferrous iron being converted to ferric iron. The end result is some  $\text{Fe}_2\text{O}_3$  in an  $\text{M}_2\text{O}_3$  solid solution with  $\text{FeTiO}_3$  together with  $\text{TiO}_2$  as a separate phase.

Together with the titanium and iron oxides, numerous impurity chemical species also occur. These include  $\text{CaO}$ ,  $\text{MgO}$ ,  $\text{MnO}$ ,  $\text{ZrO}_2$ ,  $\text{SiO}_2$ ,  $\text{Al}_2\text{O}_3$ ,  $\text{Cr}_2\text{O}_3$ ,  $\text{P}_2\text{O}_5$ ,  $\text{V}_2\text{O}_5$ ,  $\text{Nb}_2\text{O}_5$  and possibly others. Some of these species ( $\text{MgO}$ ,  $\text{MnO}$ ) can occur as part of the ilmenite solid solution, while others ( $\text{SiO}_2$  and  $\text{Cr}_2\text{O}_3$ ) report as separate phases like spinel and garnet as mentioned above. The levels of the various impurities depend on the ore body.

All of the above effects often result in natural ilmenite containing less  $\text{TiO}_2$  than the 52.6% by mass of stoichiometric pure ilmenite ( $\text{FeTiO}_3$ ).

### 2.4.2 Reductant

The reductant used in ilmenite smelting is firstly chosen to have low ash content because virtually all of the ash reports in the slag phase as impurities. Secondly, low volatile matter content is preferred. This is to ensure a lower rate of gas evolution from the reductant that can contribute to slag foaming without significantly contributing to reduction. Anthracite and charred coal are therefore mostly used as reductant.

The particle size of the reductant is chosen relatively fine, less than 10 mm. A fine particle size is beneficial for reaction rates in the furnace due to the increased surface area. Too-fine particles are not favoured because these can blow out of the furnace with the off-gas and reduce reductant efficiency.

### 2.4.3 Graphite Electrodes

The graphite electrodes used in DC ilmenite-smelting furnaces are pre-baked, consisting of more than 99% graphite. The amounts of moisture, ash and volatile matter in these electrodes are negligible. They are manufactured with a hole in the centre through which feed material enters into the furnace.

### 2.4.4 Refractory Material

Various refractory materials are used in different locations in the furnace lining. All of these will not be discussed here. The material of major importance to this work is the refractory brick used in the sidewalls on the level of the slag bath. These bricks are required to have high thermal conductivity so that heat can be extracted through them to maintain a safe freeze lining thickness. High density, high-MgO material is usually used.

The reason for discussing refractory material under the heading of process inputs is the fact that some of this material is inevitably released into the slag bath through wear of the lining. This is significant because very strict MgO content specifications are usually in place for the slag product destined for pigment production through the chloride process. The reasons behind these strict specifications are explained in paragraph 1.1.7 (page 7).

### 2.4.5 Water

Leaks in the furnace roof and off-gas duct can result in water entering the furnace. This has a dual effect on the process. Firstly, the water liquid absorbs energy from the process and is converted to water vapour. The energy associated with this effect reduces the energy efficiency of the process. Secondly, the addition of water vapour increases the oxygen partial pressure in the furnace. This adversely affects reductant efficiency. Both these effects are negligible if only small amounts of water are considered, but it could become significant for increased volumes.

Other, more dramatic influences of water include the risk of explosions in the furnace when the conversion from liquid to gas somehow occurs in a confined space; and hydration of the MgO bricks that can severely damage the refractory lining and reduce its life.

### 2.4.6 Air

During normal operation, air is drawn into the furnace through gaps between furnace roof segments. It is attempted to control the furnace atmosphere at a slight positive pressure, but conditions in the furnace still result in periods of negative pressure.

The oxygen in air can strongly increase the oxygen partial pressure in the furnace. This can be detrimental to reductant efficiency. In terms of energy, the net effect of air entering the furnace should be positive. The heat absorbed by the inert N<sub>2</sub> is less than the heat released by O<sub>2</sub> reacting with CO to form CO<sub>2</sub>. This is of course only true if air is not added in excess to what is required for the combustion of CO. This is most likely the case during normal furnace operation.

Large volumes of air are drawn into the furnace when it is placed under negative pressure while an electrode is added or one of the inspection hatches is opened. Under these conditions, air is likely to be present in excess, and it will contribute to cooling the furnace down, consuming some unreacted reductant and possibly oxidising some of the species in the slag.

### 2.4.7 Energy

Energy can enter the furnace in two ways. Since the furnace is equipped with a DC power supply, discharge of energy through the electric arc is the primary means of energy input. In addition to this, both DC ilmenite-smelting furnace operations (Namakwa Sands and Ticor South Africa) equipped their furnaces with ilmenite pre-heaters. These pre-heaters utilise the chemical energy in the CO rich furnace off-gas to heat ilmenite before discharging it into the furnace.

## 2.5 PROCESS OUTPUTS

### 2.5.1 Titania Slag

The furnace is operated with a slag bath temperature of around 1700 °C (Geldenhuis and Pistorius, 1999). Slag is therefore tapped from the furnace around this temperature. The target total TiO<sub>2</sub> content (all Ti reported as TiO<sub>2</sub>) of the slag is around 85% (Kahn, 1984).

Refer to paragraph 2.6 for a discussion of the properties of titania slag.

### 2.5.2 Pig Iron

Heat is extracted at a significant rate from the metal bath through the hearth and sidewalls. For this reason the temperature of the metal bath can be up to 150 °C lower than that of the slag bath (Pistorius, 1999). The carbon content of the metal is around 2% (Pistorius, 1999). It also contains other elements such as Si, Mn, S and P. The levels of such elements in the metal tend to increase as the level of reduction of the slag is increased.

### 2.5.3 Off-gas

The major species in the off-gas include CO (estimated at between 80 and 90%) as a product from the reduction reactions, and H<sub>2</sub> (estimated at 5 to 15%) from volatiles in the reductant. Some CO<sub>2</sub>, H<sub>2</sub>O, N<sub>2</sub> and SO<sub>2</sub> are also found. Because of the high CO and H<sub>2</sub> content, this gas is rich in chemical energy. For this reason it is recycled for purposes such as ilmenite pre-heating.

### 2.5.4 Dust and Fumes

It is likely that thermal shock is experienced by materials as they enter the zone of the electric arc and the bath just beneath it. This can cause reductant and ilmenite particles to break up, producing fine dust particles that are carried into the furnace atmosphere. This is a likely reason for the thick dust cloud present in the furnace freeboard during normal operation. In addition to this, species like Mn and SiO are fumed off at the operating temperatures of the furnace. The dust extracted from the furnace by the off-gas system is enriched in these species.

### 2.5.5 Energy

Energy leaves the furnace via a number of routes. Liquid slag (at around 1700 °C), liquid metal (at around 1600 °C), and off-gas and dust (at around 1700 °C) carry out large quantities of sensible heat. In addition to this heat is lost through the hearth, sidewalls and roof.

## 2.6 PROPERTIES OF TITANIA SLAG

Because of the specific importance of titania slag to this project, the relevant properties of this material are discussed below in more detail.

### 2.6.1 Thermodynamic Data

Valuable work on the thermodynamic properties of the Fe-Ti-O system has been done in recent time. Firstly thermodynamic data from numerous authors were critically assessed and optimised for a number of TiO<sub>2</sub>-containing binary systems (Eriksson and Pelton, 1993). The result of this study was, for each binary system, a single set of modified quasichemical model equations describing the Gibbs energy of the liquid slag phase as a function of composition and temperature, and equations for the Gibbs energy of each compound as a function of temperature. The two systems in that work that are of interest to this study are the FeO-TiO<sub>2</sub> and Ti<sub>2</sub>O<sub>3</sub>-TiO<sub>2</sub> binaries.

The 1993 work was followed up with some experimental work on the stability of pseudobrookite solid solutions in the FeTi<sub>2</sub>O<sub>5</sub>-Ti<sub>3</sub>O<sub>5</sub> range, combined with critical assessment of more literature data (Eriksson et al., 1996). All this data was combined and optimised to yield a comprehensive description of the

thermodynamic properties of the  $\text{FeTiO}_3\text{-TiO}_2\text{-Ti}_2\text{O}_3\text{-Fe}$  system. This is the system of primary importance to the current study. The data from these studies have been included into the FactSage 5.2 software system (Bale et al., 2002). This software system and the data in its databases were used for much of the work in this study.

In 1999, Pesl and Eriç did measurements in the  $\text{TiO}_2\text{-FeO-Ti}_2\text{O}_3$  ternary system. These measurements have not been incorporated into the FactSage data. For this reason only comparisons between the Pesl and Eriç data and the FactSage calculated values are presented here.

FactSage 5.2 contains three solution phase data sets that can be used for describing the liquid slag phase of interest in this study. These are as follows (FactSage 5.2):

- FACT-SLAGA  
This data set has been approved for the sub-system containing FeO,  $\text{TiO}_2$ , and  $\text{Ti}_2\text{O}_3$ .
- FACT-SLAGB  
This data set has been approved for the sub-system containing FeO,  $\text{TiO}_2$ , and  $\text{Fe}_2\text{O}_3$ .
- FACT-SLAG?  
This data set can be used for describing systems containing FeO,  $\text{TiO}_2$ ,  $\text{Ti}_2\text{O}_3$ , and  $\text{Fe}_2\text{O}_3$ . It has however not been thoroughly evaluated and approved by the developers of FactSage.

The FACT-SLAG? data set was the only one available in ChemSage data format for use with the ChemApp library used in this study. Because this data set has not been approved, it was decided to compare it with the FACT-SLAGA data set to determine if significant errors would result from the use of the FACT-SLAG? data. Such comparisons were drawn over a composition range that is applicable to the work of this project, and are shown in Figure 9.

For the most part of the binary diagrams, the difference between results from the two data sets is not visible. It is only on the high  $\text{TiO}_2$  side of the diagrams where the FACT-SLAG? results seem to deviate noticeably from the results generated with the approved data set.

The first noticeable difference is on the rutile liquidus line of all three diagrams. The FACT-SLAG? results indicate a slightly lower liquidus temperature on the high  $\text{TiO}_2$  end of this line. Such a deviation is not likely to influence the modelling work based on the data set significantly.

The second difference is on the line separating the *pseudobrookite-slag-rutile* region from the *pseudobrookite-rutile* region (the *pseudobrookite-rutile* solidus line). The temperature at which this line ends at the  $\text{TiO}_2$  mass fraction upper limit is from 100 to 155 °C lower for the unapproved data set. This inaccuracy causes an overestimation of the amount of liquid slag present in the *pseudobrookite-slag-rutile* region.



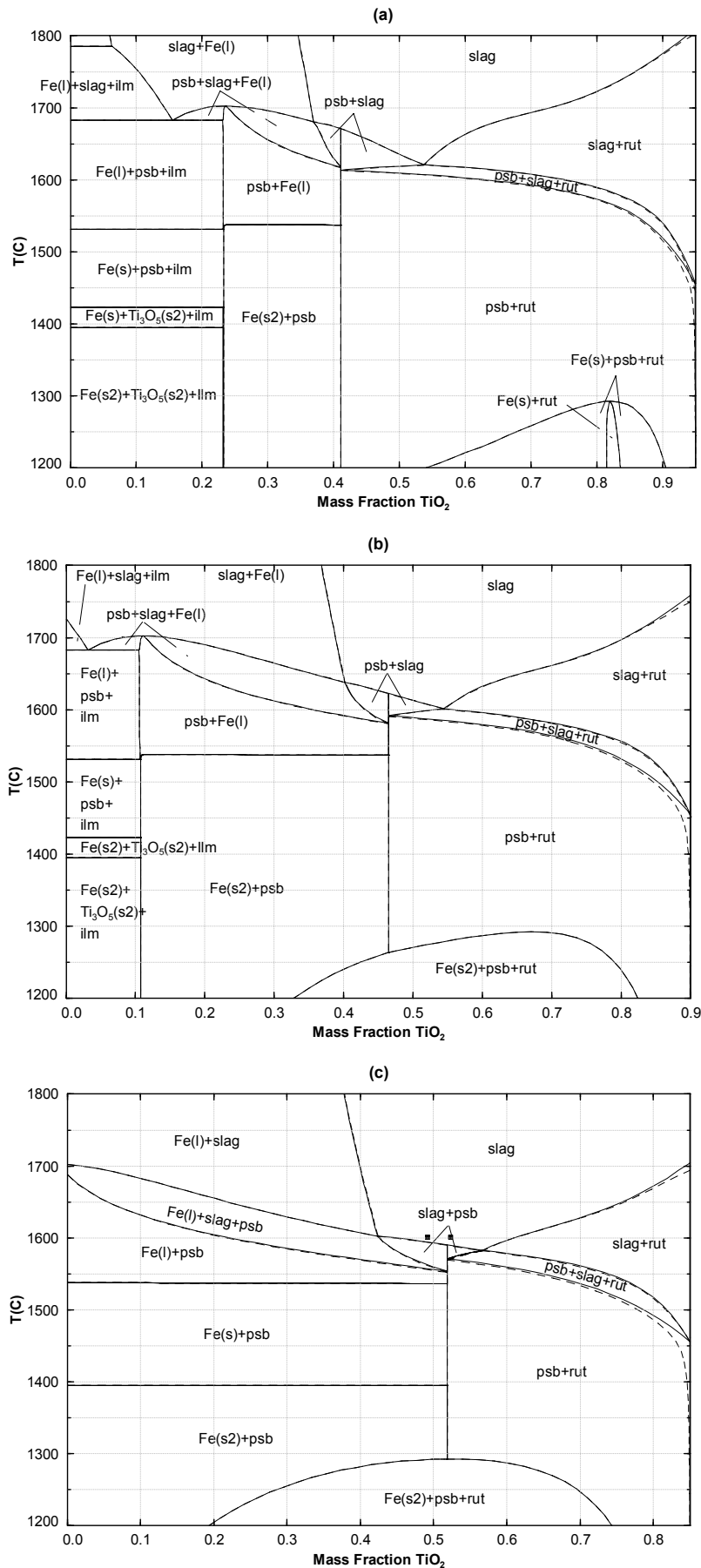


Figure 9 – Constant-FeO binary sections through the  $\text{TiO}_2$ -FeO- $\text{Ti}_2\text{O}_3$  ternary phase diagram.

Solid lines were generated using the FACT-SLAGA data set, and broken lines using the FACT-SLAG? data set in FactSage 5.2.

“rut” = rutile solid solution phase.  
 “psb” = pseudobrookite solid solution phase.  
 “ilm” = ilmenite solid solution phase.

Mass percentages of FeO:

- (a) %FeO = 5.0
- (b) %FeO = 10.0
- (c) %FeO = 15.0

Filled squares on (c) indicate data from Pesi and Eriç (1999).

Based on pilot plant slag compositions reported earlier, the  $\text{TiO}_2$  (tetravalent titanium, excluding  $\text{T}_2\text{O}_3$ ) content of the slag bath is rarely expected to become more than 60% (Pistorius and Coetzee, 2003). This  $\text{TiO}_2$  content is therefore chosen as a reference to determine the impact of the inaccuracies on the modelling work that follows. The temperature of the pseudobrookite–rutile solidus line deviates by no more than 2 °C from that of the approved data set. This means that slags with  $\text{TiO}_2$  content less than 60% should be adequately described by the FACT–SLAG? data set when modelling reduction reactions, solidification and melting.

In graph (c) of Figure 9 two measured data points from Pesl and Eriç (1999) are shown as filled squares. These two points indicate two differences between the measured data and the data calculated by FactSage 5.2. Firstly, in both cases the measured liquidus temperature is higher than the calculated values. The differences in temperature are around 7 and 13 °C for the two points, which seem insignificant. What is significant, however, is the fact that the measurements indicated that the points lie on different sides of the eutectic groove. The calculated data indicates that the eutectic groove is situated to the right of both measured points.

### 2.6.2 Liquidus and Solidus Temperatures and Solidification Behaviour

A liquidus diagram was constructed for the  $\text{TiO}_2$ – $\text{FeTiO}_3$ – $\text{Ti}_2\text{O}_3$  system with the approved data set in FactSage 5.2 and is shown in Figure 10. The dotted lines on this diagram indicate the isothermal boundary between the *slag* region above it, and the *slag-Fe* region below it. This diagram is in good agreement with the conjectural liquidus diagram constructed by Pistorius (1999). Because the conclusion drawn in that work relied strongly on the accuracy of the conjectural liquidus diagram, and because of the good agreement between that diagram and the one in Figure 10, more confidence is placed in the conclusions drawn by Pistorius that energy and reductant inputs into an ilmenite smelter cannot be changed independently.

Figure 10 also shows data as measured by Pesl and Eriç (1999). There are some significant differences between the measured and calculated data. The measured 1600 °C liquidus curve is mostly situated away from the calculated curve towards the  $\text{FeTiO}_3$  corner of the diagram. Conversely, the measured 1500 °C liquidus curve is situated away from the calculated curve towards the  $\text{TiO}_2$ – $\text{Ti}_2\text{O}_3$  join. This comparison suggests that for low-FeO compositions, liquidus temperatures are underestimated by the FactSage data, and for higher-FeO compositions, liquidus temperatures are overestimated.

The measured data also places the eutectic groove closer to the  $\text{M}_3\text{O}_5$  join at both 1500 and 1600 °C. This suggests that the rutile primary phase field can be larger than what the FactSage calculations predict.

Finally, the calculated liquidus lines indicate that the shape of the field where iron metal is stable could be different than what the FactSage calculations predict. The calculations and measurements agree fairly well at 1600 °C, but at 1500 °C the measured data indicates that Fe could be stable at higher  $\text{TiO}_2$  content. The boundary of the Fe stability field could therefore have less of a taper towards the  $\text{FeTiO}_3$  corner of the diagram.

The above differences between measured and calculated data must be taken into account when interpreting the results of this work. All of the calculations done in the present work are based on FactSage 5.2 data.

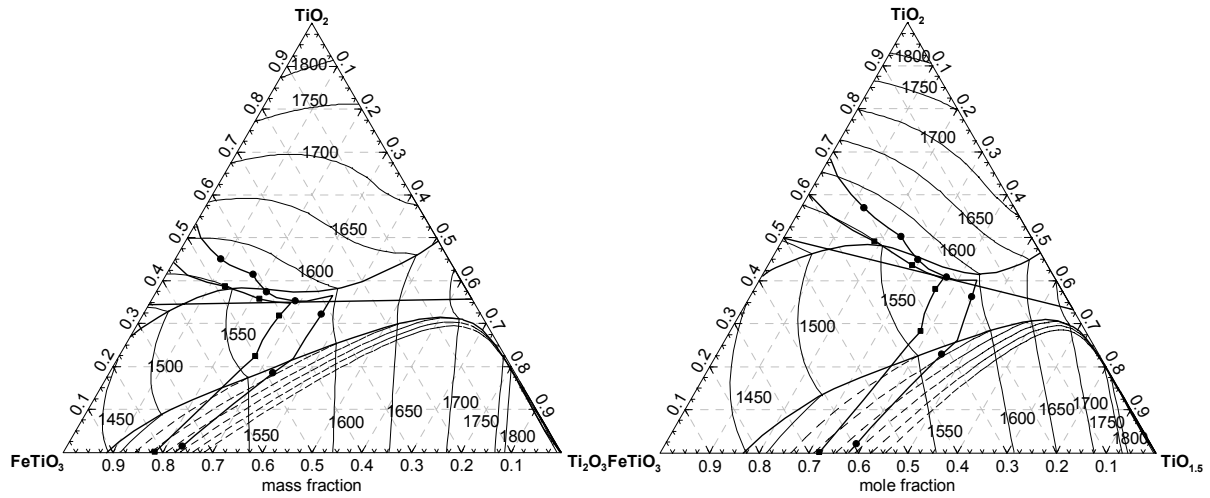


Figure 10 - Liquidus diagram for the  $\text{TiO}_2$ - $\text{FeTiO}_3$ - $\text{Ti}_2\text{O}_3$  system including Magnéli phases.

Dotted lines indicate the boundary between the *slag* region (above the line) and the *slag-Fe* region (below the line). Thick lines marked with filled squares indicate a measured 1500 °C liquidus line (Pesl and Eriç, 1999). Thick lines marked with filled circles indicate a measured 1600 °C liquidus line (Pesl and Eriç, 1999). The top curved thick line indicates the eutectic groove composition. The bottom curved thick line indicates the non-isothermal boundary between the slag region and the slag-Fe region. The straight thick line indicates the  $\text{M}_3\text{O}_5$  join.

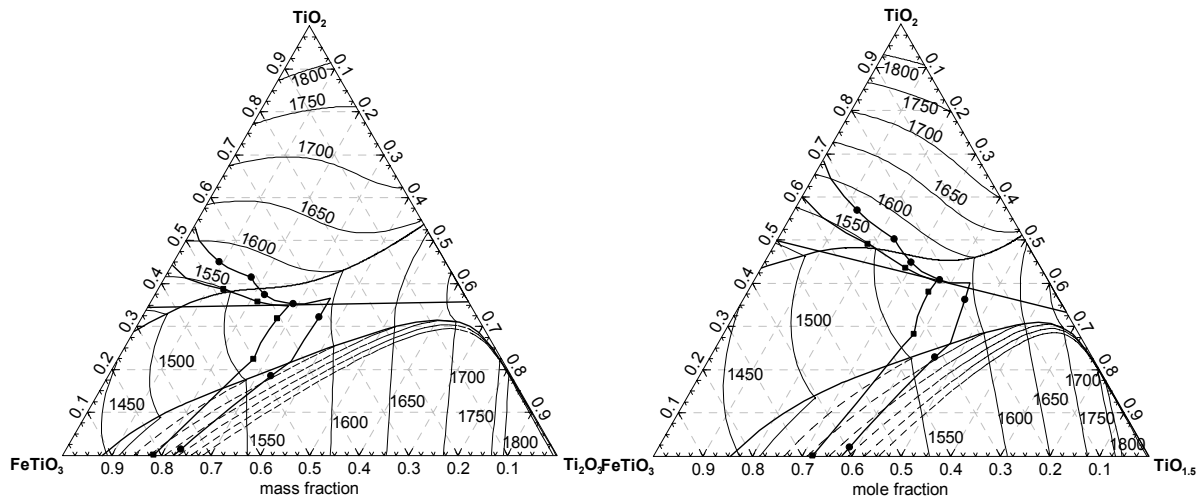


Figure 11 - Liquidus diagram for the  $\text{TiO}_2$ - $\text{FeTiO}_3$ - $\text{Ti}_2\text{O}_3$  system excluding Magnéli phases

Dotted lines indicate the boundary between the *slag* region (above the line) and the *slag-Fe* region (below the line). Thick lines marked with filled squares indicate a measured 1500 °C liquidus line (Pesl and Eriç, 1999). Thick lines marked with filled circles indicate a measured 1600 °C liquidus line (Pesl and Eriç, 1999). The top curved thick line indicates the eutectic groove composition. The bottom curved thick line indicates the non-isothermal boundary between the slag region and the slag-Fe region. The straight thick line indicates the  $\text{M}_3\text{O}_5$  join.

Figure 11 shows a liquidus diagram for the same system with Magnéli phases omitted. The reason for doing this is that these phases are not detected in high-titania slags. The liquidus diagrams in Figure 11 were therefore used during this study.

The data measured by Pesl and Eriç (1999) is also shown on Figure 11. Agreement between measurements and calculated values are worse on this diagram than on Figure 10 if one considers the relative positions of the eutectic grooves. This is to be expected if one consider that Pesl and Eriç (1999) did take Magnéli phases into account.

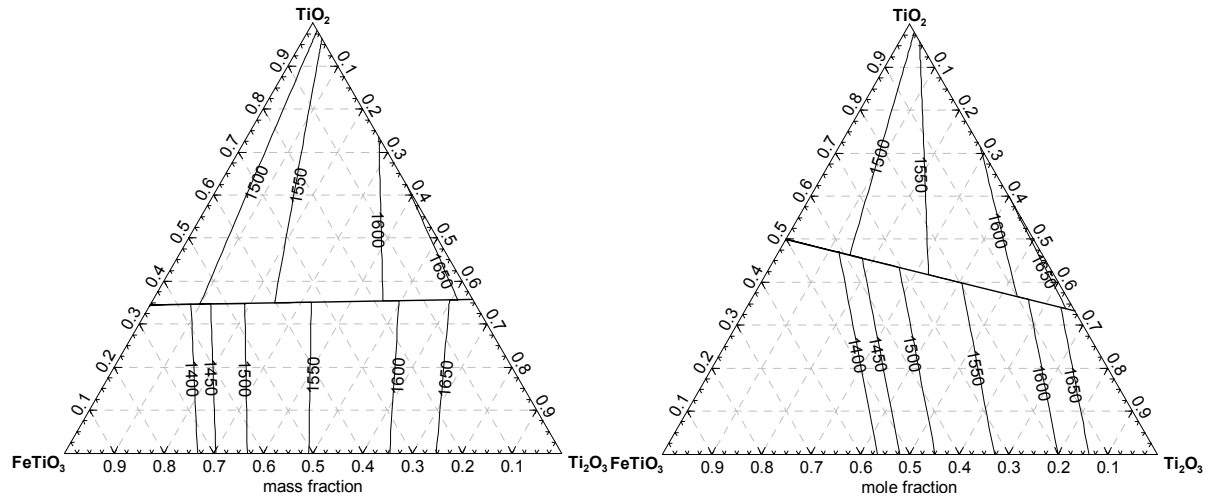


Figure 12 – Solidus diagram for the  $\text{TiO}_2$ - $\text{FeTiO}_3$ - $\text{Ti}_2\text{O}_3$  system including Magnéli phases.

The straight thick line indicates the  $\text{M}_3\text{O}_5$  join. Only slag is considered in this diagram. The solidus lines indicate the boundaries of regions, to the right of the lines, in which only solid slag occurs.

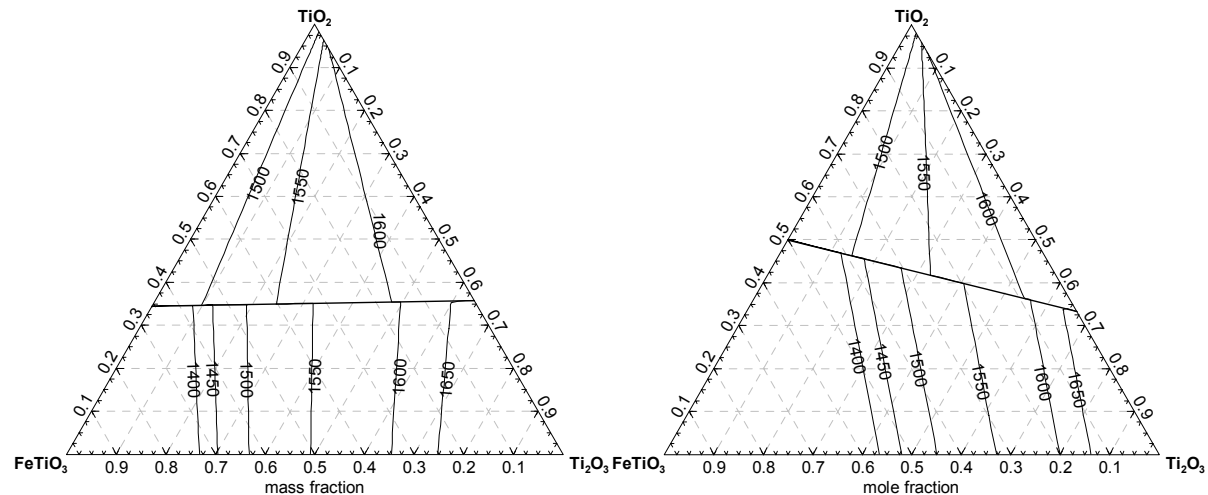


Figure 13 – Solidus diagram for the  $\text{TiO}_2$ - $\text{FeTiO}_3$ - $\text{Ti}_2\text{O}_3$  system excluding Magnéli phases

The straight thick line indicates the  $\text{M}_3\text{O}_5$  join. Only slag is considered in this diagram. The solidus lines indicate the boundaries of regions, to the right of the lines, in which only solid slag occurs.

Figure 12 and Figure 13 shows solidus diagrams of the  $\text{TiO}_2$ - $\text{FeTiO}_3$ - $\text{Ti}_2\text{O}_3$  system. Again the first set includes Magnéli phases and the second does not.

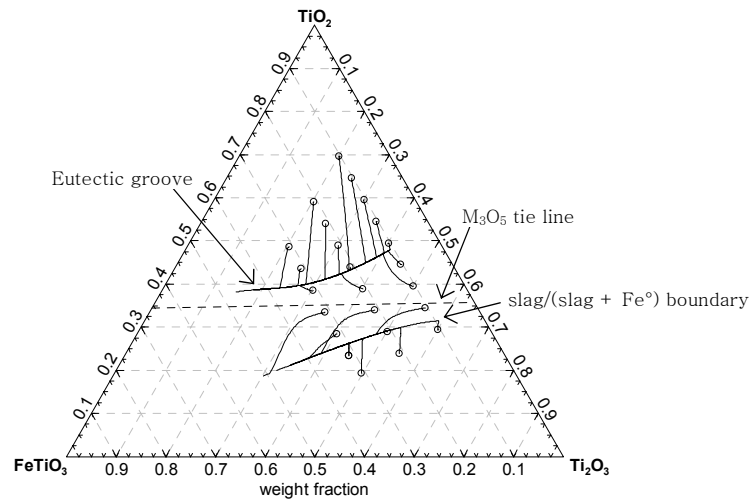


Figure 14 – Liquid slag composition trajectories during solidification.

The dotted line indicates the  $\text{Ti}_3\text{O}_5$ - $\text{FeTi}_2\text{O}_5$  join. Initial composition indicated by circles and trajectories by solid lines.

Another useful view on the behaviour of the system under consideration, given the importance of solidification and melting behaviour in this study, is the composition trajectory of the liquid slag phase during solidification. Figure 14 shows a grid of initial liquid slag compositions above the liquidus temperature (circles) and associated composition trajectories (solid lines) of the liquid slag phase as the system is cooled down to its solidus temperature. This diagram gives an indication of the direction in which solidification and melting phase equilibria can influence the composition of the slag bath. Figure 14 is based on the FACT-SLAG? data set and therefore contains some inaccuracies.

It is evident from Figure 14 that the composition of liquid slag with a starting composition above the  $\text{M}_3\text{O}_5$  join is modified through solidification to eventually end up in the eutectic groove visible in Figure 9. Liquid slag with starting composition below the  $\text{Ti}_3\text{O}_5$ - $\text{FeTi}_2\text{O}_5$  join tends to drift toward the boundary of the phase field where iron metal becomes stable. The cases converging in the eutectic groove is a demonstration of the phase chemistry behaviour during solidification that was proposed as the origin of the compositional invariance of ilmenite smelter slag close to the  $\text{M}_3\text{O}_5$  composition (Pistorius, 2002).

### 2.6.3 Heat Capacity

Figure 15 shows temperature vs. enthalpy curves for three different slag compositions under equilibrium conditions, as calculated with FactSage 5.2. For these three compositions, the latent heat of fusion represents approximately 27% of the enthalpy required to heat the material from 0 °C up to its liquidus temperature. This is a significant point, since the latent heat of fusion acts as ‘buffer’ between events occurring inside the furnace, and the brick portion of the furnace wall in which thermocouples are installed. Even without this buffer a temperature change taking place at the hot face of the freeze lining will take a long time to be detected by a thermocouple installed in the brick. The latent heat of fusion adds to this time lag, and ultimately to the degree of difficulty of the freeze lining control problem.

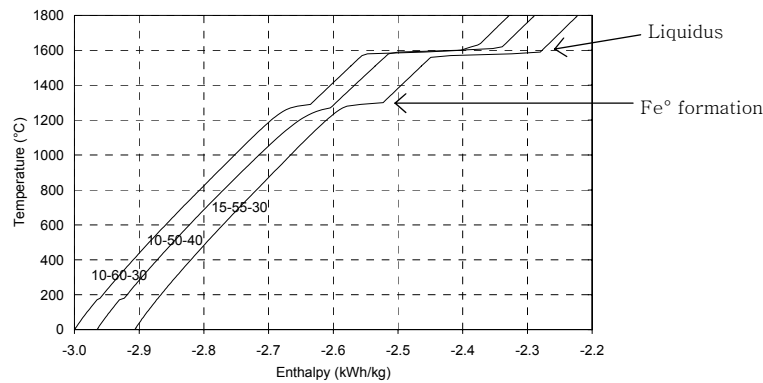


Figure 15 – Temperature vs. enthalpy curves for three difference slag compositions. Composition indicated as FeO-TiO<sub>2</sub>-Ti<sub>2</sub>O<sub>3</sub> mass percentages.

Two distinctive changes in slope are visible on Figure 15. The first is at around 1600 °C where the slag converts from solid to liquid or vice versa depending on whether temperature is increasing or decreasing. The second is visible just below 1300 °C. Below this temperature iron metal becomes stable. This can be verified on Figure 9 (page 21).

#### 2.6.4 Viscosity

The viscosity of high-titania slag has been determined previously (Handfeld and Charette, 1971). The values reported by them are around 0.03 kg/ms for slags above their liquidus temperature. This is several orders of magnitude less than the viscosity (10<sup>6</sup> kg/ms) of SiO<sub>2</sub> at its melting point (1727 °C) (Pistorius and Coetzee, 2003).

This viscosity data is of relevance to this work since it determines the validity of assumptions made about the slag being ideally mixed. Due to the strong stirring that is known to occur in the slag bath, and the low viscosity of the slag, assuming ideal mixing in the slag bath seems to be valid.

#### 2.6.5 Thermal Conductivity

Due to the nature of this study, the thermal conductivity of solid high-titania slag is of great importance. Little published data is available on this. The value of 1.0 W/(m.K) that was used in this text was obtained from Pistorius (2004, 2004b).

#### 2.6.6 Compositional Invariance

Pistorius (1999) identified a relationship between the Ti<sub>2</sub>O<sub>3</sub> and FeO content of high-titania slag. Work has been done to determine the phenomena that cause this relationship (Pistorius 2002; Pistorius and Coetzee 2003; Pistorius 2003; Pistorius 2004). Further study to determine the cause of this compositional invariance was part of the scope of this study. CHAPTER 10 is therefore dedicated to this subject.

## CHAPTER 3

### A 1D MODEL OF THE FREEZE LINING AND FURNACE WALL

This chapter describes the details of a dynamic one-dimensional model of the furnace freeze lining and wall. The development process followed during this modelling effort closely resembles the process described by Thomas and Brimacombe (1997). The same development process was used for the models discussed in following two chapters.

The model described in this chapter was used to build a more comprehensive process model (see CHAPTER 5, page 89) and in the execution of experiments to investigate phenomena related to the freeze lining (see CHAPTER 6, page 137; and CHAPTER 7, page 176).

#### 3.1 IDENTIFICATION

The model being described in this chapter is identified as follows:

Name: Freeze Lining Conductor Model

Abbreviation: FLC Model

#### 3.2 PROBLEM DEFINITION

The main objective of this study was to investigate the dynamic interaction between the freeze lining and slag bath in an ilmenite-smelting furnace. For this reason it was necessary to develop a mathematical model of the freeze lining that can describe its behaviour as a function of time. This was the most basic requirement.

The behaviour of the freeze lining that was of interest includes changes in thickness, composition and temperature as functions of time, and, in the case of composition and temperature, as functions of position in the freeze lining.

Because both slag bath temperature and composition are known to have an important influence on the behaviour of the freeze lining (Pistorius, 1999), the model had to be able to address both these aspects.

#### 3.3 SYSTEM DESCRIPTION

Before becoming involved with the details of phenomena and mathematics relevant to the model, it is necessary to first gain perspective about the physical system to be modelled. For this reason the reader is referred back to the simplified schematic representation of an ilmenite-smelting furnace (Figure 8, page 13).

The schematic shows a sectional view of a circular DC electric arc furnace with a single hollow electrode. Feed is introduced into the furnace through the hollow electrode. Metal and slag are tapped from the furnace through separate tap holes.

For the FLC model, the region including the freeze lining and furnace wall is of particular importance. This region is shown in somewhat more detail below:

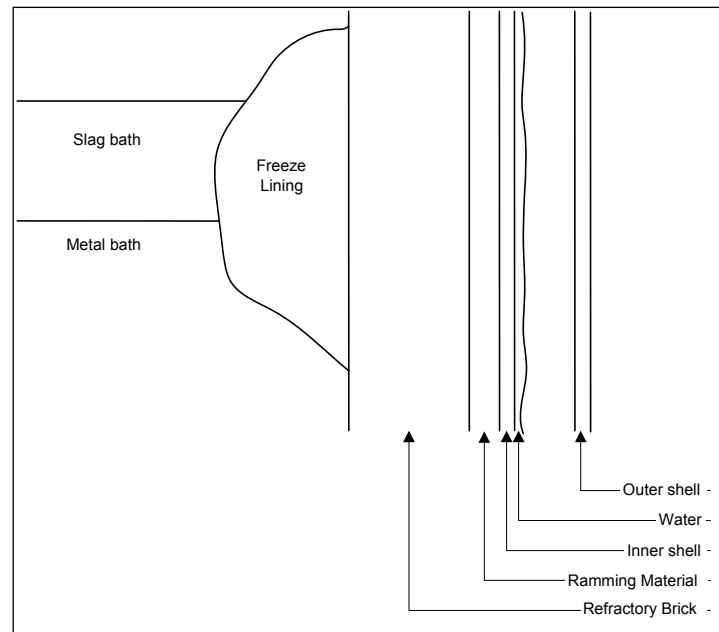


Figure 16 – Schematic representation of the freeze lining and wall region of the furnace.

### 3.3.1 System geometry

If one only focuses on the part of the furnace shown in Figure 16, the system to be modelled is cylindrical. For this reason, phenomena occurring in the furnace will be identified and described based on the cylindrical coordinate system and therefore the following geometrical dimensions:

- Radial dimension
- Axial dimension
- Angular dimension

## 3.4 KEY PHENOMENA

To be able to model a process, one needs to be aware of all or most of the phenomena that are active in the process. For this reason, the next few paragraphs aim to identify most of the phenomena that are relevant to the system being considered in this chapter. It also aims to classify these phenomena in terms of their importance to the FLC model.

### 3.4.1 Heat Transfer

#### a. Radial heat transfer

Outward radial heat transfer is the direction of heat transfer that is of primary concern in the system. The reason is that the electric arc is the main source of energy in the furnace. The arc discharges a significant portion of its energy into the slag bath (Stenkvist and Bowman, 1987). The slag bath then transfers, via conduction and convection, heat to the metal bath and freeze lining. It also radiates heat into the furnace atmosphere (Reynolds, 2002).

Focusing on the system being considered here, energy will flow

- through the slag bath by means of conduction and convection,



- from the slag bath to the freeze lining by convection,
- through the freeze lining, refractory materials and steel inner shell by conduction, and
- into the cooling water on the outer surface of the inner shell by convection.

Radial heat transfer, including all the components listed above, was seen as a key phenomenon since modelling of this phenomenon is crucial to the usefulness of the FLC model. This is because solidification and melting of the freeze lining move the interface between the freeze lining and slag bath primarily in the radial dimension.

#### b. Axial heat transfer

Because of the slag bath being the hottest part in the furnace other than the arc itself, heat flows away from it to regions of lower temperature. Heat is transferred via convection and radiation to the furnace atmosphere and by convection to the metal bath. The metal bath and furnace atmosphere can therefore be safely assumed to have lower temperatures than the slag bath. Due to this it is very likely that there is an axial heat transfer component in the system being considered.

There is likely to be upward transfer of heat in the furnace wall from the region of the slag bath towards the colder upper sidewall regions. It is also possible that there is downward heat transfer in the sidewall towards the colder lower sidewall regions that are in contact with liquid metal. The likelihood that liquid metal in these regions are in direct contact with the refractory lining (with no freeze lining) could however result in a much higher temperature boundary condition compared with the region of the sidewall that is in contact with the freeze lining. This will result in an upward axial heat transfer component from the level of the metal bath.

It is believed that the magnitude of axial components of heat transfer vectors within the system is significantly smaller than the radial components. Due to this, axial heat transfer was seen as being less important than radial heat transfer (Assumption 3.1, page 35). It was not believed to be a key phenomenon within the context of the FLC model.

#### c. Angular heat transfer

Due to the cylindrical shape of the furnace, it is convenient to assume symmetry about the cylinder's central axis in terms of freeze lining thickness, temperature, etc. However, because of the presence of tap holes on the side of the furnace, and the likelihood of the electrode (and therefore the arc) being off-centre, this symmetry does not exist in reality. For this reason temperature, freeze lining thickness and even freeze lining composition should vary with angular position.

It is believed that the magnitude of angular components of heat transfer vectors within the system is significantly smaller than the radial components. Due to this, angular heat transfer was seen as being less important than radial heat transfer (Assumption 3.1, page 35). It was not believed to be a key phenomenon within the context of the FLC model.

#### d. Heat sources

The following known heat sources are found in the system or influence the system as boundary conditions:

- Electric arc

The electric arc heats the furnace atmosphere, slag bath and metal bath directly. This heat reaches the freeze lining via convection and conduction. Heat can also be radiated to the freeze lining in the case when slag or metal tapping exposes part of the freeze lining to the arc.

This heat source was seen as key to the FLC model.

- Slag solidification

When slag solidifies on the surface of the refractory bricks or the freeze lining heat associated with the phase change is liberated.

This heat source was seen as key to the FLC model because the liberated heat must be accounted for in a heat transfer model of the furnace wall and freeze lining. Ignoring it would have resulted in a serious weakness in the model.

- Chemical reaction

Various chemical reactions (to be discussed in more detail below) can occur in the system. Some of these reactions are exothermic and therefore act as heat sources.

This heat source was seen as key to the FLC model for reasons similar to those quoted for the heat liberated during slag solidification.

e. Heat sinks

The following known heat sinks are found in the system or influence the system as boundary conditions:

- Slag melting

When material melts away on the surface of the refractory bricks or the freeze lining, heat associated with the phase change is absorbed.

This heat sink was seen as key to the FLC model for the same reasons as the slag solidification heat source.

- Chemical reaction

Various chemical reactions (to be discussed in more detail below) can occur in the system. Some of these reactions are endothermic and therefore act as heat sinks.

This heat sink was seen as key to the FLC model for the same reasons as the slag solidification heat source.

- Water cooling

Forced water cooling is applied on the outer surface of the inner steel shell. The water extracts heat as it exits the system.

This heat sink was seen as important to the FLC model, but since the extraction of heat by water cooling is not the rate-determining step in heat transfer from the slag bath to the water, it was

decided not to model this phenomenon in great detail. A simple boundary condition assumption was used to describe this heat sink (Assumption 3.8, page 38).

### 3.4.2 Mass Transfer

#### a. Convective mass transfer

Due to movement in the slag and metal baths that is induced by the impinging arc, entering feed material, electromagnetic forces and buoyancy forces, material (slag and metal) is transported to and from the freeze lining surface and the refractory brick surface (if some refractory material is exposed to the slag and metal baths).

Convective mass transfer was not seen as a critical/key phenomenon to the FLC model. The reason is that it was assumed that the slag bath is well mixed due to the momentum transferred to it by the above-mentioned forces (Assumption 4.2, page 36).

#### b. Diffusion

Due to compositional gradients inside the metal and slag baths it is expected that diffusion occurs in these zones.

Compositional gradients can also exist in the freeze lining due to slag of different compositions having solidified at different positions. Such gradients also induce diffusion.

Diffusion was not seen as a critical/key phenomenon to the FLC model. The reason for this was again the strong stirring effects that are present in the metal and slag baths. In the case of the freeze lining it was simply assumed that mass transfer does not have a significant impact on the behaviour of the freeze lining (Assumption 3.3, page 36). Ideal mixing in the liquid, with no diffusion in the solid, corresponds to the assumptions of the Scheil model of solidification (Flemings, 1997).

### 3.4.3 Momentum Transfer

#### a. Slag and metal baths

Momentum is transferred to the slag bath by the impinging arc, material fed through the centre of the electrode, and by electromagnetic and buoyancy forces. This results in movement in the slag and metal baths. This movement can influence the rates at which heat and mass are transferred to and from the freeze lining.

Momentum transfer in the slag bath was seen as an important phenomenon for the FLC model since it can significantly influence heat transfer at the freeze lining surface. This phenomenon therefore had to be addressed in the model. It was however believed that it would be adequate to incorporate this phenomenon as a simple boundary condition without modelling it in any great detail.

#### b. Water-cooling layer

Water flows down the outer surface of the inner shell (see Figure 16, page 28) under the influence of gravity. This momentum transfer influences the rate at which heat is extracted by the water from the wall.

Momentum transfer in the water cooling layer was not seen as a key phenomenon for the FLC model. The heat transfer resulting from it was believed to be important, but since it is not rate-determining, it could be addressed adequately by a simplifying assumption regarding this heat transfer boundary condition (Assumption 3.8, page 38).

### 3.4.4 Chemical Reaction

#### a. Reaction between liquid slag and liquid slag

It is likely that some chemical reactions may take place in the liquid slag. For example  $\text{Fe}_2\text{O}_3$  may be reduced by  $\text{Ti}_2\text{O}_3$  to form  $\text{FeO}$  and  $\text{TiO}_2$ .

Since the slag bath acts as a boundary condition to the heat transfer FLC model and because the calculations of solidification and melting influence liquid slag composition, these reactions were seen as important to the FLC model.

#### b. Reaction between liquid slag and solid slag

Due to strong mixing in the slag bath and the compositional variations of the slag bath with time, liquid slag coming into contact with the freeze lining will often differ in composition from the solid material of the freeze lining. Solidification by itself enriches the liquid phase in certain species resulting in a compositional difference between the solid and liquid phases at the interface between the freeze lining and slag bath. The combination of the difference in composition, the difference in phase (liquid versus solid) and likely difference in temperature could often result in a chemical potential difference/gradient between the liquid slag close to the freeze lining and the freeze lining itself. Such a gradient acts as the driving force for chemical reaction between slag bath and freeze lining. In this case chemical reaction refers to reaction between species in the same phases, between species in different phases and changes from one phase to another (for example liquid and solid phases).

These chemical reactions were seen as a critical part of the behaviour of the system since it occurs at the interface between the slag bath and freeze lining. Describing the movement of this interface in response to process changes was partly the aim of this modelling study, and these chemical reactions therefore had to be modelled.

#### c. Reaction between solid slag and solid slag

Compositional variations may occur in the freeze lining as a function of radial position. This may be due to variations in slag bath composition. These compositional variances can result in chemical potential gradients that provide a driving force for chemical reactions to take place.

Such chemical reactions were assumed to be negligible for the purpose of the FLC model (Assumption 3.3, page 36). In the solid state, the reaction rates and mass transfer rates are likely to be slow. For this reason the inaccuracies that result from the assumption were accepted.

d. Reaction between slag and refractory material

It was uncertain whether any significant reaction takes place at the interface between the freeze lining (solid slag) and the refractory material. It was expected that chemical reaction at this interface will not be important to the overall accuracy of the model since it should occur at very low rates.

If the freeze lining is completely dissolved into the slag bath, liquid slag will come into contact with refractory material. The reaction between liquid slag and refractory material becomes important in this situation. Since the aim in practice is to prevent the entire freeze lining from melting away, chemical reaction between liquid slag and refractory material is a limiting condition. For this reason it was not seen as key to the FLC modelling exercise. A complete loss of freeze lining in the FLC model can be considered indicative of refractory erosion.

**3.4.5 Mechanical Effects**

a. Tapping equipment

Tapping equipment (drills, lances and clay guns) can significantly influence the behaviour of the freeze lining in the vicinity of the tap holes. The focus of this study was however not on these regions, and these mechanical effects were not seen as important to the accuracy of the FLC model. They were therefore ignored.

b. Buoyancy in the metal bath

Due to the lower density of solid slag (approximately 3,800 kg/m<sup>3</sup>) compared with liquid metal (approximately 7,000 kg/m<sup>3</sup>), the freeze lining will experience upward buoyancy forces from below when it becomes partially submerged in the metal bath. This effect was however not the focus of the FLC model and was ignored.

**3.4.6 Summary of Key Phenomena**

The table below summarises the phenomena identified above and assigns a level of importance to each phenomenon within the context of the FLC model. A level of importance of 1 means that the phenomenon is considered unimportant and it is subsequently ignored. Level 2 indicates that the phenomenon must be incorporated into the model, but it is not necessary to model it in detail. Level 3 marks critical phenomena that must be modelled in as much detail as possible.

		Level of importance to current modelling effort		
		1	2	3
Heat transfer	Radial	In slag bath		✓
		Slag bath to freeze lining		✓
		In freeze lining		✓
		Freeze lining to refractory brick		✓
		In refractory brick		✓
		Refractory brick to ramming material		✓
		In ramming material		✓
		Ramming material to steel shell		✓
		In steel shell		✓
		Steel shell to water		✓
	Axial	In slag bath	✓	
		In freeze lining	✓	

		In refractory brick	✓					
		In ramming material	✓					
		In steel shell	✓					
		In water	✓					
	Angular	In slag bath	✓					
		In freeze lining	✓					
		In refractory brick	✓					
		In ramming material	✓					
		In steel shell	✓					
	Heat sources	In water	✓					
		Electric arc						✓
		Slag solidification						✓
	Heat sinks	Chemical reaction						✓
		Slag melting						✓
Chemical reaction			✓					
Mass transfer	Water cooling		✓					
	Convection	In slag bath	✓					
	Diffusion	In slag bath	✓					
In freeze lining		✓						
Momentum transfer	Slag bath		✓					
	Metal bath	✓						
	Water cooling layer	✓						
Chemical reaction	Liquid slag	With liquid slag	✓					
	Liquid slag	With solid slag		✓				
	Liquid slag	With refractory material	✓					
	Solid slag	With solid slag	✓					
	Solid slag	With refractory material	✓					
Mechanical effects	Tapping equipment		✓					
	Buoyancy in metal bath		✓					

Table 2 – Summary of key phenomena for the FLC model.

### 3.5 APPROACH AND MODEL COMPLEXITY

From the table summarising key phenomena it can be concluded that radial heat transfer, heat sources and sinks, and chemical reaction are of greatest importance to the FLC model. Among these the heat-related phenomena are most basic to the problem being studied. The reason is that the thermal phenomena occur right throughout the system while significant chemical reactions only occur in the slag bath, freeze lining, and perhaps on the hot face of the refractory brick.

Due to the general importance of heat-related phenomena in the system, heat transfer was used as the foundation of the model. The chemical reactions were modelled within the heat transfer framework where applicable.

#### 3.5.1 Modelling of Heat Transfer

Because axial and angular heat transfer were assumed to be of significantly lesser importance than radial heat transfer, and because this model was the first attempt at building a mathematical representation of the system, it was decided to model heat transfer in the radial dimension only. The model is therefore one-dimensional with the radial dimension being labelled the ‘focus dimension’.

The axial position in the furnace that was used for the model is one where liquid slag is found all of the time. The influence of liquid metal and the furnace atmosphere on the freeze lining was therefore ignored.

The angular position that was used is one that is representative of most of the circumference of the furnace. This means that the influence of tap holes was ignored in the FLC model.

The range of the radial dimension that was used starts at some distance away from the inner surface of the refractory wall into the slag bath. It ends at the outer surface of the inner steel shell where it is water-cooled. The distance that the model's radial dimension extends into the slag bath was chosen in such a way that there was sufficient room for the interface between the slag bath and freeze lining to move (by solidification and melting) to achieve the desired experimental results.

#### a. Solution method

A finite difference method was used to solve the heat transfer problem. An explicit formulation was used.

### 3.5.2 Modelling of Chemical Reaction

In the case of the freeze lining and the slag bath, a complete thermochemical representation of the nodes was maintained in addition to the heat transfer representation. This made it possible to calculate chemical reaction and phase changes by using a Gibbs-free-energy-minimisation approach. This approach simplified modelling of chemical reaction, because one does not need to focus on specific reactions that occur. The Gibbs-free-energy minimiser (Eriksson and Rosen, 1973; Eriksson, 1975) simply searches for the relevant thermodynamic equilibrium condition.

This approach implicitly assumes a strong drive towards thermodynamic equilibrium at the interface between the slag bath and freeze lining (Assumption 3.4, page 36).

## 3.6 MODEL FORMULATION

### 3.6.1 Assumptions

The following paragraphs list assumptions made as part of the FLC model formulation. The paragraphs clarify why the assumptions were made, their validity and the impact that the assumptions have on the model.

#### a. Assumption 3.1

Statement: Axial and angular heat transfer components are negligible and can be ignored.

Justification: This assumption was required to simplify the model. A one-dimensional model is significantly simpler and more manageable compared with two- and three-dimensional models. The results of the current study may lead to the development of such more detailed models if the additional modelling effort is justified by the perceived value that could be added.

Validity: The assumption is certainly not absolutely true since the existence of axial and angular heat transfer components can easily be proven. It is however true that the radial heat transfer components should be significantly larger than the axial and angular components. The assumption was therefore acceptable given the objectives of the current work. The most significant influence on the validity of this assumption is

probably the axial heat transfer component from the portion of the wall in direct contact with the metal bath.

Impact: This assumption causes inaccuracies in the predictions of the model. These inaccuracies were in general viewed as being in balance with other uncertainties (measurement inaccuracies, uncertainty about dimensions, and uncertainty about material properties) in the process, and they were therefore viewed as not being significant within the context of the FLC model and its current application.

#### b. Assumption 3.2

Statement: The slag bath is well mixed and can therefore be treated as ideally mixed.

Justification: This assumption was required to simplify the model. Taking compositional and thermal variations in the slag bath into account would have complicated the model significantly.

Validity: The assumption is surely not absolutely true, but since there is significant stirring in the slag bath, it could be seen as being valid within the context of the FLC model.

Impact: The impact of this assumption on the accuracy and validity of the model was believed to be minimal.

#### c. Assumption 3.3

Statement: Mass transfer and solid-state chemical reaction in the freeze lining are negligible and can be ignored.

Justification: This assumption was required to simplify the model. Incorporating mass transfer and chemical reaction between solid nodes with different compositions into the model would have complicated matters significantly. It was uncertain whether it would have added much to the accuracy and validity of the model.

Validity: If compositional gradients exist, mass transfer will occur and chemical reaction is also likely to occur. Because the solid state is being considered here, mass transfer and chemical reactions are likely to be slow relative to other phenomena being modelled. This made the assumption acceptable, even though it is not absolutely true.

Impact: The impact of this assumption on the accuracy and validity of the model was believed to be minimal.

#### d. Assumption 3.4

Statement: There is a strong drive towards thermodynamic equilibrium at the interface between the slag bath and freeze lining.

Justification: This assumption was required to simplify the modelling of chemical reactions and phase changes at the interface between the slag bath and freeze lining. This assumption made it possible to use a Gibbs-free-energy-minimisation approach to model these reactions.

Validity: Ultimately the tendency towards thermodynamic equilibrium drives all chemical reactions. In some instances this influence is less dominant because of a significant influence of mass transfer, heat transfer and reaction kinetics. In the case being considered here, it was believed that the high temperatures and strong mixing of the



slag bath prevent mass transfer and reaction kinetics from being limiting. Heat transfer plays a significant role and for this reason it was modelled in detail.

Impact: If mass transfer or reaction kinetics plays a significant role in the behaviour of the freeze lining, this assumption would result in noteworthy inaccuracies in the model. This was, however, not believed to be the case.

#### e. Assumption 3.5

Statement: The temperature dependence of the density of materials (liquid slag, solid slag, magnesia brick, ramming material, and steel) used in this model is negligible and can be ignored.

Justification: This assumption was required to simplify the model. Variations in density with changing temperature result in changes in the volume of the finite-difference nodes used in the model. To properly address such volume changes one needs to use a finite element approach. This would have complicated the model significantly.

Validity: Since it is known that the density of most materials vary with temperature, this assumption is not true. Within the context of the FLC model, it was believed that the inaccuracies introduced by this assumption were within the general uncertainties that are associated with the smelting process. The assumption could therefore be tolerated.

Impact: The assumption introduces inaccuracies into the model, but these were believed to be tolerable.

#### f. Assumption 3.6

Statement: The thermal conductivity of solid slag is assumed to be 0.001 kW/(m.°C), and independent of temperature.

Justification: No detailed information on thermal conductivity of liquid and solid slag as a function of temperature and/or composition was available for this study.

Validity: The only information regarding the thermal conductivity of high-titania slag in literature was found in the form of an assumption made by Pistorius (2004), and discussions with Pistorius (2004b). The same value used in that work is used here.

Impact: The assumption introduces inaccuracies into the model, but these were believed to be acceptable given the objectives of this study and the availability of thermal conductivity data.

#### g. Assumption 3.7

Statement: No liquid metal reaches the freeze lining.

Justification: This assumption was required to simplify the FLC model. If this assumption were omitted, the model would have to be constructed to allow liquid metal to enter into the conductor in addition to liquid slag. This would have added some complications to the model, and these complications were not believed to add significantly to the validity or accuracy of the model.

Validity: Because liquid metal is formed in reduction reactions between slag and reductant particles, it is likely that small liquid metal droplets will be dispersed throughout the slag bath. This makes the assumption false. The amount of metal was however believed to be small, which would improve the validity of the assumption.

Impact: The assumption introduces inaccuracies into the model, but these inaccuracies were believed to be minimal. Contact between liquid metal and slag was modelled in other ways in the overall process modelled discussed later.

#### h. Assumption 3.8

Statement: The outer surface of the steel shell is at a constant temperature.

Justification: This assumption was required to simplify the FLC model. By assuming a constant temperature boundary condition, all the complexity of the convective water cooling boundary condition was ignored.

Validity: The water cooling boundary condition is not the rate-determining step in the heat transfer path from the freeze lining surface to the water cooling on the outside of the steel shell. The influence of variations in water cooling was also not the focus of this study. For these reasons this assumption was acceptable even though it is not true.

Impact: The assumption introduces inaccuracies into the FLC model but because the water cooling boundary condition is not rate determining, these inaccuracies were believed to be acceptable.

#### i. Assumption 3.9

Statement: The contact resistances between the layers (solid slag, brick, ramming, steel) of the conductor are not rate-determining of heat transfer through the wall.

Justification: This assumption was required to simplify the FLC model. It is virtually impossible to measure or infer the actual contact resistances in the furnace being considered. For this reason the contact resistances are made as small as possible without causing numerical instabilities in the model.

Validity: Due to significant expansion of refractory brick and ramming when the furnace is brought into operation, it was believed that the mechanical contact between the brick and ramming, and between ramming and steel is very tight with no air gaps of note being present. This would result in these contact resistances having a smaller influence than conduction through the solid slag and brick layers.

The contact between the solid slag and the brick was also believed to be very tight due to the high temperatures experienced during the initial period when the furnace is brought into operation. For this reason this resistance was believed not to be rate-determining.

Impact: The assumption and the subsequent determination of the contact resistances introduced inaccuracies into the FLC model. Because the resistances were made as small as possible and because they are very likely not rate-determining in reality, these inaccuracies were believed to be negligible.

### 3.6.2 Simplifications

The following paragraph presents a simplification that was made in the model. The justification and impact of the simplification are also presented.

#### a. Simplification 3.1

Description: The influence of contact between the metal bath and the freeze lining on freeze lining behaviour is ignored.

Justification: This simplification was made to avoid having to treat the details of varying slag and metal bath levels in the model.

Impact: The simplification introduces inaccuracies into the model, but since the influences of tapping on freeze lining behaviour were not set as an objective of this study, it was deemed to be acceptable.

### 3.6.3 Material Definitions

#### a. Liquid Slag

Liquid Slag is found in contact with the freeze lining on the inside of the furnace. Because of the interaction between liquid slag and solid slag at this interface, it was required to include the Liquid Slag material into the model.

Liquid Slag is defined to contain only a single liquid phase. This phase is referred to as the Liquid Slag Phase.

The relevant physical properties of this material are given in APPENDIX A.

#### i. Liquid Slag Phase

Actual constituents: From chemical analyses this phase is known to contain the following constituents:  $\text{Al}_2\text{O}_3$ ,  $\text{CaO}$ ,  $\text{Cr}_2\text{O}_3$ ,  $\text{FeO}$ ,  $\text{Fe}_2\text{O}_3$ ,  $\text{K}_2\text{O}$ ,  $\text{MgO}$ ,  $\text{MnO}$ ,  $\text{Na}_2\text{O}$ ,  $\text{P}_2\text{O}_5$ ,  $\text{SiO}_2$ ,  $\text{TiO}_2$ ,  $\text{Ti}_2\text{O}_3$ ,  $\text{V}_2\text{O}_3$ , and  $\text{ZrO}_2$ .

Considered constituents: For the purpose of the FLC model, only the following phase constituents were considered:  $\text{FeO}$ ,  $\text{Fe}_2\text{O}_3$ ,  $\text{TiO}_2$ , and  $\text{Ti}_2\text{O}_3$ .

Solution model: Quasichemical Model (Eriksson et al., 1996)

Thermochemical data: ChemSage format data file from GTT Technologies.

#### b. Liquid Metal

Liquid Metal can be produced as part of the reactions taking place between liquid slag and solid slag at the interface between the slag bath and the freeze lining.

Liquid Metal is defined to contain only a single liquid phase. This phase is referred to as the Liquid Metal Phase.

The relevant physical properties of this material are given in APPENDIX A.

## i. Liquid Metal Phase

Actual constituents: From chemical analyses this phase is known to contain the following constituents: Al, Cr, Fe, Mn, P, Si, Ti, V, C, and O.

Considered constituents: For the purpose of the FLC model, the following phase constituents were considered: Fe, C, O, Ti, TiO, and Ti<sub>2</sub>O.

Solution model: Unified Interaction Parameter Formalism (Bale and Pelton, 1997)

Thermochemical data: ChemSage format data file from GTT Technologies.

## c. Solid Slag

The freeze lining consists of Solid Slag. Since the freeze lining is the primary consideration of the model, it was necessary to include this material in the model formulation.

Solid Slag is defined to contain the following phases:

- Pseudobrookite Solid Solution Phase
- Rutile Solid Solution Phase

The relevant physical properties of this material are given in APPENDIX A.

## i. Pseudobrookite Solid Solution Phase

Actual constituents: It is known (Pistorius and Coetzee, 2003; FactSage 5.2) that the following ions are found in this phase: Ti<sup>4+</sup>, Ti<sup>3+</sup>, Cr<sup>3+</sup>, Al<sup>3+</sup>, V<sup>3+</sup>, Fe<sup>2+</sup>, Mg<sup>2+</sup>, and Mn<sup>2+</sup>. They occur in a solid solution. The basic forms of the compounds that make up the solid solution are M<sup>2+</sup>(Ti<sup>4+</sup>)<sub>2</sub>O<sub>5</sub> and (M<sup>3+</sup>)<sub>2</sub>OTi<sup>4+</sup>O<sub>5</sub>.

Considered constituents: For the purpose of the FLC model, only the following phase constituents were considered: (FeTi<sub>2</sub>O<sub>5</sub>)<sup>2-</sup>, (Ti<sub>3</sub>O<sub>5</sub>)<sup>+</sup>, FeTi<sub>2</sub>O<sub>5</sub>, and (Ti<sub>3</sub>O<sub>5</sub>)<sup>-</sup>. (The solution model used to describe this phase is an ionic formalism. For this reason some of the constituents are indicated as being ions rather than neutral species.)

Solution model: 2-Sublattice Ionic Formalism (Eriksson et al., 1996; GTT Technologies 1998)

Thermochemical data: ChemSage format data file from GTT Technologies.

## ii. Rutile Solid Solution Phase

Actual constituents: This solid solution can contain the following constituents TiO<sub>2</sub>, Ti<sub>2</sub>O<sub>3</sub>, and ZrO<sub>2</sub> (Eriksson et al., 1996; FactSage 5.2).

Considered constituents: For the purpose of the model being considered in this chapter, only the following phase constituents were considered: TiO<sub>2</sub> and Ti<sub>2</sub>O<sub>3</sub>.

Solution model: General Polynomial Kohler/Toop Formalism (Eriksson et al., 1996; GTT Technologies, 1998)

Thermochemical data: ChemSage format data file from GTT Technologies.

#### d. Magnesite Brick

The furnace wall contains magnesite brick on the level of the slag bath. These bricks consist mostly of MgO with minor levels of impurities. Because no chemical reactions were considered where MgO was involved, this material and its phases were viewed in a simplified manner. For this reason impurities such as Fe<sub>2</sub>O<sub>3</sub>, Al<sub>2</sub>O<sub>3</sub>, CaO and SiO<sub>2</sub> that are known to be present in the brick, were ignored.

Magnesite Brick is defined to contain only a single phase, named Magnesite Phase.

The relevant physical properties of this material are given in APPENDIX A.

#### i. Magnesite Phase

Actual constituents: The phases occurring in the Magnesite Brick are known to contain MgO, Fe<sub>2</sub>O<sub>3</sub>, Al<sub>2</sub>O<sub>3</sub>, CaO and SiO<sub>2</sub>.

Considered constituents: For the purpose of the model being considered in this chapter, the phase is viewed as being pure MgO.

Solution model: None

Thermochemical data: FactSage 5.2. (Bale et al, 2002)

#### e. Ramming

Ramming is used between the steel shell and the refractory brick on the level of the slag bath. Very little information was available about this material, but it seems to consist of mostly graphite. Because no chemical reactions were considered where Ramming was involved, this material and its phases were viewed in a simplified manner.

Ramming is defined to contain only a single phase, named Graphite Phase.

The relevant physical properties of this material are given in APPENDIX A.

#### i. Graphite Phase

Actual constituents: Except for graphite, the phases and phase constituents actually occurring in the Ramming was not known.

Considered constituents: For the purpose of the FLC model, the phase was viewed as being pure carbon.

Solution model: None

Thermochemical data: FactSage 5.2. (Bale et al, 2002)

#### f. Steel

Steel is used for the shell that contains the Ramming, Magnesite Brick and the slag and metal baths. No information was available about this material, but, since it is steel, it could be safely assumed to consist mostly of iron.

Steel is defined to contain only a single phase, named Steel Phase.

#### i. Steel Phase

---

Actual constituents:	Except for Fe and C, the phases and phase constituents actually occurring in the Steel were not known.
Considered constituents:	For the purpose of the FLC model, the phase is viewed as consisting of Fe, C and Mn.
Solution model:	Ideal Mixture
Thermochemical data:	FactSage 5.2. (Bale et al, 2002)

### 3.6.4 Model Structure

The FLC model is primarily a one-dimensional heat transfer model. The final structure of this model is now defined. Because of the confidentiality of actual furnace parameters, the author devised a set of furnace dimensions for use in the current work. It was attempted to choose the dimensions in such a way that the results of this work are relevant to industrial furnace operations.

Heat transfer was modelled by dividing the one-dimensional representation of the region of interest (Figure 17) into layers and the layers into finite-difference nodes. A heat balance was performed on each node during each time step. An explicit finite difference formulation was used.

The following layers were used in the model:

- Freeze Lining (Abbreviated as *FL*. This layer contains both Solid Slag and Liquid Slag material.)
- Brick Layer (Abbreviated as *BL*.)
- Ramming Layer (Abbreviated as *RL*.)
- Steel Layer (Abbreviated as *SL*.)

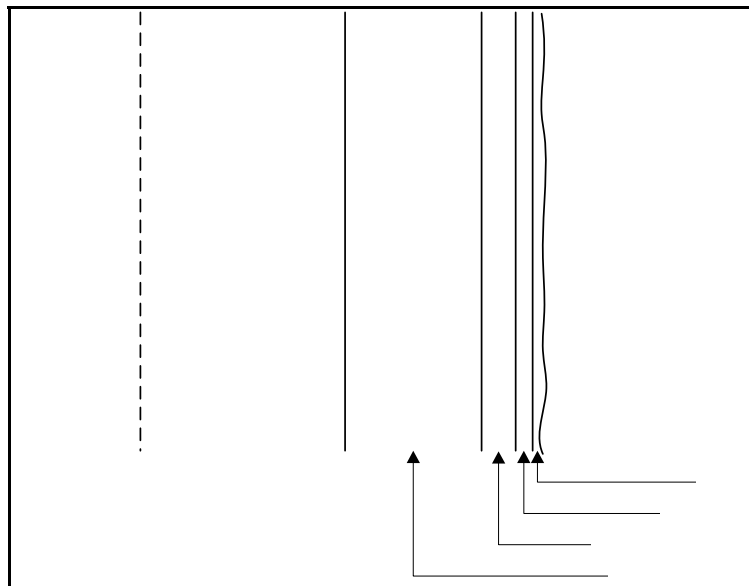


Figure 17 – One-dimensional representation of the region being modelled.

## a. Geometry and dimensions

Coordinate system: Cylindrical

Focus dimension: Radial

The radial dimension range and the freeze lining layer dimensions given below are typical values as these are adjusted to suit the objectives of specific experiments.

Dimension ranges:	Dimension	Min.	Max.	Units
	Radial:	0.000	5.000	m
	Axial:	0.000	1.000	m
	Angular:	0.000	$2\pi$	radians
Layer dimensions:	Layer	Min.	Max.	Units
	Steel Layer:	4.975	5.000	m
	Ramming Layer:	4.925	4.975	m
	Brick Layer:	4.425	4.925	m
	Freeze lining:	0.000	4.425	m
Standard node size:	Layer	Size	Units	
	Steel Layer:	0.00625	m	
	Ramming Layer:	0.010	m	
	Brick Layer:	0.010	m	
	Freeze lining	0.010	m	

The dimensions of the freeze lining layer indicate that it reaches from the centre of the furnace to the inner surface of the brick layer. This does not mean that the entire slag bath is solidified, but rather that the entire slag bath can participate in solidification and melting.

The inner position of the freeze lining can be adjusted to be away from the centre of the furnace if the application of the model requires this. Doing this will mean that the entire slag bath will not participate in solidification and melting of the freeze lining. This becomes necessary if a second conductor module (representing the crust on the slag bath, for example) is linked to the same material mixer (in this case the SlagBath).

### 3.6.5 Heat Transfer

## a. Boundary conditions

Because the conductor was divided into four distinct layers, the number of boundary conditions increased from two (for the case where the conductor is viewed as a single layer) to five.

- Steel layer outer surface boundary condition

Type: Constant temperature (50 °C)

For details about this boundary condition, see paragraph 3.6.1h Assumption 3.8 on page 38.

- Steel-ramming contact boundary condition

Type: Contact heat transfer coefficient

The heat transfer coefficient was increased to the maximum value that did not cause numerical instabilities in the FLC model. The reason for this approach is that this contact resistance was assumed not to be rate-determining. For details about this assumption, see paragraph 3.6.1i Assumption 3.9 on page 38.

- Ramming-brick contact boundary condition

Type: Contact heat transfer coefficient

The heat transfer coefficient was increased to the maximum value that did not cause numerical instabilities in the FLC model. The reason for this approach is that this contact resistance was assumed not to be rate-determining. For details about this assumption, see paragraph 3.6.1i Assumption 3.9 on page 38.

- Brick-slag contact boundary condition

Type: Contact heat transfer coefficient

The heat transfer coefficient was increased to the maximum value that did not cause numerical instabilities in the FLC model. The reason for this approach is that this contact resistance was assumed not to be rate-determining. For details about this assumption, see paragraph 3.6.1i Assumption 3.9 on page 38.

- Freeze lining layer inner surface boundary condition

Type: Ideal insulation

No heat transfer was allowed over the inner surface of the freeze lining layer. The first reason was that this layer was sometimes defined to start at the centre of the furnace, which made heat transfer into the inner surface impossible. Secondly, heat is transferred into the freeze lining layer by the bulk exchange of liquid slag with the slag bath. This is discussed in subsequent paragraphs.

b. List of symbols

SYMBOL	DESCRIPTION	UNITS OF MEASURE
$c_{p,material}(T)$	The heat capacity at constant pressure of the material identified by the subscript at temperature $T$ .	kWh/(kg.°C)
$\Delta H_m^t$	The increase (or decrease if negative) of the enthalpy of a finite-difference node identified by $m$ from time step $t-1$ to time step $t$ .	kWh
$\Delta H_{FEM}^t$	The enthalpy change associated with the equilibrium state calculated by the free energy minimiser.	kWh
$\Delta H_{ref}$	The enthalpy of the material at the reference temperature of, in this case, 298.15 K.	kWh/kg
$H_m^t$	The enthalpy of finite-difference node $m$ at time step $t$ .	kWh
$h_{c,layer1-layer2}$	The contact heat transfer coefficient between the layers identified in the subscript.	kW/(m <sup>2</sup> .°C)
$k_{material}(T)$	The thermal conductivity of the material identified by the subscript at temperature $T$ .	kW/(m.°C)
$M_{layer}$	The number of finite-difference nodes in the layer identified by the subscript.	
$M'_{layer}$	The index identifying the innermost finite-difference node in the layer identified by the subscript.	



SYMBOL	DESCRIPTION	UNITS OF MEASURE
$m$	An index identifying a finite-difference node. Nodes are indexed in ascending order as the position (radial, axial or angular) of the node increases.	
$R_{m,m'}^t$	The heat transfer resistance between finite-difference nodes $m$ and $m'$ at time step $t$ .	$^{\circ}\text{C}/\text{kW}$
$R_{c,layer1-layer2}^t$	The contact heat transfer resistance between the two layers identified in the subscript at time step $t$ .	$^{\circ}\text{C}/\text{kW}$
$r_m$	The radial position of finite-difference node $m$ .	m
$\Delta r_{layer}$	The standard radial dimension of finite-difference nodes in the layer identified by the subscript. Innermost and outermost nodes have half this dimension.	m
$T_m^t$	The temperature of finite-difference node $m$ at time step $t$ .	$^{\circ}\text{C}$
$t$	Used as a superscript to indicate the current time step.	
$V_m$	The volume of finite-difference node $m$ .	$\text{m}^3$
$\Delta z_{layer}$	The standard node size of the layer indicated by the subscript.	m
$\Delta z_{freeze\ lining}$	The axial dimension of the freeze lining.	m
$\rho_{material}$	The density of the material identified by the subscript.	$\text{kg}/\text{m}^3$
$\Delta \tau$	The size of the integration time step of the model.	s

Table 3 – List of symbols used in CHAPTER 3 heat transfer formulation.

#### c. Steel layer outermost node heat balance

Because this node was treated with a constant-temperature boundary condition, no heat balance was done on it.

#### d. Layer outermost node heat balance

The equations formulated below are applicable for all layers except the steel layer.

Change in enthalpy = Energy conducted into left face

+ Heat generated within node

– Energy transferred over contact out of right face

$$\Delta H_{M'_L+1}^{t+1} = H_{M'_L+1}^{t+1} - H_{M'_L+1}^t = \frac{T_{M'_L+2}^t - T_{M'_L+1}^t}{R_{M'_L+2,M'_L+1}^t} \cdot \Delta \tau + \Delta H_{FEM}^t - \frac{T_{M'_L+1}^t - T_{M'_L}^t}{R_{c,L-L2}^t} \cdot \Delta \tau$$

$$H_{M'_L+1}^t = \rho_{material} \cdot V_{M'_L+1} \cdot \left[ \int_{T_{ref}}^{T_{M'_L+1}^t} c_{p,material}(T) dT + H_{ref} \right]$$

$$V_{M'_L+1} = \pi \left( r_{M'_L+1}^2 - \left( r_{M'_L+1} - \frac{\Delta r_L}{2} \right)^2 \right) \cdot \Delta z_{freeze\ lining}$$

$$R_{M'_L+1,M'_L+2}^t = \frac{\Delta r_{L2}}{\left( r_{M'_L+1} - \frac{\Delta r_{L2}}{2} \right) \cdot 2\pi \cdot \Delta z_{freeze\ lining} \cdot k_{material} \left( \frac{T_{M'_L+1}^t + T_{M'_L+2}^t}{2} \right)}$$

$$R_{c,L-L2}^t = \frac{1}{r_{M'_L+1} \cdot 2\pi \cdot \Delta z_{freeze\ lining} \cdot h_{c,L-L2}}$$

$\Delta H_{FEM}^t$  represents heat associated with solidification and melting as calculated by Gibbs-free-energy minimisation. It is only applicable for  $L=FL$ .

For the ramming layer:  $L = SL$   $L2 = RL$   $material = Ramming$

For the brick layer:  $L = RL$   $L2 = BL$   $material = Magnesia Brick$

For the freeze lining:  $L = BL$   $L2 = FL$   $material = Liquid/Solid Slag$

e. Layer internal node heat balance

The equations formulated below are applicable to all layers in the model.

Change in enthalpy = Energy conducted into left face

+ Heat generated within node

– Energy conducted out of right face

$$\Delta H_m^{t+1} = H_m^{t+1} - H_m^t = \frac{T_{m+1}^t - T_m^t}{R_{m,m+1}^t} \cdot \Delta \tau + \Delta H_{FEM}^t - \frac{T_m^t - T_{m-1}^t}{R_{m,m-1}^t} \cdot \Delta \tau$$

$$H_m^t = \rho_{material} \cdot V_m \cdot \left[ \int_{T_{ref}}^{T_m^t} c_{p,material}(T) dT + H_{ref} \right]$$

$$V_m = \pi \left( \left( r_m + \frac{\Delta r_L}{2} \right)^2 - \left( r_m - \frac{\Delta r_L}{2} \right)^2 \right) \cdot \Delta z_{freeze\ lining}$$

$$R_{m,m+1} = \frac{\Delta r_L}{\left( r_m - \frac{\Delta r_L}{2} \right) \cdot 2\pi \cdot \Delta z_{freeze\ lining} \cdot k_{material} \left( \frac{T_m^t + T_{m+1}^t}{2} \right)}$$

$$R_{m,m-1} = \frac{\Delta r_L}{\left( r_m + \frac{\Delta r_L}{2} \right) \cdot 2\pi \cdot \Delta z_{freeze\ lining} \cdot k_{material} \left( \frac{T_m^t + T_{m-1}^t}{2} \right)}$$

$\Delta H_{FEM}^t$  represents heat associated with solidification and melting as calculated by Gibbs-free-energy minimisation. It is only applicable for  $L=FL$ .

For the steel layer:  $L = SL$   $material = Steel$   $1 < m < M'_{SL}$

For the ramming layer:  $L = RL$   $material = Ramming$   $M'_{SL} + 1 < m < M'_{RL}$

For the brick layer:  $L = BL$   $material = Magnesia Brick$   $M'_{RL} + 1 < m < M'_{BL}$

For the freeze lining:  $L = FL$   $material = Solid/Liquid Slag$   $M'_{BL} + 1 < m < M'_{FL}$

f. Layer innermost node heat balance

The equations formulated below are applicable to all layers except for the freeze lining.

Change in enthalpy = Energy transferred over contact into left face  
 + Heat generated within node  
 – Energy conducted out of right face

$$\Delta H_{M'_L}^{t+1} = H_{M'_L}^{t+1} - H_{M'_L}^t = \frac{T_{M'_L+1}^t - T_{M'_L}^t}{R_{c,L-L2}^t} \cdot \Delta \tau + 0 - \frac{T_{M'_L}^t - T_{M'_L-1}^t}{R_{M'_L,M'_L-1}^t} \cdot \Delta \tau$$

$$H_{M'_L}^t = \rho_{material} \cdot V_{M'_L} \cdot \left[ \int_{T_{ref}}^{T_{M'_L}^t} c_{p,material}(T) dT + H_{ref} \right]$$

$$V_{M'_L} = \pi \left( \left( r_{M'_L} + \frac{\Delta r_L}{2} \right)^2 - r_{M'_L}^2 \right) \cdot \Delta z_{freezelining}$$

$$R_{c,L-L2}^t = \frac{1}{r_{M'_L} \cdot 2\pi \cdot \Delta z_{freezelining} \cdot h_{c,L-L2}}$$

$$R_{M'_L,M'_L-1}^t = \frac{\Delta r_L}{\left( r_{M'_L} + \frac{\Delta r_L}{2} \right) \cdot 2\pi \cdot \Delta z_{freezelining} \cdot k_{material} \left( \frac{T_{M'_L}^t + T_{M'_L-1}^t}{2} \right)}$$

For the steel layer:  $L = SL$   $L2 = RL$   $material = Steel$

For the ramming layer:  $L = RL$   $L2 = BL$   $material = Ramming$

For the brick layer:  $L = BL$   $L2 = FL$   $material = Magnesia Brick$

g. Freeze lining innermost node heat balance

This node was treated with an ideal insulation boundary condition on its inner surface. This was done to simplify the model. It means that the model will stop receiving heat from the slag bath once this innermost node has become completely solid.

The radial dimension of the freeze lining layer was chosen in such a way that this never happened. This constraint of the model was therefore avoided by appropriate use of the model.

Change in enthalpy = Energy transferred into left face  
 + Heat generated within node  
 – Energy conducted out of right face

$$\Delta H_{M'_L}^{t+1} = H_{M'_L}^{t+1} - H_{M'_L}^t = 0 + \Delta H_{FEM}^t - \frac{T_{M'_L}^t - T_{M'_L-1}^t}{R_{M'_L,M'_L-1}^t} \cdot \Delta \tau$$

$$H_{M'_L}^t = \rho_{material} \cdot V_{M'_L} \cdot \left[ \int_{T_{ref}}^{T_{M'_L}^t} c_{p,material}(T) dT + H_{ref} \right]$$

$$V_{M'_L} = \pi \left( \left( r_{M'_L} + \frac{\Delta r_L}{2} \right)^2 - r_{M'_L}^2 \right) \cdot \Delta z_{freezelining}$$

$$R_{M'_L,M'_L-1}^t = \frac{\Delta r_L}{\left( r_{M'_L} + \frac{\Delta r_L}{2} \right) \cdot 2\pi \cdot \Delta z_{freezelining} \cdot k_{material} \left( \frac{T_{M'_L}^t + T_{M'_L-1}^t}{2} \right)}$$

$\Delta H'_{FEM}$  represents heat associated with solidification and melting as calculated by Gibbs-free-energy minimisation.

For this layer:  $L = FL$  *material* = Liquid/Solid Slag

#### h. Liquid slag effective thermal conductivity

Because of mixing in the slag bath, the effective thermal conductivity of the liquid slag is higher than the 0.001 kW/(m.°C) that was assumed previously for the solid slag (Assumption 3.6, page 37). The convective heat transfer from the slag bath (and therefore the higher effective thermal conductivity) was accounted for by assigning a higher thermal conductivity value to liquid slag, calculating a single temperature for the entire slag bath at each time step, and then bringing this slag into contact with the freeze lining at its surface. The end result was that virtually no temperature gradient was created in the liquid slag adjacent to the freeze lining.

The influence of effective thermal conductivity was tested during validation of the FLC model. It was not found to have a major influence on modelling results. The effective thermal conductivity that was finally used was 5 times that of the solid slag. This is similar to what has been assumed for liquid metal in the molten core of continuous casting strands (Brimacombe, 1976).

### 3.6.6 Slag Solidification and Melting

Equilibrium solidification and melting of slag was modelled by using a Gibbs-free-energy-minimisation technique. The Gibbs-free-energy minimiser calculates the most stable combination of phases and phase constituents from the material and enthalpy provided as inputs. The ChemApp library (GTT Technologies, 2001) was used for this purpose.

## 3.7 MODEL SOLUTION

### 3.7.1 Flow Sheet

Since the FLC model used the slag bath only as a boundary condition, and the slag bath and its modelling were not included, the FLC model could not be used on its own. It formed part of a larger modelling framework and always had to be incorporated into a larger model that was able to calculate the slag bath state. The modelling framework used for the construction of these models, is the one developed by Pauw (1989). A simple example is given in Figure 18. The remaining discussions about the FLC model will be done within the context of the model presented in Figure 18.

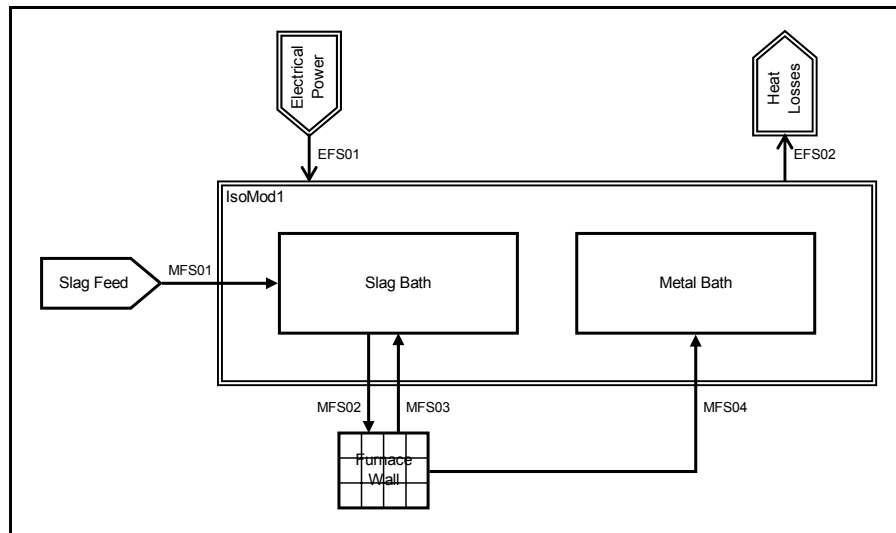


Figure 18 – Flow sheet of a simple process model incorporating the FLC model.

See APPENDIX B for a description of the various model elements.

The elements of the flow sheet presented in Figure 18 are as follows:

- SlagFeed  
The SlagFeed material input module delivers liquid slag that is poured into the SlagBath mixer to establish an initial condition. The material produced by the SlagFeed material input module is discharged into the MFS01 material flow stream.
- MFS01  
The MFS01 material flow stream connects the SlagFeed material input module with the SlagBath mixer. It assists in establishing an initial condition.
- SlagBath  
The SlagBath mixer contains all liquid slag in the system.
- MFS02  
The MFS02 material flow stream connects the SlagBath mixer with the Furnace Wall conductor. It transports material that is about to participate in solidification and melting to the freeze lining.
- FurnaceWall  
The FurnaceWall conductor contains the 4-layer FLC conductor model that is the focus of this chapter.
- MFS03  
The MFS03 material flow stream connects the FurnaceWall conductor with the SlagBath mixer. It transports material that participated in solidification and melting from the freeze lining.

- MFS04  
The MFS04 material flow stream connects the FurnaceWall conductor with the MetalBath mixer. It transports liquid metal that may form as a result of solidification and melting at the freeze lining inner surface.
- MetalBath  
The MetalBath mixer contains all liquid metal in the system.
- ElectricalPower  
The ElectricalPower energy input module delivers electrical energy and represents a furnace electrical system.
- EFS01  
The EFS01 energy flow stream connects the ElectricalPower energy input module with the IsoMod1 isothermal module. In this simplified case, all energy from ElectricalPower reaches IsoMod1.
- IsoMod1  
The IsoMod1 isothermal module represents the slag and metal baths as an isothermal zone.
- EFS02  
The EFS02 energy flow stream connects the IsoMod1 isothermal module with the HeatLosses energy output module. All heat that is lost from the SlagBath and Metal Bath mixers by means other than conduction through the FurnaceWall conductor leaves IsoMod1 through EFS02.
- HeatLosses  
The HeatLosses energy output module represents all heat losses from the SlagBath and Metal Bath mixers other than the losses through the FurnaceWall conductor.

### 3.7.2 Initial Conditions

Before the step-by-step solution of the model was started, it was set up with the following initial conditions:

- The Steel Layer was set up with all nodes being filled with Steel, and with a predetermined temperature for each node. The outermost node temperature was set equal to the constant temperature boundary condition and the other nodes equal to values that were determined not to cause instabilities when the model was started. These temperatures were close to the values that the nodes would converge to.
- The Ramming Layer was handled identically to the Steel Layer, except for its outermost node. This node temperature was also predetermined in such a way that it did not cause instabilities when the model was started.
- The Brick Layer was handled identically to the Ramming Layer.
- The Freeze Lining Layer was handled in the same way as the Ramming Layer, except that this layer was only partially filled with solid slag. The nodes containing solid slag were assigned initial

temperatures. The composition of the solid slag used to fill the slag was the same as the first product that would solidify from the liquid slag bath.

### 3.7.3 Solution

The following procedure was used to solve the model during each time step:

- Fill the Freeze Lining layer void with material from the SlagBath. The void refers to those nodes that do not contain any material. Upon start-up, this includes all freeze lining nodes except those nodes and part of nodes that were filled as part of the initial conditions. Step (a) of Figure 19 shows the condition before filling the void, and step (b) the condition after filling the void.
- For each layer L:
  - Calculate the enthalpy change for each node of L due to heat transfer and calculate the new temperature for each node of L. The result of this is indicated as step (c) of Figure 19. The temperature profile is now different.
  - If L is the Freeze Lining layer:
    - Combine all liquid slag in the layer with a layer of solid slag. The result is shown in step (d) of Figure 19.
    - Calculate the equilibrium state of the combined material by Gibbs-free-energy minimisation. The result is shown in step (e) of Figure 19. More solid slag is now present and the combined material is isothermal.
    - Should any solid material result from the equilibrium calculation, this material is assigned to the outermost node  $m$  that is partially or completely void first, then to its inner neighbour  $m+1$ , then to  $m+2$ , etc. The result is shown in step (f) of Figure 19. A complete thermal profile has been applied to the solid slag layer.
    - Once the solid material has been distributed, the liquid resulting from the equilibrium calculation is used to fill the remaining empty or partially empty nodes. The result is shown in step (f) of Figure 19.
- Drain all liquid slag from the freeze lining and add it back to the SlagBath mixer. The result is shown in step (g) of Figure 19.
- Drain all liquid metal from the freeze lining and add it to the Metal Bath mixer. For the sake of simplicity this is not indicated on Figure 19.
- Calculate new liquid slag composition and IsoMod1 temperature for the current time step ( $t$ ). This is not part of the FLC model since the slag bath is simply used as a boundary condition. It is done by other modules (SlagBath and IsoMod1) in the flow sheet.

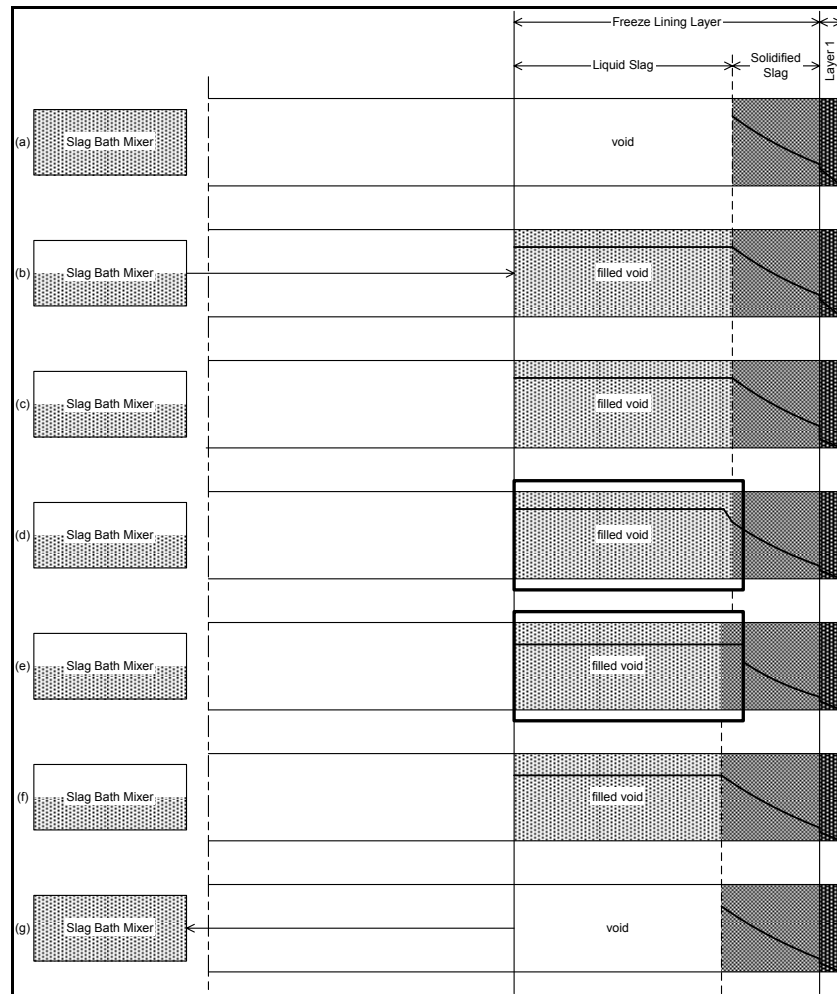


Figure 19 – Schematic representation of steps in the FLC model solution procedure.

### 3.8 MODEL VALIDATION

#### 3.8.1 Purpose

The purpose of validation is to confirm the numerical integrity of the FLC model (Thomas and Brimacombe, 1997).

#### 3.8.2 Objectives

Model validation had to achieve the following objectives:

- Confirm the integrity of the heat transfer calculations.
- Confirm that the combination of the ChemApp Gibbs-free-energy-minimisation routine and the thermochemical data files used by the model calculated realistic equilibrium results.
- Confirm that the model was able to describe solidification and melting of the freeze lining.



### 3.8.3 Methodology

The heat transfer calculations included in the model were validated by checking steady state results generated by the model against a set of analytically calculated steady state results. Example results of the analytical calculation are shown in Figure 20 and Figure 21. From Figure 21 it is clear that the freeze lining generally represents the largest thermal resistance since the steepest fall in temperature occurs in this layer.

The model was initialised with a steady state heat flow rate of 300 kW into the system and through the wall. The input heat flow rate was changed to a new value of either 250 kW or 350 kW. The model was then left to reach a new steady state. The temperatures calculated by the model were then compared with a corresponding analytical solution.

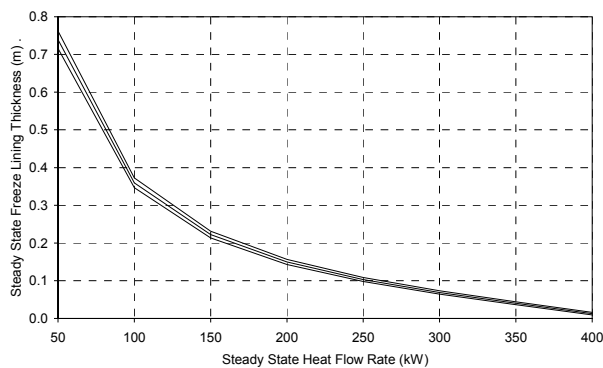


Figure 20 – Analytically calculated steady state freeze lining thickness vs. heat flow rate.

The bottom line represents a slag with a liquidus temperature of 1550 °C, the middle line 1600 °C and the top line 1650 °C.

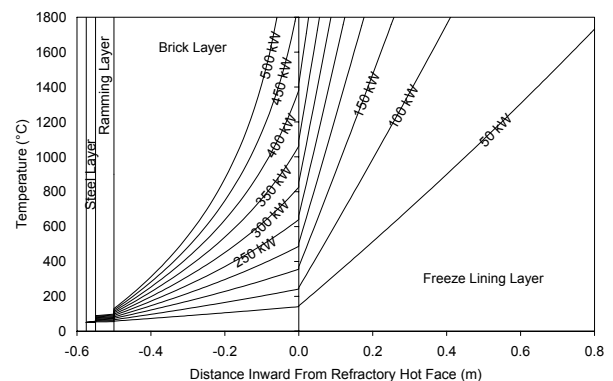


Figure 21 – Analytically calculated steady state temperature profiles.

The ChemApp Gibbs-free-energy-minimisation routine and thermochemical data files were used to generate results that were subsequently compared with results of the same calculations done by FactSage 5.2. Since FactSage contains critically evaluated data of the thermochemical system under consideration, it was believed to be a trustworthy reference. The agreement between the ChemApp and FactSage results was found to be good. This was expected because the ChemApp data file was most probably generated using FactSage 5.2. Details of these comparisons are not presented here.

The results generated by the comparison between model results and analytically calculated results were used to achieve the last validation objective. Because a change in input heat flow rate caused the freeze lining to either become thicker in the case of a reduced input heat flow rate, or thinner in the case of an increased input heat flow rate, these experiments demonstrated whether or not the model was able to describe solidification and melting of the freeze lining.

### 3.8.4 Validation Experiments

#### a. Experiment 3.1

Objective: Confirm the integrity of the model's heat transfer equations, and that the model is able to describe solidification and melting of the freeze lining.

Initial condition: The SlagBath was filled with a 10%-60%-30% (FeO-TiO<sub>2</sub>-Ti<sub>2</sub>O<sub>3</sub> mass percentages) slag at a temperature of 1633 °C. This temperature is close to the liquidus temperature of the slag. The slag composition was chosen to be on the rutile side of the eutectic groove. This meant that rutile was the primary phase that solidified.

The conductivity of the liquid slag was set equal to 0.001 kW/(m.°C), the same as the solid slag.

The freeze lining thickness and the temperature distribution through the freeze lining, brick, ramming and steel were initialised as close as possible to an analytically calculated steady state for a heat flow rate of 300 kW.

Steps: The model was allowed to run until the freeze lining thickness and the temperature distribution through the freeze lining, brick, ramming and steel reached steady state values at 300 kW. This result is referred to as the '300 kW Base Condition'.

With the 300 kW Base Condition as starting point, the input heat flow rate via the ElectricalPower energy input module was then set equal to 250 kW, and the model was allowed to reach a new steady state.

The 300 kW Base Condition was subsequently again used as starting point, the input heat flow rate via the ElectricalPower energy input module was next set equal to 350 kW, and the model was allowed to reach a new steady state.

#### b. Experiment 3.2

Objective: Confirm the integrity of the model's heat transfer equations, and that the model is able to describe solidification and melting of the freeze lining.

Determine the influence of an increase in effective thermal conductivity of the liquid slag.

Initial condition: As for Experiment 3.1, but with a liquid slag conductivity of 0.005 kW/(m.°C).

Steps: As for Experiment 3.1.

#### c. Experiment 3.3

Objective: Confirm the integrity of the model's heat transfer equations, and that the model is able to describe solidification and melting of the freeze lining.

Initial condition: As for Experiment 3.1, but with a slag composition of 10%-50%-40% (FeO-TiO<sub>2</sub>-Ti<sub>2</sub>O<sub>3</sub> mass percentages) and a temperature of 1617 °C.

Steps: As for Experiment 3.1.

d. Experiment 3.4

Objective: Confirm the integrity of the model's heat transfer equations, and that the model is able to describe solidification and melting of the freeze lining.

Determine the influence of an increase in effective thermal conductivity of the liquid slag.

Initial condition: As for Experiment 3.3, but with a liquid slag conductivity of 0.005 kW/(m.°C).

Steps: As for Experiment 3.1.

e. Experiment 3.5

Objective: Confirm the integrity of the model's heat transfer equations, and that the model is able to describe solidification and melting of the freeze lining.

Determine the influence of an increase in effective thermal conductivity of the liquid slag.

Initial condition: As for Experiment 3.3, but with a liquid slag conductivity of 0.010 kW/(m.°C).

Steps: As for Experiment 3.1.

f. Experiment 3.6

Objective: Confirm the integrity of the model's heat transfer equations, and that the model is able to describe solidification and melting of the freeze lining.

Determine the influence of an increase in effective thermal conductivity of the liquid slag.

Initial condition: As for Experiment 3.1, but with a slag composition of 15%-55%-30% (FeO-TiO<sub>2</sub>-Ti<sub>2</sub>O<sub>3</sub> mass percentages), a temperature of 1587 °C and a liquid slag conductivity of 0.005 kW/(m.°C).

Steps: As for Experiment 3.1.

### 3.8.5 Validation Results

Results of the validation experiments are presented below in the form of two graphs per experiment step. The graph on the left-hand side shows a comparison between an analytically calculated steady-state temperature profile of the furnace wall and freeze lining (solid line), and the same profile calculated by the FLC model (crosses).

The second graph shows the difference between temperatures calculated by the FLC model and analytically calculated temperature values. Positive values indicate overestimation by the FLC model.

The reference point (zero) of the radial position is the centre of the furnace.

a. Experiment 3.1

%FeO	%TiO <sub>2</sub>	%Ti <sub>2</sub> O <sub>3</sub>	k <sub>liquid slag</sub>
10	60	30	0.001 kW/(m.°C)

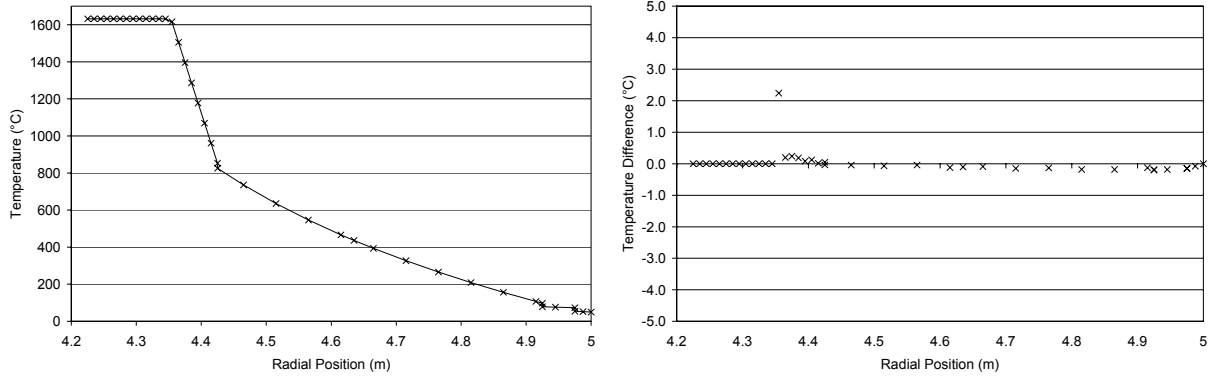


Figure 22 – Validation experiment 3.1 results for a heat flow rate of 300 kW (the 300kW Base Condition).

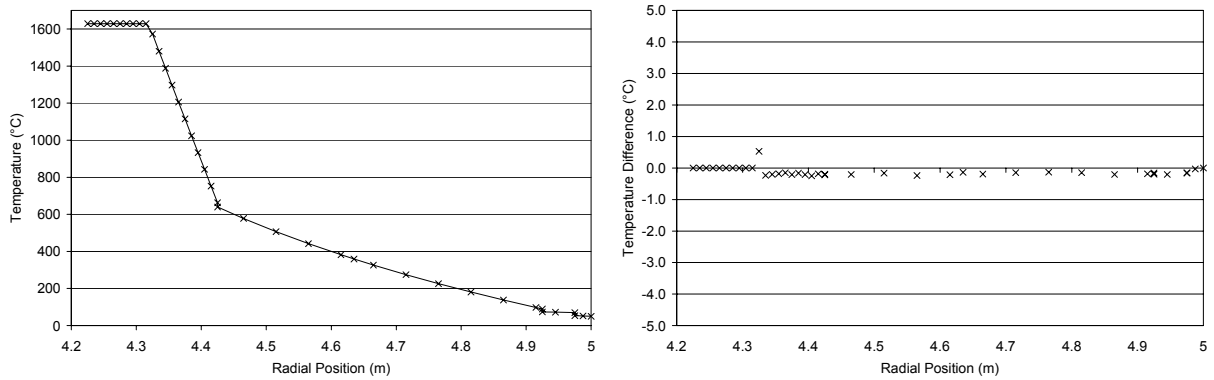


Figure 23 – Validation experiment 3.1 results for a heat flow rate of 250 kW.

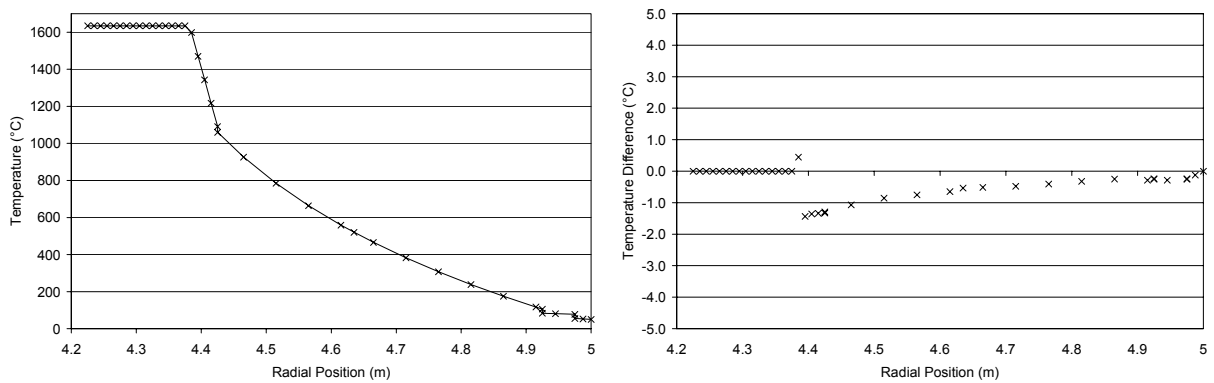


Figure 24 – Validation experiment 3.1 results for a heat flow rate of 350 kW.

b. Experiment 3.2

%FeO	%TiO <sub>2</sub>	%Ti <sub>2</sub> O <sub>3</sub>	k <sub>liquid slag</sub>
10	60	30	0.005 kW/(m.°C)

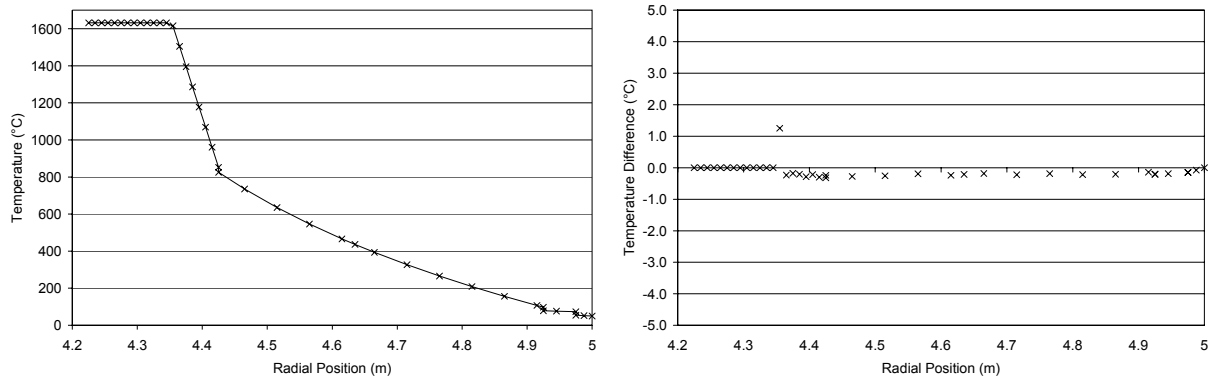


Figure 25 – Validation experiment 3.2 results for a heat flow rate of 300 kW (the 300kW Base Condition).

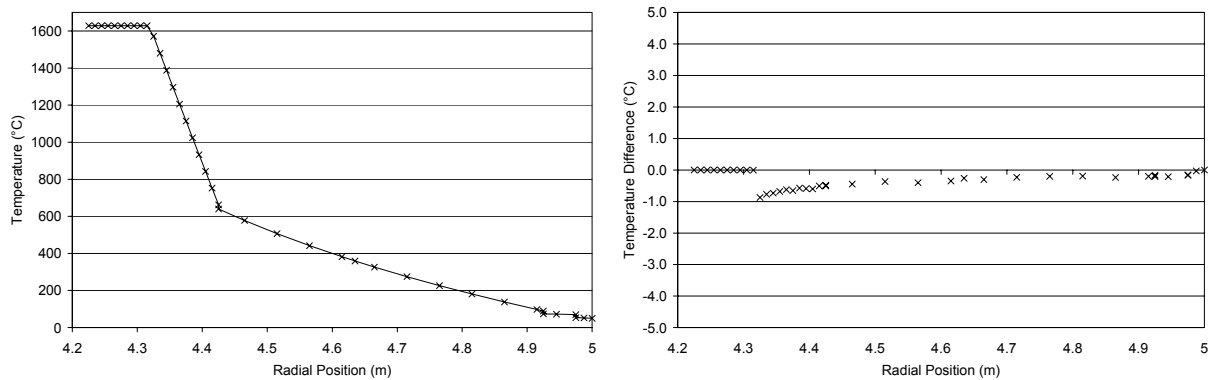


Figure 26 – Validation experiment 3.2 results for a heat flow rate of 250 kW.

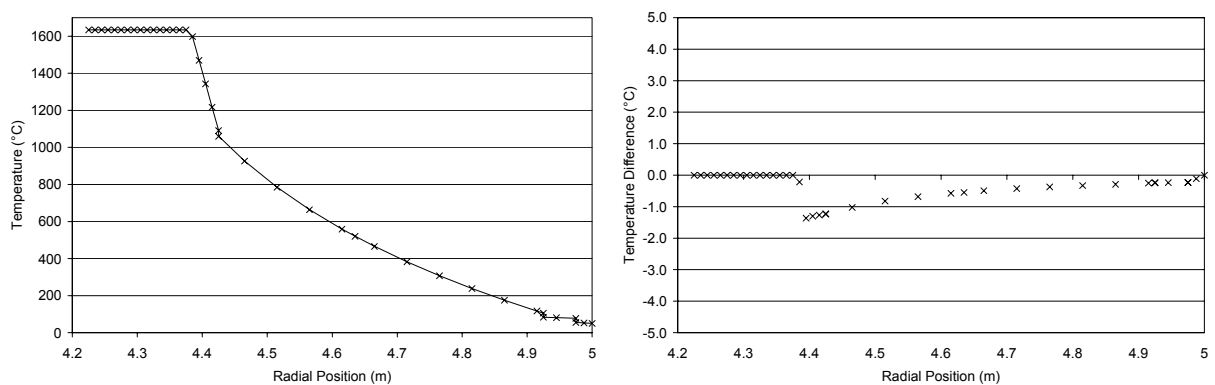


Figure 27 – Validation experiment 3.2 results for a heat flow rate of 350 kW.

c. Experiment 3.3

%FeO	%TiO <sub>2</sub>	%Ti <sub>2</sub> O <sub>3</sub>	k <sub>liquid slag</sub>
10	50	40	0.001 kW/(m.°C)

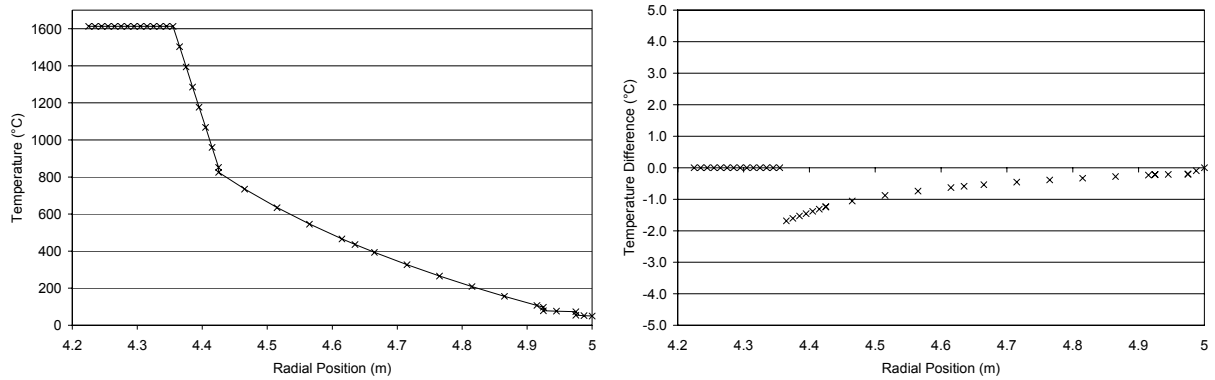


Figure 28 – Validation experiment 3.3 results for a heat flow rate of 300 kW (the 300kW Base Condition).

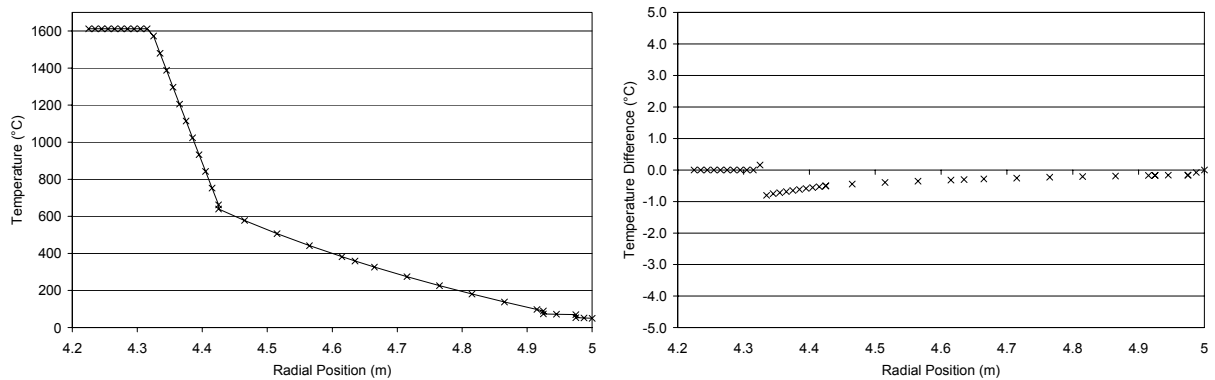


Figure 29 – Validation experiment 3.3 results for a heat flow rate of 250 kW.

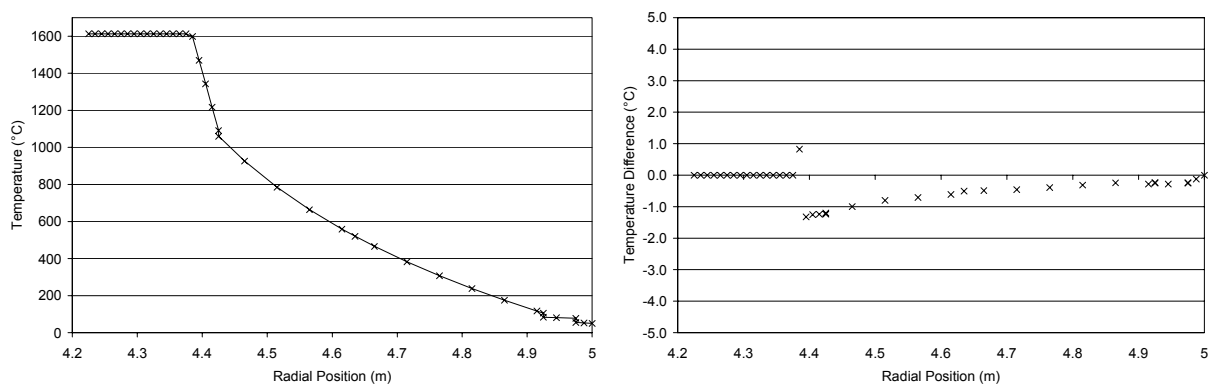


Figure 30 – Validation experiment 3.3 results for a heat flow rate of 350 kW.

d. Experiment 3.4

%FeO	%TiO <sub>2</sub>	%Ti <sub>2</sub> O <sub>3</sub>	k <sub>liquid slag</sub>
10	50	40	0.005 kW/(m.°C)

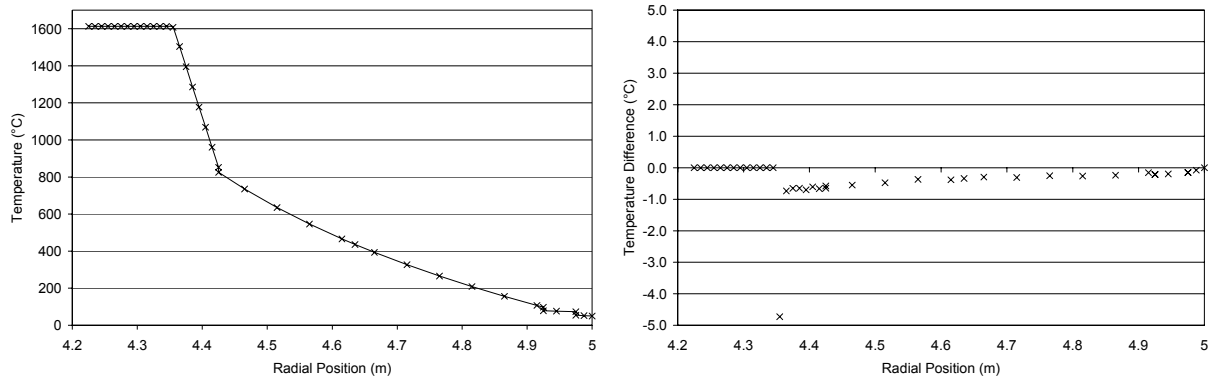


Figure 31 – Validation experiment 3.4 results for a heat flow rate of 300 kW (the 300kW Base Condition).

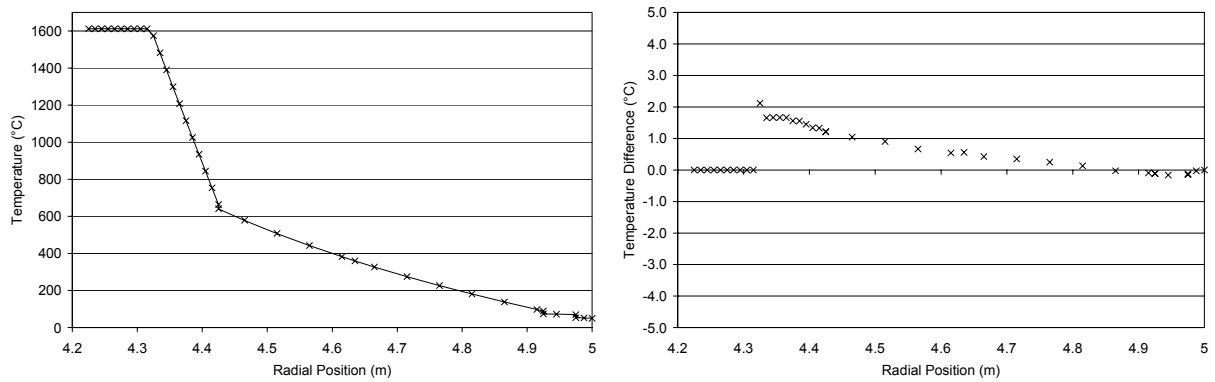


Figure 32 – Validation experiment 3.4 results for a heat flow rate of 250 kW.

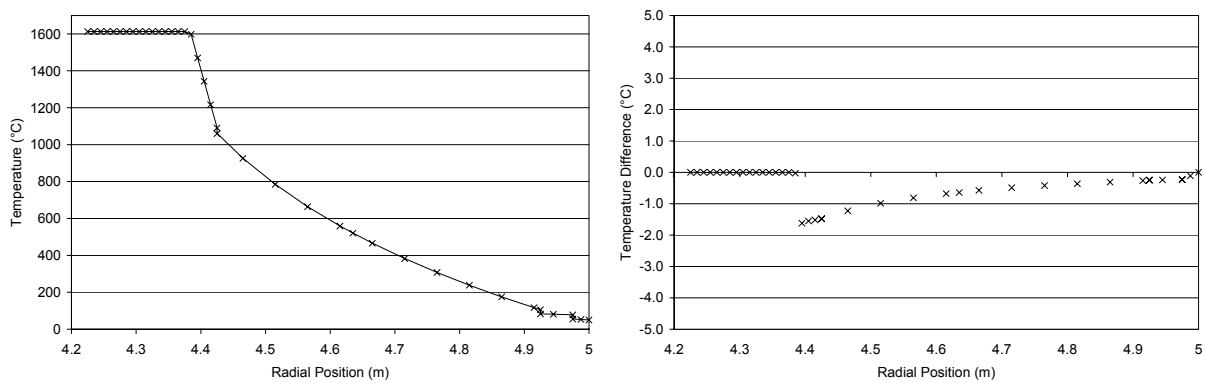


Figure 33 – Validation experiment 3.4 results for a heat flow rate of 350 kW.

e. Experiment 3.5

%FeO	%TiO <sub>2</sub>	%Ti <sub>2</sub> O <sub>3</sub>	k <sub>liquid slag</sub>
10	50	40	0.010 kW/(m.°C)

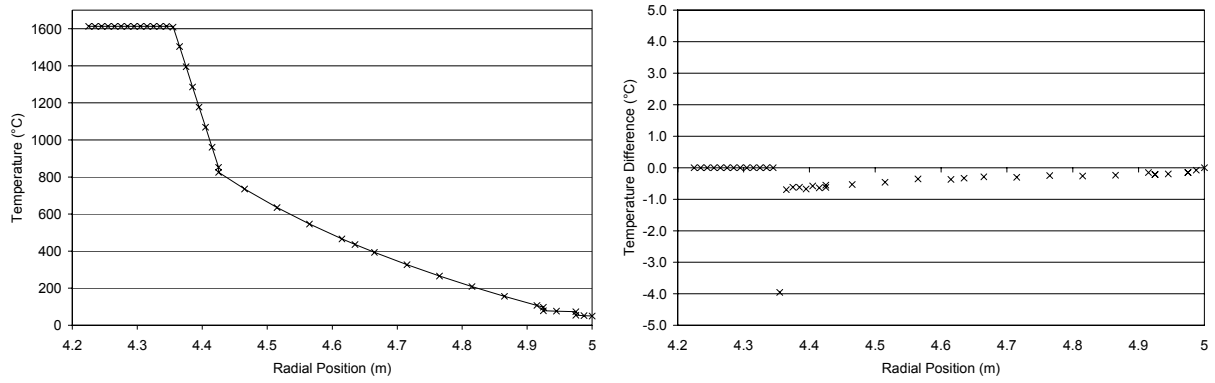


Figure 34 – Validation experiment 3.5 results for a heat flow rate of 300 kW.



f. Experiment 3.6

%FeO	%TiO <sub>2</sub>	%Ti <sub>2</sub> O <sub>3</sub>	k <sub>liquid slag</sub>
15	55	30	0.005 kW/(m.°C)

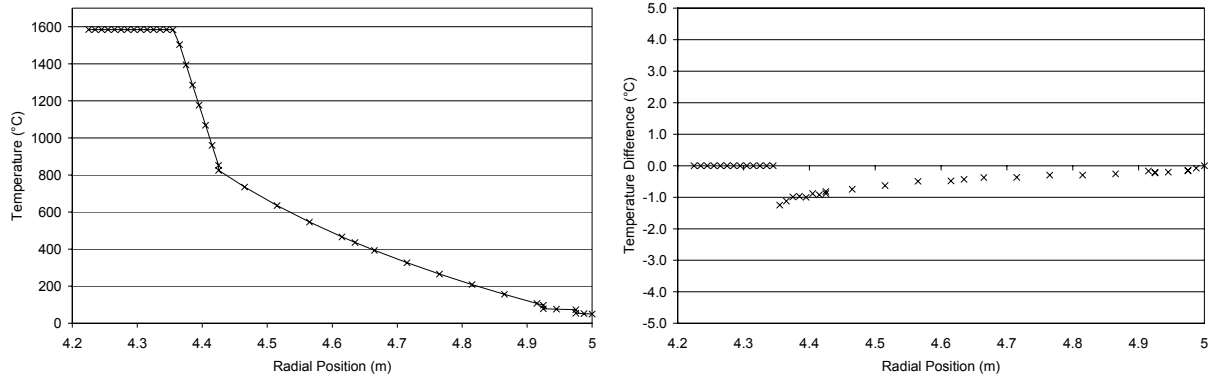


Figure 35 – Validation experiment 3.6 results for a heat flow rate of 300 kW (the 300kW Base Condition).

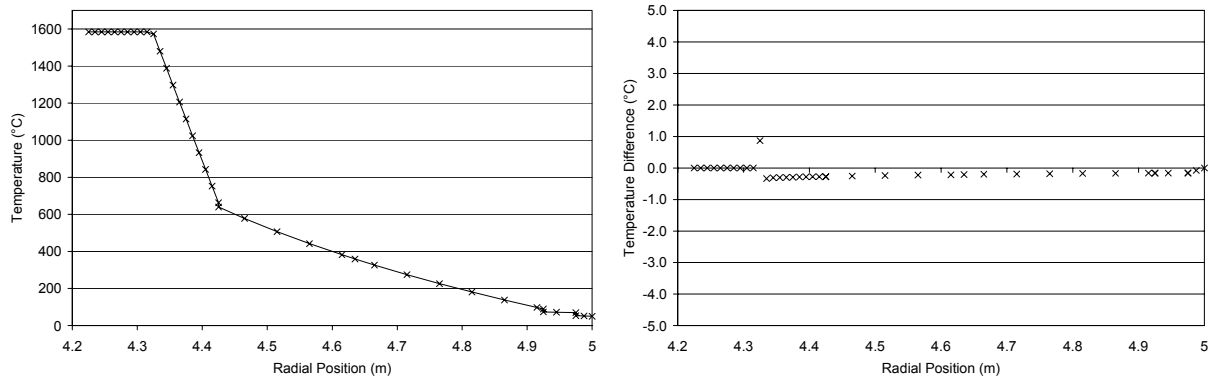


Figure 36 – Validation experiment 3.6 results for a heat flow rate of 250 kW.

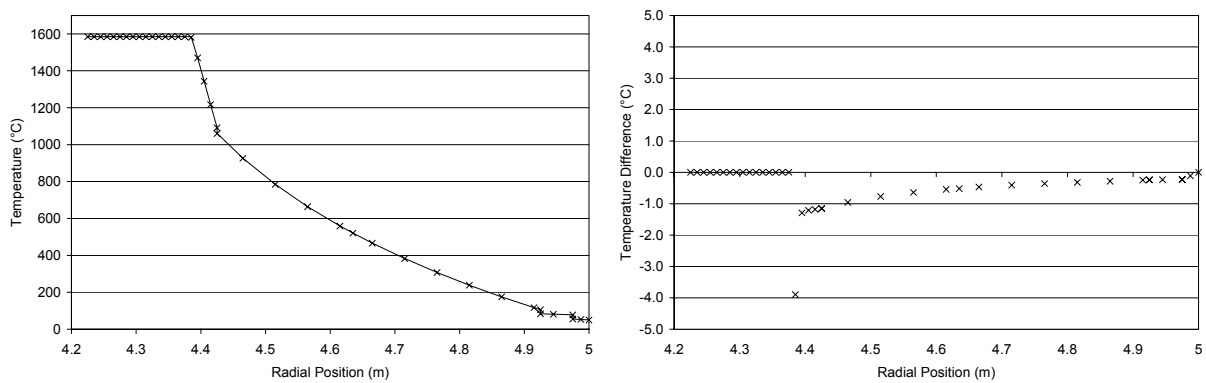


Figure 37 – Validation experiment 3.6 results for a heat flow rate of 350 kW.

g. Summary

A relatively wide range of conditions were covered by the validation experiments listed above. The model was able to reach steady state values that never deviated by more than 5 °C from the analytical solution. The deviations were believed to be due to round-off errors due to the ever-decreasing enthalpy change of the nodes as steady state is approached.

The variation in effective thermal conductivity between the various experiments did not appear to have a large influence. A figure of 0.005 kW/(m.°C) was finally decided on for use during subsequent work.

### **3.9 COMPARISON WITH ACTUAL DATA**

Due to the confidentiality of most information pertaining to the industrial process, no comparison with actual data could be published here. The comparisons against analytically calculated values therefore serve as the only validation of the FLC model.

## CHAPTER 4

### A 1D MODEL OF SOLIDIFICATION ON THE SLAG BATH SURFACE

This chapter describes a dynamic one-dimensional model of the crust that forms on the slag bath surface when furnace inputs are switched off for extended periods of time. The model is used to build a more comprehensive process model (CHAPTER 5, page 89) and in the execution of experiments to investigate phenomena. Details of both these applications are contained in subsequent chapters.

#### 4.1 IDENTIFICATION

The model being described in this chapter is identified as follows:

Name: Slag Bath Crust Conductor Model

Abbreviation: SBCC model

#### 4.2 PROBLEM DEFINITION

The main objective of this study was to investigate the dynamic interaction between the freeze lining and slag bath in an ilmenite-smelting furnace. Part of this objective was to determine whether the eutectic groove present in the FeO-TiO<sub>2</sub>-Ti<sub>2</sub>O<sub>3</sub> ternary system is the reason for the compositional invariance observed in high-titania slag (Pistorius, 2002). This requires that slag solidification and melting in the furnace be modelled as completely as possible. The phase equilibria that are active during solidification and melting change the composition of the slag bath. These changes may be strong enough to cause the mentioned compositional invariance.

The magnitude of the influence of solidification and melting on slag bath composition could partially be determined by the surface area over which solidification and melting occur. The larger the area, the larger this influence could possibly be. Solidification and melting are known to occur in two zones in the furnace. Firstly the freeze lining zone that was described in the previous chapter. Secondly, a crust forms on the surface of the slag bath when the energy and material inputs to the furnace are switched off. This crust starts to melt away again when furnace operation resumes.

It was required to model the thickness, composition and temperature of the crust as functions of time, and, in the case of composition and temperature, as functions of position in the crust.

Because both slag bath temperature and composition are known to have an important influence on the solidification and melting of solid slag, the model had to be able to address both these aspects. The differences between heat transfer from the slag bath surface when the furnace is operational and when it is not, also had to be incorporated into the model.

#### 4.3 SYSTEM DESCRIPTION

Figure 8 (page 13) can again be used as a view of the system currently being considered. In this case the surface of the slag bath is the area being focussed upon.

During normal operation, the slag bath surface is liquid and reductant particles are expected to float on the slag surface. The zone directly underneath the electrode is violently mixed by the momentum that is discharged from the arc and feed material.

Once the furnace is shut down, the thick cloud of dust that is present in the furnace freeboard during normal operation is sucked out by the off-gas system. This drastically increases the rate at which the slag bath can transfer heat to the furnace roof and walls by radiation (Reynolds, 2002). Heat therefore starts leaving the slag bath at a significant rate when the furnace is shut down. In addition to this, some slag reduction still takes place due to reaction between slag and reductant particles, and between slag and carbon dissolved in the metal bath. These endothermic reactions further lower the slag bath temperature. Once the furnace power has been turned off for some time, the slag bath surface starts to crust over.

When the furnace is switched on again, additional energy must be supplied to melt away the crust before normal operation can continue.

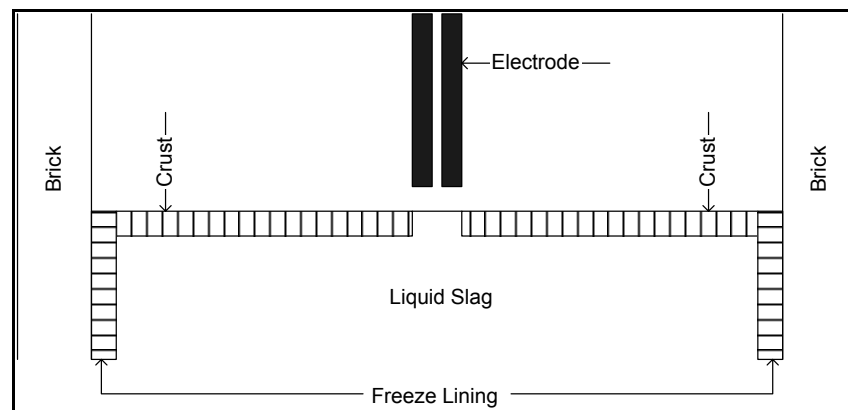


Figure 38 – Schematic representation of the slag bath and crust region of the furnace.

Figure 38 shows the region considered by the model in more detail. The region filled with vertical lines is the crust modelled with the SBCC model. The reason for the hole in the middle of the crust directly underneath the electrode is discussed in a subsequent paragraph.

### 4.3.1 System Geometry

If one only focuses on the crust shown in Figure 38, the system to be modelled is cylindrical. For this reason, phenomena occurring in the furnace will be identified and described based on the cylindrical coordinate system and therefore the following geometrical dimensions:

- Radial dimension
- Axial dimension
- Angular dimension

## 4.4 KEY PHENOMENA

To be able to model a process, one at least needs to be aware of all or most of the phenomena that are active in the process. For this reason, the next few paragraphs aim to identify most of the phenomena that are relevant to the system being considered in this chapter. It also aims to classify these phenomena in terms of their importance to the SBCC model.

#### 4.4.1 Heat Transfer

##### a. Radial heat transfer

When a crust exists in the furnace it is likely that there will be a radial heat transfer component inside the crust. The reason for this is that the centre of the slag bath is generally hotter compared with regions closer to the walls. This generates a driving force for radial heat transfer. These heat transfer vectors are believed to be relatively small due to the low thermal conductivity of the material and the length of the conduction path from the radial centre to the outer radial limit at the wall.

Once the furnace power is switched back on after a crust had formed, the region under the electrode once again becomes the hottest region in the furnace. This will heat up the radial centre of the crust as well, inducing driving forces for radial heat transfer. In this situation it is again believed that the radial heat transfer components will be small compared with axial components due to the same reasons mentioned above.

It is believed that the magnitude of the radial components of heat transfer vectors within the crust is significantly smaller than that of the axial components discussed below. Due to this, radial heat transfer was seen as being less important than axial heat transfer (Assumption 4.1, page 70). It was not believed to be a key phenomenon within the context of the SBCC model.

##### b. Axial heat transfer

When the furnace is switched off and the freeboard emptied of the thick dust cloud that is present during normal operation, the rate at which heat is radiated to the furnace roof and walls increases dramatically (Reynolds, 2002). When considering the top 1 cm layer of the slag bath, the radiation and convection boundary conditions at the top of this layer will induce significant driving forces for axial heat transfer. This extraction of heat from the slag bath top surface does not cause formation of a crust immediately, but as time passes and the slag bath temperature drops, a crust eventually starts to form.

In this crust, axial heat transfer will remain dominant. The crust will initially be thin, with its lower surface in contact with hot liquid slag and its upper surface losing heat via radiation and convection to the furnace roof and walls. With such a temperature gradient across a fairly small axial distance, it is not difficult to envisage that axial heat transfer is of greatest importance. This dominance remains in place for the duration of most down time occurrences on the furnace. It is only when the axial dimension becomes comparable to the radial dimension that radial heat transfer would be of the same order of magnitude as axial heat transfer. This is however not likely to happen since the furnace should not be off for long enough periods of time to result in the formation of such a thick crust.

The important components of axial heat transfer when a crust is not yet present are as follows:

- Forced convection heat transfer in the slag bath transporting heat to and from the surface due to stirring in the bath.
- Radiation from the slag bath surface to the furnace roof and walls.
- Natural convection from the slag bath surface into the furnace atmosphere.

When a crust is present, the important components of axial heat transfer are:

- Forced/natural convection heat transfer transporting heat to and from the crust's lower surface due to stirring in the bath.
- Conduction through the crust.
- Radiation from the crust's upper surface to the sidewalls and roof.
- Forced/natural convection from the crust's upper surface to the furnace atmosphere.

Axial heat transfer, including all the components listed above, was seen as a key phenomenon since modelling of this phenomenon was crucial to the usefulness of the SBCC model. This is due to solidification and melting of the crust moving the interface between crust and slag bath primarily in the axial dimension.

#### c. Angular heat transfer

Because the slag bath surface is some distance above the level of the slag tap holes, it is likely that strong symmetry around the central vertical axis of the furnace exists. It is believed that the slag bath surface in the vicinity of the tap holes may be influenced by the tap holes, but also that this influence should be small. Such influences will result in angular temperature gradients that will induce angular heat transfer components. These components were believed to be insignificant within the context of the SBCC model (Assumption 4.1, page 70).

#### d. Heat sources

The following known heat sources are found in the system or influence the system as boundary conditions:

- Electric arc

The electric arc heats the furnace atmosphere, slag bath and metal bath directly. This heat reaches the crust via convection and radiation.

This heat source was seen as key to the SBCC model.

- Slag solidification

When slag solidifies on the surface of the slag bath or the lower surface of an already existing crust, heat associated with the phase change is liberated.

This heat source was seen as key to the SBCC model because the liberated heat must be accounted for in a heat transfer model of the crust. Ignoring it would have resulted in a serious weakness in the model.

- Chemical reaction

Various chemical reactions (to be discussed in more detail below) can occur in the system. Some of these reactions are exothermic and therefore act as heat sources.

This heat source was seen as key to the SBCC model for reasons similar to those quoted for the heat liberated during slag solidification.

#### e. Heat sinks

The following known heat sinks are found in the system or influence the system as boundary conditions:

- Slag melting

When material melts away on the surface of the crust, heat associated with the phase change is absorbed.

This heat sink was seen as key to the SBCC model for the same reasons as the slag solidification heat source.

- Chemical reaction

Various chemical reactions (to be discussed in more detail below) can occur in the system. Some of these reactions are endothermic and therefore act as heat sinks.

This heat sink was seen as key to the SBCC model for the same reasons as the slag solidification heat source.

### 4.4.2 Mass Transfer

#### a. Convective mass transfer

Due to movement in the slag and metal baths that is induced by the impinging arc, entering feed material, electromagnetic forces and buoyancy forces, slag is transported to and from the slag bath surface.

Convective mass transfer was not seen as a critical/key phenomenon to the SBCC model. The reason is that it is assumed that the slag bath is well mixed due to the momentum transferred to it by the above-mentioned forces (Assumption 4.2, page 70).

#### b. Diffusion

Due to compositional gradients inside the metal and slag baths it is expected that diffusion occurs in these zones.

Compositional gradients can also exist in the crust due to slag of different compositions having solidified at different axial positions. Such gradients also induce diffusion.

Diffusion was not seen as a critical/key phenomenon to the SBCC model. The reason for this is again the strong stirring effects that are present in the metal and slag baths. In the case of the crust it was simply assumed that mass transfer does not have a significant impact on the behaviour of the crust. Ideal mixing in the liquid, with no diffusion in the solid, corresponds to the assumptions of the Scheil model of solidification (Flemings, 1997).

### 4.4.3 Momentum Transfer

#### a. Slag and metal baths

Momentum is transferred to the slag bath by the impinging arc, material fed through the centre of the electrode, and by electromagnetic and buoyancy forces. This results in movement in the slag bath. This

movement can influence the rates at which heat and mass is transferred to and from the slag bath surface and the crust.

Momentum transfer in the slag bath was seen as important phenomena for the model under consideration since it can significantly influence heat transfer at the lower surface of the crust. This phenomenon therefore had to be addressed in the model. It was however believed that it would be adequate to incorporate this phenomenon as a simple boundary condition without modelling it in any great detail.

#### 4.4.4 Chemical Reaction

This paragraph refers back to the description of chemical reactions provided for the FLC model. The major difference between the freeze lining and the crust is that the radial dimension is the focus in the case of the freeze lining, and the axial dimension in the case of the crust. Other than that the descriptions done for the FLC model are completely relevant here.

a. Reaction between liquid slag and liquid slag

Refer to paragraph 3.4.4a on page 32.

b. Reaction between liquid slag and solid slag

Refer to paragraph 3.4.4b on page 32.

c. Reaction between solid slag and solid slag

Refer to paragraph 3.4.4c on page 32.

#### 4.4.5 Summary of Key Phenomena

			Level of importance to current modelling effort		
			1	2	3
Heat transfer	Radial	In slag bath	✓		
		Slag bath to freeze lining	✓		
		In freeze lining	✓		
		Freeze lining to refractory brick	✓		
		In refractory brick	✓		
		Refractory brick to ramming material	✓		
		In ramming material	✓		
		Ramming material to steel shell	✓		
		In steel shell	✓		
		Steel shell to water	✓		
		Axial	In slag bath		✓
	Slag bath to crust				✓
	In crust				✓
	Out of crust top surface				✓
	Angular	In slag bath	✓		
		In crust	✓		
	Heat sources	Electric arc			✓
		Slag solidification			✓
		Chemical reaction			✓
Heat sinks	Slag melting			✓	
	Chemical reaction			✓	
Mass transfer	Convection	In slag bath	✓		
		In crust	✓		
	Diffusion				
Momentum	Slag bath		✓		



transfer	Metal bath		✓			
Chemical reaction	Liquid slag	With liquid slag	✓			
	Liquid slag	With solid slag				✓
	Solid slag	With solid slag	✓			

Table 4 – Summary of key phenomena for the SBCC model.

## 4.5 APPROACH AND MODEL COMPLEXITY

From the table summarising key phenomena it can be concluded that axial heat transfer, heat sources and sinks, and chemical reaction are of greatest importance to the SBCC model. Among these the heat-related phenomena are most basic to the problem being studied. The reason is that the thermal phenomena drive the chemical reactions that take place. Increase in temperature results in melting and decrease in temperature results in solidification. It must however also be stated that variations in slag bath composition without temperature variations could have the same influences.

Due to the general importance of heat-related phenomena in the system, heat transfer was used as the foundation of the model. The chemical reactions were modelled within the heat transfer framework where applicable.

### 4.5.1 Modelling of Heat Transfer

Because radial and angular heat transfer were identified to be of significantly less importance than axial heat transfer, and because this model was the first attempt at building a mathematical representation of the system, it was decided to model heat transfer in the axial dimension only. The model was therefore one-dimensional with the axial dimension being labelled the ‘focus dimension’.

The range of radial positions in the furnace that were used, were chosen to start at a distance equal to the radius of the graphite electrode away from the radial centre furnace up to some short distance away from the inner surface of the furnace wall.

The reason for not starting at the centre of the furnace was to avoid having the arc influence the one-dimensional crust model when the furnace is started up. The arc can transfer heat directly to the liquid slag bath through the hole in the crust. This is a simplification that was used to avoid having to consider a second dimension (Simplification 4.1, page 71).

The reason for ending the radial dimension some distance from the wall was because the FLC model described in the previous chapter would typically be used together with the SBCC model in a complete process model of the furnace. Defining the radial range of the SBCC to stop some distance away from the wall prevented the two models from overlapping. This is also a simplification (Simplification 4.2, page 71).

The angular range used is the entire circumference of the furnace. The influence of tap holes was ignored in this model.

The range of the axial dimension that was used started at top of the slag bath and ended some distance below this surface. The distance that the model’s axial dimension extends into the slag bath was chosen in such a way that there was room for the interface between the slag bath and crust to move sufficiently (by solidification and melting) to achieve the desired experimental results.

## a. Solution method

A finite difference method was used to solve the heat transfer problem. An explicit formulation was used.

### 4.5.2 Modelling of Chemical Reaction

Modelling of chemical reactions relevant to the crust was done in the same way as it was done for the FLC model. Refer to paragraph 3.5.2 on page 35. The relevant assumption in the case of the SBCC model is Assumption 4.4 (page 70).

## 4.6 MODEL FORMULATION

### 4.6.1 Assumptions

The following paragraphs list assumptions made as part of the SBCC model formulation. The paragraphs clarify why the assumptions were made, their validity and the impact that the assumptions have on the model.

## a. Assumption 4.1

Statement: Radial and angular heat transfer components are negligible and can be ignored.

Justification: This assumption is required to simplify the model. A one-dimensional model is significantly simpler and more manageable compared with two- and three-dimensional models.

Validity: The assumption is not completely true, since the existence of radial and angular heat transfer components can easily be proven. It is however true that the axial heat transfer components should be significantly larger than the radial and angular components. It was therefore acceptable given the objectives of the current work.

Impact: This assumption causes inaccuracies in the predictions of the model. These inaccuracies were viewed as being in balance with other uncertainties (measurement inaccuracies, uncertainty about dimensions, and uncertainty about material properties) in the process, and they were therefore viewed as not being significant within the context of the SBCC model and its current application.

## b. Assumption 4.2

This assumption is the same as Assumption 3.2 of the FLC model. The reader is therefore referred to page 36 for detail.

## c. Assumption 4.3

Assumption 3.3 of the FLC model applied to the crust layer is relevant here. Refer to page 36 for detail.

## d. Assumption 4.4

Assumption 3.4 of the FLC model applied to the interface between slag bath and crust is relevant here. Refer to page 36 for detail.

## e. Assumption 4.5

Assumption 3.5 of the FLC model applied only to liquid and solid slag is relevant here. Refer to page 37 for detail.

## f. Assumption 4.6

Assumption 3.6 of the FLC model is relevant here. Refer to page 37 for detail.

## g. Assumption 4.7

Assumption 3.7 of the FLC model applied to the crust layer is relevant here. Refer to page 37 for detail.

### 4.6.2 Simplifications

The following paragraphs list simplifications that were made in the model. The justification and impact of the simplifications are also presented.

## a. Simplification 4.1

Description: The inner radial limit of the crust is defined to start a distance equal to the radius of the graphite electrode away from the radial centre.

Justification: This simplification was made to avoid having to consider a second dimension (the radial dimension) when the furnace starts up after a crust had formed. The arc can simply transfer its heat through the hole left in the crust directly below the electrode.

Impact: The simplification introduces inaccuracies into the model, but since the surface area of the region under the electrode that is effectively ignored by the crust model is small relative to the remaining bath surface area, the inaccuracies were acceptable.

## b. Simplification 4.2

Description: The outer radial limit of the crust is defined to end some distance away from the inner surface of the furnace refractory wall.

Justification: This simplification was made to avoid overlap between the FLC model and the SBCC models when these models are used together in a larger process model.

Impact: The simplification introduces inaccuracies into the model, but since the surface area of the region next to the wall that is ignored by the crust model is small relative to the remaining bath surface area (between 4% and 13% of the total bath area for typical freeze lining thicknesses), the inaccuracies were tolerable.

### 4.6.3 Material Definitions

The definitions of the Liquid Slag and Solid Slag materials used in the SBCC model are identical to the definitions used for the FLC model. The reader is therefore referred back to the definitions made in the chapter on the FLC model.

## a. Liquid Slag

Refer to paragraph 3.6.3a on page 39.

## b. Liquid Metal

Refer to paragraph 3.6.3b on page 39.

## c. Solid Slag

Refer to paragraph 3.6.3c on page 40.

#### 4.6.4 Model Structure

The SBCC model is primarily a one-dimensional heat transfer model. The final structure of this model is now defined. Because of the confidentiality of actual furnace parameters, the author devised a set of furnace dimensions for use in the current work. It was attempted to choose the dimensions in such a way that the results of this work are relevant to industrial furnace operations.

Heat transfer was modelled by dividing the zone shown in Figure 39 into finite-difference nodes in the axial dimension. The boundaries between these nodes are indicated with horizontal dotted lines. A heat balance was then performed on each node during each time step. An explicit finite difference formulation was used.

In contrast with the FLC model, this model only had one layer making up the conductor. It was called the crust layer and abbreviated as CL.

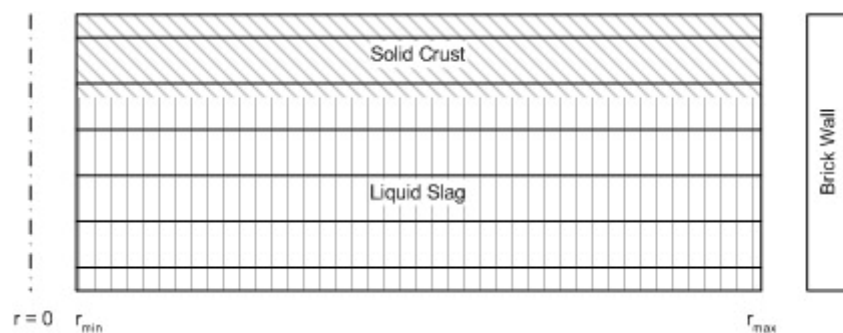


Figure 39 – Representation of the finite-difference model used to describe the crust.

## a. Geometry and dimensions

Coordinate system: Cylindrical

Focus dimension: Axial

The axial dimension range and therefore the crust layer dimensions given below are typical values as these are adjusted to suit specific experimental objectives.

Dimension ranges:	Dimension	Min.	Max.	Units
	Radial:	0.030	4.425	m
	Axial:	0.000	1.000	m
	Angular:	0.0	$2\pi$	radians
Layer dimensions:	Layer	Min.	Max.	Units
	Crust layer:	0.000	1.000	m

---

Standard node size:	Layer	Size	Units
	Crust layer	0.010	m

The dimensions of the Crust Layer can be adjusted so that it includes the entire slag bath. If this is done, the entire volume of liquid slag will be able to participate in the calculation of solidification and melting equilibria. If some portion of the slag bath is excluded, that portion will not participate. By doing this, the model can be manipulated to be closer or further from complete (thermal) equilibrium in the slag bath. Excluding some portion of the slag bath becomes necessary when additional conductor modules are included in process model.

#### 4.6.5 Heat Transfer

##### a. Boundary conditions

Because the conductor consists of only a single layer the number of boundary conditions is equal to two (the inner (lower) boundary in contact with liquid slag and the outer (upper) boundary representing the slag bath surface that is in contact with the furnace atmosphere).

- Crust layer outer surface boundary condition

Type: Effective heat transfer coefficient

Radiation and convection heat transfer are of importance at this boundary. Determining the magnitude of either of these components is difficult, especially for the conditions prevalent when the furnace is in operation. For this reason wall and roof heat losses on the furnace were used to determine an effective heat transfer coefficient.

These boundary condition values were determined from a study on radiation heat transfer in the furnace freeboard (Reynolds, 2002). The results of that study were used to determine an estimate of the effective heat transfer coefficient. It was concluded from that work that the heat transfer coefficient could vary from 0.010 to 0.050 kW/(m<sup>2</sup>.°C). The actual figures depend on numerous factors such as configuration of the sidewalls and roof, dust loading in the freeboard during operation, geometry of the roof, etc. A value of 0.019 kW/(m<sup>2</sup>.°C) was decided upon for use while the furnace is operational, and 0.027 kW/(m<sup>2</sup>.°C) when the furnace is off. In all cases 25 °C was used as the temperature towards which heat was transferred. This served as an estimate of the temperature of the cooling water on the outside of the sidewalls and roof. Because no actual plant data could be used for determination of the heat transfer coefficient, these rough estimates were used.

- Crust layer inner surface boundary condition

Type: Ideal insulation

No heat transfer was allowed over the inner surface of the crust layer. The reason is that heat is transferred into the crust layer by the bulk exchange of liquid slag with the slag bath. This is discussed in subsequent paragraphs.

## b. List of symbols

SYMBOL	DESCRIPTION	UNITS OF MEASURE
$c_{p,material}(T)$	The heat capacity at constant pressure of the material identified by the subscript at temperature $T$ .	kWh/(kg.°C)
$\Delta H_m^t$	The increase (or decrease if negative) of the enthalpy of a finite-difference node identified by $m$ from time step $t-1$ to time step $t$ .	kWh
$\Delta H_{FEM}^t$	The enthalpy change associated with the equilibrium state calculated by the free energy minimiser.	kWh
$\Delta H_{ref}$	The enthalpy of the material at the reference temperature of, in this case, 298.15 K.	kWh/kg
$H_m^t$	The enthalpy of finite-difference node $m$ at time step $t$ .	kWh
$h_{eff}^t$	Effective heat transfer coefficient at time step $t$ .	kW/(m <sup>2</sup> .°C)
$k_{material}(T)$	The thermal conductivity of the material identified by the subscript at temperature $T$ .	kW/(m.°C)
$M_{layer}$	The number of finite-difference nodes in the layer identified by the subscript.	
$m$	An index identifying a finite-difference node. Nodes are indexed in ascending order as the position (radial, axial or angular) of the node increases.	
$R_{h_{eff}}^t$	The effective heat transfer coefficient resistance from the top of the slag bath surface of crust surface at time step $t$ .	°C/kW
$R_{m,m'}^t$	The heat transfer resistance between finite-difference nodes $m$ and $m'$ at time step $t$ .	°C/kW
$r_{max,crust}$	The radial position of the outer radial surface of the crust layer.	m
$r_{min,crust}$	The radial position of the inner radial surface of the crust layer.	m
$T_\infty^t$	The temperature of the ambient environment at time step $t$ .	°C
$T_m^t$	The temperature of finite-difference node $m$ at time step $t$ .	°C
$t$	Used as a superscript to indicate the current time step.	
$V_m$	The volume of finite-difference node $m$ .	m <sup>3</sup>
$\Delta z_{layer}$	The standard node size of the layer indicated by the subscript.	m
$\rho_{material}$	The density of the material identified by the subscript.	kg/m <sup>3</sup>
$\Delta \tau$	The size of the integration time step of the model.	s

Table 5 - List of symbols used in CHAPTER 4 heat transfer formulation.

## c. Crust layer outermost node heat balance

Change in enthalpy = Energy conducted into lower face

+ Heat generated within node

- Energy transferred via radiation and convection out of upper face

$$\Delta H_1^{t+1} = H_1^{t+1} - H_1^t = \frac{T_2^t - T_1^t}{R_{1,2}^t} \cdot \Delta \tau + \Delta H_{FEM}^t - \frac{T_1^t - T_\infty^t}{R_{h_{eff}}^t} \cdot \Delta \tau$$

$$H_1^t = \rho_{slag} \cdot V_1 \cdot \left[ \int_{T_{ref}}^{T_1^t} c_{p,slag}(T) dT + H_{ref} \right]$$

$$V_1 = \pi \cdot (r_{\max,crust}^2 - r_{\min,crust}^2) \cdot \frac{\Delta z_{CL}}{2}$$

$$R_{1,2}^t = \frac{\Delta z_{CL}}{\pi \cdot (r_{\max,crust}^2 - r_{\min,crust}^2) \cdot k_{slag} \left( \frac{T_1^t + T_2^t}{2} \right)}$$

$$R_{h_{eff}}^t = \frac{1}{\pi \cdot (r_{\max,crust}^2 - r_{\min,crust}^2) \cdot h_{eff}^t}$$

$\Delta H_{FEM}^t$  represents heat associated with solidification and melting as calculated by Gibbs-free-energy minimisation.

d. Crust layer internal node heat balance

Change in enthalpy = Energy conducted into lower face

+ Heat generated within node

- Energy conducted out of upper face

$$\Delta H_m^{t+1} = H_m^{t+1} - H_m^t = \frac{T_{m+1}^t - T_m^t}{R_{m,m+1}^t} \cdot \Delta \tau + \Delta H_{FEM}^t - \frac{T_m^t - T_{m-1}^t}{R_{m,m-1}^t} \cdot \Delta \tau$$

$$H_m^t = \rho_{slag} \cdot V_m \cdot \left[ \int_{T_{ref}}^{T_m^t} c_{p,slag}(T) dT + H_{ref} \right]$$

$$V_m = \pi \cdot (r_{\max,crust}^2 - r_{\min,crust}^2) \cdot \Delta z_{CL}$$

$$R_{m,m+1}^t = \frac{\Delta z_{CL}}{\pi \cdot (r_{\max,crust}^2 - r_{\min,crust}^2) \cdot k_{slag} \left( \frac{T_m^t + T_{m+1}^t}{2} \right)}$$

$$R_{m,m-1}^t = \frac{\Delta z_{CL}}{\pi \cdot (r_{\max,crust}^2 - r_{\min,crust}^2) \cdot k_{slag} \left( \frac{T_m^t + T_{m-1}^t}{2} \right)}$$

$\Delta H_{FEM}^t$  represents heat associated with solidification and melting as calculated by Gibbs-free-energy minimisation.

e. Crust layer innermost node heat balance

Change in enthalpy = Energy transferred into lower face

+ Heat generated within node

- Energy conducted out of upper face

$$\Delta H_{M_{CL}}^{t+1} = H_{M_{CL}}^{t+1} - H_{M_{CL}}^t = 0 + \Delta H_{FEM}^t - \frac{T_{M_{CL}}^t - T_{M_{CL}-1}^t}{R_{M_{CL},M_{CL}-1}^t} \cdot \Delta \tau$$

$$H_{M_{CL}}^t = \rho_{slag} \cdot V_{M_{CL}} \cdot \left[ \int_{T_{ref}}^{T_{M_{CL}}^t} c_{p,slag}(T) dT + H_{ref} \right]$$

$$V_{M_{CL}} = \pi \cdot (r_{\max,crust}^2 - r_{\min,crust}^2) \cdot \frac{\Delta z_{CL}}{2}$$

$$R_{M_{CL},M_{CL-1}}^t = \frac{\Delta z_{CL}}{\pi \cdot (r_{\max,crust}^2 - r_{\min,crust}^2) \cdot k_{slag} \left( \frac{T_{M_{CL}}^t + T_{M_{CL-1}}^t}{2} \right)}$$

$\Delta H_{FEM}^t$  represents heat associated with solidification and melting as calculated by Gibbs-free-energy minimisation.

#### f. Liquid slag effective thermal conductivity

The liquid slag effective thermal conductivity was handled the same as in the FLC model. Refer to paragraph 3.6.5h on page 48.

### 4.6.6 Slag Solidification and Melting

Slag solidification and melting was handled the same as in the FLC model. Refer to paragraph 3.6.6 on page 48.

## 4.7 MODEL SOLUTION

### 4.7.1 Flow Sheet

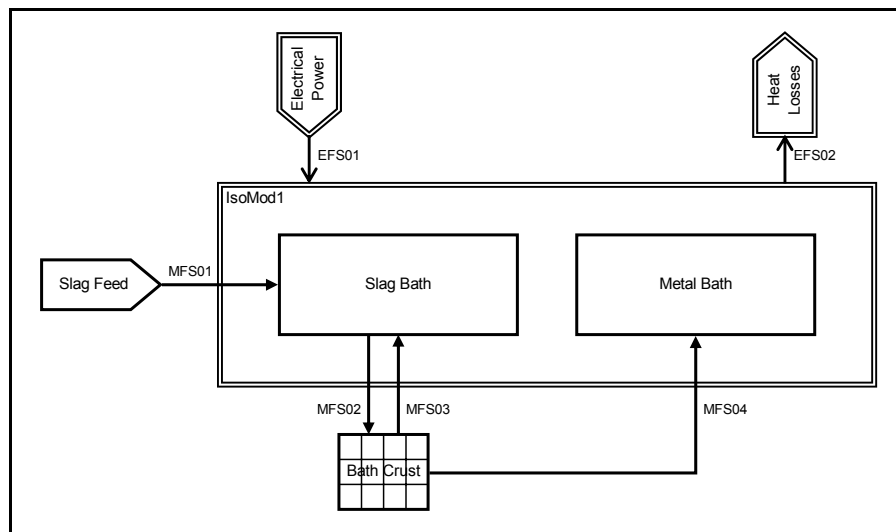


Figure 40 – Flow sheet of a simple process model incorporating the SBCC model.

Since the SBCC model used the slag bath only as a boundary condition, and the slag bath and its modelling were not included, the SBCC model could not be used on its own. It formed part of a larger modelling framework and always had to be incorporated into a larger model that was able to calculate the slag bath state. The modelling framework used for the construction of such models, is the one developed by Pauw (1989). A simple example is given in Figure 40. The remaining discussions about the SBCC model will be done within the context of the model presented in Figure 40.

See APPENDIX B for a description of the various model elements.



The elements of the flow sheet presented in Figure 40 are as follows:

- SlagFeed  
The SlagFeed material input module delivers liquid slag that is poured into the SlagBath mixer to establish an initial condition. The material produced by the SlagFeed material input module is discharged into the MFS01 material flow stream.
- MFS01  
The MFS01 material flow stream connects the SlagFeed material input module with the SlagBath mixer. It assists in establishing an initial condition.
- SlagBath  
The SlagBath mixer contains all liquid slag in the system.
- MFS02  
The MFS02 material flow stream connects the SlagBath mixer with the BathCrust conductor. It transports material that is about to participate in solidification and melting to the crust.
- BathCrust  
The BathCrust conductor is the single-layer SBCC model that is the main focus of this chapter.
- MFS03  
The MFS03 material flow stream connects the BathCrust conductor with the SlagBath mixer. It transports material that participated in solidification and melting from the crust.
- MFS04  
The MFS04 material flow stream connects the BathCrust conductor with the MetalBath mixer. It transports liquid metal that may form as a result of solidification and melting at the crust.
- MetalBath  
The MetalBath mixer contains all liquid metal in the system.
- ElectricalPower  
The ElectricalPower energy input module delivers electrical energy and represents a furnace electrical system.
- EFS01  
The EFS01 energy flow stream connects the ElectricalPower energy input module with the IsoMod1 isothermal module. In this simplified case, all energy from ElectricalPower reaches IsoMod1.
- IsoMod1  
The IsoMod1 isothermal module represents the slag and metal baths as an isothermal zone.
- EFS02  
The EFS02 energy flow stream connects the IsoMod1 isothermal module with the HeatLosses energy output module. All heat that is lost from the SlagBath and Metal Bath mixers by means other than conduction through the BathCrust conductor leaves IsoMod1 through EFS02.

- HeatLosses

The HeatLosses energy output module represents all heat losses from the SlagBath and Metal Bath mixers other than the losses through the BathCrust conductor.

#### 4.7.2 Initial Conditions

Before the step-by-step solution of the model was started, it was set up with the following initial conditions:

- The crust layer was set up with all nodes being empty and containing neither solid nor liquid slag.

#### 4.7.3 Solution

The following procedure was used to solve the model during each time step:

- Fill the crust layer void with material from the SlagBath. The void refers to those nodes that do not contain any material. Upon start-up, this will include all Crust Layer nodes. Figure 41 shows the model solution procedure schematically for a time step where some solid slag is already present. Step (a) of Figure 41 shows the condition before filling the void, and step (b) the condition after filling the void.
  - For the Crust Layer:
    - Calculate the enthalpy change for each node due to heat transfer and calculate the new temperature for each node. The result of this is indicated as step (c) of Figure 41. The temperature profile is now different.
    - Combine all liquid slag in the layer with a layer of solid slag. The result is shown in step (d) of Figure 41.
    - Calculate the equilibrium state of the combined material by Gibbs-free-energy minimisation. The result is shown in step (e) of Figure 41. More solid slag is now present and the combined material is isothermal.
    - Should any solid material result from the equilibrium calculation, this material is assigned to the outermost node  $m$  that is partially or completely void first, then to its inner neighbour  $m+1$ , then to  $m+2$ , etc. The result is shown in step (f) of Figure 41. A complete thermal profile has been applied to the Crust Layer.
    - Once the solid material has been distributed, the liquid resulting from the equilibrium calculation is used to fill the remaining empty or partially empty nodes. The result is shown in step (f) of Figure 41.
  - Drain all liquid slag from the crust layer and add it back to the SlagBath. The result is shown in step (g) of Figure 41.
  - Drain all liquid metal from the crust layer and add it to the Metal Bath mixer. For the sake of simplicity this is not indicated on Figure 19.
  - Calculate new liquid slag composition and IsoMod1 temperature for the current time step ( $t$ ).
-

This is not part of the SBCC model since the slag bath is simply assumed to be a boundary condition. It is done by other modules (SlagBath and IsoMod1) in the flow sheet.

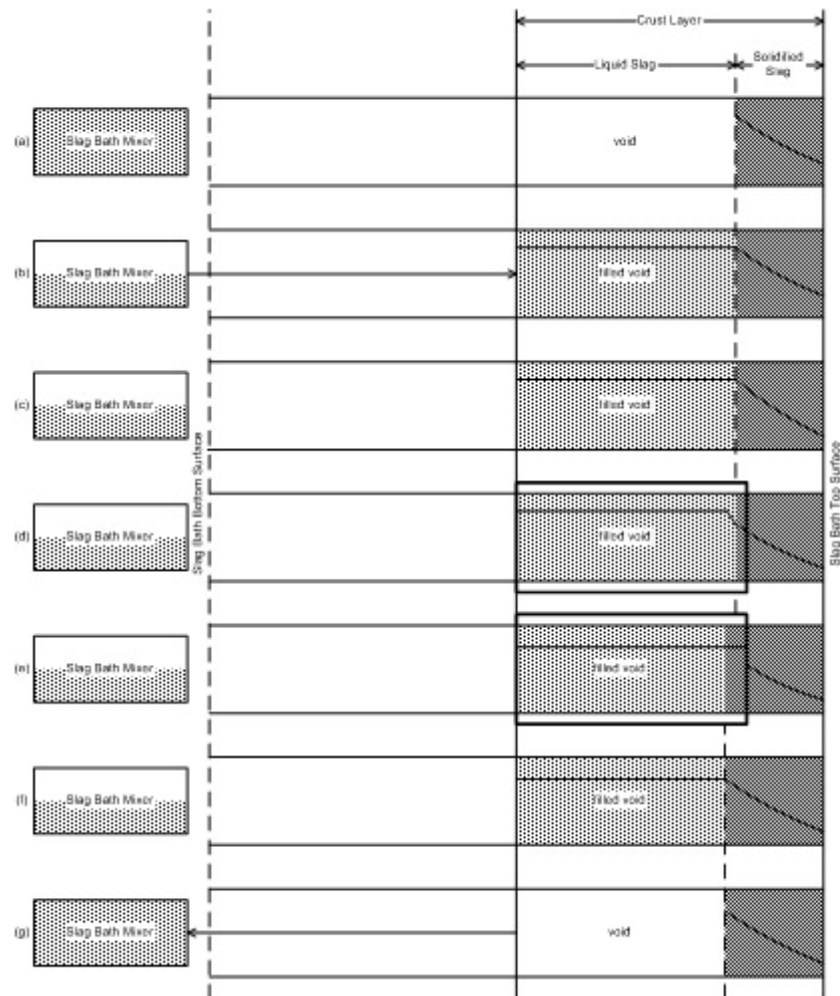


Figure 41 – Schematic representation of steps in the SBCC model solution procedure.

## 4.8 MODEL VALIDATION

### 4.8.1 Purpose

The purpose of validation is to verify the numerical integrity of the SBCC model (Thomas and Brimacombe, 1997).

### 4.8.2 Objectives

Model validation had to achieve the following objectives:

- Confirm the integrity of the basic heat transfer calculations.
- Confirm that the combination of the ChemApp Gibbs-free-energy-minimisation routine and the thermochemical data files used by the model calculate realistic equilibrium results.
- Confirm that the model is able to achieve solidification and melting of the freeze lining.

### 4.8.3 Methodology

The same ChemApp Gibbs-free-energy-minimisation routine and thermochemical data files used for the FLC model are used for the SBCC model. These were also assumed to be valid after the validation was performed for the FLC model.

Because there are differences (boundary conditions, number of layers) between the final FLC and SBCC models, the validation results of the FLC model could not be assumed to prove the validity of the SBCC. A number of experiments using the model shown in Figure 40 (page 76) therefore had to be done to inspect whether the results displayed the expected behaviour or not. If the slag bath is simply allowed to cool down, solidification is expected. If adequate amounts of energy are added to the slag bath, the crust is expected to melt away.

The heat transfer calculations included in the model were again validated by checking steady state results generated by the model against a set of analytically calculated steady state results. Example results of the analytical calculation are shown in Figure 42 and Figure 43.

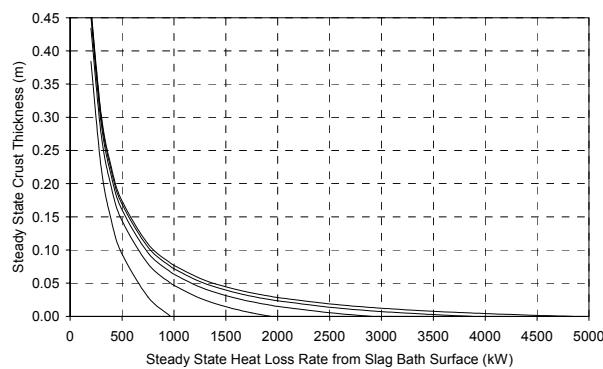


Figure 42 – Analytically calculated steady state crust thickness vs. heat loss rate from slag surface.

The left-most line represents an effective heat transfer coefficient of  $0.010 \text{ kW}/(\text{m}^2 \cdot ^\circ\text{C})$ . It is followed to the right by lines for  $0.020$ ,  $0.030$ ,  $0.040$  and  $0.050 \text{ kW}/(\text{m}^2 \cdot ^\circ\text{C})$ .

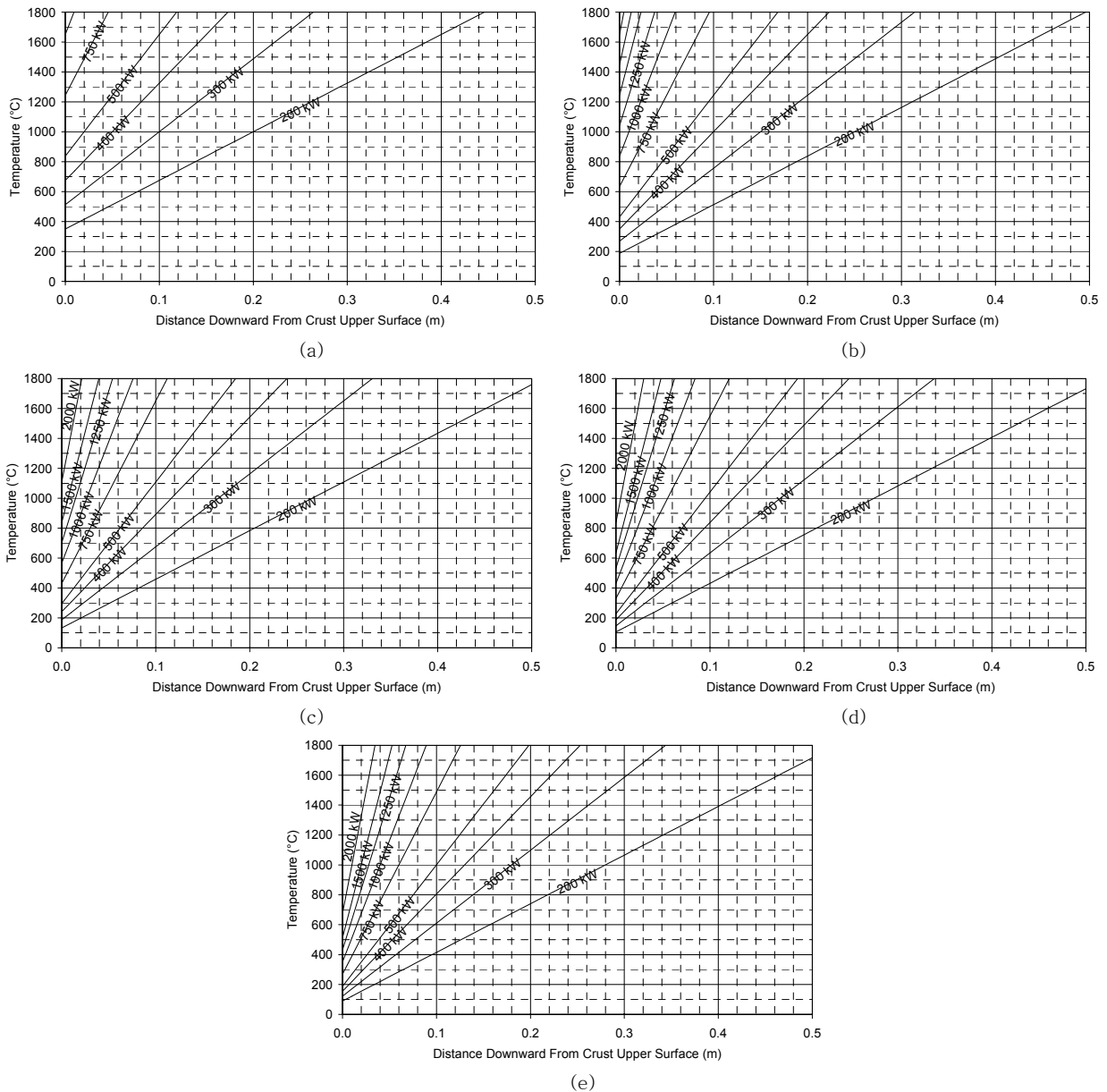


Figure 43 – Analytically calculated steady state temperature profiles in the crust layer.

Graph (a) was constructed with an effective heat transfer coefficient of  $0.010 \text{ kW}/(\text{m}^2 \cdot ^\circ\text{C})$ , (b) with  $0.020 \text{ kW}/(\text{m}^2 \cdot ^\circ\text{C})$ , (c) with  $0.030 \text{ kW}/(\text{m}^2 \cdot ^\circ\text{C})$ , (d) with  $0.040 \text{ kW}/(\text{m}^2 \cdot ^\circ\text{C})$  and (e) with  $0.050 \text{ kW}/(\text{m}^2 \cdot ^\circ\text{C})$ .

The results generated by the comparison between model results and analytically calculated results were also used to achieve the last validation objective. Because a change in input heat flow rate caused the crust to either become thicker in the case of a reduced input heat flow rate or thinner in the case of an increased input heat flow rate, these experiments demonstrated whether the model was able to describe solidification and melting of the crust.

#### 4.8.4 Validation Experiments

##### a. Experiment 4.1

Objective: Confirm the integrity of the model's heat transfer equations, and that the model is able to describe solidification and melting of the crust.

Initial condition: Fill up the SlagBath with a 10%-60%-30% (FeO-TiO<sub>2</sub>-Ti<sub>2</sub>O<sub>3</sub> mass percentages) slag at a temperature of 1635 °C. This temperature is just above the liquidus temperature of the slag. The slag composition is chosen to be on the rutile side of the eutectic groove. This means that rutile will be the primary phase that solidifies.

The effective heat transfer coefficient was set equal to 0.030 kW/(m<sup>2</sup>.°C).

The model was started with no crust present.

Steps: Run the model with a heat flow rate of 3000 kW through the ElectricalPower energy input module until the model reaches a steady state. No crust was expected to form under these conditions.

Run the model with a heat flow rate of 1000 kW through the ElectricalPower energy input module until the model reaches a steady state. A crust was expected to form.

Run the model using the steady state results of the previous step as starting condition and apply a heat flow rate of 2000 kW through the ElectricalPower energy input module until the model reaches a steady state.

##### b. Experiment 4.2

Objective: Confirm the integrity of the model's heat transfer equations, and that the model is able to describe solidification and melting of the crust.

Initial condition: As for Experiment 4.1, but with a liquid slag composition of 10%-50%-40% (FeO-TiO<sub>2</sub>-Ti<sub>2</sub>O<sub>3</sub> mass percentages), and a liquid slag temperature of 1617 °C.

Steps: As for Experiment 4.1.

##### c. Experiment 4.3

Objective: Confirm the integrity of the model's heat transfer equations, and that the model is able to describe solidification and melting of the crust.

Determine the influence of a decrease in the effective heat transfer coefficient from the top of the slag bath or crust.

Initial condition: As for Experiment 4.1, but with an effective heat transfer coefficient of 0.020 kW/(m<sup>2</sup>.°C).

Steps: Run the model with a heat flow rate of 2000 kW through the ElectricalPower energy input module until the model reaches a steady state. No crust was expected to form under these conditions.

Run the model with a heat flow rate of 500 kW through the ElectricalPower energy input module until the model reaches a steady state. A crust was expected to form.

Run the model using the steady state results of the previous step as starting condition and apply a heat flow rate of 1000 kW through the ElectricalPower energy input module until the model reaches a steady state.

#### d. Experiment 4.4

Objective: Confirm the integrity of the model's heat transfer equations, and that the model is able to describe solidification and melting of the crust.

Determine the influence of a decrease in the effective heat transfer coefficient from the top of the slag bath or crust.

Initial condition: As for Experiment 4.3, but with a liquid slag composition of 10%-50%-40% (FeO-TiO<sub>2</sub>-Ti<sub>2</sub>O<sub>3</sub> mass percentages), and a liquid slag temperature of 1617 °C.

Steps: As for Experiment 4.3.

### 4.8.5 Validation Results

Results of the validation experiments are presented below in the form of two graphs per experiment step. The graph on the left-hand side shows a comparison between an analytically calculated steady-state temperature profile of the furnace wall and freeze lining (solid line), and the same profile calculated by the SBCC model (crosses).

The second graph shows the difference between temperatures calculated by the SBCC model and analytically calculated temperature values. Positive values indicate overestimation by the SBCC model.

a. Experiment 4.1

%FeO	%TiO <sub>2</sub>	%Ti <sub>2</sub> O <sub>3</sub>	k <sub>liquid slag</sub>	h <sub>effective</sub>
10	60	30	0.001 kW/(m.°C)	0.030 kW/(m <sup>2</sup> .°C)

Step 1 of this experiment was executed with an ElectricalPower input of 3000 kW. The conditions modelled yielded no crust, as was expected. For this reason no graphs are shown for this step. The analytical calculation predicted a steady state slag bath temperature of 1650.6 °C. This was the temperature achieved by the model.

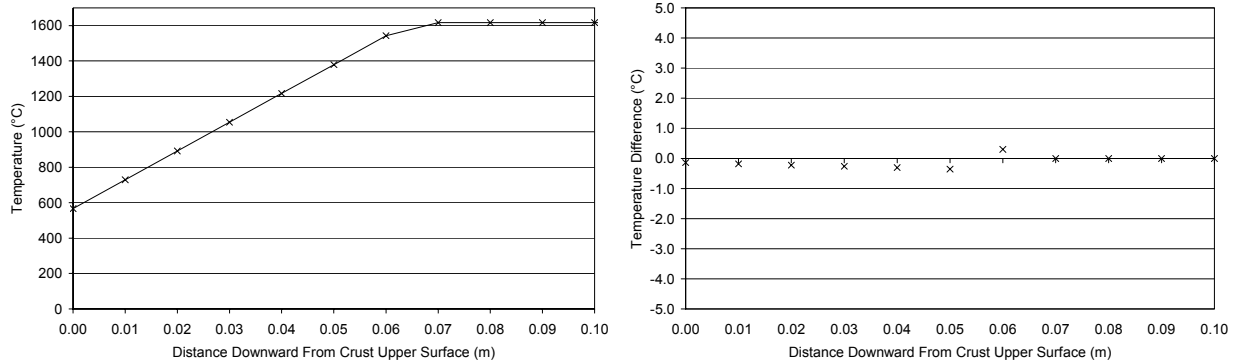


Figure 44 – Validation experiment 4.1 results for a heat input of 1000 kW.

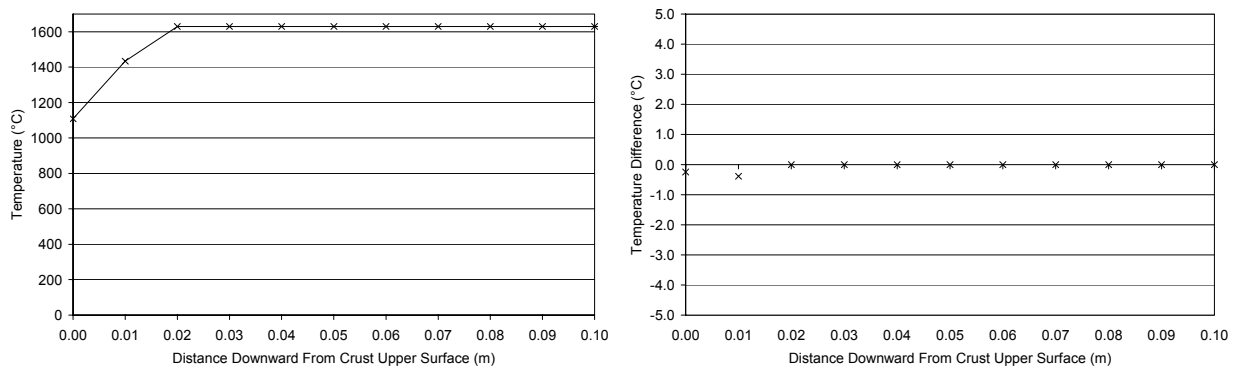


Figure 45 – Validation experiment 4.1 results for a heat input of 2000 kW.



b. Experiment 4.2

%FeO	%TiO <sub>2</sub>	%Ti <sub>2</sub> O <sub>3</sub>	k <sub>liquid slag</sub>	h <sub>effective</sub>
10	50	40	0.001 kW/(m.°C)	0.030 kW/(m <sup>2</sup> .°C)

Step 1 of this experiment was executed with an ElectricalPower input of 3000 kW. The conditions modelled yielded no crust, as was expected. For this reason no graphs are shown for this step. The analytical calculation predicted a steady state slag bath temperature of 1650.6 °C. This was the temperature achieved by the model.

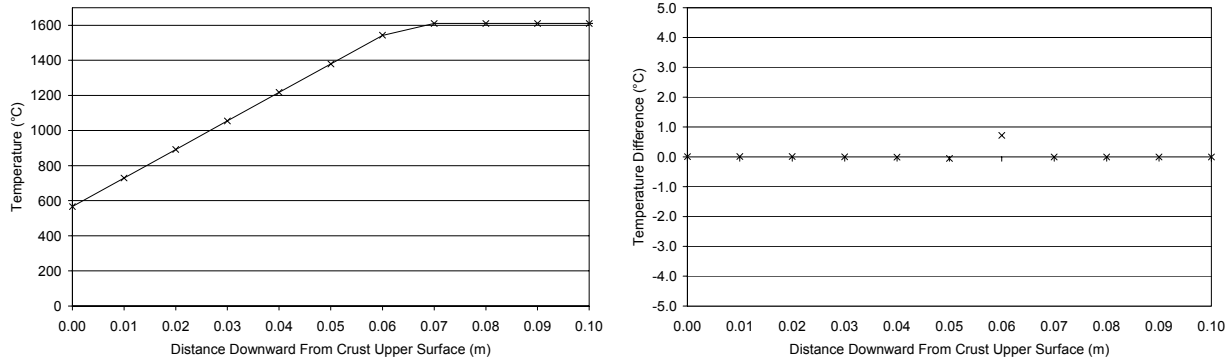


Figure 46 – Validation experiment 4.2 results for a heat input of 1000 kW.

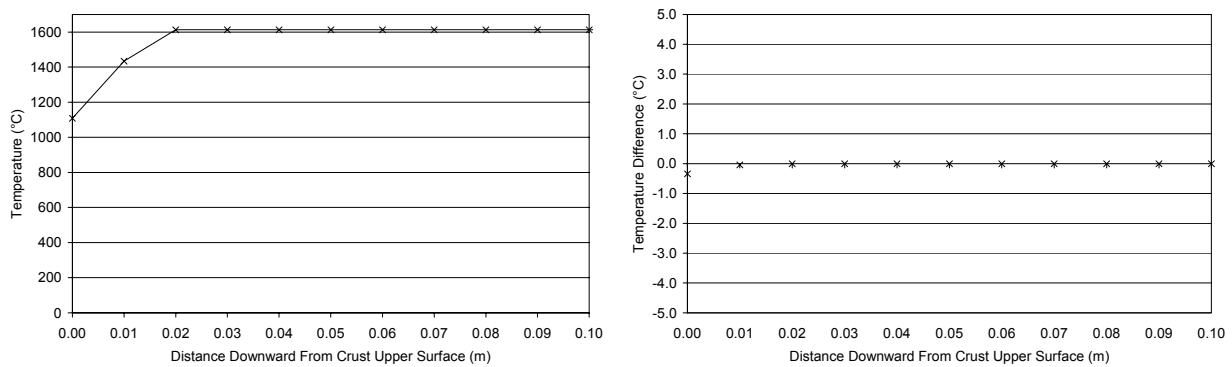


Figure 47 – Validation experiment 4.2 results for a heat input of 2000 kW.

c. Experiment 4.3

%FeO	%TiO <sub>2</sub>	%Ti <sub>2</sub> O <sub>3</sub>	k <sub>liquid slag</sub>	h <sub>effective</sub>
10	60	30	0.001 kW/(m.°C)	0.020 kW/(m <sup>2</sup> .°C)

Step 1 of this experiment was executed with an ElectricalPower input of 2000 kW. The conditions modelled yielded no crust, as was expected. For this reason no graphs are shown for this step. The analytical calculation predicted a steady state slag bath temperature of 1650.6 °C. This was the temperature achieved by the model.

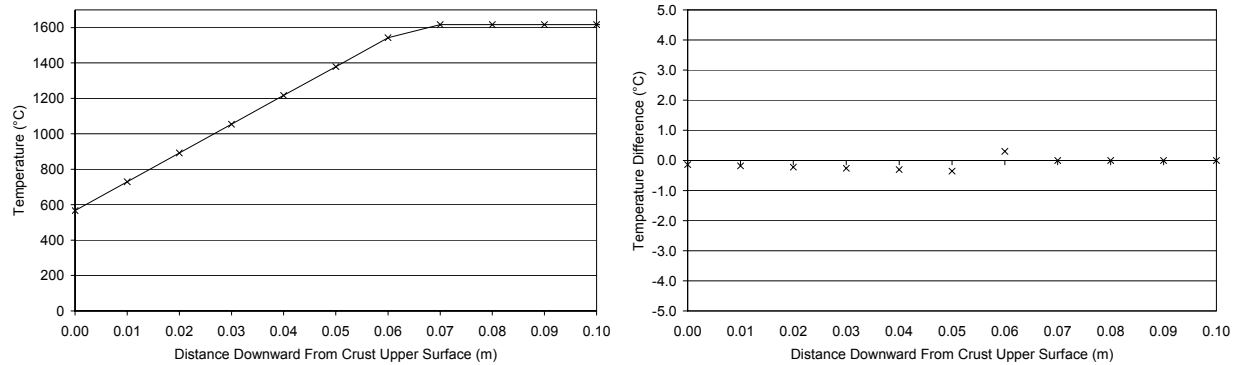


Figure 48 – Validation experiment 4.3 results for a heat input of 500 kW.

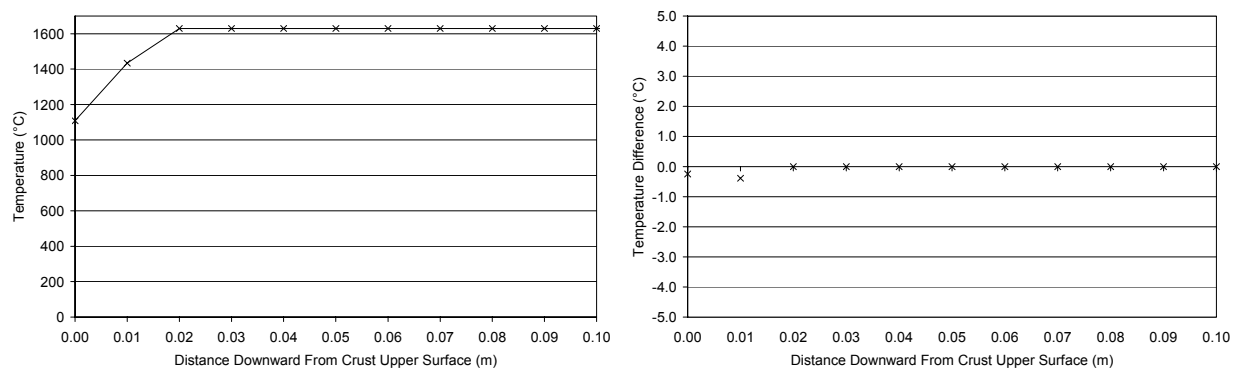


Figure 49 – Validation experiment 4.3 results for a heat input of 1000 kW.

d. Experiment 4.4

%FeO	%TiO <sub>2</sub>	%Ti <sub>2</sub> O <sub>3</sub>	k <sub>liquid slag</sub>	h <sub>effective</sub>
10	50	40	0.001 kW/(m.°C)	0.020 kW/(m <sup>2</sup> .°C)

Step 1 of this experiment was executed with an ElectricalPower input of 2000 kW. The conditions modelled yielded no crust, as was expected. For this reason no graphs are shown for this step. The analytical calculation predicted a steady state slag bath temperature of 1650.6 °C. This was the temperature achieved by the model.

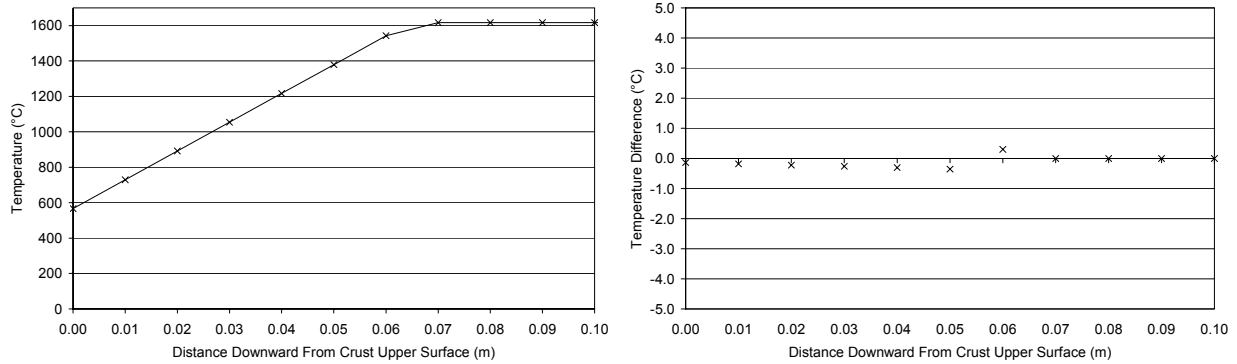


Figure 50 – Validation experiment 4.4 results for a heat input of 500 kW.

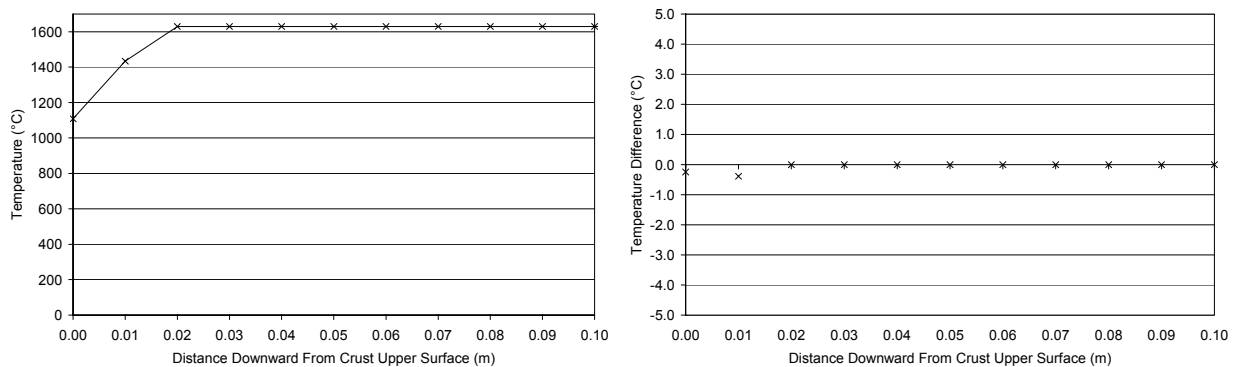


Figure 51 – Validation experiment 4.4 results for a heat input of 1000 kW.

e. Summary

Slag composition, steady state heat flow rate and effective heat transfer coefficient from the top of the slag bath or crust were the parameters covered by the validation experiments listed above. The model was able to reach steady state values that never deviated by more than 5 °C from the analytical solution. The deviations were believed to be due to round-off errors due to the ever-decreasing enthalpy change of the nodes as steady state is approached.

#### **4.9 COMPARISON WITH ACTUAL DATA**

Due to the confidentiality of most information pertaining to the industrial process, no comparison with actual data could be published here. The comparisons against analytically calculated values therefore serve as the only validation of the SBCC model.

## CHAPTER 5

### A DYNAMIC MODEL OF THE ENTIRE ILMENITE-SMELTING FURNACE PROCESS

This chapter describes a dynamic model of the entire process contained in an ilmenite-smelting furnace. The model was used to conduct experiments to determine, under various circumstances, the influence of the slag bath on the freeze lining and crust, and the reverse influence of the freeze lining and crust on the slag bath. Details of these experiments are provided in CHAPTER 8 and CHAPTER 9.

#### 5.1 IDENTIFICATION

The model being described in this chapter is identified as follows:

Name: Ilmenite-smelting Furnace Process Model

Abbreviation: ISFP model

#### 5.2 PROBLEM DEFINITION

The main focus of this study was to investigate the dynamic interaction between the freeze lining and slag bath in an ilmenite-smelting furnace. All the influences to be considered have their origin in the slag bath, or first reach the slag bath before reaching the freeze lining. The slag bath therefore acts as a very important boundary condition to the freeze lining and crust models described in the previous two chapters. Because of the significance of the slag bath in this study, it was necessary to model, to a reasonable degree of accuracy, this part of the process for the use of the freeze lining and crust models to become more meaningful. Once the freeze lining and crust models had been integrated with a model that describes the slag bath well, this integrated model could be used as an improved representation of the dynamic behaviour of the slag bath, the freeze lining, the crust and of the process as a whole.

Since reduction reactions in the smelting process produce slag, metal and gas, modelling of the slag bath in isolation was not a meaningful option. For this reason the ISFP model described in this chapter had to be a comprehensive model of the ilmenite-smelting process. It had to take as inputs the material and energy inputs of the actual process (ilmenite, reductant, electrical energy). It also had to calculate as its final outputs the outputs of the actual process (liquid slag, liquid metal, off-gas and heat losses). Finally, intermediate states had to be calculated. These included the state of the slag bath, metal bath and furnace atmosphere.

In addition to the above, the model also had to integrate the freeze lining and crust models described earlier. This would enable it to also provide state information about the freeze lining and crust. These sub-models, especially the freeze lining sub-model, were the focus of most of the experiments described in subsequent chapters.

Because the focus of this study was more on the freeze lining and slag bath than on the rest of the process, the ISFP model was not required to provide the ultimate in accuracy in terms of modelling the metal bath, furnace atmosphere, etc. These aspects were modelled to such a degree of accuracy that satisfied the objectives of the study.

### 5.3 SYSTEM DESCRIPTION

Figure 8 (page 13) shows the aspects addressed by the ISFP model. A scale drawing was also made to present the furnace as it is described by the ISFP model (Figure 52 below). In this drawing the metal and slag baths are shown, as well as the areas (freeze lining and crust) described by the two conductor models presented in CHAPTER 3 and CHAPTER 4. The freeze lining as described by the FLC model is shown as being in contact with the sidewalls and slag bath. The crust described by the SBCC model is shown at the top part of the slag bath.

Material inputs enter the furnace through a hollow electrode. These materials include ilmenite and a reductant (typically anthracite or char). Material exits from the furnace as off-gas through an off-gas duct installed in the furnace roof, as slag through a slag tap hole and as metal through a metal tap hole. The metal tap hole is situated on a level lower than the slag tap hole because the metal has a higher density than the slag and it settles at the bottom of the furnace as a metal bath. Heat exits the furnace together with the material outputs just listed, and as heat lost through the furnace roof, sidewalls and hearth.

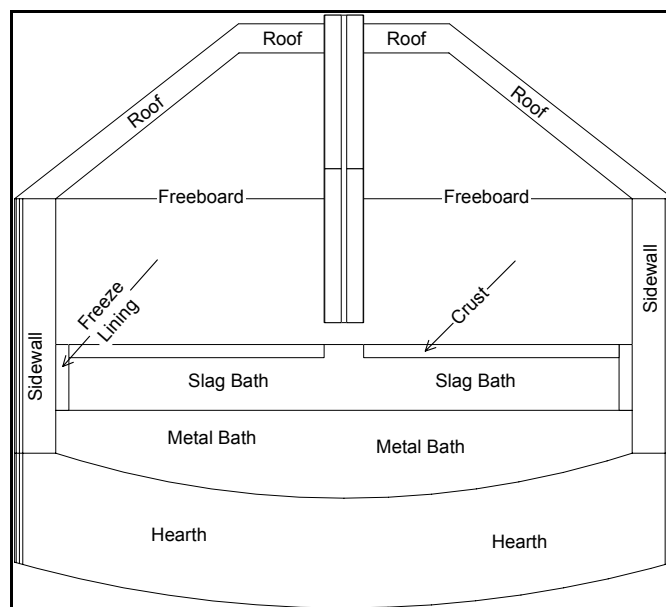


Figure 52 – Schematic of the furnace and process as described by the ISFP model.

The main areas of chemical reaction include the top of the slag bath where floating reductant particles react with liquid slag, the interface between the slag and metal baths where dissolved carbon in the metal reacts with liquid slag, and the turbulent region underneath the electrode where the arc attaches to the bath and material discharges into the bath. In all these zones the reaction products include slag, metal and gas.

#### 5.3.1 Dimensions

The dimensions of the hypothetical system under consideration are presented in Figure 53 below.

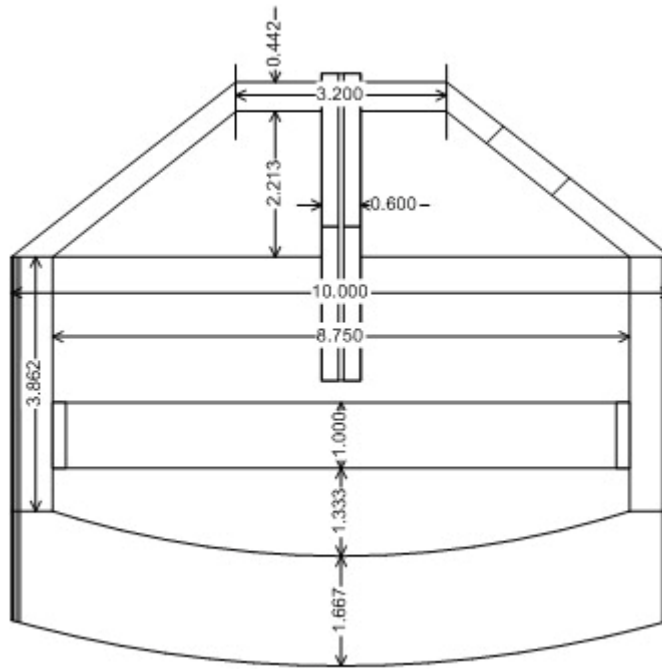


Figure 53 – Dimensions in meters of the furnace configuration used in CHAPTER 5.

## 5.4 KEY PHENOMENA

### 5.4.1 Heat Transfer

Figure 54 identifies the various heat transfer phenomena discussed in this section. The phenomena are referenced using the Q symbols presented in the schematic.

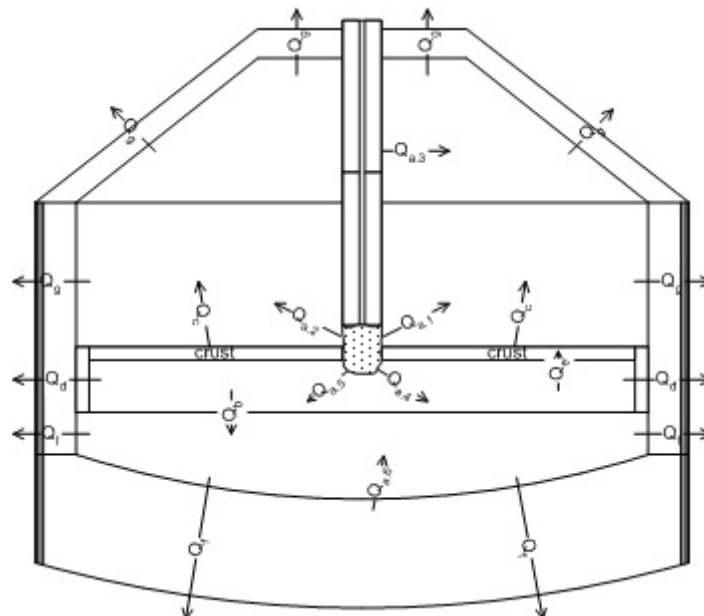


Figure 54 – Heat transfer phenomena in an ilmenite-smelting furnace.

#### a. Heat transfer from the arc

Because of the ilmenite-smelting furnace being powered by an electric arc, the arc is the main source of energy in the process. The electrical energy discharged into the furnace is distributed, in summary, between the furnace (walls, roof and freeboard) and the melt (slag and metal baths) (Stenkvist and Bowman, 1987). For an arc of 10 kA and 125 V, the distribution has been set out as follows (Stenkvist and Bowman, 1987):

- 28% to furnace
  - 20% via radiation ( $Q_{a,1}$  in Figure 54)
  - 4% via convection ( $Q_{a,2}$  in Figure 54)
  - 4% via the electrode effect ( $Q_{a,3}$  in Figure 54)
- 72% to melt
  - 10% via radiation ( $Q_{a,4}$  in Figure 54)
  - 50% via convection ( $Q_{a,5}$  in Figure 54)
  - 12% via the electrode effect ( $Q_{a,6}$  in Figure 54)

The electrode effect mentioned above refers to energy dissipated by resistance heating in either the graphite electrode (cathode) or in the slag bath, metal bath and bottom connection (anode).

The distribution presented above is specifically representative of a 10 kA and 125 V arc (power of 1.25 MW and resistance of 12.5 m $\Omega$ ). Arcs with other current and voltage settings will result in different energy distributions. A higher arc resistance results in a longer arc and more radiation to walls, roof and freeboard, and less convection to the melt. However, the trend visible in the above distribution (that most of the energy is discharged into the melt via convection) should be present in general during the operation of actual furnaces.

Heat transfer from the arc was seen as a key phenomenon within the context of the ISFP model because of the arc being the main energy source of the process. However, the exact distribution of energy from the arc to the process was not viewed as being of major importance. For this reason it was decided to model the arc simply as an energy source into the bath. Details of the relative influences of radiation, convection and electrode effects were therefore ignored.

#### b. Heat transfer between slag bath and metal bath

Temperature gradients exist in the furnace from the high-temperature zone of the arc towards the outside boundaries of the furnace where the temperature is close to ambient. For this reason it has been observed that the metal bath (being further away from the arc) has a somewhat lower temperature than the slag bath. Energy flows from the slag bath into the metal bath, from which it flows into part of the freeze lining, sidewalls and hearth.

The mode of heat transfer from the slag bath to the metal bath is expected to be a combination of conduction and convection ( $Q_b$  in Figure 54). In the turbulent region below the electrode, convection is expected to be the dominant mechanism due to the intense movement and mixing in this region. In areas further away from the centre of the furnace convection is still expected to be dominant due to mixing that



is known to occur in these areas in both the slag and metal baths. Conduction should however play a relatively larger role compared with the zone under the electrode.

Heat transfer between the slag and metal baths was not viewed as critical to the ISFP model. It was decided to assume that the slag and metal baths existed at the same temperature (Assumption 5.1, page 110).

c. Heat transfer from the slag bath surface to the furnace freeboard

Extensive modelling work was done on radiation in the freeboards of DC smelting furnaces (Reynolds, 2002). That study showed that radiation from the bath surface is the main source of energy loss into the freeboard and through the upper sidewalls and roof.

The impact of heat losses from the slag bath surface was seen as important to the ISFP model. The detailed mechanisms of heat transfer in this region were however not viewed as being that important. For this reason it was decided to describe heat transferred from the slag bath surface by a simple heat transfer coefficient boundary condition derived from the work by Reynolds (2002).

d. Heat transfer from the slag bath to the freeze lining and sidewall

Heat transfer from the slag bath to the freeze lining and sidewall was of critical importance to the ISFP model because the model was required to describe interactions between the slag bath and the freeze lining. For details about the heat transfer phenomenon, refer to CHAPTER 3.

e. Heat transfer from the slag bath to the crust

Because the ISFP model was also required to model interactions between the crust and the slag bath (in cases when a crust exists), this heat transfer phenomenon was viewed as being important. Details about this heat transfer component are included in CHAPTER 4.

f. Heat transfer from the metal bath to the sidewalls and hearth

A significant amount of energy is lost from the metal bath to the lower sidewalls and hearth. The heat is transferred through convection to these surfaces, and by conduction through the sidewalls and hearth towards the outside of the furnace. Heat is removed by water cooling in the case of the sidewalls and either water or air cooling in the case of the hearth.

This phenomenon was seen as important to the ISFP model. It was however decided to incorporate it into the model as two simple boundary conditions, and not as comprehensive models describing convection and conduction heat transfer.

g. Heat transfer through the upper sidewalls and roof

Heat transferred into the freeboard from the arc and slag bath surface by convection and radiation reaches the upper sidewalls and roof. This heat is transferred toward the outside of the furnace through conduction. The upper sidewalls, the conical part of the roof and the flat part of the roof are all covered with a layer of process material (Reynolds, 2002). In an ilmenite-smelting furnace, this layer consists of slag, ilmenite and reductant particles.

In the case of the upper sidewalls (the walls above the level of the slag bath surface), the heat that arrives at the hot face from the furnace freeboard is removed by conduction through the layer of process material, the brick layer, potentially a ramming layer and the steel shell. Forced water cooling is often applied on the outside of the shell.

The conical part of the roof often does not contain a brick layer. Heat from the freeboard is therefore removed by conduction through the layer of process material and steel shell, and by forced water cooling on the outside of the steel shell.

The flat part of the roof again has a layer of refractory material. Conduction is therefore responsible for removing heat from the freeboard. On the outer surface of the flat part of the roof no forced cooling is used.

The heat removed from the system by the above-mentioned mechanisms was seen as important to the ISFP model, but the detailed mechanisms were not viewed as being important enough to include in the model. As mentioned in paragraph c above, an effective heat transfer coefficient from the top of the slag bath surface was used to model all heat transferred upward from the slag bath surface.

### 5.4.2 Mass Transfer

When describing mass transfer below, the phenomena were classified as follows:

- Bulk flow.

Bulk flow refers to phenomena such as ore and reductant that are fed into the furnace through the hollow electrode, or metal and slag that are tapped from the furnace through the tap holes.

- Convective mass transfer.

This refers to mass flow resulting from fluid flow within a single phase. For example, carbon dissolved in iron is transported to the surface between the slag and metal baths as a result of stirring in the metal bath.

- Diffusion

Diffusion refers to mass transfer resulting from concentration gradients in a phase. For example,  $Ti_2O_3$  diffuses away from the interfaces at which reduction takes place into the bulk slag phase due to reduction increasing the  $Ti_2O_3$  concentration at the reaction interface.

In the drawings describing the various mass flow phenomena below, the symbol  $m_B$  is used to indicate bulk mass flow.

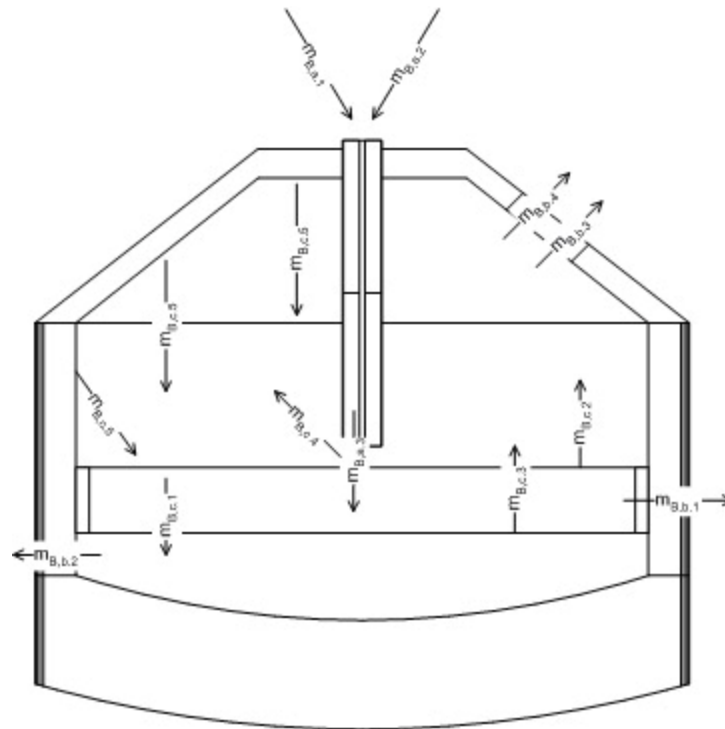


Figure 55 – Bulk mass flow phenomena in an ilmenite-smelting furnace.

#### a. Bulk mass flow of feed materials

The main feed materials, ilmenite ( $m_{B,a,1}$ ) and reductant ( $m_{B,a,2}$ ), are fed into the furnace through the hollow graphite electrode. The material accelerates under the influence of gravity and enters the slag bath with significant momentum. This momentum adds to the turbulence in the zone below the electrode.

The graphite electrode is consumed at its tip. Graphite released into the process in this way also represents a bulk mass flow stream ( $m_{B,a,3}$ ). This graphite is expected to enter into the slag bath and freeboard as a result of the flow of the arc plasma.

Because ilmenite and the carbon-based reductant are the main feed components of the process, the bulk flows of these materials were very important within the context of the ISFP model. Both these flows were therefore incorporated in the model. The flow of graphite (from the electrode material), however, was not seen as equally important. This flow was ignored, but it can be viewed that the graphite flow was incorporated in the reductant bulk flow.

#### b. Bulk mass flow of product materials

The main products of the process are slag tapped from the slag bath ( $m_{B,b,1}$ ) and metal tapped from the metal bath ( $m_{B,b,2}$ ). The third stream exiting the furnace contains gas (mainly CO;  $m_{B,b,3}$ ), fume and dust ( $m_{B,b,4}$ ).

Three of these four bulk mass flow streams had to be incorporated into the model. This is because slag, metal and gas are inevitably produced inside the furnace when feed materials and energy are charged. It

was however decided that the dust bulk flow stream ( $m_{B,b,4}$ ) was of lesser importance to the ISFP model, and it was therefore ignored.

#### c. Internal bulk mass flow phenomena

The reduction reactions taking place between slag and reductant particles in and on top of the slag bath produce metal droplets as one of its products. Such droplets continuously travel down through the slag bath and coalesce with the metal bath ( $m_{B,c,1}$ ).

This bulk flow was incorporated into the ISFP model in a crude way by moving all metal produced by reduction reactions immediately to the metal bath once it was produced.

Another product of the same reduction reactions is gas. Gas travels up through the slag bath and into the freeboard as it is produced ( $m_{B,c,2}$ ).

Reduction reactions also occur at the interface between the slag and metal baths due to the relatively high carbon content of the metal bath (around 2%). These reactions also produce gas that travels up through the slag bath and into the freeboard ( $m_{B,c,3}$ ).

The two gas bulk flows described above were handled similar to the metal bulk flow by moving all gas produced by reduction reactions immediately to the freeboard.

Due to the significant momentum transferred to the slag bath by the entering feed material and arc, material is thrown from the zone underneath the arc into the freeboard and towards the sidewalls and roof ( $m_{B,c,4}$ ). Since these furnaces do not continue to build up material on the sidewalls and roof and eventually clog up completely, it can be safely assumed that some material also travels back from the sidewalls and roof into the slag bath ( $m_{B,c,5}$ ). This is likely due to melting of such material by heat radiated to these surfaces.

The bulk flow of material to and from the upper sidewalls and roof was not seen as important to the ISFP model. These flows were therefore ignored.

#### d. Mass transfer at the slag–reductant interface

The most important reaction interface in the process is believed to be the interface between liquid slag and reductant particles. Reactions at this interface result in the formation of metal, gas and a slag enriched in  $Ti_2O_3$ .

It is expected that diffusion will occur in the slag phase due to the  $Ti_2O_3$  concentration gradient created by reduction reactions. Due to stirring in the slag bath, it is also expected that liquid slag and reductant particles will move relative to each other. In the case of the slag phase, this can be viewed as convective mass transfer to and from the slag–reductant interface. This causes a renewal of liquid slag taking part in reduction reactions at this interface.

Metal and gas formed during reduction reactions are carried away from the slag–reductant interface by buoyancy forces due to the marked difference in density between these materials and liquid slag. These phenomena were classified as bulk mass flows in paragraph c above.

The diffusion and convective mass transfer phenomena identified above were viewed as important to the ISFP model. However, it was decided not to model these phenomena in any great detail, but rather to incorporate it into the model by a simple approach (paragraph 5.6.8a, page 125).

e. Mass transfer at the interface between the slag and metal baths

Reduction reactions also take place at the interface between the slag and metal baths. The reason for these reactions is the relatively high carbon content of the metal (around 2%) that is not in equilibrium with the liquid slag. Carbon therefore reacts with FeO and TiO<sub>2</sub> in the slag to form CO gas, Fe metal and Ti<sub>2</sub>O<sub>3</sub>. The metal product of the reduction reaction is expected to coalesce with the metal bath virtually immediately. The CO gas bubbles move upward through the slag bath to eventually escape into the freeboard (paragraph c above).

The slag at the interface becomes depleted in FeO and TiO<sub>2</sub>, and enriched in Ti<sub>2</sub>O<sub>3</sub>. This causes concentration gradients in the slag phase that will result in diffusion of these species. Ti<sub>2</sub>O<sub>3</sub> will tend to diffuse away from the interface and FeO and TiO<sub>2</sub> are expected to diffuse toward the interface.

In the case of the metal phase carbon is consumed at the interface. The metal will therefore become depleted in carbon. The resulting carbon concentration gradient will cause carbon to diffuse toward the interface from the bulk metal.

Significant stirring is known to occur in both the slag and metal baths. This stirring causes convective mass transfer on both sides of the interface. This convective mass transfer results in the renewal of both slag and metal at the interface from the respective bulk phases. It is expected that convective mass transfer is the dominant mass transfer mechanism at this interface.

The mass transfer phenomena identified above were viewed as important to the ISFP model. The detailed modelling of these phenomena was however excluded to simplify the model. The phenomena were incorporated into the model by a simple approach (paragraph 5.6.8b, page 129).

f. Mass transfer of carbon into the metal bath

One phenomenon in the ilmenite-smelting process that is not yet understood clearly is the transfer of carbon into the metal bath. As mentioned above, the metal carbon content of around 2% observed in ilmenite-smelting processes (Geldenhuis and Pistorius, 1999) is far from the composition for metal in equilibrium with slag (which is less than 0.2% according to simple FactSage equilibrium calculations). This causes reduction reactions to take place at the interface between the slag and metal baths. These reactions contribute to lowering the carbon concentration of the metal bath. This creates a question: What causes the carbon content of the metal to increase to a value of around 2% if reduction reactions at the interface between the slag and metal bath tend to lower the composition toward 0.2% carbon?

At least two possible phenomena exist that can contribute to increasing the carbon content of the metal. Firstly, it is possible that the turbulent zone underneath the electrode may consist of a mixture of slag, reductant particles and metal droplets. Assuming that this is true, the metal droplets in the region can come into contact with reductant particles under conditions of high temperature. It is not certain what the typical

temperature in this region is, but with slag being tapped at temperatures in excess of 1700°C, it is likely that the temperature of the zone underneath the electrode could be substantially higher.

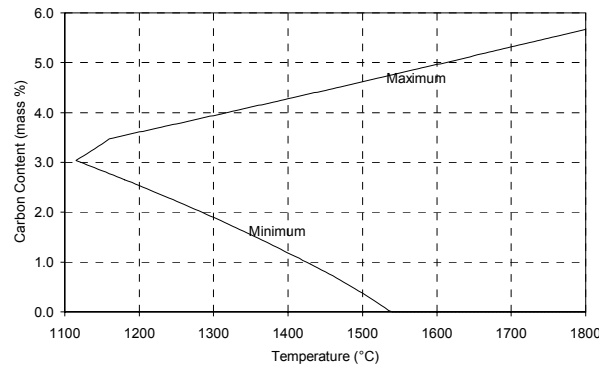


Figure 56 – Solubility limits of carbon in liquid iron as functions of temperature. (FactSage 5.2)

Figure 56 shows the solubility limits of carbon in liquid iron. The maximum solubility indicates the maximum carbon content of liquid iron at a specific temperature. The minimum limit indicates the minimum carbon content of liquid iron at a specific temperature. Both these limits are indicated for equilibrium conditions. Other solute elements such as Ti, Mn, S, etc. were not taken into account. From this figure it is clear that the maximum solubility of carbon increases with increasing temperature. At a temperature of 1800°C liquid iron can contain up to 5.67 % carbon (by mass).

If the turbulent zone under the electrode is at a temperature of 1800°C and liquid metal droplets come into contact with reductant particles, these droplets can be carburised up to a carbon content of around 5.67 % before reaching carbon saturation. It is however expected that droplets will not have long residence times in the turbulent zone before being reabsorbed into the metal bath. It is therefore not certain whether these droplets will reach the point of carbon saturation. Nevertheless, it is likely that these droplets will be carburised to some extent in this zone, thereby contributing to an increase in metal bath carbon content.

The second phenomenon that may increase the carbon content of the metal bath also involves small metal droplets, but in this case the droplets originating from reduction reactions at the slag-reductant interface. These droplets may leave the reduction reaction zone with high carbon contents as a result of contact with reductant particles present. Once again Figure 56 indicates that up to 5.31% carbon (by mass) can be dissolved in liquid iron at a temperature of 1700 °C that can be attained in this area.

The droplets produced at the slag-reductant interface still have to travel down through the slag bath and into the metal bath. During this journey the droplets are likely to be in contact with liquid slag, but less likely to remain in contact with reductant particles. Because it was already calculated that metal with high carbon content will tend to react with slag, these droplets will tend to lose most of their carbon while travelling to the metal bath.

The phenomenon of carbon mass transfer into the metal bath was seen as important to the ISFP model because realistic metal bath carbon contents were required to make reduction reactions possible at the

interface between the slag and metal baths. For this reason both of the phenomena described above had to be incorporated into the model. The second phenomenon could be implicitly incorporated in the reduction reactions between slag and reductant particles. The carbon content of metal produced from these reactions could simply be a function of the thermodynamic equilibrium behaviour of this part of the process. The first phenomenon where reductant particles come into contact with metal droplets in the turbulent zone underneath the electrode had to be incorporated explicitly into the model by a reaction interface between metal and reductant.

#### g. Mass transfer at the interface between the slag bath and freeze lining

As observed from the experimental results in CHAPTER 6, solidification and melting at the interface between the slag bath and freeze lining cause changes in liquid slag composition at this interface. In the case of solidification the FeO and TiO<sub>2</sub> contents increase and the Ti<sub>2</sub>O<sub>3</sub> content decreases. During melting of the freeze lining the opposite was observed.

These changes in liquid slag composition at the interface cause diffusion in the liquid slag. More importantly, the convective mass transfer resulting from strong mixing in the slag bath transports liquid slag to and from this interface.

These phenomena were addressed in CHAPTER 3 as part of the FLC model and were treated in the same way in the ISFP model.

### 5.4.3 Momentum Transfer

#### a. Momentum sources

There are five main sources of momentum in the process:

- The plasma arc.
- Feed material falling into the bath.
- Electromagnetic stirring.
- Gas rising up through the metal bath and into the freeboard.
- Buoyancy forces in the slag and metal baths.

The momentum sources discussed below were viewed to be important collectively to the ISFP model. However, details of flow phenomena associated with these sources were not viewed as important. It was decided to incorporate the influence of these momentum sources into the ISFP model by assuming that the slag and metal baths both are ideally mixed (Assumption 5.2, page 110; Assumption 5.3, page 111).

#### i. The plasma arc

The plasma arc on its own and in combination with feed material transfers a significant amount of momentum to the bath. No quantitative information was available for inclusion here, but some qualitative and some related quantitative information should give the reader an indication of the amount of momentum involved.

It was reported by Stenkvis and Bowman (1987) that a 40 kA arc operating with a gap of 300 mm between the cathode tip and the bath surface creates a 160 mm depression in a bath of molten iron metal. The same authors reported that the maximum axial velocity associated with an arc current of a mere 200 A was measured to be approximately 330 m/s.

Ramírez-Argáez (2003) reported that shear stresses of the arc on the bath surface, when viewed in isolation, can cause velocities of around 0.5 m/s in a metal bath (depth 0.5 m and diameter 3 m). Shear stresses, however, are never the only influence causing movement in the bath. It is always combined with effects of buoyancy and electromagnetic stirring.

From the above it can be concluded that the plasma arc acts as a major momentum source in the process.

#### ii. Feed material

In the case of the scale drawing shown in Figure 52, material entering the furnace would fall a minimum of around 5 m through the hollow electrode column. The roof configuration in this drawing is probably higher than for furnaces found in practice. It is expected that the minimum distance material would fall in practice would be around 3 m. Assuming unconstrained movement of feed material in the hollow electrode, the velocity of the feed material after a fall of 3 m is approximately 7.75 m/s (27.9 km/h). This relates to momentum of 71 kg.m/s being added to the bath per second when feeding 30 ton of ilmenite and 3 ton of reductant per hour (a total of 33 ton/h or 9.2 kg/s). The actual momentum is expected to be less than this due to movement of feed material in the hollow electrode being constrained to some degree.

The momentum carried into the furnace with the feed material is expected to cause significant motion in at least the zone underneath the electrode. This momentum together with the momentum of the arc is responsible for the turbulence in this zone.

#### iii. Electromagnetic stirring

Ramírez-Argáez (2003) reported that electromagnetic forces are dominant in establishing velocity gradients in a metal bath. The motion caused by electromagnetic stirring was shown to be opposed by the motion caused by shear stresses from the arc and buoyancy forces. The combination of these influences resulted in a maximum velocity of 1.22 m/s in a metal bath without a slag covering. When a slag layer was introduced, the maximum velocity in the system dropped to 0.4 m/s. The system modelled by Ramírez-Argáez (2003) had a metal bath depth of 0.5 m and a diameter of 3 m.

#### iv. Rising gas

Gas bubbles produced by reduction reactions at the interface between the slag and metal baths, and at interfaces between slag and reductant particles dispersed throughout the slag bath rise up through the slag bath and escape into the freeboard. The creation and movement of this gas is expected to transfer some momentum to the surrounding liquid slag, thereby influencing fluid flow in the slag bath.

#### v. Buoyancy forces

Temperature gradients in the slag and metal baths cause variations in density of these materials. This causes lower-density material to travel upward, and higher-density material to travel downward under the



influence of buoyancy forces. The influence of buoyancy was studied by Ramírez-Argáez (2003), and it was found to have a lesser influence on flow in a metal bath compared to shear forces from the arc and electromagnetic influences.

#### b. Momentum transfer in the slag bath

All five sources of momentum listed and described above are expected to influence fluid flow in the slag bath. The most pronounced influence is expected to result from momentum transferred from the arc and feed material entering the bath in the centre underneath the electrode. The impinging stream of plasma and feed material is believed to be so intense that it will cause some material to be projected toward the sidewalls of the furnace. This effect can be compared with blowing air through a straw onto the surface of a glass of water. When one blows hard enough some water droplets are projected toward the sides of the glass.

Due to the relatively high electrical conductivity of high-titania slag (Pistorius and Coetzee, 2003) it is expected that electromagnetic forces will have some influence on fluid flow in the bath. The exact magnitude of these influences is however not known.

Because gas is produced by reduction reactions at the interface between the slag and metal baths, gas will rise up through the slag bath. This gas is expected to influence fluid flow in the slag bath to some degree. Since most reduction reactions are expected to occur at the interface between reductant particles and liquid slag, and not at the interface between the metal and slag baths, the flow of gas rising through the slag bath from the top of the metal bath is expected to be low. For this reason the contribution to fluid flow in the slag bath from gas bubbles rising up through the slag bath is expected to be small relative to the influences of feed material, the arc and electromagnetic stirring.

Some vertical temperature gradients are expected in the slag bath due to the heat sink caused by reduction reactions occurring between reductant particles and liquid slag on the slag bath surface. Such temperature gradients are expected to cause variations in density. The extent of the flow caused by the resulting buoyancy forces is unknown.

Details of flow phenomena occurring in the slag bath were ignored. The influence of these phenomena was incorporated into the ISFP model by assuming ideal mixing in the slag bath (Assumption 5.2, page 110).

#### c. Momentum transfer in the metal bath

Momentum from the arc and feed material is expected to influence the metal bath. The extent of this influence depends on feed rate, electrical parameters (power, current) and the depth of the slag bath. Because of the metal bath being somewhat separated from the arc and feed material by the slag bath, it is expected that these momentum sources will have a lesser influence on flow patterns in the metal bath.

Because of the metal bath being similar to the metal bath studied by Ramírez-Argáez (2003) in terms of composition, the relative influences of different phenomena on flow in the metal bath of an ilmenite-smelting furnace can be expected to be similar. For this reason it is expected that electromagnetic stirring will also be dominant in establishing flow patterns in the metal bath of an ilmenite-smelting furnace. It was reported (Ramírez-Argáez, 2003) that velocities in the metal bath can be around 0.4 m/s when a slag layer

is present. This was calculated for a metal bath with a depth of 0.5 m and a diameter of 3 m. It is unknown what the velocities in the metal bath would be for the geometry used in the current study.

Finally, buoyancy forces are expected to have only a slight influence on flow in the metal bath. The reason for this is that the direction of heat transfer in the bath is predominantly downward. Such heat transfer would cause thermal stratification of the metal bath with colder material collecting at the bottom of the furnace and hotter material remaining above. The metal bath is not stagnant, however. As already mentioned the arc, entering feed material and electromagnetic forces are all expected to cause flow in the metal bath. Such flow is likely to cause hot material to move toward the bottom of the furnace. In such a case buoyancy forces will tend to 'push' such material upward.

Again, details of flow phenomena in the metal bath were not seen as critically important for the ISFP model. All these phenomena were incorporated into the model using the assumption that the metal bath is ideally mixed (Assumption 5.3, page 111).

#### d. Momentum transfer in the freeboard

Flow in the freeboard of the furnace is expected to be influenced mostly by the following factors:

- The arc.
- Gas rising up from the slag bath.
- Buoyancy forces.

Figure 57 shows flow patterns in an empty (no feed) arc operating at 30 kA and 270 V. On this drawing it is clear that gas from the surroundings of the arc (the freeboard) is drawn into the arc at the top and middle of the arc column, and then ejected at the bottom of column. Because of the high velocities that have been measured for even small arcs (330 m/s for a 200 A arc (Stenkvist and Bowman, 1987)) the arc can be viewed as a 'pump' causing significant motion in the furnace freeboard.

Reduction reactions cause gas (approximately 150 kg per ton of ilmenite fed) to be released into the furnace freeboard. This relates to 3.75 t/h and approximately 21,600 m<sup>3</sup>/h (or 1.04 kg/s and 6.01 m<sup>3</sup>/s) of gas released into the freeboard when operating a furnace at 25 ton/h ilmenite. (Volumes were calculated at 1 atm pressure and 1700 °C.) Because this gas has to exit the furnace through a gas off-take installed in the furnace roof, the average flow of gas in the furnace freeboard has to be directed upwards and towards the off-take. Because this bulk flow rate of gas is relatively low, the flow velocities caused by it are expected to be small.

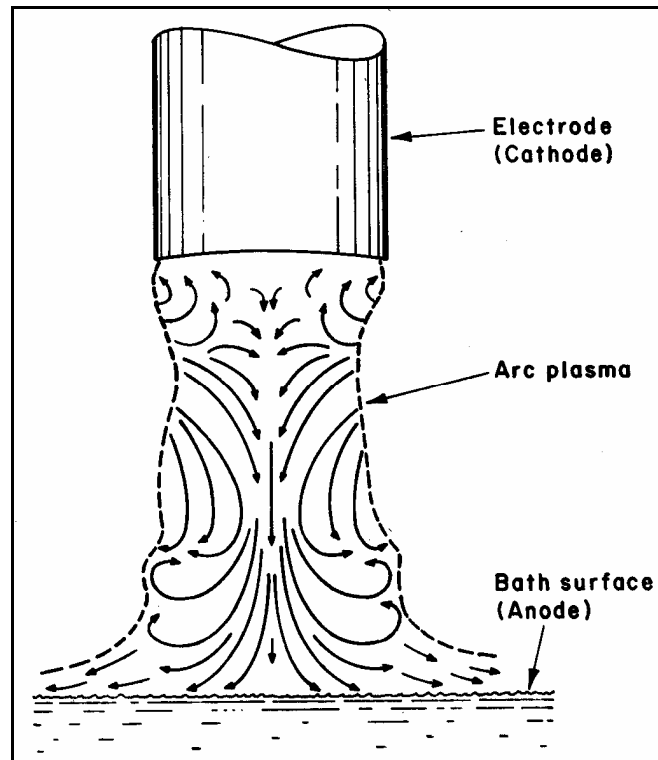


Figure 57 – Flow patterns in a 30 kA, 270 V arc. (Stenkvist and Bowman, 1987)

Gas enters the freeboard at approximately the temperature of the slag bath. Gas in the freeboard exchanges heat with the sidewalls and roof by convection and radiation. These exchanges are expected to cause variations in gas temperature (and therefore gas density) in the freeboard. These variations are then expected to result in buoyancy forces and flow in the freeboard.

Because gas has a relatively low contact and residence time in the system being considered, details of flow phenomena in the freeboard were viewed as unimportant to the ISFP model. For this reason the freeboard was assumed to be ideally mixed (Assumption 5.4, page 111).

#### 5.4.4 Chemical Reaction

Chemical reactions take place at numerous locations in the furnace between and within various phases. This paragraph describes briefly most of the reactions occurring in the furnace and their importance to the ISFP model. The discussions are organised by focussing on specific phases or materials and grouping reactions that are of specific interest to that phase or material. The following list presents the phases and materials that are used to organise the discussions below:

- Liquid slag
- Solid slag
- Liquid metal
- Reduction product gas
- Air
- Graphite

a. Chemical reactions involving liquid slag

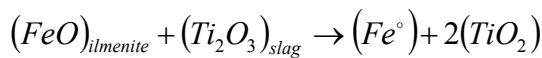
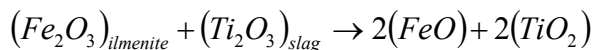
Since liquid slag is the primary product of the process, chemical reactions involving this phase are naturally very important. Of specific relevance to the liquid slag are its chemical reaction with ilmenite, reductant, refractory material and chemical reactions within the liquid slag phase.

i. Reaction between liquid slag and ilmenite

As feed material enters the furnace through the hollow electrode, through the arc and into the turbulent zone beneath the arc, at least some ilmenite particles are expected to melt. Due to the relatively short residence time of material flowing at high rates through small volume occupied by the arc some ilmenite particles are expected to arrive in the bath still in the solid state.

Due to the high temperature of the slag bath (1620 to 1680 °C [Geldenhuis and Pistorius, 1999]) and the even higher temperatures prevailing in the zone beneath the arc, ilmenite particles arriving in the bath in the solid state are expected to melt quickly. This is due to the relatively low melting point of ilmenite of around 1397 °C (FactSage 5.2).

Because of the reduction work that is continuously being done in the furnace, the liquid slag in the slag bath exists in a more reduced state compared with molten ilmenite. The newly-melted ilmenite will therefore tend to oxidise the liquid slag. The following reactions are expected to occur:

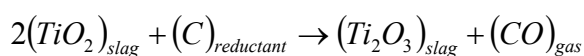
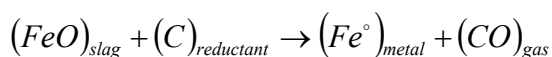
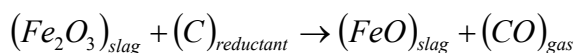


The subscripts *ilmenite* and *slag* used above indicate the origin of the species within the context of the current discussion. Liquid ilmenite and slag do not exist as two separate phases. Further, the species indicated above exist in ionic form in the slag and the reactions will tend to be redox reactions between cations. This applies to all reactions described subsequently that involve liquid slag phase constituents.

The reactions described above were of critical importance to the ISFP model and was incorporated into the model.

ii. Reaction between liquid slag and reductant

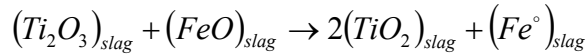
Reduction of liquid slag by solid reductant particles is the primary means of converting feed material to products in the process. The following reactions are expected to occur:



The reactions described above were of critical importance to the ISFP model and were incorporated into the model.

## iii. Reaction between liquid slag and liquid slag

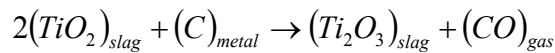
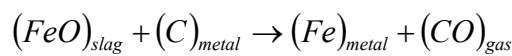
Reduction reactions occurring at the interface between liquid slag and reductant particles may occur to such an extent that the products of these reactions are more reduced than the bulk liquid slag. In such a case the reduction products would tend to reduce some species in the bulk liquid slag.



The above reaction was of critical importance to the ISFP model and was incorporated into the model.

## iv. Reaction between liquid slag and liquid metal

Reduction reactions occurring at the interface between the slag and metal baths occur because of the high carbon content of the liquid metal. The following reactions are expected to occur.



The above reactions were of critical importance to the ISFP model and were incorporated into the model.

## v. Reaction between liquid slag and refractory material

As has been discussed in CHAPTER 2, no known refractory material can withstand the chemical attack of liquid high-titania slag. The high-MgO refractory brick used in ilmenite-smelting furnaces simply dissolves in liquid slag if it is not protected by a freeze lining.

Reactions involving refractory materials were not viewed as important to the current study and were therefore omitted from the ISFP model.

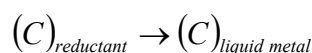
## b. Chemical reactions involving solid slag

Chemical reactions involving solid slag have been discussed in CHAPTER 3 and CHAPTER 4. The reader is referred to paragraphs 3.4.4 (page 32) and 4.4.4 (page 68).

## c. Chemical reactions involving liquid metal

## i. Reaction between liquid metal and reductant

It is suspected that reductant particles come into contact with liquid metal in the turbulent zone underneath the electrode. This contact is expected to result in the dissolution of carbon and other species in liquid metal.



The above reaction was viewed as important and was included in the ISFP model.

## ii. Reaction between liquid metal and refractory material

According to equilibrium calculations with FactSage 5.2, some interaction between the liquid metal phase and MgO refractory brick can occur. The calculations indicated a very small amount of FeO (0.001%) being

taking up into a monoxide solid solution phase with MgO. Some Mg (0.004%) and MgO (0.002) were also observed in the calculated state of the liquid metal phase.

The above dissolution reactions were not viewed as being of significant importance to the ISFP model. For this reason they were omitted from the model.

#### d. Chemical reactions involving reduction product gas

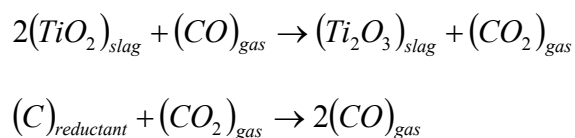
##### i. Reaction between gas and liquid slag

Gas bubbles rising up through the liquid slag layer are expected to interact with the surrounding slag. Should this gas come into contact with slag that is more oxidised (higher  $P_{O_2}$ ) than the environment in which the gas was formed, the composition of the gas bubble would shift to containing more  $CO_2$  and  $H_2O$  and less  $CO$  and  $H_2$ . If it comes into contact with slag that is more reduced than its initial composition, the composition of the gas in the bubble will shift in the opposite direction.

Reactions involving gas after reduction were seen as unimportant to the ISFP model. The reason for this is that the shifts in gas composition mentioned above proved to be very slight when studying it with FactSage 5.2. These reactions were therefore ignored. It was assumed that all gas formed as a result of reduction reactions immediately escapes into the freeboard and does not come into contact with slag, metal or reductant again (Assumption 5.5, page 111).

##### ii. Reaction between gas and reductant

It is expected that gas that formed as a result of reaction between liquid slag and solid reductant may remain in contact with the reductant particle that it originated from. This gas may act as an intermediate layer between liquid slag and solid reductant. The reactions taking place in this gaseous layer with liquid slag on one side and solid reductant on the other are expected to be as follows:



FactSage 5.2 was used to determine the limiting extents of the two reactions above. First pure  $CO$  was brought into contact with a 15-55-30 (FeO-TiO<sub>2</sub>-Ti<sub>2</sub>O<sub>3</sub> mass percentages) slag at 1700 °C. The result was that the gas phase reached a composition of 93.3-6.7 ( $CO$ - $CO_2$  volume percentages) and some  $TiO_2$  was reduced to  $Ti_2O_3$ . Pure  $CO_2$  was then brought into contact with pure graphite at the same temperature. The result was a gas containing virtually 100%  $CO$ .

These results show that pure  $CO$  gas has only limited capacity to reduce liquid high-titania slag at furnace operating temperatures. It was concluded that inclusion of a gas-reductant interface would not add significantly to the ability of the ISFP model to describe the process. These reactions were therefore excluded from the model and the assumption that all gas formed as a result of reduction reactions immediately escapes into the freeboard was applied again (Assumption 5.5, page 111).

#### e. Chemical reactions involving air

It is well known that some air is drawn into the furnace during operation due to fluctuations in furnace pressure. The oxygen entering the system in this way tends to increase the oxygen potential in the system slightly. This results in increased consumption of reductant. The entrained air is expected to react primarily with gas in the freeboard to combust CO and H<sub>2</sub> to CO<sub>2</sub> and H<sub>2</sub>O. Since the freeboard gas is extracted via the gas off-take, the residence time of the combusted species in the furnace is expected to be small. The influence of entrained air on the process is therefore expected to be limited.

Reactions of air with gas during operation were seen as unimportant to the current work. For this reason these reactions were omitted from the ISFP model. It was assumed that no air enters the furnace during operation (Assumption 5.6, page 112).

Large volumes of air are drawn into the system when the furnace is shut down for maintenance and inspections. During such times the furnace pressure is controlled at a negative value relative to ambient. The air entering the furnace during such periods is expected to react with reductant on the slag bath surface, liquid slag at the slag bath surface and with the solid slag crust once such a crust has formed. The implications of these reactions are that oxygen is added to the process and carbon is removed. This exactly opposes the objectives of the process. The end result of such periods of down time is that additional energy and reductant have to be added to the process to bring it back to the desired operating state.

The influence of air on the process during periods of down time can certainly be significant. Phenomena associated with air exposure were however not the focus of the current work. For this reason all reactions related to air exposure during periods of down time were omitted from the ISFP model. It was assumed that no air enters the furnace during periods of down time (Assumption 5.7, page 112).

#### f. Chemical reactions involving graphite

The graphite electrode column is exposed to reaction with many phases in the process. It is expected that slag and, to a lesser extent, metal are splashed onto the lower part of the column. Slag is expected to be reduced by the graphite and some graphite is expected to dissolve into liquid metal droplets. In both these cases graphite is consumed on the surface of the column. This results in increased electrode consumption.

The largest part of the electrode column present inside the furnace is exposed to gases in the furnace freeboard. Since reduction product gas is highly reduced (low P<sub>O<sub>2</sub></sub>), this gas is not expected to have a major influence on the column.

Air drawn into the furnace during normal operation could adversely affect the electrode. Because it is likely that at least some of the air drawn in will enter the furnace between the electrode column and the seal surrounding it in the flat part of the furnace roof, it is also likely that some of this air will react with the hot electrode column at this location. This can increase electrode consumption significantly if the seal is leaking badly.

During periods of down time when the furnace is kept under negative pressure, air drawn in is also expected to react with the electrode column, especially the hot tip. As the column cools down the rate of these reactions are expected to decrease.

All reactions involving electrode graphite were viewed as unimportant to the ISFP model. For this reason all such reactions were omitted from the model.

### 5.4.5 Mechanical Effects

Some mechanical effects were discussed in paragraph 3.4.5 (page 33). The reader is referred to this paragraph for details.

#### a. Slag and metal tapping

The ilmenite-smelting process is operated in a semi-continuous manner. This means that inputs are supplied to the process as continuously as possible, while all products except gas and dust are extracted in batches. This practice results in continuous variation in slag and metal levels in the furnace. The levels of both slag and metal rise as material is fed. The slag level drops when slag is tapped. Both the metal and slag levels drop when metal is tapped.

The varying slag layer thickness and position have a marked influence on the behaviour of the freeze lining. These variations cause the freeze lining's properties to vary in at least two dimensions (radial and axial). The freeze lining was however modelled using a 1-dimensional approach in CHAPTER 3. This was done to simplify the modelling work. This simplification now has a significant impact on how the ISFP model is to be approached. The axial variations caused by varying slag and metal bath levels cannot be described in the ISFP model when using the FLC model to describe the freeze lining. For this reason a simplification had to be introduced (Simplification 5.1, page 113).

It was decided to keep slag and metal bath levels constant in the ISFP model by extracting slag and metal continuously from the system (equivalent to continuous tapping). This is not an accurate description of the actual process, but the consequences of this simplification were accepted within the scope of this study.

#### b. Cave-in of accretions

Material projected towards the walls by the force of the arc and dust from the freeboard collect on the furnace sidewalls and roof to form accretions. These accretions do not simply grow until the entire freeboard is clogged up, but they are also continuously melted away and dripping into the slag bath. In some cases large pieces of accretions detach from the sidewalls and/or roof and fall into the slag bath. This can cause sudden mixing of portions of the slag and metal baths. Such mixing can cause accelerated reaction between the high carbon metal and the slag.

The cave-in of accretions was not of interest during the current study and this phenomenon was therefore omitted from the ISFP model.

#### c. Water leaks

Water cooling is used to extract heat from the roof and gas off-take of the furnace. These water cooling systems sometimes rupture or crack, causing water to enter the freeboard or off-gas duct. When the flow of water from such a leak is significant it can result in water reaching the slag bath surface. This poses a very real threat in terms of explosions. Furnaces have been damaged in the past by such explosions.



Water leaks and their influence on the process and equipment were not relevant to this study. These phenomena were therefore omitted from the ISFP model.

### 5.4.6 Summary of Key Phenomena

The table below summarises the phenomena identified above and assigns a level of importance to each phenomenon within the context of the ISFP model. A level of importance of 1 means that the phenomenon was considered unimportant and it was subsequently ignored. Level 2 indicates that the phenomenon had to be incorporated into the model, but it was not necessary to model it in detail. Level 3 marks critical phenomena that had to be modelled in as much detail as possible.

		Level of importance to current modelling effort			
		1	2	3	
Heat transfer	From the arc			✓	
	Between slag bath and metal bath		✓		
	From slag bath surface to freeboard			✓	
	From slag bath to freeze lining and sidewall				✓
	From slag bath to crust and freeboard				✓
	From metal bath to sidewalls and hearth			✓	
	Through upper sidewalls and roof			✓	
Mass transfer	Bulk flow	Feed materials			✓
		Product materials			✓
		Metal droplets through slag bath	✓		
		Gas from slag bath surface into freeboard	✓		
		Gas through slag bath into freeboard	✓		
		Process material to sidewalls and roof	✓		
		Process material from sidewalls and roof into slag bath	✓		
	At slag-reductant interface			✓	
	At interface between slag and metal baths			✓	
	Carbon into metal bath			✓	
At interface between slag bath and freeze lining			✓		
Momentum transfer	Momentum sources	The arc	✓		
		Feed material	✓		
		Electromagnetic stirring	✓		
		Rising gas	✓		
		Buoyancy forces	✓		
	In the slag bath			✓	
In the metal bath			✓		
In the freeboard		✓			
Chemical reaction	Liquid slag	With ilmenite			✓
		With reductant			✓
		With liquid slag			✓
		With liquid metal			✓
	Solid slag	With refractory material	✓		
		With liquid slag			✓
		With solid slag	✓		
	Liquid metal	With liquid metal	✓		
		With reductant		✓	
	Reduction product gas	With refractory material	✓		
		With liquid slag	✓		
Air	With reductant	✓			
	With refractory material	✓			
Mechanical effects	Slag and metal tapping		✓		
	Cave-in of accretions		✓		

	Water leaks	✓				
--	-------------	---	--	--	--	--

Table 6 – Summary of key phenomena for the ISFP model.

## 5.5 APPROACH AND MODEL COMPLEXITY

From Table 6 it is clear that heat transfer to the freeze lining and crust, bulk mass flow of feed and product materials, and chemical reactions involving liquid slag are most important to the ISFP model. Details related to the freeze lining and crust have been addressed in the FLC and SBCC models. These models were therefore incorporated into the ISFP model.

Describing bulk flow of mass and energy into and out of the system requires first of all a mass and energy balance. In addition to this some framework is required to model the important reactions taking place at the various phase boundaries. The modelling methodology developed by Pauw (1989) addresses all these requirements and it was therefore chosen as the approach for the ISFP model. Definitions and descriptions of the model elements used in the Pauw approach are given in APPENDIX B.

Within the methodology developed by Pauw (1989) Gibbs-free-energy minimisation is used to model chemical reactions. This was discussed in paragraph 3.5.2 (page 35) and the reader is referred to this paragraph for details.

## 5.6 MODEL FORMULATION

### 5.6.1 Assumptions

The following paragraphs list assumptions made as part of the ISFP model formulation. The paragraphs clarify why the assumptions were made, their validity and the impact that the assumptions have on the model.

#### a. Assumption 5.1

Statement: The slag bath, metal bath and furnace freeboard are all at the same temperature.

Justification: The assumption was made to simplify the model. If the model had to describe different temperatures for the three zones, it would have been significantly more complicated in addition to the fact that other assumptions would have been required to formulate heat transfer between the metal bath and slag bath, and between the slag bath and freeboard.

Validity: The assumption statement is not true in the actual process. It has already been stated that the metal bath is usually colder than the slag bath because the slag bath is located between the metal bath and the arc. A significant amount of heat is also extracted from the metal bath through the lower sidewalls and hearth. Differences between slag and metal temperatures have been reported to be between 50 and 90 °C (Geldenhuis and Pistorius, 1999).

The assumption also does not hold for gas in the freeboard because heat is extracted from this gas by radiation and convection to the furnace roof and walls. It is however

believed that the difference in temperature between freeboard and slag bath will be less than the difference in temperature between the slag and metal baths.

Impact: Inaccuracies were caused by this assumption. The errors made with either slag or metal temperature were expected to be less than the actual difference in temperature between these two phases (between 50 and 90 °C) since the model was configured to calculate an average temperature for the system. Temperature variations in this range proved to have a relatively small effect on the result of equilibrium calculations describing reduction reactions. These calculations were done with FactSage. The inaccuracies associated with the assumption were therefore deemed to be acceptable.

#### b. Assumption 5.2

Statement: The slag bath is ideally mixed.

Justification: The assumption was introduced to simplify the model. The alternatives to this assumption were the introduction of additional slag mixers in the model, and the development of a complete fluid flow model of the slag bath. Both alternatives introduce significant additional complexity into the model. The first alternative would also required assumptions regarding flow in the bath based on the same information available when the current assumption was made. It did not seem that any significant value could be added to the model in this way.

The second alternative could have proved more fruitful, but at the expense of significant additional complexity and longer model execution times.

Validity: The assumption statement is not absolutely true in the actual process. However, due to significant momentum transferred to the slag bath by entering feed material, the arc, electromagnetic forces, rising gas and buoyancy forces, it is expected that this assumption is a fair approximation of conditions in an actual slag bath.

Impact: Because the assumption is not an absolutely accurate description of conditions in the actual process, it caused inaccuracies in the model. Because of the mixing occurring in the slag bath, these inaccuracies were believed to be negligible.

#### c. Assumption 5.3

Statement: The metal bath is ideally mixed.

Justification: The same justification supplied for Assumption 5.2 holds for this assumption regarding the metal bath.

Validity: This assumption, similar to Assumption 5.2, was believed to be a good approximation of reality. This is due to significant stirring in the metal bath as a result of momentum transferred from the arc, entering feed material, electromagnetic forces and buoyancy forces.

Impact: It was believed that inaccuracies resulting from this assumption were negligible.

#### d. Assumption 5.4

Statement: Gas in the freeboard is ideally mixed.

- Justification: This assumption was made because the gas phase in the furnace freeboard is not very important within the context of the model.
- Validity: This assumption was believed to be a fair approximation of the actual condition in the furnace freeboard. The reason for this was the significant fluid flow caused in the freeboard by the arc.
- Impact: The assumption had virtually no impact on the model due to the way in which the gas phase was handled in the model. Any gas formed during reduction was simply removed from the system virtually as soon as it was produced.

#### e. Assumption 5.5

- Statement: Gas produced by any form of reduction reaction in the process immediately escapes into the freeboard and does not come into contact with slag, metal or reductant again.
- Justification: This assumption was introduced to simplify the model. Without it interfaces between liquid slag and gas and between reductant and gas would have been required. Inclusion of such interfaces in the model would have required more assumptions and would not have added significantly to the functionality of the model.
- Validity: It is well known that gas does not instantly escape into the freeboard once formed. Gas formed at the interface between the slag and metal baths has to rise through the slag bath before it reaches the freeboard. Gas formed at the interface between liquid slag and reductant is also expected to remain attached to the reductant particle for at least a small period of time. The assumption statement is therefore not true.
- Impact: It was deemed that the impact of this assumption would have negligible influence on the model's accuracy.

#### f. Assumption 5.6

- Statement: No air enters the furnace during operation.
- Justification: This assumption was made so that air entrainment could be ignored in the model. The influence of air on the system was not the focus of the study and inclusion of air entrainment would have caused unnecessary complexities in the model. Such inclusion would have required at least one additional assumption to be made anyway.
- Validity: Fluctuations in furnace pressure during operation cause air to be drawn into the furnace from time to time. For this reason the assumption statement is not true.
- Impact: Air entrainment causes post combustion and a reduction in reductant efficiency. Since air entrainment is not included in the model, these phenomena could not be described by it.

#### g. Assumption 5.7

- Statement: No air enters the furnace during periods of down time.
- Justification: This assumption was made for the same reasons as Assumption 5.6.
- Validity: The statement of this assumption is certainly not true since large volumes of air are drawn into the furnace while it is under negative pressure during periods of down time.

Impact: This assumption causes inaccuracies in the description of transient behaviour associated with furnace down time. Such behaviour was however not the focus of this study. For this reason such inaccuracies could be tolerated.

### 5.6.2 Simplifications

The following paragraphs list simplifications that were made in the model. The justification and impact of the simplifications are also presented.

#### a. Simplification 5.1

Description: The model was configured in such a way that slag and metal were tapped continuously from the furnace.

Justification: This simplification was required because the FLC model used to describe the freeze lining is a one-dimensional model describing melting and solidification in only the radial dimension. This meant that variations in the axial dimension caused by changing slag and metal levels could not be described with the FLC model.

Impact: This simplification caused a significant difference between the dynamic behaviour of the process as described by the ISFP model and the dynamic behaviour of the actual process. Even though this was the case, it was concluded that the description of process behaviour provided by the ISFP model inclusive of this simplification would be adequate given the objectives of the current work.

#### b. Simplification 5.2

Description: A collection of stoichiometric condensed phases was used to describe ilmenite instead of a collection of solid solution phases.

Justification: This simplification was required because of the fact that no detailed mineralogical analyses of ilmenite were available for use in this study.

Impact: The simplification caused inaccuracies in describing the enthalpy of ilmenite and other of its thermodynamic properties. These inaccuracies were deemed to be acceptable within the context of the ISFP model.

### 5.6.3 Material Definitions

The definitions of the liquid slag and solid slag materials used in the ISFP model are in many respects identical to the definitions used for the FLC model. For many of the materials used in the ISFP model, the reader is referred back to the definitions made in the chapter describing the FLC model.

#### a. Ilmenite

The titanium-bearing material fed into the ilmenite-smelting furnace is named Ilmenite within the context of the ISFP model.

Ilmenite was defined to contain the following phases:

- Rutile stoichiometric condensed phase.
- Hematite stoichiometric condensed phase.

- Ilmenite stoichiometric condensed phase.

#### i. Rutile Stoichiometric Condensed Phase

Actual constituents: It is known that a rutile solid solution can contain  $\text{TiO}_2$ ,  $\text{Ti}_2\text{O}_3$ ,  $\text{ZrO}_2$  (Eriksson et al., 1996; FactSage 5.2). However, due to no detailed mineralogical analyses being available, a simple stoichiometric condensed phase was used.

Considered constituents:  $\text{TiO}_2$ .

Solution model: None.

Thermochemical data: ChemSage format data file from GTT Technologies.

#### ii. Hematite Stoichiometric Condensed Phase

Actual constituents: Hematite occurs as a solid solution (with  $\text{FeTiO}_3$ ) in reality (FactSage 5.2). However, due to no detailed mineralogical analyses being available, a simple stoichiometric condensed phase was used.

Considered constituents:  $\text{Fe}_2\text{O}_3$ .

Solution model: None.

Thermochemical data: ChemSage format data file from GTT Technologies.

#### iii. Ilmenite Stoichiometric Condensed Phase

Actual constituents: In reality ilmenite is a solid solution containing, for example,  $\text{Ti}_2\text{O}_3$ ,  $\text{MgTiO}_3$ ,  $\text{FeTiO}_3$  and  $\text{MnTiO}_3$  (FactSage 5.2). However, due to no detailed mineralogical analyses being available, a simple stoichiometric condensed phase was used.

Considered constituents:  $\text{FeTiO}_3$ .

Solution model: None.

Thermochemical data: ChemSage format data file from GTT Technologies.

#### b. Reductant

Anthracite and charred coal are used as reductants in the ilmenite-smelting process. These materials contain ash, volatile matter, moisture and carbon. Reductant is however represented here as pure graphite.

Reductant was defined to contain only a single phase, named Graphite Phase.

#### i. Graphite Phase

Actual constituents: Numerous organic species are found in the carbonaceous phase of coals and anthracite. Detail regarding most of these species was ignored here.

Considered constituents: For the purpose of the ISFP model, the phase was viewed as being pure carbon.

Solution model: None

Thermochemical data: FactSage 5.2. (Bale et al, 2002)

c. Liquid Slag

Refer to paragraph 3.6.3a on page 39.

d. Liquid Metal

Refer to paragraph 3.6.3b on page 39.

e. Gas

Gas is produced as a product of reduction reactions in the process.

Gas was defined to contain only a single phase, named Gas Phase.

i. Gas Phase

Actual constituents: It is likely that numerous species exist in the gas phase in the actual process. It is virtually impossible to compile a complete list of constituents here.

Considered constituents: C, C<sub>2</sub>, C<sub>3</sub>, C<sub>4</sub>, C<sub>5</sub>, O, O<sub>2</sub>, O<sub>3</sub>, CO, C<sub>2</sub>O, CO<sub>2</sub>, C<sub>3</sub>O<sub>2</sub>, Ar, Ti, TiO, Fe, FeO, and Fe(CO)<sub>5</sub>. (Of these constituents only CO and CO<sub>2</sub> occurred in significant amounts.)

Solution model: Ideal mixture.

Thermochemical data: ChemSage format data file from GTT Technologies.

f. Solid Slag

Refer to paragraph 3.6.3c on page 40.

g. Magnesite Brick

Refer to paragraph 3.6.3d on page 41.

h. Ramming

Refer to paragraph 3.6.3e on page 41.

i. Steel

Refer to paragraph 3.6.3f on page 41.

### 5.6.4 Model Structure

This paragraph and its sub-paragraphs show and describe the various elements of the ISFP model's structure. The model structure was built using energy and material modules and flow streams as defined by Pauw (1989).

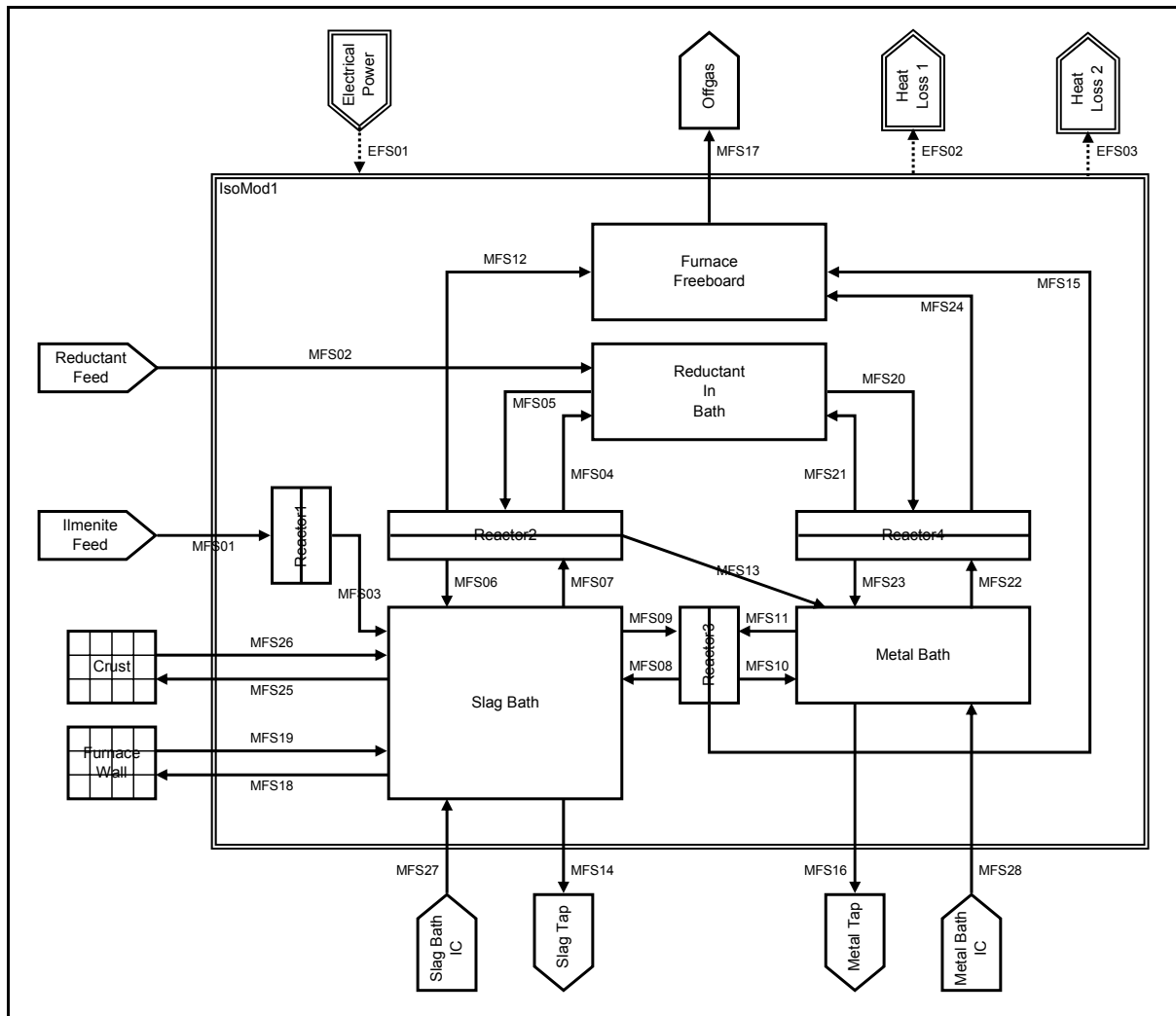


Figure 58 – Flow sheet of ISFP model.

a. Energy Modules

NAME	DESCRIPTION	CALCULATIONS
<b>Energy Input Modules</b>		
ElectricalPower	This energy input module represents the DC electrical power supply of the furnace. It supplies energy to fuel heating, melting and reduction reactions occurring in the process.	The power supplied via the ElectricalPower module was specified as a fixed parameter forming part of the definition of the scenario being modelled, or as a ratio to the feed rate of the IlmeniteFeed module.
<b>Energy Output Modules</b>		
HeatLoss1	This energy output module represents a portion of the heat loss from the process that is lost through the upper sidewalls and roof.	None.
HeatLoss2	This energy output module represents heat losses from the process through the lower sidewalls and hearth.	None.
<b>Isothermal Modules</b>		
IsoMod1	This isothermal module represents virtually the entire content of the furnace. The only exclusions from it are the solid slag of the freeze lining and the solid slag of the crust when a crust is present. Since these parts of the process contain temperature gradients that are important to the current study, they could not be described using an isothermal module.	Enthalpy integration.

Table 7 – Description of energy modules used in the ISFP model.



## b. Energy Flow Streams

NAME	DESCRIPTION	CALCULATIONS
EFS01	This energy flow stream delivers energy supplied by the ElectricalPower module to the IsoMod1 module.	None.
EFS02	This energy flow stream calculates the rate at which energy is lost via the upper sidewalls and roof as a result of convection and radiation from the portion of the bath surface that is not covered by the Crust conductor module. It withdraws energy at this rate from the IsoMod1 module and delivers it to the HeatLoss1 module.	§ 5.6.6a, p. 121.
EFS03	This energy flow stream calculates the rate at which energy is lost via the lower sidewalls and hearth that is in contact with the metal bath. It withdraws energy at this rate from the IsoMod1 module and delivers it to the HeatLoss2 module.	§ 5.6.6b, p. 122.

Table 8 – Description of energy flow streams used in the ISFP model.

## c. Material Modules

NAME	DESCRIPTION	CALCULATIONS
<b>Material Input Modules</b>		
SlagBathIC	This material input module does not refer to any physical part of the actual process. It was included into the model to generate an initial condition (IC) of the slag bath state.	The feed rate of the SlagBathIC module was specified as fixed parameters forming part of the definition of the scenario being modelled.
MetalBathIC	This material input module does not refer to any physical part of the actual process. It was included into the model to generate an initial condition (IC) of the metal bath state.	The feed rate of the MetalBathIC module was specified as fixed parameters forming part of the definition of the scenario being modelled.
IlmeniteFeed	This material input module represents the part of the feed system that charges ilmenite into the furnace.	The feed rate of the IlmeniteFeed module was specified as a fixed parameter forming part of the definition of the scenario being modelled.
ReductantFeed	This material input module represents the part of the feed system that charges reductant into the furnace.	The feed rate of the ReductantFeed module was specified as a fixed parameter forming part of the definition of the scenario being modelled, or as a ratio to the feed rate of the IlmeniteFeed module.
<b>Material Output Modules</b>		
SlagTap	This material output module represents slag being tapped from the furnace through a slag tap hole.	None.
MetalTap	This material output module represents metal being tapped from the furnace through a metal tap hole.	None.
Offgas	This material output module represents gas being extracted from the furnace off-gas system.	None.
<b>Ideal Mixers</b>		
SlagBath	This mixer represents all liquid slag in the furnace.	Mass integration.
ReductantInBath	This mixer represents all reductant particles in the furnace.	Mass integration.
MetalBath	This mixer represents all liquid metal in the furnace.	Mass integration.
FurnaceFreeboard	This mixer represents all gas in the furnace.	Mass integration.
<b>Reactors</b>		
Reactor1	This reactor represents the melting of ilmenite occurring in the process as this feed material heats up.	Gibbs-free-energy minimisation.
Reactor2	This reactor represents all reduction reactions taking place at an interface between liquid slag and reductant.	Gibbs-free-energy minimisation.
Reactor3	This reactor represents all reduction reactions taking place at an interface between liquid slag and liquid metal.	Gibbs-free-energy minimisation.
Reactor4	This reactor represents contact between reductant particles and liquid metal in the turbulent zone underneath the electrode. The contact results in dissolution of carbon in liquid metal.	Gibbs-free-energy minimisation.

NAME	DESCRIPTION	CALCULATIONS
<b>Conductors</b>		
FurnaceWall	This conductor represents the freeze lining and furnace wall.	See CHAPTER 3.
Crust	This conductor represents a solid slag crust that forms on the slag bath surface during periods of down time.	See CHAPTER 4.

Table 9 – Description of material modules used in the ISFP model.

## d. Material Flow Streams

NAME	DESCRIPTION	CALCULATIONS
MFS01	This flow stream delivers material supplied by the IlmeniteFeed module to the Reactor1 module.	None.
MFS02	This flow stream delivers material supplied by the ReductantFeed module to the ReductantInBath module.	None.
MFS03	This flow stream delivers ilmenite melted by Reactor1 to the SlagBath module.	None.
MFS04	This flow stream delivers solid carbon not consumed by reduction reactions in Reactor2 to the ReductantInBath module.	None.
MFS05	This flow stream represents reductant involved in reduction reactions due to contact with liquid slag. It draws material from the ReductantInBathModule and delivers it to Reactor2.	§ 5.6.8a, p. 125.
MFS06	This flow stream delivers the liquid slag product of reduction reactions in Reactor2 to the SlagBath module.	None.
MFS07	This flow stream represents liquid slag involved in reduction reactions due to contact with reductant particles. It draws material from the SlagBath and delivers it to Reactor2.	§ 5.6.8a, p. 125.
MFS08	This flow stream delivers the liquid slag product of reduction reactions in Reactor3 to the SlagBath module.	None.
MFS09	This flow stream represents liquid slag involved in reduction reactions due to contact with liquid metal having high carbon content. It draws material from the SlagBath and delivers it to Reactor3.	§ 5.6.8b, p. 129.
MFS10	This flow stream delivers the liquid metal product of reduction reactions in Reactor3 to the MetalBath module.	None.
MFS11	This flow stream represents high-carbon liquid metal involved in reduction reactions due to contact with liquid slag. It draws material from the MetalBath and delivers it to Reactor3.	§ 5.6.8b, p. 129.
MFS12	This flow stream delivers the gaseous product of reduction reactions in Reactor2 to the FurnaceFreeboard module.	None.
MFS13	This flow stream delivers the liquid metal product of reduction reactions in Reactor2 to the MetalBath module.	None.
MFS14	This flow stream represents liquid slag tapped from the furnace through a slag tap hole. It extracts material from the SlagBath module and delivers it to the SlagTap output module.	§ 5.6.7a, p. 124.
MFS15	This flow stream delivers the gaseous product of reduction reactions in Reactor3 to the FurnaceFreeboard module.	None.
MFS16	This flow stream represents liquid metal tapped from the furnace through a metal tap hole. It extracts material from the MetalBath module and delivers it to the MetalTap output module.	§ 5.6.7b, p. 124.
MFS17	This flow stream represents gas extracted from the furnace by the off-gas system. It extracts material from the FurnaceFreeboard module and delivers it to the Offgas module.	None.
MFS18	This flow stream represents liquid slag circulating past the freeze lining due to stirring in the slag bath. It extracts liquid slag from the SlagBath module and delivers it to the FurnaceWall conductor.	§ 5.6.8c.i, p. 131.
MFS19	This flow stream delivers liquid slag that had been melted or that had not been solidified by the FurnaceWall conductor to the SlagBath module.	None.
MFS20	This flow stream represents reductant involved in dissolution reactions due to contact with liquid metal in the turbulent zone underneath the arc. It draws material from the ReductantInBath and delivers it to Reactor4.	§ 5.6.8b.i, p. 129.
MFS21	This flow stream delivers solid carbon not consumed by dissolution in Reactor4 to the ReductantInBath module.	None.
MFS22	This flow stream represents liquid metal involved in dissolution reactions due to contact with reductant particles in the turbulent zone underneath the arc. It draws material from the MetalBath and delivers it to Reactor4.	§ 5.6.8b.i, p. 129.

NAME	DESCRIPTION	CALCULATIONS
MFS23	This flow stream delivers the liquid metal product of dissolution reactions in Reactor4 to the MetalBath module.	None.
MFS24	This flow stream delivers the gaseous product of reactions in Reactor4 to the FurnaceFreeboard module. It is fairly unlikely that gas will be generated by this reactor, but this flow stream was nevertheless added.	None.
MFS25	This flow stream represents liquid slag circulating past the slag bath surface or crust (when it is present) due to stirring in the slag bath. It extracts liquid slag from the SlagBath module and delivers it to the Crust conductor.	§ 5.6.8d.i, p. 132.
MFS26	This flow stream delivers liquid slag that had been melted or that had not been solidified by the Crust conductor to the SlagBath module.	None.
MFS27	This flow stream delivers material supplied by the SlagBathIC module to the SlagBath module.	None.
MFS28	This flow stream delivers material supplied by the MetalBathIC module to the MetalBath module.	None.

Table 10 – Description of material flow streams used in the ISFP model.

### 5.6.5 From Model Structure to Process Model

The model structure presented above is a representation of the ilmenite–smelting process built by using the language of fairly generic flow streams and modules proposed by Pauw (1989). The flow streams and modules constitute a layer of modelling infrastructure that is able to do the following routine process modelling tasks:

- Mass balancing.
- Energy balancing.
- Temperature calculations.
- Gibbs–free–energy–minimisation calculations.
- One–dimensional conduction combined with solidification and melting.

However useful this layer of infrastructure may seem, it is not yet able to describe the behaviour of the process of interest. Some additional information must be specified and some more knowledge needs to be embedded into the structure before it can be viewed as a complete process model. The following aspects still need to be addressed:

- Specification of initial conditions.
- Specification of model inputs.
- Formulation of sub–models to describe phenomena that influence the dynamic behaviour of the process.
- Specification of values for sub–model parameters.

#### a. Initial conditions

It is necessary to generate initial conditions for a modelling experiment so that the starting point of the experiment can be controlled. One would not, for example, want to execute an experiment starting with an empty furnace at ambient temperature. It would be far less cumbersome to start the model with filled metal and slag baths with desired compositions, the system at a desired temperature, and some chosen initial states for the freeze lining and crust conductor modules.

In the structure shown in Figure 58 (page 116) all the modules that are able to describe part of the state of the process are candidates for requiring initial conditions. The following is a list of such modules:

- Isothermal modules  
Because isothermal modules contain mixer modules that contain material, an isothermal module itself does not need to be given an initial condition. Proper initialisation of its contained mixers would be adequate.
- Mixers  
The mass and composition of material contained in mixers are initialised by feeding material into these mixers by material input modules that are included into the model structure specifically for the purpose of generating initial conditions. The initial temperature of an isothermal module is set by feeding material into its contained mixers at the desired temperature.

In the case of the model presented in Figure 58 (page 116) it was decided that only the SlagBath and MetalBath mixers need initial conditions. Material was fed into these mixers at the start of experiments to set up the desired initial conditions.

- Conductor modules  
Conductor models are initialised by specifying an initial steady-state heat flow rate and an initial composition of the solid slag layer if solid slag is present at the specified heat flow rate. In the case of the FurnaceWall conductor this results in an initial temperature profile in each of the conductor layers as well as an initial freeze lining thickness and composition. In the case of the Crust conductor module it results in an initial temperature profile and composition for the solid slag layer if the specified heat flow rate can sustain such a layer.

#### b. Model inputs

Model inputs refer to parameters in the actual process that are usually manipulated from outside the process. For example, an operator decides on the feed rate at which the process must be operated. Similarly in the case of the model, parameters such as ilmenite feed rate, reductant feed rate, electrical power, and slag and metal tapping rates must be specified as functions of time so that the model can react to the variations in these parameters.

In the case of the ISFP model, however, slag and metal tapping rates were not manipulated as model inputs. Due to Simplification 5.1 (page 113) two very simple sub-models were used to specify the tapping rates. These sub-models are discussed in paragraph 5.6.7 (page 124).

#### c. Sub-models and their parameters

Initial conditions and specification of model inputs combined with the model structure shown in Figure 58 (page 116) goes some way towards creating a realistic scenario to be used in an experiment. These elements provide a representation of the process, realistic initial conditions of the slag and metal baths in terms of mass, composition and temperature, and even variations in process parameters that can mimic operating conditions that had actually been used on the process or are planned to be used.

One important element is however not yet present; the sub-models that describe the phenomena that determine the dynamic behaviour of the process in question. Without these sub-models, the process model (in the case of the ISFP model) will not function at all. In other cases the model may function, but it may produce entirely unrealistic results.

Sub-models are required for each flow stream (material and energy) of which the flow is not simply the consequence of the behaviour of the module connected at its input end. For example, the flow of MFS01 is simply the consequence of the feed rate, composition and temperature specified as model inputs on the IlmeniteFeed input module. Similarly the flow of MFS12 is defined as a consequence of the results of the Gibbs-free-energy-minimisation calculations done by Reactor2. Finally, the flow definition of MFS19 is the direct consequence of the heat transfer and Gibbs-free-energy-minimisation calculations done by the FurnaceWall conductor module.

In contrast, the flows of MFS05 and MFS07 are not defined because mixers such as the SlagBath and ReductantInBath modules do not by definition push material at a specific flow rate and composition to their output flow streams. In terms of the actual process a sub-model is required for estimating the rate at which liquid slag and reductant are exposed to reduction reactions through contact between these phases. Similarly, sub-models are required for defining the flows of MFS09 and MFS11, MFS20 and MFS22, MFS18, MFS25, MFS14, MFS16, EFS02 and EFS03.

Sub-models involve numerous input and output values in their calculations. These values are classified as follows:

- Input variables  
Input variables change automatically due to calculations performed internally by the ISFP model.
- Output variables  
Output variables are those values calculated by the sub-model as functions of input variables and model parameters.
- Model parameters  
Model parameters are values set by the user of the ISFP model. These parameters are used to fit or tune the ISFP model to describe the actual process more accurately.

The sub-models used for defining the flows of the above-mentioned flow streams are described and formulated in subsequent paragraphs.

### 5.6.6 Sub-models to Calculate Heat Losses

a. HeatLoss1Rate: Heat losses through upper sidewalls and roof

i. Modelled phenomena

Heat losses from the slag bath surface through the upper sidewalls and roof have been discussed in paragraphs 5.4.1c (page 93) and 5.4.1g (page 93). The reader is referred to these paragraphs for a description of the phenomena described by this sub-model.

## ii. Approach

The approach for calculating heat losses from the top of the slag bath that was followed for the SBCC model in CHAPTER 4 was also applied here. The heat lost through the upper sidewalls and roof was therefore based on a simple heat transfer coefficient boundary condition applied at the top of the slag bath. The largest part of this heat loss was already incorporated as a boundary condition in the Crust conductor module. The heat lost from the remaining part of the slag bath surface that was not covered by the Crust conductor module, had to be calculated with this sub-model, and routed to the HeatLoss1 module.

## iii. Formulation

The sub-model was formulated with the following equation:

$$Q = h_{effective} \cdot A \cdot (T_{slag\ bath\ surface} - T_{environment})$$

SYMBOL	DESCRIPTION	CLASS	UNITS
$Q$	The rate at which heat is lost through the upper sidewalls and roof as a result of radiation and convection for the part of the slag bath surface not covered by the Crust conductor module.	Output Variable	kW
$h_{effective}$	The effective heat transfer coefficient applied on the slag bath surface to calculate the heat flow rate.	Model Parameter	kW/(m <sup>2</sup> .°C)
$A$	The surface area of the slag bath over which the effective heat transfer coefficient is applied to calculate the heat flow rate.	Model Parameter	m <sup>2</sup>
$T_{slag\ bath\ surface}$	The temperature of the slag bath surface. This value is obtained from the uppermost node of the Crust conductor module.	Input Variable	°C
$T_{environment}$	The temperature of the environment outside the furnace (ambient temperature).	Model Parameter	°C

Table 11 – Variables and parameters of the HeatLoss1Rate sub-model of the ISFP model.

## iv. Values of model parameters

The value of the surface area model parameter ( $A$ ) was calculated as the surface area of the bath that was not covered by the Crust conductor module.

Refer to paragraph 4.6.5a (page 73) for details about the effective heat transfer coefficient used here. This model parameter ( $h_{effective}$ ) was set equal to 0.019 kW/(m<sup>2</sup>.°C) when the furnace was in operation, and equal to 0.027 kW/(m<sup>2</sup>.°C) when the furnace was off.

The value of the ambient temperature model parameter ( $T_{environment}$ ) was set equal to 25 °C.

## b. HeatLoss2Rate: Heat losses through lower sidewalls and hearth

## i. Modelled phenomena

Heat losses from the metal bath through the lower sidewalls and hearth have been discussed in paragraph 5.4.1f (page 93). The reader is referred to this paragraph for a description of the phenomena described by this sub-model.

ii. Approach

The rate of heat losses through the lower sidewalls and hearth was estimated by a simple calculation. The rate-limiting heat transfer resistance in the heat transfer path was identified and only this resistance was used to calculate the heat flow rate through the wall or hearth.

Heat transfer from the metal bath through both the sidewalls and hearth involves convective heat transfer from the liquid metal to the refractory material surface, conduction through the refractory material, conduction through a ramming layer, conduction through a steel shell, and convection heat transfer from the steel shell to either water or air. In the case of the sidewalls and hearth the largest resistance was calculated to be conduction through the refractory material. This resistance was used to estimate the heat losses. The resistance offered by all other heat transfer steps (convection and conduction through other layers) were ignored. This heat was extracted from the system via the HeatLoss2 energy output module.

iii. Formulation

The sub-model was formulated with the following equation:

$$Q = k_{refractory}(T_{average}) \cdot A_{hearth} \cdot \frac{T_{metal\ bath} - T_{environment}}{\Delta x_{refractory,hearth}} + k_{refractory}(T_{average}) \cdot A_{lower\ sidewall} \cdot \frac{T_{metal\ bath} - T_{environment}}{\Delta x_{refractory,sidewall}}$$

SYMBOL	DESCRIPTION	CLASS	UNITS
$Q$	The rate at which heat is lost through the lower sidewalls and hearth as a result of convection and conduction.	Output Variable	kW
$k_{refractory}(T)$	The thermal conductivity of the refractory material as a function of temperature. The function for magnesia brick presented in APPENDIX A was used.	Input Variable	kW/(m.°C)
$A_{hearth}$	The mean surface area over which heat is conducted from the metal bath to the environment through the hearth.	Model Parameter	m <sup>2</sup>
$A_{lower\ sidewall}$	The mean surface area over which heat is conducted from the metal bath to the environment through the lower sidewalls.	Model Parameter	m <sup>2</sup>
$\Delta x_{refractory,hearth}$	The mean distance over which heat is conducted through the hearth.	Model Parameter	m
$\Delta x_{refractory,sidewall}$	The mean distance over which heat is conducted through the lower sidewalls.	Model Parameter	m
$T_{metal\ bath}$	The temperature of the metal bath. This value is obtained from the IsoMod1 module containing the MetalBath mixer.	Input Variable	°C
$T_{environment}$	The temperature of the environment outside the furnace (ambient temperature).	Model Parameter	°C
$T_{average}$	The average of $T_{metal\ bath}$ and $T_{environment}$ .	Input Variable	°C

Table 12 – Variables and parameters of the HeatLoss2Rate sub-model of the ISFP model.

iv. Values of model parameters

The values of the surface area model parameters ( $A_{hearth}$  and  $A_{lower\ sidewall}$ ) and the distance model parameters ( $\Delta x_{refractory,hearth}$  and  $\Delta x_{refractory,sidewall}$ ) were calculated based on the dimensions of the scale drawing shown in Figure 52 (page 90) and paragraph 5.3.1 (page 90).

The value of the ambient temperature model parameter ( $T_{environment}$ ) was set equal to 25 °C.

### 5.6.7 Sub-models to Calculate Product Flow Rates

#### a. SlagTapFlow: Tapping rate of slag

##### i. Modelled phenomena

Slag tapping was discussed in paragraph 5.4.5a (page 108). The way in which it was treated in the ISFP model was different from actual slag tapping due to the introduction of Simplification 5.1 (page 113). The reader is referred to these paragraphs for a description of the phenomena described by this sub-model.

##### ii. Approach

The introduction of Simplification 5.1 required that the mass of material contained in the SlagBath module remained constant after initial conditions had been established. For this reason the flow rate of slag through the SlagTap module had to be calculated in such a way that a constant slag bath mass was achieved. This was done by simply calculating the difference between the current slag bath mass and the initial slag bath mass. This mass was used to calculate the tapping flow rate.

##### iii. Formulation

The sub-model was formulated with the following equation:

$$\dot{m}^t = \frac{m^{t-1} - m^0}{\Delta t}$$

SYMBOL	DESCRIPTION	CLASS	UNITS
$\dot{m}^t$	The rate at which slag is tapped from the furnace during time step $t$ .	Output Variable	kg/h
$m^{t-1}$	The mass of slag in the SlagBath module at the end of time step $t-1$ .	Input Variable	kg
$m^0$	The mass of slag with which the SlagBath module was initialised.	Input Variable	kg
$\Delta t$	The integration time step of the ISFP model.	Input Variable	h

Table 13 – Variables and parameters of the SlagTapFlow sub-model of the ISFP model.

#### b. MetalTapFlow: Tapping rate of metal

##### i. Modelled phenomena

Metal tapping was discussed in paragraph 5.4.5a (page 108). The way in which it was treated in the ISFP model was different from actual metal tapping due to the introduction of Simplification 5.1 (page 113). The reader is referred to these paragraphs for a description of the phenomena described by this sub-model.

##### ii. Approach

The introduction of Simplification 5.1 required that the mass of material contained in the MetalBath module remained constant after initial conditions had been established. For this reason the flow rate of metal through the MetalTap module had to be calculated in such a way that a constant metal bath mass was achieved. This was done by simply calculating the difference between the current metal bath mass and the initial metal bath mass. This mass was used to calculate the tapping flow rate.



## iii. Formulation

The sub-model was formulated with the following equation:

$$\dot{m}^t = \frac{m^{t-1} - m^0}{\Delta t}$$

SYMBOL	DESCRIPTION	CLASS	UNITS
$\dot{m}^t$	The rate at which metal is tapped from the furnace during time step $t$ .	Output Variable	kg/h
$m^{t-1}$	The mass of metal in the MetalBath module at the end of time step $t-1$ .	Input Variable	kg
$m^0$	The mass of metal with which the MetalBath module was initialised.	Input Variable	kg
$\Delta t$	The integration time step of the ISFP model.	Input Variable	h

Table 14 - Variables and parameters of the MetalTapFlow sub-model of the ISFP model.

### 5.6.8 Sub-models to Calculate Mass Transfer Rates to Phase Boundaries

#### a. Reactor2Flow: Mass flow to the reductant-slag interface

##### i. Modelled phenomena

Mass transfer to the reductant-slag interface has been discussed in paragraph 5.4.2d (page 96) and chemical reaction between slag and reductant in paragraph 5.4.4a.ii (page 104). The reader is referred to these paragraphs for background on these phenomena.

This sub-model was required calculate the rates at which liquid slag and reductant are exposed to reduction reactions due to contact between these phases. Because contact between solid particles and a liquid plays a large part in this rate, it is useful to track the path of reductant particles from the point of entry into the furnace to the likely points at which these particles are completely consumed.

Reductant particles enter the furnace together with ilmenite particles through the hollow electrode in a mass ratio of around 1:10. The particles fall down the electrode and into the arc, coming in contact with high temperature plasma (12,000 to 18,000 K for plasma without feed (Stenkvisst and Bowman, 1987)). Feed material travelling through the plasma cools down the plasma to some degree. The temperatures in the arc are nevertheless expected to be extremely high. The temperature of the cathode spot that should not be influenced strongly by the introduction of feed has been reported to be around 4000 °C (Stenkvisst and Bowman, 1987). The sudden rise in temperature around reductant particles is likely to cause thermal shock and initiate devolatilisation, resulting in at least some of these particles breaking up.

The flow patterns in the arc are likely to project some reductant particles toward the furnace walls. The bulk of the particles should however pass through or past the arc in to the turbulent zone underneath the arc. Here the particles come into contact with liquid slag and probably some liquid metal. The flow patterns in this zone likely result in the newly introduced feed material to be carried down and away from the centre of the furnace. The ilmenite particles that have not melted up to this point are likely to do so and then coalesce with the liquid slag phase. Due to the difference in density between reductant (1700 kg/m<sup>3</sup> for

graphite) and liquid slag ( $3800 \text{ kg/m}^3$ ), buoyancy forces will tend to push reductant particles to the slag bath surface. These forces may however be opposed by flow patterns in the liquid slag bath.

Depending on the rate of reaction between liquid slag and reductant, small reductant particles may never arrive at the surface of the slag bath but be consumed while submerged. Larger particles may end up at the surface where they will be only partially surrounded by liquid slag. This will result in only part of their surface area being exposed to contact and reaction with liquid slag.

From the above it is obvious that a multitude of complex phenomena combine to determine the total reductant surface area exposed to contact with liquid slag. Detailed modelling of all these phenomena was outside the scope of this study. However, it was still necessary to create some basis, however conjectural, from which the rates of exposure of liquid slag and reductant could be calculated.

Another distinctive phenomenon that had to be addressed by this sub-model was the cause behind the compositional invariance of the slag composition close to the  $\text{M}_3\text{O}_5$  composition (Figure 59). From experimental results provided in CHAPTER 6 and CHAPTER 7 it seems unlikely that the explanation for the compositional invariance lies in phase chemistry effects as initially suggested by Pistorius (2002). The explanation is therefore likely to be found in some kinetic mechanism. Since detailed knowledge of such a mechanism is not available, one has to rely on data regarding the effects of the mechanism in attempts to mimic its behaviour in the ISFP model. The simplest characterisation of the mechanism's effects is the relationship between equivalent mass % $\text{Ti}_2\text{O}_3$  and equivalent mass % $\text{FeO}$  reported by Pistorius (2002).

The relationship for the  $\text{M}_3\text{O}_5$  composition is as follows (dotted line in Figure 59):

$$\text{Equivalent \%Ti}_2\text{O}_3 = -2.0722 \cdot \text{Equivalent \%FeO} + 64.282$$

Based on the results of actual furnaces published by Pistorius (2002) the following relationship was decided on for use in this sub-model (solid line in Figure 59):

$$\text{Equivalent \%Ti}_2\text{O}_3 = -2.0722 \cdot \text{Equivalent \%FeO} + 61.6$$

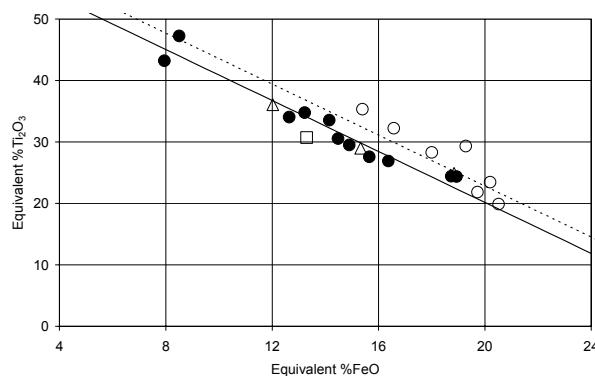


Figure 59 – Compositional invariance of ilmenite smelter slags close to  $\text{M}_3\text{O}_5$  composition.

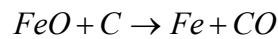
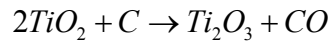
The symbols indicate actual industrial data points. The dotted line at the top is the stoichiometric  $\text{M}_3\text{O}_5$  composition and the solid line is the fitted relationship used in the Reactor2 sub-model (Pistorius 2002).

## ii. Approach

The approach used in this sub-model started with calculating an estimated total surface area of all reductant particles in the ReductantInBath mixer. This calculation is based on the assumption that all reductant particles are perfectly spherical. A single surface-area-averaged particle diameter ( $D_{average}$ ) was used to describe the size distribution of the entire population of reductant particles. This diameter was used to calculate the number of particles in the system and the surface area of a single particle. The product of these two results yielded an estimate of the total surface area of all reductant particles in the system.

The surface area then needed to be converted to volume of liquid slag and volume of reductant to be involved in reduction reactions. This was done by assuming a layer thickness for each of these materials ( $\Delta r_{slag}$  and  $\Delta r_{reductant}$ ). For example, it could be assumed that a 1 mm layer of slag around a reductant particle of size  $D_{average}$  combined with a 0.2 mm layer of reductant in the particle to participate in reduction reactions during one time step. These layer thicknesses were used to calculate volumes, and the volumes were converted to masses by multiplication with material densities. The masses were converted to mass flow rates by dividing them by the integration time step size of the ISFP model.

The composition of the liquid slag produced by reduction reactions at the reductant-slag interface had to be maintained close to the compositional relationship between  $Ti_2O_3$  and  $FeO$  described above. The Gibbs-free-energy-minimisation routine could not be used for this purpose because this would have involved modification of thermochemical data to manipulate the system into displaying the observed kinetic behaviour. It was therefore decided to manipulate the composition of the liquid slag stream flowing to the reductant-slag interface. The purpose of the manipulation was to control the extents to which the following reactions occurred:



When the extents of these reactions are simply allowed to be calculated by the Gibbs-free-energy-minimisation routine (equilibrium) too much  $Ti_2O_3$  is produced. The sub-model therefore had to restrict the extent of the first reaction. The desired results were achieved by controlling the amounts of  $TiO_2$  and  $Ti_2O_3$  allowed to reach the interface.

The approach just described represents a mass transfer restriction applied as part of the Reactor2Flow sub-model. By doing this it is not implied that mass transfer is the cause of the compositional invariance in the actual process. It is simply used as a means to reproduce the effects of whatever mechanism is responsible for the invariance.

## iii. Formulation

The sub-model formulation consists of the following equations:

$$n_{reductant\ particles}^t = m_{reductant}^t \div \left[ \frac{4}{3} \pi \left( \frac{D_{average}}{2} \right)^3 \cdot \rho_{reductant} \right]$$

$$A_{total}^t = 4\pi \left( \frac{D_{average}}{2} \right)^2 \cdot n_{reductant\ particles}^{t-1}$$

$$\dot{m}_{liquid\ slag}^t = n_{reductant\ particles}^{t-1} \cdot \left[ \frac{4}{3}\pi \left( \frac{D_{average}}{2} + \Delta r_{slag} \right)^3 - \frac{4}{3}\pi \left( \frac{D_{average}}{2} \right)^3 \right] \cdot \rho_{slag} \div \Delta t$$

$$\dot{m}_{reductant}^t = n_{reductant\ particles}^{t-1} \cdot \left[ \frac{4}{3}\pi \left( \frac{D_{average}}{2} \right)^3 - \frac{4}{3}\pi \left( \frac{D_{average}}{2} - \Delta r_{reductant} \right)^3 \right] \cdot \rho_{reductant} \div \Delta t$$

Because of the simplified liquid slag phase used in the ISFP model, the relationship between equivalent mass %Ti<sub>2</sub>O<sub>3</sub> and equivalent mass %FeO could be rewritten as:

$$\%Ti_2O_3^t = -2.0722 \cdot \%FeO^t + 61.6$$

SYMBOL	DESCRIPTION	CLASS	UNITS
$A_{total}^t$	The total surface area of all reductant particles in the system at the end of time step $t-1$ .	Output Variable	m <sup>2</sup>
$D_{average}$	The surface-area-averaged diameter of reductant particles in the system.	Model Parameter	m
$\%FeO^t$	The FeO content of the liquid slag at the end of time step $t$ .	Input Variable	Mass %
$m_{reductant}^t$	The total mass of reductant in the system at the end of time step $t$ .	Input Variable	kg
$\dot{m}_{liquid\ slag}^t$	The mass flow rate of liquid slag to the reductant-slag interface during time step $t$ .	Output Variable	kg/h
$\dot{m}_{reductant}^t$	The mass flow rate of reductant to the reductant-slag interface during time step $t$ .	Output Variable	kg/h
$n_{reductant\ particles}^t$	The number of reductant particles in the system at the end of time step $t$ .	Output Variable	
$\Delta r_{slag}$	The layer thickness of slag that is involved in reduction reactions at the reductant-slag interface. The parameter is expressed per unit time to make it independent of the model's integration time step size.	Model Parameter	m/h
$\Delta r_{reductant}$	The layer thickness of reductant that is involved in reduction reactions at the reductant-slag interface. The parameter is expressed per unit time to make it independent of the model's integration time step size.	Model Parameter	m/h
$\rho_{reductant}$	The density of reductant.	Model Parameter	kg/m <sup>3</sup>
$\rho_{slag}$	The density of liquid slag.	Model Parameter	kg/m <sup>3</sup>
$\%Ti_2O_3^t$	The Ti <sub>2</sub> O <sub>3</sub> content of the liquid slag at the end of time step $t$ .	Input Variable	Mass %
$\Delta t$	The integration time step of the ISFP model.	Input Variable	h

Table 15 – Variables and parameters of the Reactor2Flow sub-model of the ISFP model.

#### iv. Values of model parameters

Because reductant particles fed into an ilmenite-smelting furnace are generally smaller than 10 mm diameter, the value of the  $D_{average}$  model parameter was varied between 0.1 and 10 mm.

The values of the layer thickness parameters ( $\Delta r_{slag}$  and  $\Delta r_{reductant}$ ) were dependent on the value of  $D_{average}$ . The layer thicknesses were adjusted in such a way that the mass of liquid slag involved in reduction reactions was always significantly more than the mass of reductant. If this was not done, reduction products were produced that are not observed in the actual process.

Values for the density model parameters were taken from APPENDIX A.

## b. Reactor3Flow: Mass flow to the interface between the slag and metal baths

### i. Modelled phenomena

Mass transfer to the interface between the slag and metal baths has been discussed in paragraph 5.4.2e (page 97) and chemical reaction between liquid slag and liquid metal in paragraph 5.4.4a.iv (page 105). The reader is referred to these paragraphs for background on these phenomena.

This sub-model was required to calculate the rates at which liquid slag and liquid metal are exposed to reduction reactions due to contact between these phases.

Because it is likely that most of the reduction reactions between these two phases will occur in the vicinity of the interface between the two baths, the surface area of this interface can be used as a basis for calculating flow rates to the phase boundary. It is expected that the actual surface between the slag and metal baths is not flat during operation. The reason for this is stirring in both the metal and slag baths, and the turbulence in the zone underneath the electrode. It is likely that some metal droplets will enter the bulk slag phase near the interface between the two baths, and similarly that some slag droplets will enter the bulk metal phase. Such droplets will of course tend to rejoin their bulk phases due to the difference in density between liquid slag and metal.

Due to the influences of stirring on the interface between the two baths the actual contact surface area between liquid metal and slag will be larger than a flat circular surface between the two baths. The area of such a surface can however provide a good starting point for estimating the surface area of contact.

### ii. Approach

The inner diameter of the refractory brick at the axial position of the interface between the slag and metal baths was used as the basis for estimating the surface area between the two phases. Since it is known that the actual surface area is larger than such a flat circular surface, a multiplication factor was used to arrive at a final estimation of the contact surface area. Once this area was available, the approach used in the Reactor2Flow sub-model to estimate the volumes of the two phases to involve in reduction reactions was also applied here.

Two layer thicknesses ( $\Delta Z_{slag}$  and  $\Delta Z_{metal}$ ) were assumed. These layer thicknesses were used to calculate volumes of liquid slag and liquid metal, and the volumes were converted to mass by multiplication with the density of each material.

It was also necessary to apply the same approach as in the Reactor2Flow sub-model for mimicking the compositional invariance of the liquid slag close to the  $M_3O_5$  composition.

## iii. Formulation

The sub-model formulation consists of the following equations:

$$A = \alpha \cdot (\pi r_{\text{refractory inner}}^2)$$

$$\dot{m}'_{\text{liquid slag}} = \frac{A \cdot \Delta z_{\text{slag}} \cdot \rho_{\text{slag}}}{\Delta t}$$

$$\dot{m}'_{\text{liquid metal}} = \frac{A \cdot \Delta z_{\text{metal}} \cdot \rho_{\text{metal}}}{\Delta t}$$

$$\%Ti_2O_3^t = -2.0722 \cdot \%FeO^t + 61.6$$

SYMBOL	DESCRIPTION	CLASS	UNITS
$A$	The total contact surface area between liquid slag and liquid metal.	Output Variable	m <sup>2</sup>
$\alpha$	The multiplication factor used to estimate the total contact surface area between liquid metal and liquid slag.	Model Parameter	
$\%FeO^t$	The FeO content of the liquid slag at the end of time step $t$ .	Input Variable	Mass %
$\dot{m}'_{\text{liquid slag}}$	The mass flow rate of liquid slag to the slag-metal interface during time step $t$ .	Output Variable	kg/h
$\dot{m}'_{\text{liquid metal}}$	The mass flow rate of liquid metal to the slag-metal interface during time step $t$ .	Output Variable	kg/h
$r_{\text{refractory inner}}$	The inner diameter of the refractory lining at the axial position of the interface between the slag and metal baths.	Model Parameter	m
$\rho_{\text{metal}}$	The density of liquid metal.	Model Parameter	kg/m <sup>3</sup>
$\rho_{\text{slag}}$	The density of liquid slag.	Model Parameter	kg/m <sup>3</sup>
$\%Ti_2O_3^t$	The Ti <sub>2</sub> O <sub>3</sub> content of the liquid slag at the end of time step $t$ .	Input Variable	Mass %
$\Delta t$	The integration time step of the ISFP model.	Input Variable	h
$\Delta z_{\text{slag}}$	The layer thickness of slag that is involved in reduction reactions at the slag-metal interface. The parameter is expressed per unit time to make it independent of the model's integration time step size.	Model Parameter	m/h
$\Delta z_{\text{metal}}$	The layer thickness of metal that is involved in reduction reactions at the slag-metal interface. The parameter is expressed per unit time to make it independent of the model's integration time step size.	Model Parameter	m/h

Table 16 - Variables and parameters of the Reactor3Flow sub-model of the ISFP model.

## iv. Values of model parameters

A value for the  $r_{\text{refractory inner}}$  model parameter was obtained from the scale drawing and dimensions presented in Figure 52 (page 90) and paragraph 5.3.1 (page 90).

The values of parameters  $\alpha$ ,  $\Delta z_{\text{slag}}$  and  $\Delta z_{\text{metal}}$  were adjusted together with a number of parameters of other sub-models until the ISFP model produced realistic results.

Values for the density model parameters were taken from APPENDIX A.

c. Reactor4Flow: Mass flow to the reductant–metal interface

i. Modelled phenomena

Mass transfer of carbon into the metal bath to the interface between the slag and metal baths has been discussed in paragraph 5.4.2f (page 97). The reader is referred to this paragraph for background on this phenomenon.

ii. Approach

Because very little is known about mechanisms occurring in the turbulent zone underneath the arc where it is believed that reductant particles come into contact with liquid metal, a very simple approach was used in this sub-model. A fraction of the reductant present in the ReductantInBath mixer was simply routed to Reactor4 to come into contact with liquid metal. The same was done with liquid metal from the MetalBath mixer.

iii. Formulation

The sub-model formulation consists of the following equations:

$$\dot{m}_{reductant}^t = \frac{\chi_{reductant} \cdot m_{reductant}^{t-1}}{\Delta t}$$

$$\dot{m}_{liquid\ metal}^t = \frac{\chi_{liquid\ metal} \cdot m_{liquid\ metal}^{t-1}}{\Delta t}$$

SYMBOL	DESCRIPTION	CLASS	UNITS
$m_{liquid\ metal}^t$	The mass of liquid metal present in the MetalBath mixer at the end of time step $t$ .	Input Variable	kg
$m_{reductant}^t$	The mass of liquid reductant present in the ReductantInBath mixer at the end of time step $t$ .	Input Variable	kg
$\dot{m}_{liquid\ metal}^t$	The mass flow rate of liquid metal to the reductant–metal interface during time step $t$ .	Output Variable	kg/h
$\dot{m}_{reductant}^t$	The mass flow rate of reductant to the reductant–metal interface during time step $t$ .	Output Variable	kg/h
$\Delta t$	The integration time step of the ISFP model.	Input Variable	h
$\chi_{liquid\ metal}$	The fraction of liquid metal routed to the reductant–metal interface.	Model Parameter	
$\chi_{reductant}$	The fraction of reductant routed to the reductant–metal interface.	Model Parameter	

Table 17 – Variables and parameters of the Reactor4Flow sub-model of the ISFP model.

iv. Values of model parameters

The values of the model parameters  $\chi_{liquid\ metal}$  and  $\chi_{reductant}$  were adjusted to achieve realistic results with the ISFP model.

d. FreezeLiningFlow: Mass flow to interface between liquid slag and freeze lining

i. Modelled phenomena

Due to significant stirring in the slag bath, liquid slag is circulated past the interface between the freeze lining and the liquid slag bath. This contact between the freeze lining and liquid slag causes heat transfer from liquid slag to the freeze lining and ultimately solidification and melting of the freeze lining. The purpose of the FreezeLiningFlow sub-model is to calculate the mass of liquid slag that must flow to the FurnaceWall conductor for participation in heat transfer, and solidification and melting.

ii. Approach

The liquid slag flow to the freeze lining was assigned a lower priority than the flows to tapping, to the reductant-slag interface and to the slag-metal interface. For this reason this sub-model calculates its flow output by simply taking a fraction of the liquid slag left in the SlagBath mixer after the flows of the SlagTapFlow, Reactor2Flow and Reactor3Flow sub-models had been removed from the mixer. This fraction is the model's only parameter and can be used to adjust the ISFP model's overall behaviour.

iii. Formulation

The sub-model was formulated with the following equation:

$$\dot{m}^t = \frac{\chi_{FreezeLiningFlow} \cdot (m^{t-1} - (\dot{m}_{SlagTapFlow}^t + \dot{m}_{Reactor2Flow}^t + \dot{m}_{Reactor3Flow}^t) \Delta t)}{\Delta t}$$

SYMBOL	DESCRIPTION	CLASS	UNITS
$\dot{m}^t$	The rate at which slag flows to the interface between liquid slag and the freeze lining during time step $t$ .	Output Variable	kg/h
$\chi_{FreezeLiningFlow}$	The fraction of liquid slag to be removed from the SlagBath module and sent to the FurnaceWall conductor.	Model Parameter	
$m^{t-1}$	The mass of slag in the SlagBath module at the end of time step $t-1$ .	Input Variable	kg
$\dot{m}_{SlagTapFlow}^t$	The tapping flow rate of liquid slag during time step $t$ .	Input Variable	kg
$\dot{m}_{Reactor2Flow}^t$	The rate at which liquid slag flows to the interface between liquid slag and reductant during time step $t$ .	Input Variable	kg
$\dot{m}_{Reactor3Flow}^t$	The rate at which liquid slag flows to the interface between liquid slag and liquid metal during time step $t$ .	Input Variable	kg
$\Delta t$	The integration time step of the ISFP model.	Input Variable	s

Table 18 – Variables and parameters of the FreezeLiningFlow sub-model of the ISFP model.

iv. Values of model parameters

The value of the model parameter  $\chi_{FreezeLiningFlow}$  was set equal to a value between 0 and 1. The sum of this model parameter and its equivalent in the CrustFlow sub-model ( $\chi_{CrustFlow}$ ) had to be greater than or equal to 0 and less than or equal to 1.

e. CrustFlow: Mass flow to interface between liquid slag and crust

i. Modelled phenomena



Due to significant stirring in the slag bath liquid slag is circulated past the interface between the slag bath surface or crust (when it is present) and the liquid slag bath. This contact between the crust and liquid slag causes heat to be transferred from liquid slag to the crust, and ultimately solidification and melting of the crust. The purpose of the CrustFlow sub-model is to calculate the mass of liquid slag that must flow to the Crust conductor for participation in heat transfer, and solidification and melting.

ii. Approach

The approach used for this sub-model was exactly the same as for the FreezeLiningFlow sub-model. Please refer to paragraph 5.6.8d.ii on page 132.

iii. Formulation

The sub-model was formulated with the following equation:

$$\dot{m}^t = \frac{\chi_{CrustFlow} \cdot (m^{t-1} - (\dot{m}_{SlagTapFlow}^t + \dot{m}_{Reactor2Flow}^t + \dot{m}_{Reactor3Flow}^t) \Delta t)}{\Delta t}$$

SYMBOL	DESCRIPTION	CLASS	UNITS
$\dot{m}^t$	The rate at which slag flows to the interface between liquid slag and the crust during time step $t$ .	Output Variable	kg/h
$\chi_{CrustFlow}$	The fraction of liquid slag to be removed from the SlagBath module and sent to the Crust conductor.	Model Parameter	
$m^{t-1}$	The mass of slag in the SlagBath module at the end of time step $t-1$ .	Input Variable	kg
$\dot{m}_{SlagTapFlow}^t$	The tapping flow rate of liquid slag during time step $t$ .	Input Variable	kg
$\dot{m}_{Reactor2Flow}^t$	The rate at which liquid slag flows to the interface between liquid slag and reductant during time step $t$ .	Input Variable	kg
$\dot{m}_{Reactor3Flow}^t$	The rate at which liquid slag flows to the interface between liquid slag and liquid metal during time step $t$ .	Input Variable	kg
$\Delta t$	The integration time step of the ISFP model.	Input Variable	s

Table 19 – Variables and parameters of the CrustFlow sub-model of the ISFP model.

iv. Values of model parameters

The value of the model parameter  $\chi_{CrustFlow}$  was set equal to a value between 0 and 1. The sum of this model parameter and its equivalent in the FreezeLiningFlow sub-model ( $\chi_{FreezeLiningFlow}$ ) had to be greater than or equal to 0 and less than or equal to 1.

### 5.7 MODEL SOLUTION

Solution of the ISFP involved the following steps:

- Assign initial conditions to all modules that contain state.
- Solve the set of differential equations at each time step using Euler integration.

The size of the integration time step was set at 30 seconds.

### 5.7.1 Initial Conditions

The ISFP model has six modules that contain state and therefore require initial conditions. The modules include the following:

- FurnaceWall conductor module  
The initial conditions of this module were discussed in paragraph 3.7.2 (page 50).
- Crust conductor module  
The initial conditions of this module were discussed in paragraph 4.7.2 (page 78)
- SlagBath ideal mixer module  
The SlagBathIC material input module was used to add an initial mass of liquid slag to the furnace. The added mass filled the empty space between the slag and metal bath surfaces that had not already been filled with solid slag from the freeze lining (see Figure 52 on page90).
- MetalBath ideal mixer module  
The MetalBathIC material input module was used to add an initial mass of liquid metal to the furnace. The added mass filled the volume below the metal bath surface (see Figure 52 on page90).
- ReductantInBath ideal mixer module  
This mixer was left empty.
- FurnaceFreeboard ideal mixer module  
This mixer was left empty.

### 5.7.2 Solution

The model flow sheet shown in Figure 58 (page 116) represents a set of differential equations that needs to be integrated with respect to time. The integration was done at time steps of 30 seconds using the Euler method. At each time step all of the data associated with each module and flow stream was logged to a database. Model results were drawn from this database.

## 5.8 MODEL VALIDATION

### 5.8.1 Purpose

The purpose of validation is to verify the numerical integrity of the ISFP model (Thomas and Brimacombe, 1997).

### 5.8.2 Objectives

Model validation had to achieve the following objectives:

- Confirm that the basic mass and energy balancing of the model is functioning properly.
- Confirm that the FurnaceWall conductor (FLC model) produced realistic results within the ISFP model.
- Confirm that the Crust conductor (SBCC model) produced realist results within the ISFP model.
- Confirm that Reactor1 is able to heat and melt incoming ilmenite and produce realistic results.
- Confirm that Reactor2 is able to reduce slag with reductant and produce realistic results.

- Confirm that Reactor3 is able to reduce slag with carbon dissolved in liquid metal and produce realistic results.
- Confirm that Reactor4 is able to dissolve carbon into liquid metal realistic results.

### 5.8.3 Methodology

Because of the complexity of the ISFP model compared with the FLC and SBCC models, it was not possible to create an analytical solution as a reference during model validation. For this reason the most basic check of mass and energy balancing was the starting point of validation. The inputs, outputs and internal quantities of the model were compared and evaluated using mass and energy balances.

The next step was to run the model and, based on experience with actual ilmenite-smelting furnaces, determine whether the various modules in the model produced realistic results. This involved detailed inspection of data generated by the model. For example, the input flow stream compositions and temperatures of Reactor2 were compared with that of the output flow streams and with the enthalpy change calculated by the Gibbs-free-energy-minimisation routine under various circumstances. The functioning of the other reactors and conductor modules was studied in a similar way.

While studying results of the various modules, adjustments were made to the sub-models to produce more realistic results. This was an iterative and time-consuming process.

### 5.8.4 Validation Experiments

Numerous experiments were done while validating the model and improving sub-models to enhance the realism of the model's results. Because of the nature of the process followed while doing this, no structured set of validation experiments can be presented here.

### 5.8.5 Validation Results

The result of the validation phase of the ISFP model was a configuration of modules and sub-models that produced fairly realistic results. Results of specific validation experiments are not presented here, because experimental results provided in CHAPTER 8 and CHAPTER 9 demonstrate most of what was observed during the validation phase. Specifically, mass and energy balance checks are presented with each set of experimental results.

The values of model parameters resulting from the validation exercise are summarized in Table 20.

PARAMETER	VALUE	COMMENTS
<b>HeatLoss1Rate</b>		
A	5.438 m <sup>2</sup>	
h <sub>effective</sub>	0.019 kW/(m <sup>2</sup> .°C)	When furnace is operational.
	0.027 kW/(m <sup>2</sup> .°C)	When furnace is off.
T <sub>environment</sub>	25 °C	
<b>HeatLoss2Rate</b>		
A <sub>hearth</sub>	61.514 m <sup>2</sup>	
A <sub>sidewall</sub>	14.687 m <sup>2</sup>	
ΔX <sub>refractory,hearth</sub>	2.000 m	
ΔX <sub>refractory,sidewall</sub>	0.500 m	
T <sub>environment</sub>	25 °C	
<b>SlagTapFlow</b>		
None.		

PARAMETER	VALUE	COMMENTS
<b>MetalTapFlow</b>		
None.		
<b>Reactor2Flow</b>		
$D_{average}$	0.005 m	
$\Delta r_{slag}$	0.080 m/h	
$\Delta r_{reductant}$	0.0002 m/h	
$\rho_{slag}$	3800 kg/m <sup>3</sup>	
$\rho_{reductant}$	1700 kg/m <sup>3</sup>	
<b>Reactor3Flow</b>		
$r_{refractory\ inner}$	4.425 m	
$\alpha$	1.0	
$\Delta z_{slag}$	0.024 m/h	
$\Delta z_{metal}$	0.024 m/h	
$\rho_{slag}$	3800 kg/m <sup>3</sup>	
$\rho_{reductant}$	1700 kg/m <sup>3</sup>	
<b>Reactor4Flow</b>		
$\chi_{liquid\ metal}$	0.049	Fraction per hour
$\chi_{reductant}$	6.000	Fraction per hour
<b>FreezeLiningFlow</b>		
$\chi_{FreezeLiningFlow}$	0.09	
<b>CrustFlow</b>		
$\chi_{CrustFlow}$	0.91	

Table 20 – Values of parameters of sub-models of the ISFP model.

## 5.9 COMPARISON WITH ACTUAL DATA

Due to the confidentiality of most information pertaining to the industrial process, no comparison with actual data could be published here. The author was only able to rely on his own experience with actual industrial ilmenite–smelting processes to do validation of the ISFP model.

## CHAPTER 6

### THE DYNAMIC RESPONSE OF A FREEZE-LINING TO STEP CHANGES IN INPUT HEAT FLOW RATE

This chapter describes a series of experiments conducted with the FLC model. The purpose of these experiments was to study the influence of step changes in input heat flow rate on the dynamic behaviour of the furnace wall and freeze lining. The following aspects were considered:

- Freeze lining thickness.
- Temperature distribution through the furnace wall and freeze lining.
- Time lag in temperature response of the refractory brick wall relative to the time when conditions were changed in the slag bath.
- Liquid slag temperature.
- Composition distribution through the freeze lining.
- Liquid slag composition.

#### 6.1 EXPERIMENTAL SETUP

The model flow diagram used for all experiments in this chapter is shown in Figure 18 (page 49). The geometry and dimensions used are all the same as those given in paragraph 3.6.4a (page 43) except for the layer dimension of the freeze lining layer. This dimension was adjusting according to the nature of each experiment. For experiments where much solidification occurred, a layer thickness of 1.0 to 2.0 m was used. For most of the experiments, however, a thickness of 0.2 m was adequate.

The initial mass of slag used was around 11 ton solid and 230 ton liquid for those cases where a thicker initial freeze lining was used and about 7 ton solid and 234 ton liquid for cases started with a thinner freeze lining. No slag was added or removed from the system during the experiments.

The initial liquid slag composition of all experiments was chosen as 15%-55%-30% (FeO-TiO<sub>2</sub>-Ti<sub>2</sub>O<sub>3</sub> mass percentages) and the effective thermal conductivity of the liquid slag as 0.005 kW/(m.°C). The liquid slag composition used is located between the eutectic groove and the stoichiometric M<sub>3</sub>O<sub>5</sub> line. The average composition of slag in the furnace (solid together with liquid) will differ from this composition due to the difference in composition between the liquid slag and both the pseudobrookite and rutile freeze linings used.

All experiments were run for a period of 24 hours, or until the freeze lining had been melted away completely.

#### 6.2 EXPERIMENTS

The parameters that were varied over the series of experiments include the following:

- Initial steady state heat flow rate.
- Initial freeze lining composition.
- Net input heat flow rate.

The initial steady state heat flow rate fixed the initial temperature distribution in the freeze lining and furnace wall, and the initial freeze lining thickness. The net input heat flow rate was achieved by setting the heat flow rate of the ElectricalPower energy input module and of the HeatLosses energy output module shown in Figure 18 (page 49). The HeatLosses heat flow represented all heat losses from the slag bath other than through the sidewalls and freeze lining in contact with the slag bath. The set of experiments with the various parameters of interest to each experiment are listed in Table 21 below. The set of 26 experiments consists of 3 subsets.

The first subset consists of experiments 6.1 to 6.14. The aim of this set was to test the influence of the net input heat flow rate into the slag bath. Seven experiments were conducted with a net input heat flow rate less than the initial steady state heat flow rate of 250 kW, and seven experiments with a net input heat flow rate greater than the initial steady state heat flow rate. No other parameters were changed. In all cases the freeze lining was filled with solid slag consisting of only pseudobrookite and no rutile. The composition of the pseudobrookite was 37.6%  $\text{FeTi}_2\text{O}_5$  and 62.4%  $\text{Ti}_3\text{O}_5$  (mass basis). This is the composition of the first solid slag to form from liquid slag with the composition of 15%–55%–30% ( $\text{FeO}$ – $\text{TiO}_2$ – $\text{Ti}_2\text{O}_3$  mass percentages) used for all the experiments in this chapter.

The second subset includes experiments 6.15 to 6.20. These experiments were aimed at testing once again the influence of net input heat flow rate, but this time with a different initial steady state heat flow rate (and consequently a different initial freeze lining thickness). Three experiments were conducted with a net input heat flow rate less than the initial steady state heat flow rate of 300 kW, and three experiments with a net input heat flow rate greater than the initial steady state heat flow rate. The freeze lining composition used was the same as for experiments 6.1 to 6.14.

The third subset includes experiments 6.21 to 6.26. The same initial conditions as the first subset were used, except for the composition of the freeze lining. The pseudobrookite solid solution used in the first two subsets was replaced with 100% rutile ( $\text{TiO}_2$ ). The aim of these experiments was to test the influence of the freeze lining composition on the slag bath composition, and to test the influence of net input heat flow rate.

EXPERIMENT NO.	INITIAL STEADY STATE HEAT FLOW	INITIAL FREEZE LINING THICKNESS	INITIAL FREEZE LINING COMPOSITION	ELECTRICAL POWER HEAT FLOW	HEAT LOSSES HEAT FLOW	NET INPUT HEAT FLOW
6.1	250 kW	0.102 m	Pseudobrookite	0 kW	1000 kW	-1000 kW
6.2	250 kW	0.102 m	Pseudobrookite	0 kW	500 kW	-500 kW
6.3	250 kW	0.102 m	Pseudobrookite	0 kW	200 kW	-200 kW
6.4	250 kW	0.102 m	Pseudobrookite	0 kW	100 kW	-100 kW
6.5	250 kW	0.102 m	Pseudobrookite	0 kW	0 kW	0 kW
6.6	250 kW	0.102 m	Pseudobrookite	100 kW	0 kW	100 kW
6.7	250 kW	0.102 m	Pseudobrookite	200 kW	0 kW	200 kW
6.8	250 kW	0.102 m	Pseudobrookite	300 kW	0 kW	300 kW
6.9	250 kW	0.102 m	Pseudobrookite	400 kW	0 kW	400 kW
6.10	250 kW	0.102 m	Pseudobrookite	500 kW	0 kW	500 kW
6.11	250 kW	0.102 m	Pseudobrookite	1000 kW	0 kW	1000 kW
6.12	250 kW	0.102 m	Pseudobrookite	2000 kW	0 kW	2000 kW
6.13	250 kW	0.102 m	Pseudobrookite	5000 kW	0 kW	5000 kW
6.14	250 kW	0.102 m	Pseudobrookite	10000 kW	0 kW	10000 kW
6.15	300 kW	0.066 m	Pseudobrookite	0 kW	1000 kW	-1000 kW
6.16	300 kW	0.066 m	Pseudobrookite	0 kW	0 kW	0 kW

EXPERIMENT NO.	INITIAL STEADY STATE HEAT FLOW	INITIAL FREEZE LINING THICKNESS	INITIAL FREEZE LINING COMPOSITION	ELECTRICAL POWER HEAT FLOW	HEAT LOSSES HEAT FLOW	NET INPUT HEAT FLOW
6.17	300 kW	0.066 m	Pseudobrookite	200 kW	0 kW	200 kW
6.18	300 kW	0.066 m	Pseudobrookite	400 kW	0 kW	400 kW
6.19	300 kW	0.066 m	Pseudobrookite	1000 kW	0 kW	1000 kW
6.20	300 kW	0.066 m	Pseudobrookite	10000 kW	0 kW	10000 kW
6.21	250 kW	0.102 m	Rutile	0 kW	1000 kW	-1000 kW
6.22	250 kW	0.102 m	Rutile	0 kW	0 kW	0 kW
6.23	250 kW	0.102 m	Rutile	200 kW	0 kW	200 kW
6.24	250 kW	0.102 m	Rutile	400 kW	0 kW	400 kW
6.25	250 kW	0.102 m	Rutile	1000 kW	0 kW	1000 kW
6.26	250 kW	0.102 m	Rutile	10000 kW	0 kW	10000 kW

Table 21 - List of experiments conducted for CHAPTER 6.

### 6.3 EXPERIMENTAL RESULTS

The results from each experiment are presented below using a series of graphs marked from (a) to (h). The set of graphs is presented consistently for all experiments in this chapter. For this reason each graph type in the set is explained below. A discussion of the experimental results follows after the graphical presentation of the results of all experiments conducted as part of this chapter.

#### (a) Freeze Lining Thickness and Isotherm Graph

This graph contains two sets of lines. The first set is the thick lines indicating the boundaries of the various layers. From bottom to top, these thick lines represent the outer surface of the steel shell (at a radial position of  $-0.575$  m), the interface between the steel shell and the ramming layer (at  $-0.550$  m), the interface between the ramming layer and the brick layer (at  $-0.500$  m), the interface between the brick layer and the freeze lining (at  $0.000$  m), and the interface between the freeze lining and the liquid slag. Only the last of these lines varies as a function of time as the freeze lining becomes thinner or thicker depending on the scenario.

The second set of lines is drawn thinner and represents isotherms as a function of time and position in the furnace wall or freeze lining. The first isotherm is drawn at a temperature of  $100$  °C and is found towards the bottom of the graph near the cold steel shell. This curve is followed by more isotherms at intervals of  $100$  °C towards the top of the graph.

The vertical axis indicates the radial position of layer interfaces and isotherms. The reference point used on this axis is the interface between the brick layer and solid slag. This position is referred to as the hot face of the refractory brick. A positive deviation from this reference point moves towards the centre of the furnace. This axis configuration was chosen to facilitate reading of freeze lining thickness and of isotherm position relative to the refractory hot face.

#### (b) Liquid Slag Temperature Graph

This graph shows the variation of the liquid slag bath temperature as a function of time. Since the liquid slag temperature cannot vary independently from melting and solidification at the freeze lining, the temperature plotted on this graph provides an indication of the liquidus temperature of the slag.

#### (c) Temperature Response Time Delay Graph

This graphs aims to show the influence of thermal inertia of the freeze lining and refractory brick on temperature measurements made in the refractory brick.

The horizontal axis indicates the distance from the refractory hot face at which a hypothetical thermocouple is installed. The vertical axis indicates the lag from the time when a change is enforced on the inside of the furnace to when that change is detected by the thermocouple as a temperature change of specified magnitude.

For example, the results of experiment 6.1 (Figure 60, page 144) indicate that a thermocouple installed 0.4 m from the hot face will take just over 4 hours to detect a 1.0 °C change that resulted from the changes enforced on the inside of the furnace. The same thermocouple will take 5.5 hours to detect a 2.5 °C change, 6.75 hours to detect a 5.0 °C change, and 9 hours to detect a 10.0 °C change. This is in strong contrast with a thermocouple installed 0.1 m away from the hot face. Such a thermocouple detects a 1.0 °C change after 1.75 hours, a 2.5 °C change after 2.25 hours, a 5.0 °C change after 2.75 hours and a 10.0 °C after 3.5 hours.

(d) Liquid Slag Composition Graph

This graph shows the mass fractions of the three liquid slag phase constituents (FeO, TiO<sub>2</sub> and Ti<sub>2</sub>O<sub>3</sub>) as functions of time. Only a single thin solid line is shown for FeO. This line indicates the calculated mass fraction of FeO in the liquid slag as a function of time. Similarly, the thin solid lines for TiO<sub>2</sub> and Ti<sub>2</sub>O<sub>3</sub> indicate the calculated mass fraction of these phase constituents as functions of time. The thick solid lines shown for TiO<sub>2</sub> and Ti<sub>2</sub>O<sub>3</sub> indicate the eutectic groove composition for these constituents with the calculated mass fraction of FeO as reference.

This graph can for example be interpreted as follows. The results of experiment 6.1 (Figure 60, page 144) indicate that the liquid slag initially contains less TiO<sub>2</sub> and more Ti<sub>2</sub>O<sub>3</sub> than the eutectic composition. However, due to solidification and the resulting change in liquid slag composition, the liquid slag reaches the eutectic composition after about 10.25 hours.

(e) Solid Slag Composition Graph

This graph shows the composition of the freeze lining at the interface between the freeze lining and liquid slag as a function of freeze lining thickness. An additional horizontal axis is shown at the top of the graph. This axis indicates time in hours from the start of the experiment. Because the freeze lining thickness does not vary linearly with time, this second axis is not linear. It is only used to provide an indication of the time at which the slag solidified on the surface of the freeze lining. The tick marks on this axis are always 2 hours apart.

The composition of the solid slag is presented by showing both the distribution of mass between phases (rutile and pseudobrookite), and by showing the distribution of mass between constituents of a specific phase. The phases are separated by a thick solid line, and the constituents within a phase are separated by a thin solid line. The rutile phase is always plotted in the lower part of the graph, and pseudobrookite above it.



Refer to the results of experiment 6.1 (Figure 60, page 144) once again as an example. The freeze lining was initialised with only pseudobrookite having a composition of roughly 38%–62% ( $\text{FeTiO}_5$ – $\text{Ti}_3\text{O}_5$ ). As time progressed, the slag solidifying on the surface of the freeze lining became more and more enriched in  $\text{FeTi}_2\text{O}_5$ . After about 10.25 hours (the time when the liquid slag reached the eutectic composition), rutile started to solidify as part of the solid slag. The rutile phase consisted of mostly  $\text{TiO}_2$  and only a small amount of  $\text{Ti}_2\text{O}_3$ .

This graph is only included in the result set of experiments that showed an increase in freeze lining thickness. The time axis at the top of this graph is only useful for experiments in which only an increase in freeze lining thickness occurred. The arrow in graph (a) indicates the point in time to which the data in graph (e) belongs.

(f) Liquid Slag Composition Ternary Graph

This graph shows four series. The first is a broken line connecting the  $\text{Ti}_3\text{O}_5$  and  $\text{FeTi}_2\text{O}_5$  (or  $\text{M}_3\text{O}_5$ ) compositions. Second is the upper thin solid line that indicates the composition location of the eutectic groove. Thirdly is the lower thin solid line that traces the composition below which (on the ternary graph) iron metal is a stable phase. Finally, the thick solid line shows the compositional variation of the liquid slag. The starting composition of the liquid slag is marked with a circle.

This graph is only shown for experiments during which a significant change in liquid slag composition took place. For most experiments this was not the case, and the variation would have been difficult to view on this type of graph.

(g) Energy Balance Error Graph

This graph shows the energy balance error of the model as a function of time. It is always included as part of the result set to serve as a confirmation of the numerical integrity of the model in addition to the validation experiments that had been done. The energy balance error calculation is outlined below.

The law of energy conservation states that the difference between the enthalpy that has entered the system and the enthalpy that has exited the system is the enthalpy content of the system. All the terms mentioned are calculated relative to the same reference point in time. In the case of the experiments in this chapter, this reference point is always a time zero (00:00:00). In equation form it can be written as:

$$H_{input} - H_{output} = H_{content}$$

In the case of the numerical solution of the model this equation does not hold absolutely since round-off errors and possibly model errors may occur. For this reason, the balance equation can be rewritten as the following error equation.

$$H_{error} = (H_{input} - H_{output}) - H_{content}$$

The details of the three right-hand-side enthalpy terms can be written based on the model flow sheet shown in Figure 18.

The only enthalpy input is through the ElectricalPower energy input module. The power input of this module is integrated to obtain an enthalpy figure. The balance reference point of time zero is set after the initial mass of slag is added to the MetalBath mixer via the SlagFeed material input module. For this reason no enthalpy from this input is used in the balance.

$$H_{input} = H_{ElectricalPower}$$

Energy exits from the system via the HeatLosses energy output module, and as losses through the FurnaceWall conductor module. The power figures of both these modules are integrated to obtain enthalpy figures.

$$H_{output} = H_{HeatLosses} + H_{FurnaceWall}$$

The enthalpy content of the system is calculated as the sum of the enthalpy contained in the IsoMod1 isothermal module (this includes the content of the MetalBath and MetalBath mixers), and the enthalpy of each of the four layers (steel, ramming, brick and freeze lining) of the FurnaceWall conductor module.

$$H_{content} = H_{IsoMod1} + H_{FurnaceWall,SteelLayer} + H_{FurnaceWall,RammingLayer} \\ + H_{FurnaceWall,BrickLayer} + H_{FurnaceWall,FreezeLining}$$

The typical change in enthalpy content of the IsoMod1 isothermal module over the period of 24 hours modelled during the experiments conducted is 29,000 kWh. When comparing a typical energy balance error of less than 1.0 kWh with this figure it becomes clear that the errors are negligible.

(h) Mass Balance Error Graph

This graph shows the mass balance error of the model as a function of time for the same purpose as graph (g).

The same approach that was used for the energy balance error was used for calculating the mass balance error. Time zero (00:00:00) was also used as reference point. The following mass balance and error equations were used:

$$m_{input} - m_{output} = m_{content}$$

$$m_{error} = (m_{input} - m_{output}) - m_{content}$$

Figure 18 was once again used as basis for the right-hand-side terms. Because no material entered or exited the system within the 24 hours covered by the experiment, both the input and output terms in the equations can be omitted. The only term that remains is the content term, which was calculated as the sum of the mass of the slag bath, metal bath and the mass of solid slag in the freeze lining layer of the FurnaceWall conductor module. The other three layers of the conductor were not

included in the calculations because the masses of these layers remained constant during the experiments. The right-hand-side terms are detailed as follows:

$$m_{input} = 0$$

$$m_{output} = 0$$

$$m_{content} = m_{SlagBath} + m_{MetalBath} + m_{FurnaceWall,FreezeLining,SolidSlag}$$

The typical total slag mass (both liquid and solid) in the system was around 241 ton. Typical mass balance errors of less than 1 kg that were recorded during experiments can again be seen as negligible.

6.3.1 Experiment 6.1

INITIAL STEADY STATE HEAT FLOW	INITIAL FREEZE LINING THICKNESS	INITIAL FREEZE LINING COMPOSITION	ELECTRICAL POWER HEAT FLOW	HEAT LOSSES HEAT FLOW	NET INPUT HEAT FLOW
250 kW	0.102 m	Pseudobrookite	0 kW	1000 kW	-1000 kW

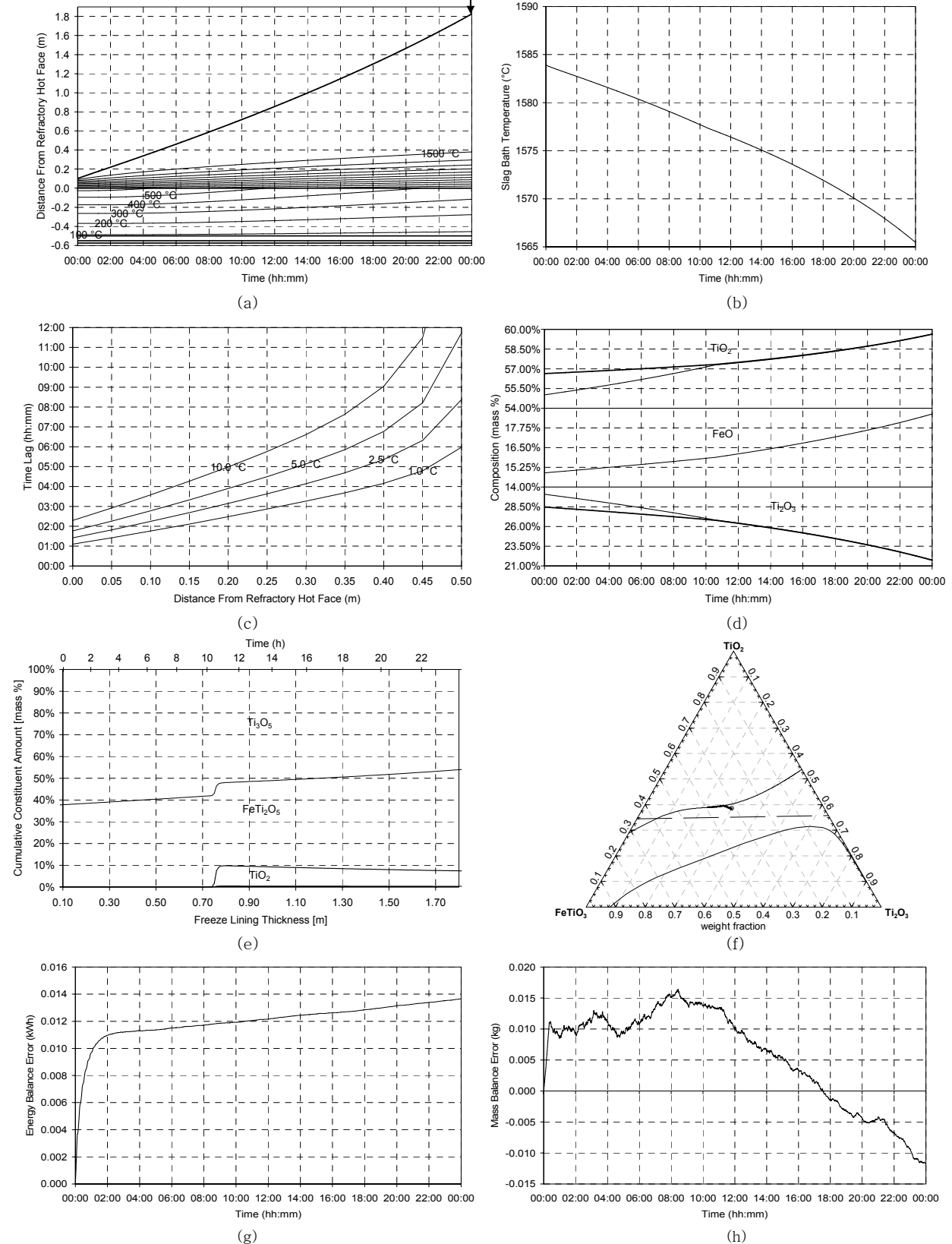


Figure 60 – Experiment 6.1 results.

6.3.2 Experiment 6.2

INITIAL STEADY STATE HEAT FLOW	INITIAL FREEZE LINING THICKNESS	INITIAL FREEZE LINING COMPOSITION	ELECTRICAL POWER HEAT FLOW	HEAT LOSSES HEAT FLOW	NET INPUT HEAT FLOW
250 kW	0.102 m	Pseudobrookite	0 kW	500 kW	-500 kW

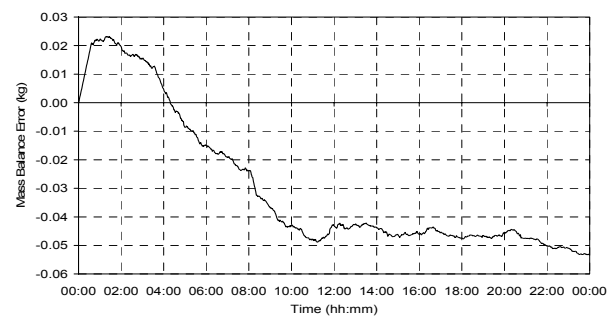
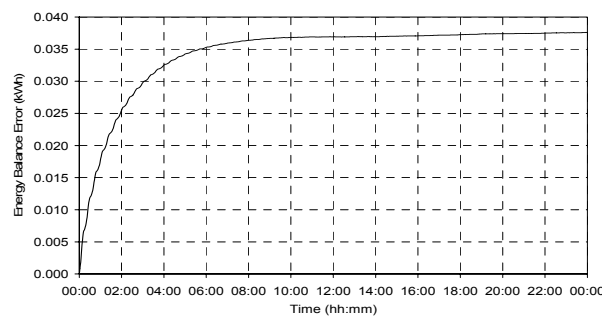
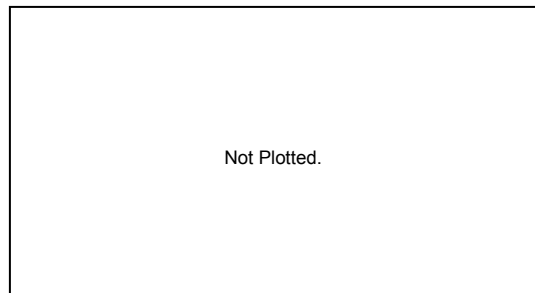
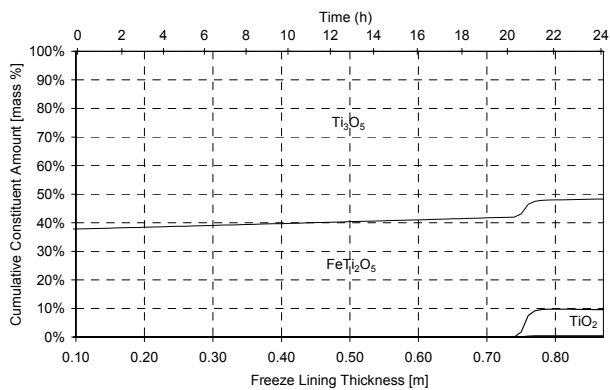
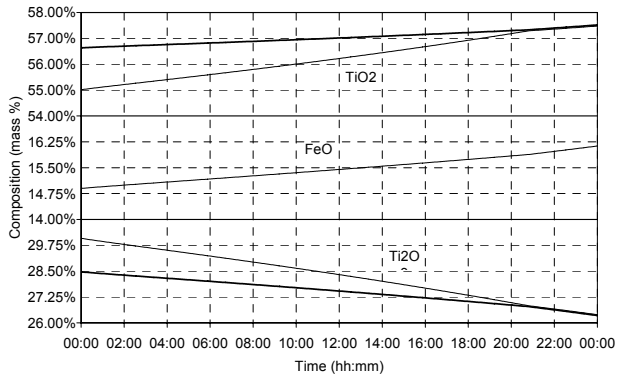
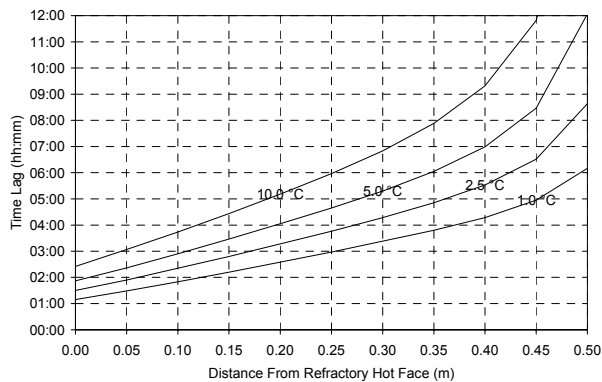
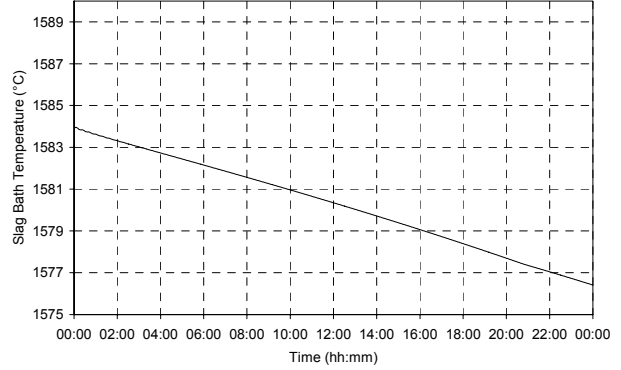
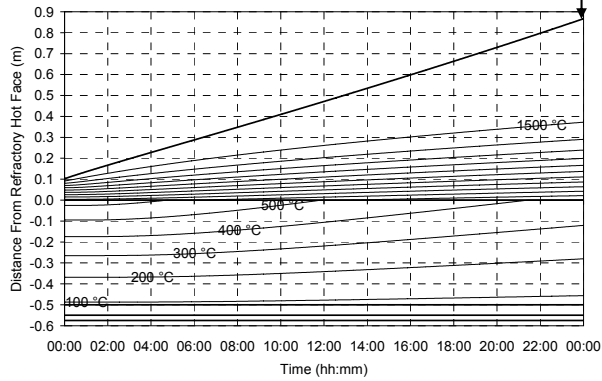
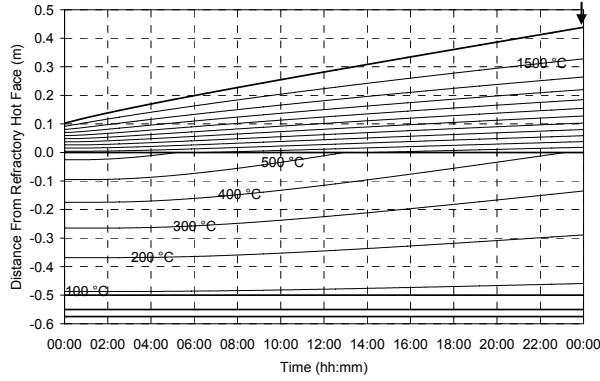


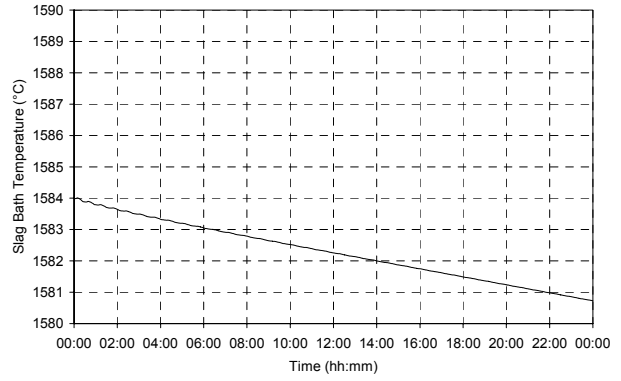
Figure 61 – Experiment 6.2 results.

6.3.3 Experiment 6.3

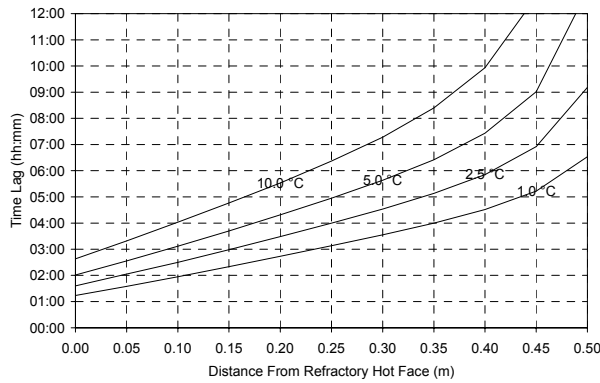
INITIAL STEADY STATE HEAT FLOW	INITIAL FREEZE LINING THICKNESS	INITIAL FREEZE LINING COMPOSITION	ELECTRICAL POWER HEAT FLOW	HEAT LOSSES HEAT FLOW	NET INPUT HEAT FLOW
250 kW	0.102 m	Pseudobrookite	0 kW	200 kW	-200 kW



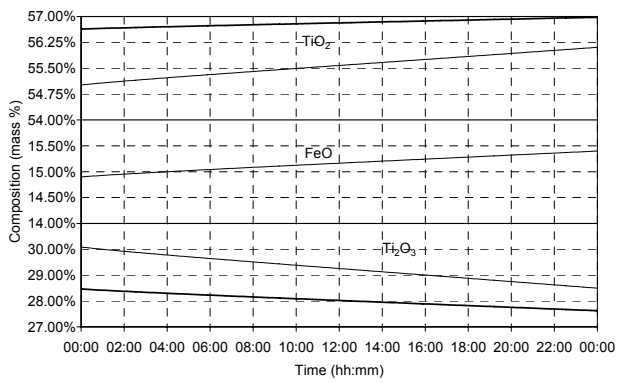
(a)



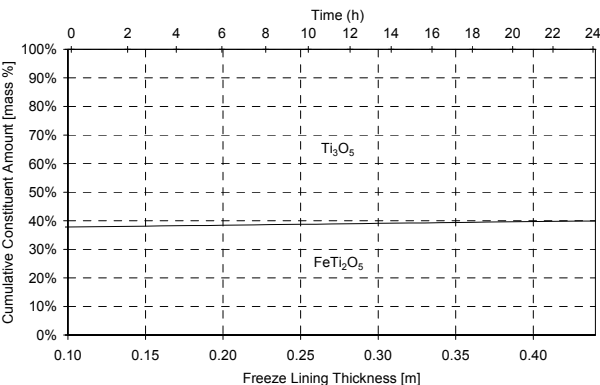
(b)



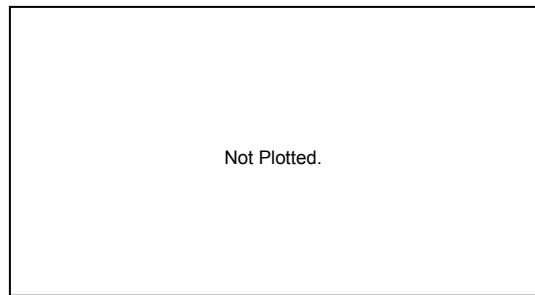
(c)



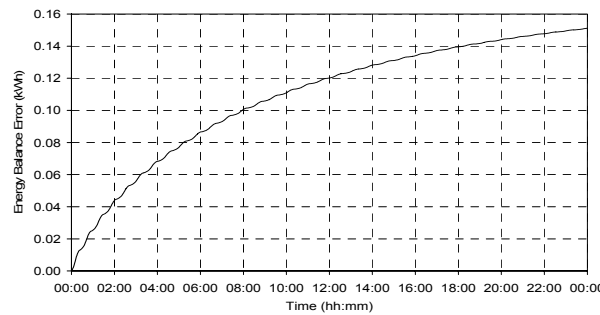
(d)



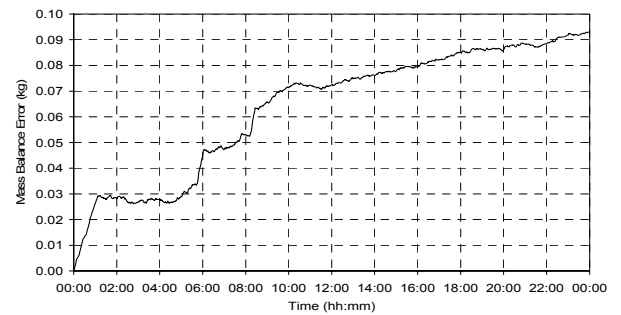
(e)



(f)



(g)

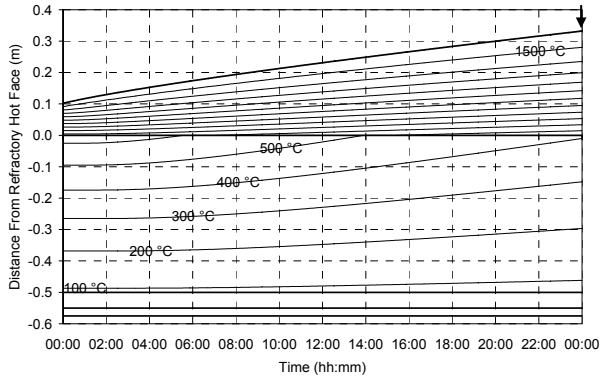


(h)

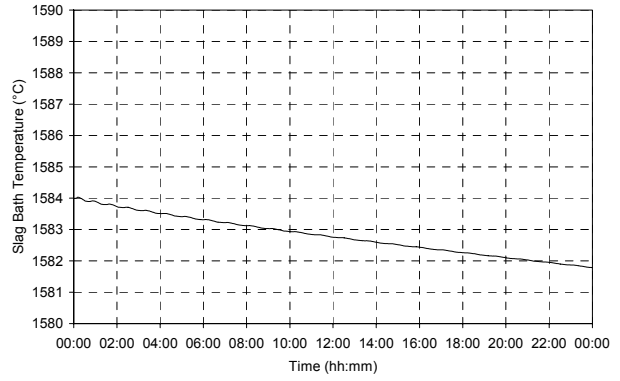
Figure 62 – Experiment 6.3 results.

6.3.4 Experiment 6.4

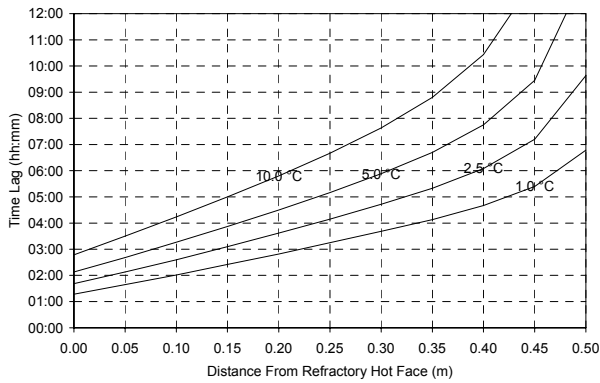
INITIAL STEADY STATE HEAT FLOW	INITIAL FREEZE LINING THICKNESS	INITIAL FREEZE LINING COMPOSITION	ELECTRICAL POWER HEAT FLOW	HEAT LOSSES HEAT FLOW	NET INPUT HEAT FLOW
250 kW	0.102 m	Pseudobrookite	0 kW	100 kW	-100 kW



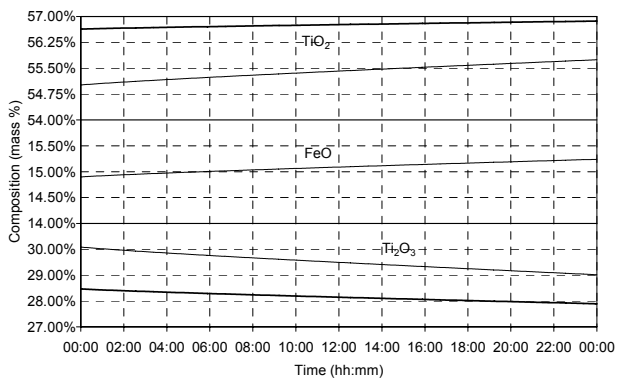
(a)



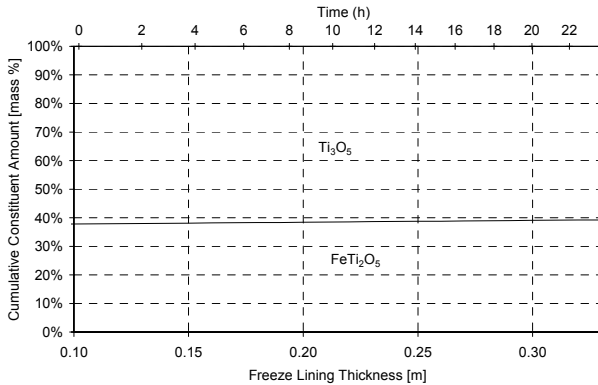
(b)



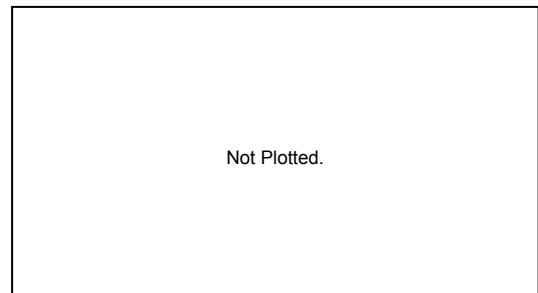
(c)



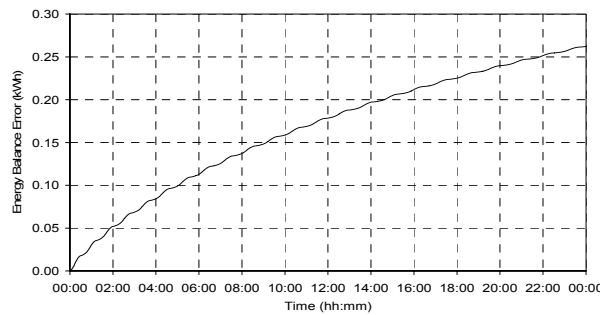
(d)



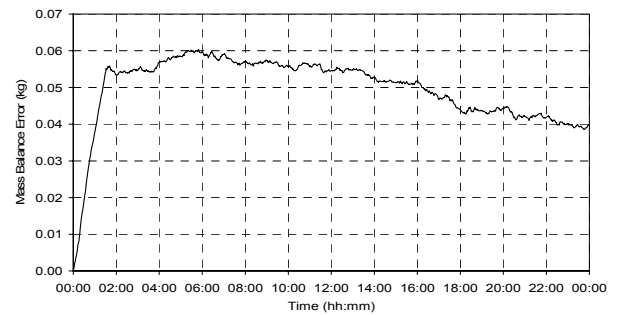
(e)



(f)



(g)

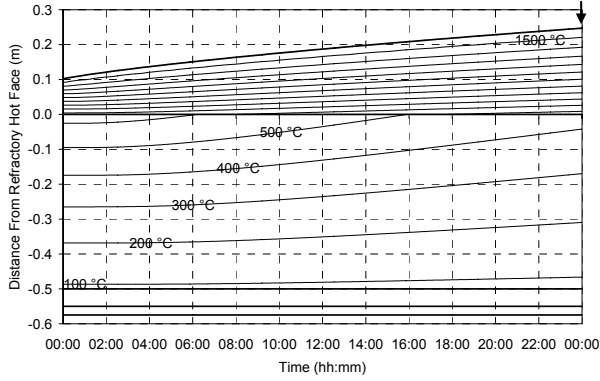


(h)

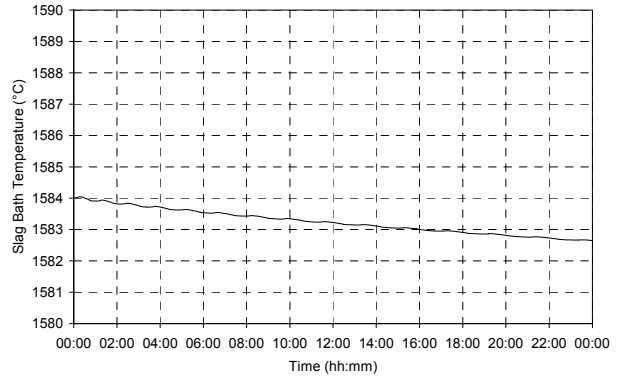
Figure 63 – Experiment 6.4 results.

6.3.5 Experiment 6.5

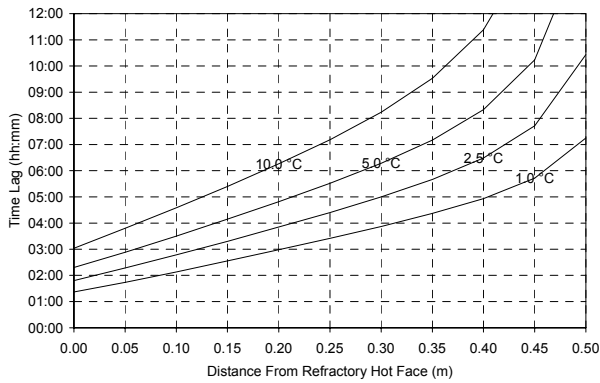
INITIAL STEADY STATE HEAT FLOW	INITIAL FREEZE LINING THICKNESS	INITIAL FREEZE LINING COMPOSITION	ELECTRICAL POWER HEAT FLOW	HEAT LOSSES HEAT FLOW	NET INPUT HEAT FLOW
250 kW	0.102 m	Pseudobrookite	0 kW	0 kW	0 kW



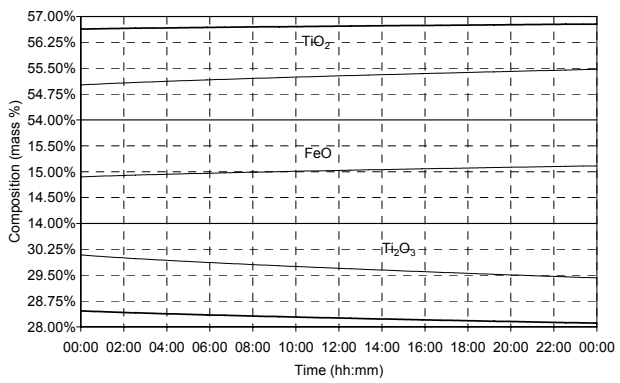
(a)



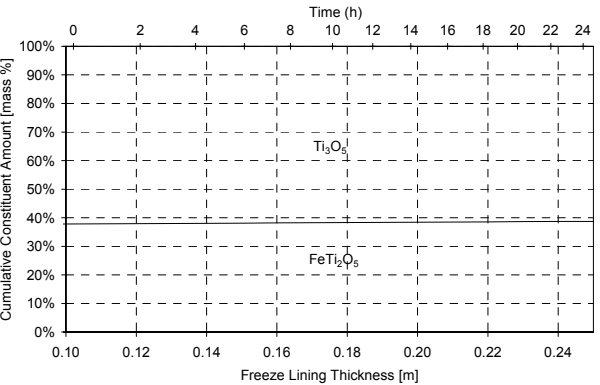
(b)



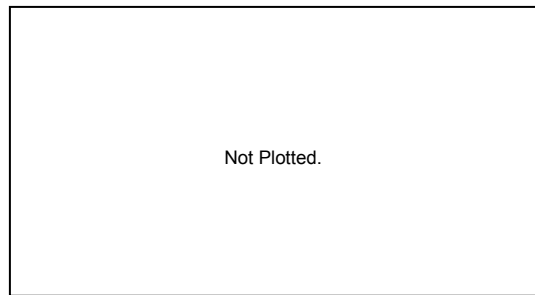
(c)



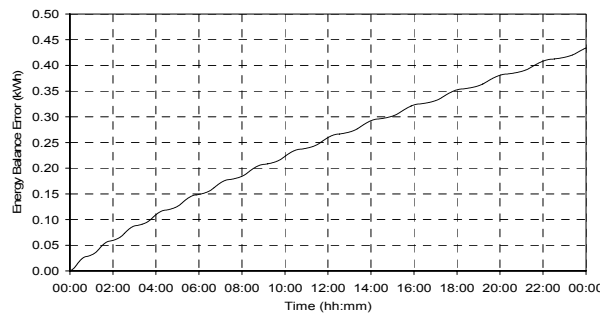
(d)



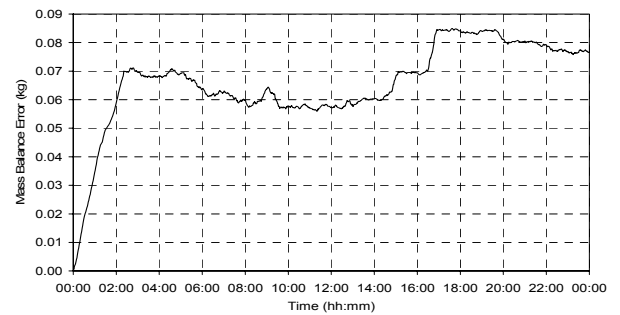
(e)



(f)



(g)



(h)

Figure 64 – Experiment 6.5 results.



6.3.6 Experiment 6.6

INITIAL STEADY STATE HEAT FLOW	INITIAL FREEZE LINING THICKNESS	INITIAL FREEZE LINING COMPOSITION	ELECTRICAL POWER HEAT FLOW	HEAT LOSSES HEAT FLOW	NET INPUT HEAT FLOW
250 kW	0.102 m	Pseudobrookite	100 kW	0 kW	100 kW

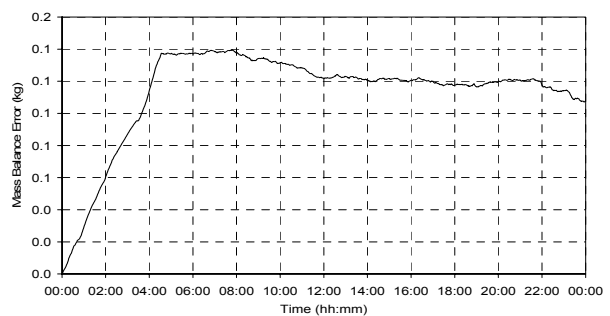
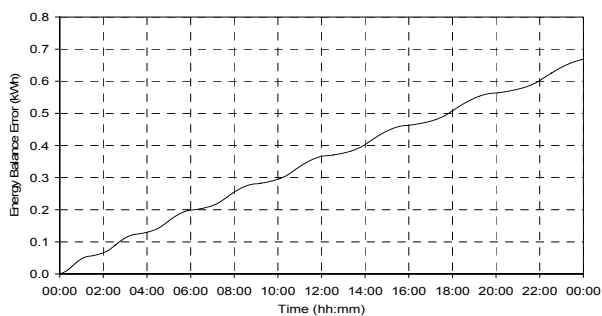
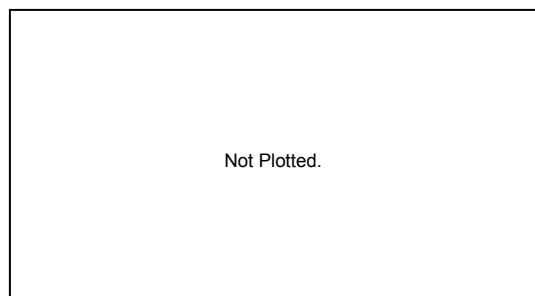
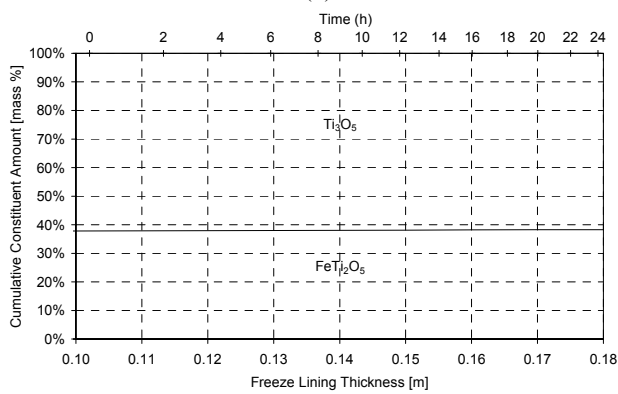
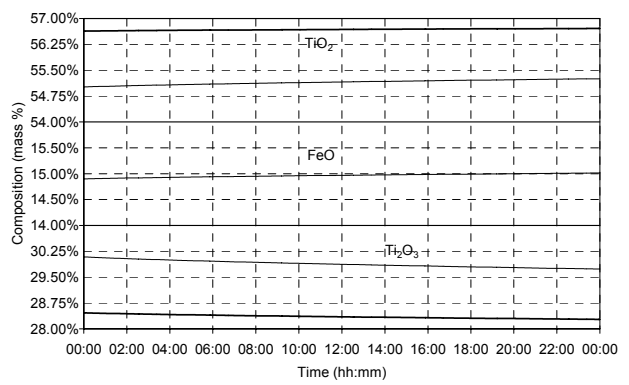
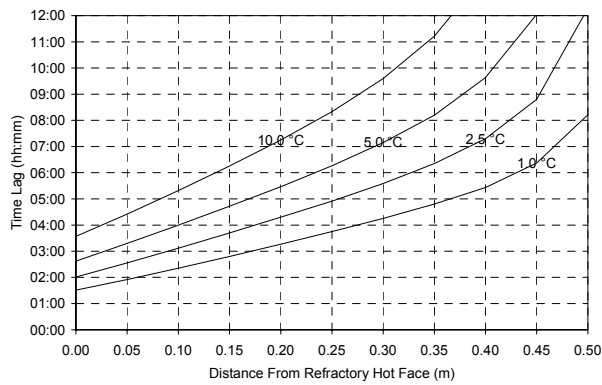
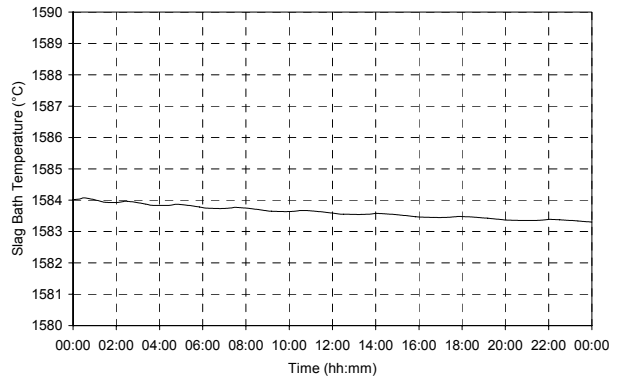
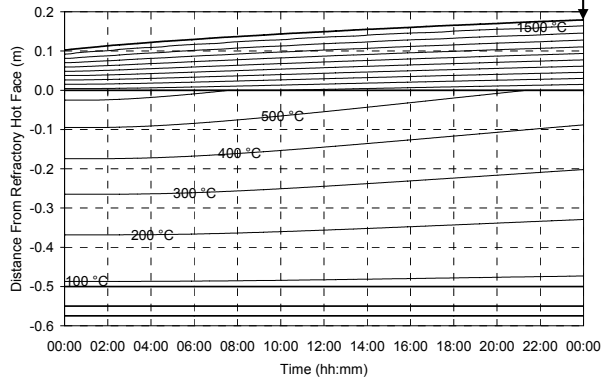


Figure 65 – Experiment 6.6 results.

6.3.7 Experiment 6.7

INITIAL STEADY STATE HEAT FLOW	INITIAL FREEZE LINING THICKNESS	INITIAL FREEZE LINING COMPOSITION	ELECTRICAL POWER HEAT FLOW	HEAT LOSSES HEAT FLOW	NET INPUT HEAT FLOW
250 kW	0.102 m	Pseudobrookite	200 kW	0 kW	200 kW

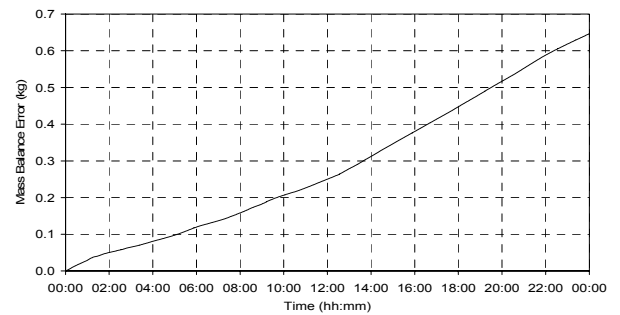
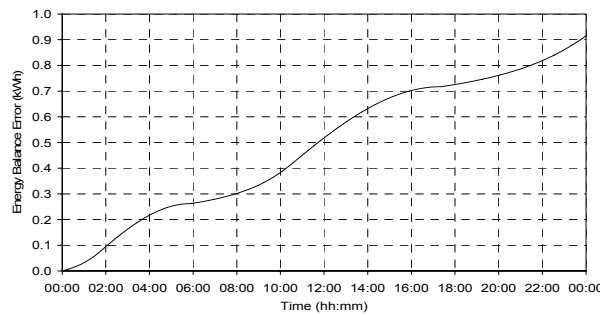
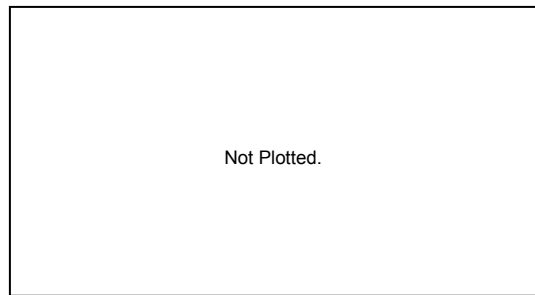
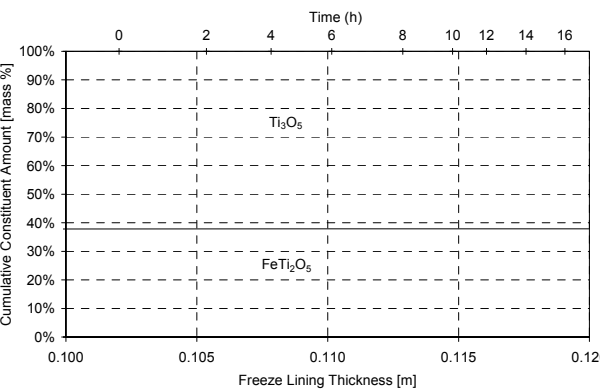
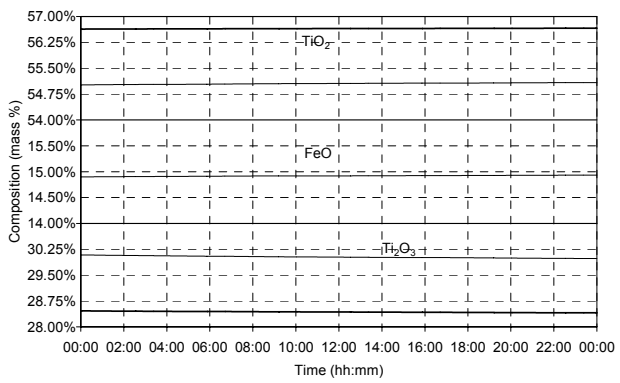
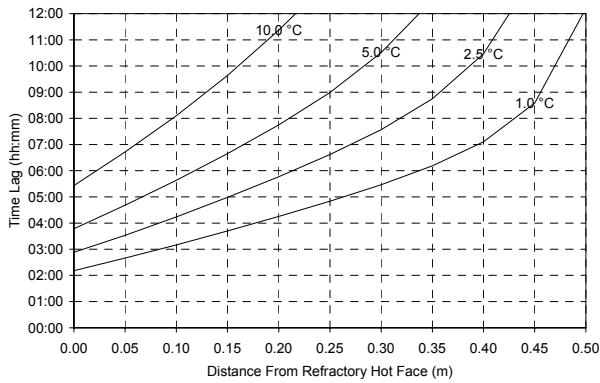
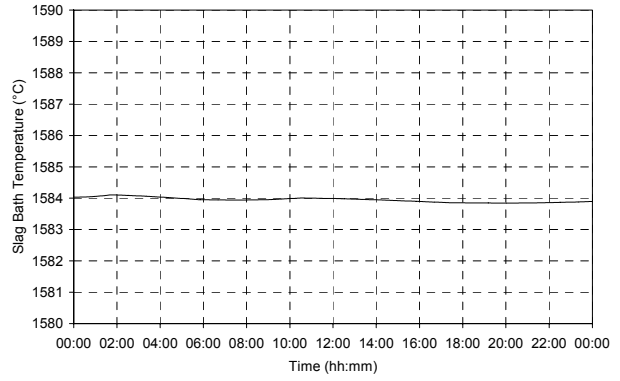
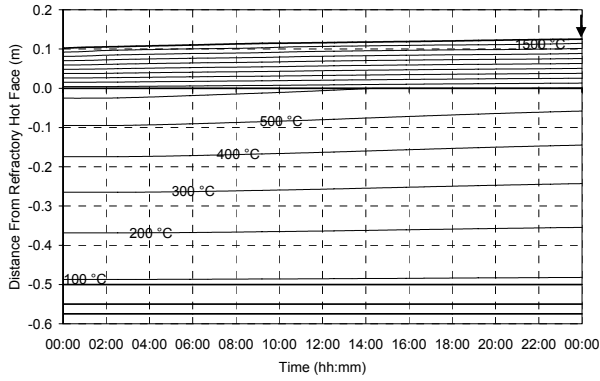
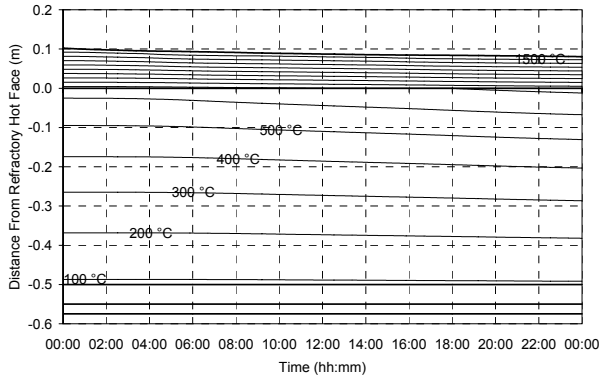


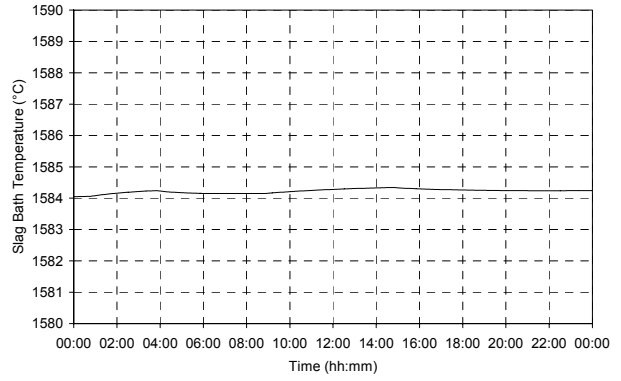
Figure 66 – Experiment 6.7 results.

6.3.8 Experiment 6.8

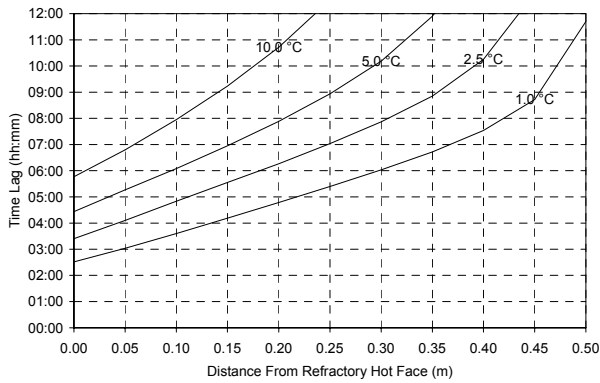
INITIAL STEADY STATE HEAT FLOW	INITIAL FREEZE LINING THICKNESS	INITIAL FREEZE LINING COMPOSITION	ELECTRICAL POWER HEAT FLOW	HEAT LOSSES HEAT FLOW	NET INPUT HEAT FLOW
250 kW	0.102 m	Pseudobrookite	300 kW	0 kW	300 kW



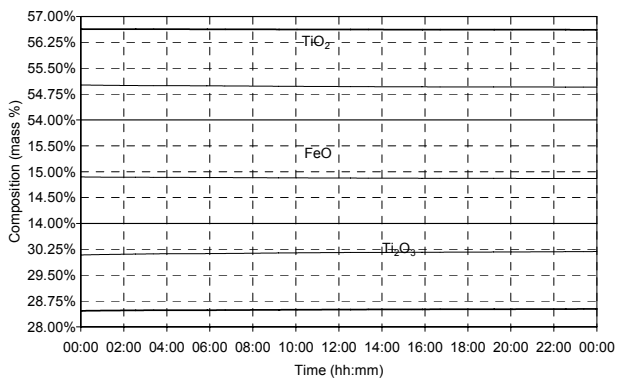
(a)



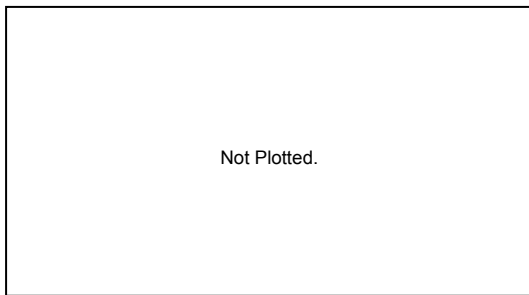
(b)



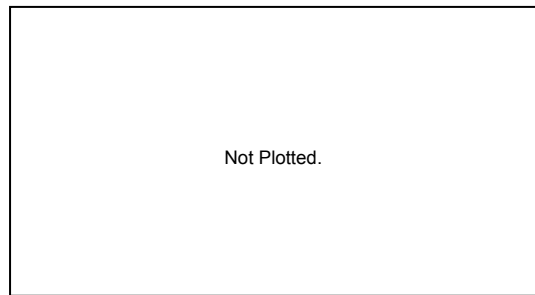
(c)



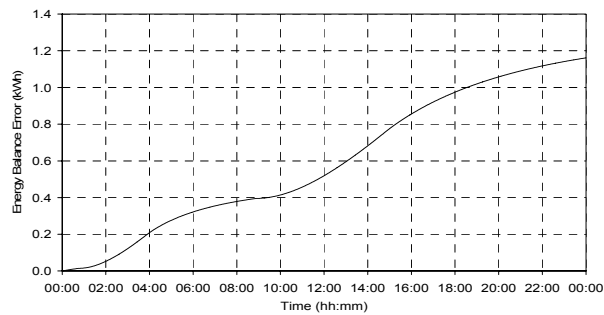
(d)



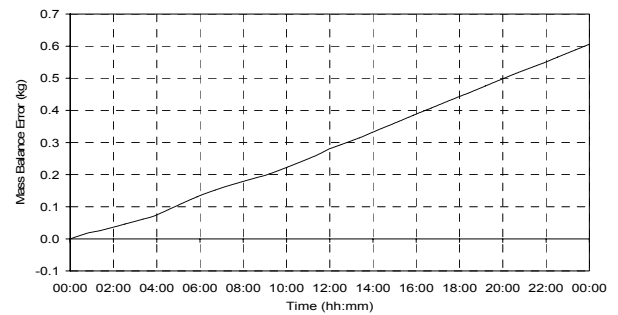
(e)



(f)



(g)

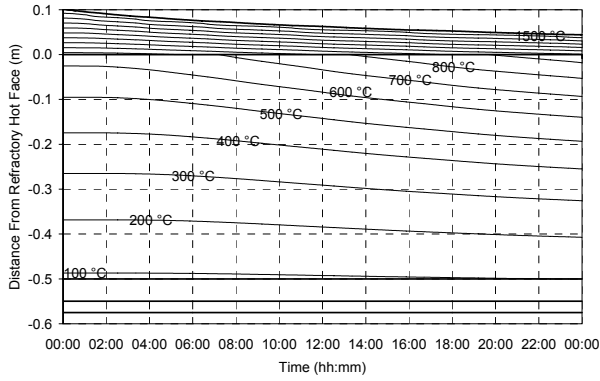


(h)

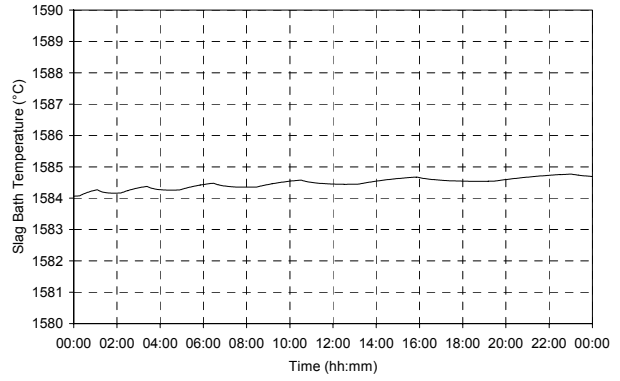
Figure 67 – Experiment 6.8 results.

6.3.9 Experiment 6.9

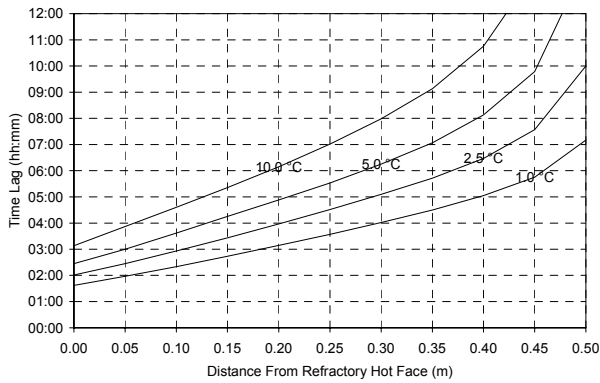
INITIAL STEADY STATE HEAT FLOW	INITIAL FREEZE LINING THICKNESS	INITIAL FREEZE LINING COMPOSITION	ELECTRICAL POWER HEAT FLOW	HEAT LOSSES HEAT FLOW	NET INPUT HEAT FLOW
250 kW	0.102 m	Pseudobrookite	400 kW	0 kW	400 kW



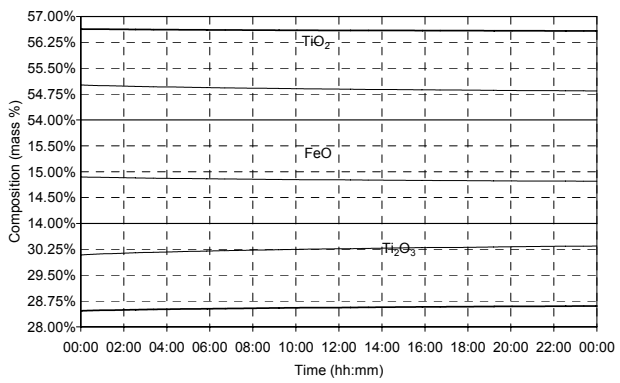
(a)



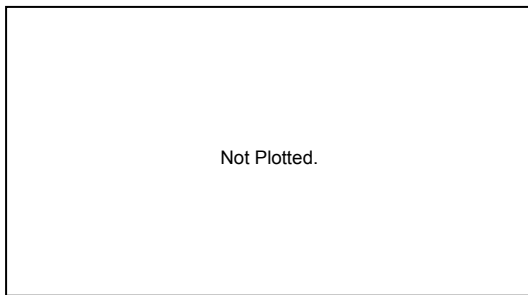
(b)



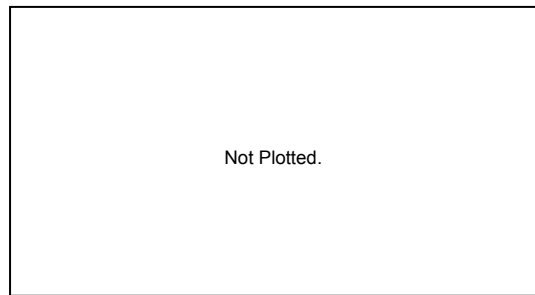
(c)



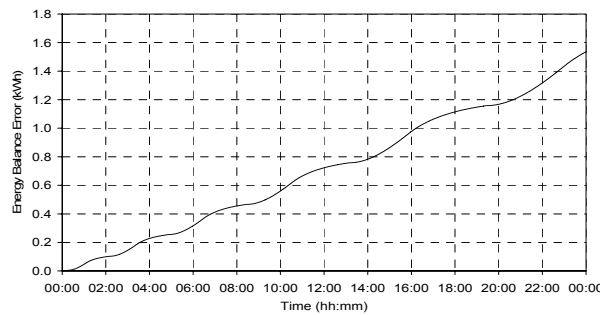
(d)



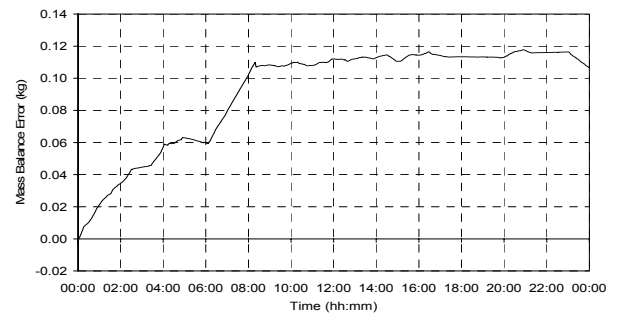
(e)



(f)



(g)

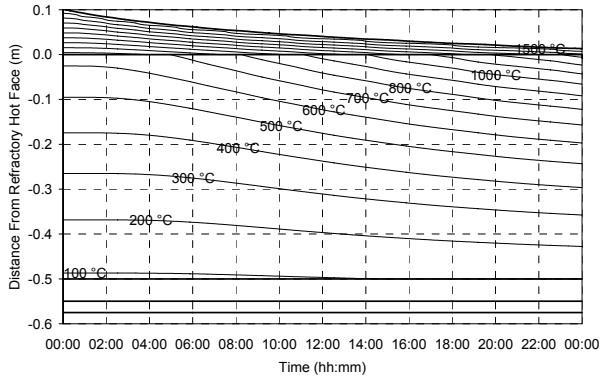


(h)

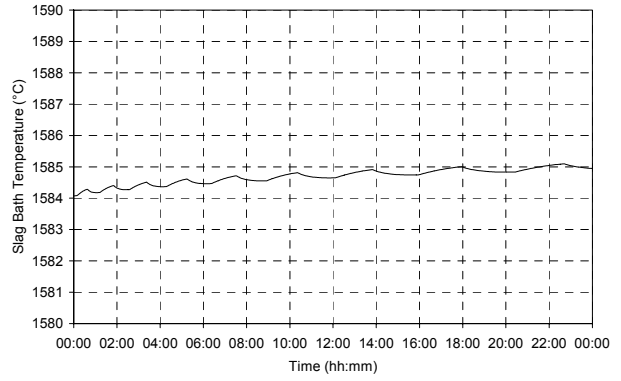
Figure 68 – Experiment 6.9 results.

6.3.10 Experiment 6.10

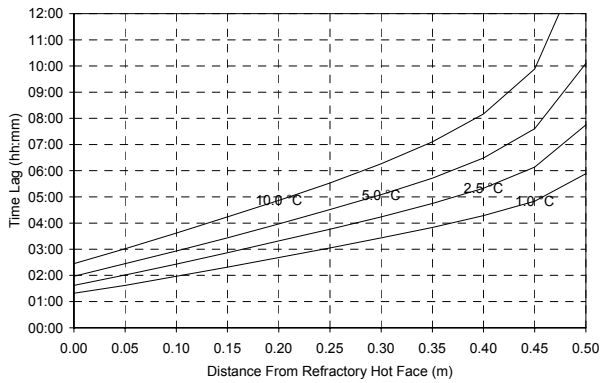
INITIAL STEADY STATE HEAT FLOW	INITIAL FREEZE LINING THICKNESS	INITIAL FREEZE LINING COMPOSITION	ELECTRICAL POWER HEAT FLOW	HEAT LOSSES HEAT FLOW	NET INPUT HEAT FLOW
250 kW	0.102 m	Pseudobrookite	500 kW	0 kW	500 kW



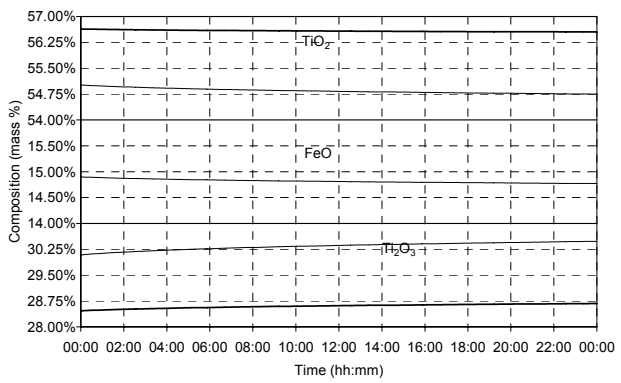
(a)



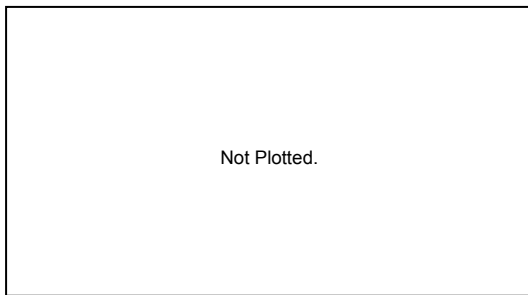
(b)



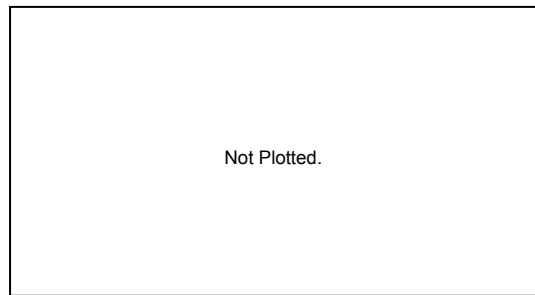
(c)



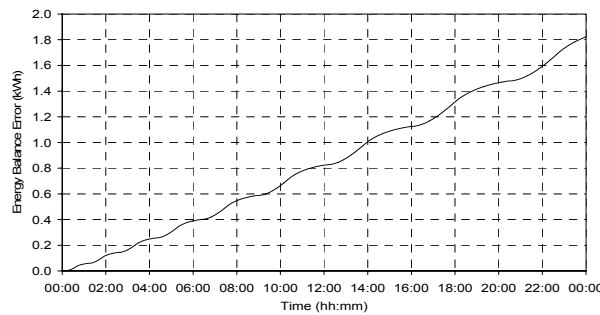
(d)



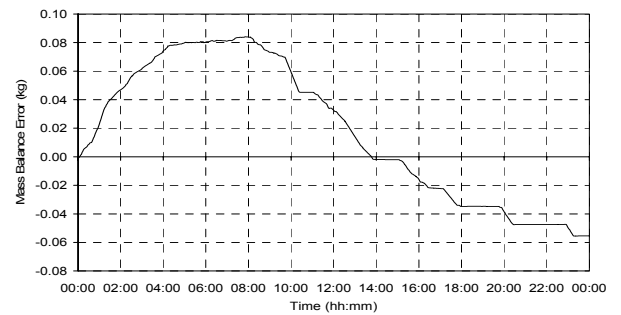
(e)



(f)



(g)

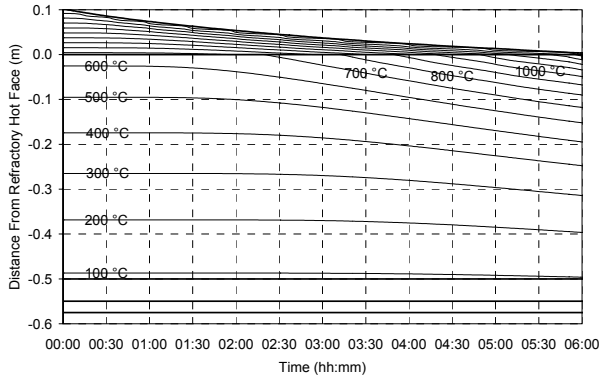


(h)

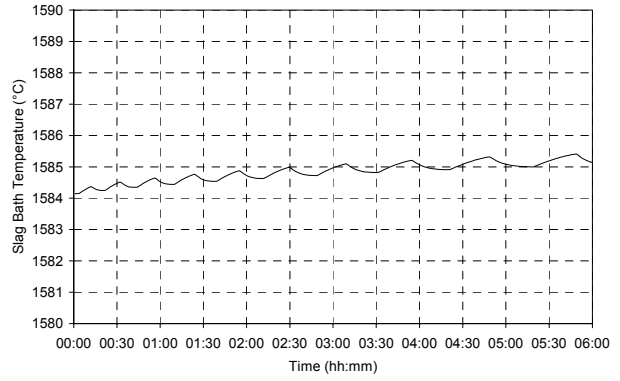
Figure 69 – Experiment 6.10 results.

6.3.11 Experiment 6.11

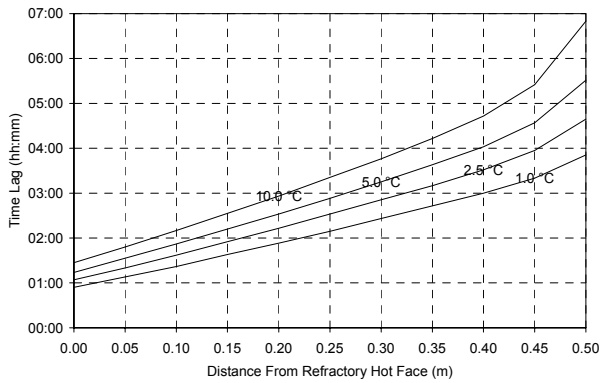
INITIAL STEADY STATE HEAT FLOW	INITIAL FREEZE LINING THICKNESS	INITIAL FREEZE LINING COMPOSITION	ELECTRICAL POWER HEAT FLOW	HEAT LOSSES HEAT FLOW	NET INPUT HEAT FLOW
250 kW	0.102 m	Pseudobrookite	1000 kW	0 kW	1000 kW



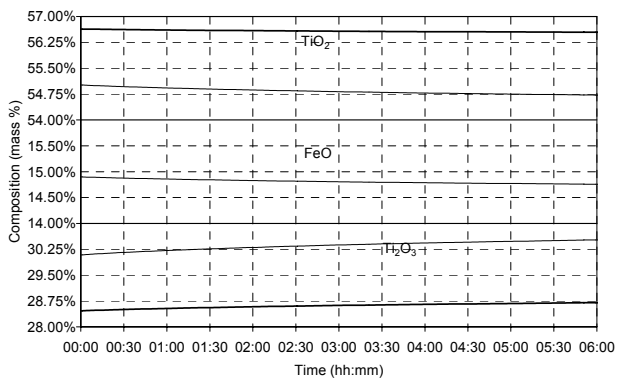
(a)



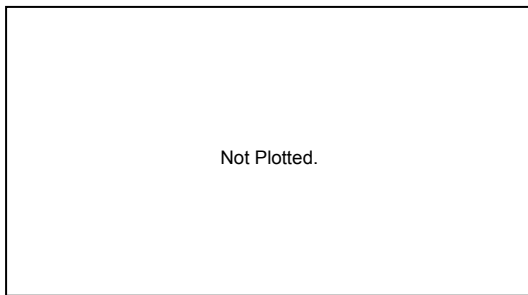
(b)



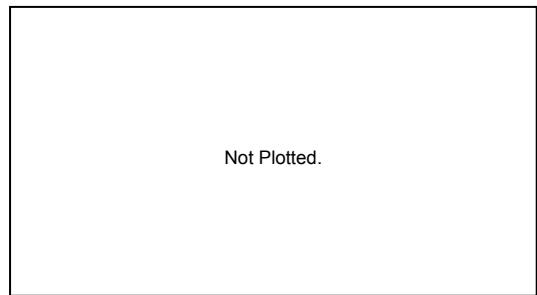
(c)



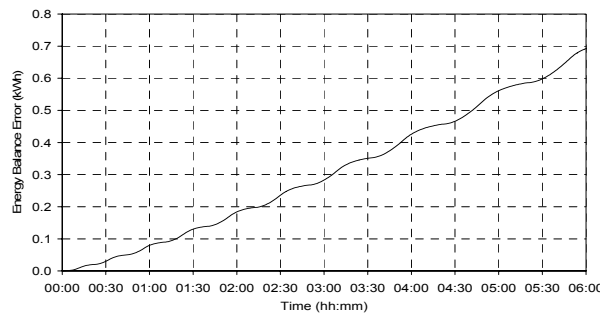
(d)



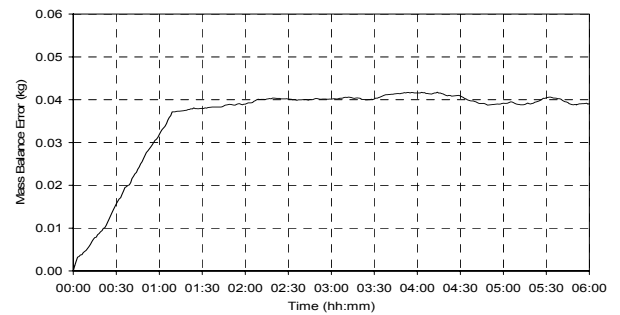
(e)



(f)



(g)

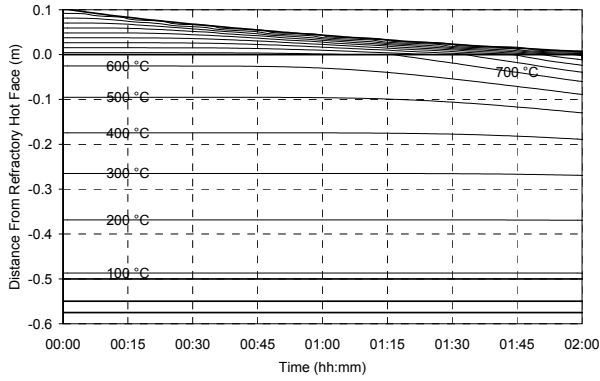


(h)

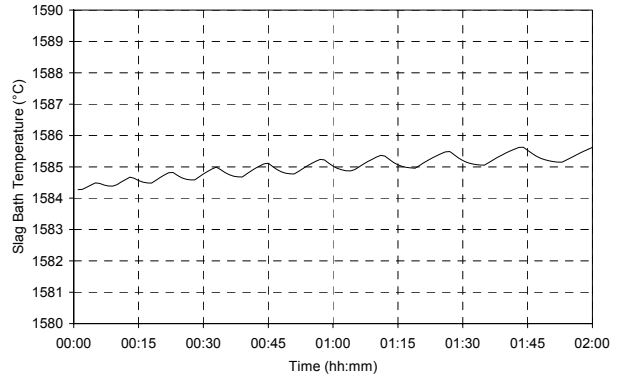
Figure 70 – Experiment 6.11 results.

6.3.12 Experiment 6.12

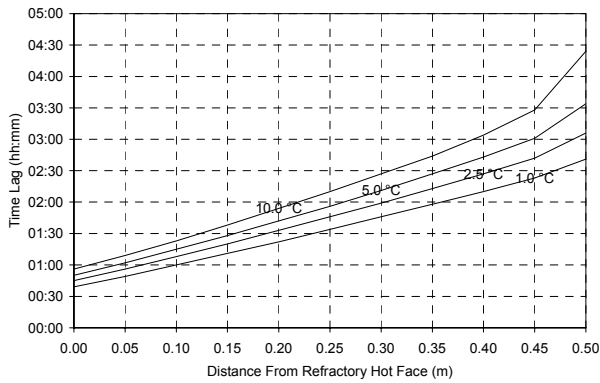
INITIAL STEADY STATE HEAT FLOW	INITIAL FREEZE LINING THICKNESS	INITIAL FREEZE LINING COMPOSITION	ELECTRICAL POWER HEAT FLOW	HEAT LOSSES HEAT FLOW	NET INPUT HEAT FLOW
250 kW	0.102 m	Pseudobrookite	2000 kW	0 kW	2000 kW



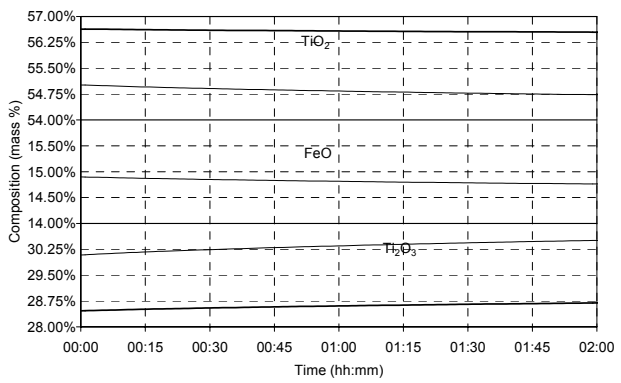
(a)



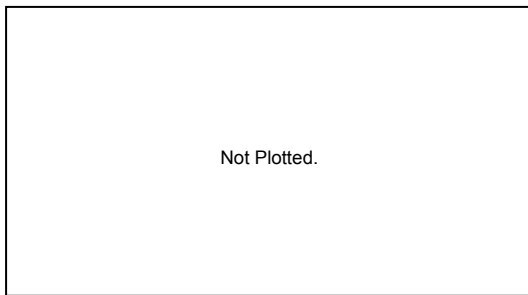
(b)



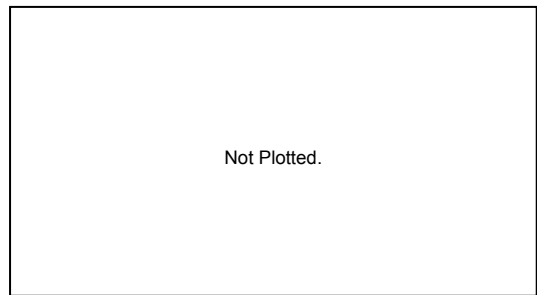
(c)



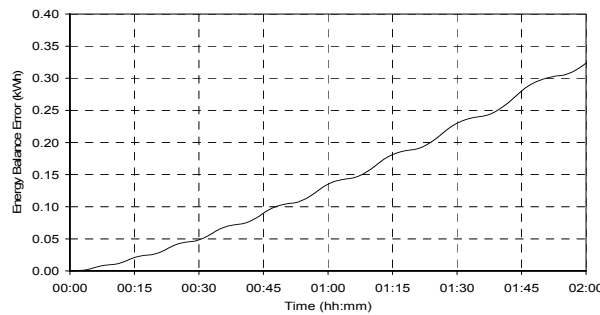
(d)



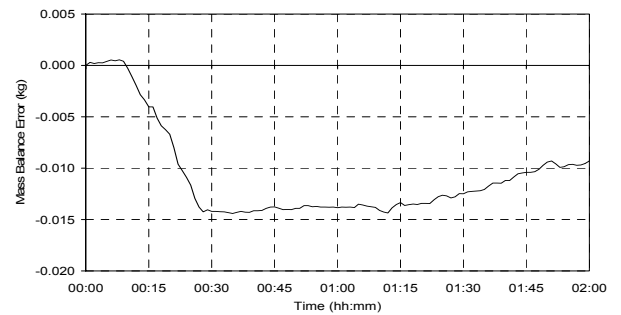
(e)



(f)



(g)



(h)

Figure 71 – Experiment 6.12 results.

6.3.13 Experiment 6.13

INITIAL STEADY STATE HEAT FLOW	INITIAL FREEZE LINING THICKNESS	INITIAL FREEZE LINING COMPOSITION	ELECTRICAL POWER HEAT FLOW	HEAT LOSSES HEAT FLOW	NET INPUT HEAT FLOW
250 kW	0.102 m	Pseudobrookite	5000 kW	0 kW	5000 kW

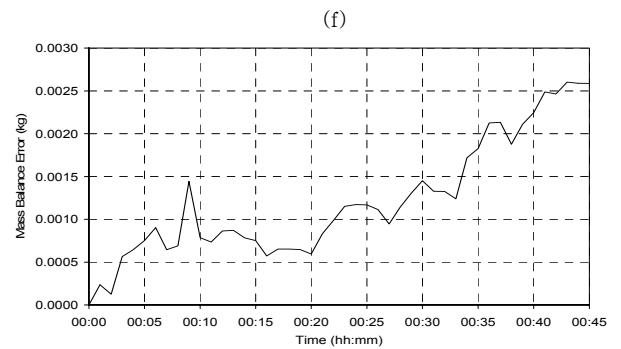
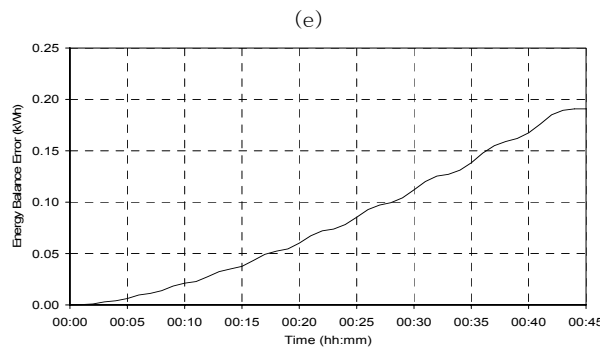
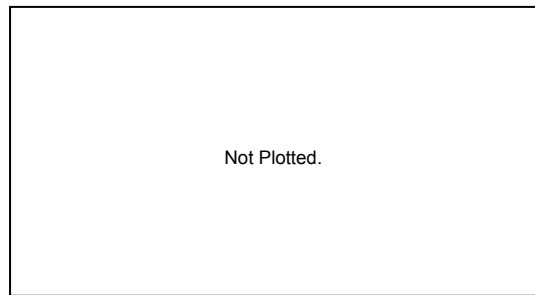
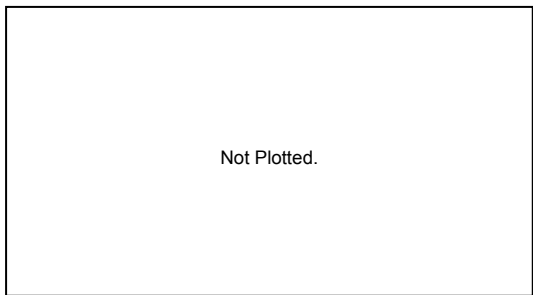
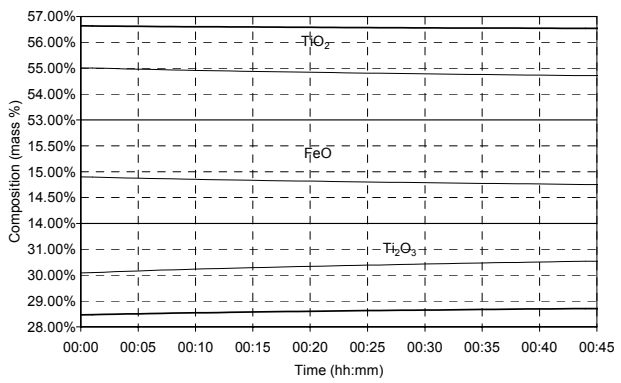
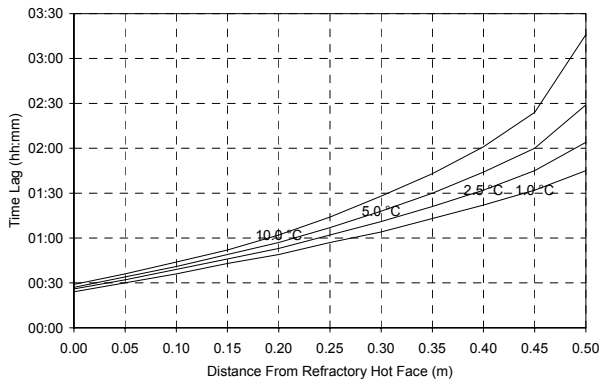
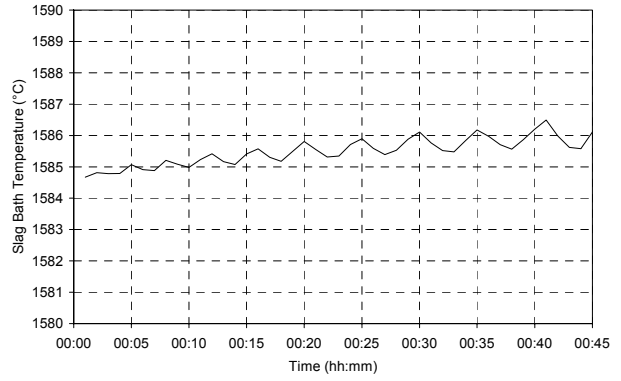
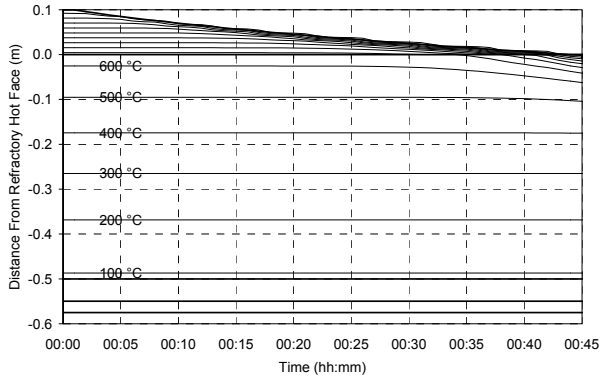
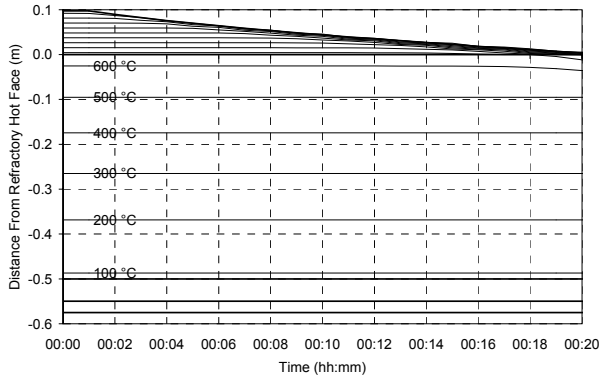


Figure 72 – Experiment 6.13 results.

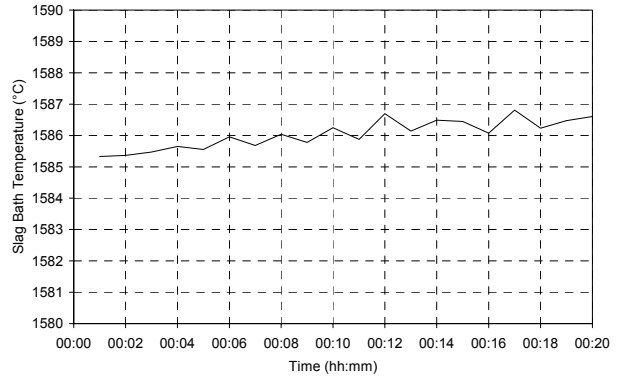


6.3.14 Experiment 6.14

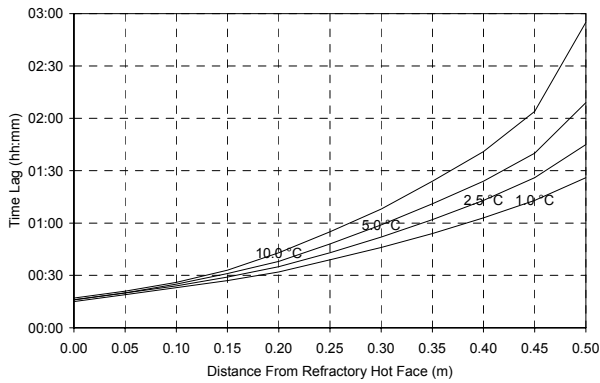
INITIAL STEADY STATE HEAT FLOW	INITIAL FREEZE LINING THICKNESS	INITIAL FREEZE LINING COMPOSITION	ELECTRICAL POWER HEAT FLOW	HEAT LOSSES HEAT FLOW	NET INPUT HEAT FLOW
250 kW	0.102 m	Pseudobrookite	10000 kW	0 kW	10000 kW



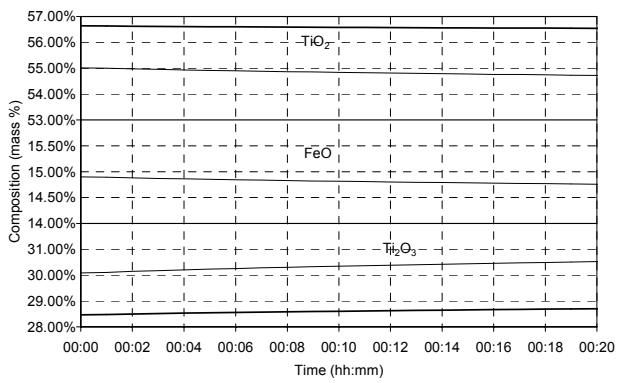
(a)



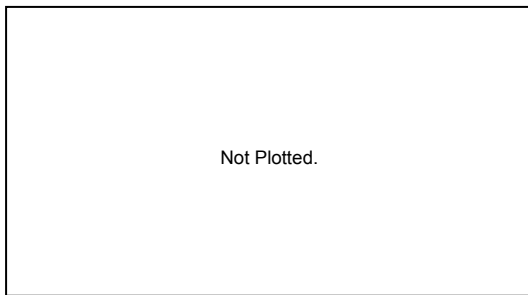
(b)



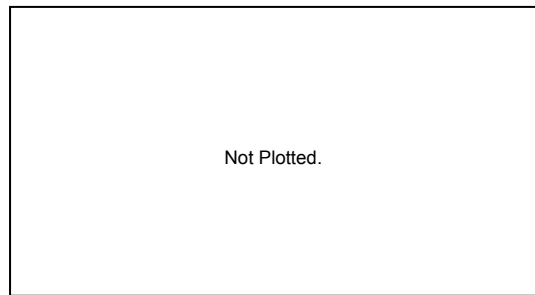
(c)



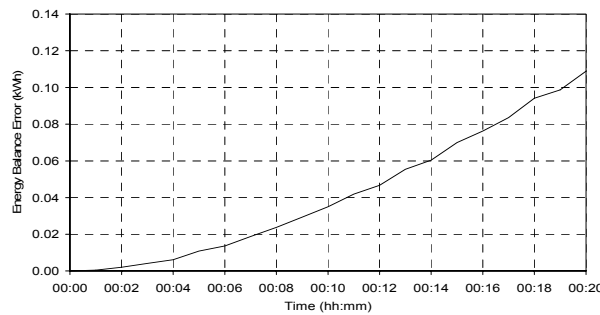
(d)



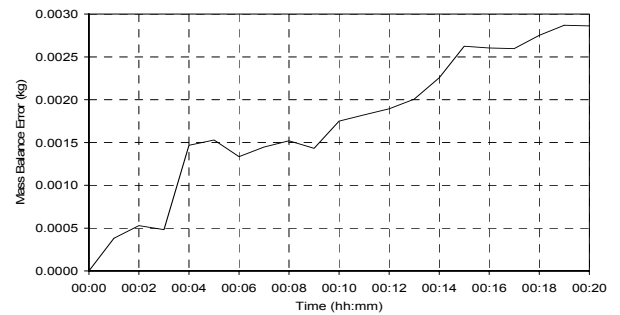
(e)



(f)



(g)

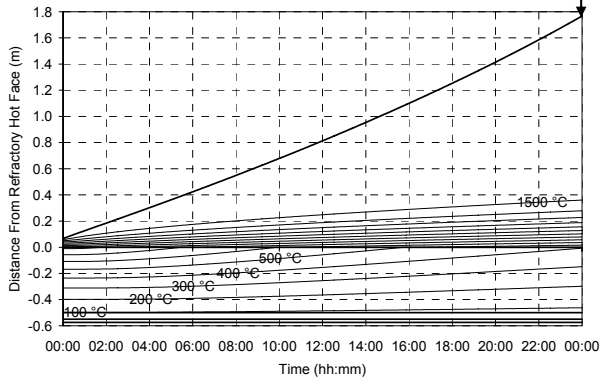


(h)

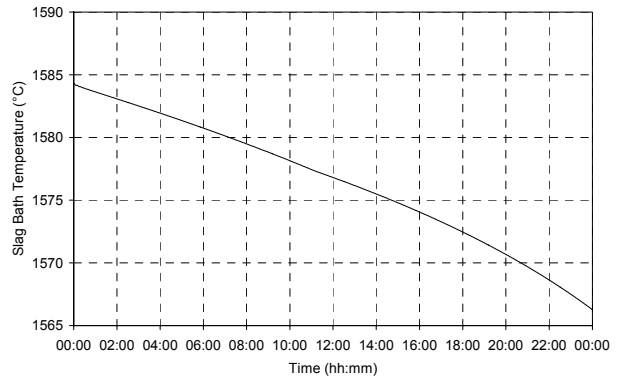
Figure 73 – Experiment 6.14 results.

6.3.15 Experiment 6.15

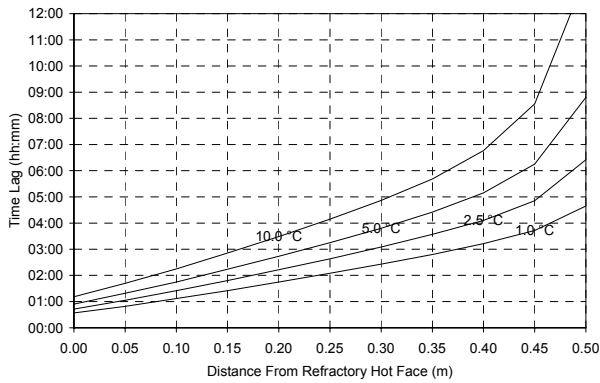
INITIAL STEADY STATE HEAT FLOW	INITIAL FREEZE LINING THICKNESS	INITIAL FREEZE LINING COMPOSITION	ELECTRICAL POWER HEAT FLOW	HEAT LOSSES HEAT FLOW	NET INPUT HEAT FLOW
300 kW	0.066 m	Pseudobrookite	0 kW	1000 kW	-1000 kW



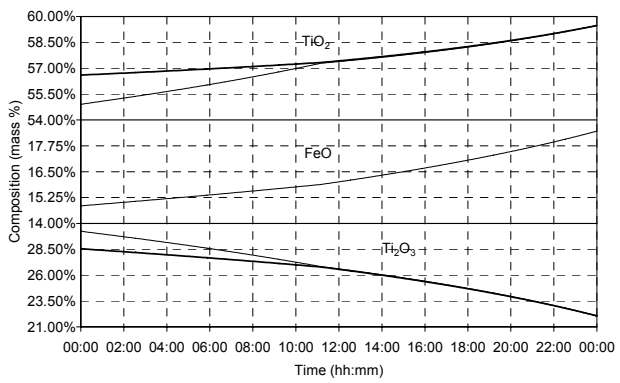
(a)



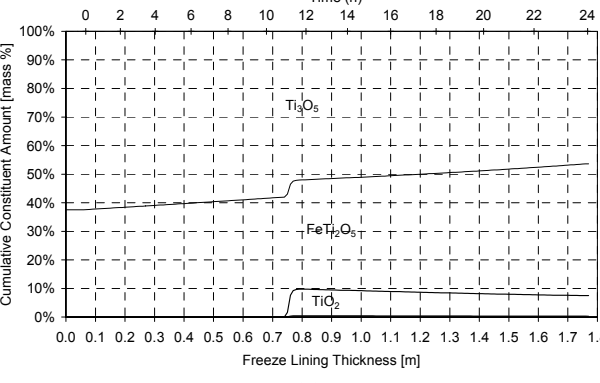
(b)



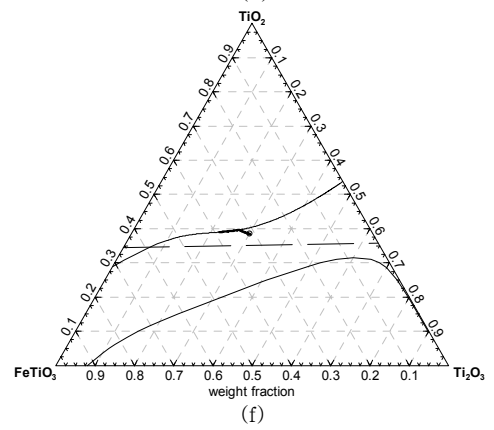
(c)



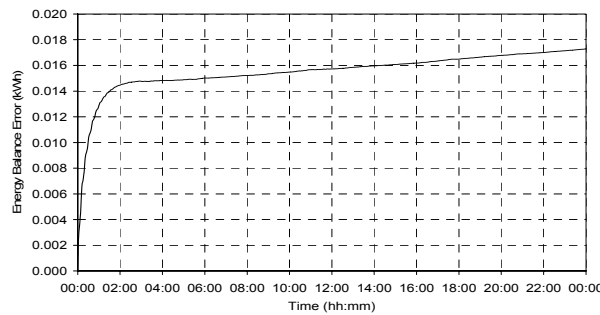
(d)



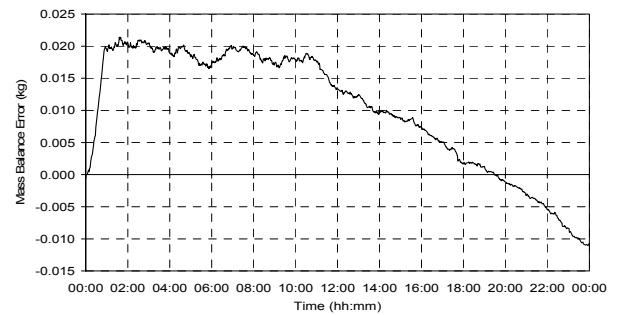
(e)



(f)



(g)



(h)

Figure 74 – Experiment 6.15 results.

6.3.16 Experiment 6.16

INITIAL STEADY STATE HEAT FLOW	INITIAL FREEZE LINING THICKNESS	INITIAL FREEZE LINING COMPOSITION	ELECTRICAL POWER HEAT FLOW	HEAT LOSSES HEAT FLOW	NET INPUT HEAT FLOW
300 kW	0.066 m	Pseudobrookite	0 kW	0 kW	0 kW

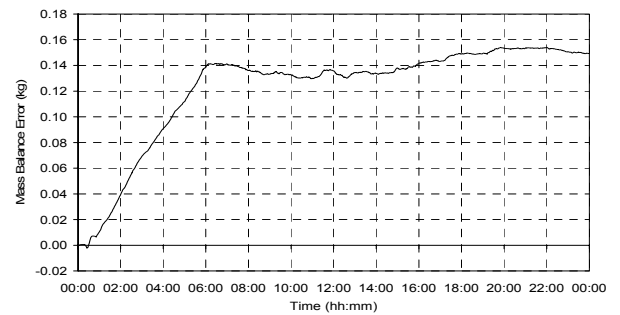
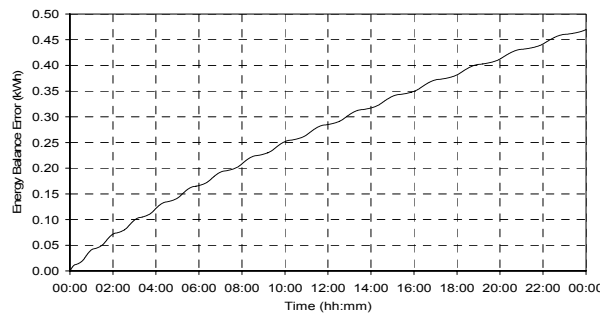
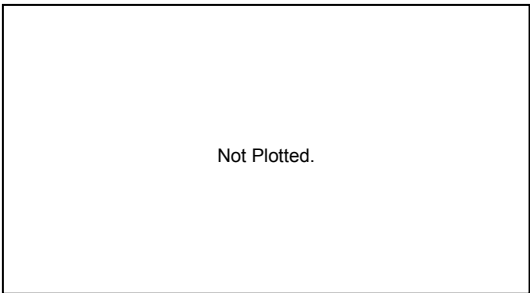
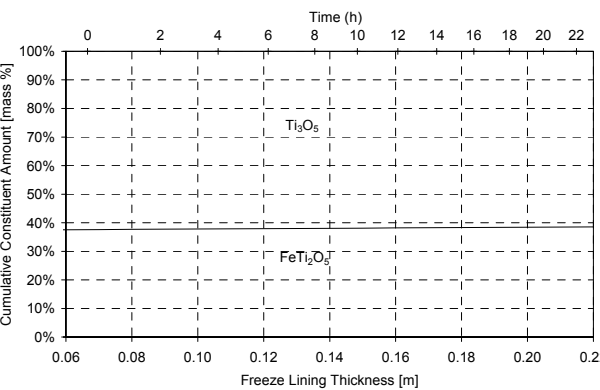
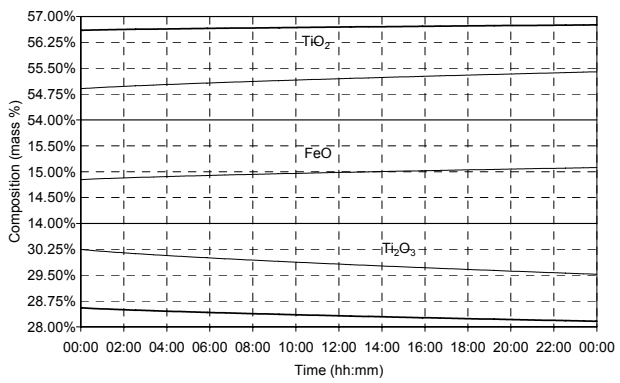
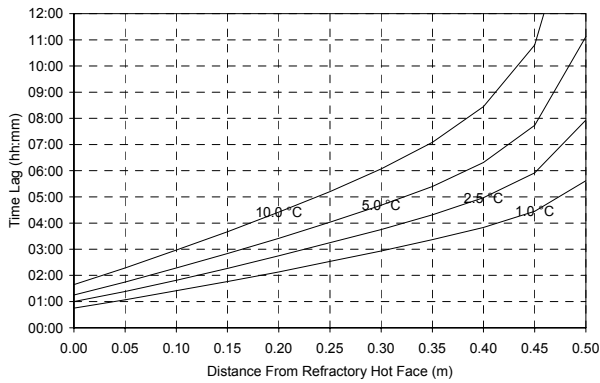
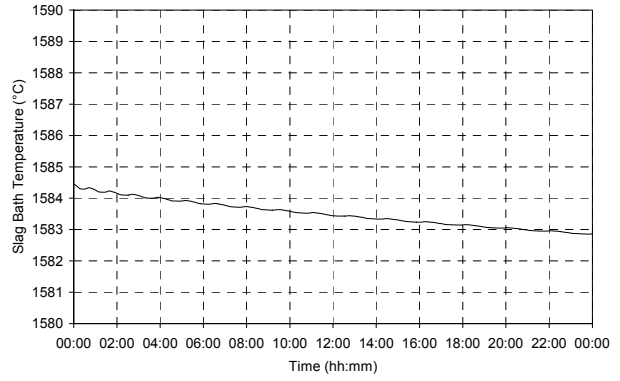
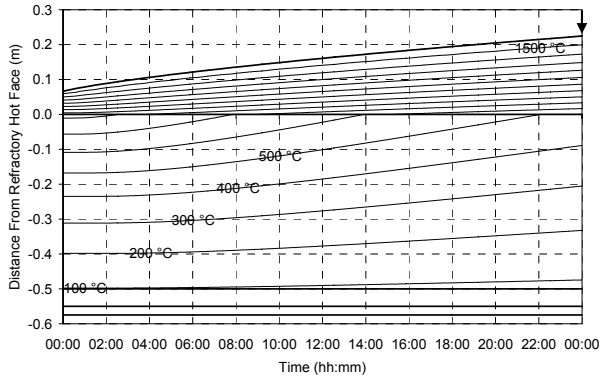
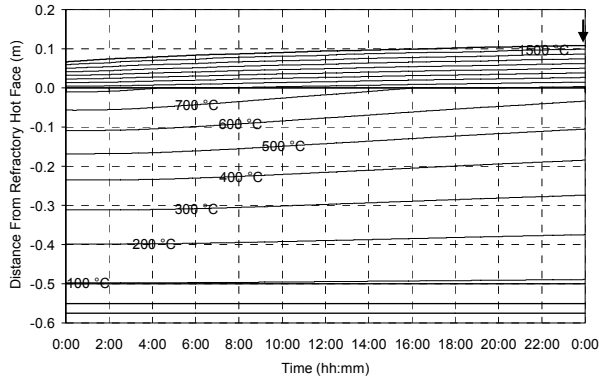


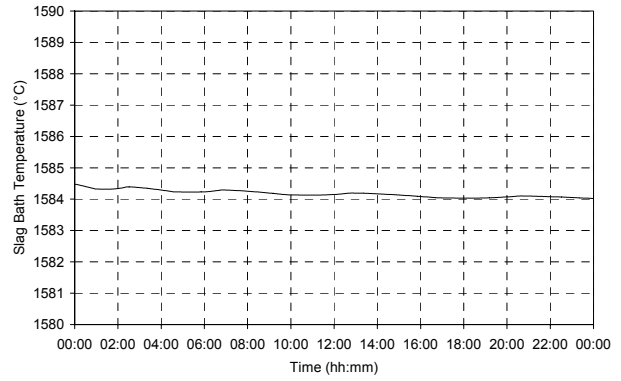
Figure 75 – Experiment 6.16 results.

6.3.17 Experiment 6.17

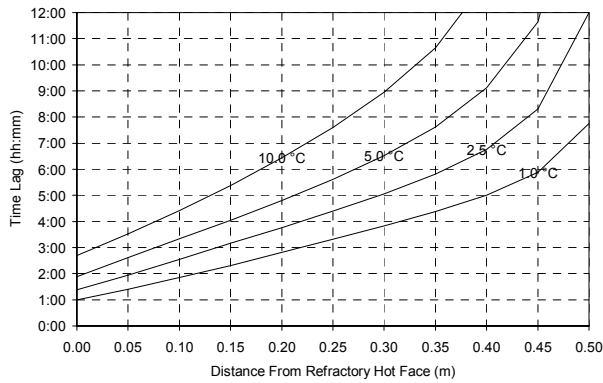
INITIAL STEADY STATE HEAT FLOW	INITIAL FREEZE LINING THICKNESS	INITIAL FREEZE LINING COMPOSITION	ELECTRICAL POWER HEAT FLOW	HEAT LOSSES HEAT FLOW	NET INPUT HEAT FLOW
300 kW	0.066 m	Pseudobrookite	200 kW	0 kW	200 kW



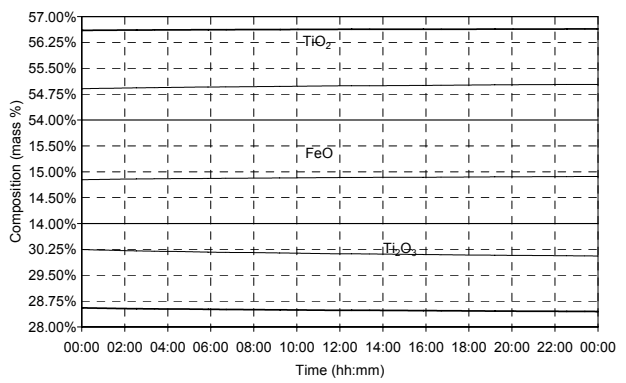
(a)



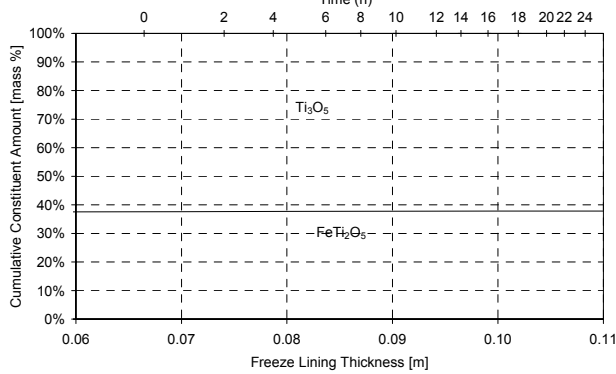
(b)



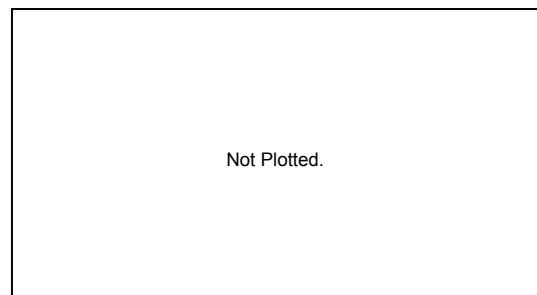
(c)



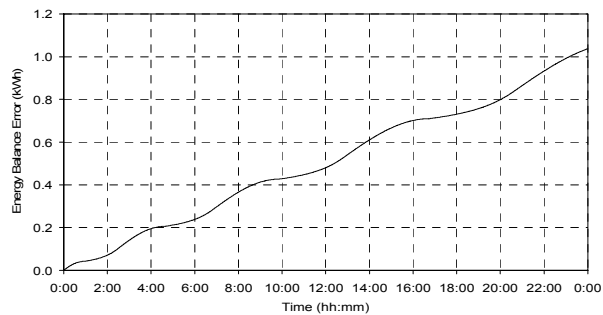
(d)



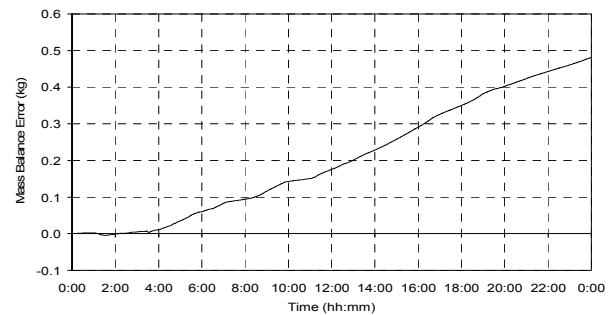
(e)



(f)



(g)

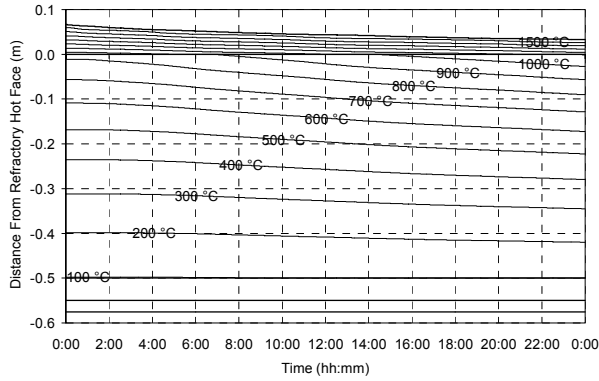


(h)

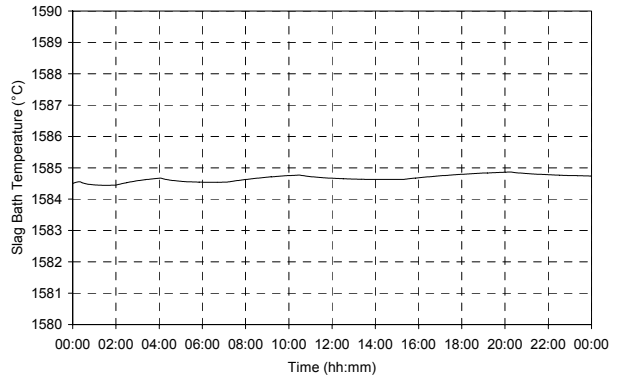
Figure 76 – Experiment 6.17 results.

6.3.18 Experiment 6.18

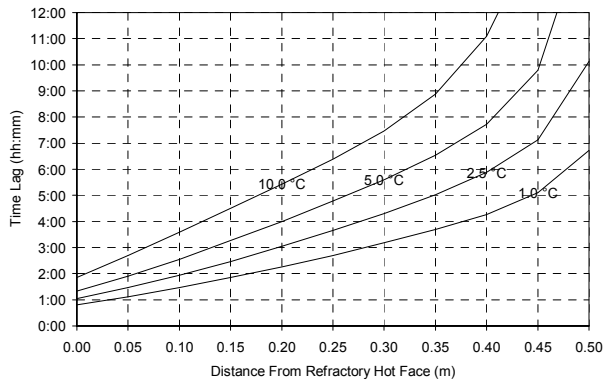
INITIAL STEADY STATE HEAT FLOW	INITIAL FREEZE LINING THICKNESS	INITIAL FREEZE LINING COMPOSITION	ELECTRICAL POWER HEAT FLOW	HEAT LOSSES HEAT FLOW	NET INPUT HEAT FLOW
300 kW	0.066 m	Pseudobrookite	400 kW	0 kW	400 kW



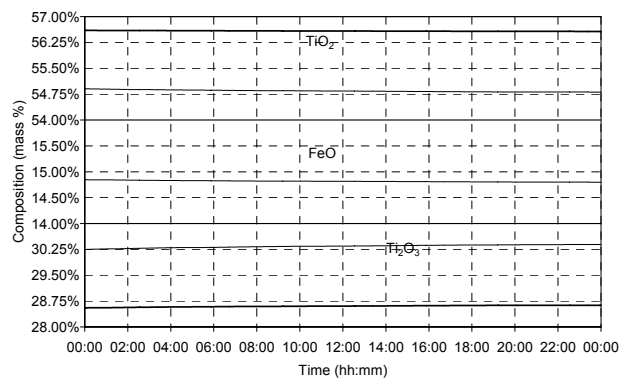
(a)



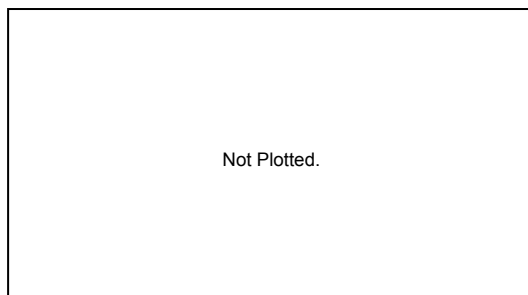
(b)



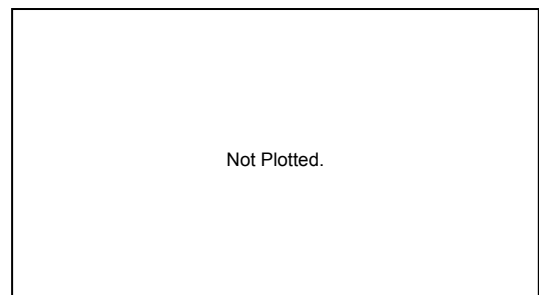
(c)



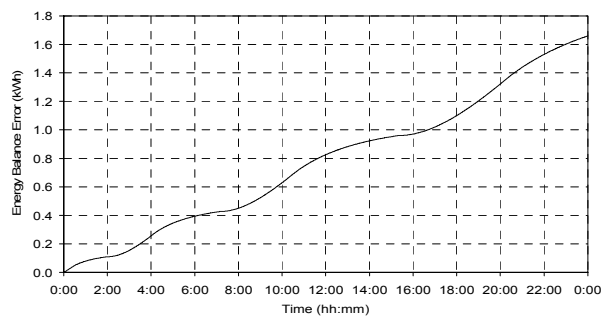
(d)



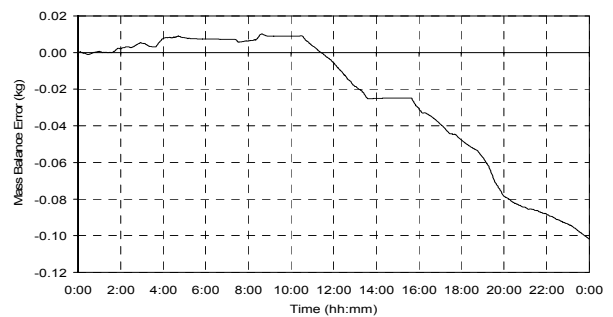
(e)



(f)



(g)

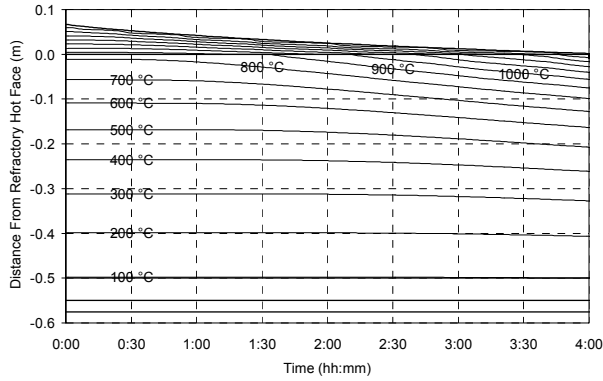


(h)

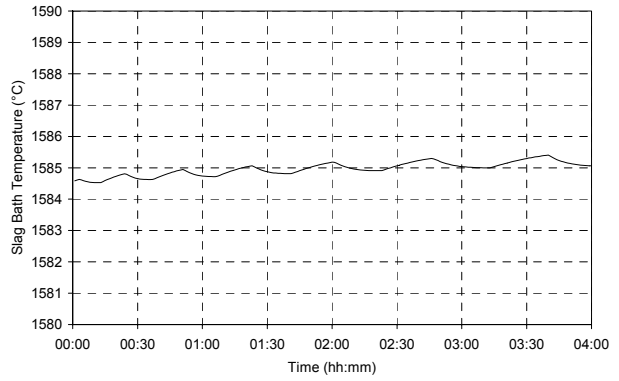
Figure 77 – Experiment 6.18 results.

6.3.19 Experiment 6.19

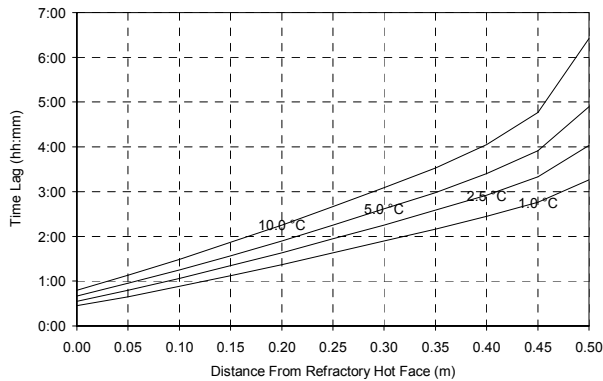
INITIAL STEADY STATE HEAT FLOW	INITIAL FREEZE LINING THICKNESS	INITIAL FREEZE LINING COMPOSITION	ELECTRICAL POWER HEAT FLOW	HEAT LOSSES HEAT FLOW	NET INPUT HEAT FLOW
300 kW	0.066 m	Pseudobrookite	1000 kW	0 kW	1000 kW



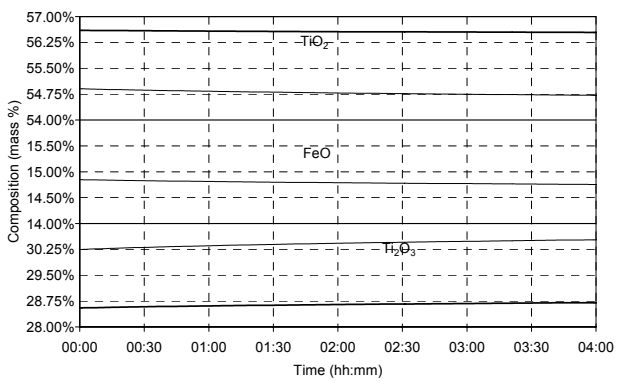
(a)



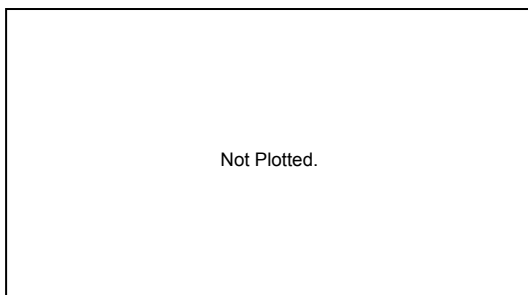
(b)



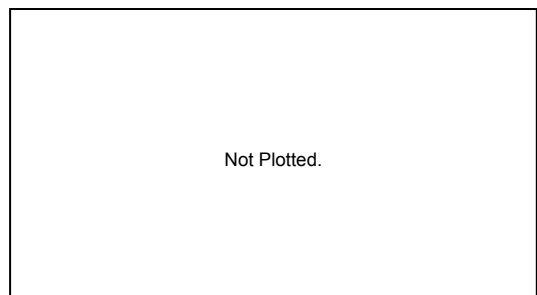
(c)



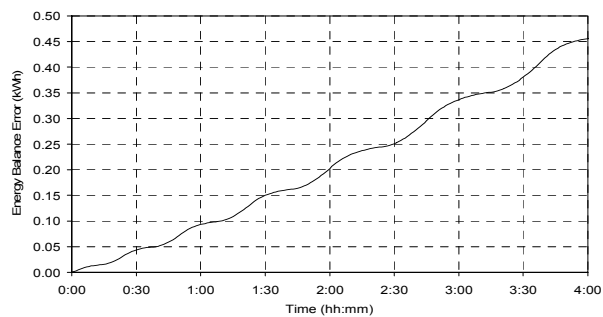
(d)



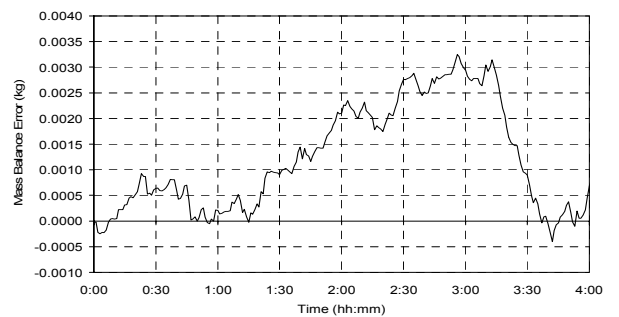
(e)



(f)



(g)

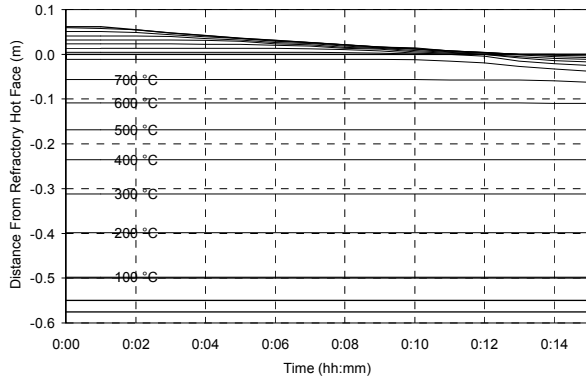


(h)

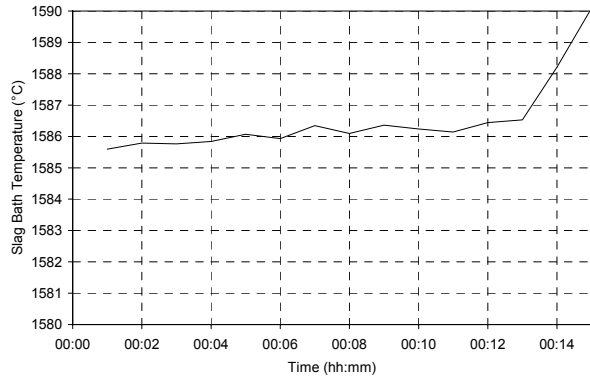
Figure 78 – Experiment 6.19 results.

6.3.20 Experiment 6.20

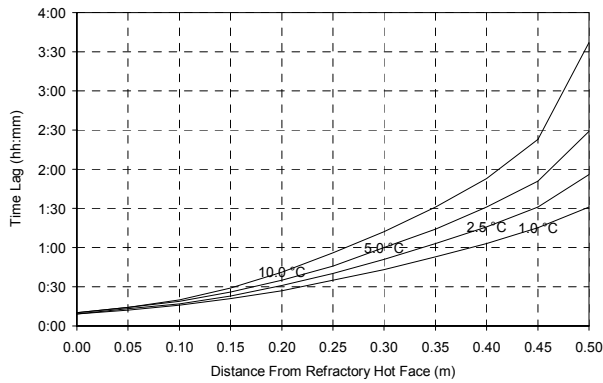
INITIAL STEADY STATE HEAT FLOW	INITIAL FREEZE LINING THICKNESS	INITIAL FREEZE LINING COMPOSITION	ELECTRICAL POWER HEAT FLOW	HEAT LOSSES HEAT FLOW	NET INPUT HEAT FLOW
300 kW	0.066 m	Pseudobrookite	10000 kW	0 kW	10000 kW



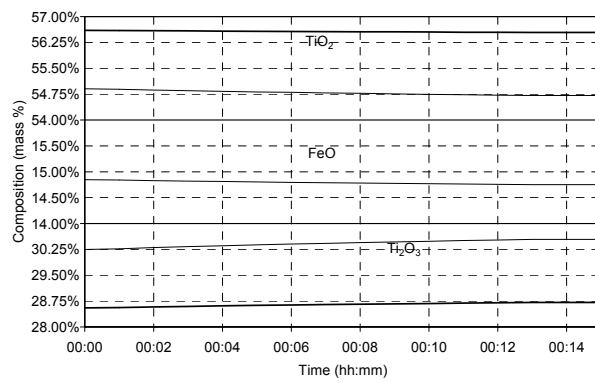
(a)



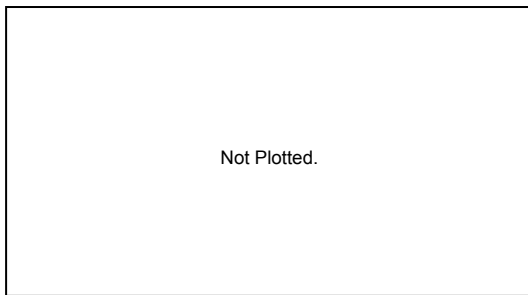
(b)



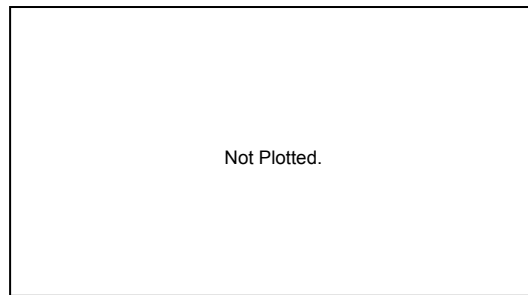
(c)



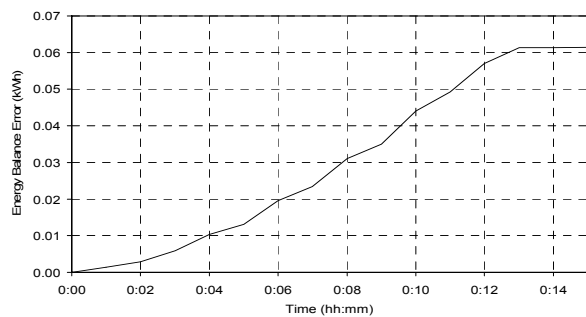
(d)



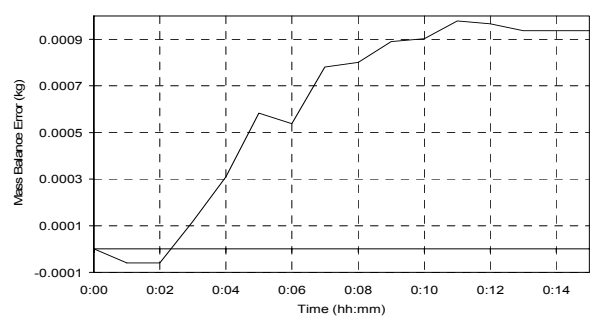
(e)



(f)



(g)

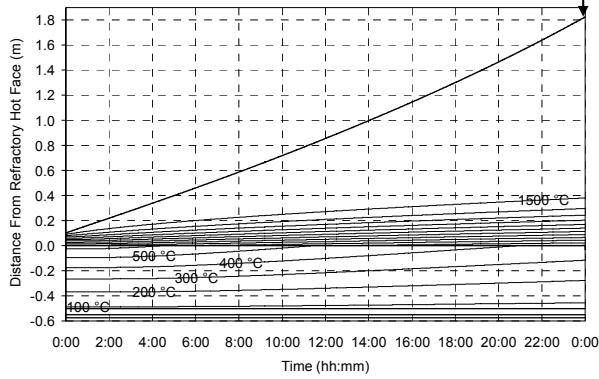


(h)

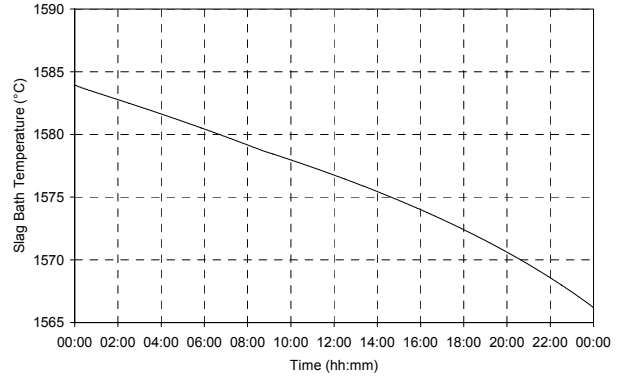
Figure 79 – Experiment 6.20 results.

6.3.21 Experiment 6.21

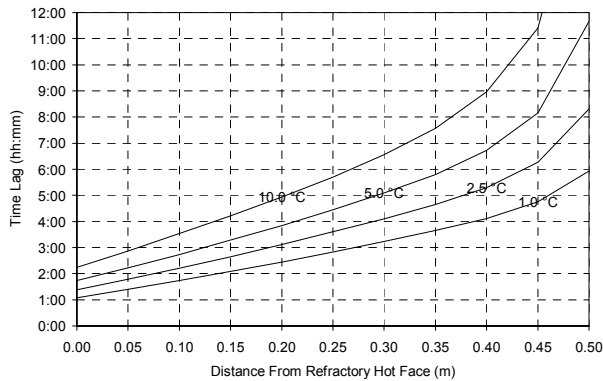
INITIAL STEADY STATE HEAT FLOW	INITIAL FREEZE LINING THICKNESS	INITIAL FREEZE LINING COMPOSITION	ELECTRICAL POWER HEAT FLOW	HEAT LOSSES HEAT FLOW	NET INPUT HEAT FLOW
250 kW	0.102 m	Rutile	0 kW	1000 kW	-1000 kW



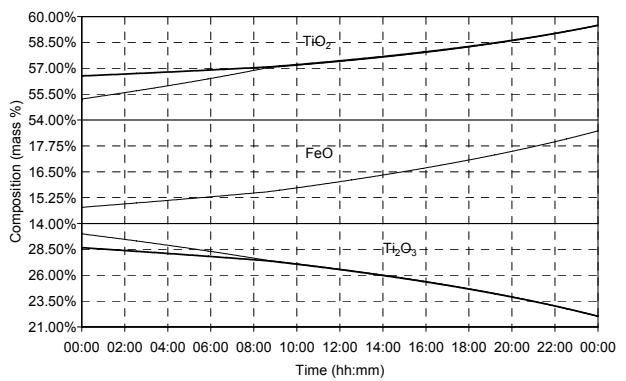
(a)



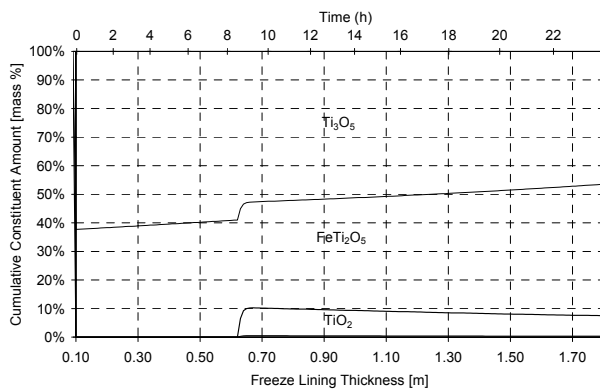
(b)



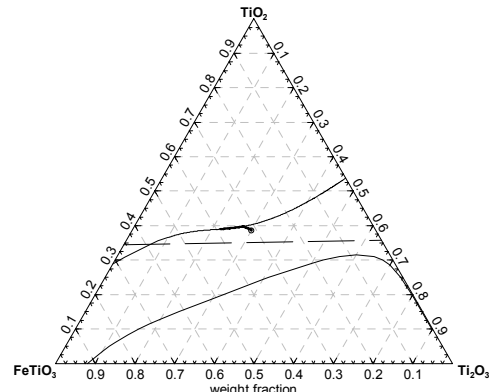
(c)



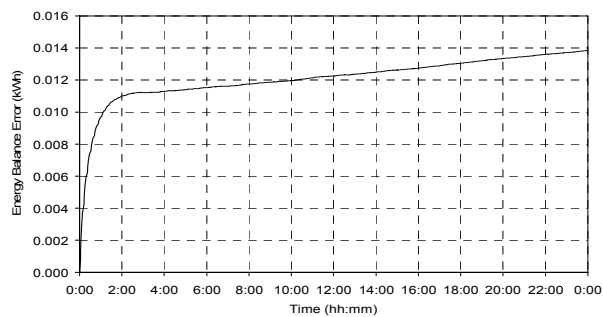
(d)



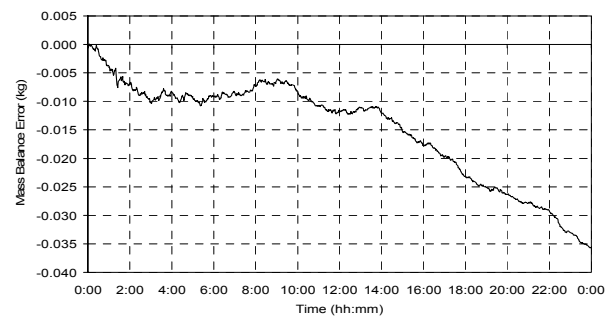
(e)



(f)



(g)



(h)

Figure 80 – Experiment 6.21 results.



6.3.22 Experiment 6.22

INITIAL STEADY STATE HEAT FLOW	INITIAL FREEZE LINING THICKNESS	INITIAL FREEZE LINING COMPOSITION	ELECTRICAL POWER HEAT FLOW	HEAT LOSSES HEAT FLOW	NET INPUT HEAT FLOW
250 kW	0.102 m	Rutile	0 kW	0 kW	0 kW

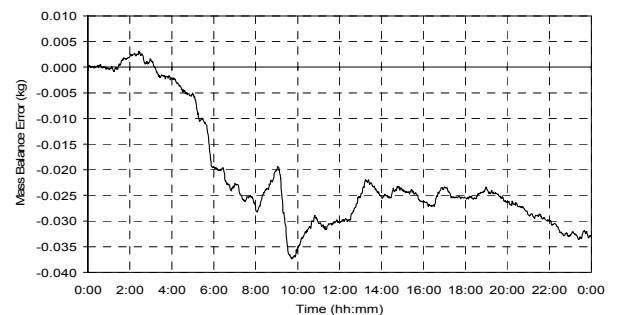
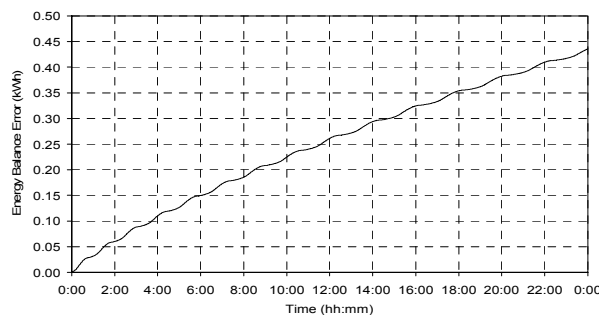
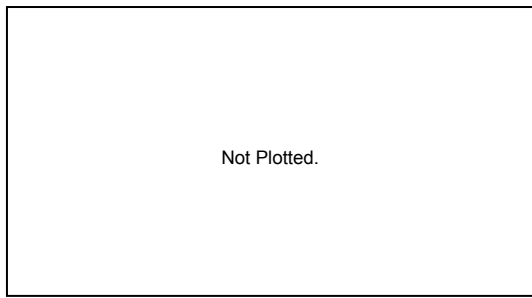
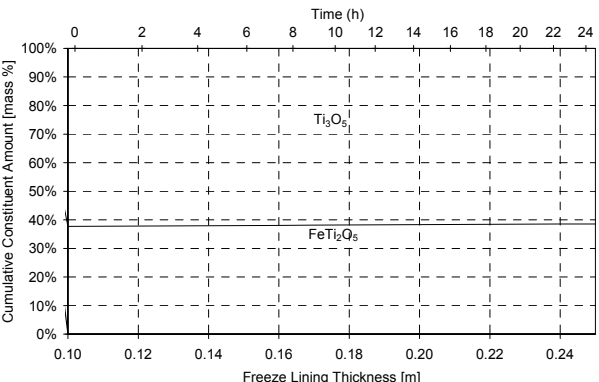
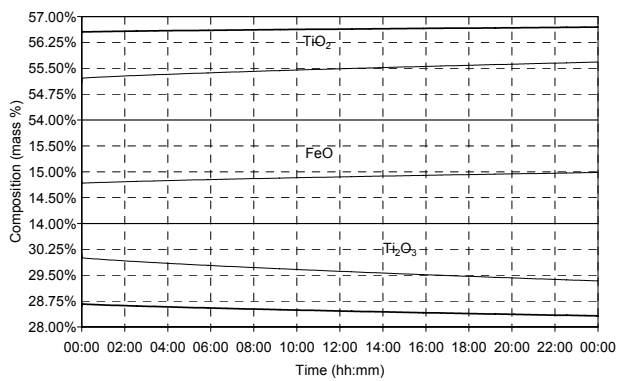
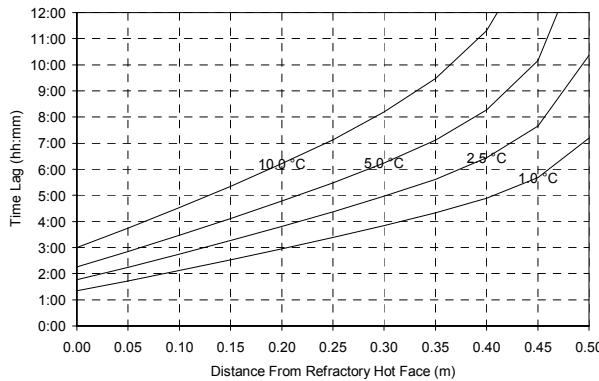
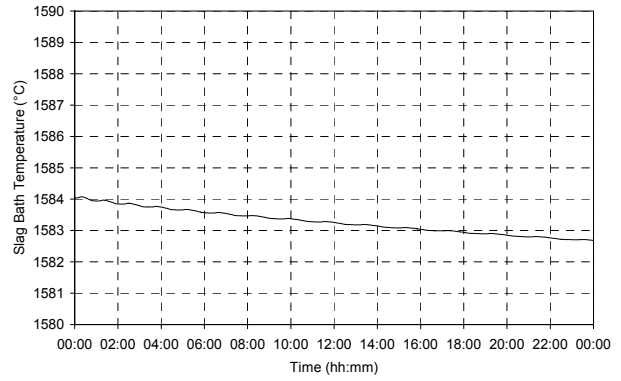
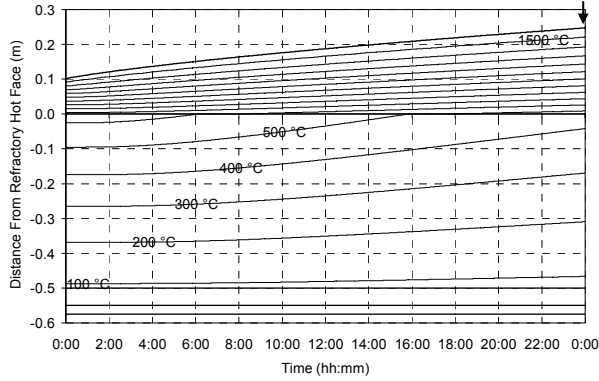
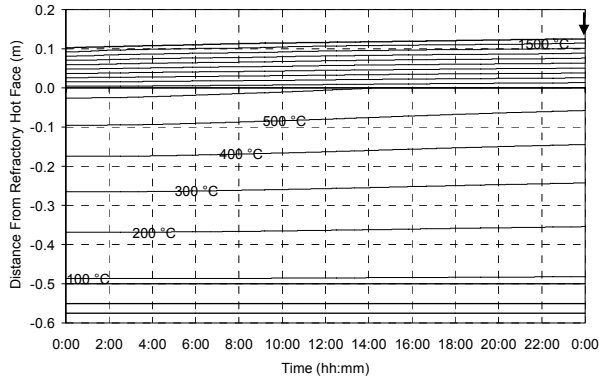


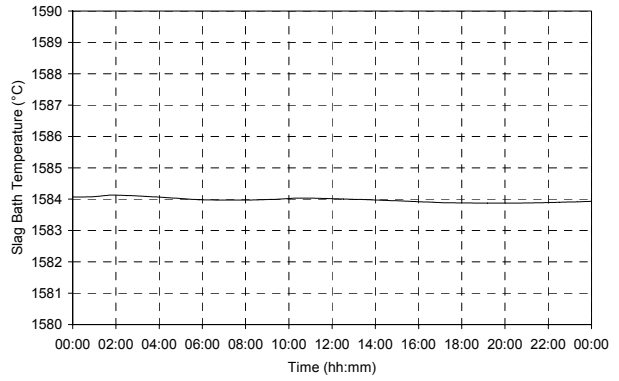
Figure 81 – Experiment 6.22 results.

6.3.23 Experiment 6.23

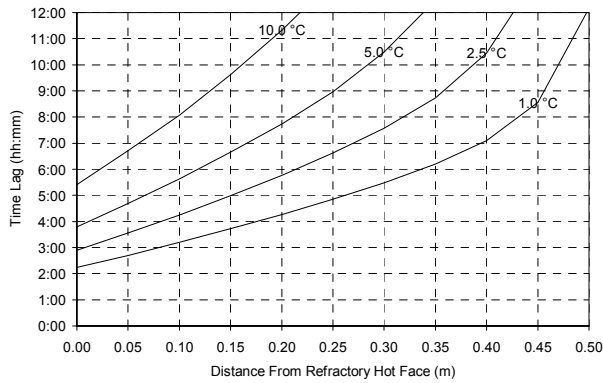
INITIAL STEADY STATE HEAT FLOW	INITIAL FREEZE LINING THICKNESS	INITIAL FREEZE LINING COMPOSITION	ELECTRICAL POWER HEAT FLOW	HEAT LOSSES HEAT FLOW	NET INPUT HEAT FLOW
250 kW	0.102 m	Rutile	200 kW	0 kW	200 kW



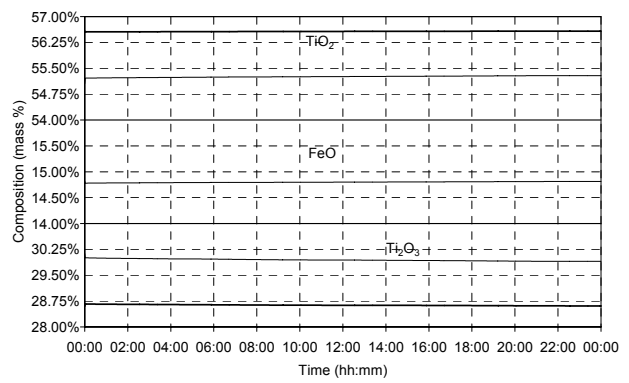
(a)



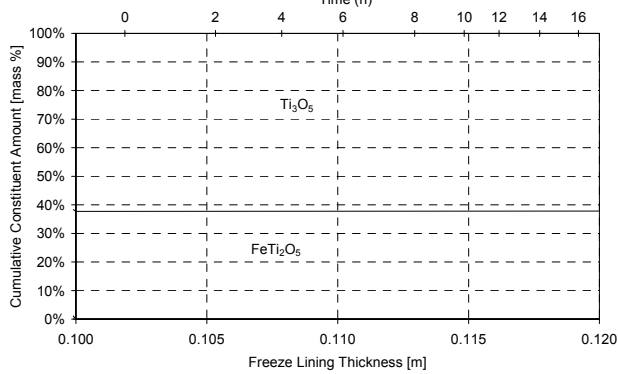
(b)



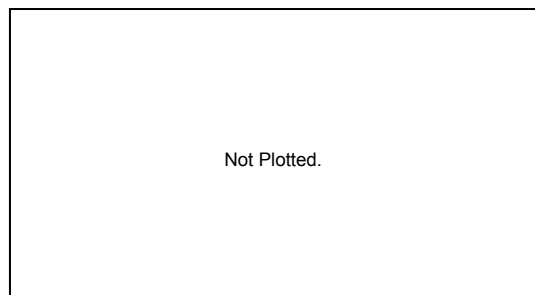
(c)



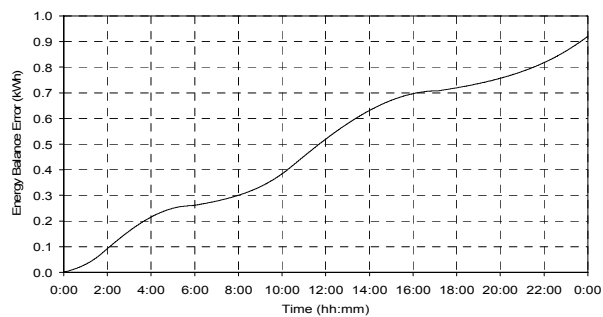
(d)



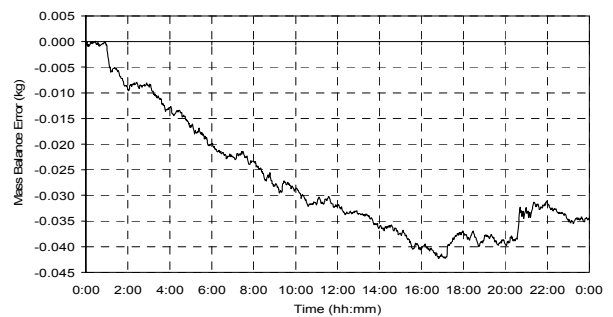
(e)



(f)



(g)

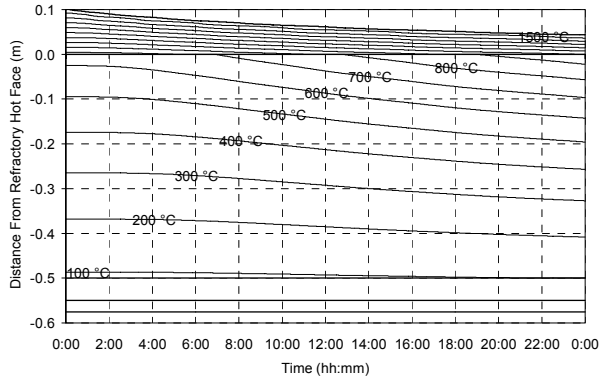


(h)

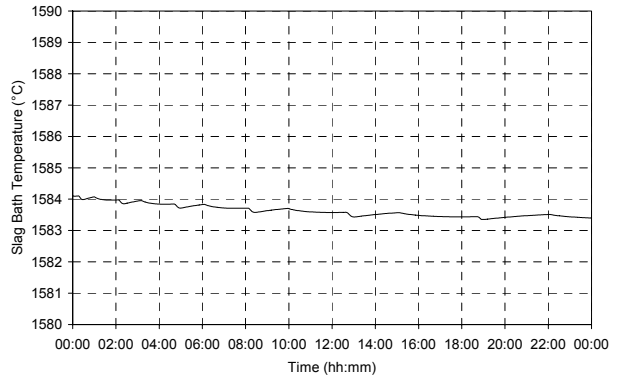
Figure 82 – Experiment 6.23 results.

6.3.24 Experiment 6.24

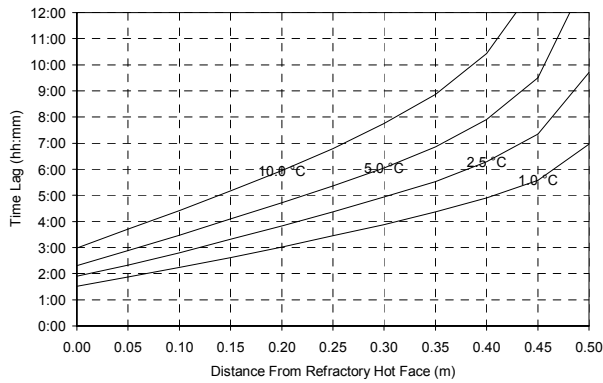
INITIAL STEADY STATE HEAT FLOW	INITIAL FREEZE LINING THICKNESS	INITIAL FREEZE LINING COMPOSITION	ELECTRICAL POWER HEAT FLOW	HEAT LOSSES HEAT FLOW	NET INPUT HEAT FLOW
250 kW	0.102 m	Rutile	400 kW	0 kW	400 kW



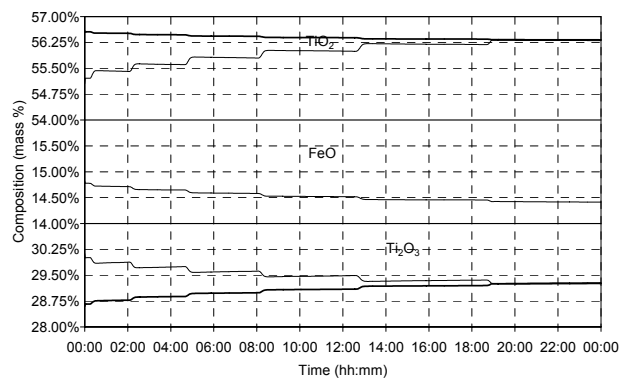
(a)



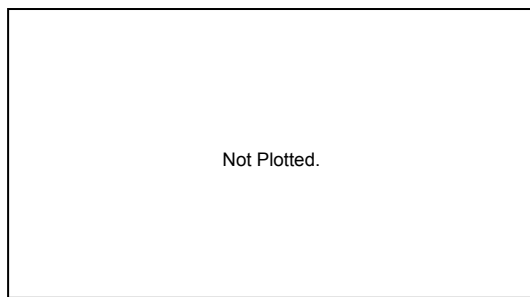
(b)



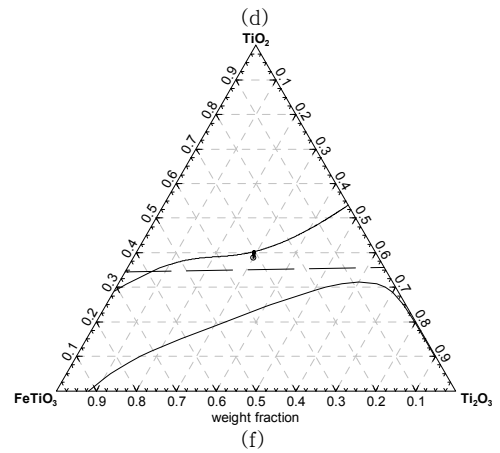
(c)



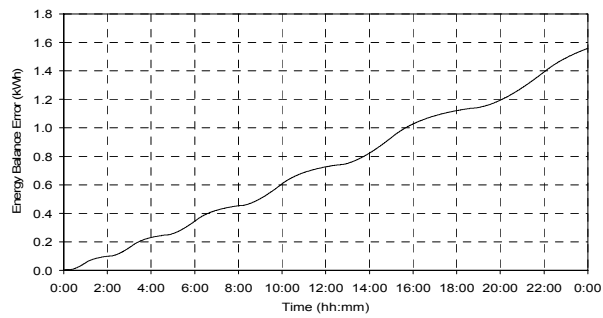
(d)



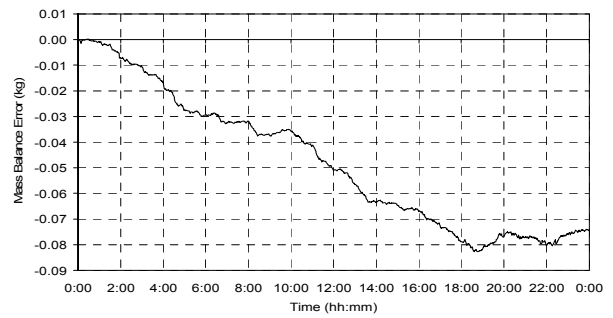
(e)



(f)



(g)

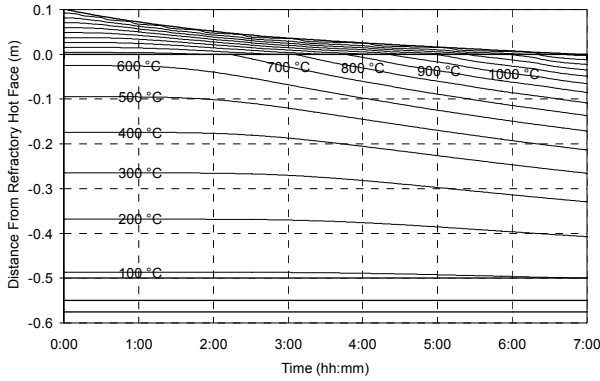


(h)

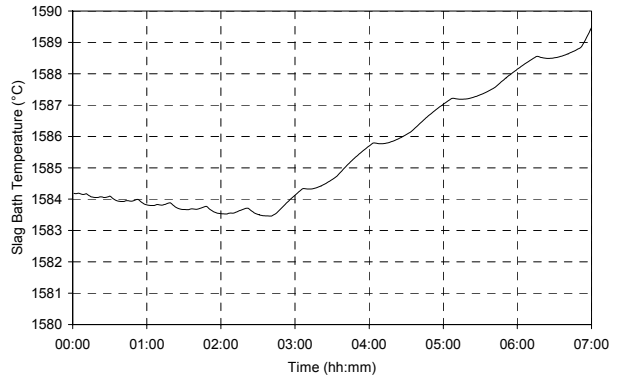
Figure 83 – Experiment 6.24 results.

6.3.25 Experiment 6.25

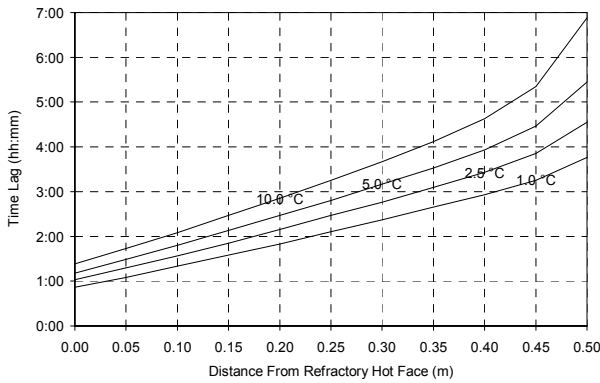
INITIAL STEADY STATE HEAT FLOW	INITIAL FREEZE LINING THICKNESS	INITIAL FREEZE LINING COMPOSITION	ELECTRICAL POWER HEAT FLOW	HEAT LOSSES HEAT FLOW	NET INPUT HEAT FLOW
250 kW	0.102 m	Rutile	1000 kW	0 kW	1000 kW



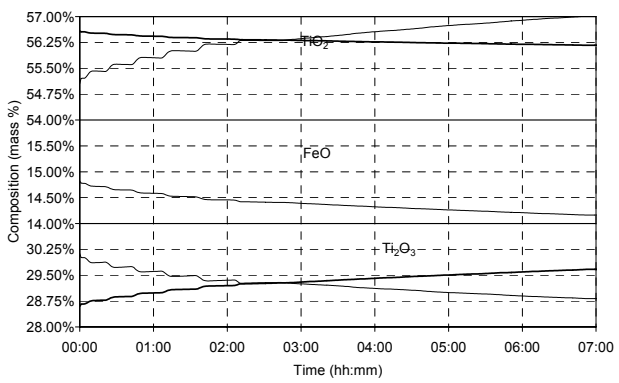
(a)



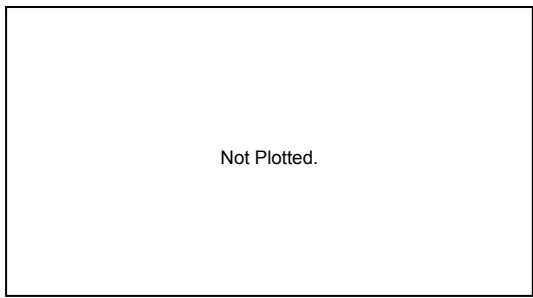
(b)



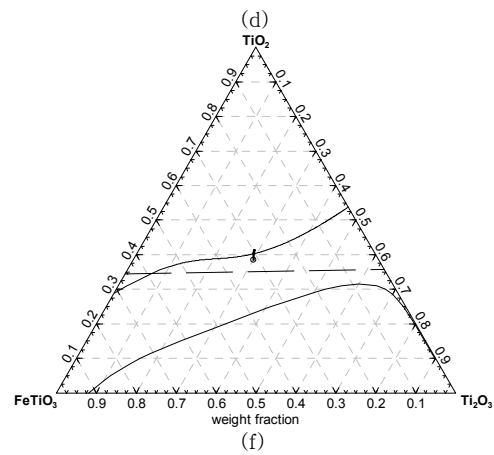
(c)



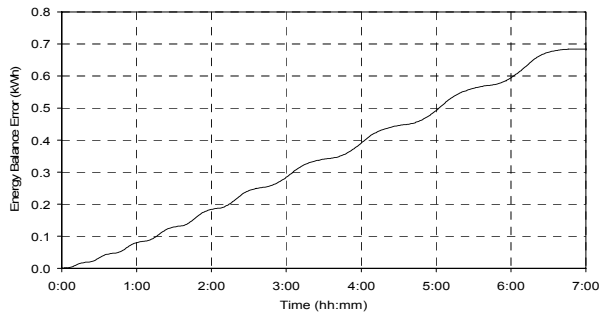
(d)



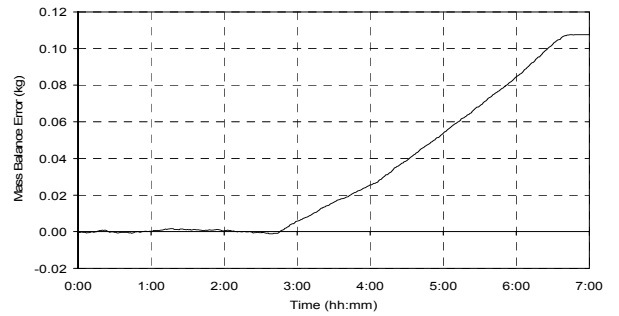
(e)



(f)



(g)

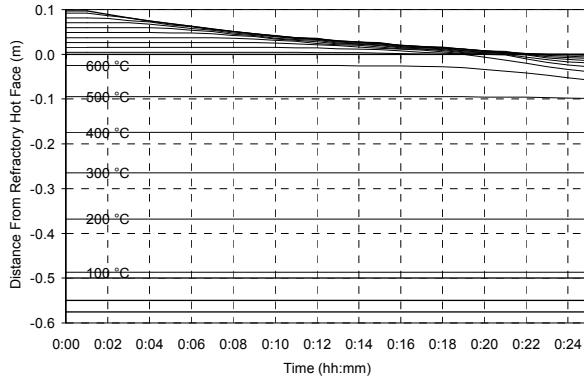


(h)

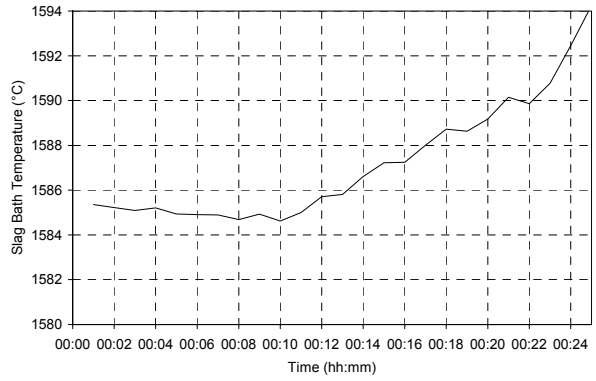
Figure 84 – Experiment 6.25 results.

6.3.26 Experiment 6.26

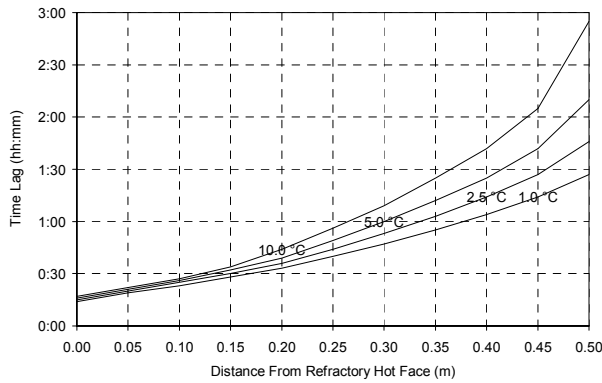
INITIAL STEADY STATE HEAT FLOW	INITIAL FREEZE LINING THICKNESS	INITIAL FREEZE LINING COMPOSITION	ELECTRICAL POWER HEAT FLOW	HEAT LOSSES HEAT FLOW	NET INPUT HEAT FLOW
250 kW	0.102 m	Rutile	10000 kW	0 kW	10000 kW



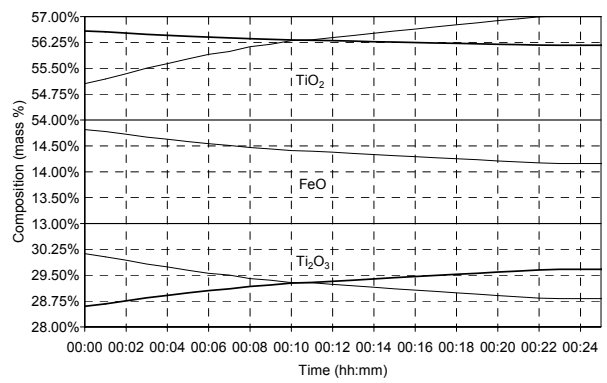
(a)



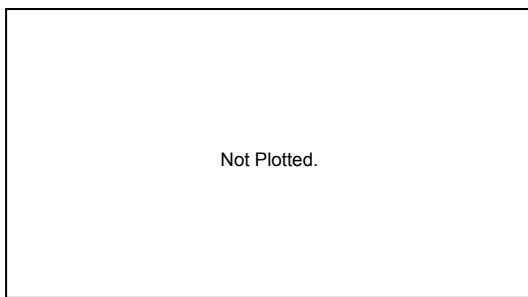
(b)



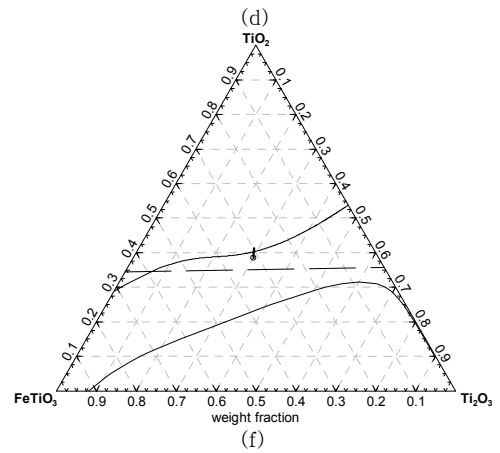
(c)



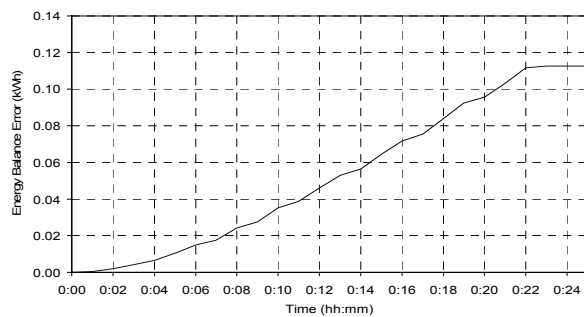
(d)



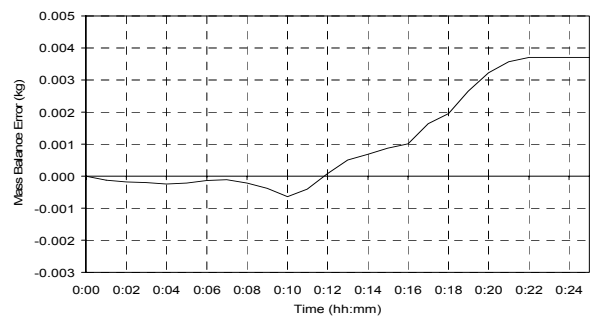
(e)



(f)



(g)



(h)

Figure 85 – Experiment 6.26 results.

## 6.4 DISCUSSION

### 6.4.1 Freeze Lining Thickness

From the experimental results the expected relationship between freeze lining thickness and net input heat flow rate is evident. A net input heat flow rate less than the initial steady state heat flow rate through the freeze lining and wall causes the freeze lining to become thicker. Conversely the freeze lining becomes thinner when the net input heat flow rate is greater than the initial steady state heat flow rate. This relationship is shown in Figure 86.

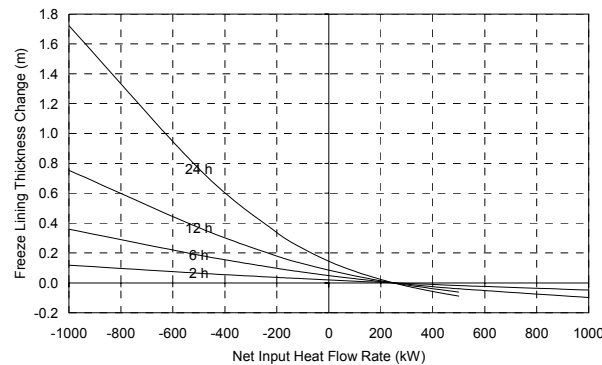


Figure 86 – Change in freeze lining thickness as a function of net input heat flow rate.

The chart was constructed with results from experiments 6.1 to 6.14. The initial freeze lining thickness for these experiments was 0.102 m.

When a net input heat flow rate of  $-1000$  kW was applied, the freeze lining reached a thickness of around 1.8 m after 24 hours. It is unlikely that this will happen in reality. The experiments were set up to only allow solidification at the freeze lining hot face. In the actual process solidification will also occur on the slag bath surface, forming a crust. Such crust formation will tend, in time, to thermally insulate the slag bath and reduce the heat losses from the slag bath. This will result in slower increase in freeze lining thickness.

The results of those experiments with high net input heat flow rates (6.11, 6.12, 6.13, 6.14, 6.19, 6.20, 6.25 and 6.26) clearly show the damage that too high energy input rates can do to the freeze lining. Given that smelting furnaces in practice are equipped with power supplies with capacities between 20 MW and 40 MW, it is possible to melt away an entire freeze lining in a matter of minutes.

### 6.4.2 Thermal Response of Freeze Lining and Furnace Wall

From graph (a) in the experimental results the first observation is that the largest fall in temperature between the freeze lining hot face and the outer surface of the steel shell occurs in the freeze lining. This clearly demonstrates that the freeze lining represents the largest thermal resistance in the heat transfer circuit. The temperature falls by about  $900$  °C in the freeze lining in many instances.

A consequence of the large thermal resistance of the freeze lining is a slow thermal response in the brick layer of the furnace wall. The time lags at various positions in the wall are shown in graph (c). All the graph (c) results of experiments 6.1 to 6.14 are summarised in Figure 87 below. The graphs in Figure 87 show an asymptotic approach to the initial steady state heat flow rate (250 kW) from net input heat flow rate values less than and greater than the initial steady state value. This makes sense, since a net input heat flow rate equal to the initial steady state value will take an infinite period of time to register any temperature change at any position in the brick layer of the wall.

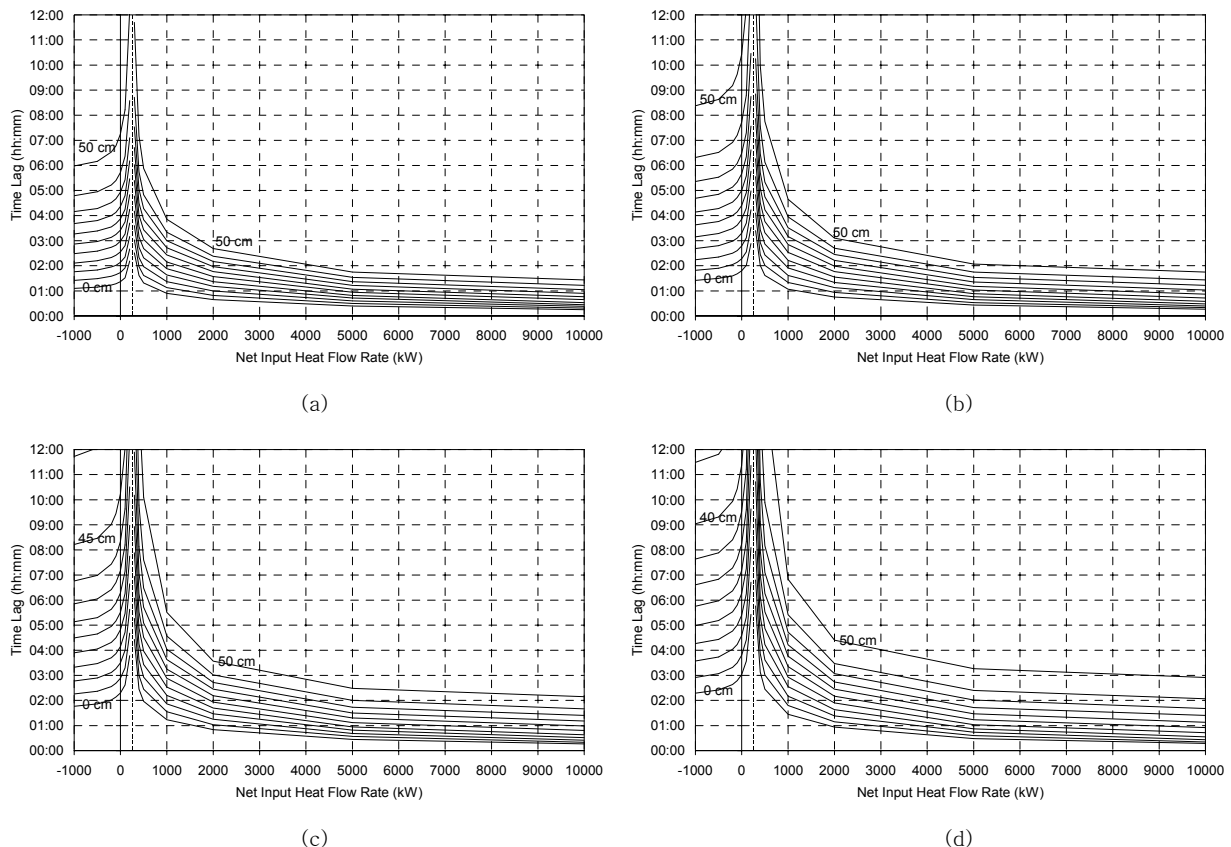


Figure 87 – Influence of net input heat flow rate on time lag in thermal response inside the brick wall.

The different curves on each graph represent different positions from the refractory hot face at 5 cm increments. The bottom curve represents a position on the refractory hot face. Chart (a) shows the time lag in detecting a 1.0 °C temperature change, (b) a 2.5 °C change, (c) a 5.0 °C change and (d) a 10.0 °C change. Data was taken from the results of experiments 6.1 to 6.14.

Also of interest is the lack of symmetry around the initial steady state heat flow rate value. In cases where the freeze lining thickness increased, temperatures in the brick layer were slower to respond compared with cases where the freeze lining thickness decreased. One can also conclude that temperatures in the brick layer take longer to fall than to rise. This is important to know when one is considering control of a freeze lining. The asymmetry in thermal response can be explained by considering the influence of solidification and melting on heat transfer in the freeze lining layer.

Figure 88 shows the temperature profile in the freeze lining layer 1 hour after changing the net input heat flow rate from the initial steady state value of 250 kW. For the -1000 kW case the difference in net input heat flow rate compared with the initial value is -1250 kW. For the 1000 and 2000 kW cases it is 750 kW and 1750 kW respectively. From this chart it is again clear that the melting cases have resulted in quicker thermal response inside the freeze lining than did the solidifying case. This, in turn, results in quicker thermal response in the brick layer of the furnace wall.

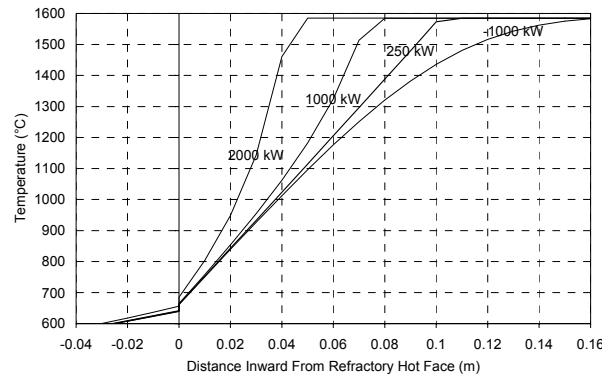


Figure 88 – Temperature profile in the freeze lining after 1 hour.

Cases shown include both solidification and melting.

Melting causes a reduction in freeze lining thickness and a reduction in the heat transfer resistance associated with the freeze lining. Heat therefore flows through the freeze lining and into the brick layer at a higher rate. This higher heat flow rate raises temperatures in the freeze lining and brick layer and yields a thermal response.

Solidification increases freeze lining thickness and the associated heat transfer resistance. In this case the rate at which heat is transferred into the freeze lining is reduced. For the brick layer to respond, the new lower heat flow rate must be propagated through the freeze lining and through the brick layer.

An increase in temperature is therefore dependent on conduction from the freeze lining hot face to the point in the brick layer where the temperature is monitored. This is because heat only needs to flow from the freeze lining hot face to the point of measurement to change the temperature at this point. In contrast, a decrease in temperature is dependent on conduction from the freeze lining hot face to the outside surface of the steel shell. The reason is that a reduction in temperature at the point of measurement needs heat to be removed from the outside surface of the steel shell. The heat transfer path is therefore generally shorter when detecting melting than when detecting solidification. This causes the asymmetric behaviour described above.

### 6.4.3 Slag Bath Composition

The 'wavy' profile of many of the graphs is the result of transitions from one finite difference node to the next.

The slag bath's composition was influenced in three ways during the experiments:



1. When the freeze lining grew thicker the slag bath  $\text{TiO}_2$  and  $\text{FeO}$  content increased, and  $\text{Ti}_2\text{O}_3$  content decreased.

This observation can be made from the (d) graph of experiments 6.1 to 6.7, 6.15 to 6.17 and 6.21 to 6.23. It is also evident from the (f) graph of these experiments where such a graph was included, although it is slightly more difficult to detect due to the choice of axes ( $\text{TiO}_2$ - $\text{FeTiO}_3$ - $\text{Ti}_2\text{O}_3$  rather than  $\text{TiO}_2$ - $\text{FeO}$ - $\text{Ti}_2\text{O}_3$ ).

This effect is simply the result of the phase chemistry of the slag. The composition of the slag that initially solidifies from the liquid is approximately 38%-62% ( $\text{FeTi}_2\text{O}_5$ - $\text{Ti}_3\text{O}_5$  by mass). This translates to a composition of approximately 12%-48%-40% ( $\text{FeO}$ - $\text{TiO}_2$ - $\text{Ti}_2\text{O}_3$  by mass). Since the initial liquid slag composition is 15%-55%-30% ( $\text{FeO}$ - $\text{TiO}_2$ - $\text{Ti}_2\text{O}_3$  by mass), the observed change in liquid slag composition is easily understood.

2. In the case of experiments 6.1 to 6.20, when the freeze lining was melted away the slag bath  $\text{TiO}_2$  and  $\text{FeO}$  content decreased, and  $\text{Ti}_2\text{O}_3$  content increased.

This can be seen on the (d) graph of experiments 6.8 to 6.14 and 6.18 to 6.20.

For these experiments the initial composition of the freeze lining was approximately 38%-62% ( $\text{FeTi}_2\text{O}_5$ - $\text{Ti}_3\text{O}_5$  by mass), or 12%-48%-40% ( $\text{FeO}$ - $\text{TiO}_2$ - $\text{Ti}_2\text{O}_3$  by mass). Adding such material to liquid slag with composition 15%-55%-30% ( $\text{FeO}$ - $\text{TiO}_2$ - $\text{Ti}_2\text{O}_3$  by mass) once again must yield the observed influence on liquid slag composition.

3. In the case of experiments 6.21 to 6.26, when the freeze lining was melted away the slag bath  $\text{TiO}_2$  content increased, and the  $\text{FeO}$  and  $\text{Ti}_2\text{O}_3$  content decreased.

This is evident on the (d) and (f) graphs of experiments 6.24 to 6.26.

Here the effect can again be explained based on a simple mass balance. Because the freeze lining used in these experiments initially consisted of pure  $\text{TiO}_2$ , melting this material into the bath can only result in an increase of liquid slag  $\text{TiO}_2$  content.

Another observation of note is the convergence of liquid slag composition into the eutectic groove. This is entirely expected given the phase chemistry information presented in CHAPTER 2. The convergence into the eutectic groove is only observed for experiments in which a large degree of solidification took place. Such experiments include 6.1, 6.2, 6.15 and 6.21. From these experiments it is concluded that at least 0.7 m of additional freeze lining must solidify before the liquid slag composition reaches the eutectic groove.

The results of experiment 6.24 also show the liquid slag composition converging into the eutectic groove. This can however not be attributed to the same mechanism prevalent in experiments 6.1, 6.2, 6.15 and 6.21. In fact, the apparent convergence in the experiment 6.24 results occurred as a coincidence due to the choice of parameters used in the experiment. The results of experiments 6.25 and 6.26 shed some light on this matter. In both cases the liquid slag composition approaches the eutectic groove, but then crosses it. This is expected, since pure  $\text{TiO}_2$  is being added from the freeze lining. Had experiment 6.24 therefore

been run for longer than 24 hours, its liquid slag composition would also have crossed over the eutectic groove.

#### 6.4.4 Slag Bath Temperature

The 'wavy' profile of many of the temperature graphs is the result of transitions from one finite difference node to the next.

The observed changes in liquid slag composition discussed in the previous paragraph had a direct influence on liquid slag temperature. This is due to the model combining the slag bath with a portion of the freeze lining and bringing this combined mass of material to equilibrium. The end result of this procedure must be that the slag bath should follow closely the liquidus temperature of the slag. This is precisely what was observed. The same behaviour is expected in the actual process because of the inevitable interaction between slag bath and freeze lining.

For those experiments where the freeze lining became thicker, the liquid slag temperature dropped. This is consistent with the observed tendency of the liquid slag composition towards the eutectic groove. For those experiments where the freeze lining became thinner, the liquid slag temperature increased. This is because the material that is being absorbed from the freeze lining alters the slag bath composition in such a way that the slag's liquidus temperature becomes higher. If the initial freeze lining had consisted of pure ilmenite (This is of course a hypothetical possibility, given the low melting point of ilmenite.), the effect would have been reversed because adding pure ilmenite to the slag bath would lower its liquidus temperature. This is evident from the Figure 11 liquidus diagram.

There were some exceptions to the observed increase in liquid slag temperature with a decrease in freeze lining thickness. The results of experiments 6.24, 6.25 and 6.26 show the liquid slag temperature decreasing (at least initially) as the freeze lining becomes thinner. These experiments, specifically 6.25 and 6.26, are excellent examples of the liquid slag temperature following the slag's liquidus temperature.

Both these experiments show the liquid slag temperature decreasing until the slag composition reaches the eutectic groove. When the slag composition moves away from the eutectic groove, the liquid slag temperature starts to increase. This is expected, since the eutectic groove is after all a series of compositions where the slag liquidus temperature is lower than for compositions on either side of it.

#### 6.4.5 Freeze Lining Composition

The variation of freeze lining composition with time is shown in graph (e) for those experiments where the freeze lining became thicker (6.1 to 6.7, 6.15 to 6.17 and 6.21 to 6.23). Because a relatively small amount of slag solidified during most of these experiments, the composition of slag that solidified at the freeze lining hot face remained mostly constant.

Significant changes in solid slag composition were only observed for experiments 6.1, 6.2, 6.15 and 6.21. During these experiments the liquid slag composition reached the eutectic groove, which resulted in slag solidification producing rutile in addition to the pseudobrookite phase that was always present. A change in the composition of the pseudobrookite phase is also evident before the point where rutile becomes stable.

The pseudobrookite phase tended to become richer in the  $\text{FeTi}_2\text{O}_5$  end member as solidification progressed. This is expected, since the liquid slag phase became richer in  $\text{FeO}$  and  $\text{TiO}_2$  with time.

## CHAPTER 7 THE DYNAMIC RESPONSE OF A FREEZE-LINING TO CHANGES IN SLAG BATH COMPOSITION

This chapter, similar to CHAPTER 6, describes a series of experiments conducted with the FLC model. The purpose of these experiments was to study the influence of changes in slag bath composition on the dynamic behaviour of the furnace wall and freeze lining. The same aspects as in CHAPTER 6 were considered:

- Freeze lining thickness.
- Temperature distribution through the furnace wall and freeze lining.
- Time lag in temperature response of the refractory brick wall relative to the time when conditions were changed in the slag bath.
- Liquid slag temperature.
- Composition distribution through the freeze lining.
- Liquid slag composition.

### 7.1 EXPERIMENTAL SETUP

The flow sheet of the model used for all experiments in this chapter is shown in Figure 89. For the largest part the flow sheet has been documented in paragraph 3.7.1 (page 48). Only the added modules and flow streams are described below.

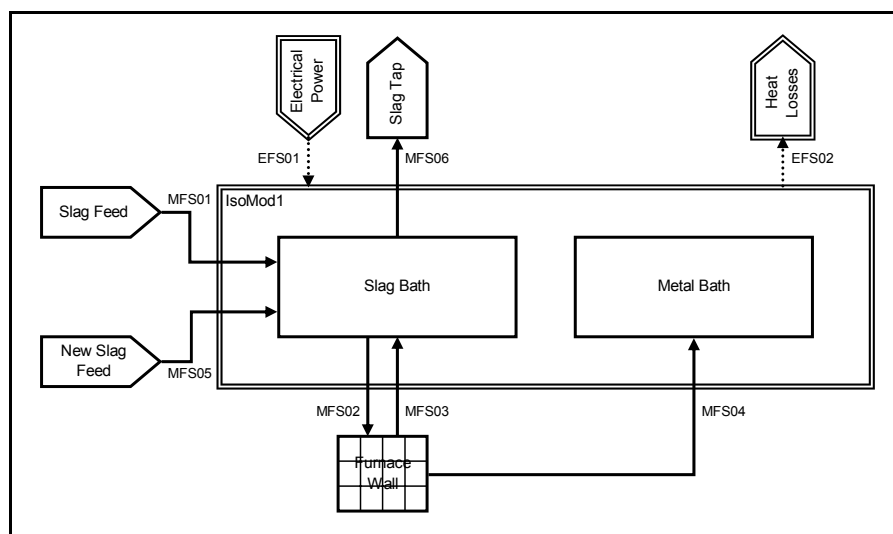


Figure 89 – Flow sheet of the model used for CHAPTER 7 experiments.

- NewSlagFeed  
The NewSlagFeed material input module delivers liquid slag that is poured into the SlagBath mixer for the duration of each experiment. The material produced by the NewSlagFeed material input module is discharged into the MFS05 material flow stream.

- MFS05  
The MFS05 material flow stream connects the NewSlagFeed material input module with the SlagBath mixer. It assists in delivering slag to the SlagBath mixer during experiments.
- SlagTap  
The SlagTap material output module extracts liquid slag from the SlagBath mixer for the duration of each experiment. It receives liquid slag via the MFS06 material flow stream.
- MFS06  
The MFS06 material flow stream connects the SlagBath mixer with the SlagTap material output module. It assists in delivering slag to the SlagTap material output module.

The following conditions were common to all experiments:

- An initial liquid slag composition equal of 15%-55%-30% (FeO-TiO<sub>2</sub>-Ti<sub>2</sub>O<sub>3</sub>).
- A liquid slag effective thermal conductivity of 0.005 kW/(m.°C).
- An initial steady state heat flow rate of 250 kW.
- An electrical power input of 250 kW through the ElectricalPower energy input module.
- A heat loss rate of 0 kW through the HeatLosses energy output module.
- An initial freeze lining thickness of 0.102 m.
- An initial freeze lining consisting of only pseudobrookite with a composition of 37.6% FeTi<sub>2</sub>O<sub>5</sub> and 62.4% Ti<sub>3</sub>O<sub>5</sub> (mass basis).

Further, all experiments were run for a period of 24 hours, or until the entire freeze lining had disappeared. During this period slag was introduced into the system at a constant rate through the NewSlagFeed material input module. Slag was removed from the system at the same rate via the SlagTap material output module. This meant that the total mass of slag in the system remained constant throughout the experiments (although the amounts of individual species could vary).

The conditions described above are of course not in complete agreement with conditions in an actual furnace. Slag is produced continuously due to the continuous addition of ilmenite, reductant and energy to the system. Tapping of metal and slag is done in batches. Batch extraction of material could not be modelled with the FLC model presented earlier. The main cause was the decision to represent the freeze lining and wall using only a one-dimensional model. This meant that only phenomena varying along the radial dimension could be studied with the model. Since changes in slag and metal levels in the furnace result in variations in the axial dimension, influences of such variations were automatically eliminated from the set of conditions that the model could be applied to. This was a conscious decision aimed at restricting the scope of work in such a way that it could realistically be completed.

An aspect that must be highlighted is the temperature at which slag was introduced into the system through the NewSlagFeed material input module. This temperature was allowed to vary with the temperature of the slag bath. The new slag therefore entered the system at exactly the same temperature as the slag bath at any point in time. This was done in an attempt to isolate the chemical influence that the new slag would have in the system from possible thermal influences since thermal influences had already been addressed

in CHAPTER 6. By doing this, it is implied that supercooled slag was discharged into the system in some cases.

## 7.2 EXPERIMENTS

The parameters that were varied over the series of experiments include the following:

- Composition of the liquid slag introduced with the NewSlagFeed material input module.
- Residence time of slag in the system. (Given the constant total mass, the residence time is inversely proportional to feed rate.)

The initial steady state heat flow rate fixed the initial temperature distribution in the freeze lining and the initial freeze lining thickness. The set of experiments with the various parameters of interest to each experiment are listed in Table 22 below. The set of experiments consists of 3 subsets.

EXPERIMENT NO.		NEW SLAG COMPOSITION			NEW SLAG FEED RATE	SLAG RESIDENCE TIME
		FeO	TiO <sub>2</sub>	Ti <sub>2</sub> O <sub>3</sub>		
7.1	A	15.0	50.0	35.0	57.5 t/h	4 h
7.2	B	15.0	60.0	25.0	57.5 t/h	4 h
7.3	C	10.0	55.0	35.0	57.5 t/h	4 h
7.4	D	20.0	55.0	25.0	57.5 t/h	4 h
7.5	E	10.0	60.0	30.0	57.5 t/h	4 h
7.6	F	20.0	50.0	30.0	57.5 t/h	4 h
7.7	G	10.0	50.0	40.0	57.5 t/h	4 h
7.8	H	20.0	60.0	20.0	57.5 t/h	4 h
7.9	I	35.5	59.5	5.0	57.5 t/h	4 h
7.10	J	pure stoichiometric ilmenite			57.5 t/h	4 h
7.11	A	15.0	50.0	35.0	23.0 t/h	10 h
7.12	B	15.0	60.0	25.0	23.0 t/h	10 h
7.13	C	10.0	55.0	35.0	23.0 t/h	10 h
7.14	D	20.0	55.0	25.0	23.0 t/h	10 h
7.15	E	10.0	60.0	30.0	23.0 t/h	10 h
7.16	F	20.0	50.0	30.0	23.0 t/h	10 h
7.17	G	10.0	50.0	40.0	23.0 t/h	10 h
7.18	H	20.0	60.0	20.0	23.0 t/h	10 h
7.19	I	35.5	59.5	5.0	23.0 t/h	10 h
7.20	J	pure stoichiometric ilmenite			23.0 t/h	10 h
7.21	A	15.0	50.0	35.0	14.38 t/h	16 h
7.22	B	15.0	60.0	25.0	14.38 t/h	16 h
7.23	C	10.0	55.0	35.0	14.38 t/h	16 h
7.24	D	20.0	55.0	25.0	14.38 t/h	16 h
7.25	E	10.0	60.0	30.0	14.38 t/h	16 h
7.26	F	20.0	50.0	30.0	14.38 t/h	16 h
7.27	G	10.0	50.0	40.0	14.38 t/h	16 h
7.28	H	20.0	60.0	20.0	14.38 t/h	16 h
7.29	I	35.5	59.5	5.0	14.38 t/h	16 h
7.30	J	pure stoichiometric ilmenite			14.38 t/h	16 h

Table 22 – List of experiments conducted for CHAPTER 7.

The same set of 10 new slag compositions was used in each of the three subsets. The distribution of these compositions within the TiO<sub>2</sub>-FeTiO<sub>3</sub>-Ti<sub>2</sub>O<sub>3</sub> ternary system around the initial slag composition is shown in Figure 90. The first eight compositions (A to H) were chosen in such a way that they surrounded the initial slag composition. This would result in the slag bath composition being shifted into these eight surrounding

directions over time. The remaining two compositions were chosen to represent a much less reduced slag (I) and unreduced molten ilmenite (J).

The only parameter that was varied between the three sets is slag residence time. The first set of experiments was done with a residence time of 4 hours. This short residence time and associated extremely high slag feed rate was used to provide an exaggerated view of the influence that changing slag chemistry could have within the system. The second set used a residence time of 10 hours. The associated feed rate is again high, but probably achievable in a unit with the same dimensions as those used in the model. A slag residence time of 16 hours was used in the final set of experiments. This is the most realistic of the three feed rates used.

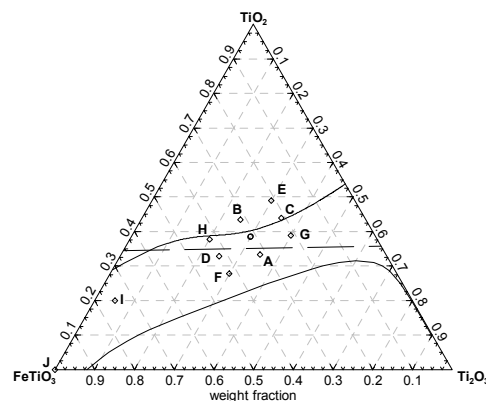


Figure 90 – New slag compositions used in CHAPTER 7 experiments.

The circle indicates the initial slag composition. Diamonds indicate new slag compositions. The dashed line is the  $Ti_3O_5$  and  $FeTi_2O_5$  (or  $M_3O_5$ ) join. The top solid line is the eutectic groove, and the bottom solid line is the slag/slag+  $Fe^\circ$  phase boundary.

### 7.3 EXPERIMENTAL RESULTS

The results from each experiment are presented below using much the same series of graphs (marked from (a) to (h)) that was used in CHAPTER 6. Only the differences in presentation between CHAPTER 6 and the current chapter are highlighted below. The reader is referred to paragraph 6.3 (page 139) for details about the various graphs. A discussion of the experimental results follows after the graphical presentation of the results of all experiments conducted as part of this chapter.

The top time axis used in graph (e) in CHAPTER 6 was omitted here because the freeze lining showed both an increase and a decrease in thickness in most of the experiments. It was therefore not possible to use such an axis to give an indication of time on these graphs. To be able to use the same axes in all cases, graph (e) was drawn for freeze lining thickness values from zero, even in cases where the freeze lining thickness did not reach zero during the simulation.

In cases such as experiments 7.2 and 7.3 the liquid slag composition crossed the eutectic groove towards the  $TiO_2$  corner of the ternary diagram. This caused rutile to become the primary solidification phase. When

this happens, graph (e) shows the freeze lining at the solid-liquid interface as consisting of mostly  $\text{TiO}_2$  with a small amount of  $\text{Ti}_2\text{O}_3$  dissolved in the rutile matrix.

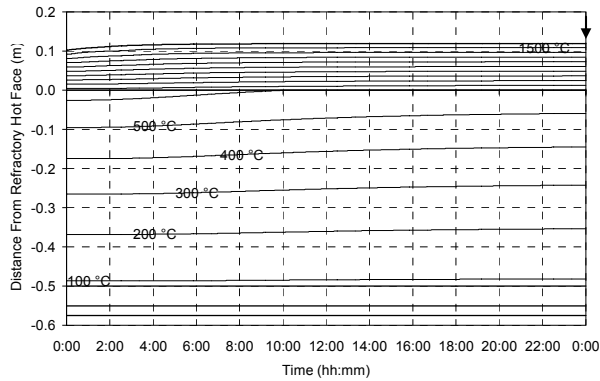
Graph (e) is not provided for experiments 7.20 and 7.30 because virtually the entire freeze lining had melted away by the end of these experiments.

Two fixed compositions are highlighted on graph (f). The initial liquid slag composition is shown as a circle, and the composition of the new liquid slag with a diamond. This was done to give the reader perspective about the change in liquid slag composition relative to these two points.

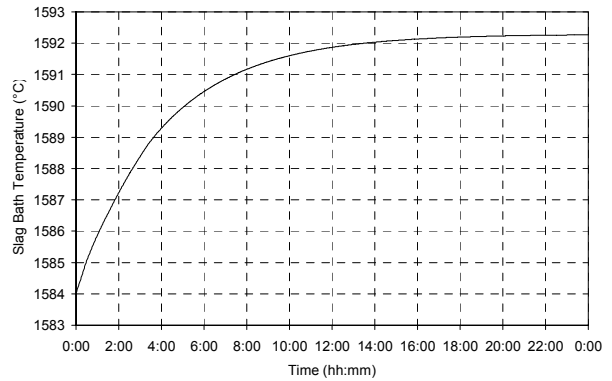


7.3.1 Experiment 7.1

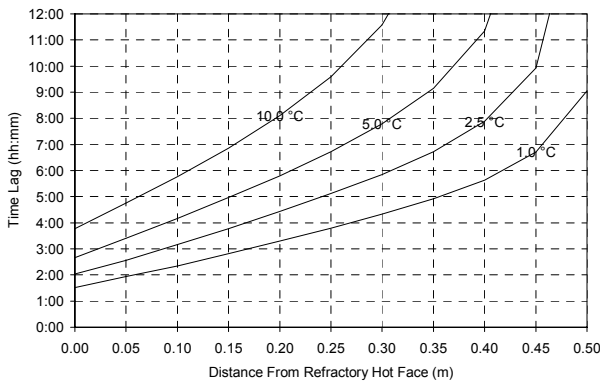
FEED COMPOSITION	%FeO	%TiO <sub>2</sub>	%Ti <sub>2</sub> O <sub>3</sub>	NEW SLAG FEED RATE	SLAG RESIDENCE TIME
A	15.0	50.0	35.0	57.5 t/h	4 h



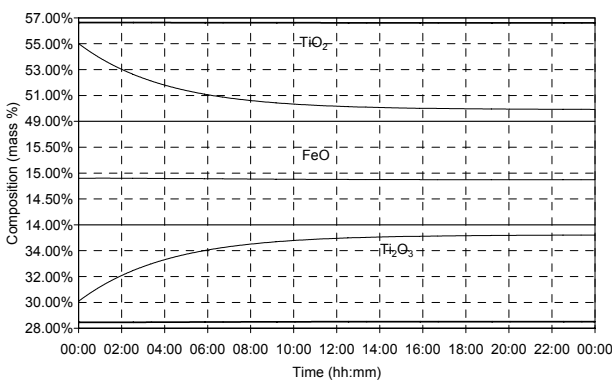
(a)



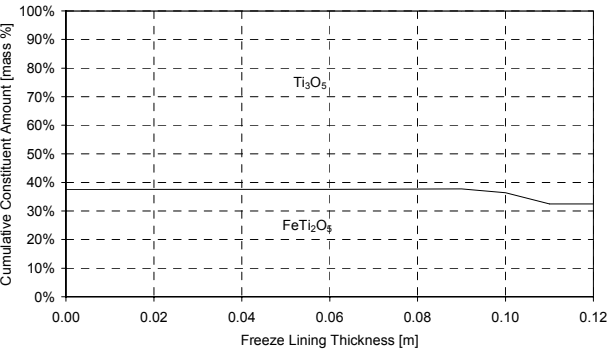
(b)



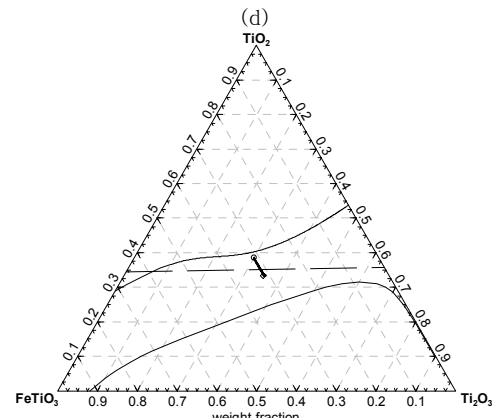
(c)



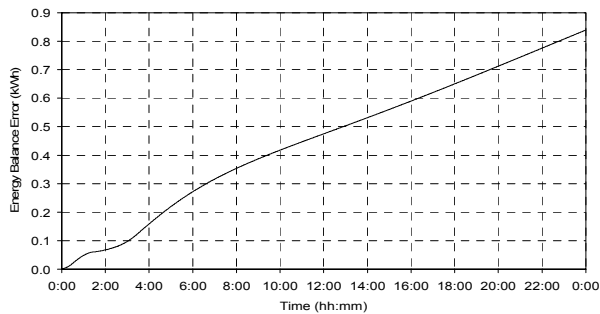
(d)



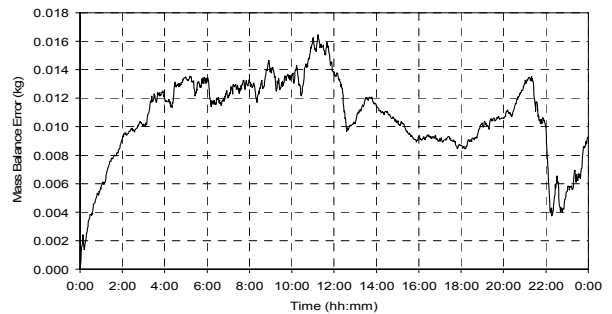
(e)



(f)



(g)

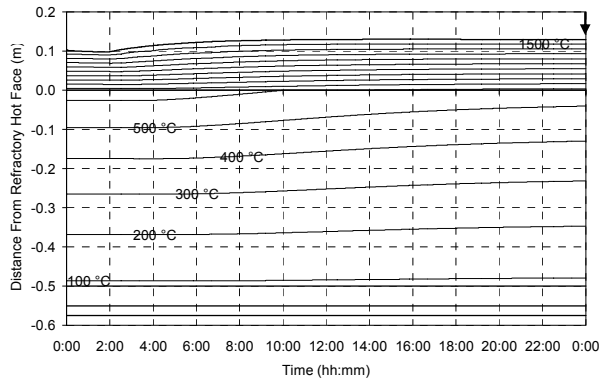


(h)

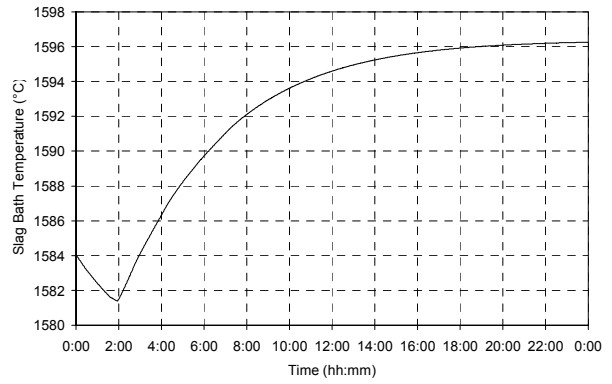
Figure 91 – Experiment 7.1 results.

7.3.2 Experiment 7.2

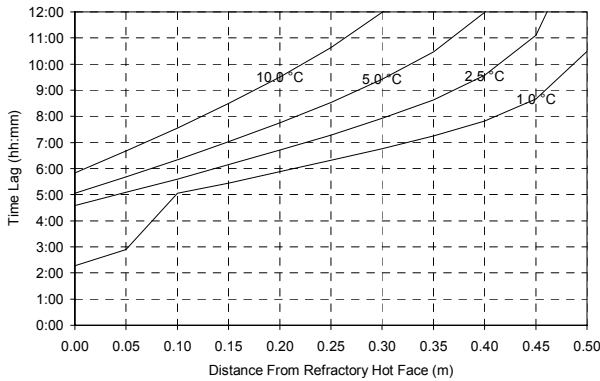
FEED COMPOSITION	%FeO	%TiO <sub>2</sub>	%Ti <sub>2</sub> O <sub>3</sub>	NEW SLAG FEED RATE	SLAG RESIDENCE TIME
B	15.0	60.0	25.0	57.5 t/h	4 h



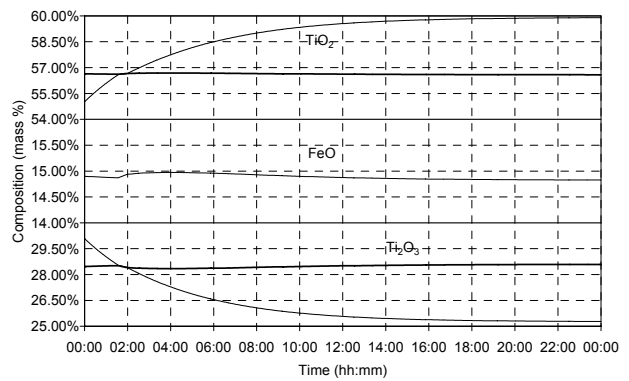
(a)



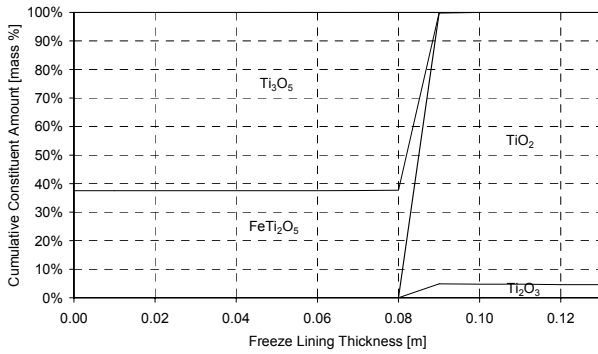
(b)



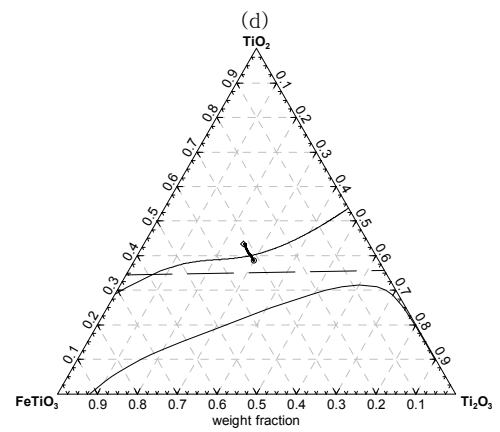
(c)



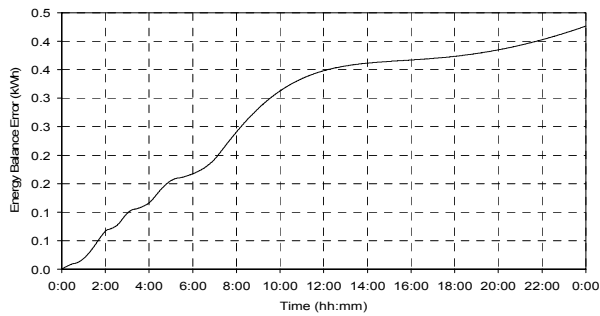
(d)



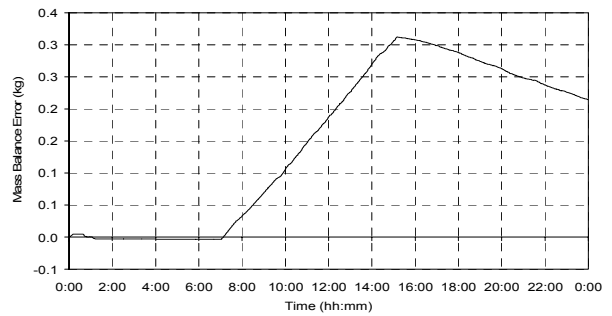
(e)



(f)



(g)



(h)

Figure 92 – Experiment 7.2 results.

7.3.3 Experiment 7.3

FEED COMPOSITION	%FeO	%TiO <sub>2</sub>	%Ti <sub>2</sub> O <sub>3</sub>	NEW SLAG FEED RATE	SLAG RESIDENCE TIME
C	10.0	55.0	35.0	57.5 t/h	4 h

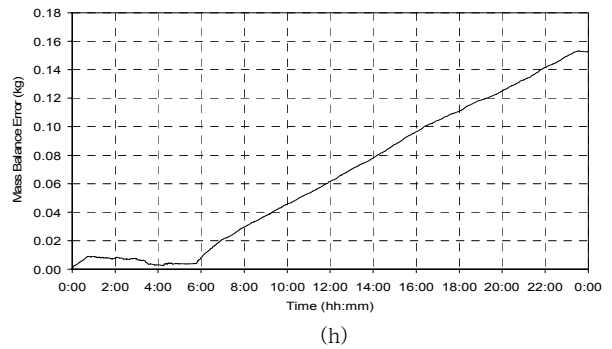
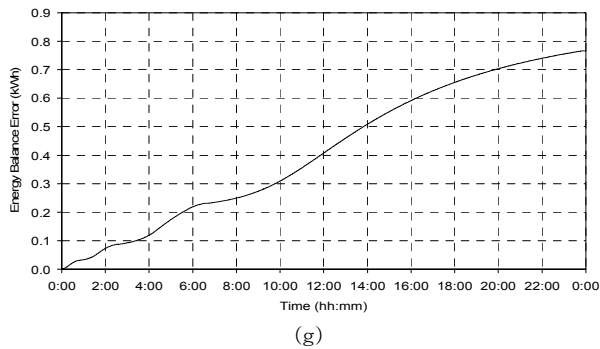
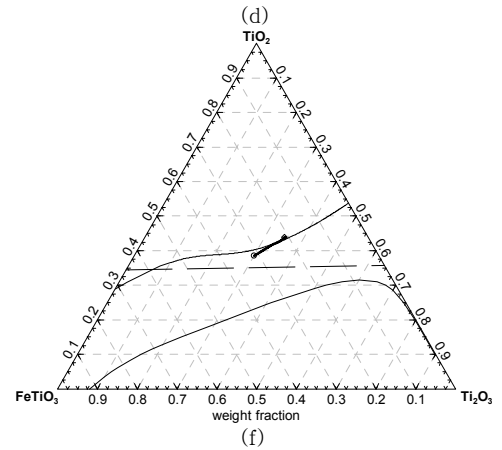
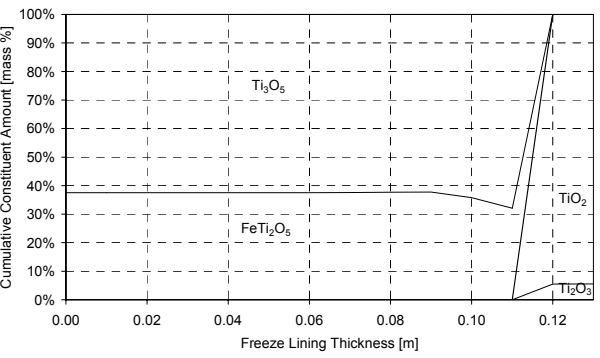
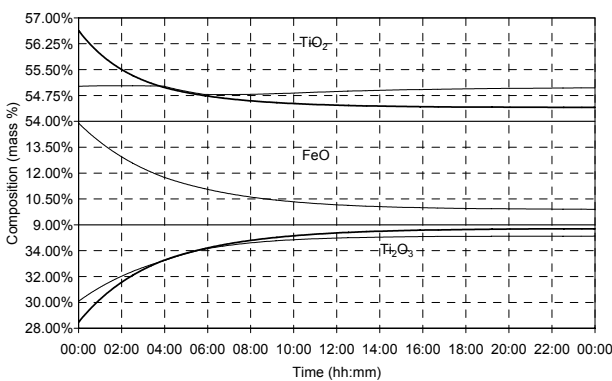
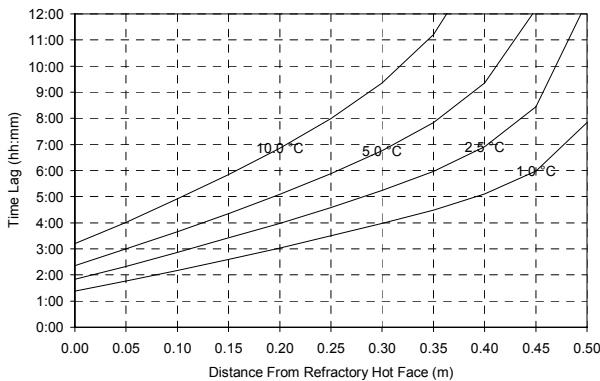
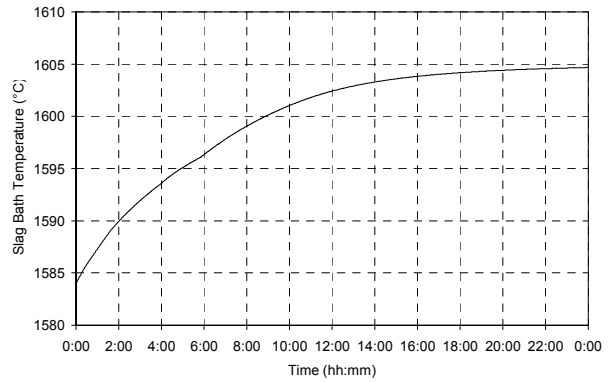
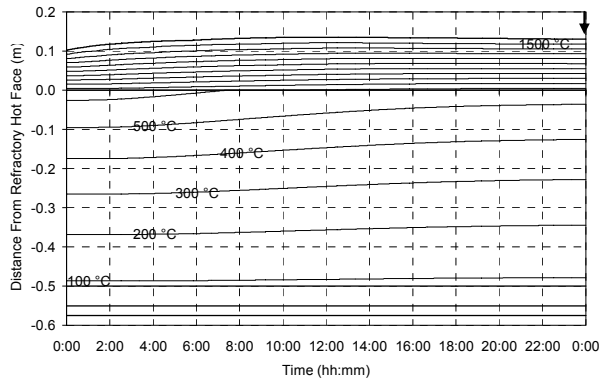


Figure 93 – Experiment 7.3 results.

7.3.4 Experiment 7.4

FEED COMPOSITION	%FeO	%TiO <sub>2</sub>	%Ti <sub>2</sub> O <sub>3</sub>	NEW SLAG FEED RATE	SLAG RESIDENCE TIME
D	20.0	55.0	25.0	57.5 t/h	4 h

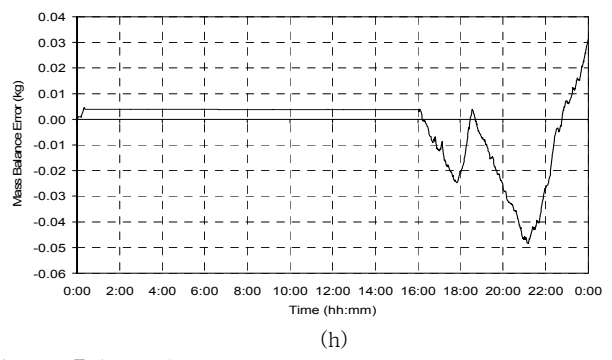
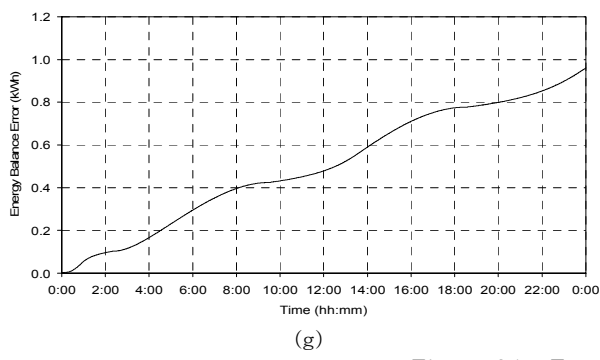
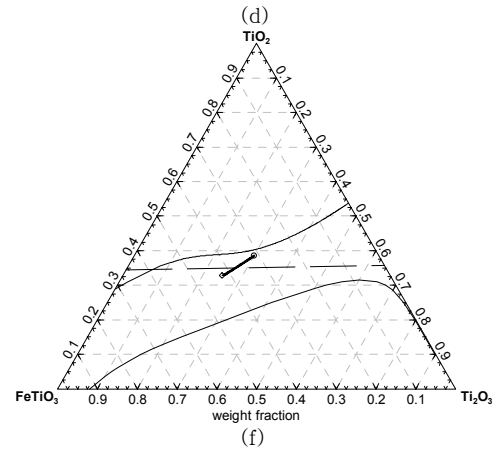
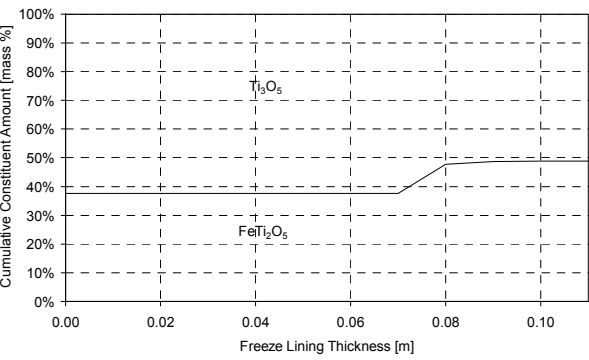
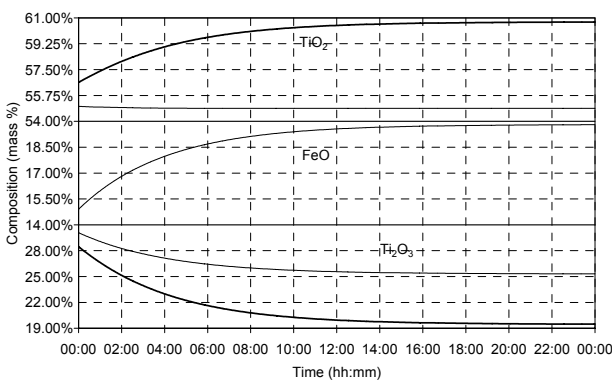
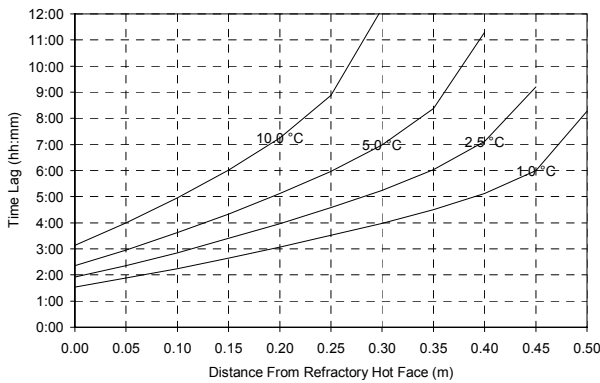
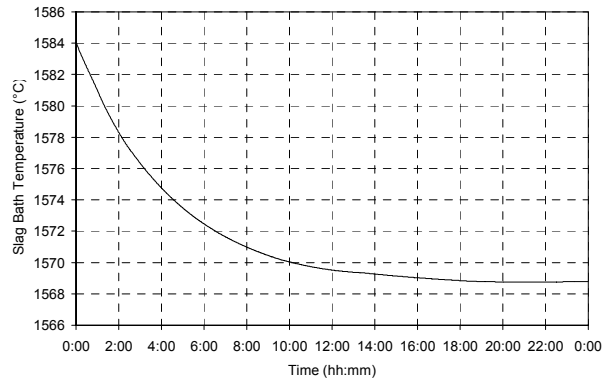
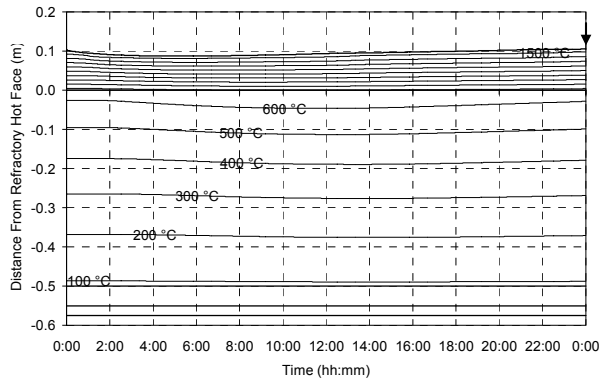


Figure 94 – Experiment 7.4 results.

7.3.5 Experiment 7.5

FEED COMPOSITION	%FeO	%TiO <sub>2</sub>	%Ti <sub>2</sub> O <sub>3</sub>	NEW SLAG FEED RATE	SLAG RESIDENCE TIME
E	10.0	60.0	30.0	57.5 t/h	4 h

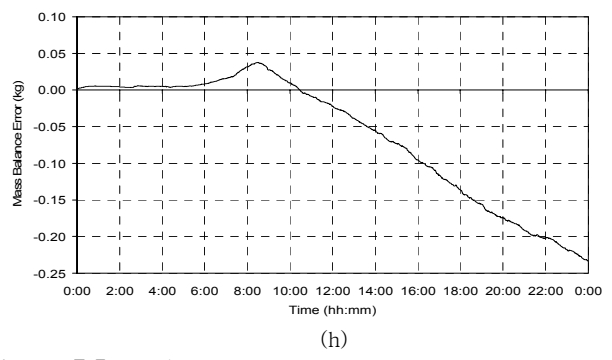
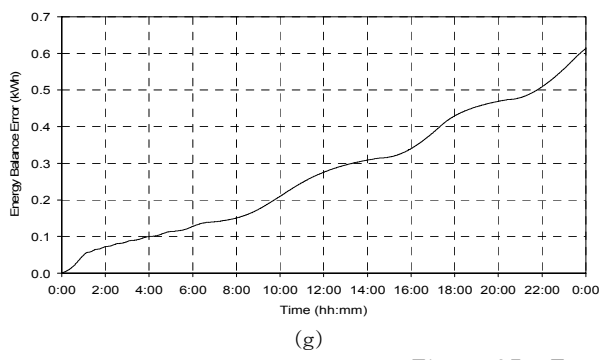
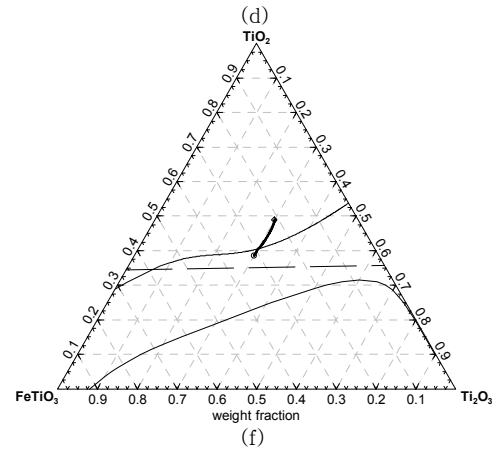
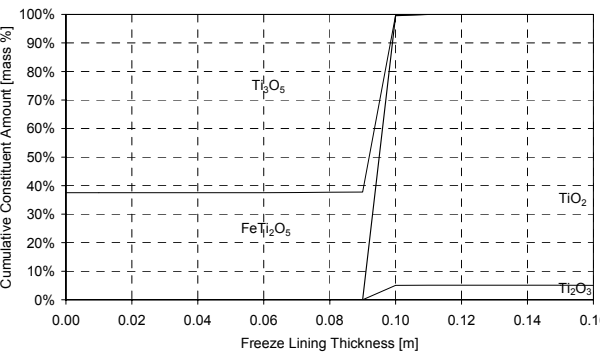
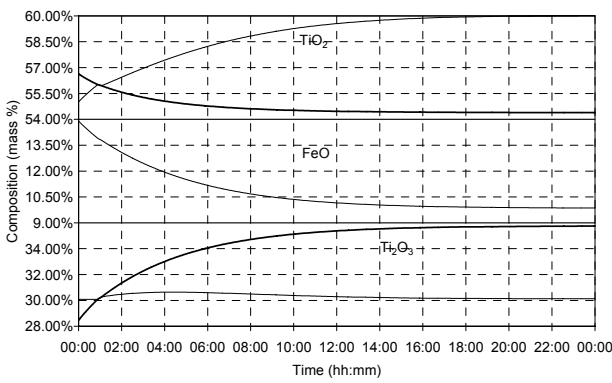
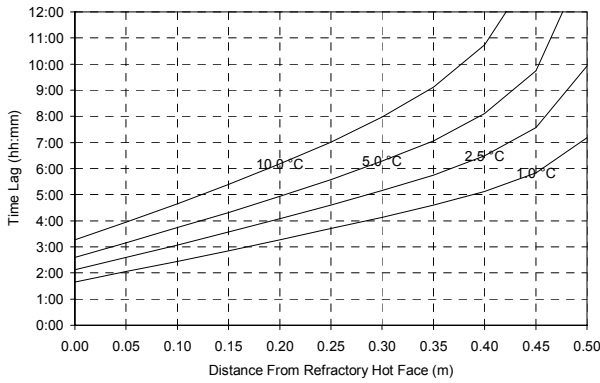
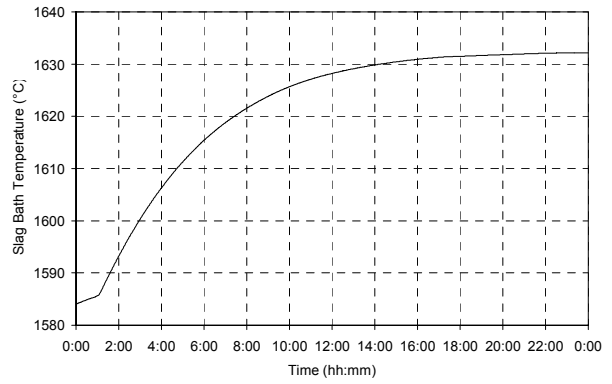
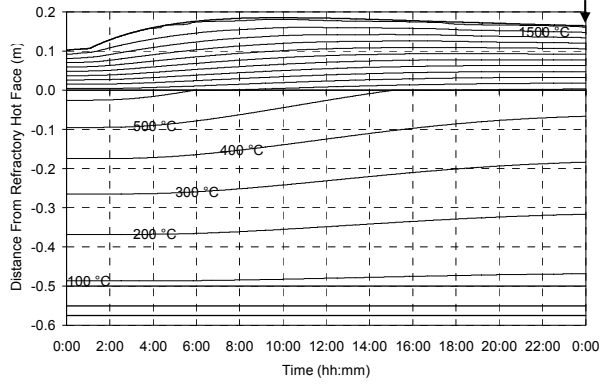
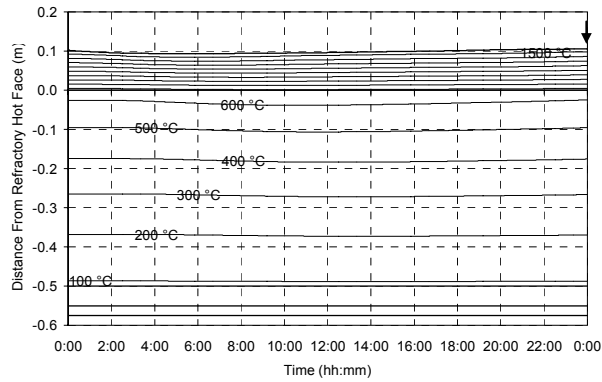


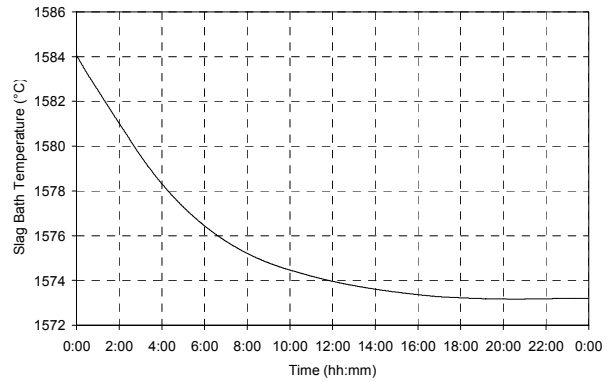
Figure 95 – Experiment 7.5 results.

7.3.6 Experiment 7.6

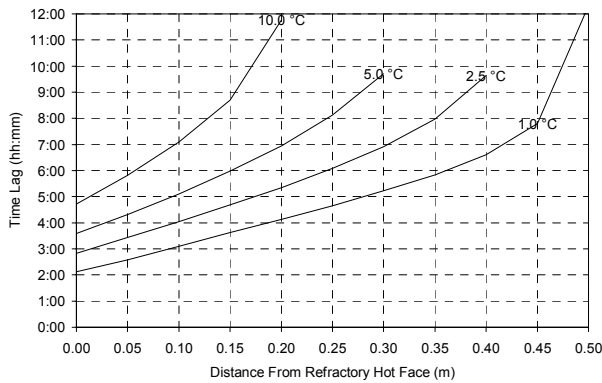
FEED COMPOSITION	%FeO	%TiO <sub>2</sub>	%Ti <sub>2</sub> O <sub>3</sub>	NEW SLAG FEED RATE	SLAG RESIDENCE TIME
F	20.0	50.0	30.0	57.5 t/h	4 h



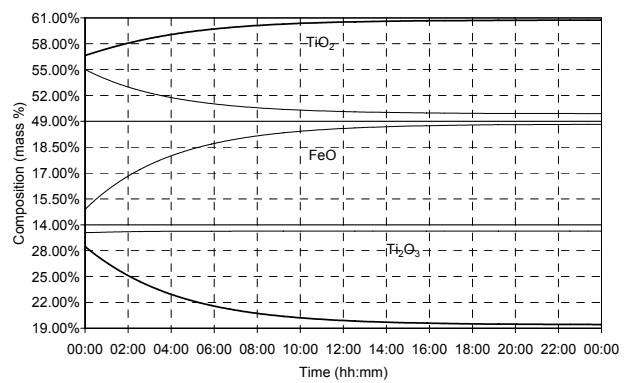
(a)



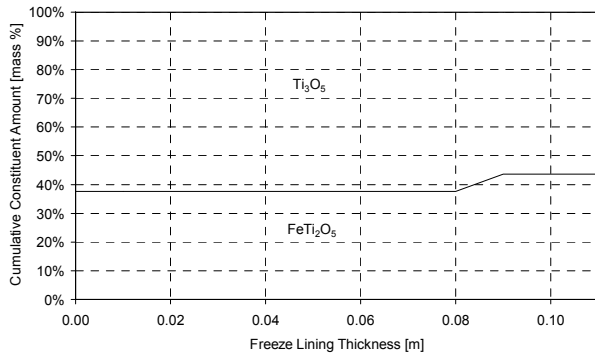
(b)



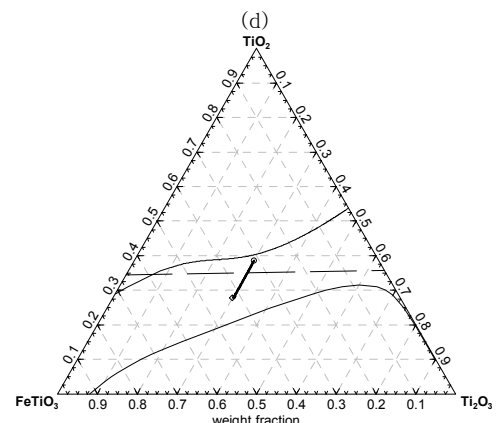
(c)



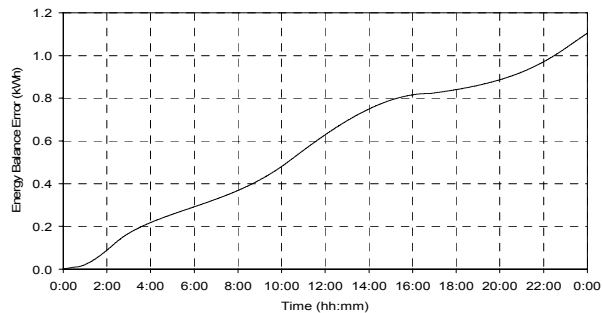
(d)



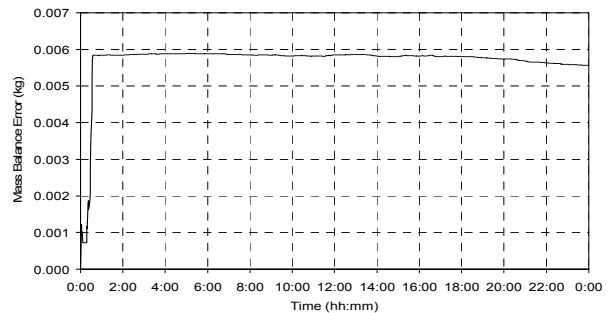
(e)



(f)



(g)



(h)

Figure 96 – Experiment 7.6 results.

7.3.7 Experiment 7.7

FEED COMPOSITION	%FeO	%TiO <sub>2</sub>	%Ti <sub>2</sub> O <sub>3</sub>	NEW SLAG FEED RATE	SLAG RESIDENCE TIME
G	10.0	50.0	40.0	57.5 t/h	4 h

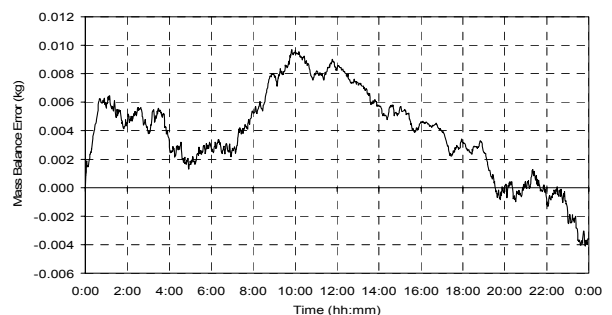
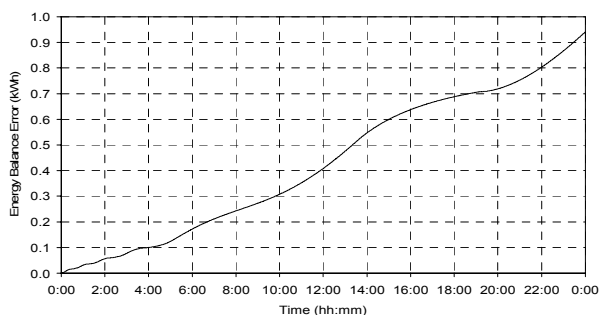
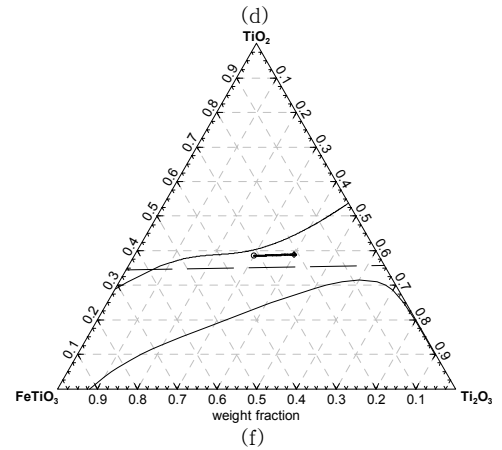
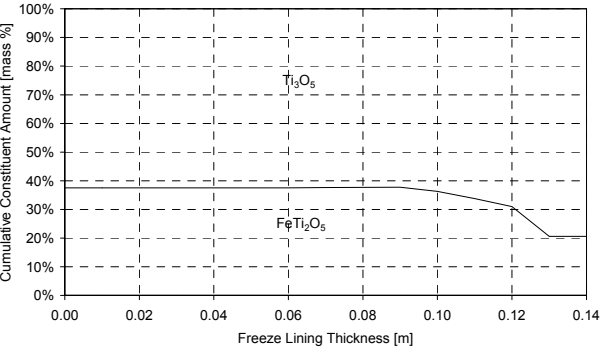
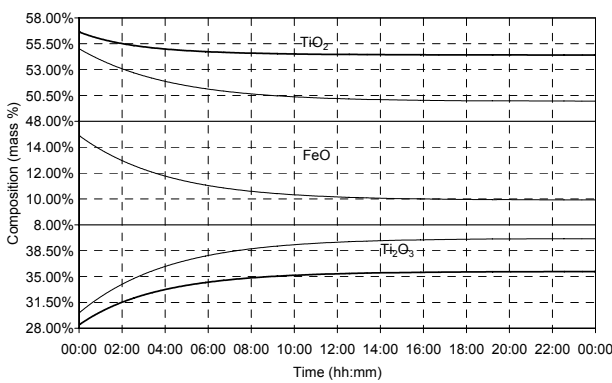
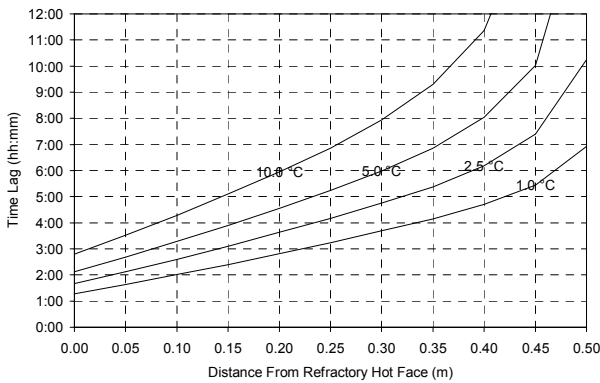
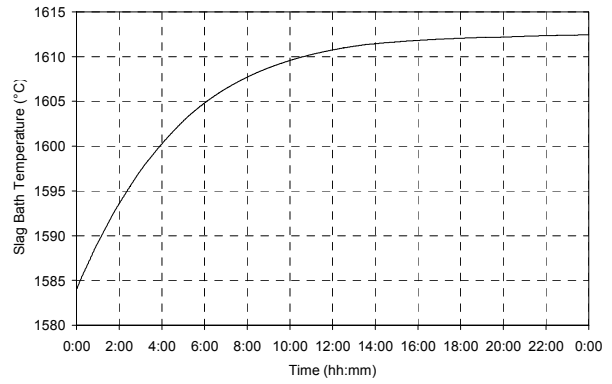
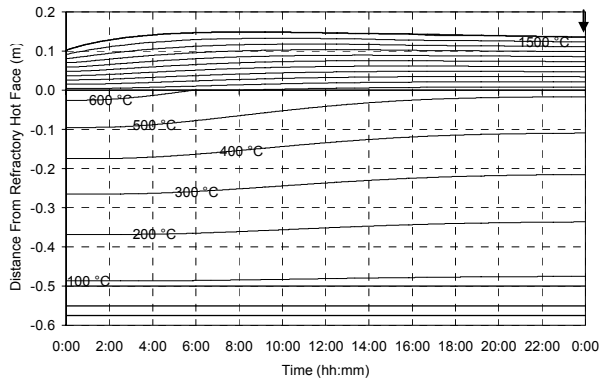
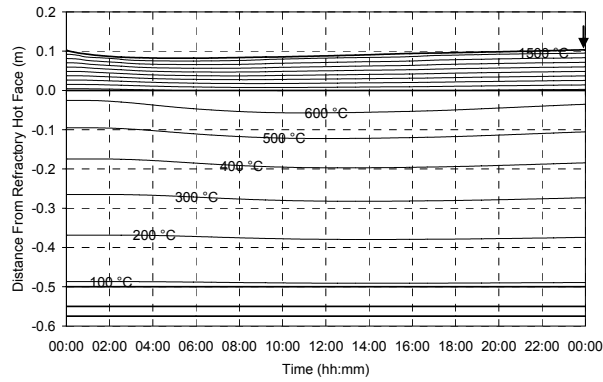


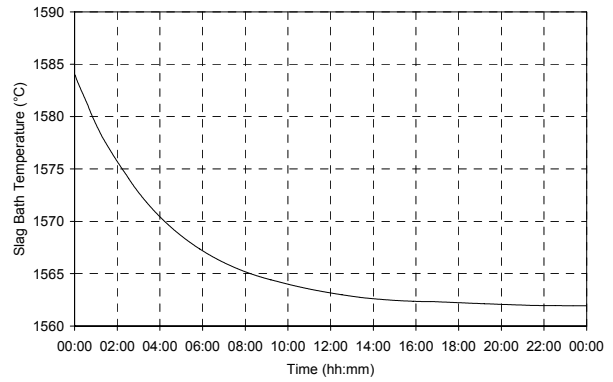
Figure 97 – Experiment 7.7 results.

7.3.8 Experiment 7.8

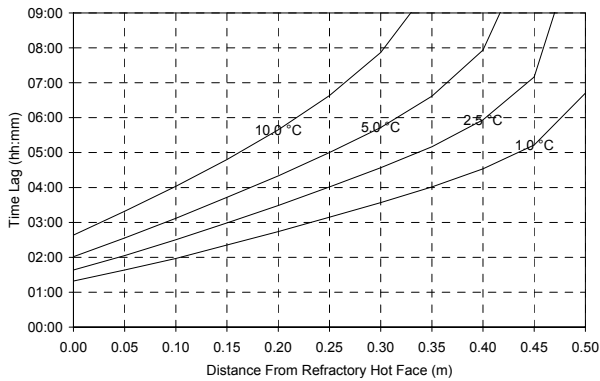
FEED COMPOSITION	%FeO	%TiO <sub>2</sub>	%Ti <sub>2</sub> O <sub>3</sub>	NEW SLAG FEED RATE	SLAG RESIDENCE TIME
H	20.0	60.0	20.0	57.5 t/h	4 h



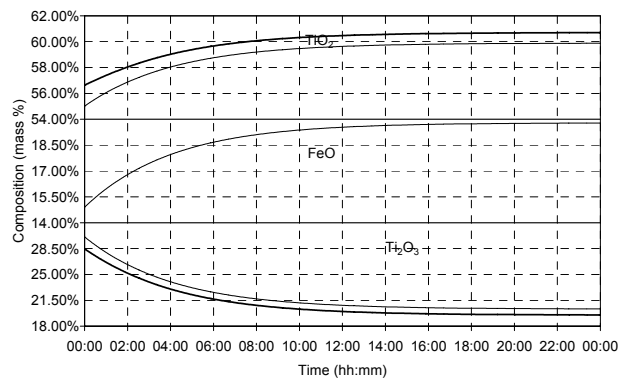
(a)



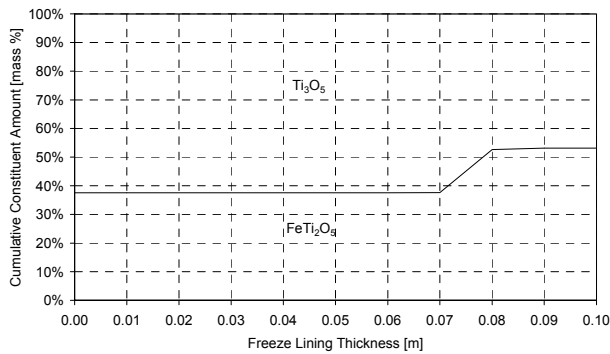
(b)



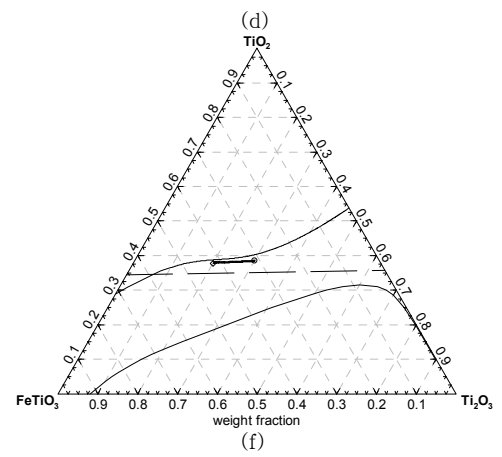
(c)



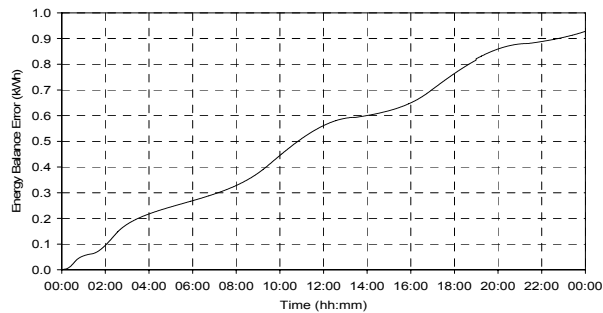
(d)



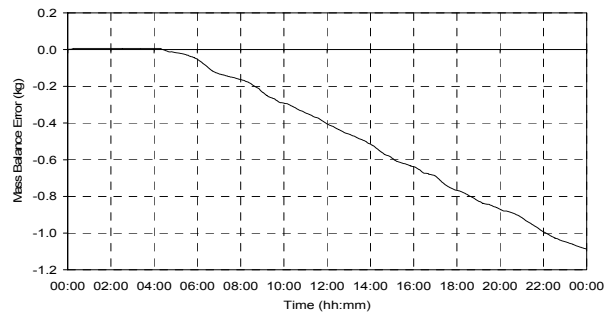
(e)



(f)



(g)



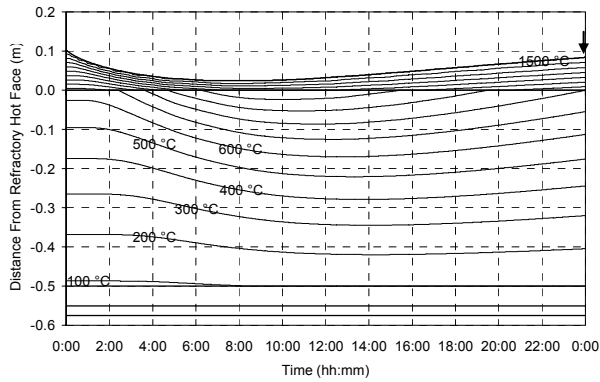
(h)

Figure 98 – Experiment 7.8 results.

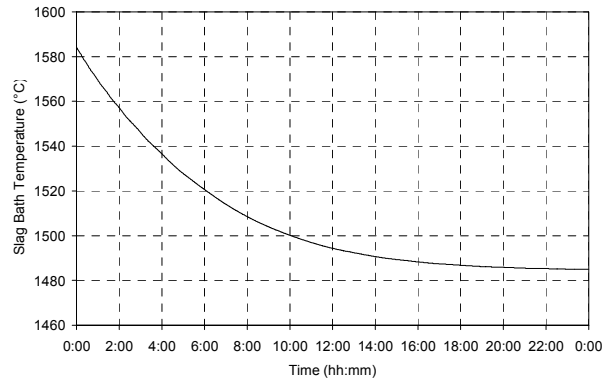


7.3.9 Experiment 7.9

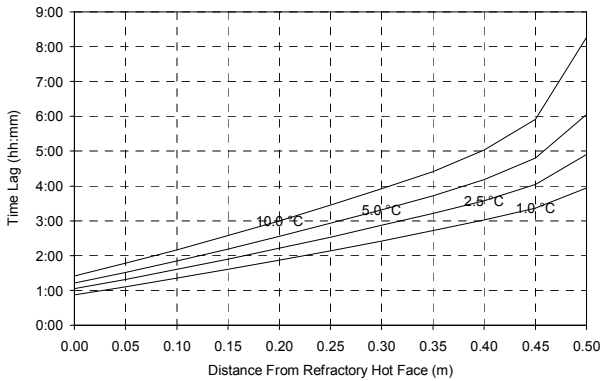
FEED COMPOSITION	%FeO	%TiO <sub>2</sub>	%Ti <sub>2</sub> O <sub>3</sub>	NEW SLAG FEED RATE	SLAG RESIDENCE TIME
I	35.5	59.5	5.0	57.5 t/h	4 h



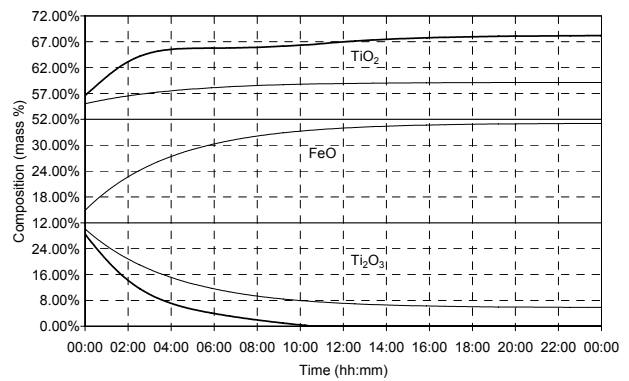
(a)



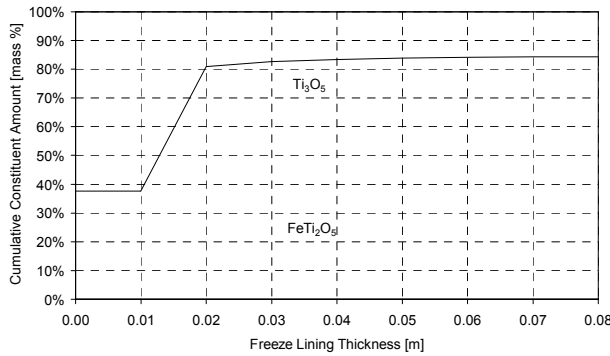
(b)



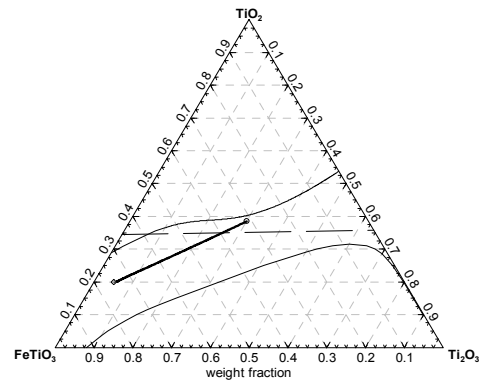
(c)



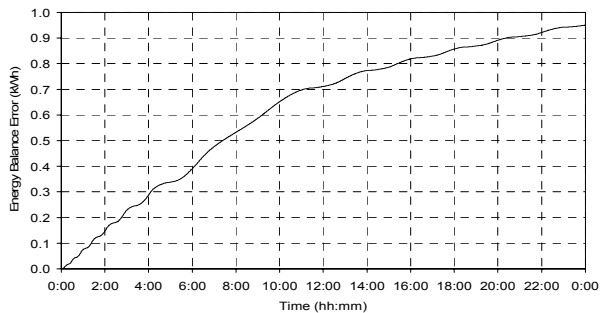
(d)



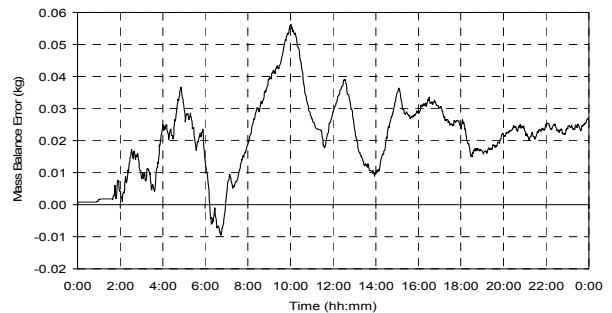
(e)



(f)



(g)

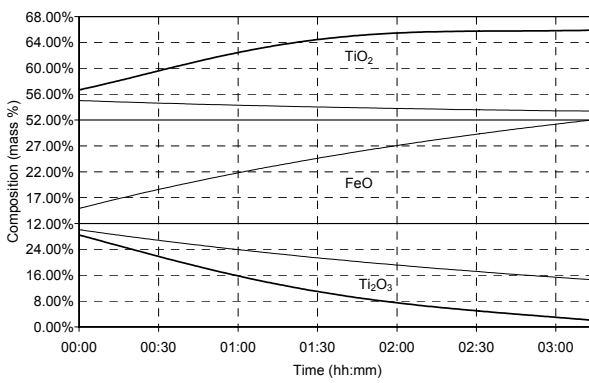
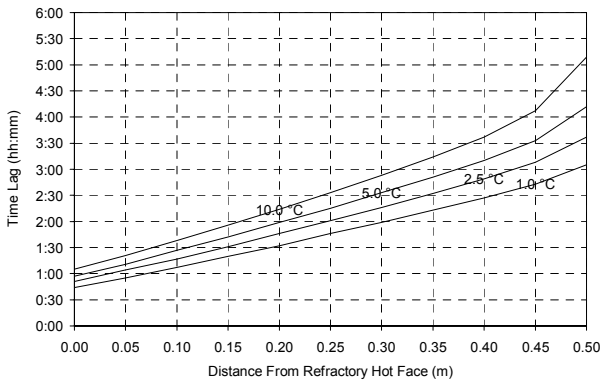
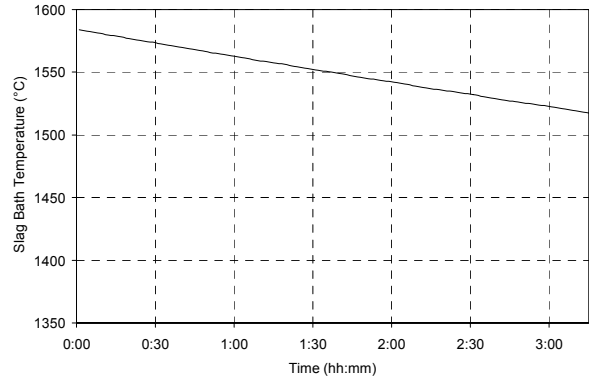
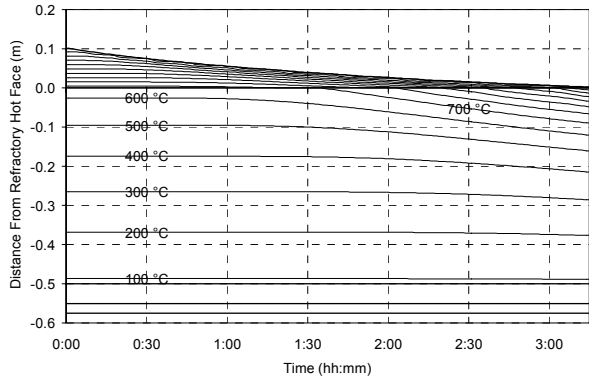


(h)

Figure 99 – Experiment 7.9 results.

7.3.10 Experiment 7.10

FEED COMPOSITION	%FeO	%TiO <sub>2</sub>	%Ti <sub>2</sub> O <sub>3</sub>	NEW SLAG FEED RATE	SLAG RESIDENCE TIME
J	pure	stoichiometric	ilmenite	57.5 t/h	4 h



Not Plotted.

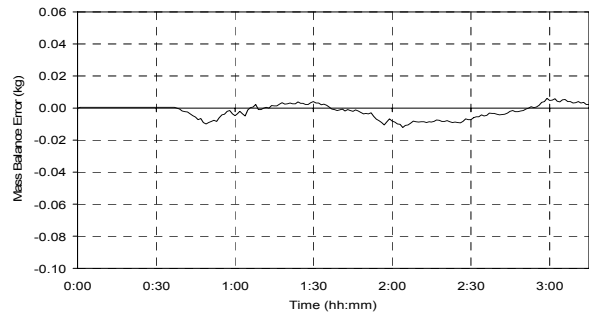
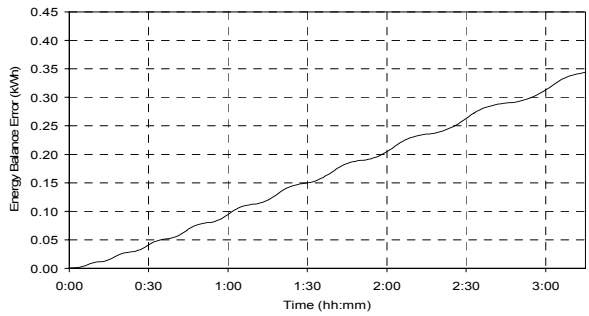
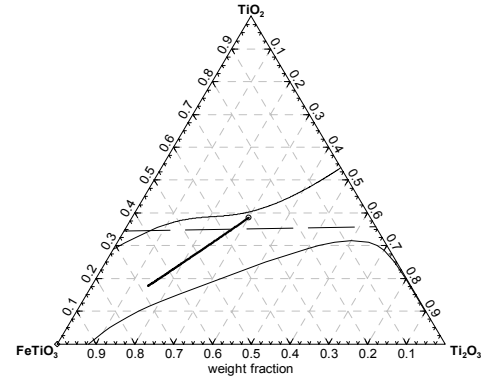
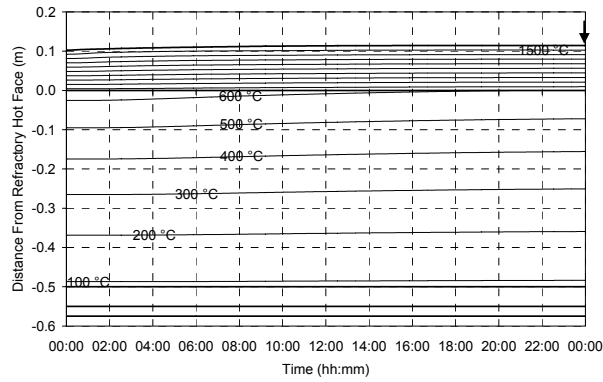


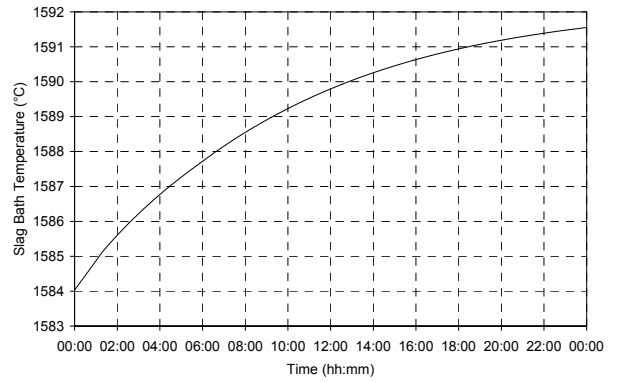
Figure 100 – Experiment 7.10 results.

7.3.11 Experiment 7.11

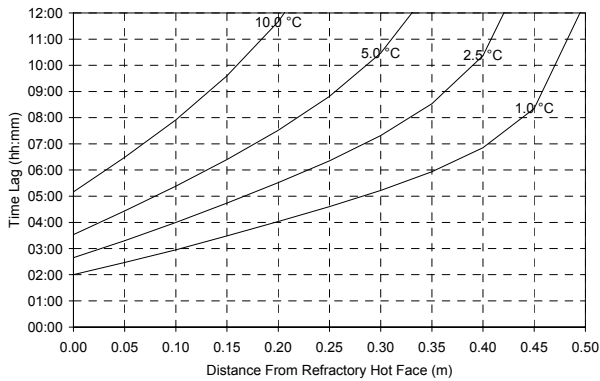
FEED COMPOSITION	%FeO	%TiO <sub>2</sub>	%Ti <sub>2</sub> O <sub>3</sub>	NEW SLAG FEED RATE	SLAG RESIDENCE TIME
A	15.0	50.0	35.0	23.0 t/h	10 h



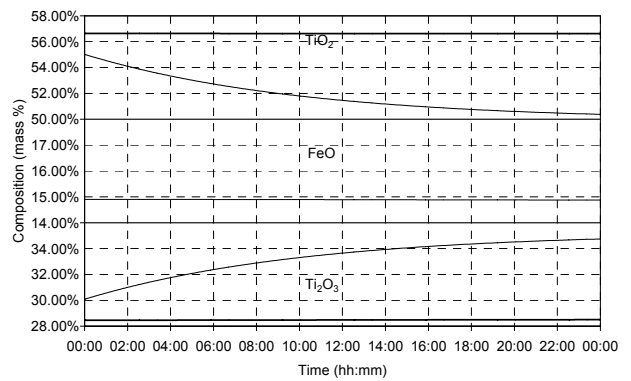
(a)



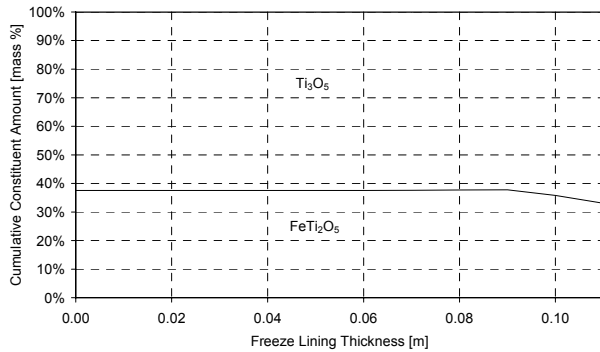
(b)



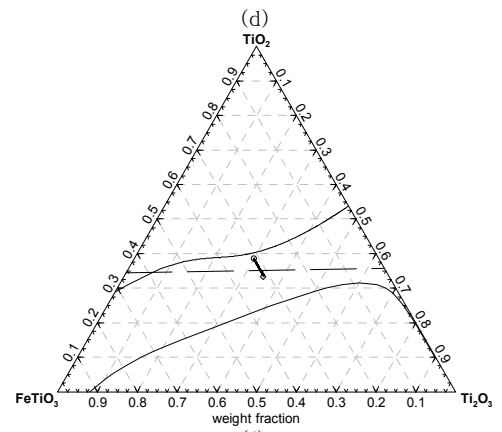
(c)



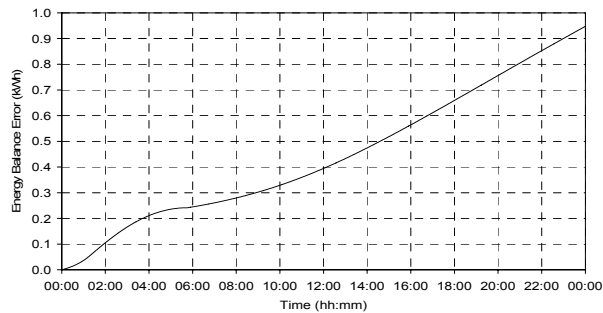
(d)



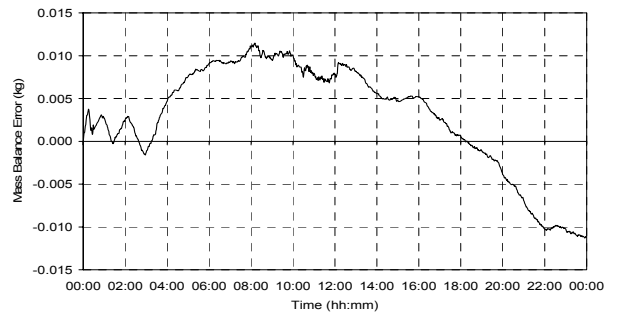
(e)



(f)



(g)



(h)

Figure 101 – Experiment 7.11 results.

7.3.12 Experiment 7.12

FEED COMPOSITION	%FeO	%TiO <sub>2</sub>	%Ti <sub>2</sub> O <sub>3</sub>	NEW SLAG FEED RATE	SLAG RESIDENCE TIME
B	15.0	60.0	25.0	23.0 t/h	10 h

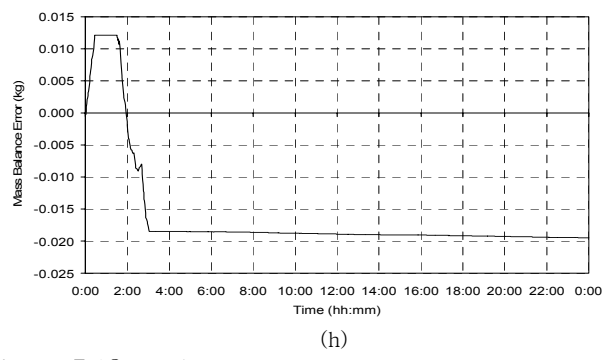
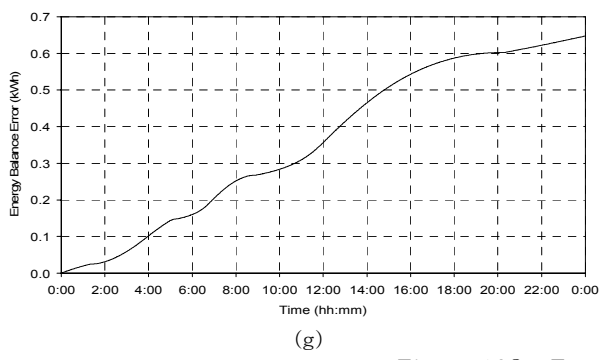
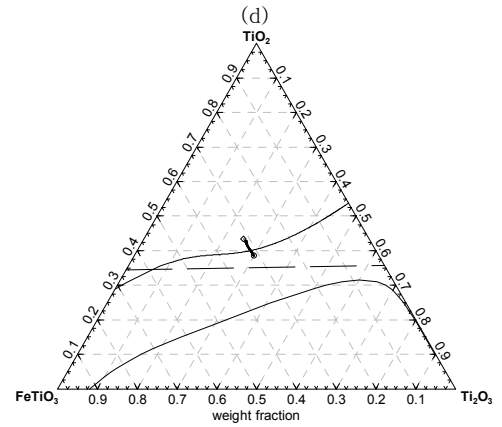
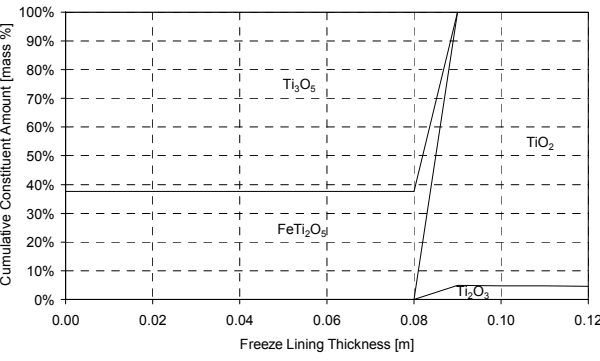
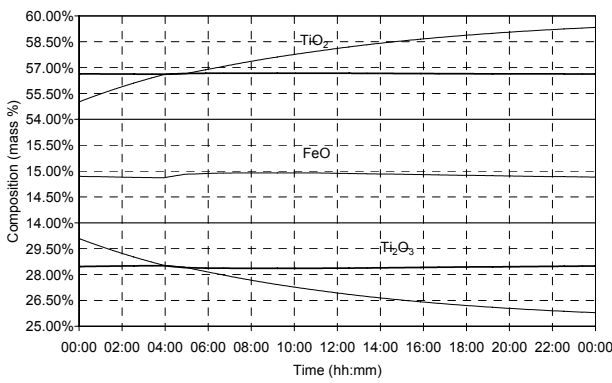
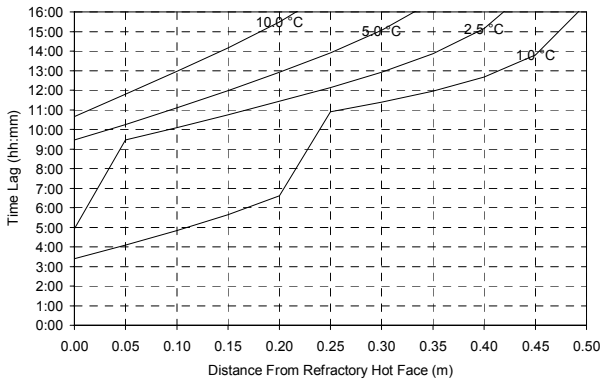
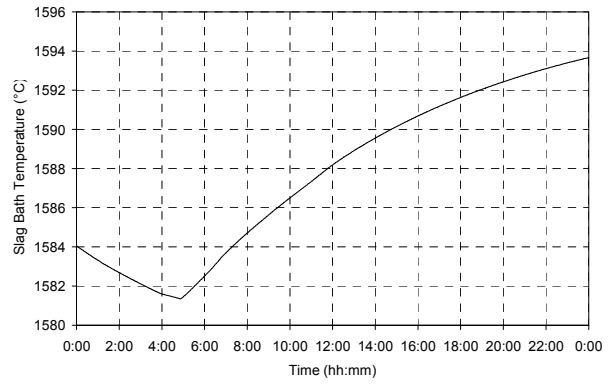
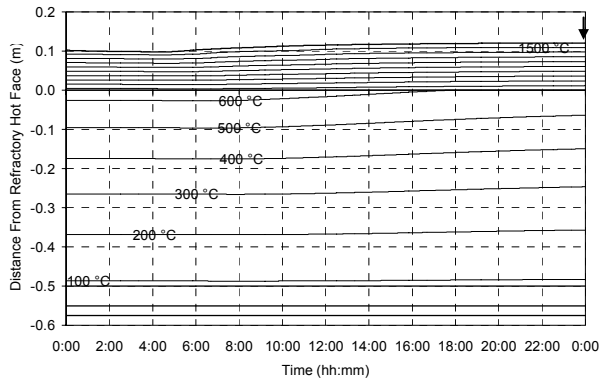
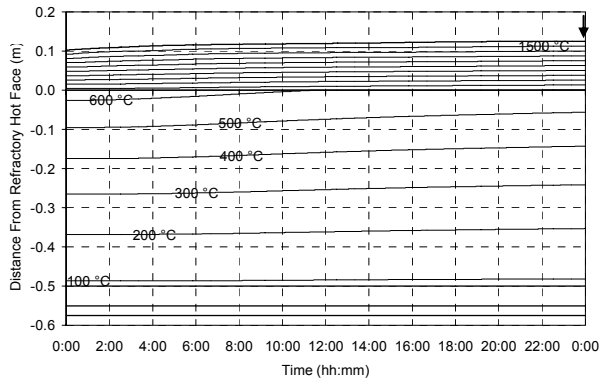


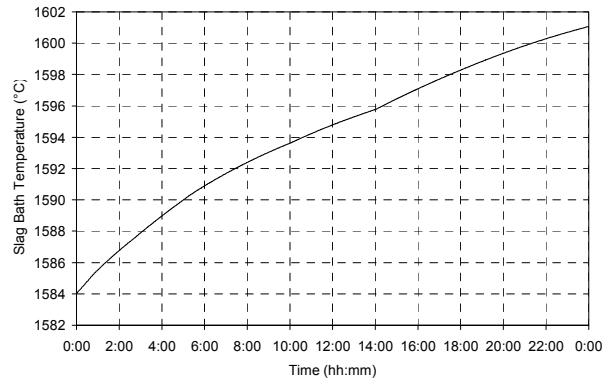
Figure 102 – Experiment 7.12 results.

7.3.13 Experiment 7.13

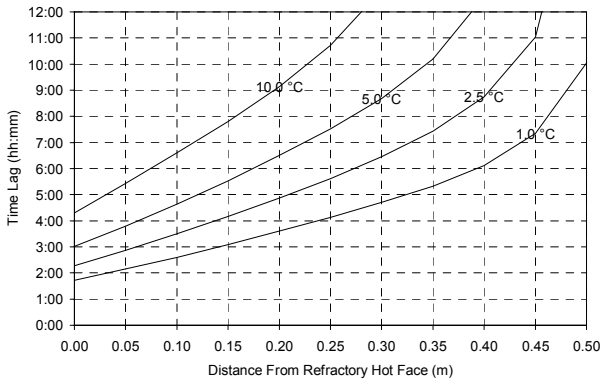
FEED COMPOSITION	%FeO	%TiO <sub>2</sub>	%Ti <sub>2</sub> O <sub>3</sub>	NEW SLAG FEED RATE	SLAG RESIDENCE TIME
C	10.0	55.0	35.0	23.0 t/h	10 h



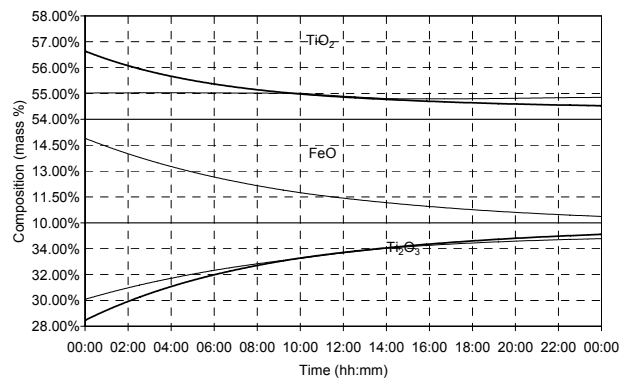
(a)



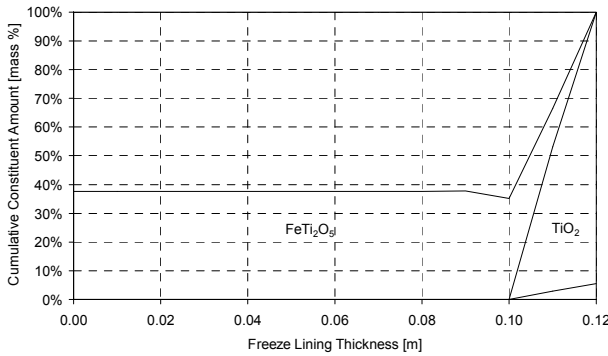
(b)



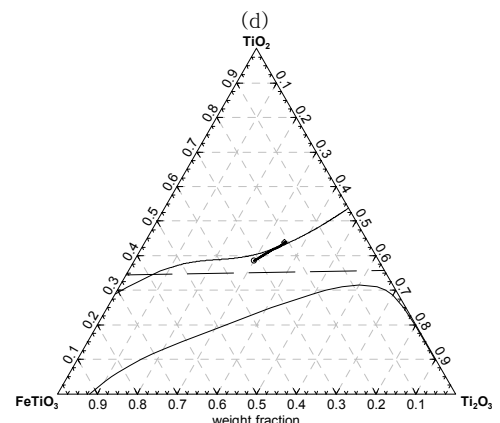
(c)



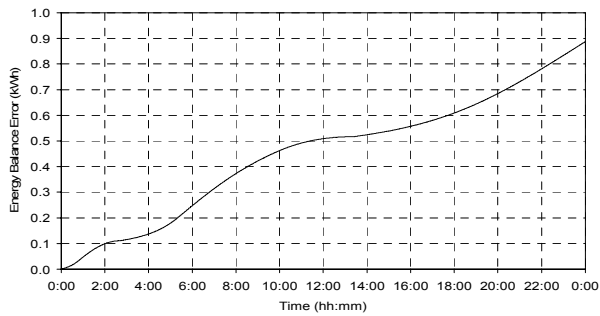
(d)



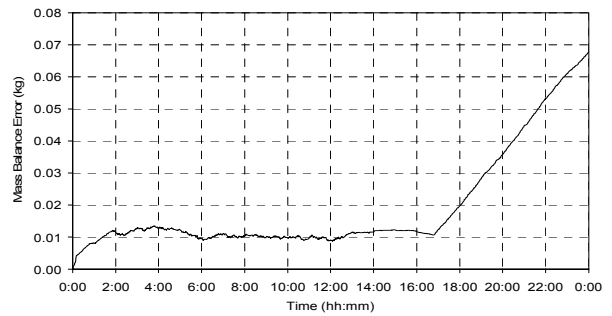
(e)



(f)



(g)



(h)

Figure 103 – Experiment 7.13 results.

7.3.14 Experiment 7.14

FEED COMPOSITION	%FeO	%TiO <sub>2</sub>	%Ti <sub>2</sub> O <sub>3</sub>	NEW SLAG FEED RATE	SLAG RESIDENCE TIME
D	20.0	55.0	25.0	23.0 t/h	10 h

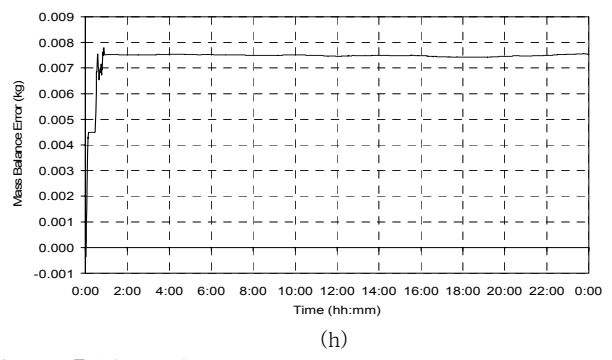
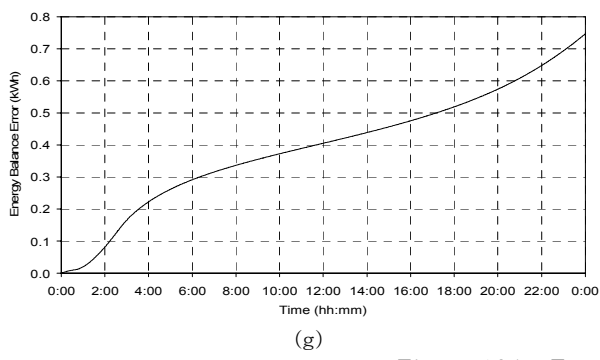
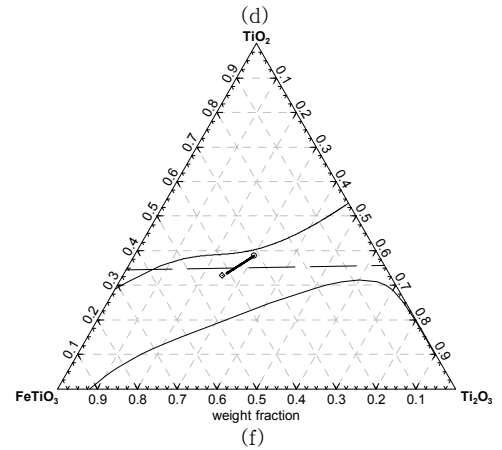
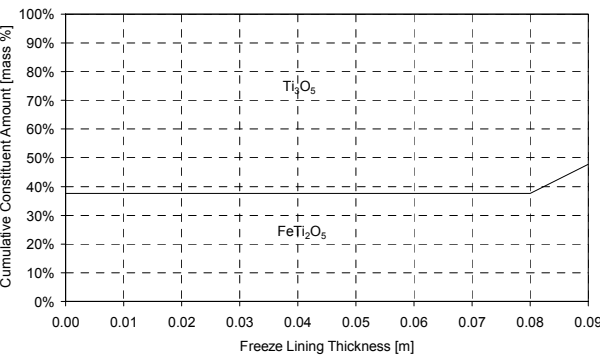
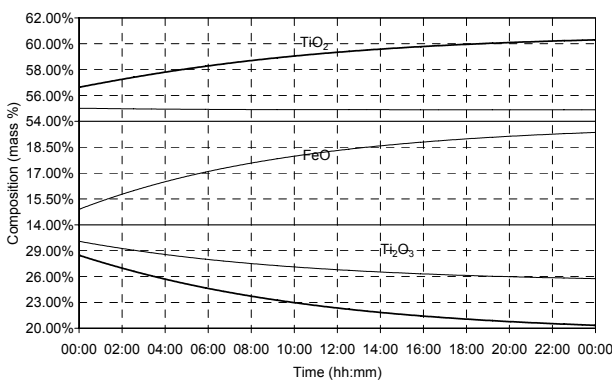
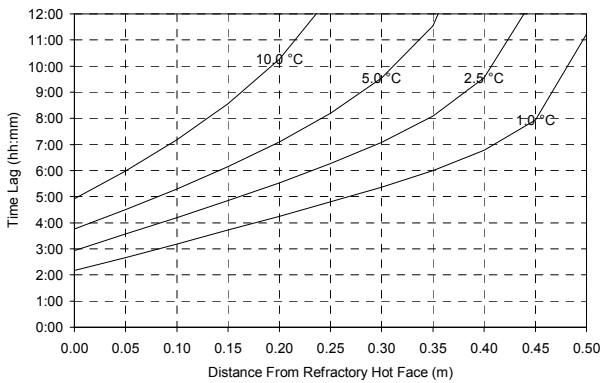
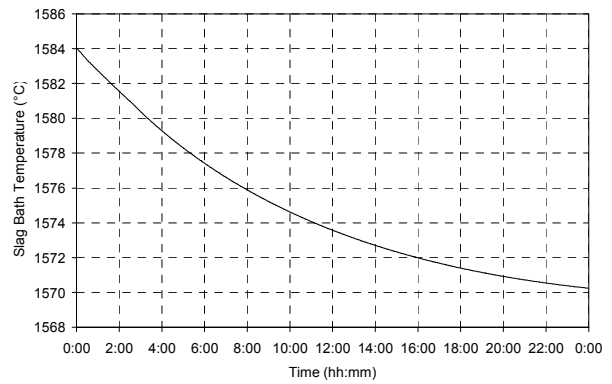
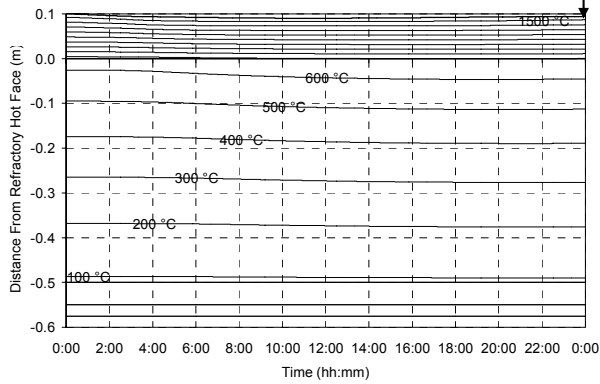
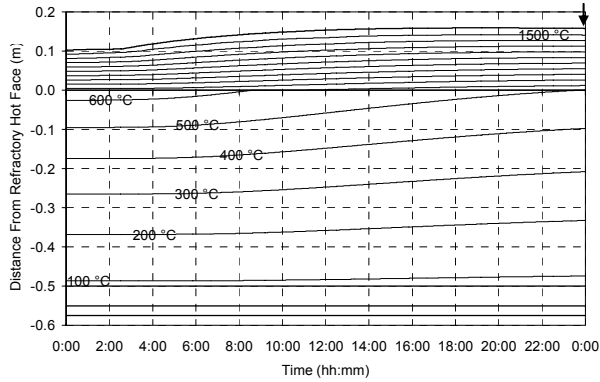


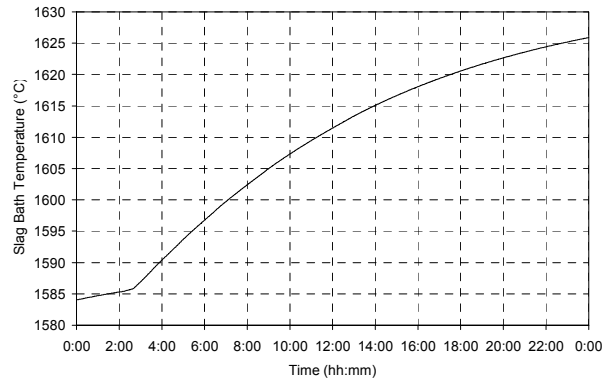
Figure 104 – Experiment 7.14 results.

7.3.15 Experiment 7.15

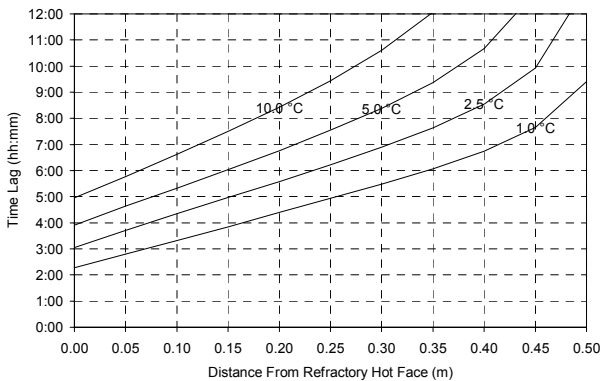
FEED COMPOSITION	%FeO	%TiO <sub>2</sub>	%Ti <sub>2</sub> O <sub>3</sub>	NEW SLAG FEED RATE	SLAG RESIDENCE TIME
E	10.0	60.0	30.0	23.0 t/h	10 h



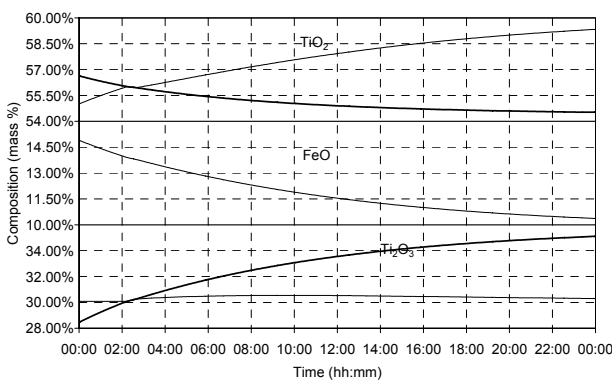
(a)



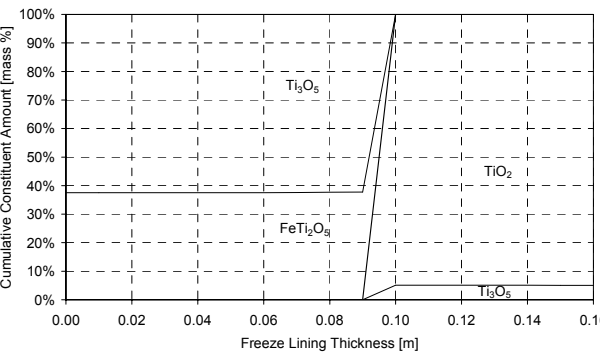
(b)



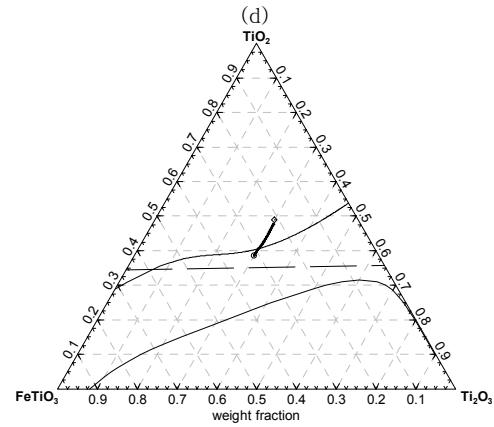
(c)



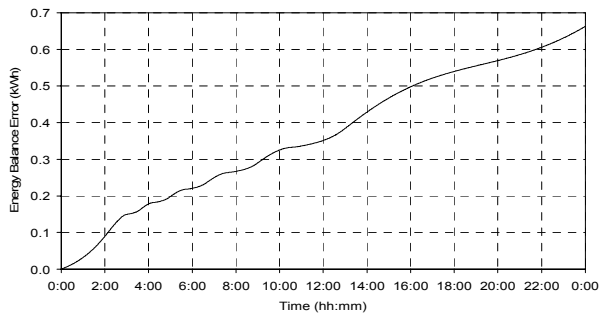
(d)



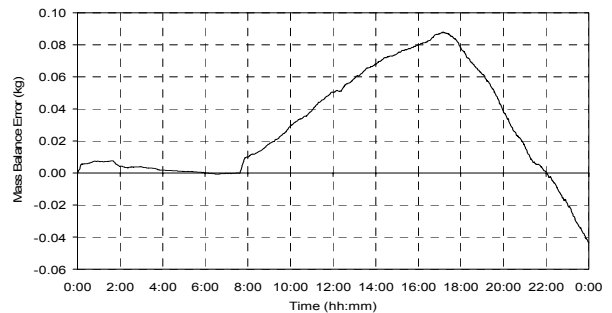
(e)



(f)



(g)



(h)

Figure 105 – Experiment 7.15 results.

7.3.16 Experiment 7.16

FEED COMPOSITION	%FeO	%TiO <sub>2</sub>	%Ti <sub>2</sub> O <sub>3</sub>	NEW SLAG FEED RATE	SLAG RESIDENCE TIME
F	20.0	50.0	30.0	23.0 t/h	10 h

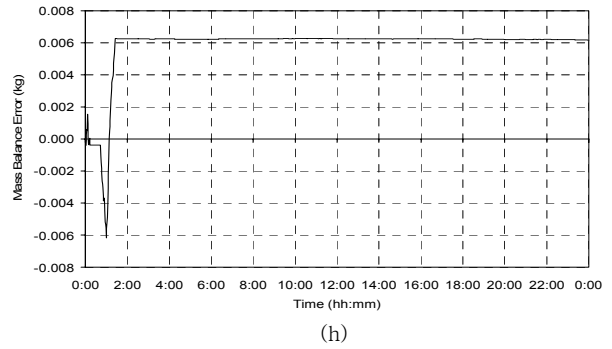
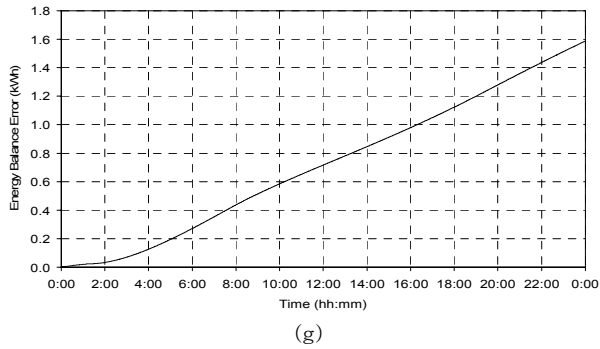
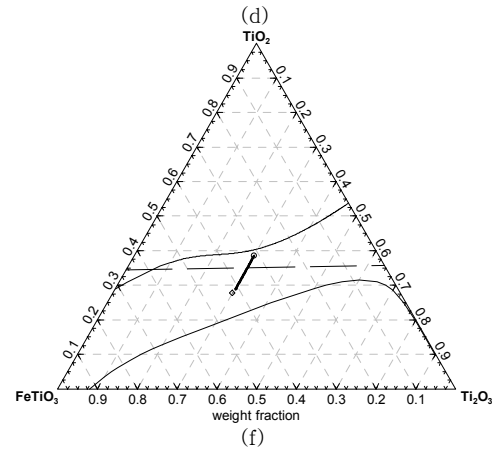
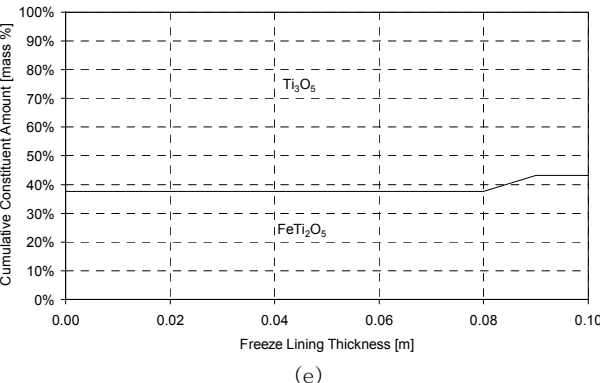
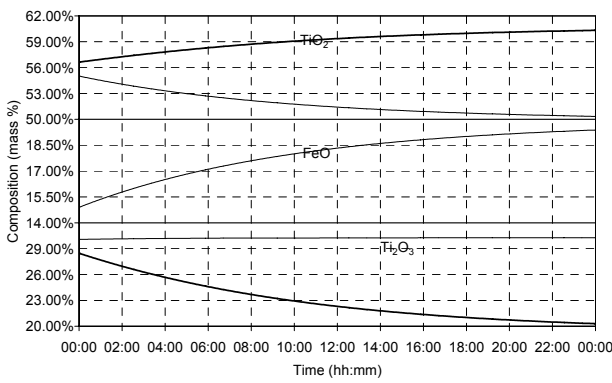
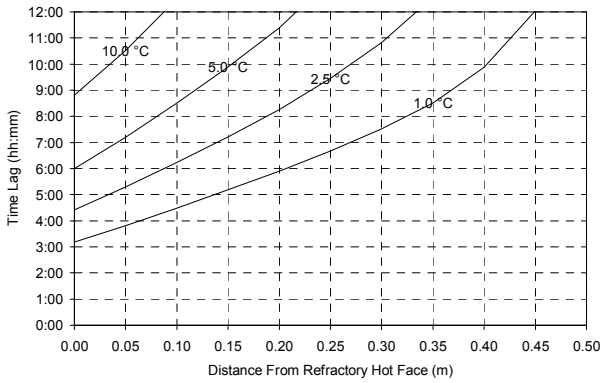
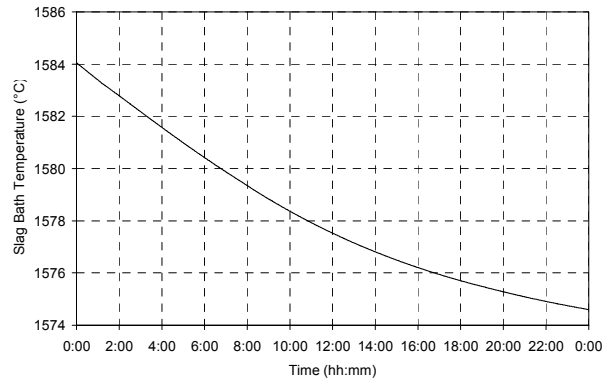
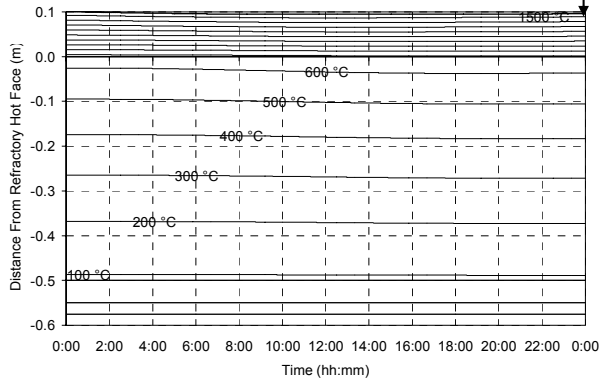


Figure 106 – Experiment 7.16 results.



7.3.17 Experiment 7.17

FEED COMPOSITION	%FeO	%TiO <sub>2</sub>	%Ti <sub>2</sub> O <sub>3</sub>	NEW SLAG FEED RATE	SLAG RESIDENCE TIME
G	10.0	50.0	40.0	23.0 t/h	10 h

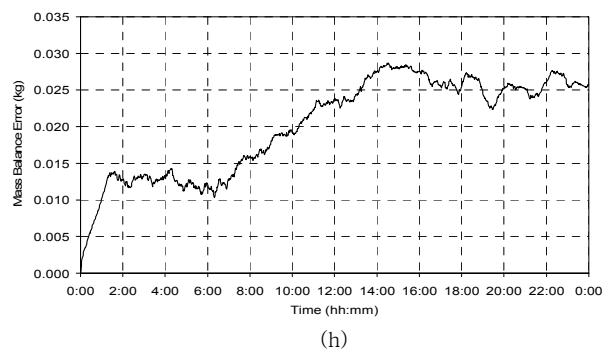
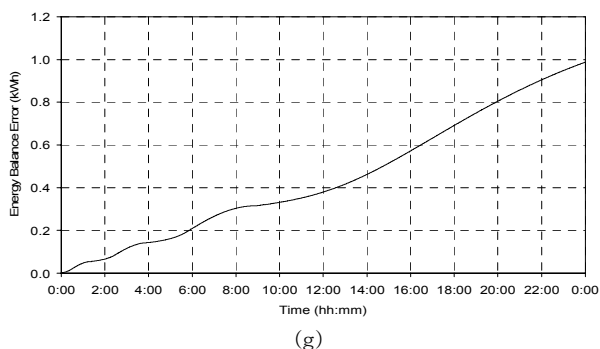
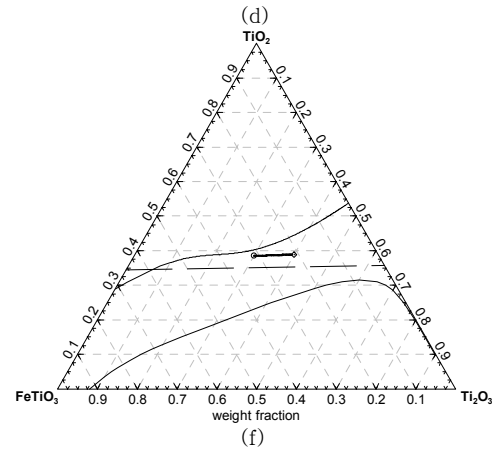
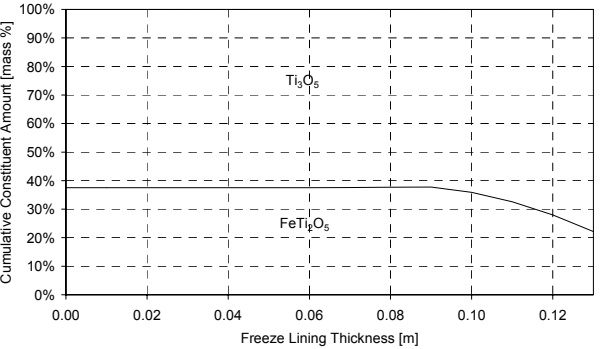
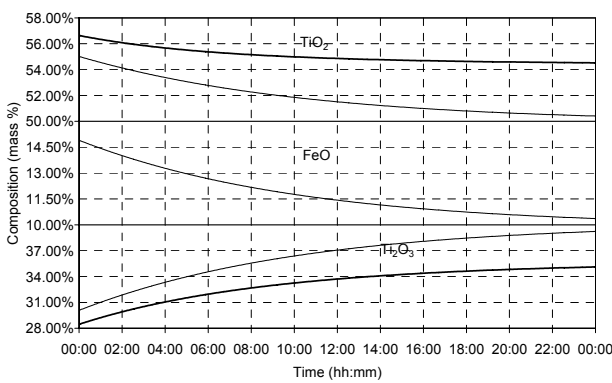
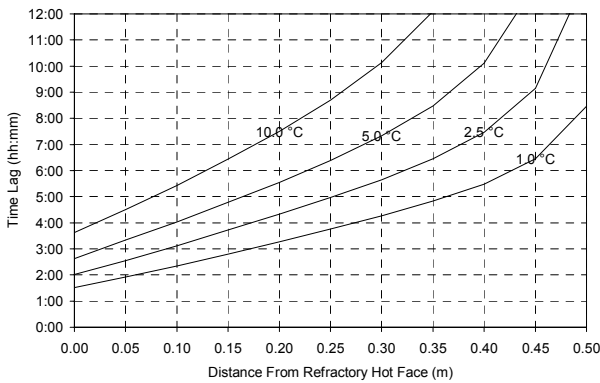
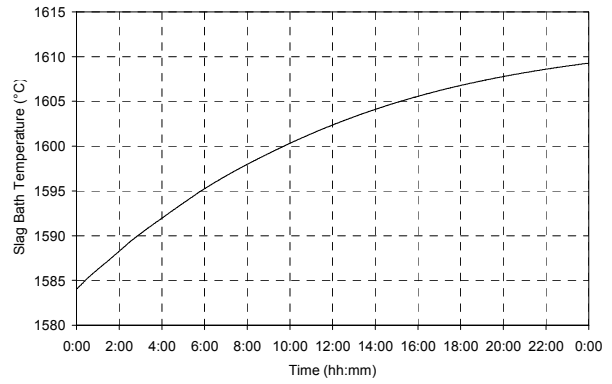
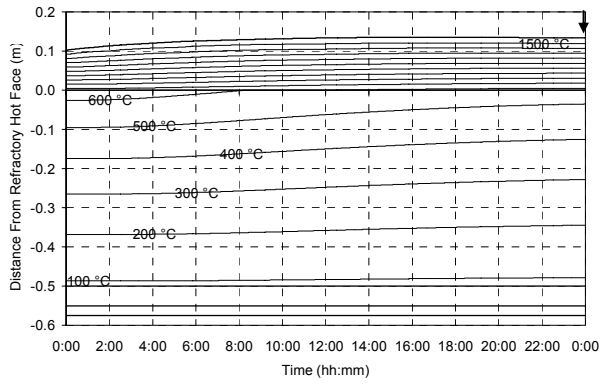
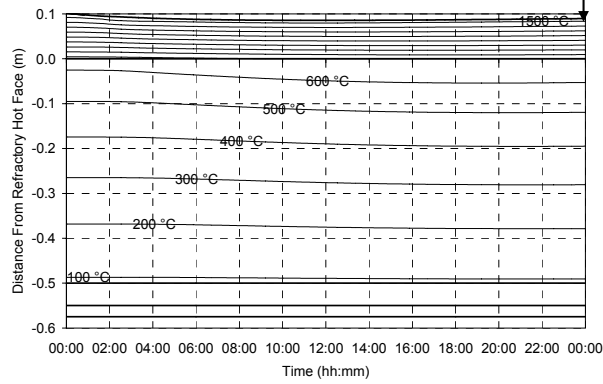


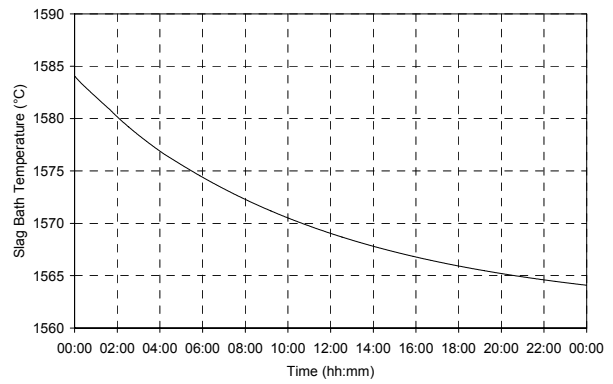
Figure 107 – Experiment 7.17 results.

7.3.18 Experiment 7.18

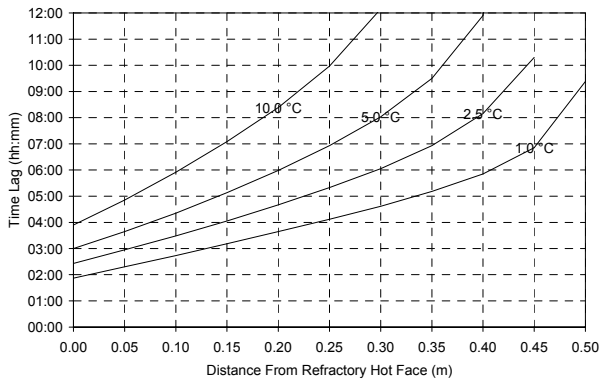
FEED COMPOSITION	%FeO	%TiO <sub>2</sub>	%Ti <sub>2</sub> O <sub>3</sub>	NEW SLAG FEED RATE	SLAG RESIDENCE TIME
H	20.0	60.0	20.0	23.0 t/h	10 h



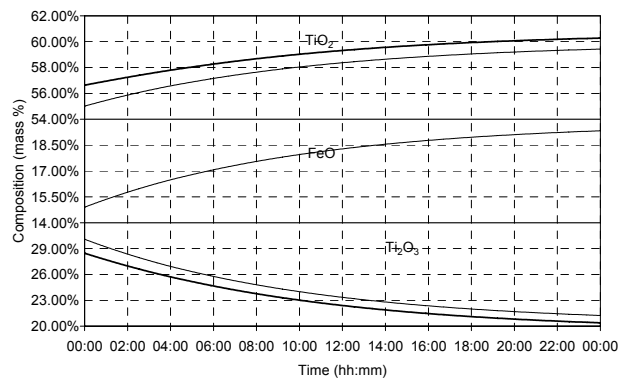
(a)



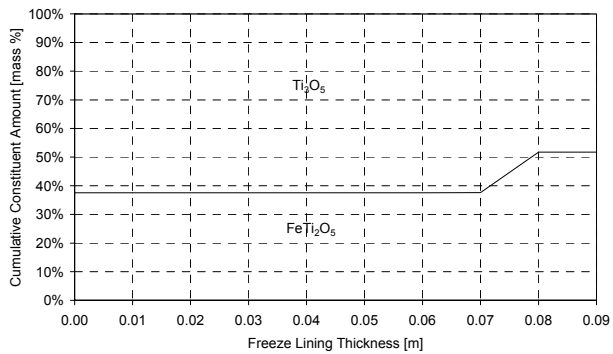
(b)



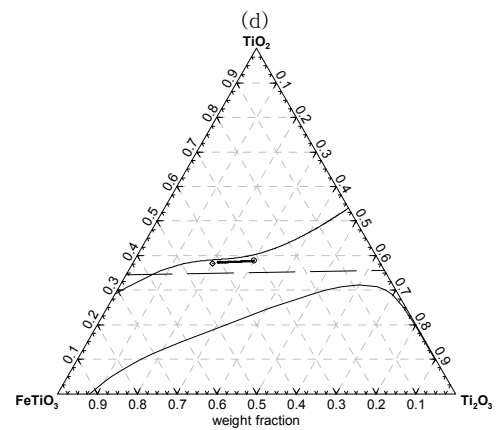
(c)



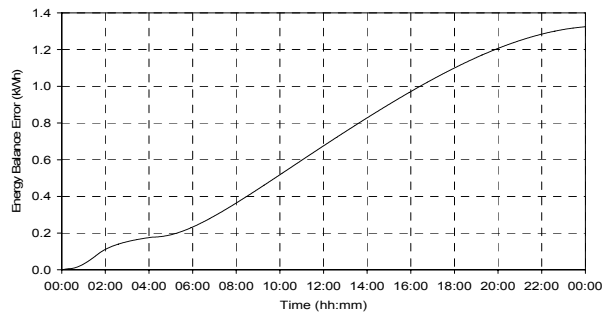
(d)



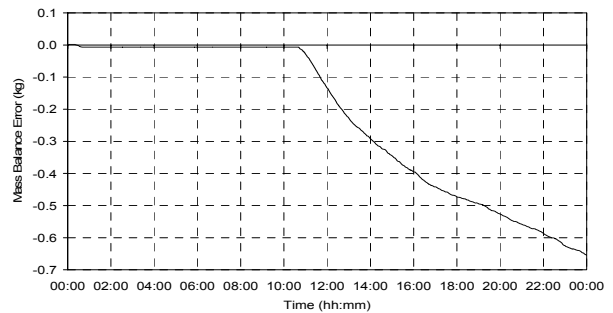
(e)



(f)



(g)

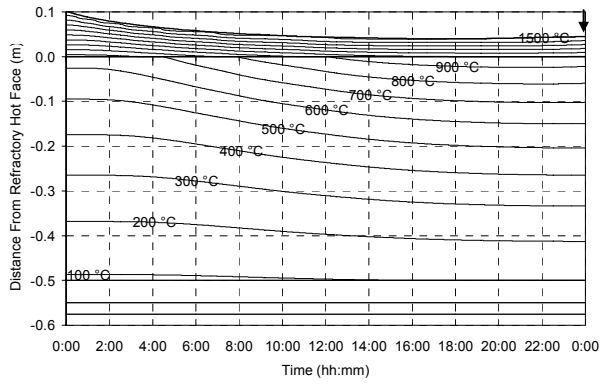


(h)

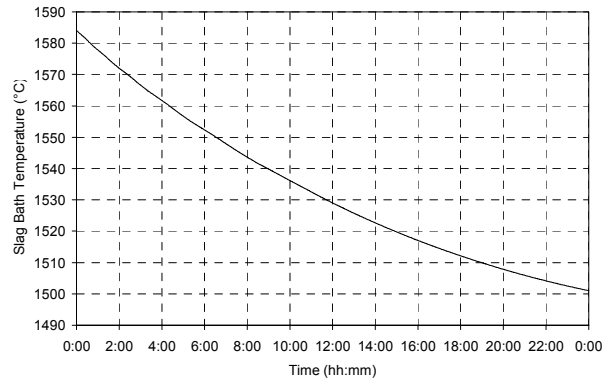
Figure 108 – Experiment 7.18 results.

7.3.19 Experiment 7.19

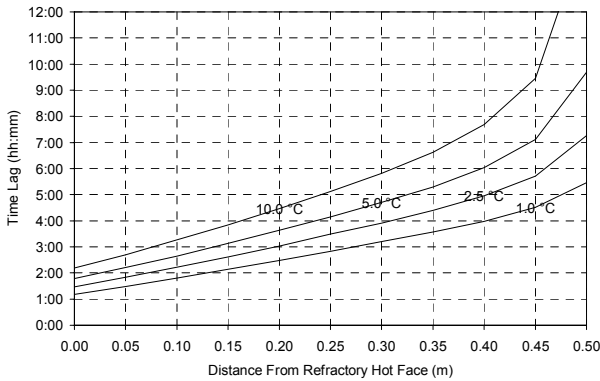
FEED COMPOSITION	%FeO	%TiO <sub>2</sub>	%Ti <sub>2</sub> O <sub>3</sub>	NEW SLAG FEED RATE	SLAG RESIDENCE TIME
I	35.5	59.5	5.0	23.0 t/h	10 h



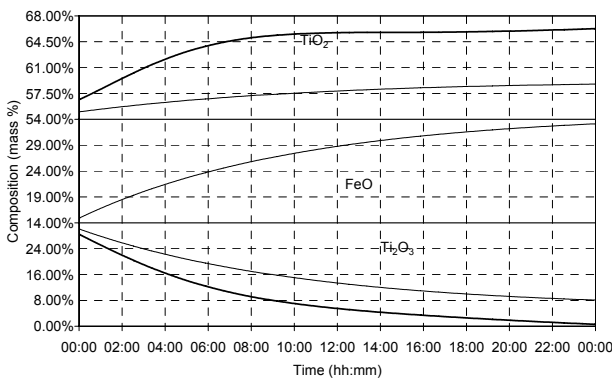
(a)



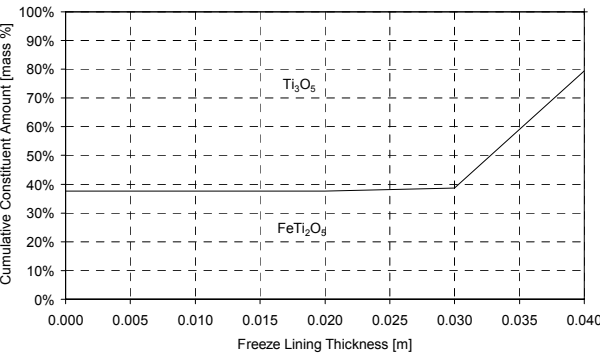
(b)



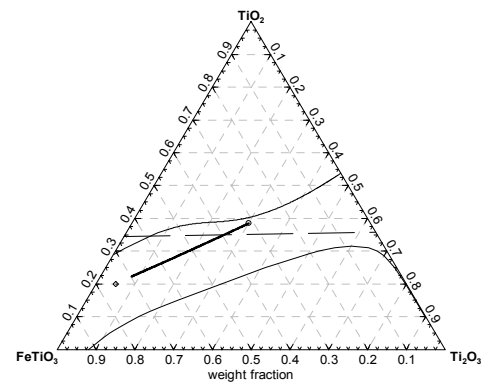
(c)



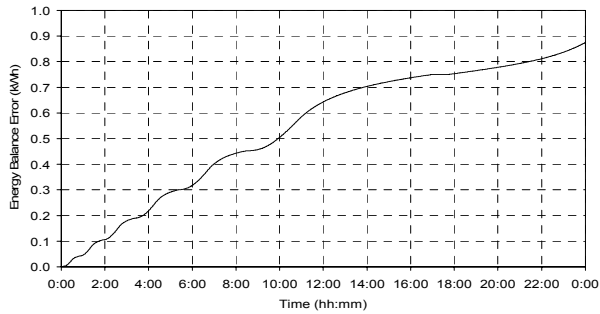
(d)



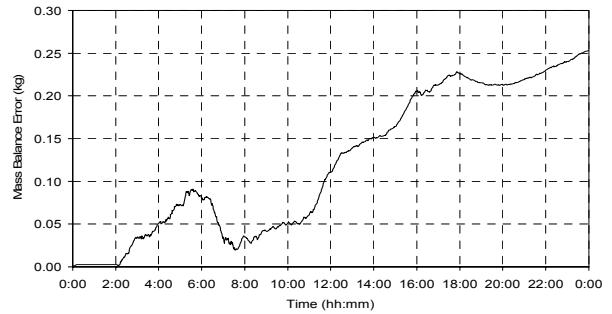
(e)



(f)



(g)

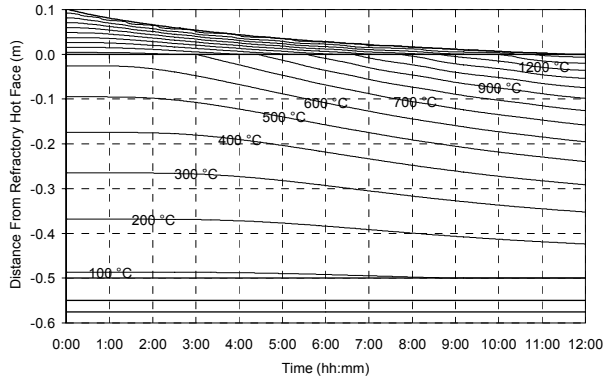


(h)

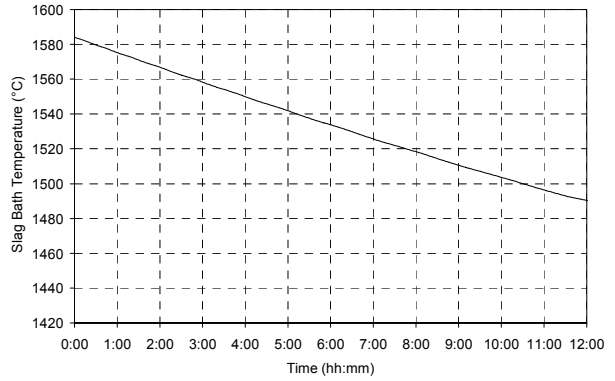
Figure 109 – Experiment 7.19 results.

7.3.20 Experiment 7.20

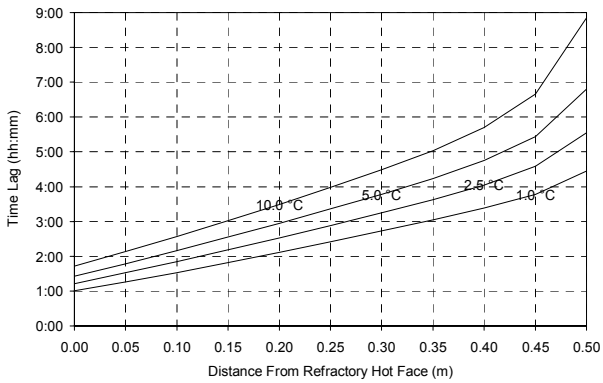
FEED COMPOSITION	%FeO	%TiO <sub>2</sub>	%Ti <sub>2</sub> O <sub>3</sub>	NEW SLAG FEED RATE	SLAG RESIDENCE TIME
J	pure stoichiometric ilmenite			23.0 t/h	10 h



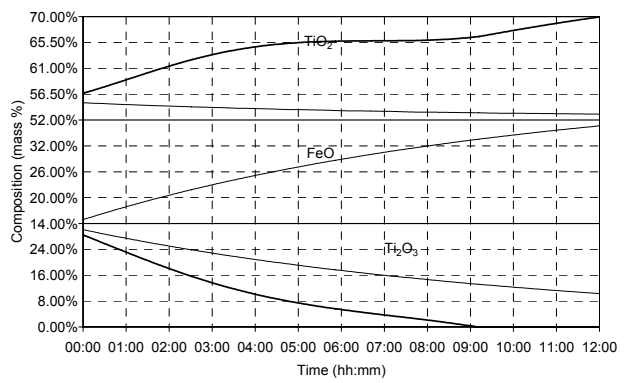
(a)



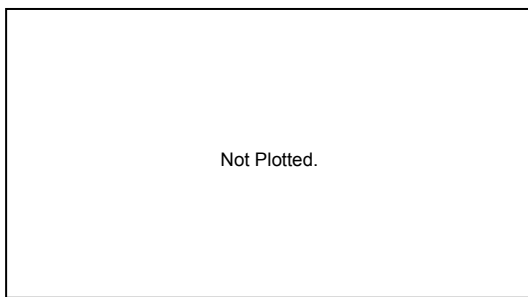
(b)



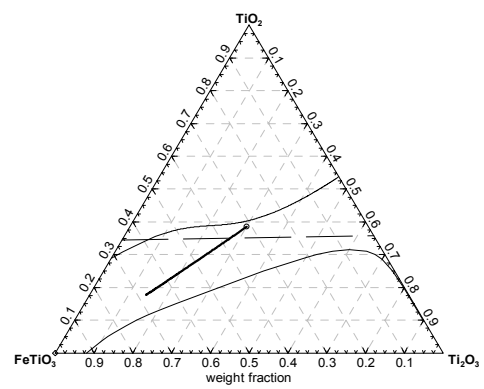
(c)



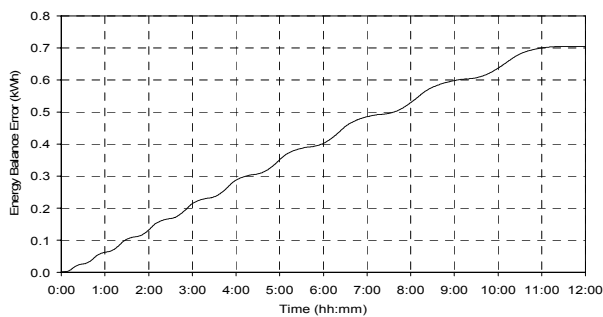
(d)



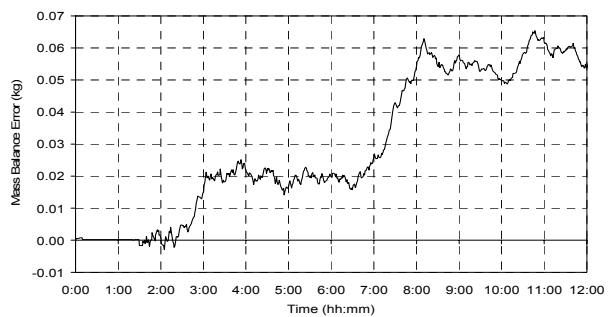
(e)



(f)



(g)



(h)

Figure 110 – Experiment 7.20 results.

7.3.21 Experiment 7.21

FEED COMPOSITION	%FeO	%TiO <sub>2</sub>	%Ti <sub>2</sub> O <sub>3</sub>	NEW SLAG FEED RATE	SLAG RESIDENCE TIME
A	15.0	50.0	35.0	14.4 t/h	16 h

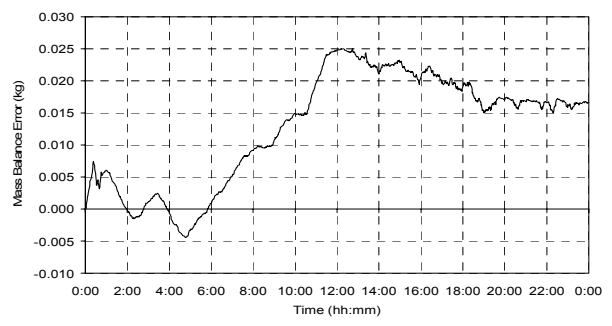
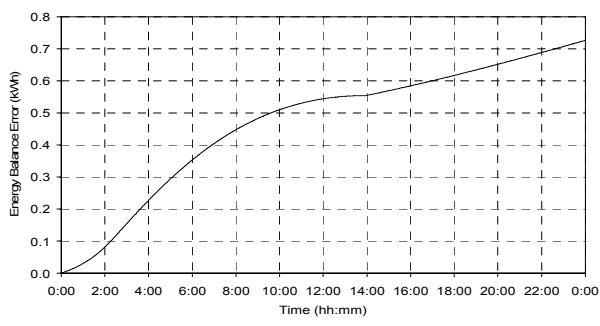
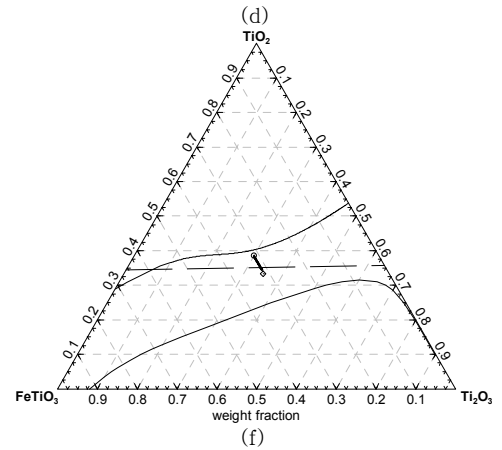
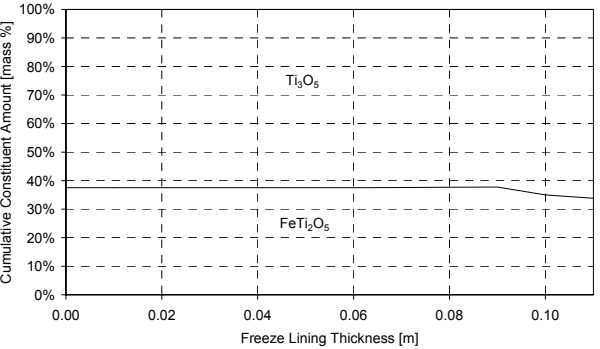
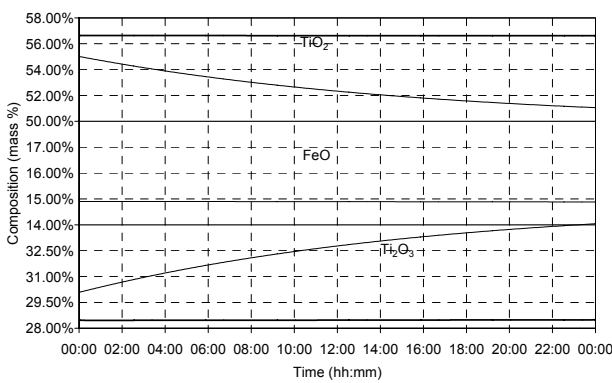
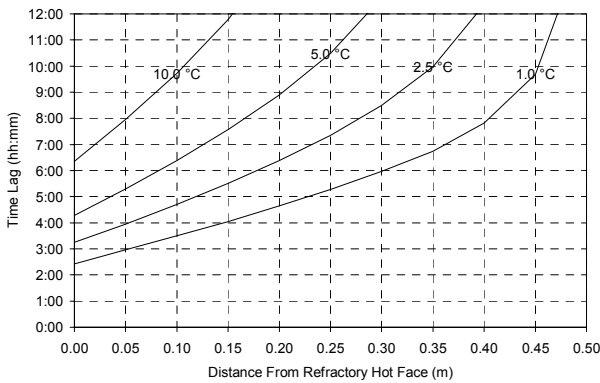
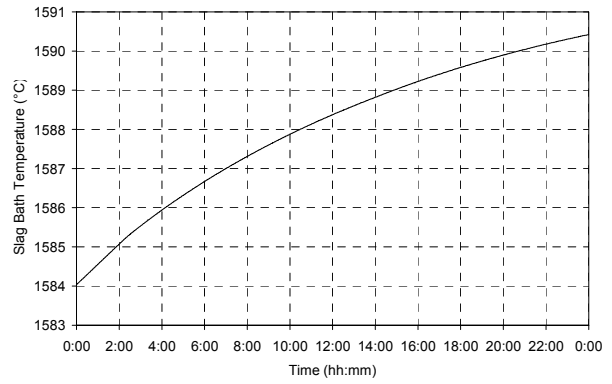
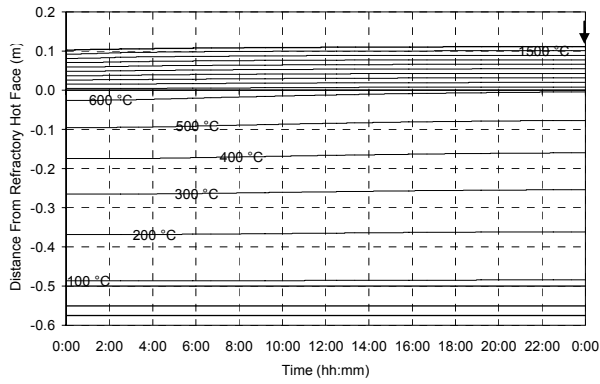


Figure 111 – Experiment 7.21 results.

7.3.22 Experiment 7.22

FEED COMPOSITION	%FeO	%TiO <sub>2</sub>	%Ti <sub>2</sub> O <sub>3</sub>	NEW SLAG FEED RATE	SLAG RESIDENCE TIME
B	15.0	60.0	25.0	14.4 t/h	16 h

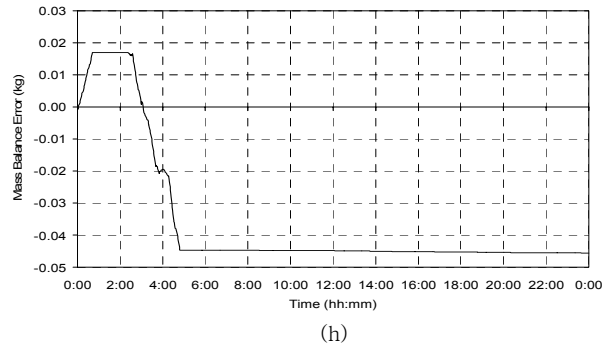
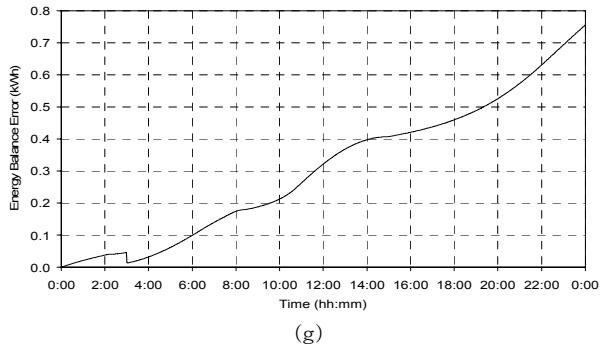
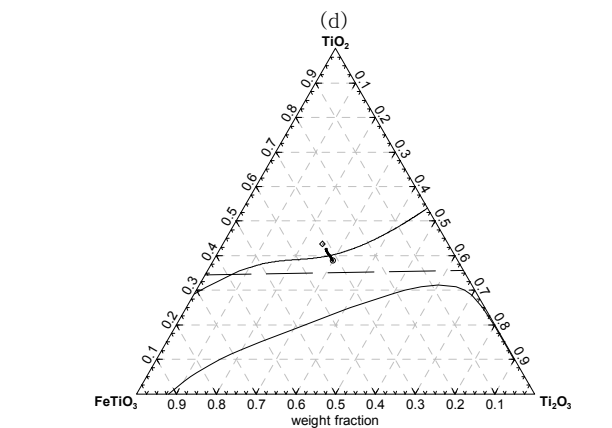
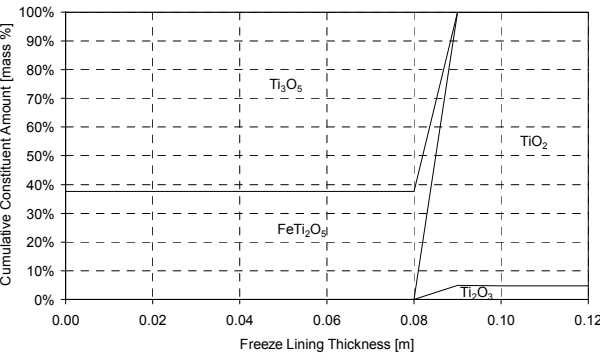
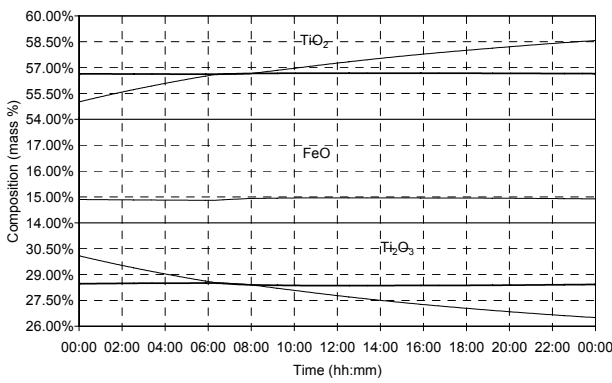
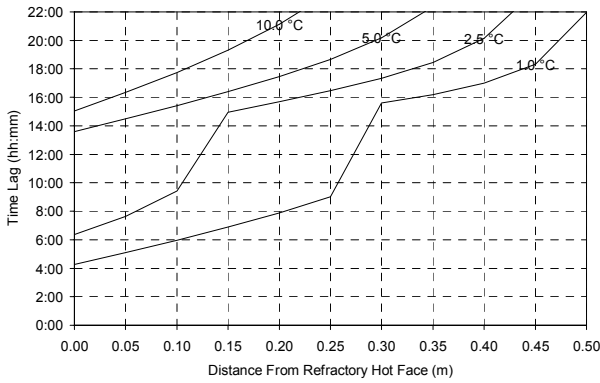
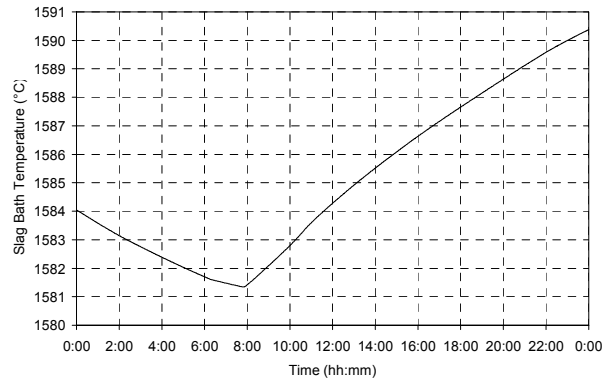
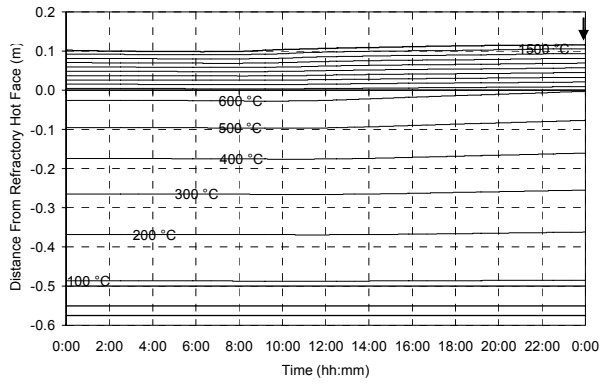
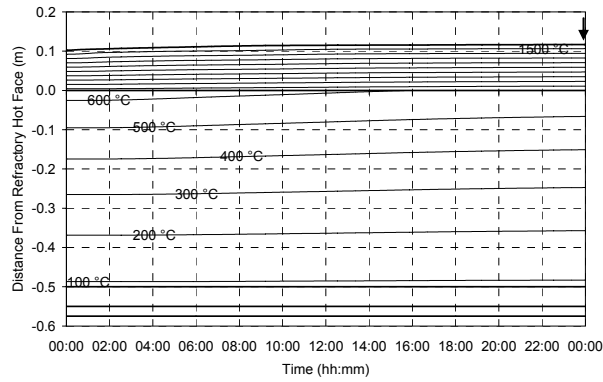


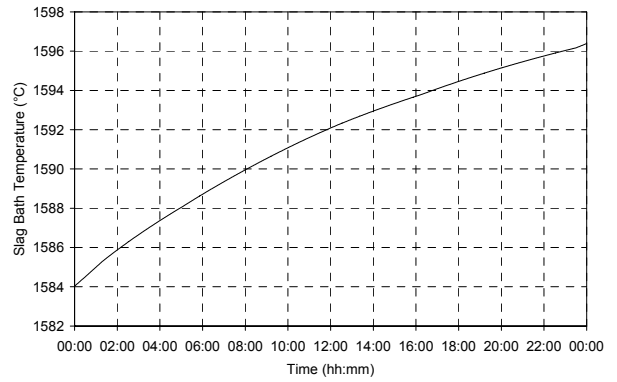
Figure 112 – Experiment 7.22 results.

7.3.23 Experiment 7.23

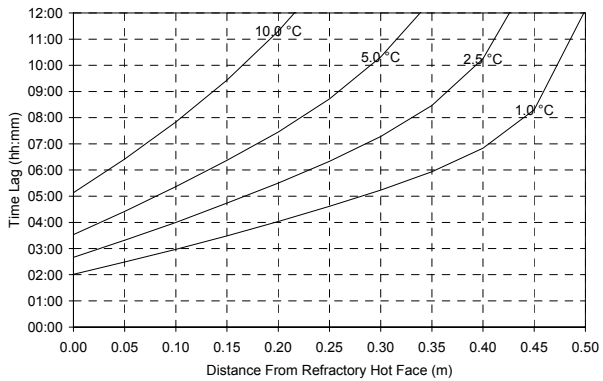
FEED COMPOSITION	%FeO	%TiO <sub>2</sub>	%Ti <sub>2</sub> O <sub>3</sub>	NEW SLAG FEED RATE	SLAG RESIDENCE TIME
C	10.0	55.0	35.0	14.4 t/h	16 h



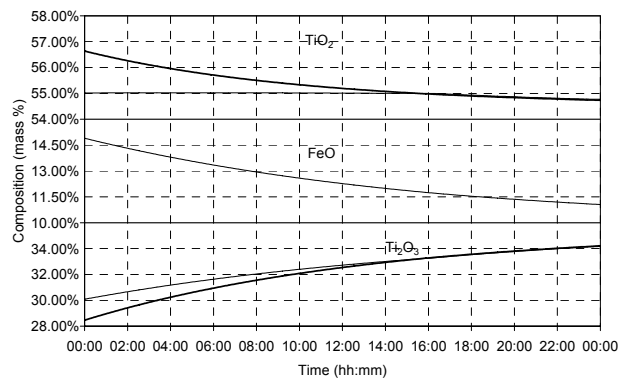
(a)



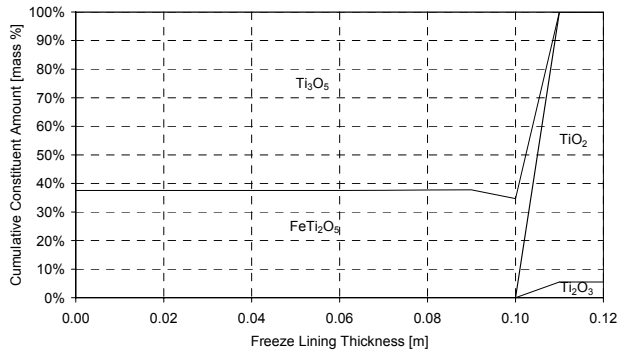
(b)



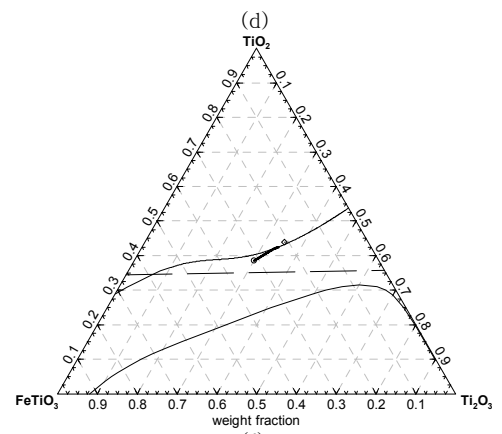
(c)



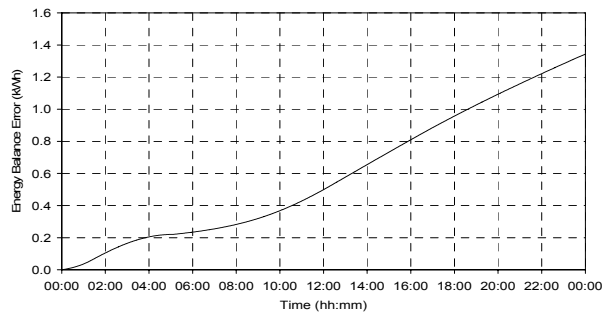
(d)



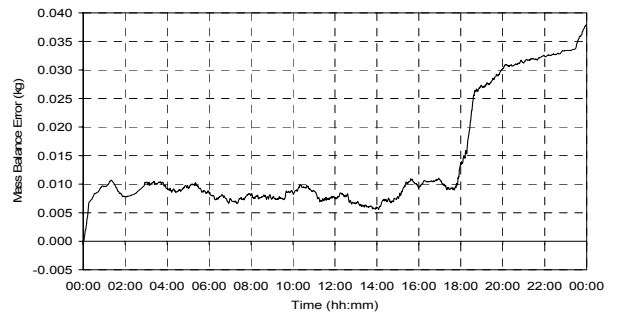
(e)



(f)



(g)



(h)

Figure 113 – Experiment 7.23 results.

7.3.24 Experiment 7.24

FEED COMPOSITION	%FeO	%TiO <sub>2</sub>	%Ti <sub>2</sub> O <sub>3</sub>	NEW SLAG FEED RATE	SLAG RESIDENCE TIME
D	20.0	55.0	25.0	14.4 t/h	16 h

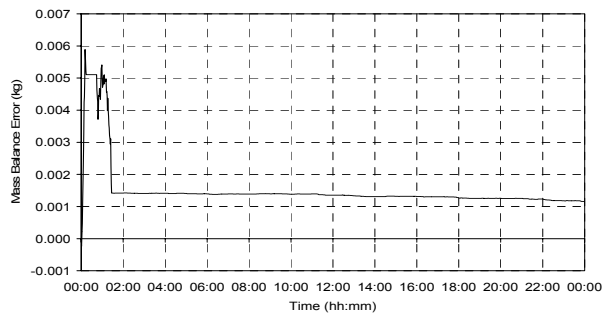
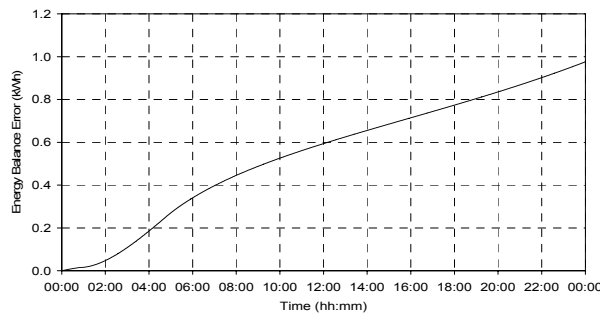
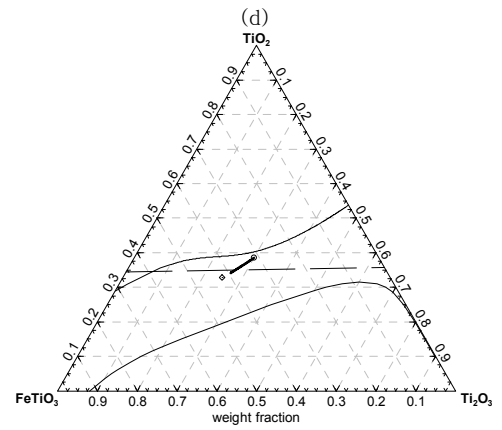
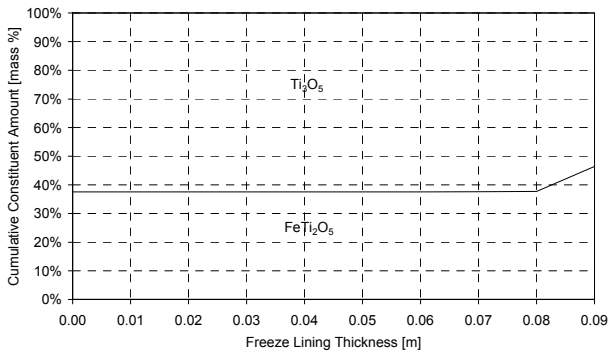
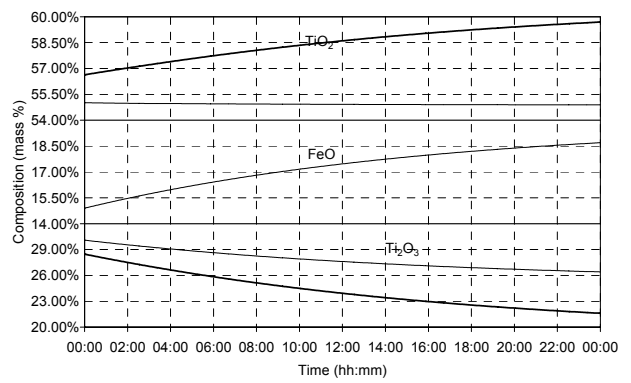
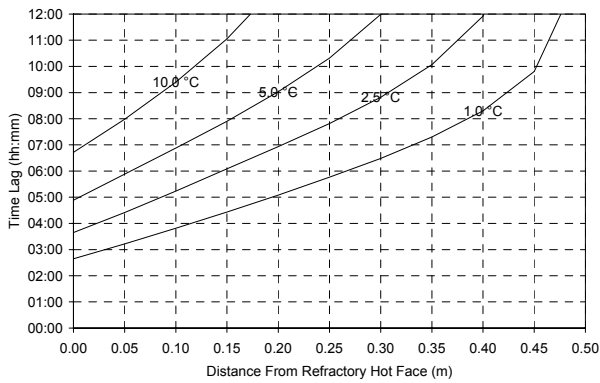
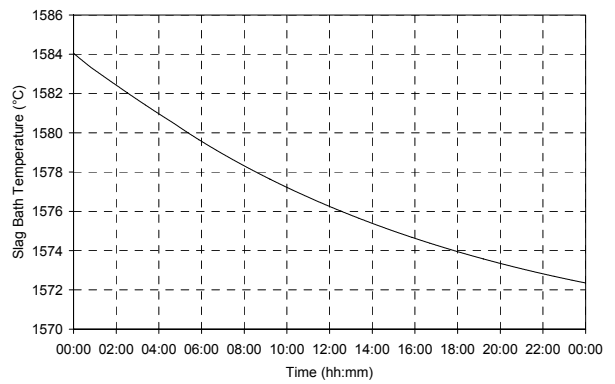
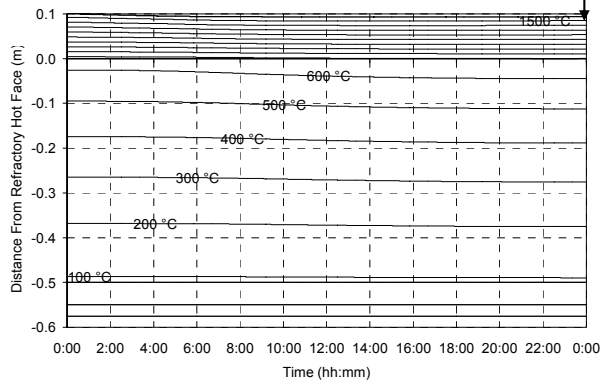


Figure 114 – Experiment 7.24 results.



7.3.25 Experiment 7.25

FEED COMPOSITION	%FeO	%TiO <sub>2</sub>	%Ti <sub>2</sub> O <sub>3</sub>	NEW SLAG FEED RATE	SLAG RESIDENCE TIME
E	10.0	60.0	30.0	14.4 t/h	16 h

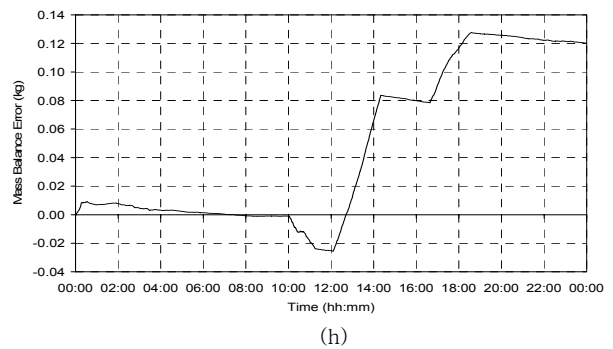
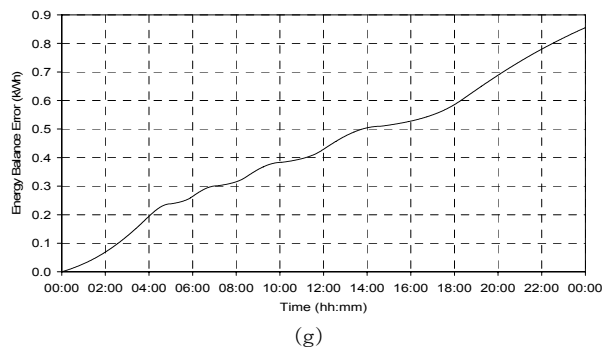
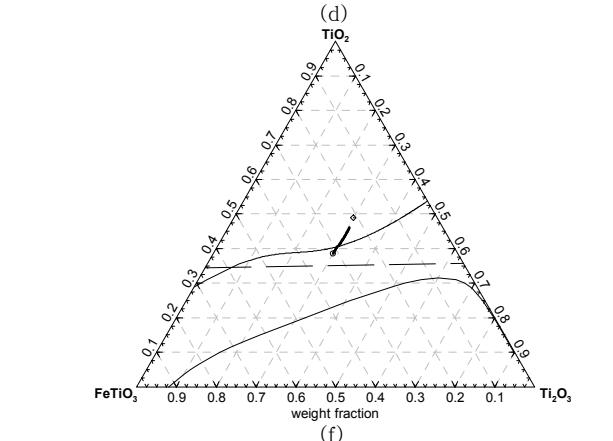
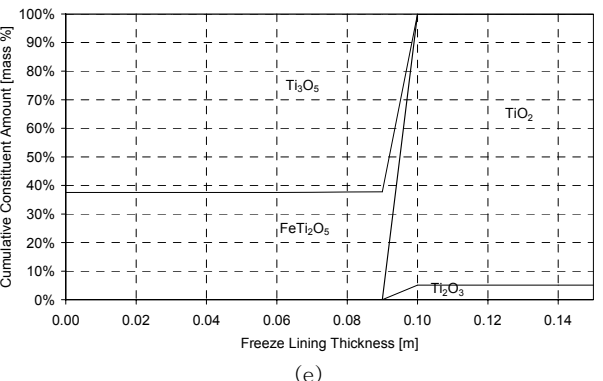
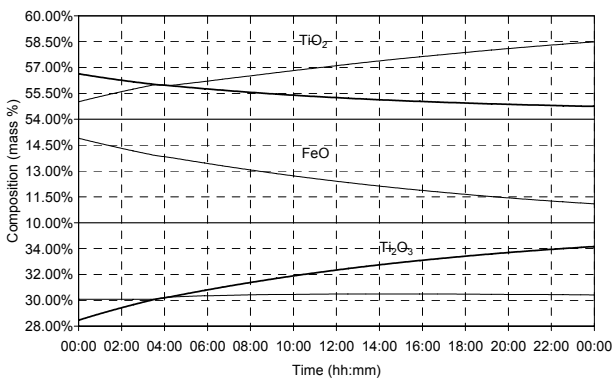
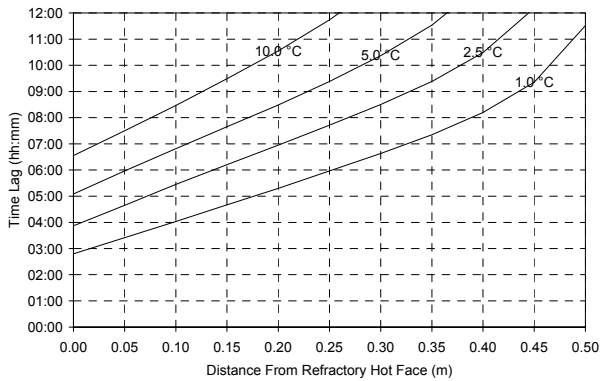
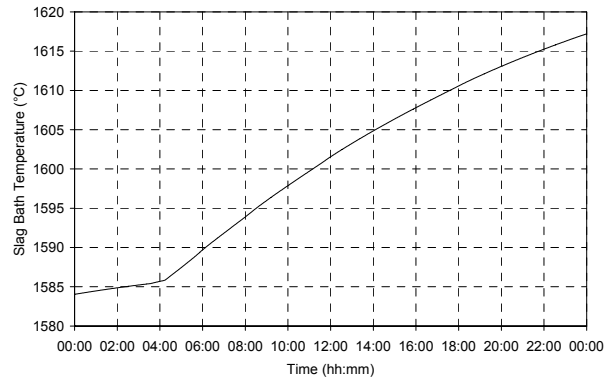
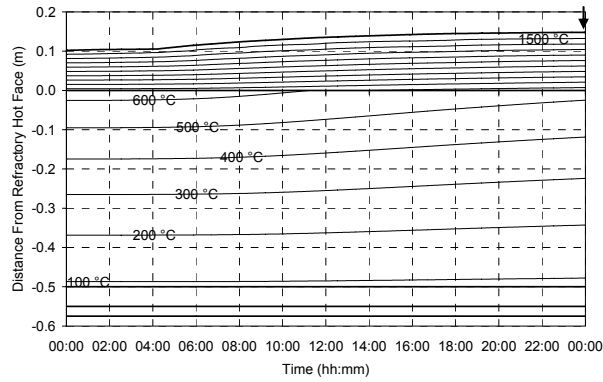


Figure 115 – Experiment 7.25 results.

7.3.26 Experiment 7.26

FEED COMPOSITION	%FeO	%TiO <sub>2</sub>	%Ti <sub>2</sub> O <sub>3</sub>	NEW SLAG FEED RATE	SLAG RESIDENCE TIME
F	20.0	50.0	30.0	14.4 t/h	16 h

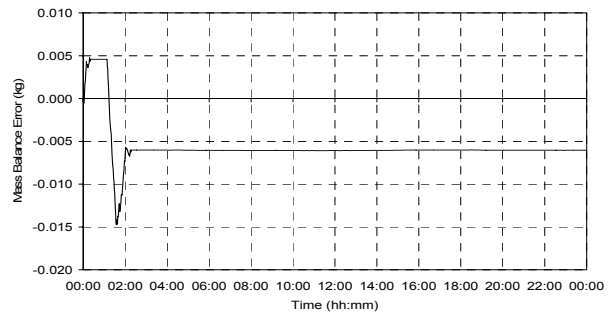
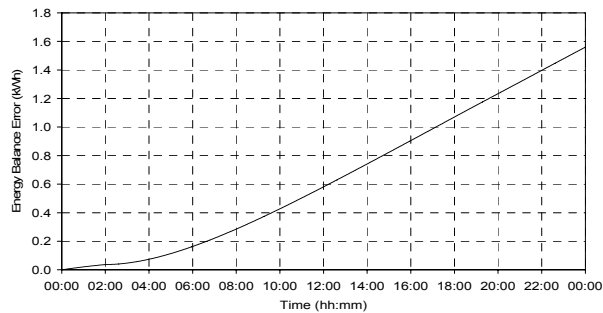
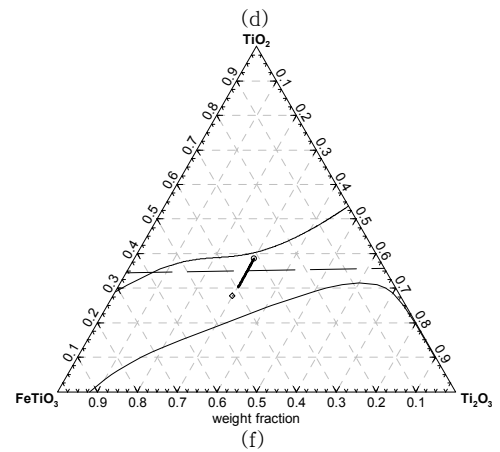
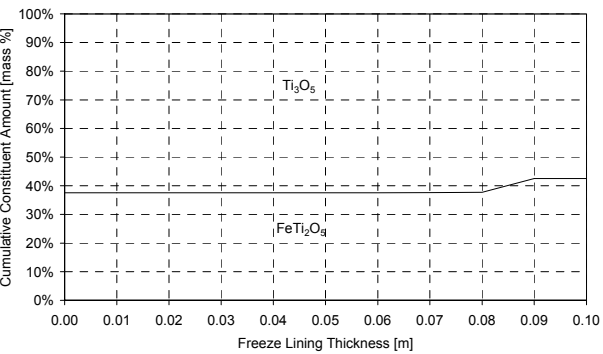
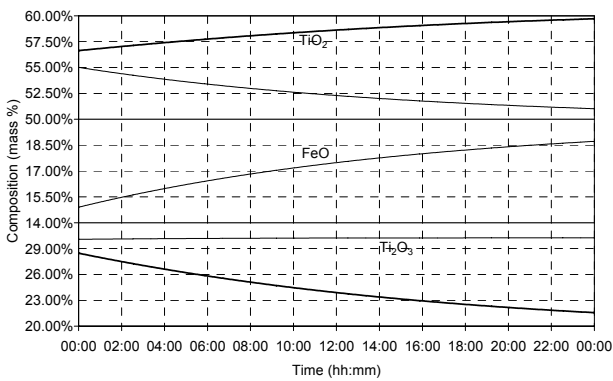
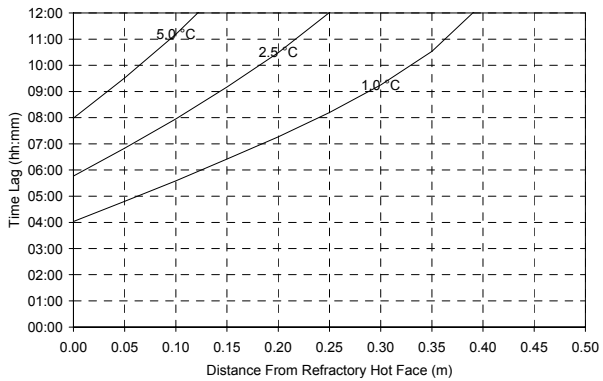
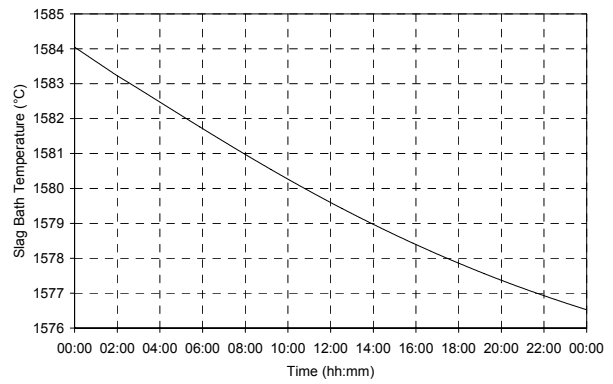
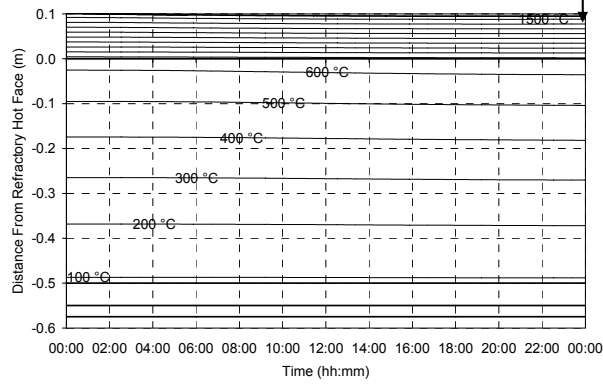
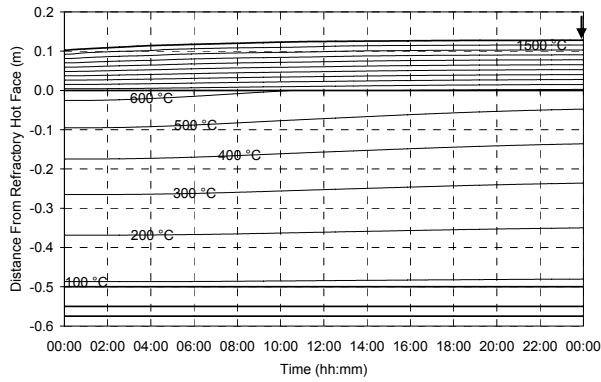


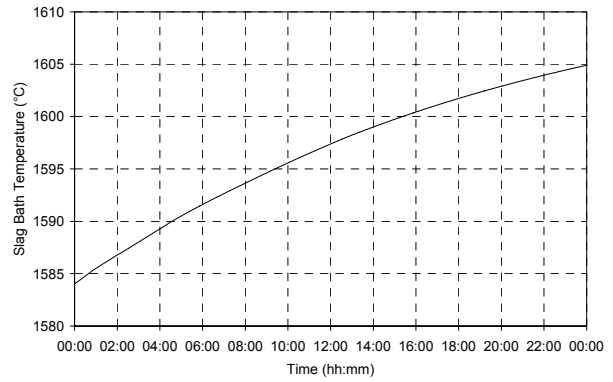
Figure 116 – Experiment 7.26 results.

7.3.27 Experiment 7.27

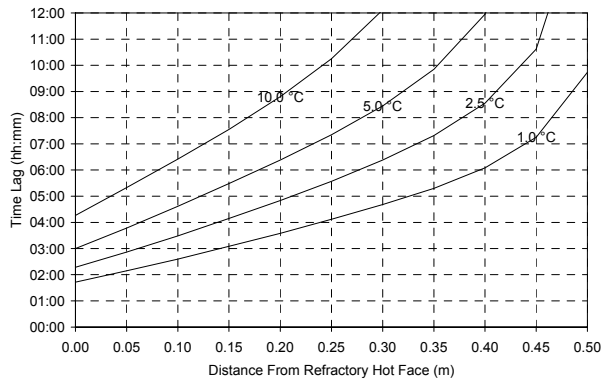
FEED COMPOSITION	%FeO	%TiO <sub>2</sub>	%Ti <sub>2</sub> O <sub>3</sub>	NEW SLAG FEED RATE	SLAG RESIDENCE TIME
G	10.0	50.0	40.0	14.4 t/h	16 h



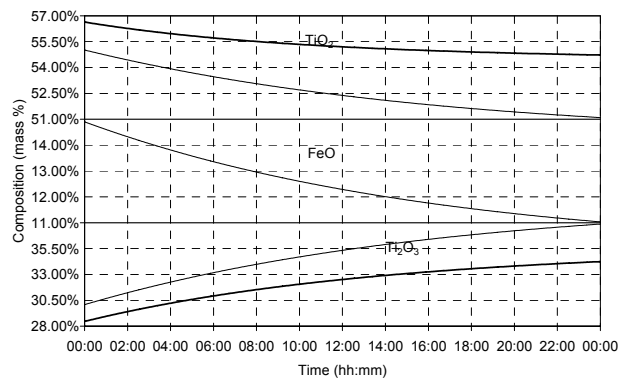
(a)



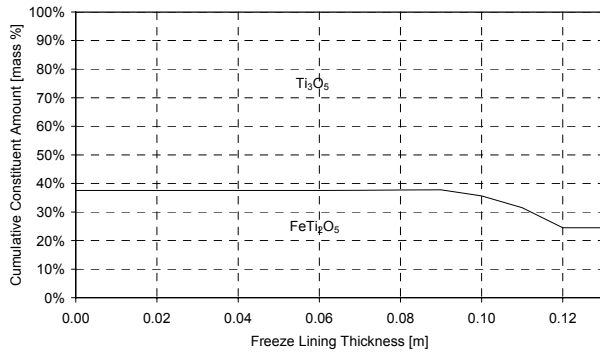
(b)



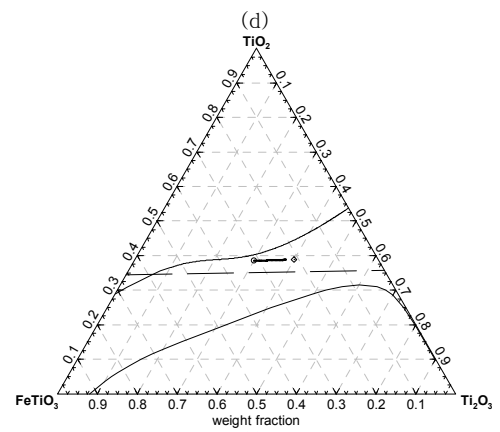
(c)



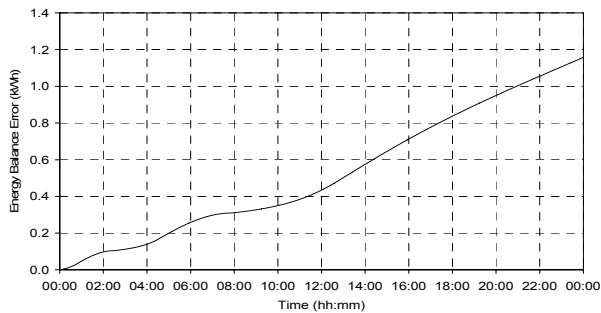
(d)



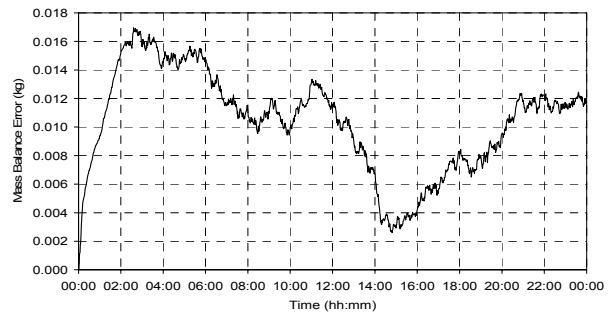
(e)



(f)



(g)



(h)

Figure 117 – Experiment 7.27 results.

7.3.28 Experiment 7.28

FEED COMPOSITION	%FeO	%TiO <sub>2</sub>	%Ti <sub>2</sub> O <sub>3</sub>	NEW SLAG FEED RATE	SLAG RESIDENCE TIME
H	20.0	60.0	20.0	14.4 t/h	16 h

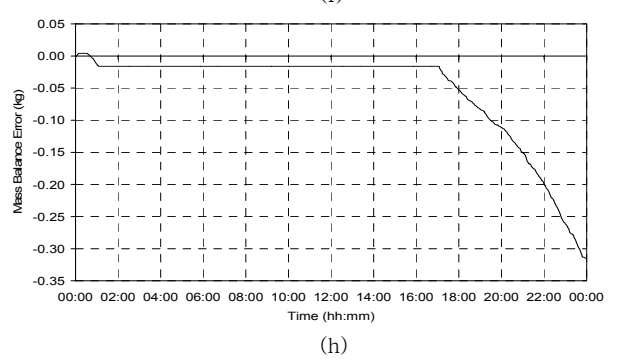
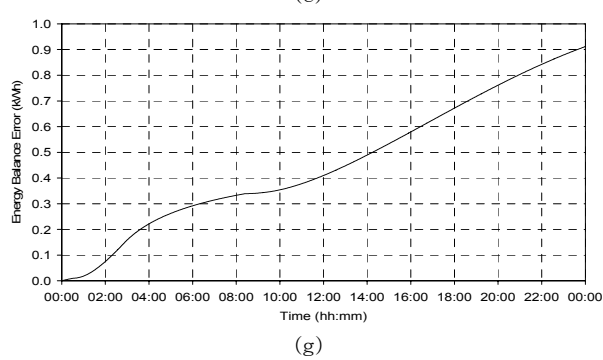
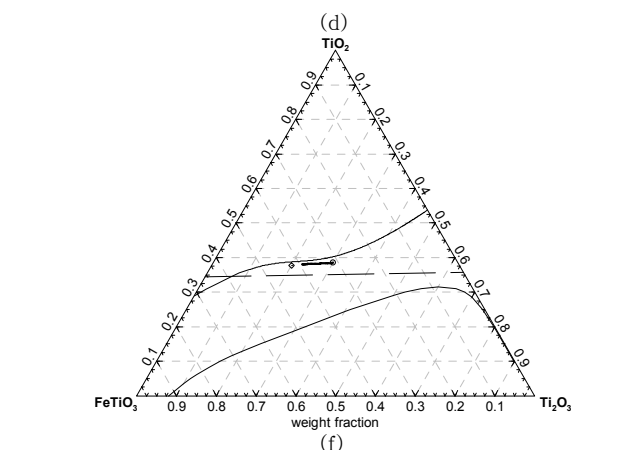
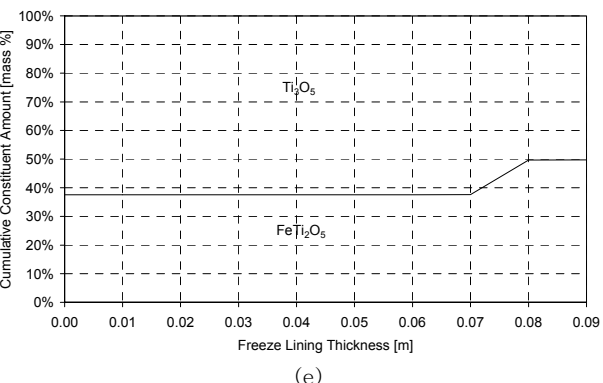
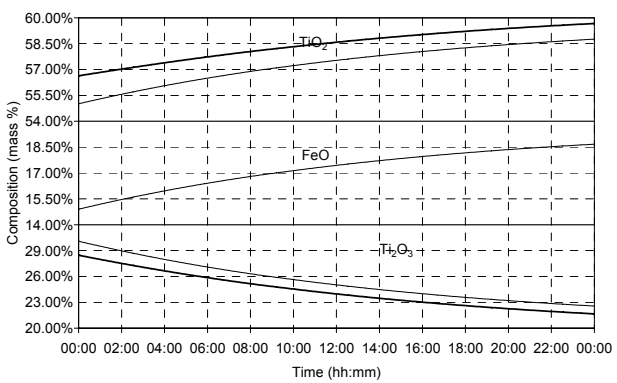
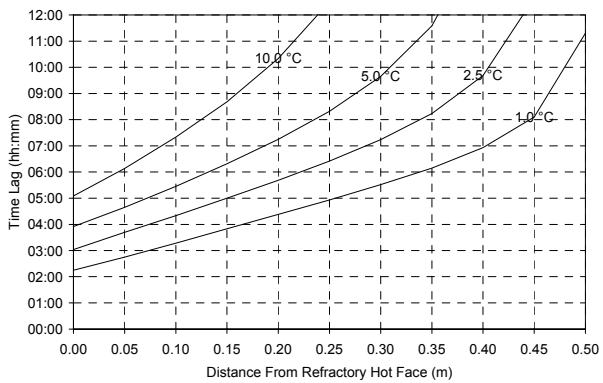
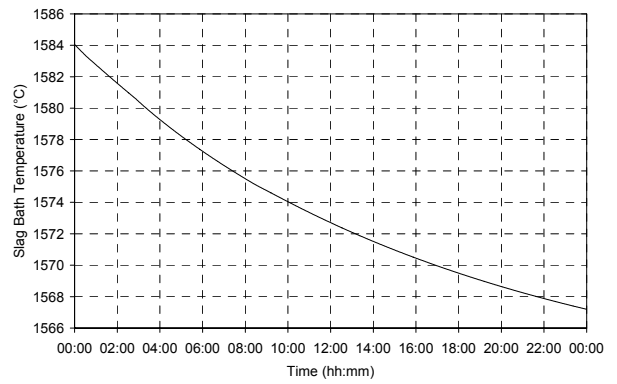
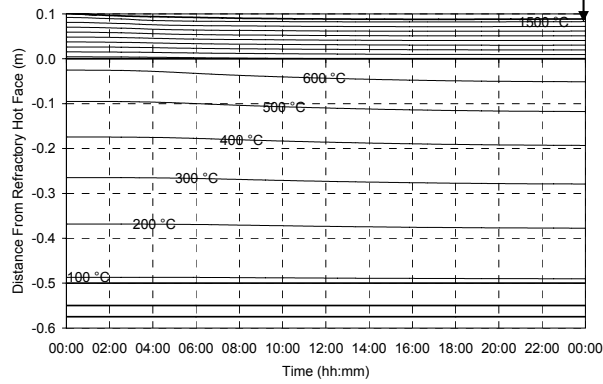
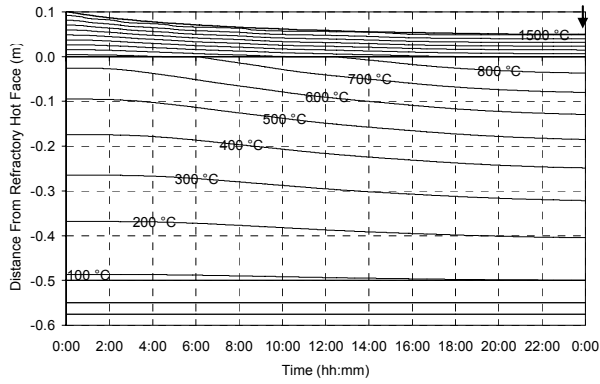


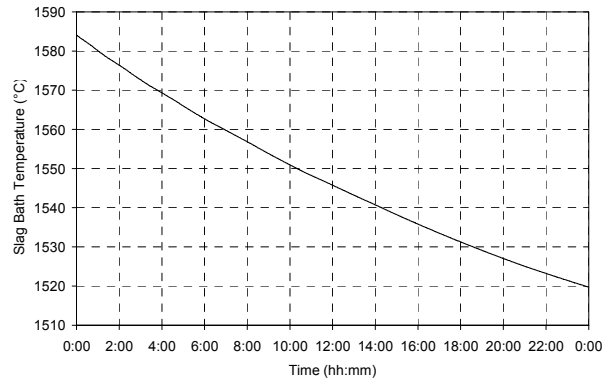
Figure 118 – Experiment 7.28 results.

7.3.29 Experiment 7.29

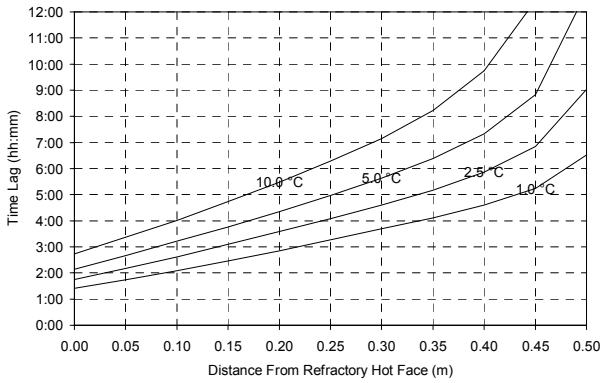
FEED COMPOSITION	%FeO	%TiO <sub>2</sub>	%Ti <sub>2</sub> O <sub>3</sub>	NEW SLAG FEED RATE	SLAG RESIDENCE TIME
I	35.5	59.5	5.0	14.4 t/h	16 h



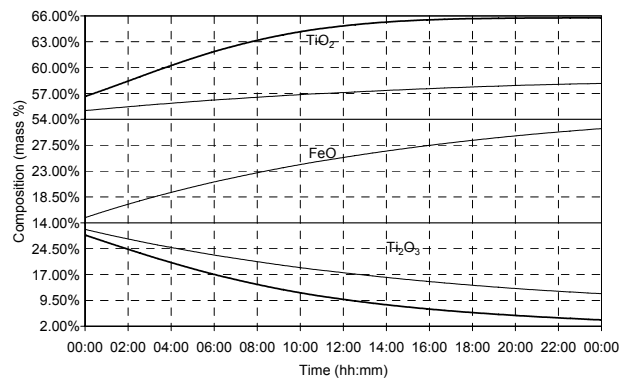
(a)



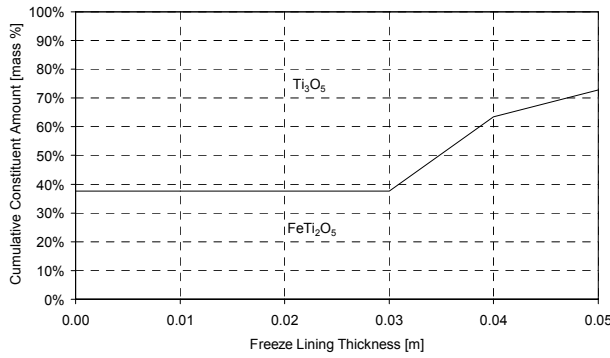
(b)



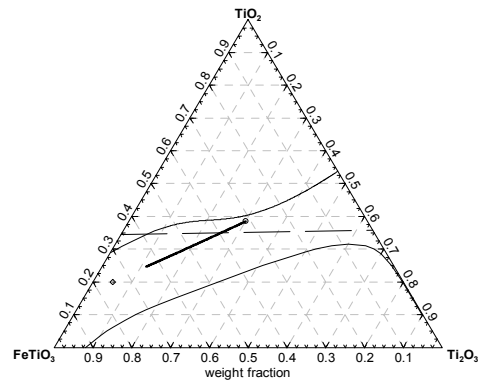
(c)



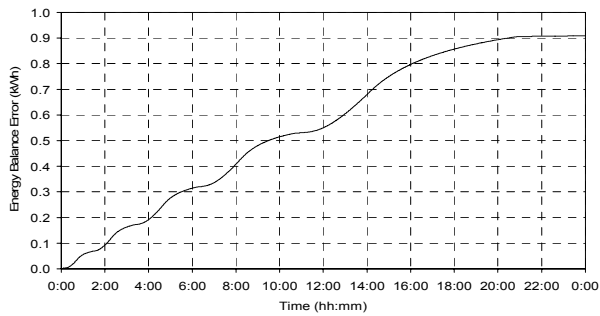
(d)



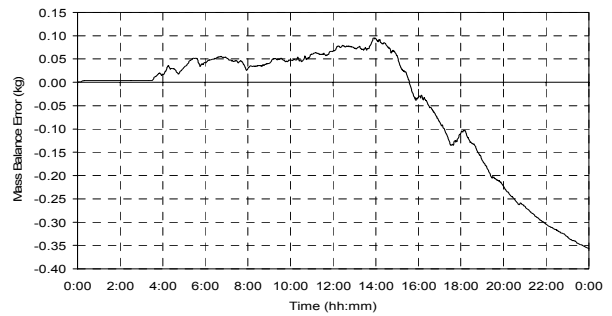
(e)



(f)



(g)

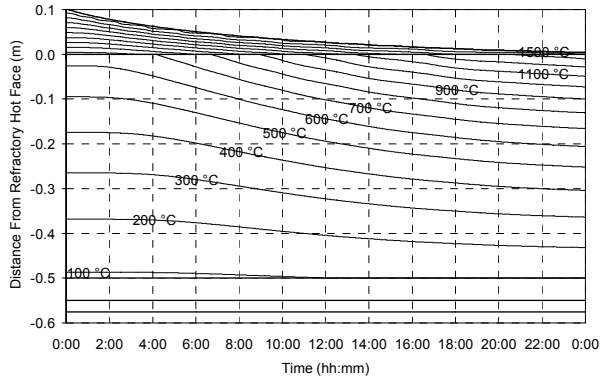


(h)

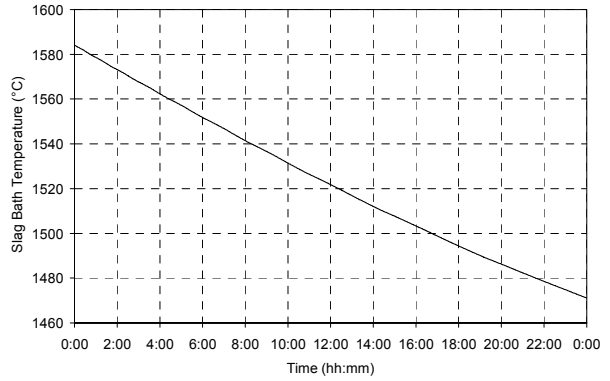
Figure 119 – Experiment 7.29 results.

7.3.30 Experiment 7.30

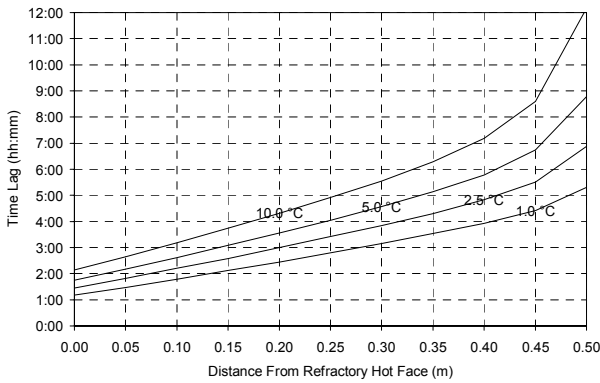
FEED COMPOSITION	%FeO	%TiO <sub>2</sub>	%Ti <sub>2</sub> O <sub>3</sub>	NEW SLAG FEED RATE	SLAG RESIDENCE TIME
J	pure stoichiometric ilmenite			14.4 t/h	16 h



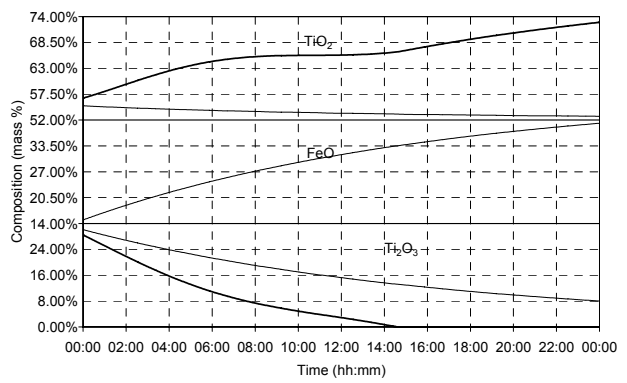
(a)



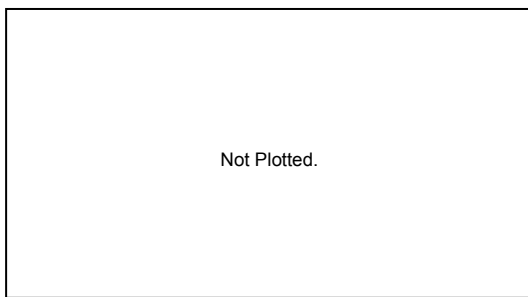
(b)



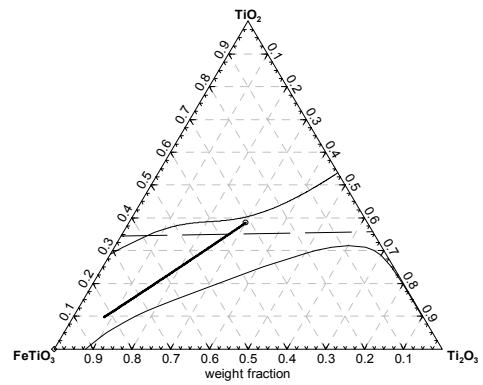
(c)



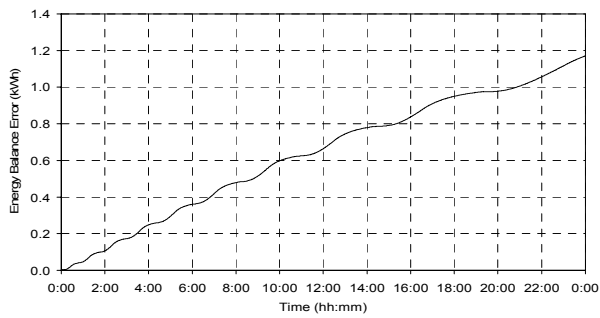
(d)



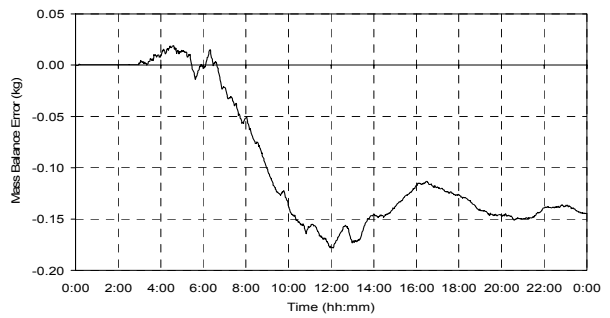
(e)



(f)



(g)



(h)

Figure 120 – Experiment 7.30 results.

## 7.4 DISCUSSION

One of the objectives of the set of experiments was to isolate the influence of slag composition on the interaction between slag bath and freeze lining as much as possible so that it can be studied clearly. Because heat transfer plays such a significant role in the system being considered in this chapter, its influence could not be completely removed from the experiments conducted. This is clear from the experimental results, especially in those of experiments 7.1 to 7.10 where the slag feed rate was set extremely high.

Before discussing the results in detail, the expected behaviour of the system must be considered. New liquid slag with composition different from the initial composition of the slag bath is fed into the system. The slag is ideally mixed in the SlagBath mixer and then extracted by the SlagTap material output module. The expected behaviour of such a system is that the composition of the slag bath will ultimately become equal to the composition of the new slag being fed. As a result of the changing slag composition, the liquidus temperature of the slag should change according to the liquidus surface of the system (as shown in Figure 11 on page 23) while its composition is moving from the initial to the new slag composition. The changing state of the slag bath should therefore influence the interface between the freeze lining and slag bath in two ways.

Firstly there is a thermal influence. It is expected, purely from heat transfer considerations, that the freeze lining will grow thicker when the slag bath temperature increases, and thinner when the slag bath temperature decreases. This statement takes into account that the slag bath temperature is always very nearly equal to the slag's liquidus temperature, that slag is fed at the current bath temperature, and that the power input into the system was kept constant at 250 kW. Hotter slag thus implies a lower rate of heat loss.

The second influence is a chemical one. The changing composition of the slag bath changes the compositional combination of solid slag and liquid slag that are present at the interface between the freeze lining and slag bath. If the composition of the new slag being fed is decreasing the liquidus temperature of the slag, the liquidus temperature of the combination of material at the interface is also likely to drop. This will result in solid slag being dissolved in the slag bath and in a thinner freeze lining. The opposite is expected if the liquidus temperature of the slag bath is increased by the new slag being fed.

It is therefore expected – based on both thermal and compositional considerations – that an increase in slag bath temperature will be associated with an increase in freeze lining thickness, and a decrease in slag bath temperature will be associated with thinner freeze lining to become thinner.

### 7.4.1 Freeze Lining Thickness

In most of the experiments, the above-mentioned expected influence of the new slag on freeze lining thickness was observed. The best examples are the results of experiments 7.2, 7.12 and 7.22. In these experiments the slag bath liquidus temperature first dropped as the composition approached the eutectic groove, and then started to rise after the eutectic groove had been crossed. As expected, the freeze lining thickness first decreased slightly and then became thicker.

The results of experiments 7.4 and 7.8 (and, to a lesser extent, experiments 7.6, 7.9, 7.14 and 7.16) appeared to display behaviour contrary to what was expected. Generally in these cases, a slight decrease followed by an increase in freeze lining thickness was observed even though the slag bath temperature decreased by 15 to 20 °C. It is not clear what the reason for this is, but it is likely related to the sharp increase in FeO content of the slag in all of these cases, which causes the slag liquidus temperature to drop. There is also an effect of the time lag in heat transfer changes, as discussed below.

Also of interest are cases (7.3, 7.5 and 7.7) where the freeze lining, in line with expectations, became thicker, but after some time started to become thinner. The origin of opposite trends with time (7.4, 7.6, 7.8 and 7.9) is likely to be related. The cases mentioned are all from the first subset where the highest feed rate was used. The same tendencies were either less pronounced or not present at all in the results of corresponding experiments executed with lower slag feed rates.

The reason for the observed increase and subsequent decrease in freeze lining thickness as well as the opposite behaviour is the difference in the dynamics of the thermal and chemical influences identified above. Because of the slag bath being well-mixed, the chemical influence of liquid slag on the freeze lining causes the freeze lining to grow thicker or thinner virtually immediately when a compositional change takes place. The thermal influence, however, is subject to the inertia of heat transfer through the furnace wall and freeze lining.

Experiment 7.5 is used as an example. The new slag used in this experiment has a liquidus temperature that is about 45 °C higher than the initial slag. The temperature of the slag bath immediately started increasing once the new slag was introduced. As expected, the freeze lining thickness also started to increase. The increase in thickness continued for 10 hours and then started decreasing. Heat transfer stepped in and resulted in the decrease in freeze lining thickness. The reason is that the freeze lining thickness that had been established after 10 hours could not conduct heat out of the system at the rate of 250 kW that was used as an energy input into the system. The freeze lining started to become thinner to again establish a heat transfer steady state in which the 250 kW input is conducted out of the system through the freeze lining and furnace wall.

Experiment 7.9 is another clear example. In this case, however, the freeze lining first became thinner due to the chemical influence of the slag bath, and then grew thicker to establish a heat transfer configuration that could remove 250 kW from the system.

### **7.4.2 Thermal Response of Freeze Lining and Furnace Wall**

Because the freeze lining thickness changed very little in many of the experiments, and because it often both increased and decrease, the same type of analysis that was done in paragraph 6.4.2 on the experimental results of CHAPTER 6 was not possible here. The reader is referred to paragraph 6.4.2 for a discussion on the thermal response of the freeze lining and furnace wall.

### **7.4.3 Slag Bath Composition**

The slag bath consistently displayed the expected behaviour in terms the change in its composition. In all cases the composition changed with virtually a straight line trajectory on the ternary graph (f) of the



experimental results. The slag bath reached the composition of the new slag in cases with high feed rates, and it was still approaching the new slag composition after 24 hours in cases where low feed rates were used.

In cases where the slag composition crossed the eutectic groove, the trajectory followed the eutectic groove for a period of time. When the average direction of the trajectory was roughly perpendicular to the eutectic groove, the slag composition followed the eutectic groove for only a short period of time. When the average direction was more parallel to the eutectic groove, the slag composition followed the groove for longer periods of time.

#### **7.4.4 Slag Bath Temperature**

The expected slag bath temperature changes were evident in the results of all the experiments. This temperature is simply a function of the slag bath composition, and it followed the liquidus temperature surface shown in Figure 11 on page 23.

#### **7.4.5 Freeze Lining Composition**

The freeze lining consisted of pseudobrookite as the only phase for most of the cases (new slag compositions A, D, F, G, H, I, J) since these slag composition in these cases were below the eutectic groove. This resulted in pseudobrookite being the primary solidification phase. In a few of the cases (new slag compositions B, C and E) the slag bath composition crossed over the eutectic groove. Once this happened, rutile became the primary solidification phase. This behaviour can be clearly seen on graph (e) of the results of the various experiments.

## CHAPTER 8

### THE DYNAMIC PROCESS RESPONSE TO STEP CHANGES IN FURNACE OPERATING PARAMETERS

This chapter describes a series of experiments conducted with the ISFP model. The purpose of these experiments was to study the influence of step changes in furnace operating parameters on the dynamic behaviour of the furnace wall, freeze lining, crust and slag bath. The focus was on the following aspects:

- Freeze lining and crust thickness.
- Temperature distribution through the furnace wall, freeze lining and crust.
- Time lag in temperature response of the refractory brick wall relative to the time when conditions changed in the slag bath.
- Liquid slag temperature.
- Composition distribution through the freeze lining and crust.
- Liquid slag composition.

In addition to the above list, metal bath composition data, off-gas composition data, heat loss data and reactor power data are also presented to provide a comprehensive set of results for each experiment.

#### 8.1 EXPERIMENTAL SETUP

The model flow diagram used for all experiments in this chapter is shown in Figure 58 (page 116). The geometry and dimensions used are all the same as those given in paragraph 5.3.1 (page 90).

A single steady state was generated and used for all experiments conducted in this chapter. The details of this steady state are as follows:

- Inputs
  - ElectricalPower: 21,715 kW
  - IlmeniteFeed: 20,000 kg/h
  - ReductantFeed: 1,700 kg/h
- Contents
  - IsoMod1:
    - Temperature: 1,589 °C
  - SlagBath:
    - Mass: 225,859 kg
    - Composition: 14.7-54.0-31.9 (FeO-TiO<sub>2</sub>-Ti<sub>2</sub>O<sub>3</sub> mass percentages)
  - MetalBath:
    - Mass: 323,002 kg
    - Composition: 2 mass percent carbon. Trace amounts of O, Ti and TiO. Balance as Fe.
  - ReductantInBath:
    - Mass: 52.4 kg
  - FurnaceFreeboard:
    - Mass: 30.9 kg
    - Composition: 98.8-1.2 (CO-CO<sub>2</sub> volume percentages)
  - FurnaceWall:
    - Freeze lining thickness: 76.3 mm
    - Freeze lining mass: 7,992 kg
  - Crust:
    - Crust thickness: 0 mm
- Outputs
  - HeatLoss1: 161.5 kW
  - HeatLoss2: 434.8 kW

- FurnaceWall: 280 kW
- Crust: 2,631 kW
- SlagTap: 11,842 kg/h
- MetalTap: 6,151 kg/h
- Offgas: 3,707 kg/h

The effective thermal conductivity of the liquid slag was assumed to be 0.005 kW/(m.°C).

All experiments were run for a period of 24 hours, or until the freeze lining had been melted away completely.

## 8.2 EXPERIMENTS

The parameters that were varied over the series of experiments include the following:

- Ilmenite feed rate.
- Reductant feed rate.
- Electrical power.

The set of experiments with the various parameters of interest to each experiment are listed in Table 23 below. The set of 20 experiments consists of 4 subsets.

EXPERIMENT NO.	ILMENITE FEED RATE CHANGE	ILMENITE FEED RATE	REDUCTANT FEED RATE CHANGE	REDUCTANT FEED RATE	ELECTRICAL POWER CHANGE	ELECTRICAL POWER
8.1	-20,000 kg/h	0 kg/h	-1,700 kg/h	0 kg/h	-	21,715 kW
8.2	-	20,000 kg/h	-1,700 kg/h	0 kg/h	-	21,715 kW
8.3	-	20,000 kg/h	+ 1 kg/t ilm.	1,720 kg/h	-	21,715 kW
8.4	-	20,000 kg/h	-1 kg/ton ilm.	1,680 kg/h	-	21,715 kW
8.5	-	20,000 kg/h	+ 2 kg/ton ilm.	1,740 kg/h	-	21,715 kW
8.6	-	20,000 kg/h	-2 kg/ton ilm.	1,660 kg/h	-	21,715 kW
8.7	-	20,000 kg/h	-	1,700 kg/h	+ 5 kWh/ton ilm.	21,815 kW
8.8	-	20,000 kg/h	-	1,700 kg/h	-5 kWh/ton ilm.	21,615 kW
8.9	-	20,000 kg/h	-	1,700 kg/h	+ 10 kWh/ton ilm.	21,915 kW
8.10	-	20,000 kg/h	-	1,700 kg/h	-10 kWh/ton ilm.	21,515 kW
8.11	-	20,000 kg/h	+ 1 kg/ton ilm.	1,720 kg/h	+ 5 kWh/ton ilm.	21,815 kW
8.12	-	20,000 kg/h	-1 kg/ton ilm.	1,680 kg/h	-5 kWh/ton ilm.	21,615 kW
8.13	-	20,000 kg/h	+ 2 kg/ton ilm.	1,740 kg/h	+ 10 kWh/ton ilm.	21,915 kW
8.14	-	20,000 kg/h	-2 kg/ton ilm.	1,660 kg/h	-10 kWh/ton ilm.	21,515 kW
8.15	-	20,000 kg/h	+ 5 kg/ton ilm.	1,800 kg/h	+ 25 kWh/ton ilm.	22,215 kW
8.16	-	20,000 kg/h	-5 kg/ton ilm.	1,600 kg/h	-25 kWh/ton ilm.	21,215 kW
8.17	-	20,000 kg/h	+ 10 kg/ton ilm.	1,900 kg/h	+ 50 kWh/ton ilm.	22,715 kW
8.18	-	20,000 kg/h	-10 kg/ton ilm.	1,500 kg/h	-50 kWh/ton ilm.	20,715 kW
8.19	-	20,000 kg/h	+ 10 kg/ton ilm.	1,900 kg/h	+ 52 kWh/ton ilm.	22,755 kW
8.20	-	20,000 kg/h	-10 kg/ton ilm.	1,500 kg/h	-53 kWh/ton ilm.	20,655 kW

Table 23 – List of experiments conducted for CHAPTER 8.

The first subset consists of experiments 8.1 and 8.2. The objective of these experiments was to investigate the influence of two severe operational errors on the process. In experiment 8.1 all feed was stopped while maintaining the initial power input. In experiment 8.2 only the reductant feed was stopped and the initial ilmenite feed rate and electrical power was maintained.

The second subset consists of experiments 8.3 to 8.10. The aim of these experiments was to determine the influence on the process of independent adjustment of the reductant feed rate and electrical power operating parameters. Increasing and decreasing adjustments were made to both operating parameters. It

was reported by Pistorius (1999) that energy and reductant inputs cannot be changed independently while maintaining stable process conditions. It was further suggested in that work that the ratio between reductant and energy change must be 1 kg:5 kWh. Therefore, each 1kg/(ton ilmenite) reductant change must be combined with a 5 kWh/(ton ilmenite) energy change. The second subset of experiments therefore ignored this suggestion. The impact of the changes were expected to be clear because the steady state initial condition used by all of the experiments represented stable operating conditions.

The third subset included experiments 8.11 to 8.18. These experiments aimed to test the validity of the 1 kg:5 kWh ratio proposed by Pistorius (1999). Experiments covered both increases and decreases in reductant and energy operating parameters. The magnitudes of the changes were also varied to study dynamic process responses further.

The results of the third subset showed excellent agreement with the 1:5 ratio proposed by Pistorius (1999). At large operating parameter changes the freeze lining thickness did however vary. In the fourth and last subset it was attempted to adjust the 1 kg:5 kWh ratio so that very little variation in freeze lining thickness occurred over the duration of the experiment.

### 8.3 EXPERIMENTAL RESULTS

The results from each experiment are presented below using a series of graphs marked from (a) to (n). The set of graphs is presented consistently for all experiments in this chapter. For this reason each graph type in the set is explained below. A discussion of the experimental results follows after the graphical presentation of the results of all experiments conducted as part of this chapter.

(a) Freeze Lining Thickness and Isotherm Graph

Refer to paragraph 6.3, item (a) on page 139 for details.

(b) Freeze Lining Composition Graph

This graph shows the composition of the freeze lining as a function of position within the freeze lining at the point in time when the freeze lining thickness was at its maximum.

The composition of the solid slag is presented by showing both the distribution of mass between phases (rutile and pseudobrookite), and by showing the distribution of mass between constituents of a specific phase. The phases are separated by a thick solid line, and the constituents within a phase are separated by a thin solid line. The rutile phase is always plotted in the lower part of the graph, and pseudobrookite above it.

Refer to paragraph 6.3, item (e) on page 140 for more details.

(c) Crust Thickness Graph

This graph shows the thickness of the solid slag crust as a function of time.

(d) Crust Composition Graph

This graph shows the composition of the crust as a function of crust thickness at the point in time when the crust thickness was at its maximum.

This graph is presented similarly to graph (b). Refer to that paragraph above for more details.

(e) Temperature Response Time Delay Graph

Refer to paragraph 6.3, item (c) on page 139 for details.

(f) Liquid Slag Temperature Graph

Refer to paragraph 6.3, item (b) on page 139 for details.

(g) Liquid Slag Composition Graph

Refer to paragraph 6.3, item (d) on page 140 for details.

(h) Liquid Slag Composition Ternary Graph

Refer to paragraph 6.3, item (f) on page 141 for details.

(i) Liquid Metal Composition Graph

This graph shows the variation (with time) of the liquid metal C, O and Ti content. Carbon content is expressed in mass percentage and oxygen and titanium content in parts per million (ppm) by mass.

(j) Off-gas Composition Graph

This graph shows the variation (with time) of off-gas composition. Firstly the CO and CO<sub>2</sub> contents are give in volume percentage. The bottom-most sub-graph shows the variation of the logarithm of the oxygen partial pressure.

(k) Reactor Power Graph

Each of the four reactors in the model flow sheet (Figure 58, page 116) describes one or more chemical reactions. The net enthalpy change calculated by the Gibbs-free-energy minimisation in each reactor is always endothermic. The power indicated on this graph is therefore the rate at which energy is consumed by each of the reactors.

(l) Heat Loss Graph

This graph presents time series heat loss data of the process. It consists of three sub-graphs. The 'Upper' sub-graph shows the sum of the Crust conductor module and HeatLoss1 energy output module heat losses. This represents all radiation and convection losses from the slag bath surface. The 'Middle' sub-graph shows the heat loss calculated by the FurnaceWall conductor module. This only describes heat lost through the portion of the sidewall that is covered by the freeze lining. The 'Lower' sub-graph shows the heat loss represented by the HeatLoss2 energy output module. This heat loss includes heat lost through the portion of the sidewalls below the freeze lining and heat lost through the furnace hearth.

(m) Energy Balance Error Graph

Refer to paragraph 6.3, item (g) on page 141 for details.

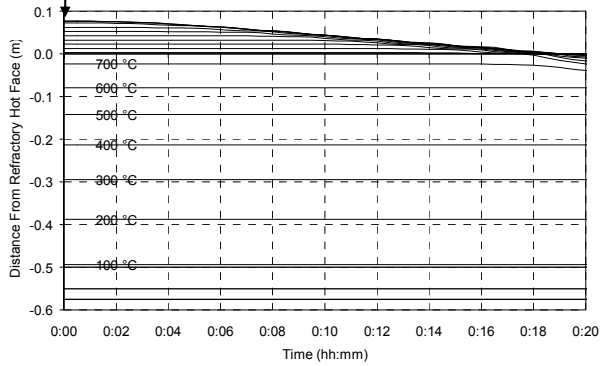
(n) Mass Balance Error Graph

Refer to paragraph 6.3, item (h) on page 142 for details.

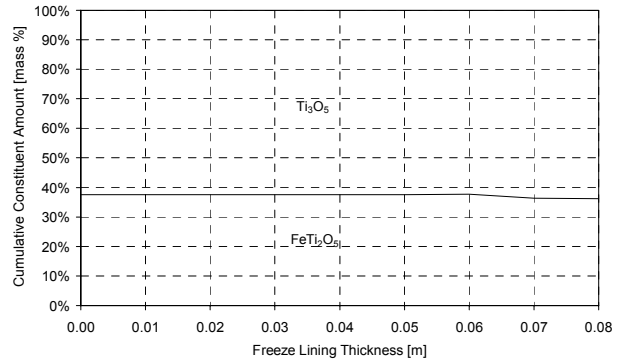
Fluctuations are present in many of the signals presented in graphs (i), (j) and (k). These fluctuations were caused by the method used to regulate the liquid slag composition close to the stoichiometric  $M_3O_5$  line. See paragraphs 5.6.8a (page 125) and 5.6.8b (page 129) for details about the approach used.

8.3.1 Experiment 8.1

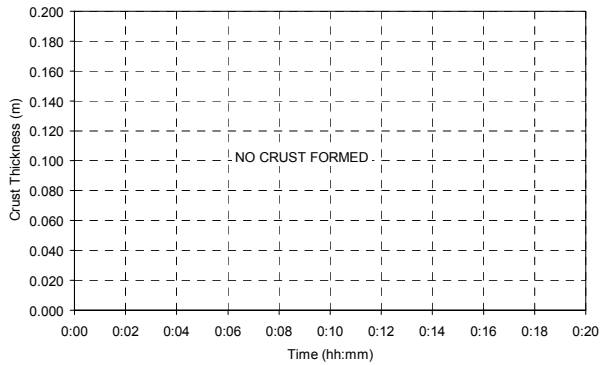
ILMENITE FEED RATE CHANGE	ILMENITE FEED RATE	REDUCTANT FEED RATE CHANGE	REDUCTANT FEED RATE	ELECTRICAL POWER CHANGE	ELECTRICAL POWER
-20,000 kg/h	0 kg/h	-1,700 kg/h	0 kg/h	-	21,715 kW



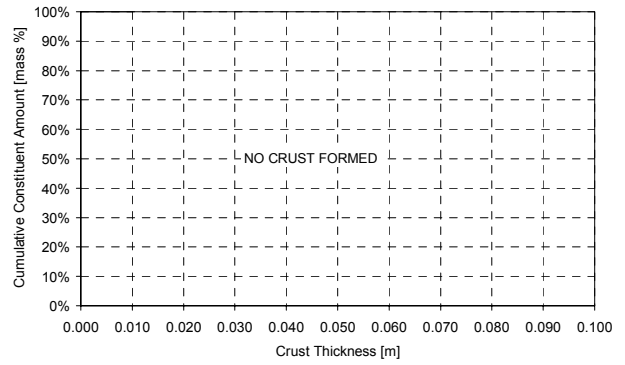
(a)



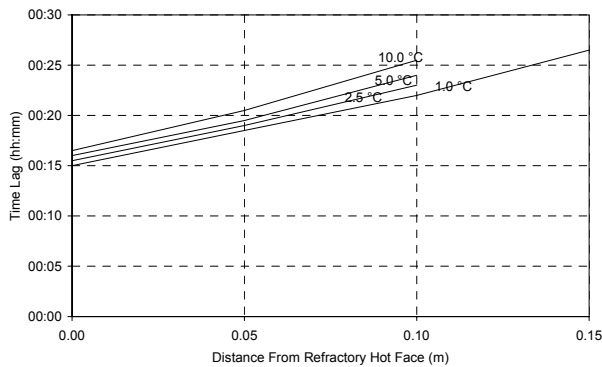
(b)



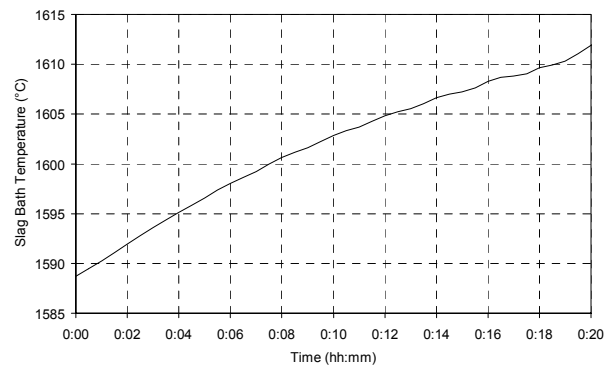
(c)



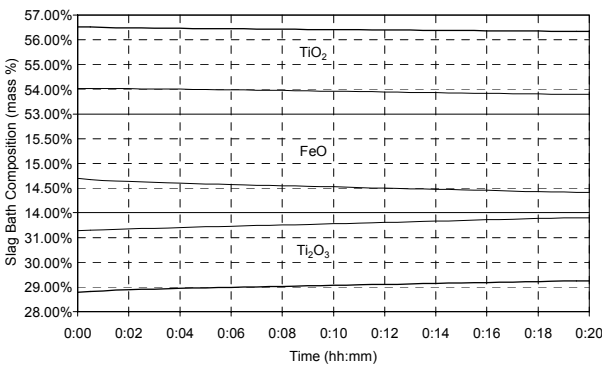
(d)



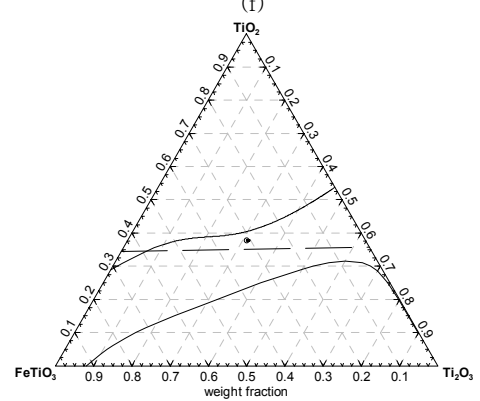
(e)



(f)



(g)



(h)

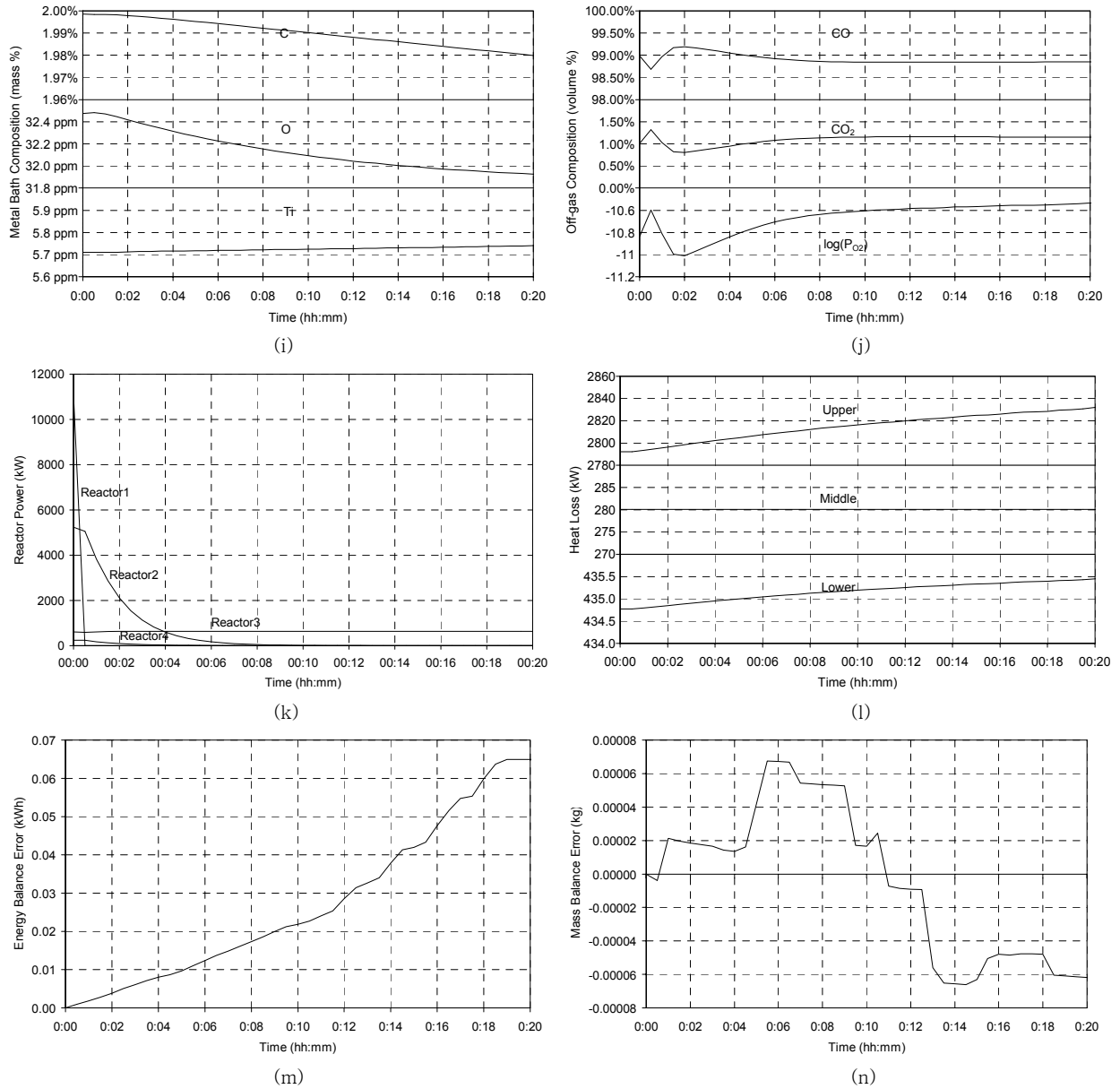
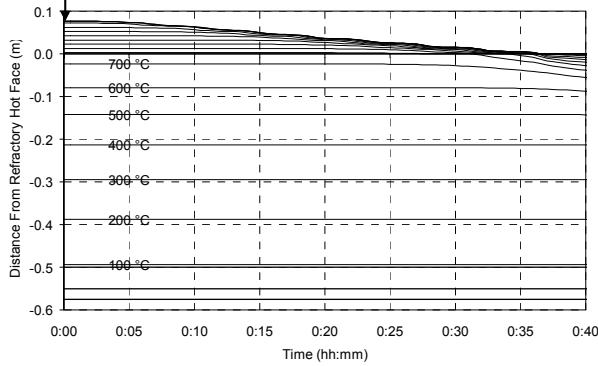


Figure 121 – Experiment 8.1 results.

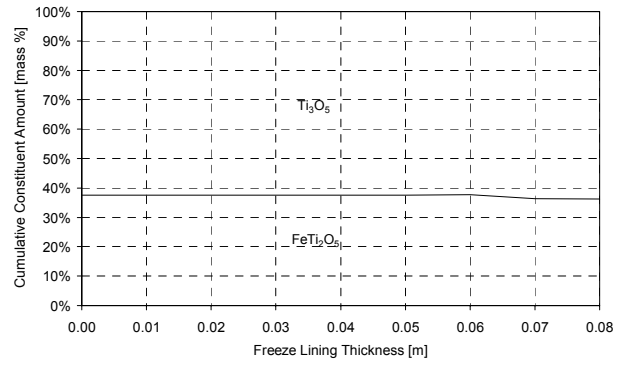


8.3.2 Experiment 8.2

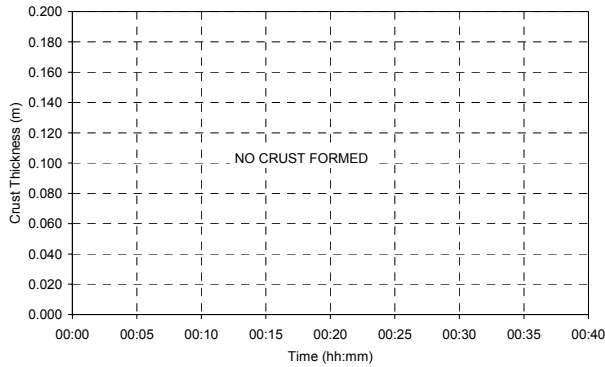
ILMENITE FEED RATE CHANGE	ILMENITE FEED RATE	REDUCTANT FEED RATE CHANGE	REDUCTANT FEED RATE	ELECTRICAL POWER CHANGE	ELECTRICAL POWER
-	20,000 kg/h	-1,700 kg/h	0 kg/h	-	21,715 kW



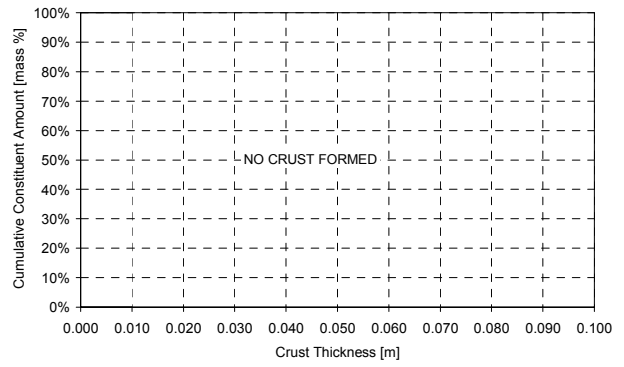
(a)



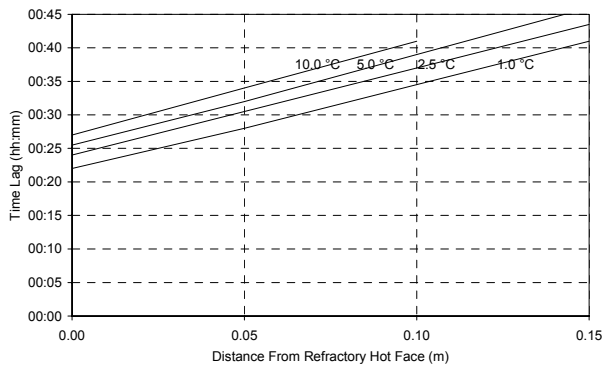
(b)



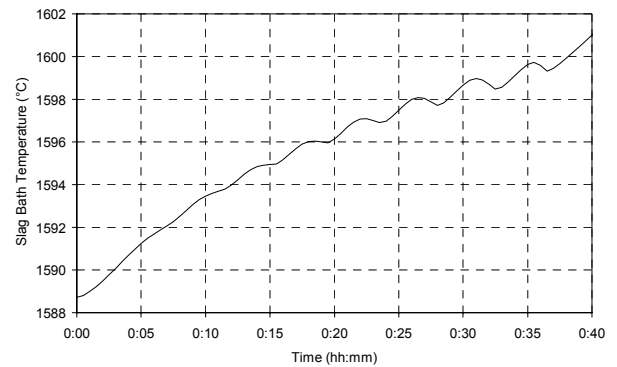
(c)



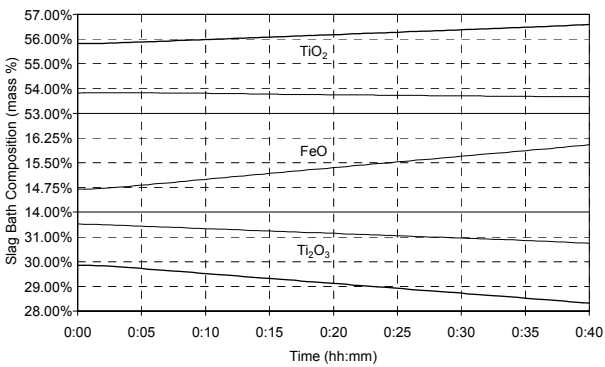
(d)



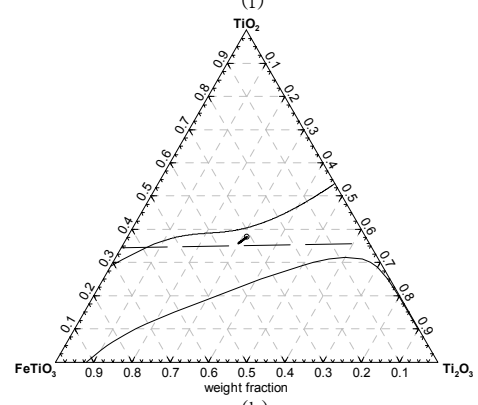
(e)



(f)



(g)



(h)

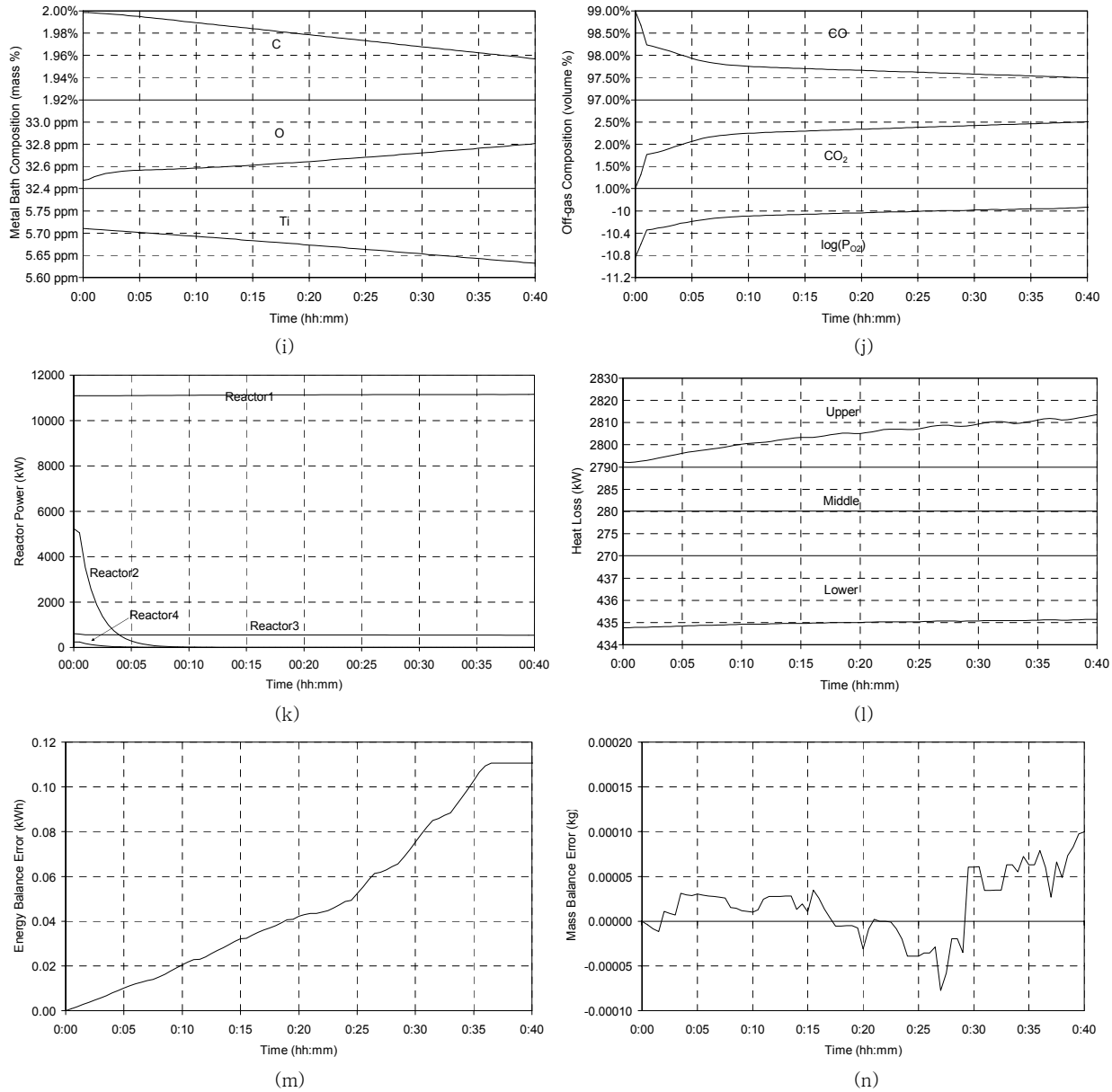
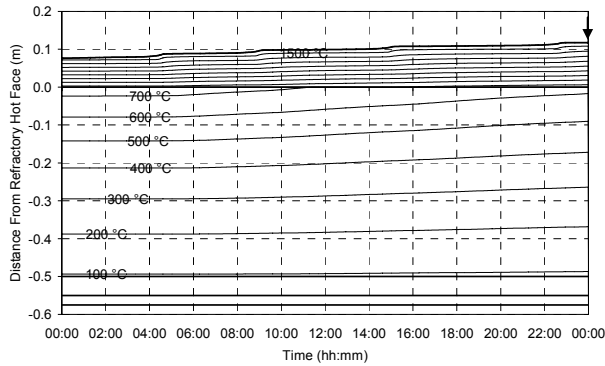


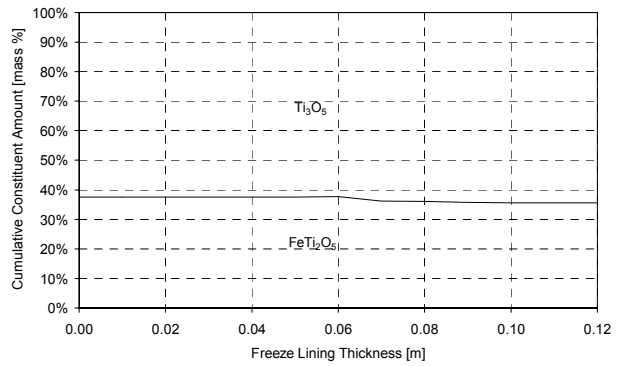
Figure 122 - Experiment 8.2 results.

8.3.3 Experiment 8.3

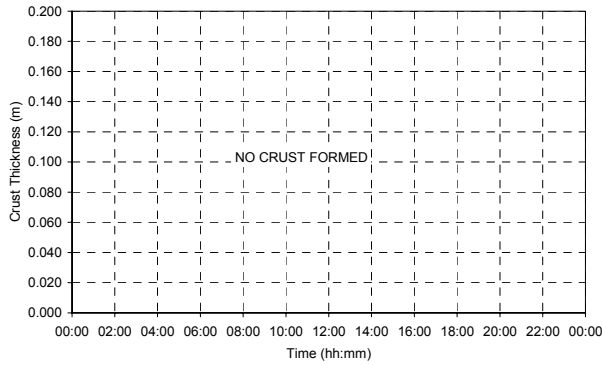
ILMENITE FEED RATE CHANGE	ILMENITE FEED RATE	REDUCTANT FEED RATE CHANGE	REDUCTANT FEED RATE	ELECTRICAL POWER CHANGE	ELECTRICAL POWER
-	20,000 kg/h	+ 1 kg/t ilm.	1,720 kg/h	-	21,715 kW



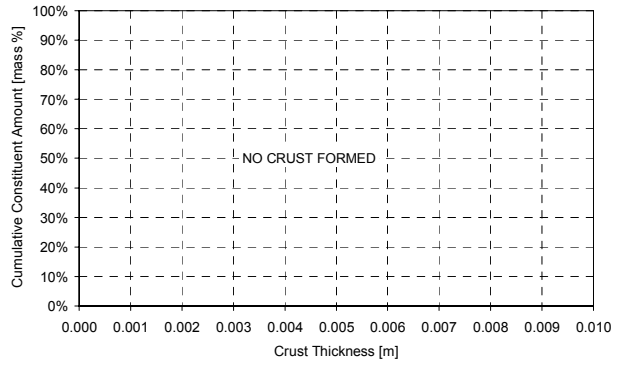
(a)



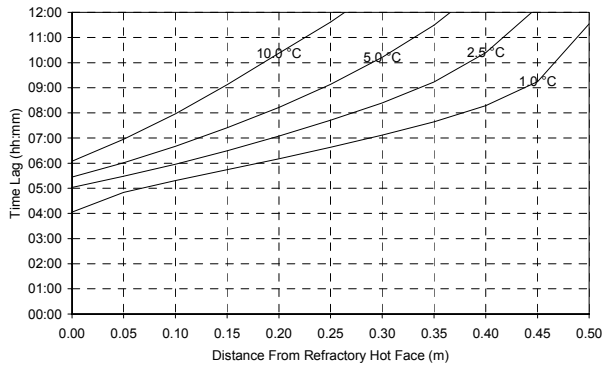
(b)



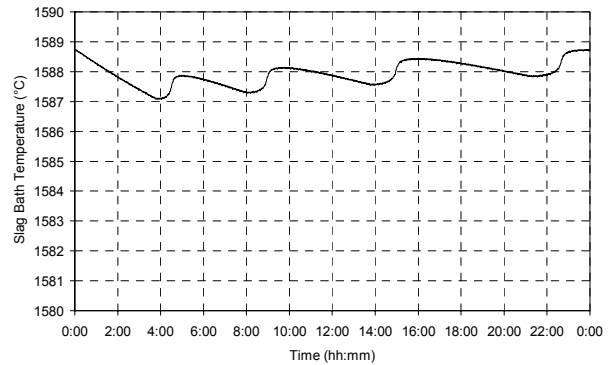
(c)



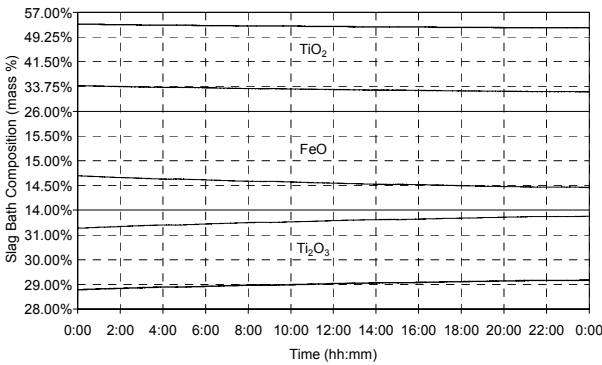
(d)



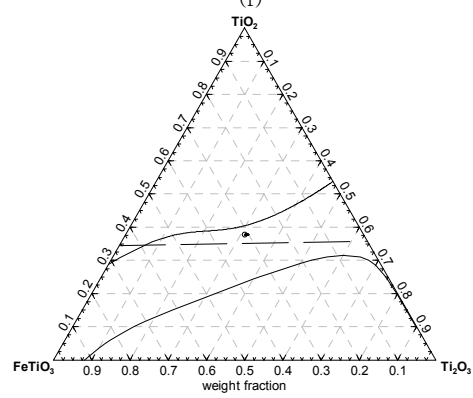
(e)



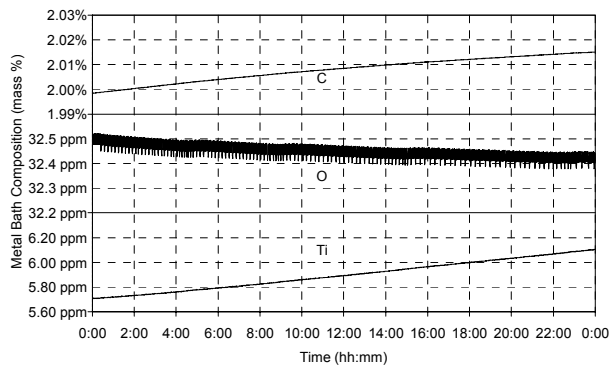
(f)



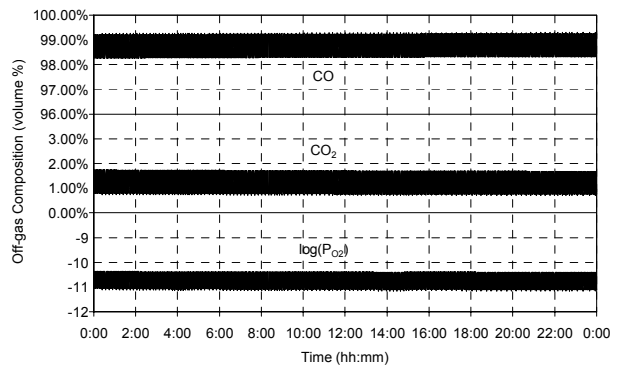
(g)



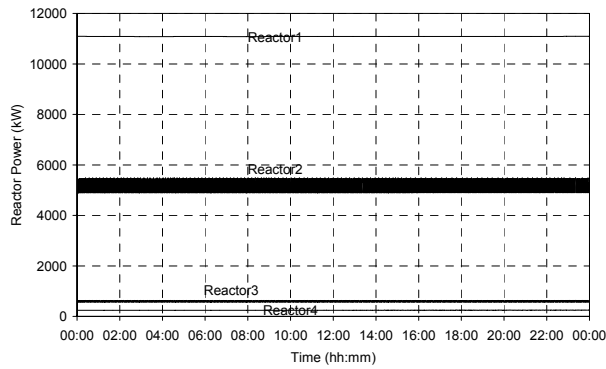
(h)



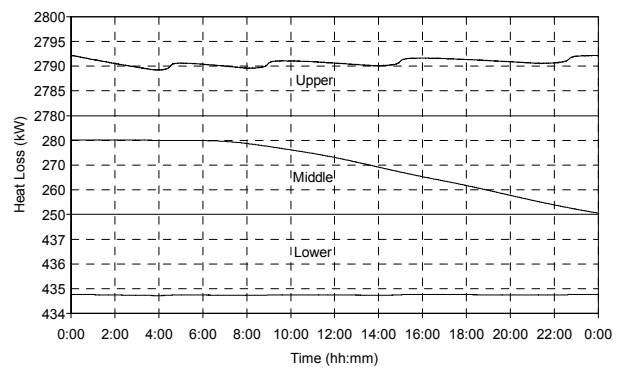
(i)



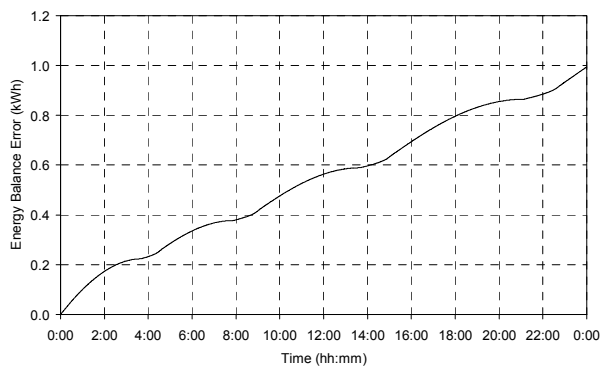
(j)



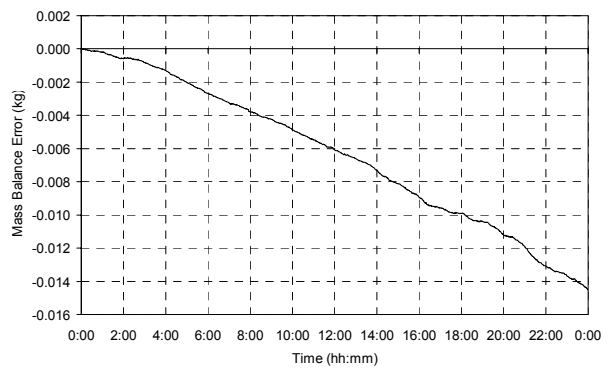
(k)



(l)



(m)

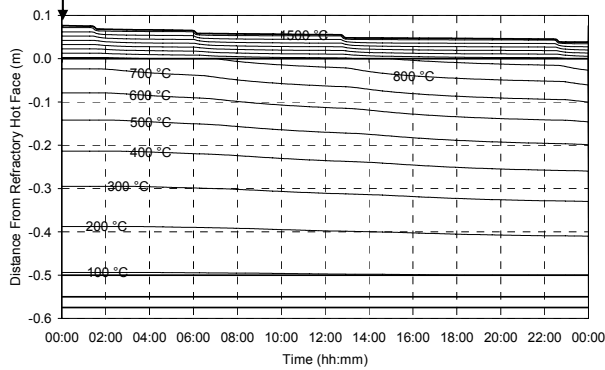


(n)

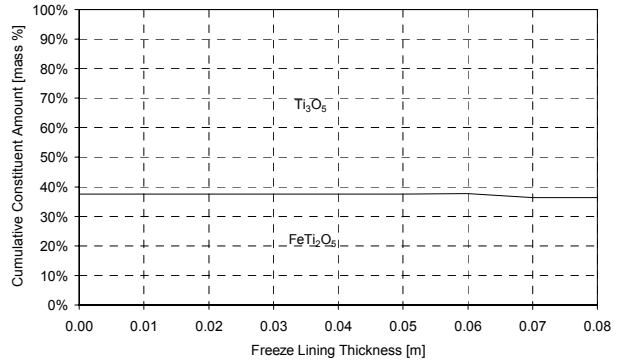
Figure 123 – Experiment 8.3 results.

8.3.4 Experiment 8.4

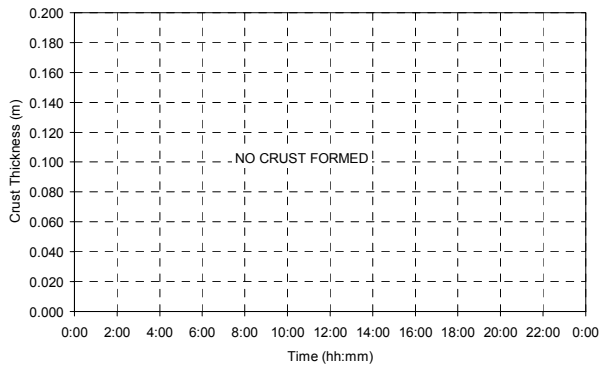
ILMENITE FEED RATE CHANGE	ILMENITE FEED RATE	REDUCTANT FEED RATE CHANGE	REDUCTANT FEED RATE	ELECTRICAL POWER CHANGE	ELECTRICAL POWER
-	20,000 kg/h	-1 kg/ton ilm.	1,680 kg/h	-	21,715 kW



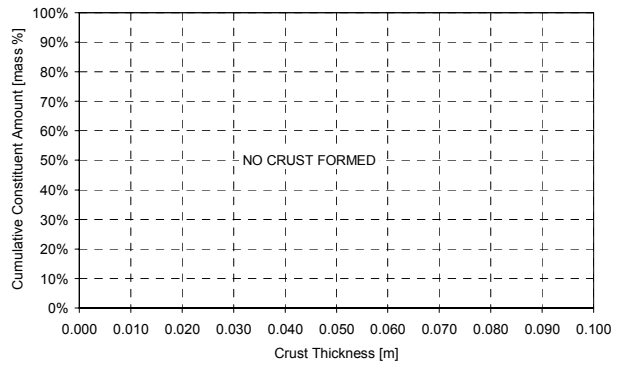
(a)



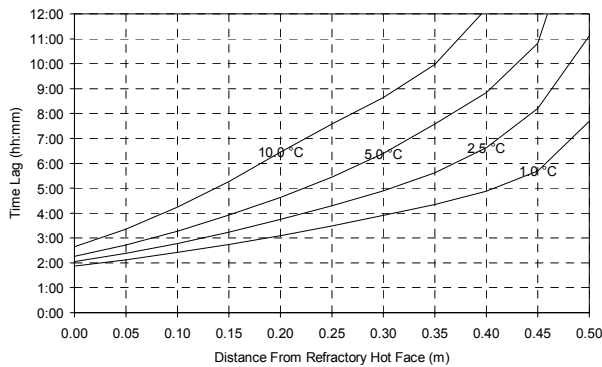
(b)



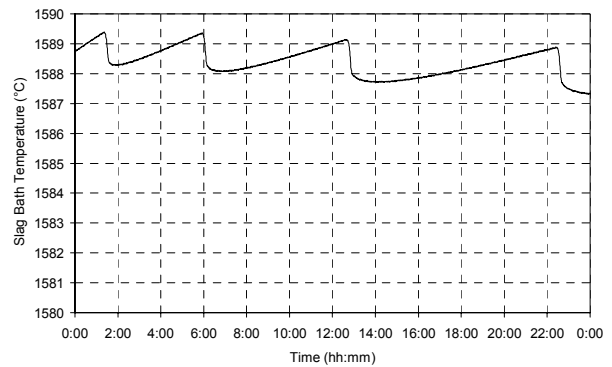
(c)



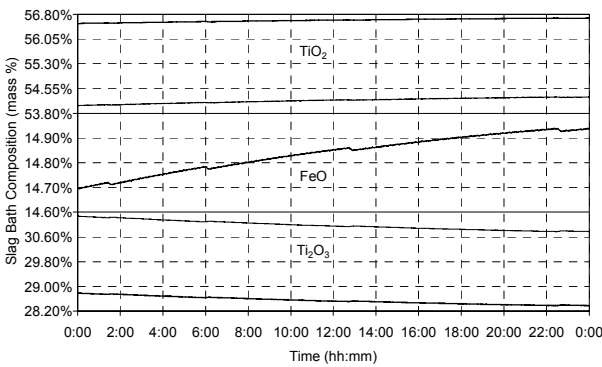
(d)



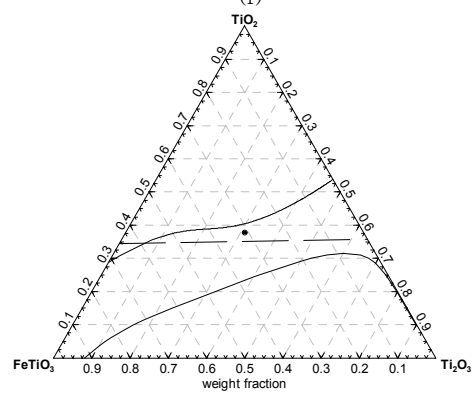
(e)



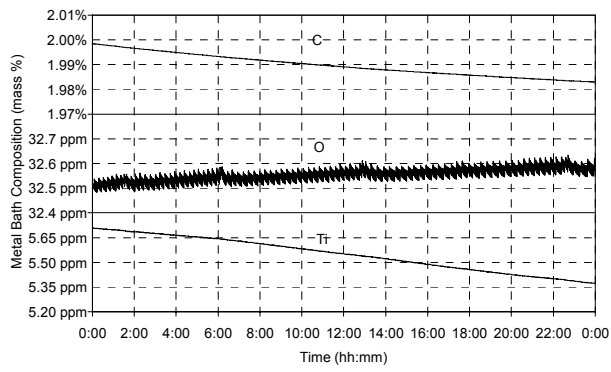
(f)



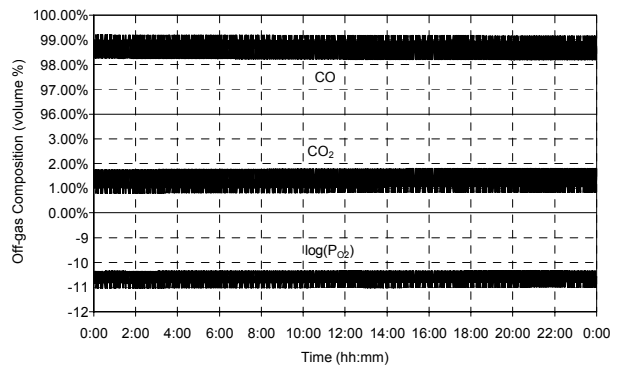
(g)



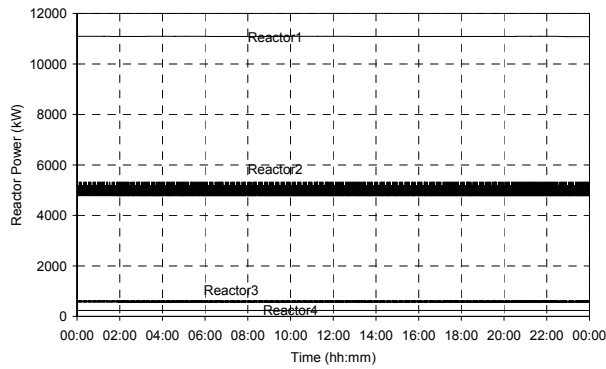
(h)



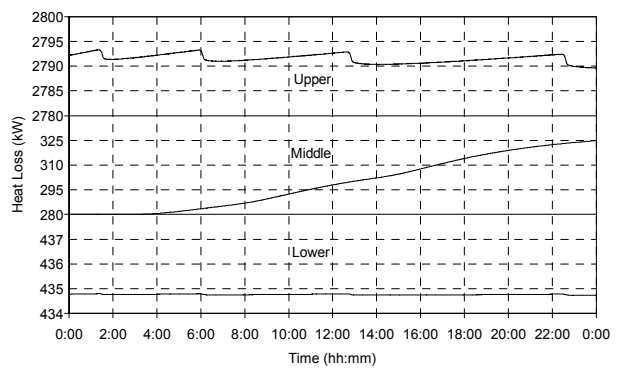
(i)



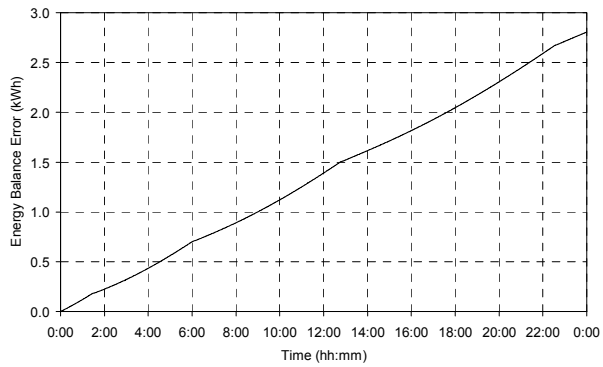
(j)



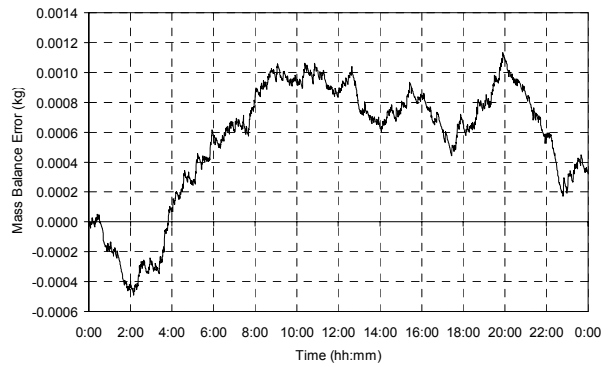
(k)



(l)



(m)

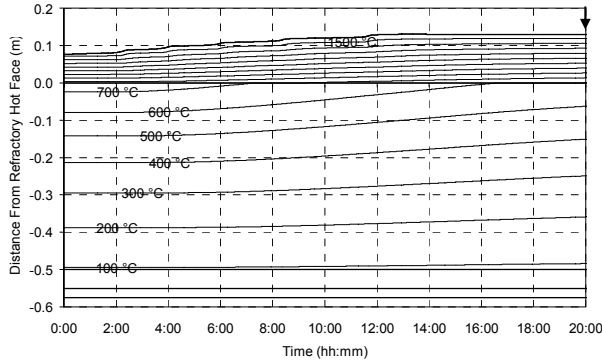


(n)

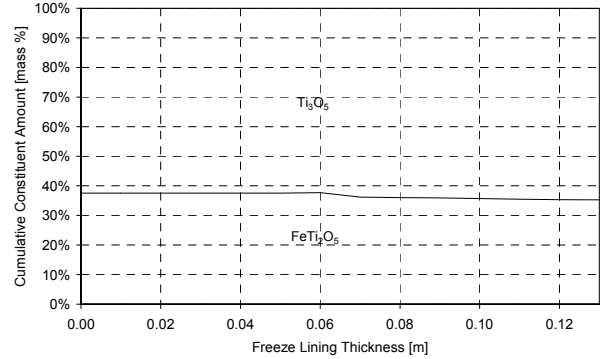
Figure 124 – Experiment 8.4 results.

8.3.5 Experiment 8.5

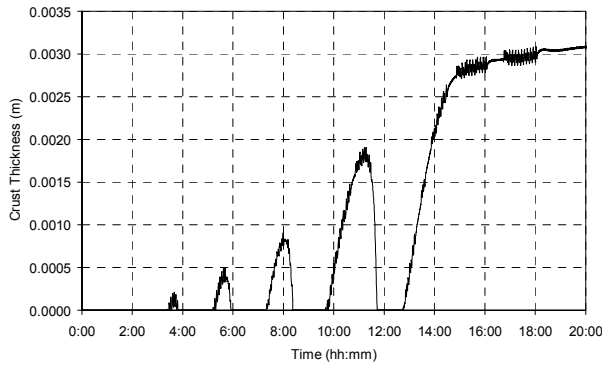
ILMENITE FEED RATE CHANGE	ILMENITE FEED RATE	REDUCTANT FEED RATE CHANGE	REDUCTANT FEED RATE	ELECTRICAL POWER CHANGE	ELECTRICAL POWER
-	20,000 kg/h	+ 2 kg/ton ilm.	1,740 kg/h	-	21,715 kW



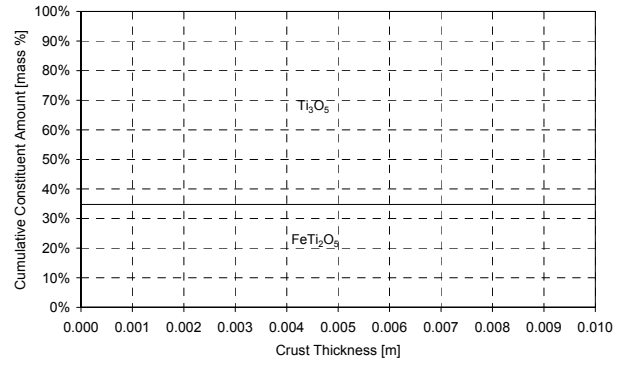
(a)



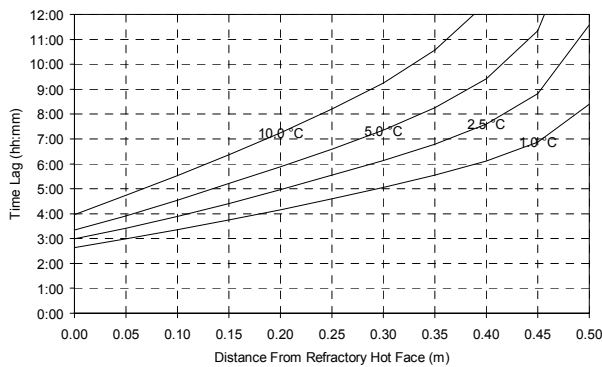
(b)



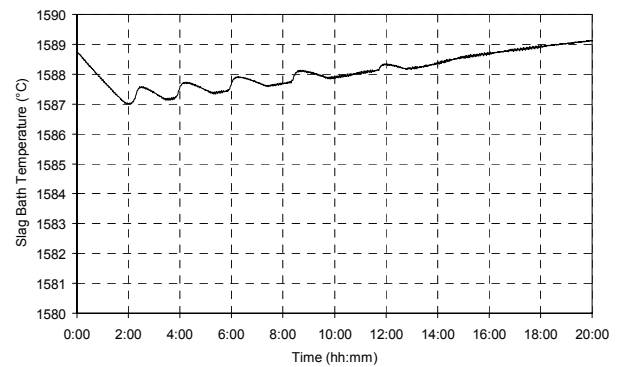
(c)



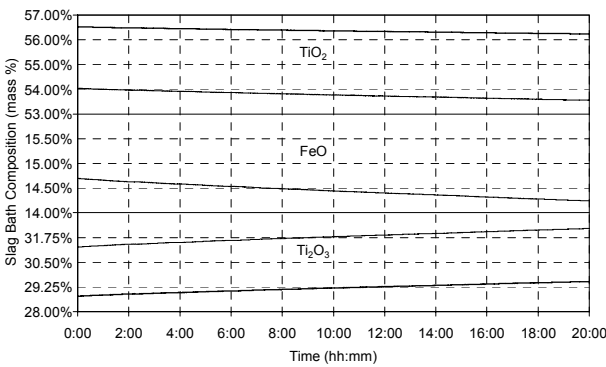
(d)



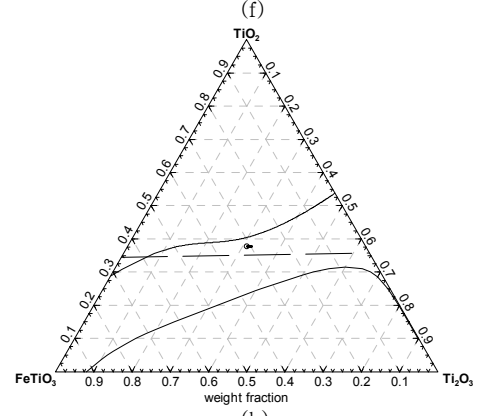
(e)



(f)



(g)



(h)

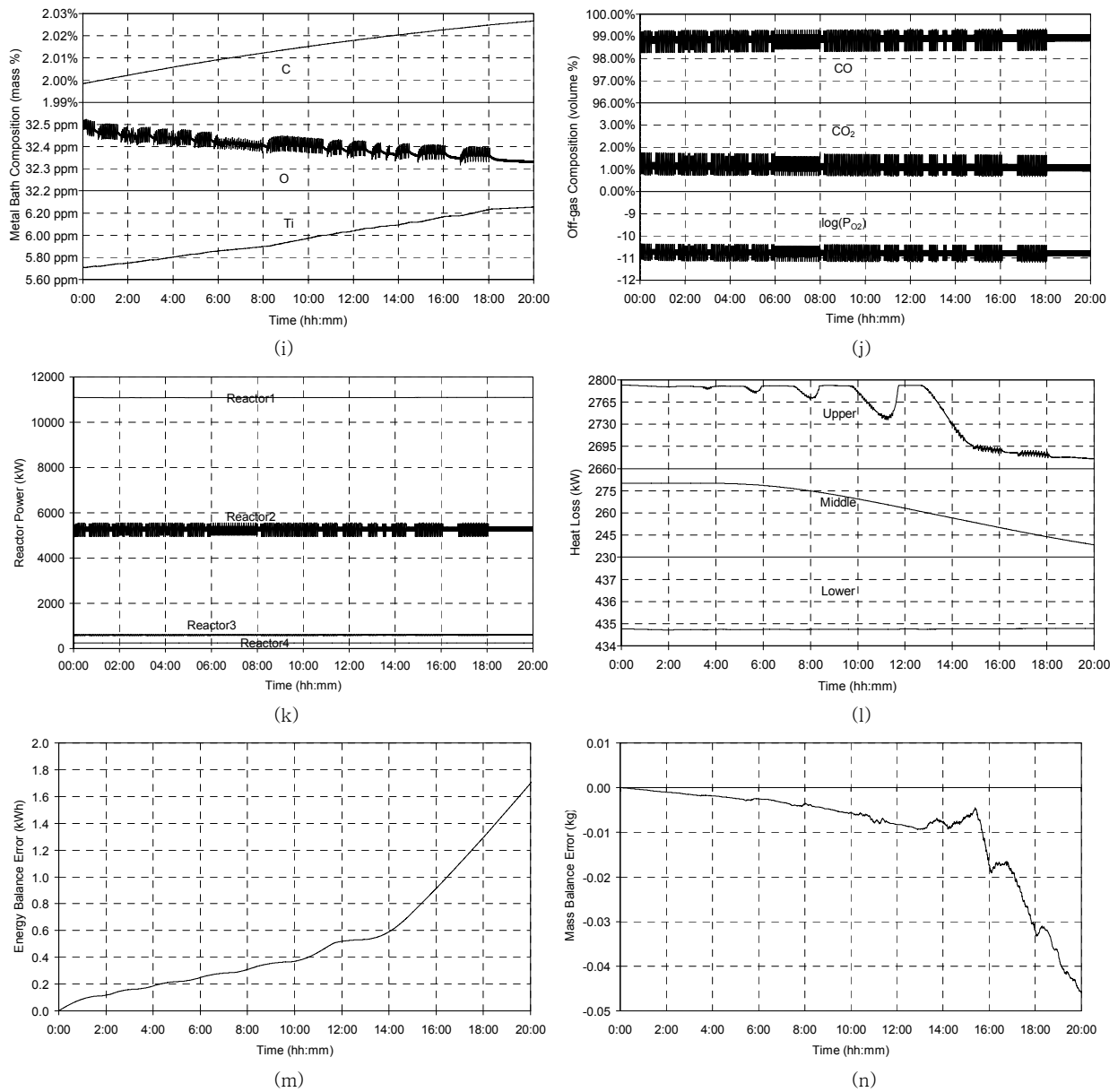
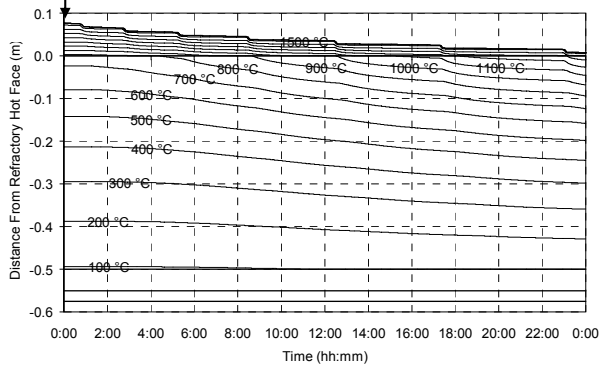


Figure 125 – Experiment 8.5 results.

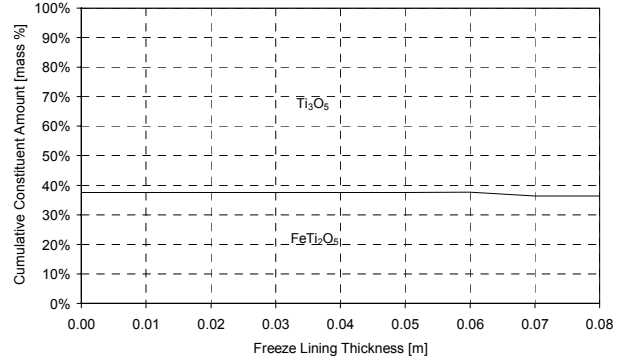


8.3.6 Experiment 8.6

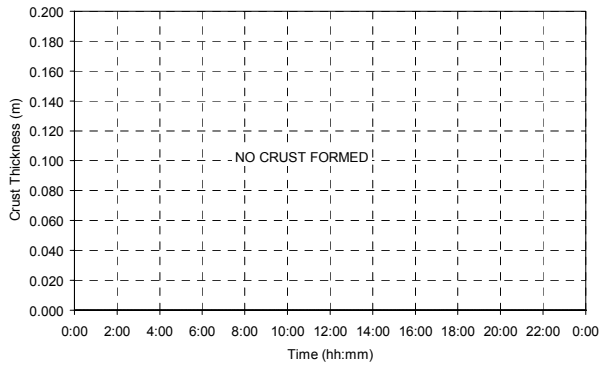
ILMENITE FEED RATE CHANGE	ILMENITE FEED RATE	REDUCTANT FEED RATE CHANGE	REDUCTANT FEED RATE	ELECTRICAL POWER CHANGE	ELECTRICAL POWER
-	20,000 kg/h	-2 kg/ton ilm.	1,660 kg/h	-	21,715 kW



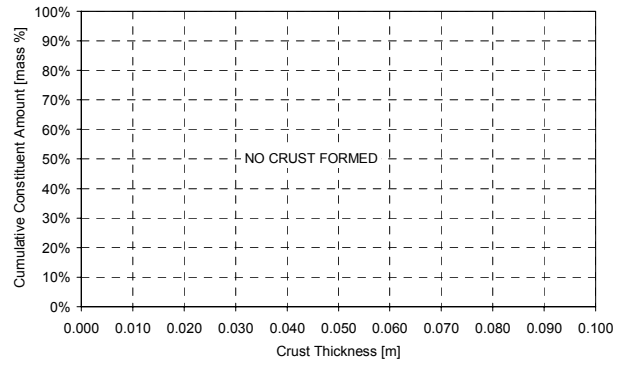
(a)



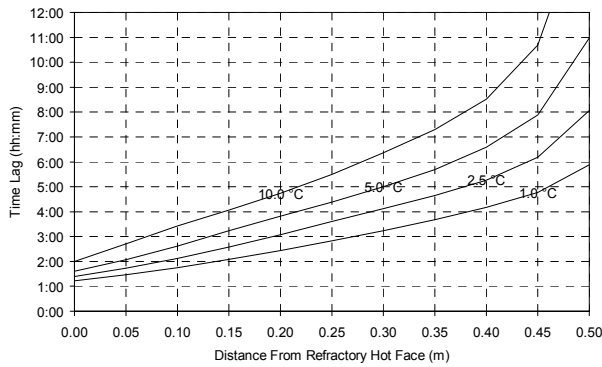
(b)



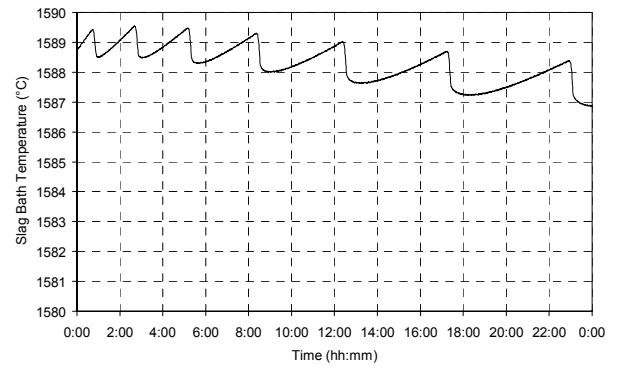
(c)



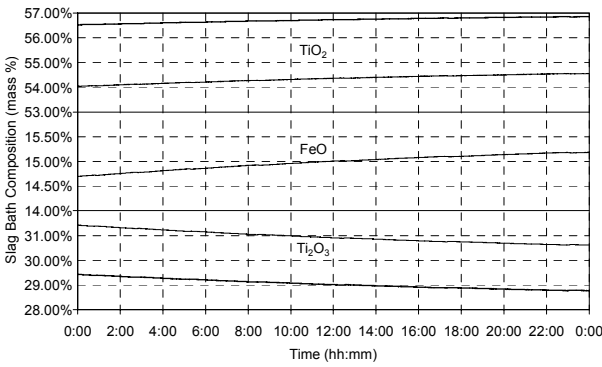
(d)



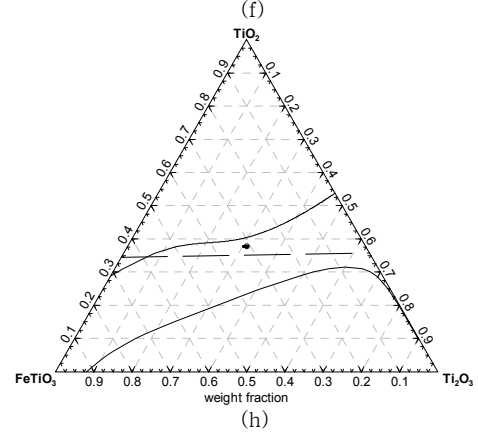
(e)



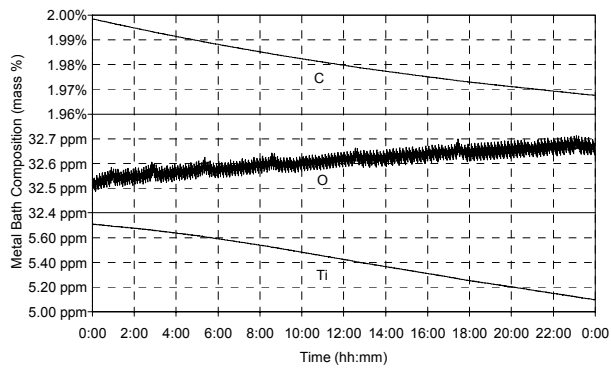
(f)



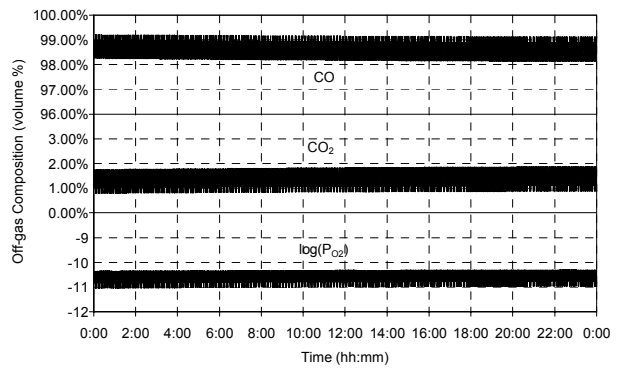
(g)



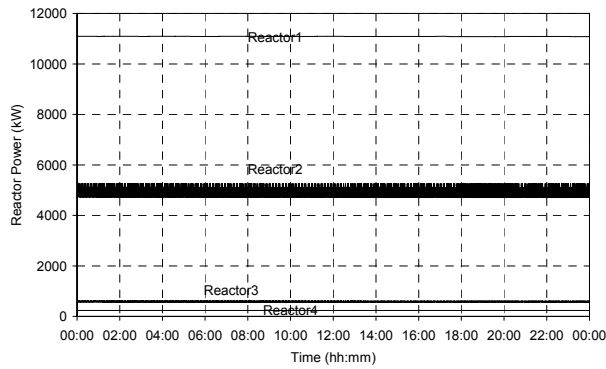
(h)



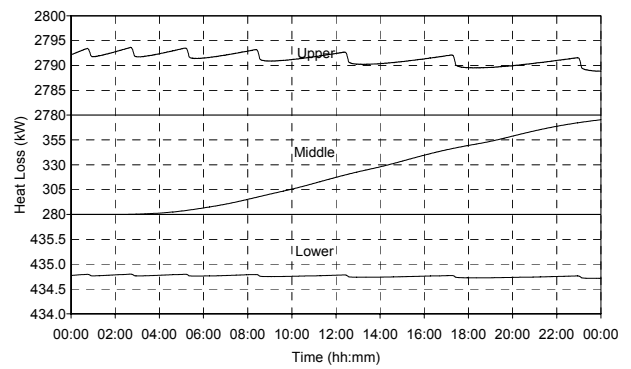
(i)



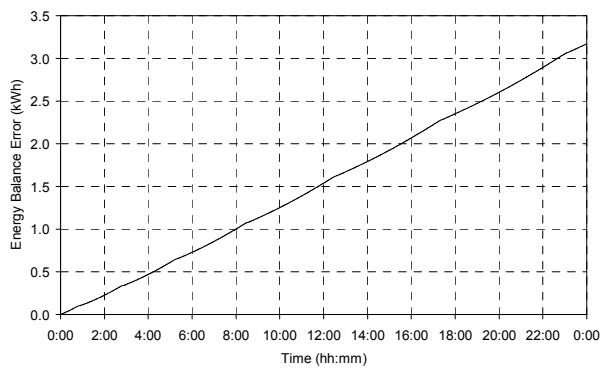
(j)



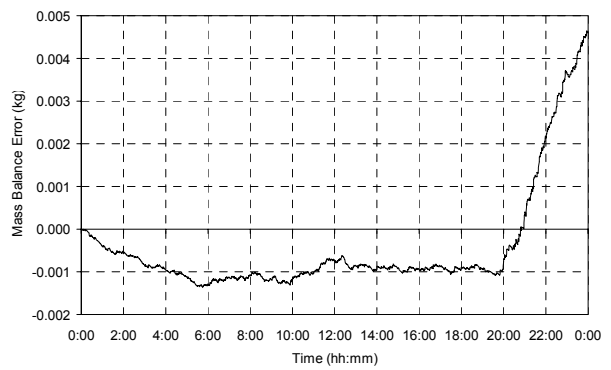
(k)



(l)



(m)

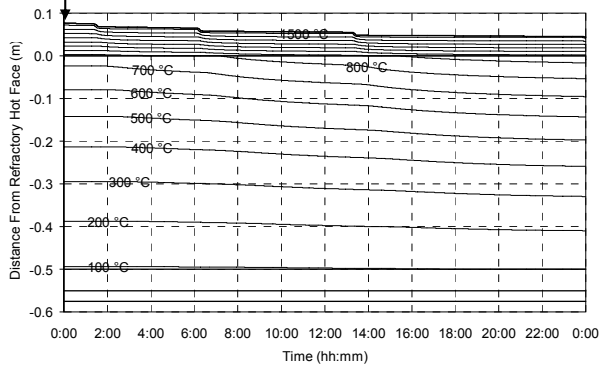


(n)

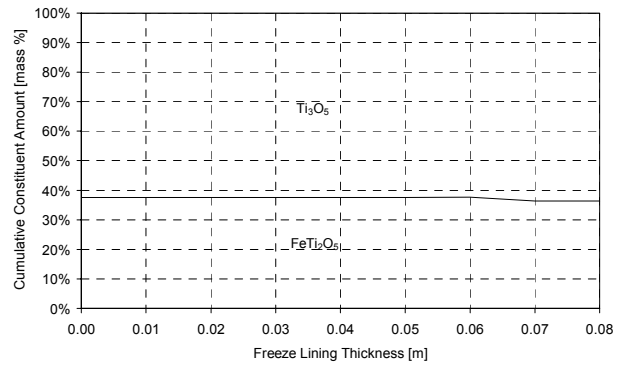
Figure 126 – Experiment 8.6 results.

8.3.7 Experiment 8.7

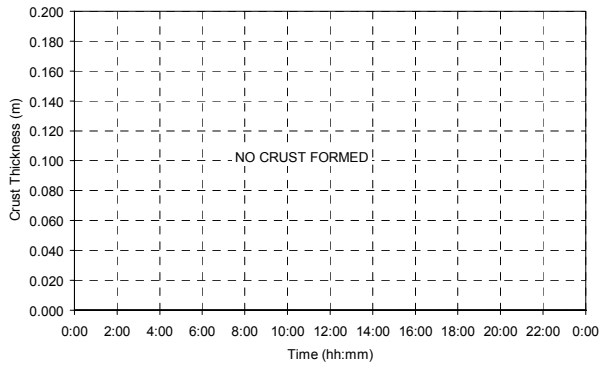
ILMENITE FEED RATE CHANGE	ILMENITE FEED RATE	REDUCTANT FEED RATE CHANGE	REDUCTANT FEED RATE	ELECTRICAL POWER CHANGE	ELECTRICAL POWER
-	20,000 kg/h	-	1,700 kg/h	+ 5 kWh/ton ilm.	21,815 kW



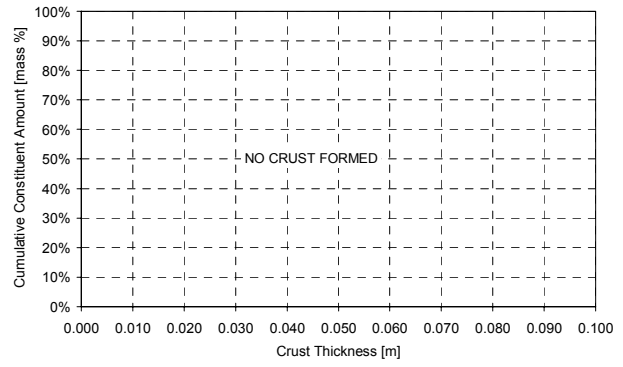
(a)



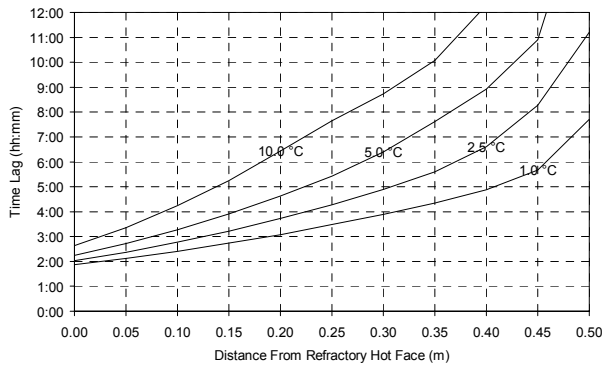
(b)



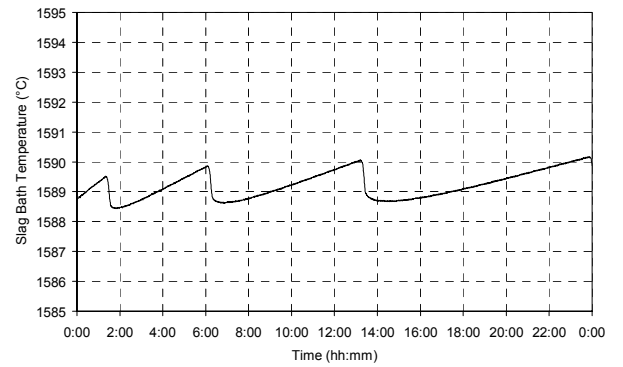
(c)



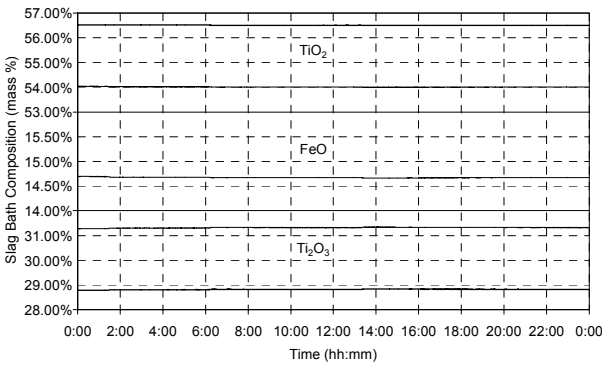
(d)



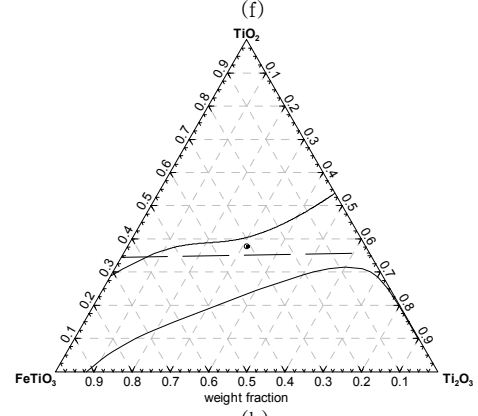
(e)



(f)



(g)



(h)

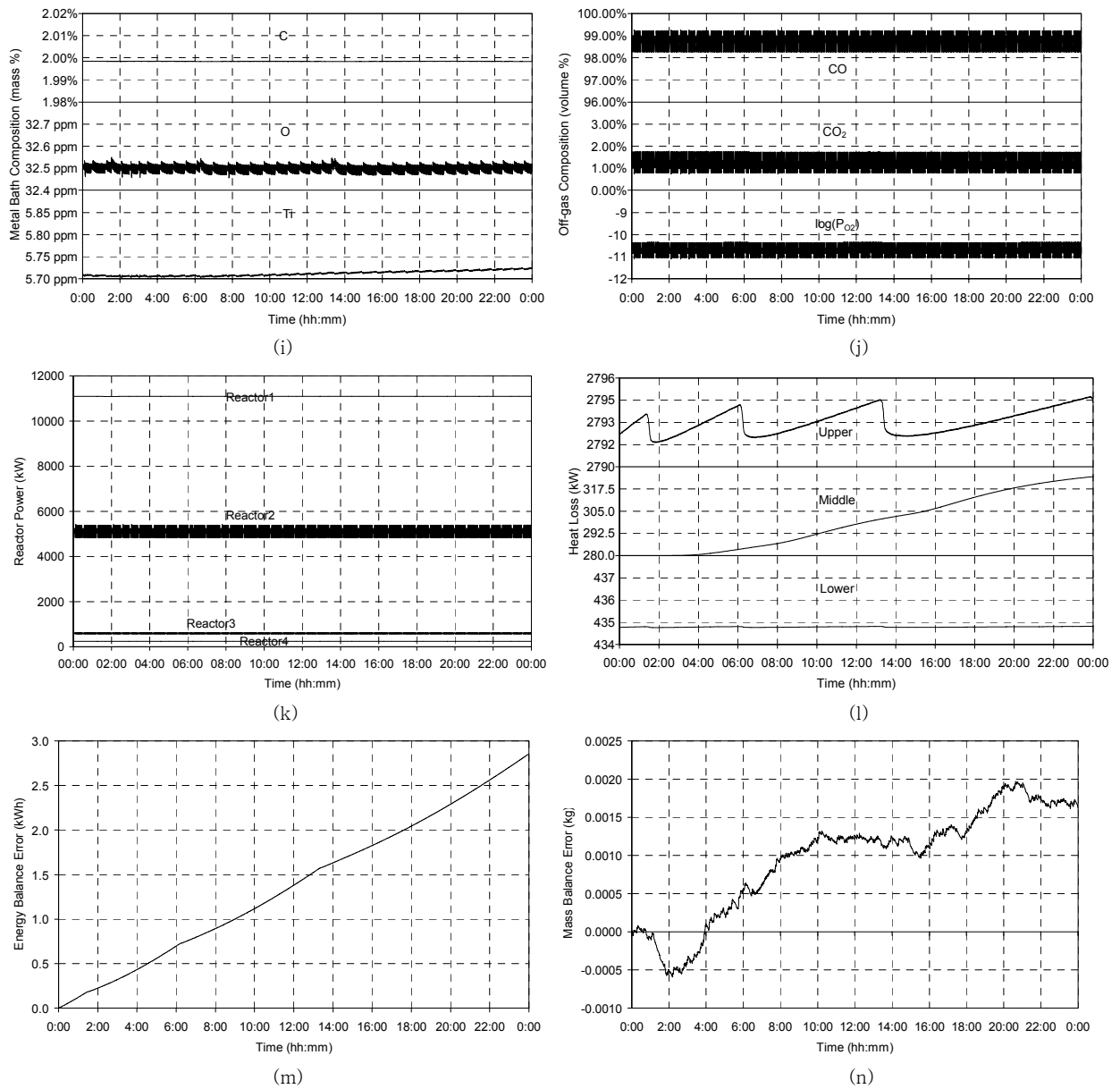
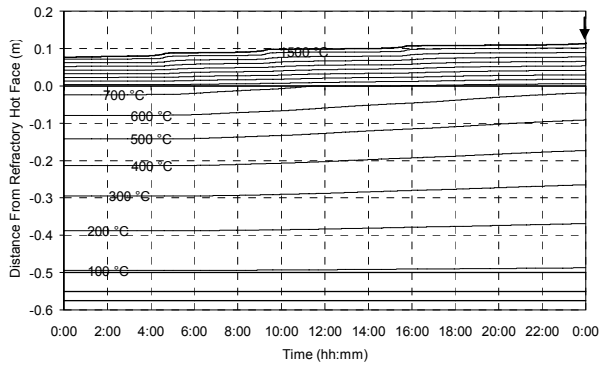


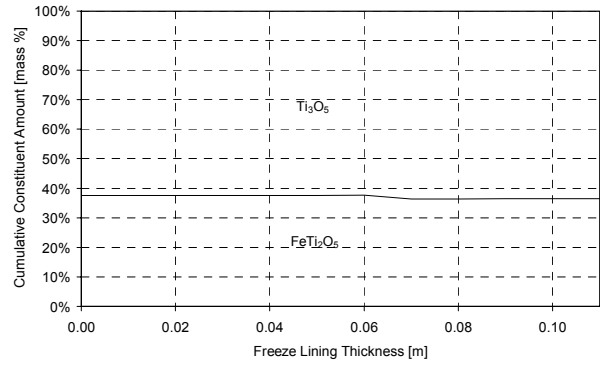
Figure 127 - Experiment 8.7 results.

8.3.8 Experiment 8.8

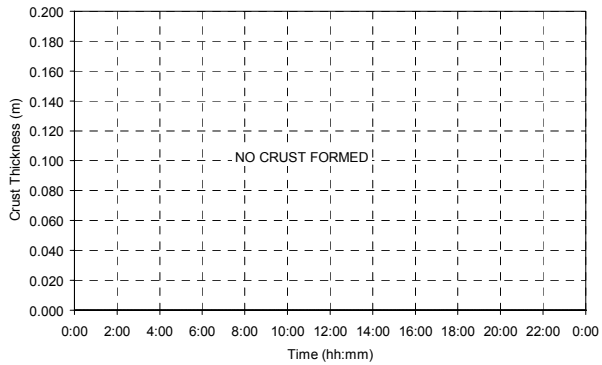
ILMENITE FEED RATE CHANGE	ILMENITE FEED RATE	REDUCTANT FEED RATE CHANGE	REDUCTANT FEED RATE	ELECTRICAL POWER CHANGE	ELECTRICAL POWER
-	20,000 kg/h	-	1,700 kg/h	-5 kWh/ton ilm.	21,615 kW



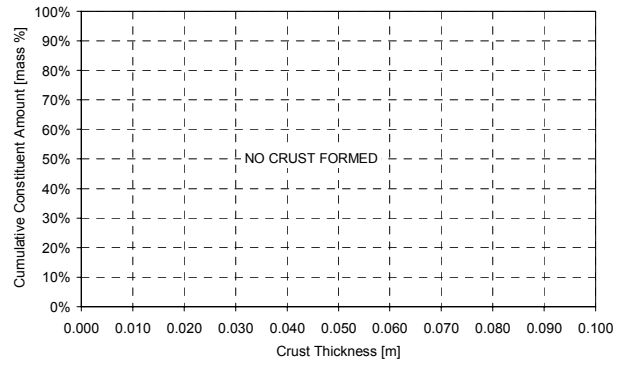
(a)



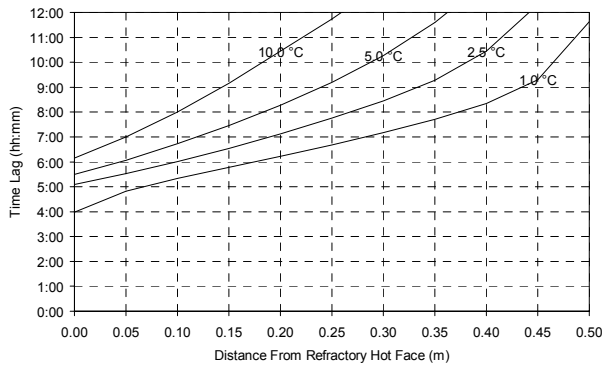
(b)



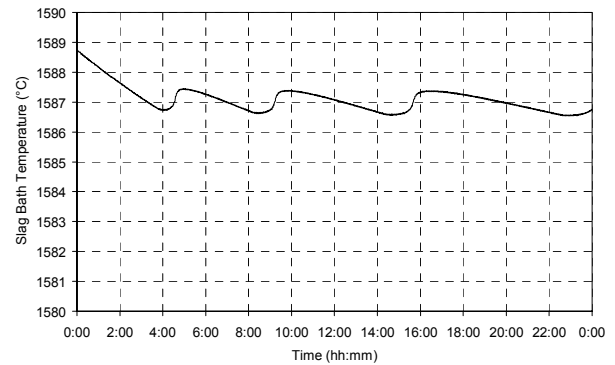
(c)



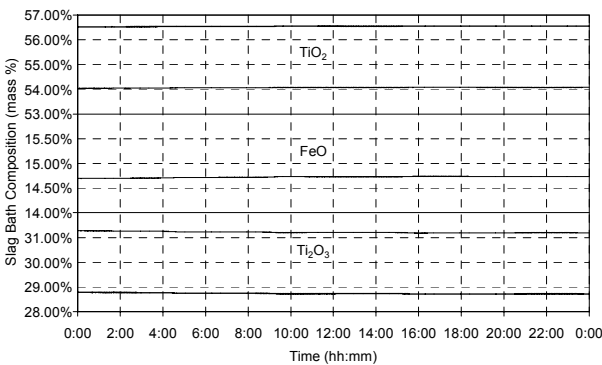
(d)



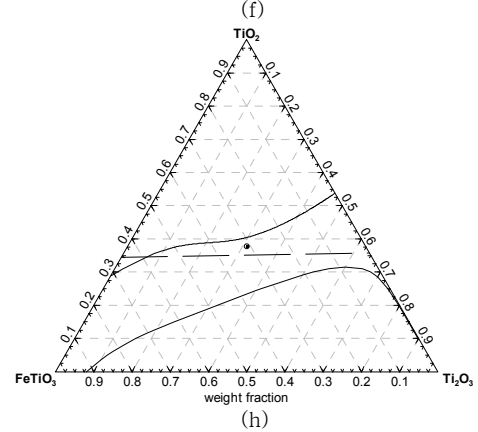
(e)



(f)



(g)



(h)

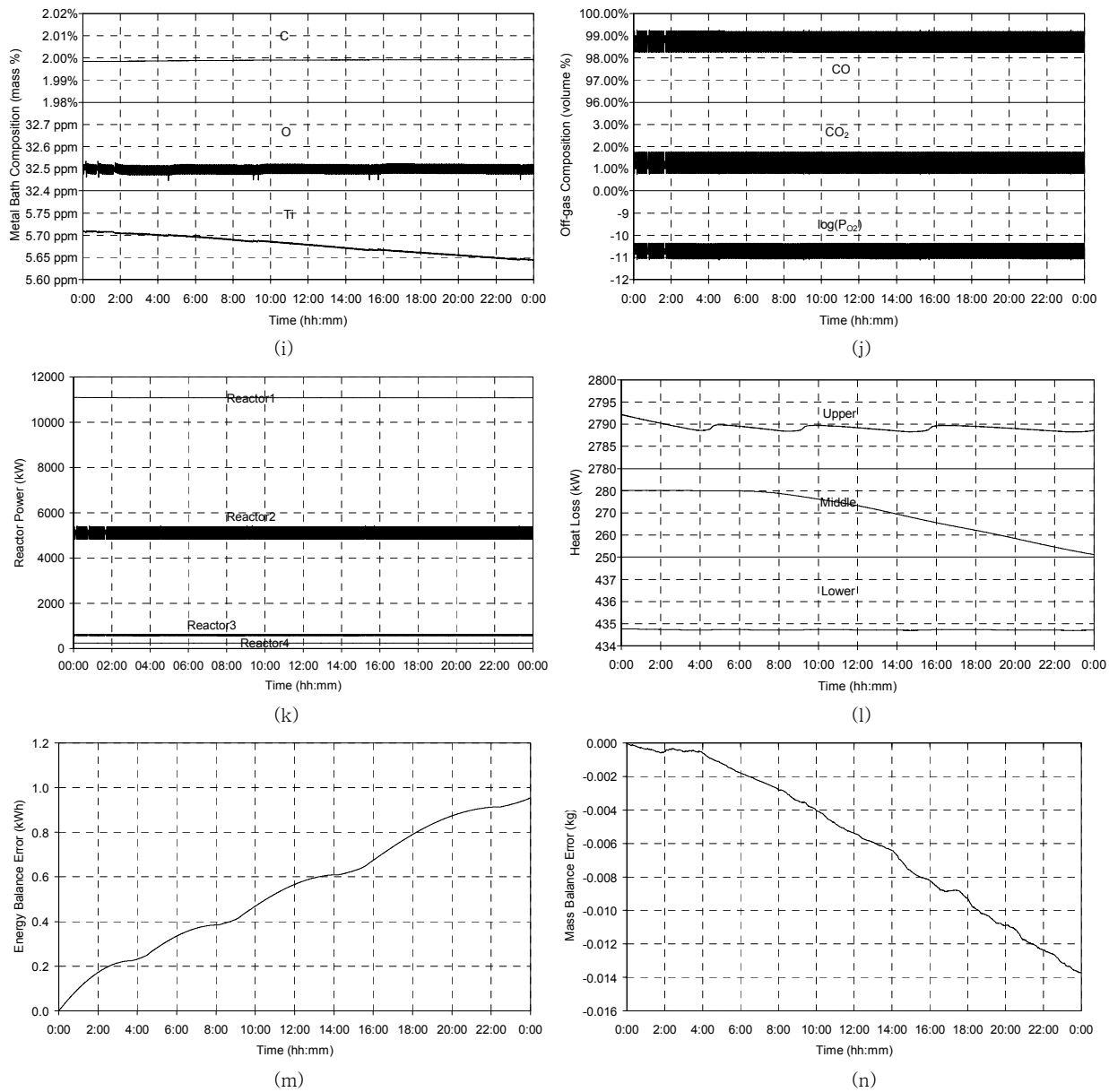
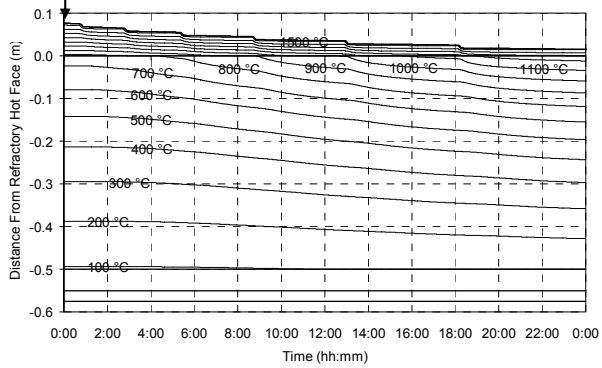


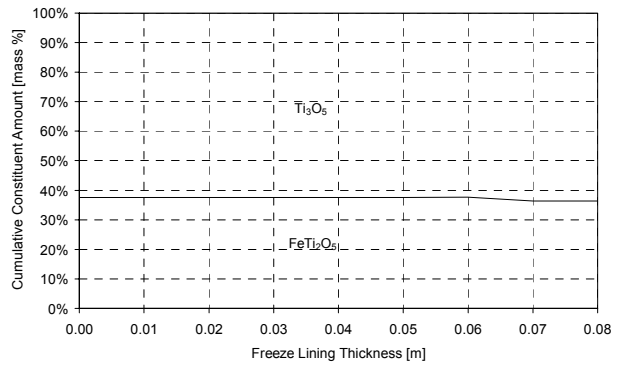
Figure 128 – Experiment 8.8 results.

8.3.9 Experiment 8.9

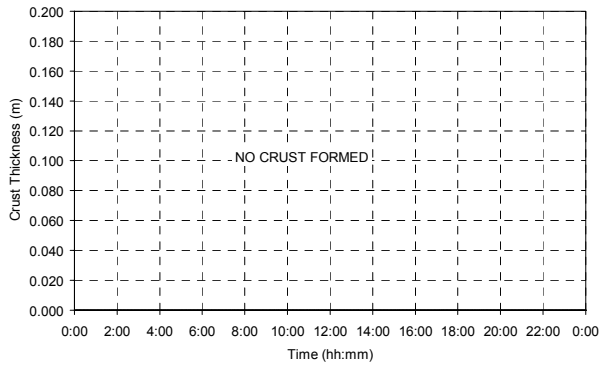
ILMENITE FEED RATE CHANGE	ILMENITE FEED RATE	REDUCTANT FEED RATE CHANGE	REDUCTANT FEED RATE	ELECTRICAL POWER CHANGE	ELECTRICAL POWER
-	20,000 kg/h	-	1,700 kg/h	+ 10 kWh/ton ilm.	21,915 kW



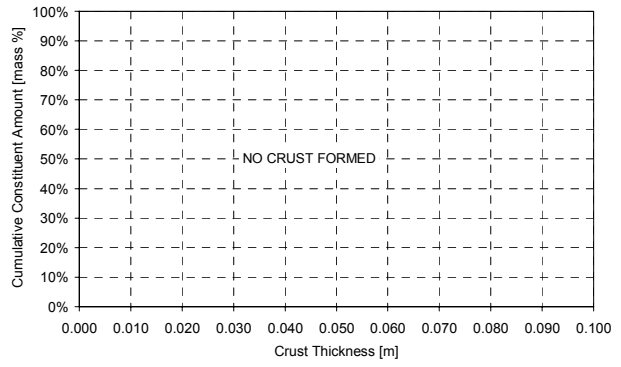
(a)



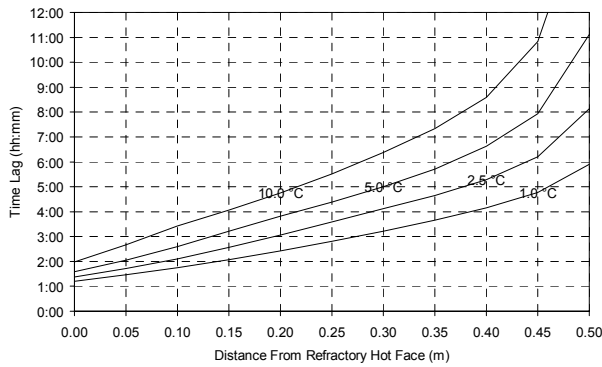
(b)



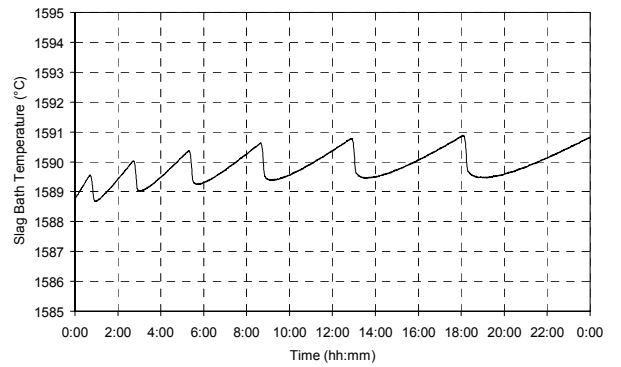
(c)



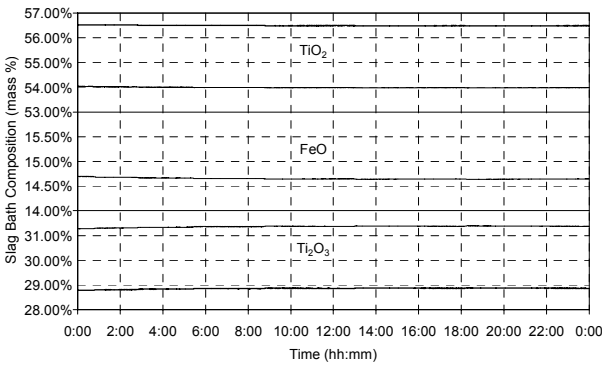
(d)



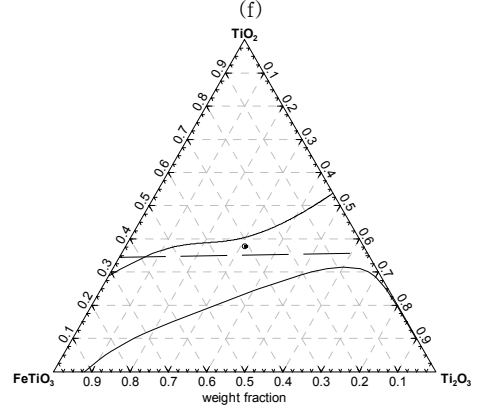
(e)



(f)



(g)



(h)

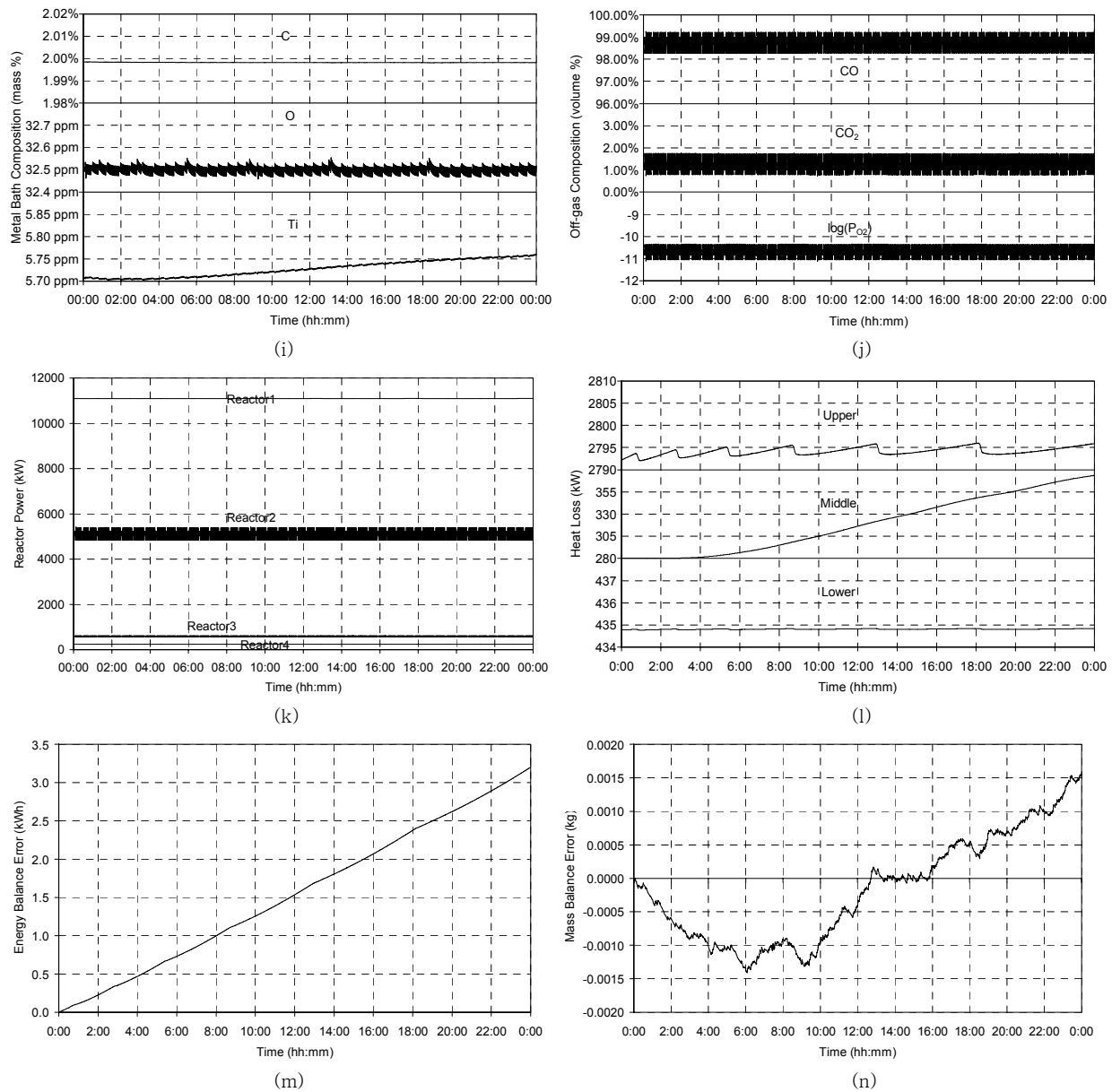
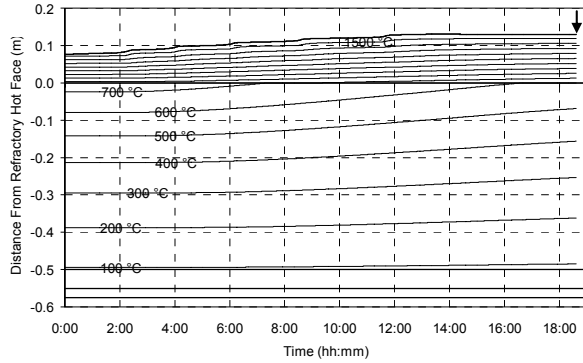


Figure 129 – Experiment 8.9 results.

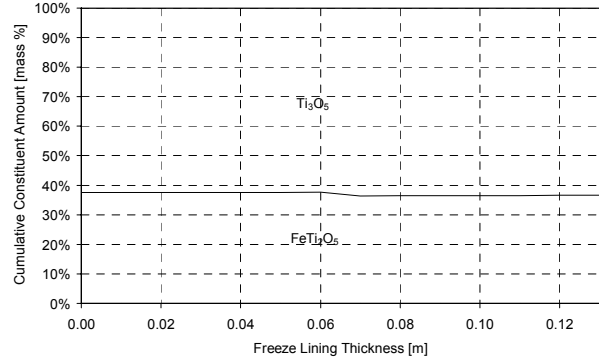


8.3.10 Experiment 8.10

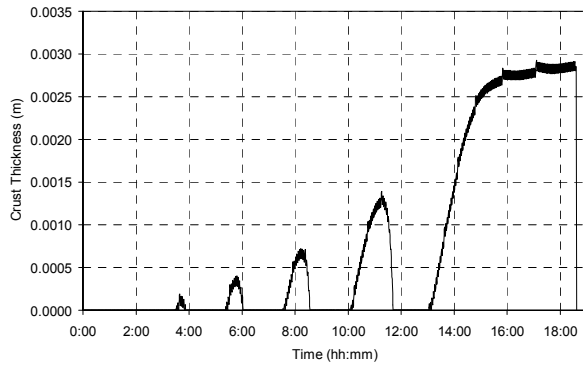
ILMENITE FEED RATE CHANGE	ILMENITE FEED RATE	REDUCTANT FEED RATE CHANGE	REDUCTANT FEED RATE	ELECTRICAL POWER CHANGE	ELECTRICAL POWER
-	20,000 kg/h	-	1,700 kg/h	-10 kWh/ton ilm.	21,515 kW



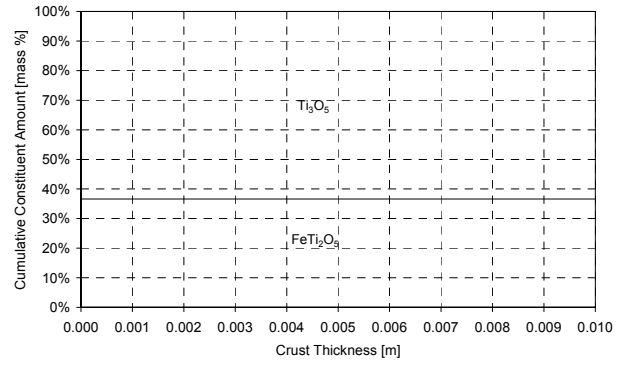
(a)



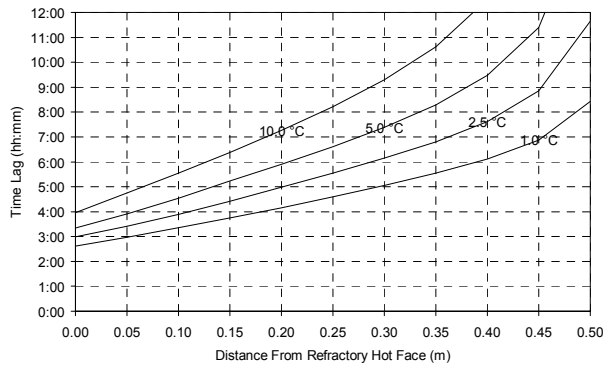
(b)



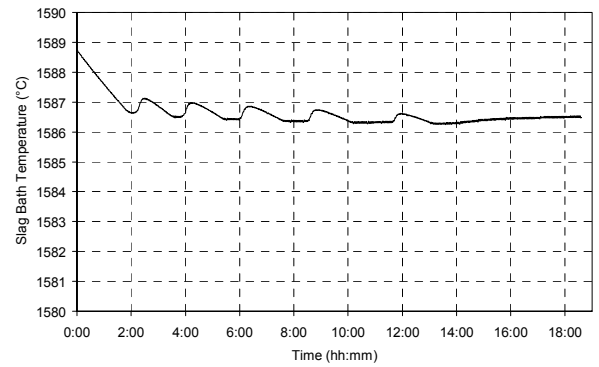
(c)



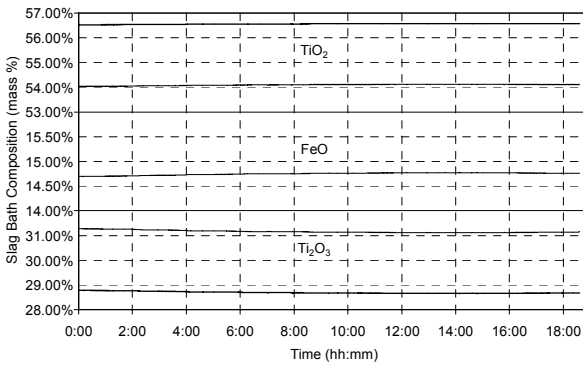
(d)



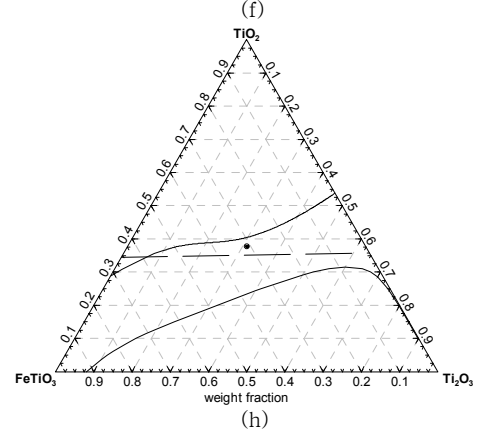
(e)



(f)



(g)



(h)

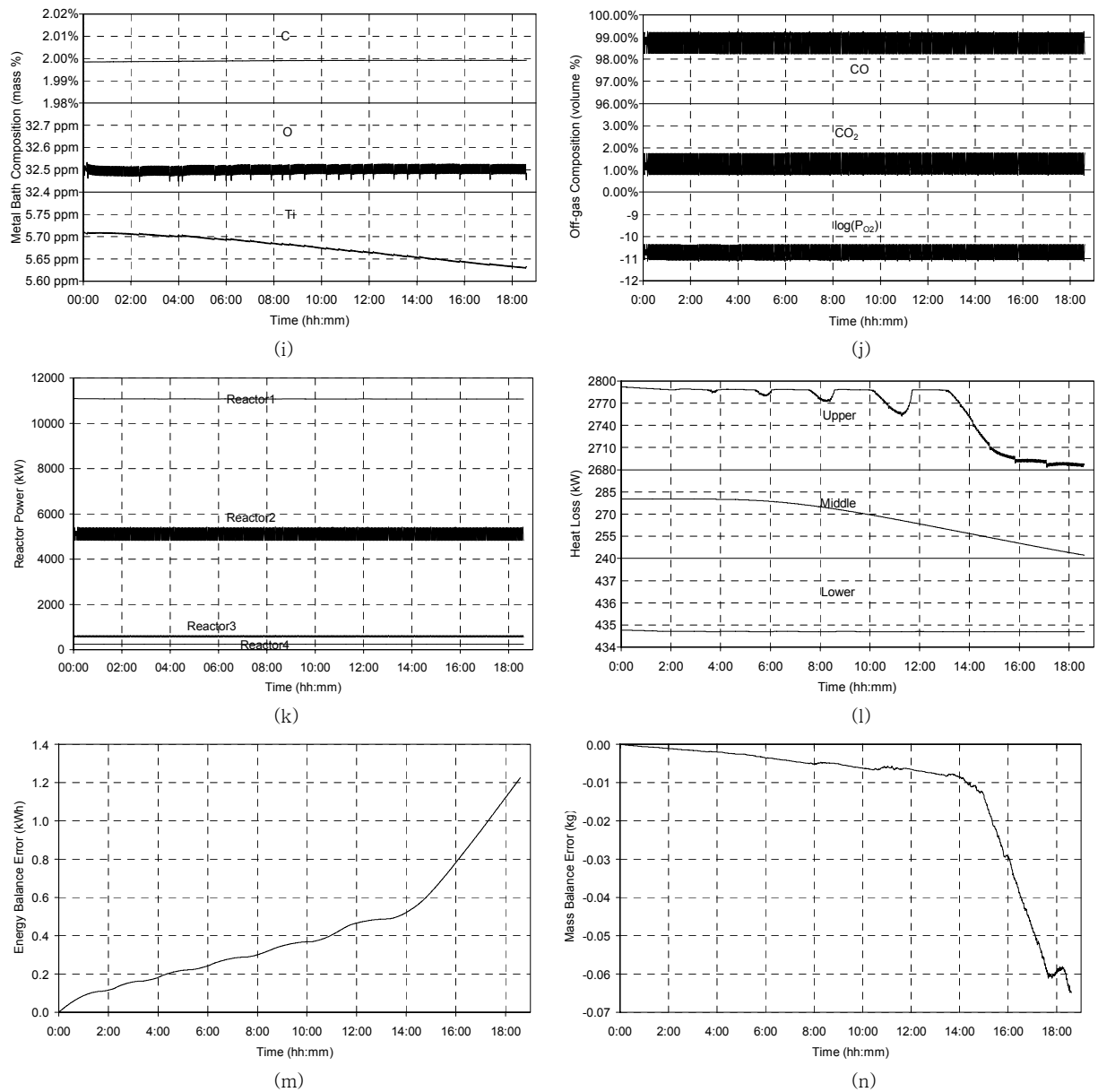
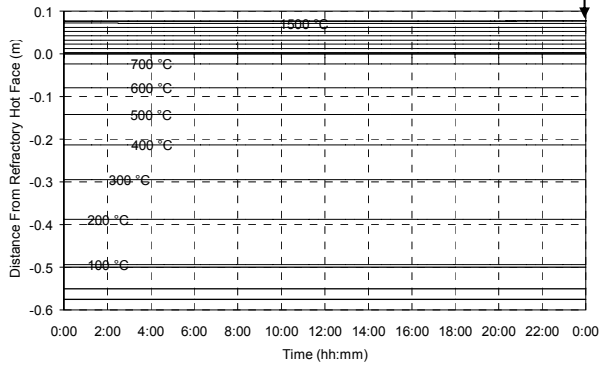


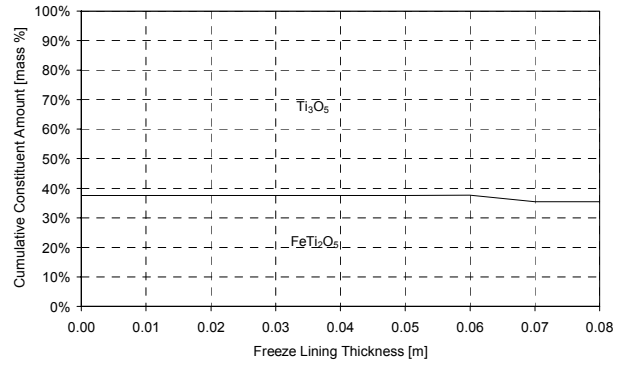
Figure 130 – Experiment 8.10 results.

8.3.11 Experiment 8.11

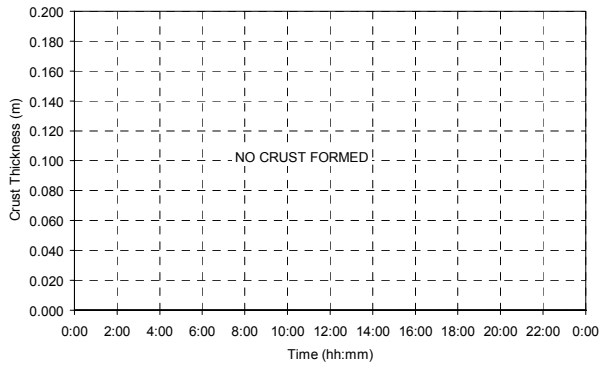
ILMENITE FEED RATE CHANGE	ILMENITE FEED RATE	REDUCTANT FEED RATE CHANGE	REDUCTANT FEED RATE	ELECTRICAL POWER CHANGE	ELECTRICAL POWER
-	20,000 kg/h	+ 1 kg/ton ilm.	1,720 kg/h	+ 5 kWh/ton ilm.	21,815 kW



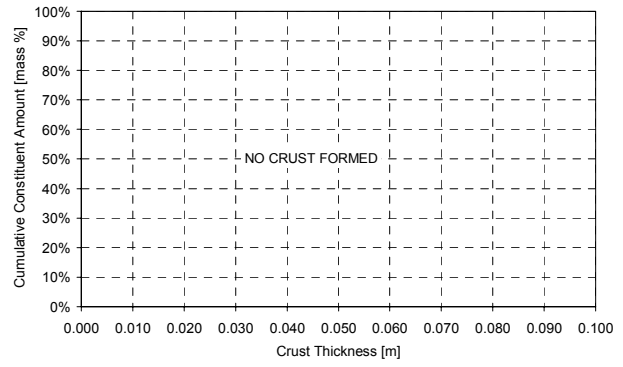
(a)



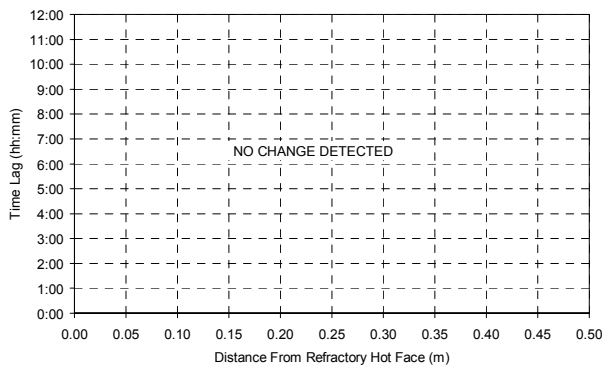
(b)



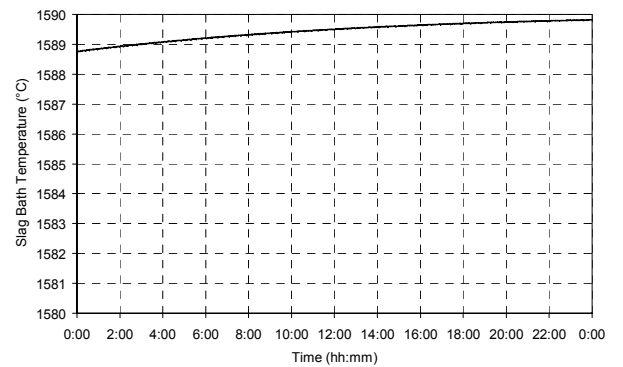
(c)



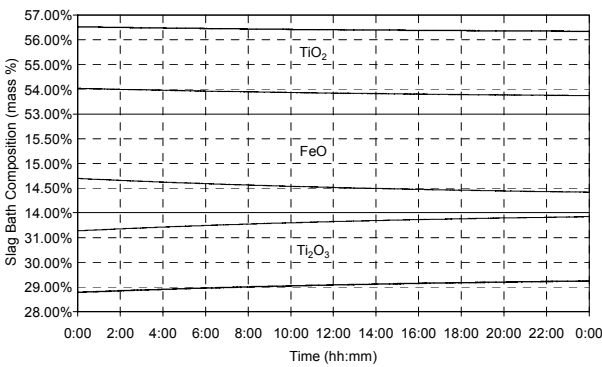
(d)



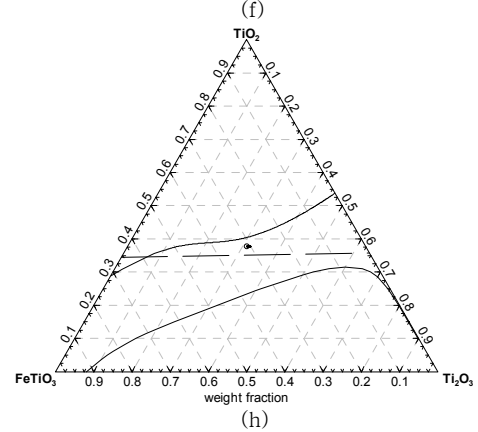
(e)



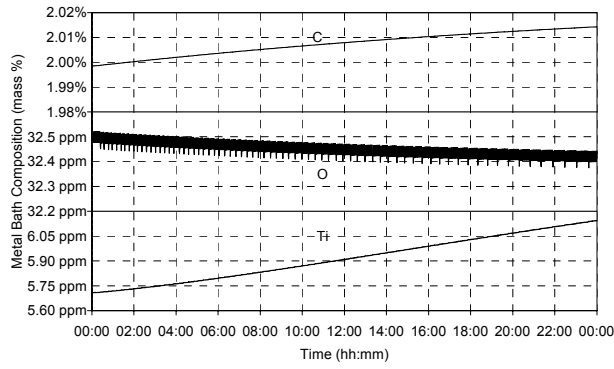
(f)



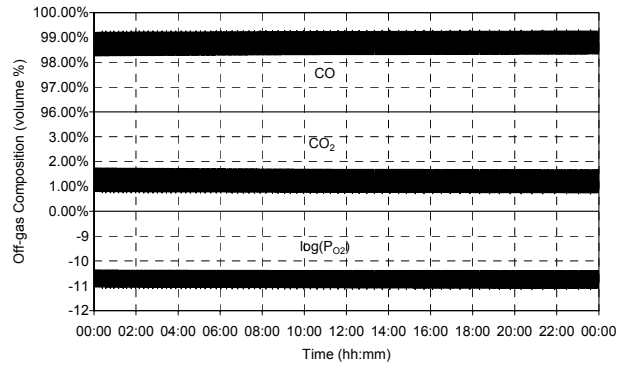
(g)



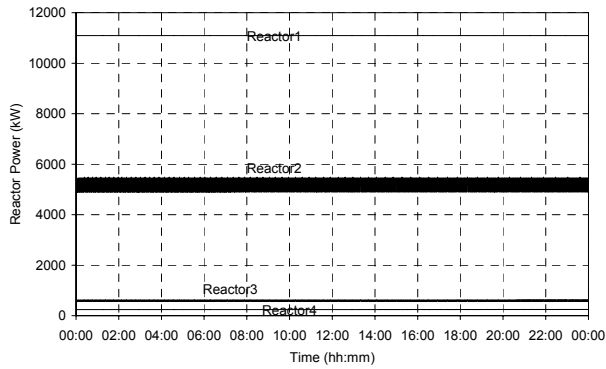
(h)



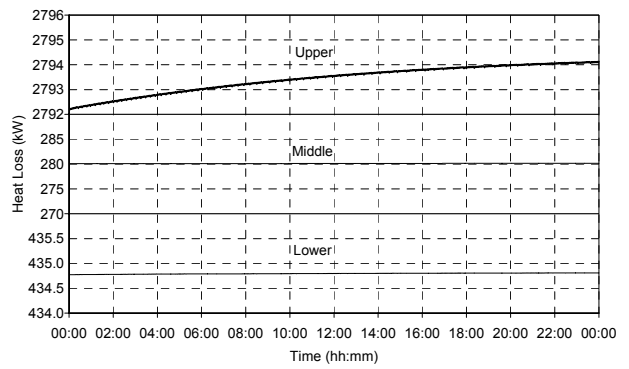
(i)



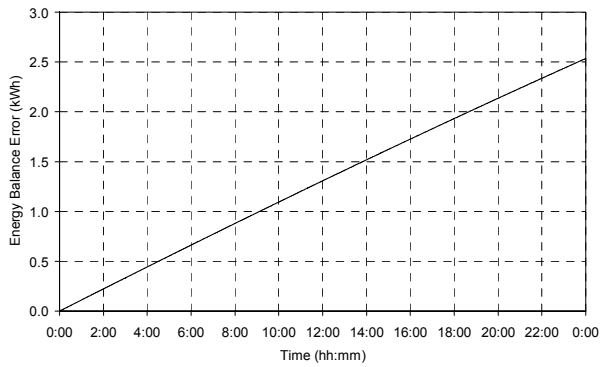
(j)



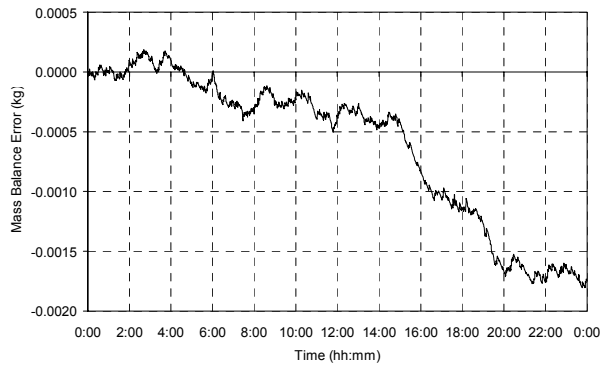
(k)



(l)



(m)

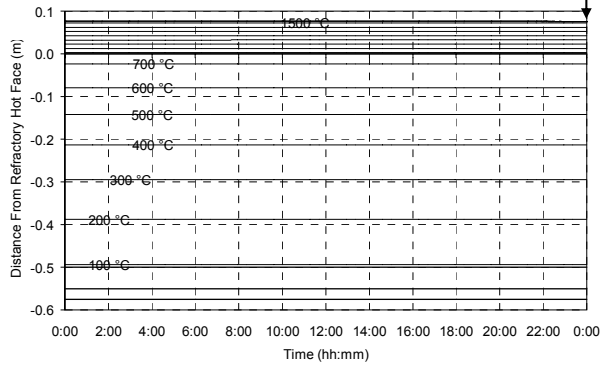


(n)

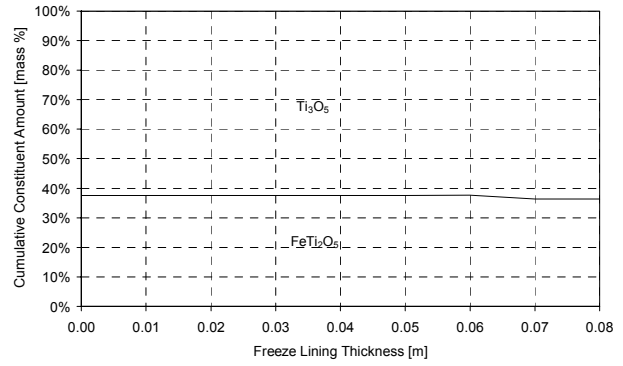
Figure 131 – Experiment 8.11 results.

8.3.12 Experiment 8.12

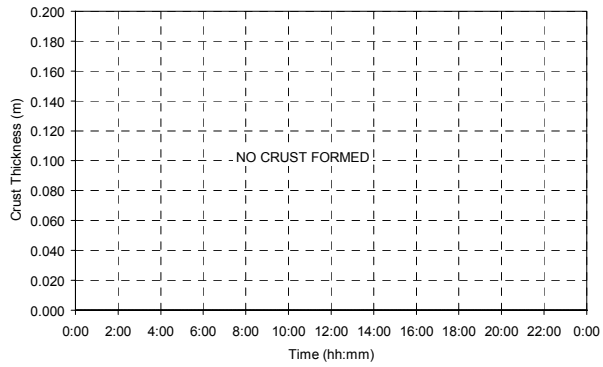
ILMENITE FEED RATE CHANGE	ILMENITE FEED RATE	REDUCTANT FEED RATE CHANGE	REDUCTANT FEED RATE	ELECTRICAL POWER CHANGE	ELECTRICAL POWER
-	20,000 kg/h	-1 kg/ton ilm.	1,680 kg/h	-5 kWh/ton ilm.	21,615 kW



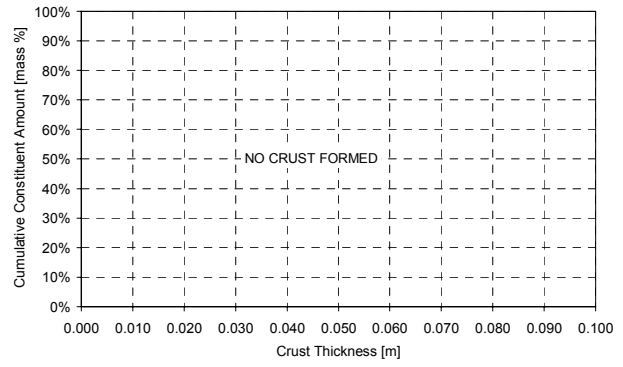
(a)



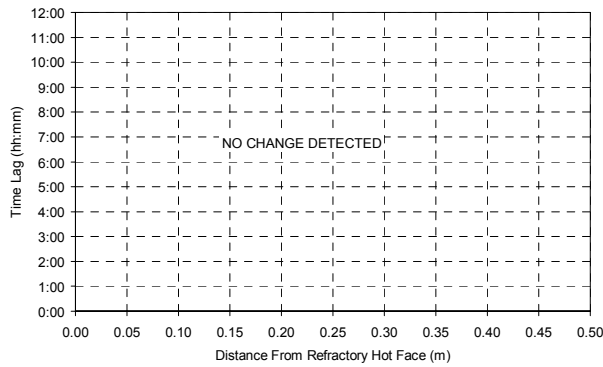
(b)



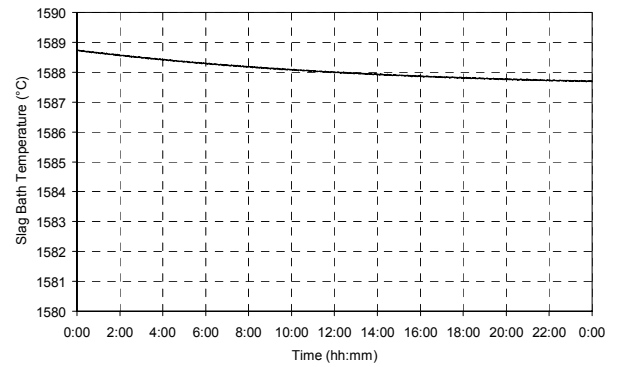
(c)



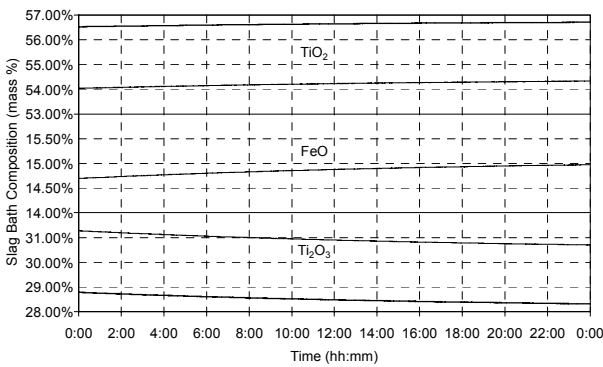
(d)



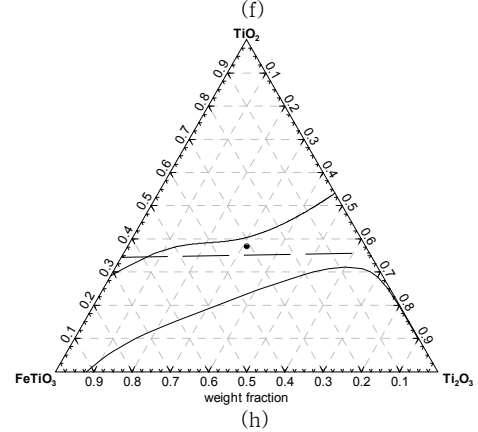
(e)



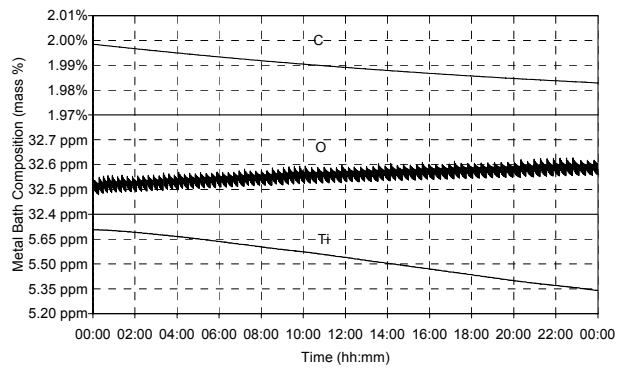
(f)



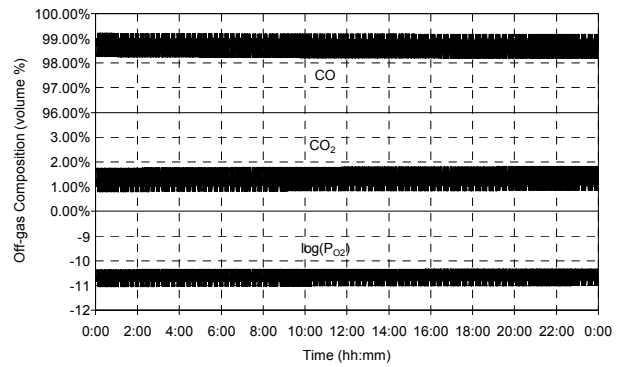
(g)



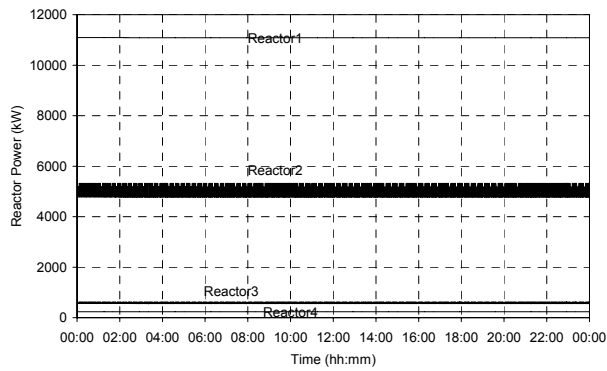
(h)



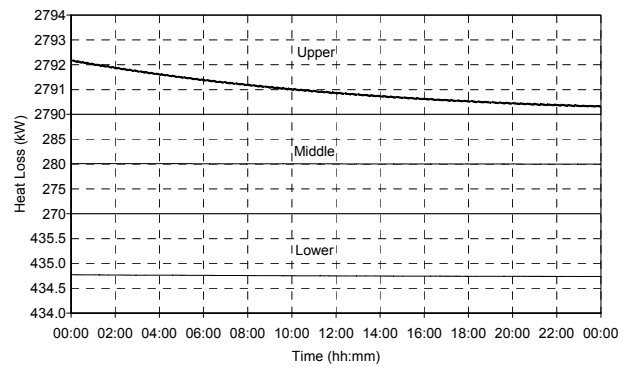
(i)



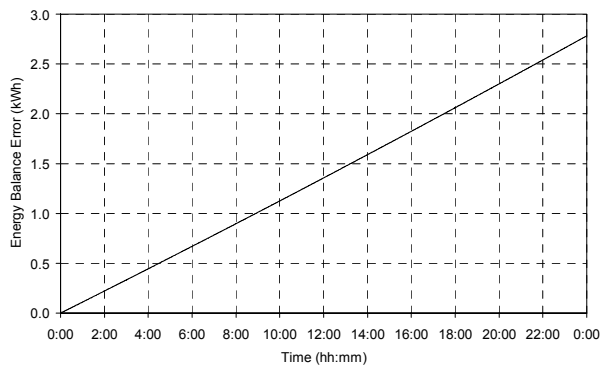
(j)



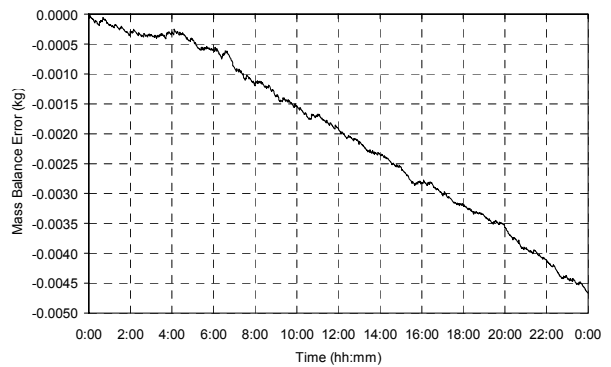
(k)



(l)



(m)

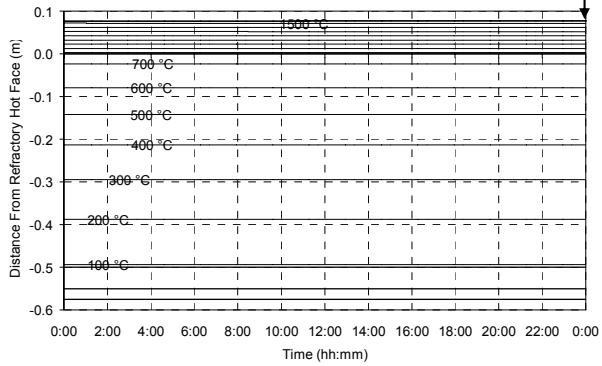


(n)

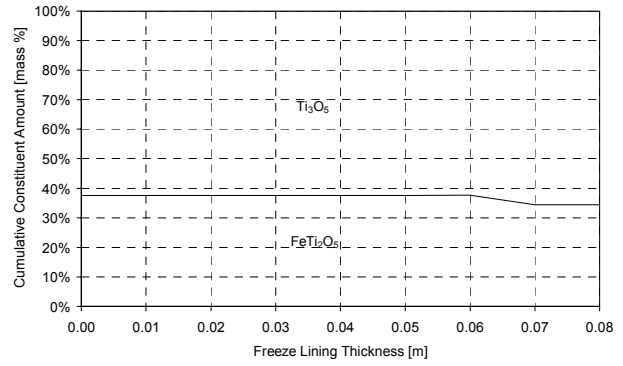
Figure 132 – Experiment 8.12 results.

8.3.13 Experiment 8.13

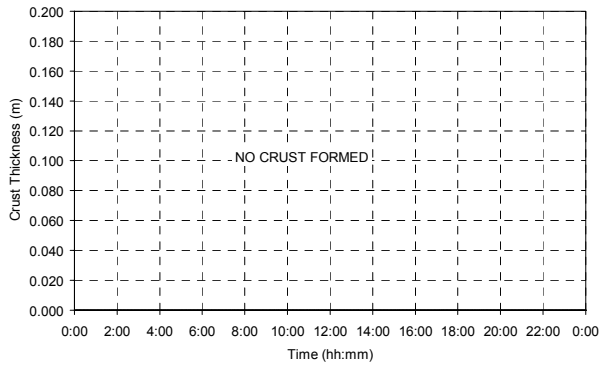
ILMENITE FEED RATE CHANGE	ILMENITE FEED RATE	REDUCTANT FEED RATE CHANGE	REDUCTANT FEED RATE	ELECTRICAL POWER CHANGE	ELECTRICAL POWER
-	20,000 kg/h	+ 2 kg/ton ilm.	1,740 kg/h	+ 10 kWh/ton ilm.	21,915 kW



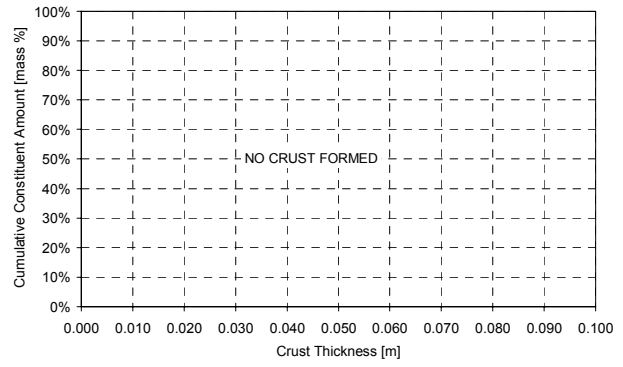
(a)



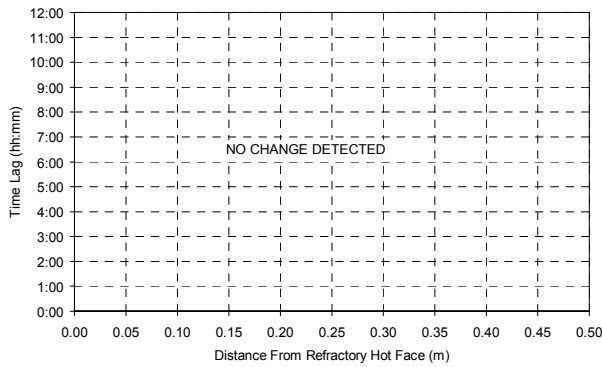
(b)



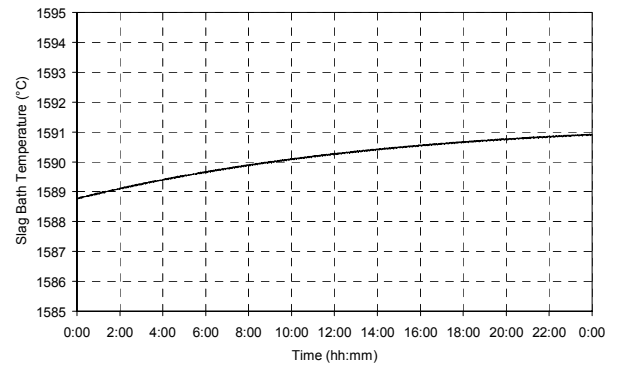
(c)



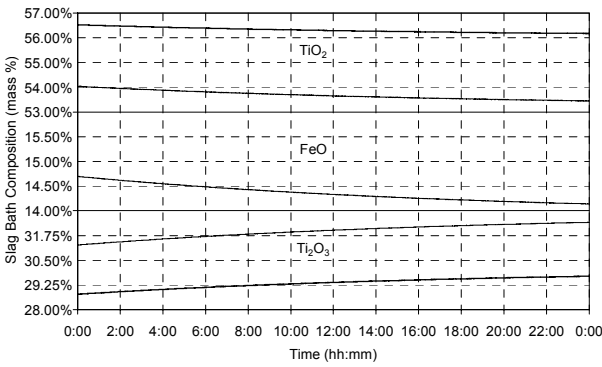
(d)



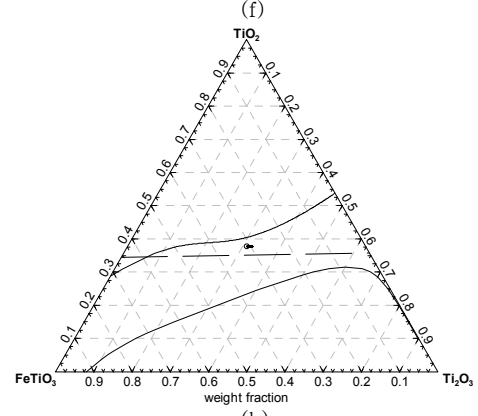
(e)



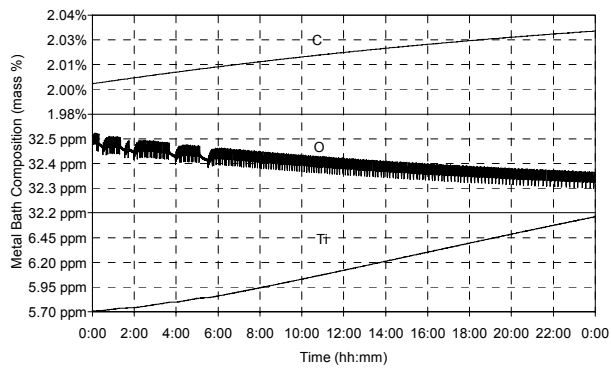
(f)



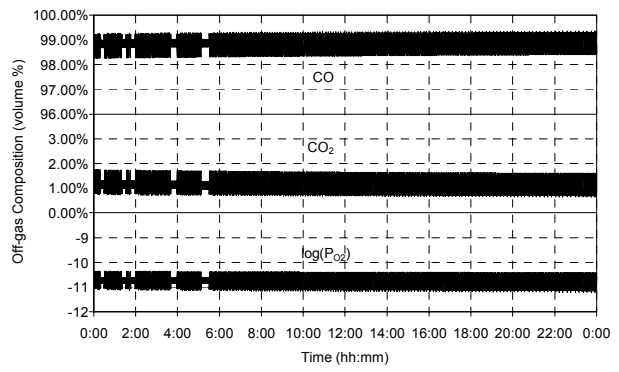
(g)



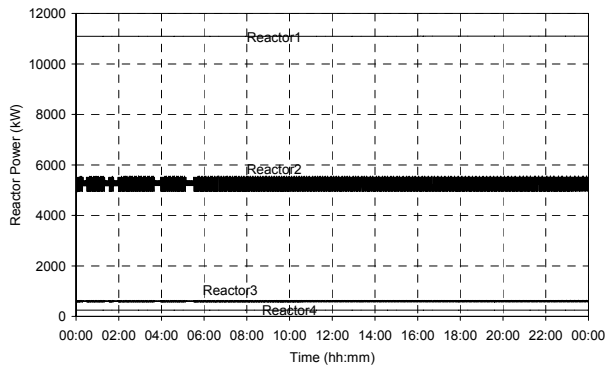
(h)



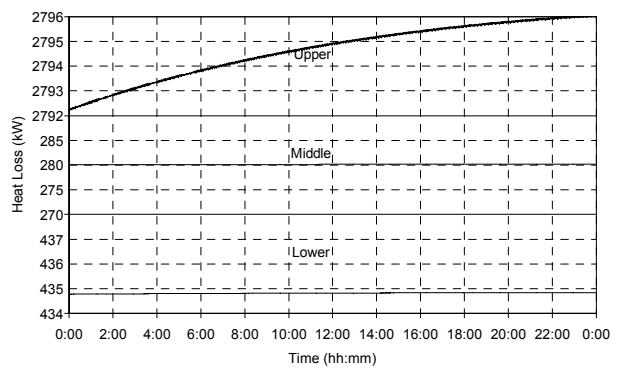
(i)



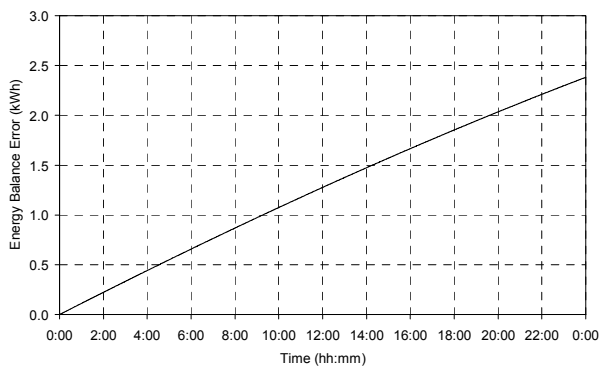
(j)



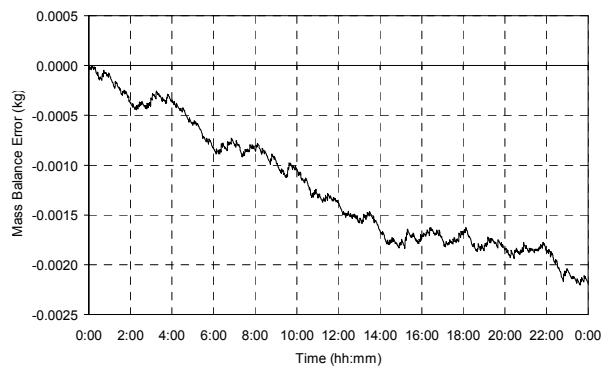
(k)



(l)



(m)



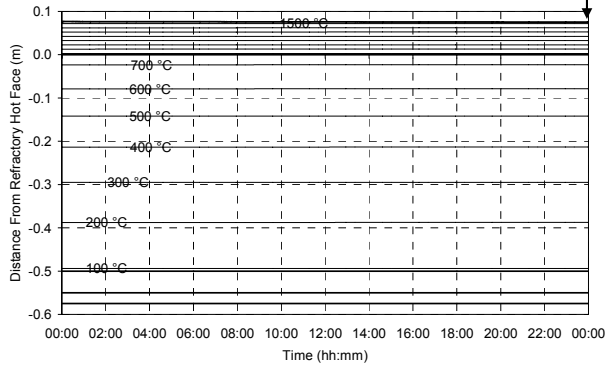
(n)

Figure 133 – Experiment 8.13 results.

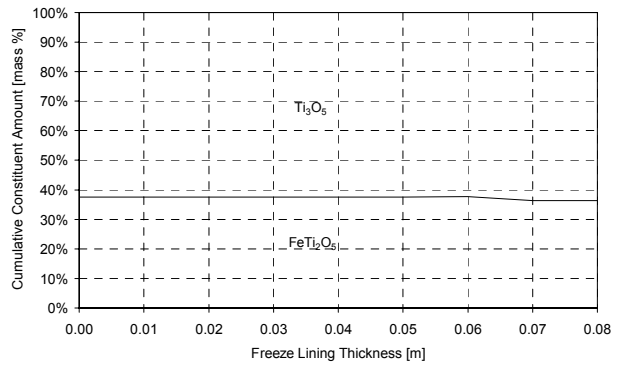


8.3.14 Experiment 8.14

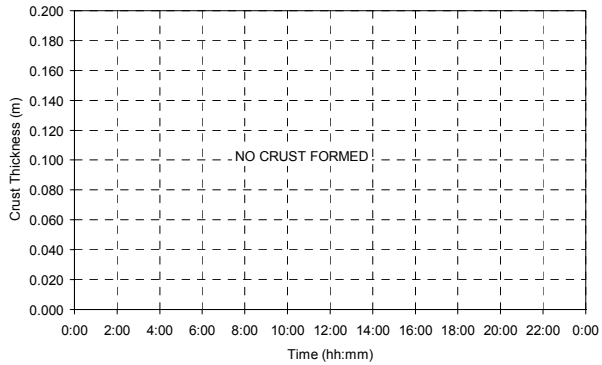
ILMENITE FEED RATE CHANGE	ILMENITE FEED RATE	REDUCTANT FEED RATE CHANGE	REDUCTANT FEED RATE	ELECTRICAL POWER CHANGE	ELECTRICAL POWER
-	20,000 kg/h	-2 kg/ton ilm.	1,660 kg/h	-10 kWh/ton ilm.	21,515 kW



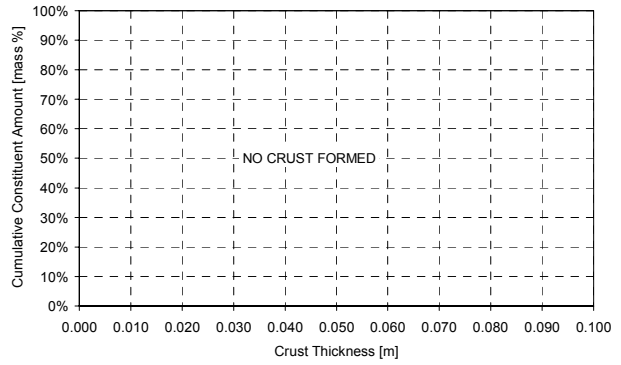
(a)



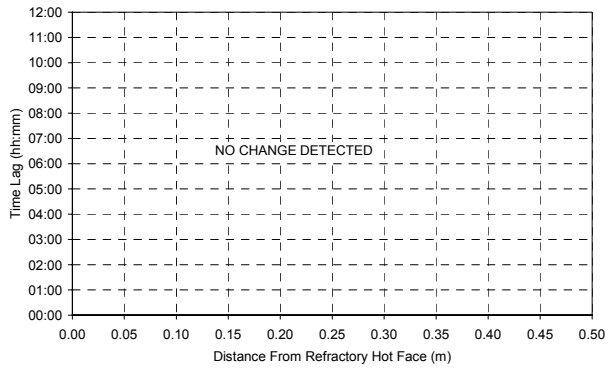
(b)



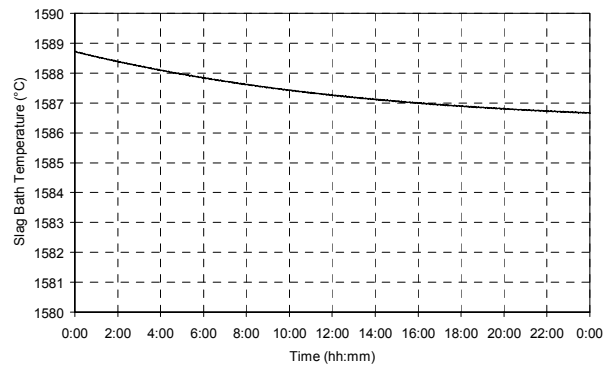
(c)



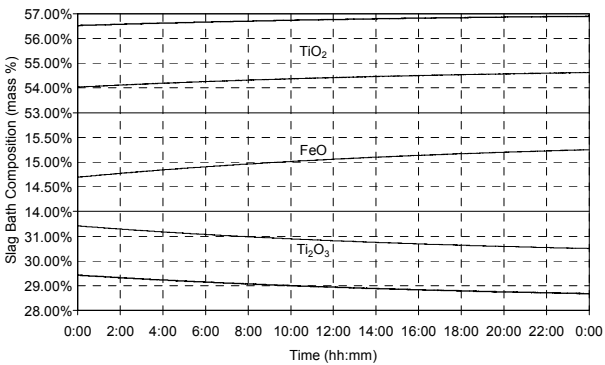
(d)



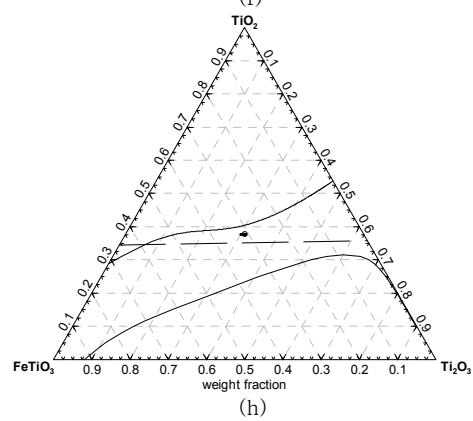
(e)



(f)



(g)



(h)

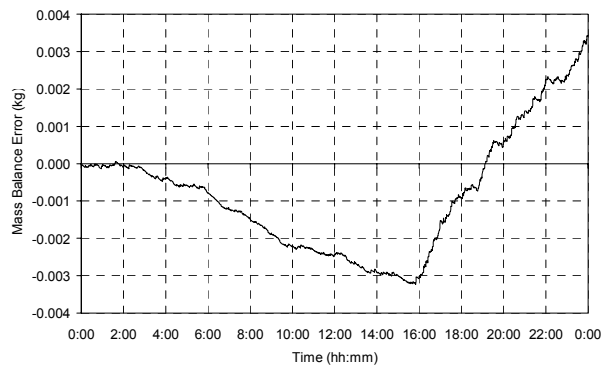
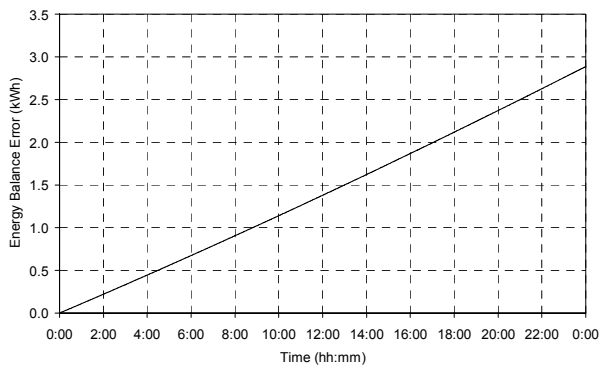
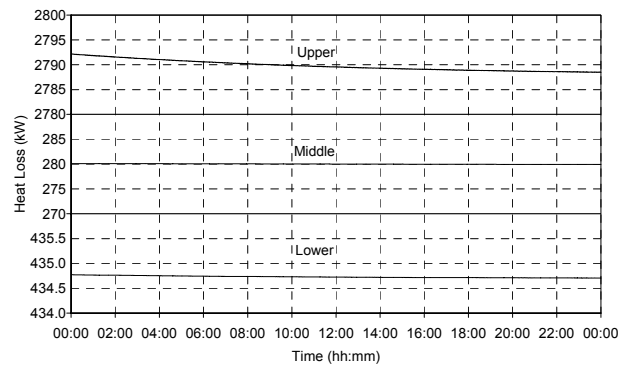
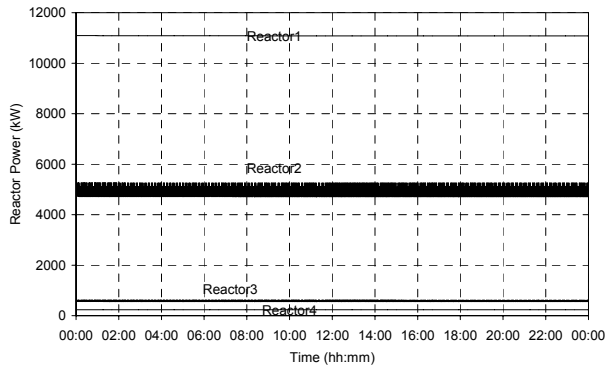
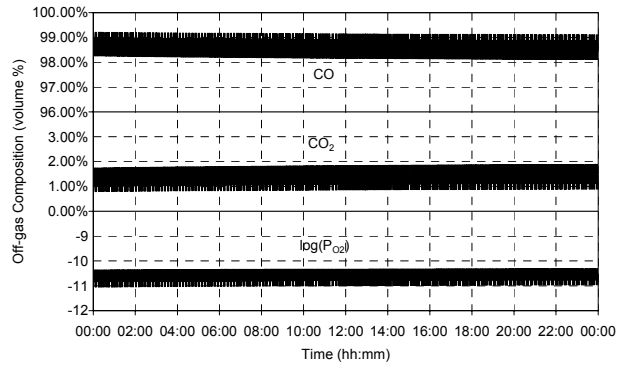
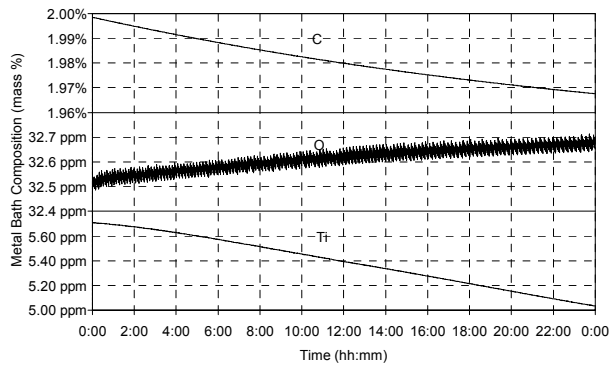
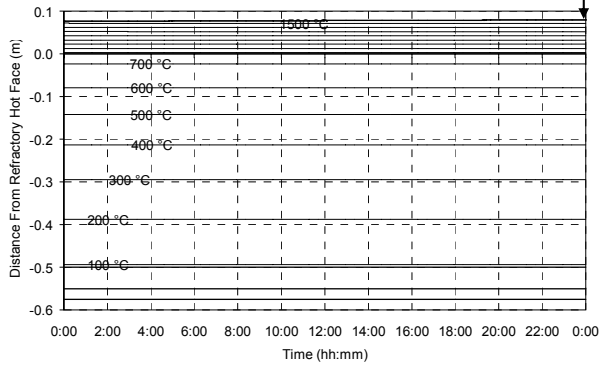


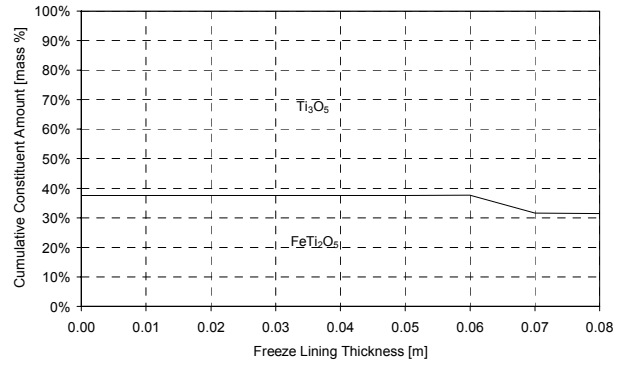
Figure 134 – Experiment 8.14 results.

8.3.15 Experiment 8.15

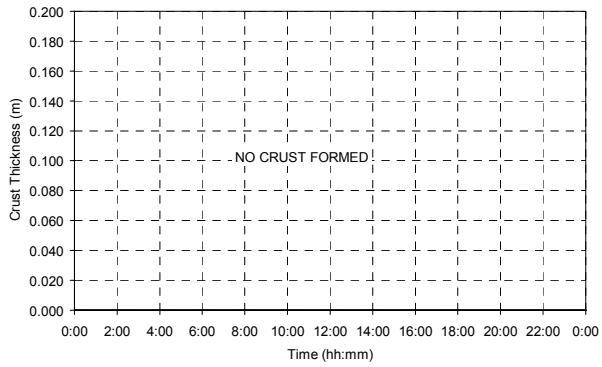
ILMENITE FEED RATE CHANGE	ILMENITE FEED RATE	REDUCTANT FEED RATE CHANGE	REDUCTANT FEED RATE	ELECTRICAL POWER CHANGE	ELECTRICAL POWER
-	20,000 kg/h	+ 5 kg/ton ilm.	1,800 kg/h	+ 25 kWh/ton ilm.	22,215 kW



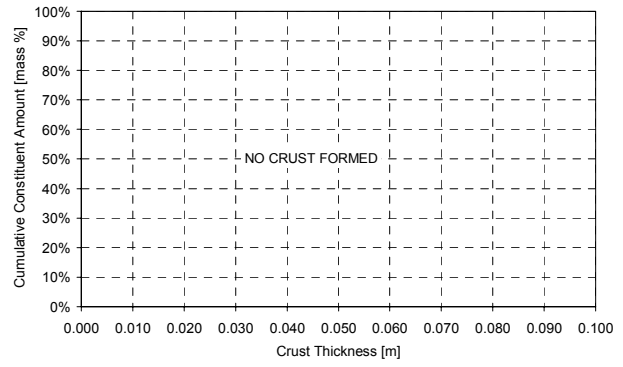
(a)



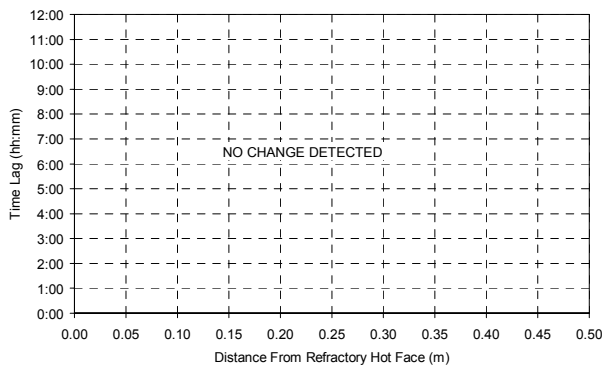
(b)



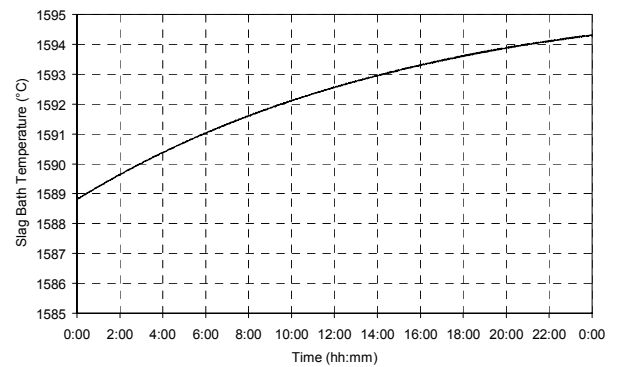
(c)



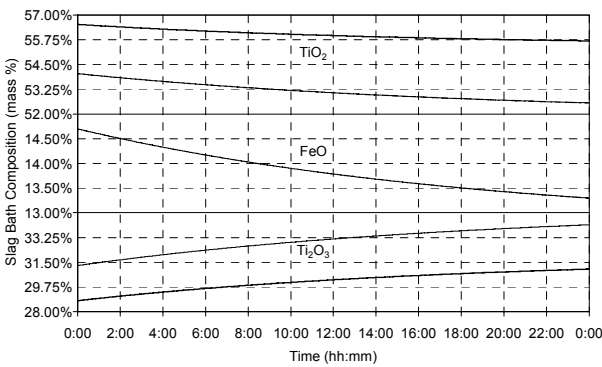
(d)



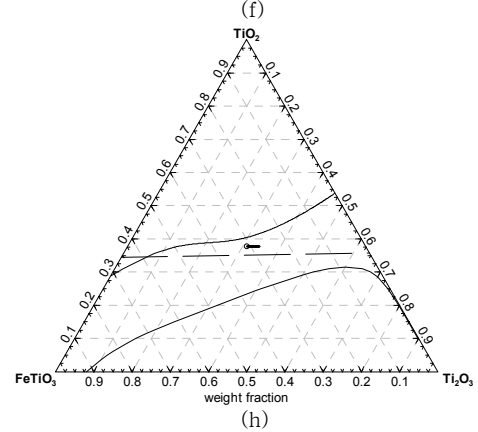
(e)



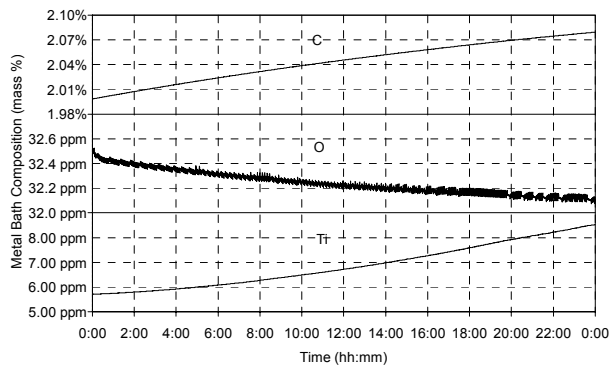
(f)



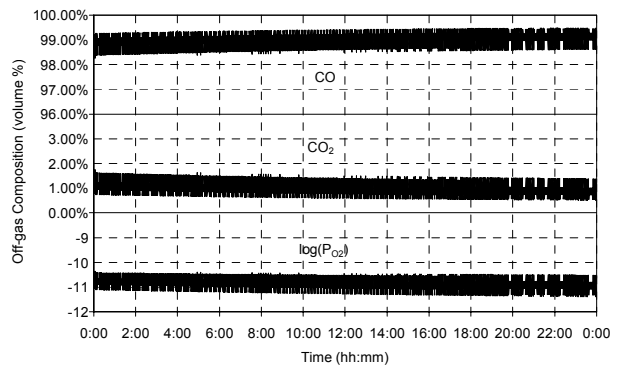
(g)



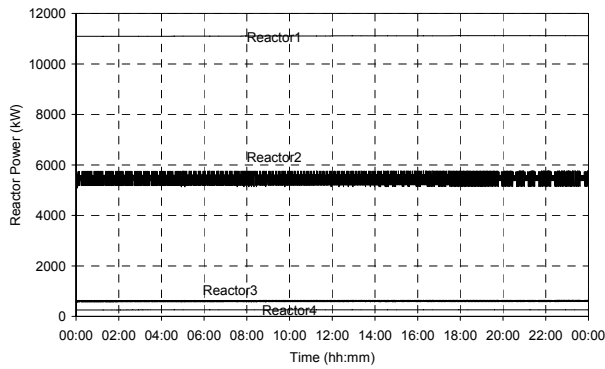
(h)



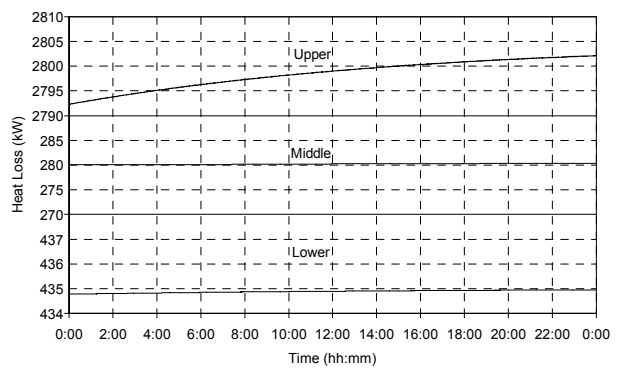
(i)



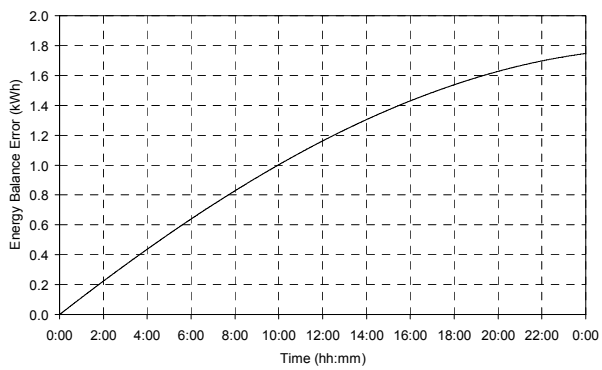
(j)



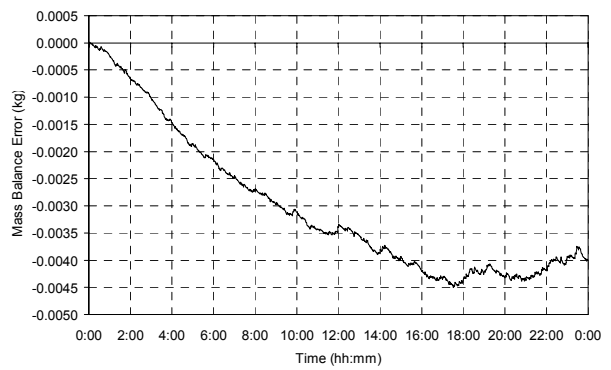
(k)



(l)



(m)

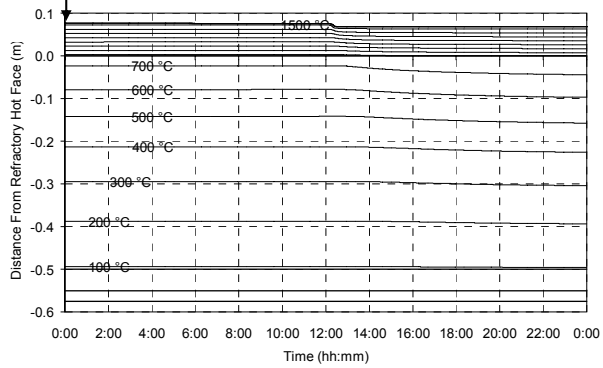


(n)

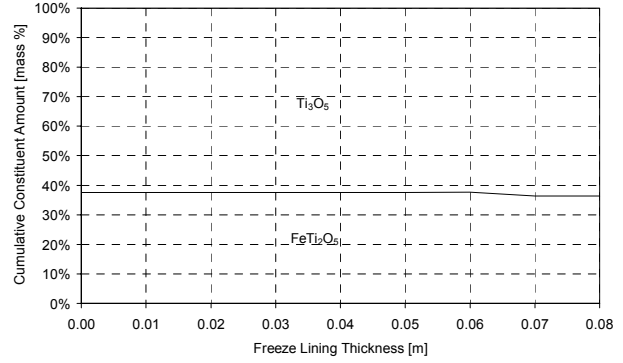
Figure 135 – Experiment 8.15 results.

8.3.16 Experiment 8.16

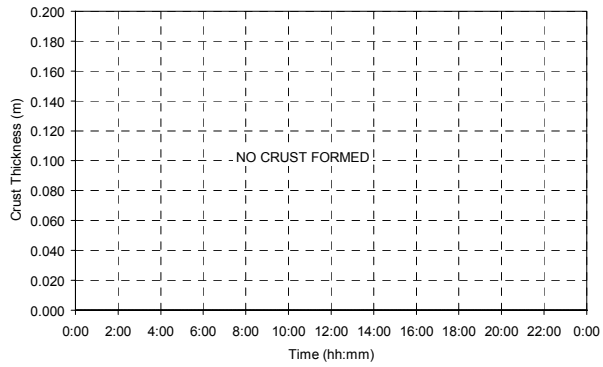
ILMENITE FEED RATE CHANGE	ILMENITE FEED RATE	REDUCTANT FEED RATE CHANGE	REDUCTANT FEED RATE	ELECTRICAL POWER CHANGE	ELECTRICAL POWER
-	20,000 kg/h	-5 kg/ton ilm.	1,600 kg/h	-25 kWh/t ilm	21,215 kW



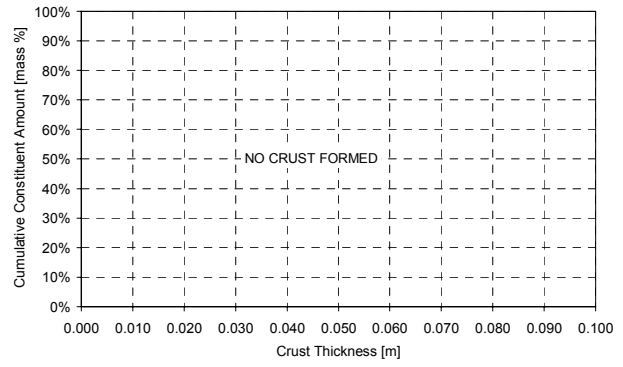
(a)



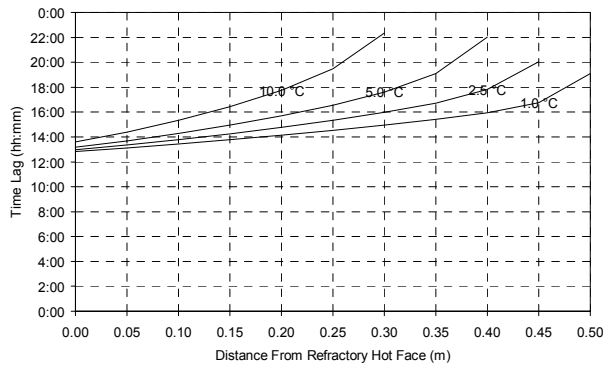
(b)



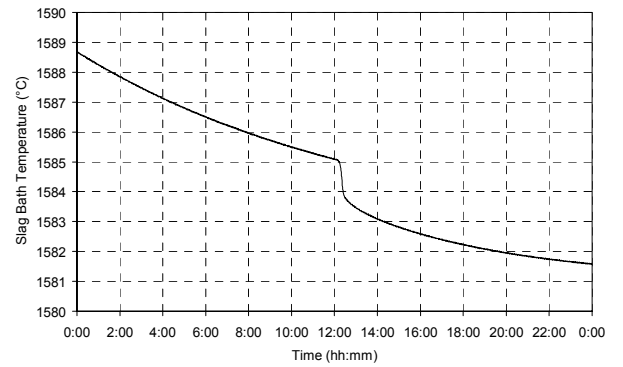
(c)



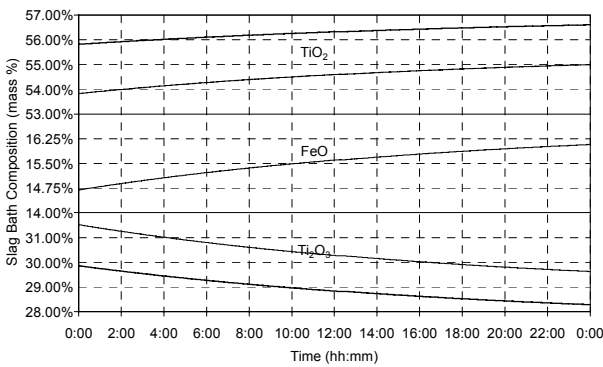
(d)



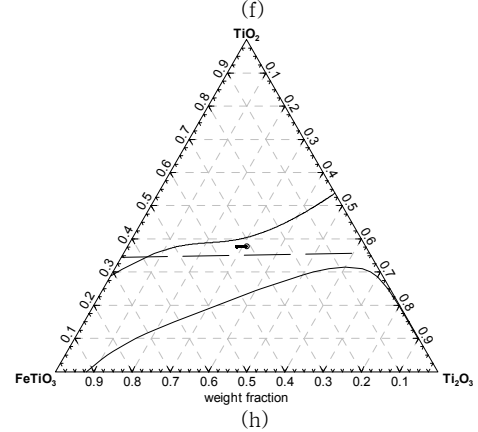
(e)



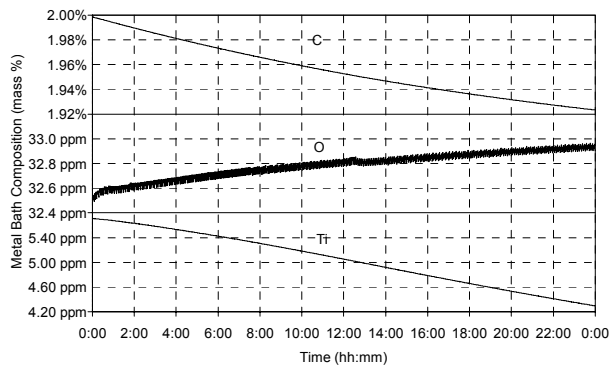
(f)



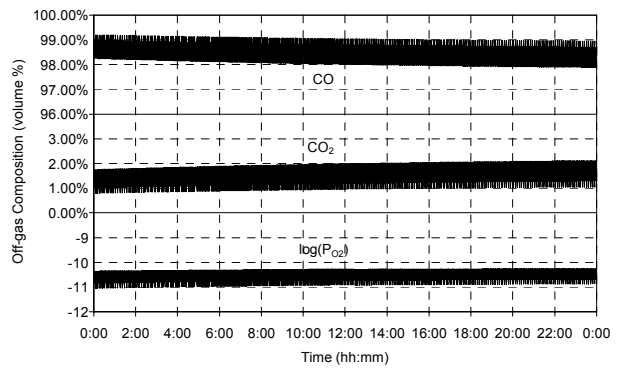
(g)



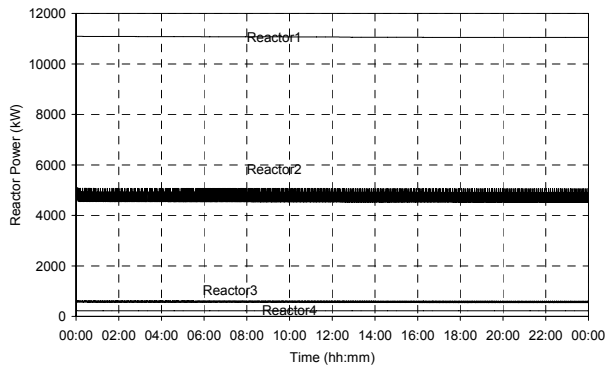
(h)



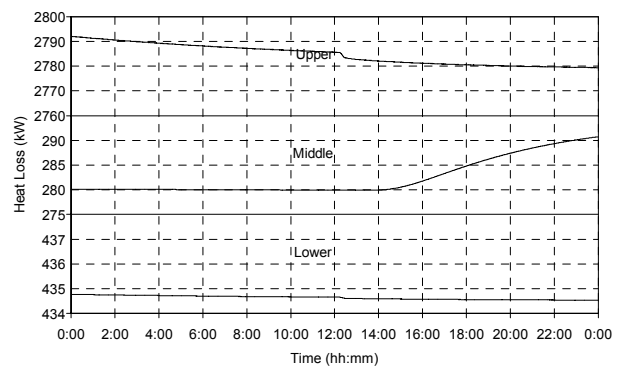
(i)



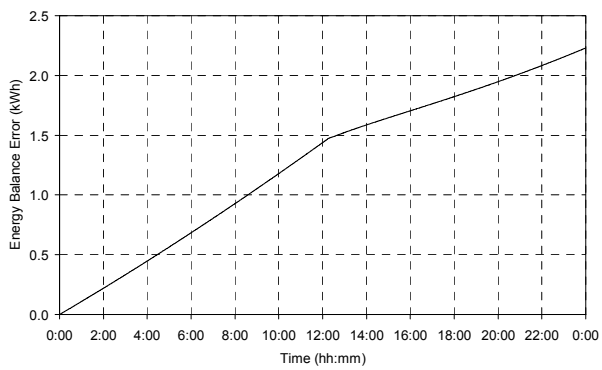
(j)



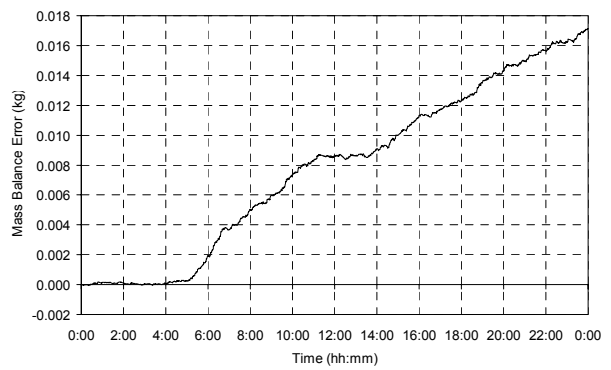
(k)



(l)



(m)

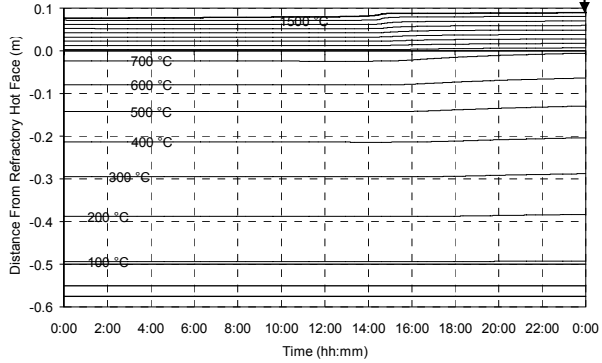


(n)

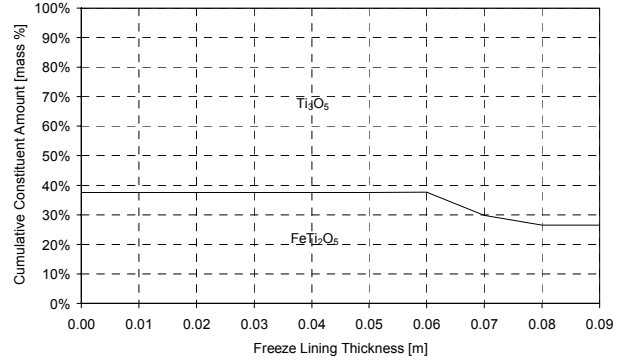
Figure 136 – Experiment 8.16 results.

8.3.17 Experiment 8.17

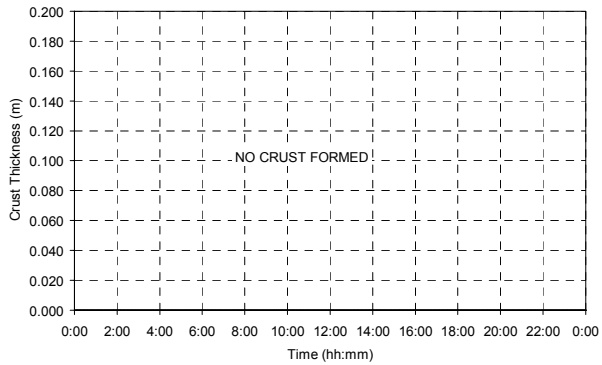
ILMENITE FEED RATE CHANGE	ILMENITE FEED RATE	REDUCTANT FEED RATE CHANGE	REDUCTANT FEED RATE	ELECTRICAL POWER CHANGE	ELECTRICAL POWER
-	20,000 kg/h	+ 10 kg/ton ilm.	1,900 kg/h	+ 50 kWh/ton ilm.	22,715 kW



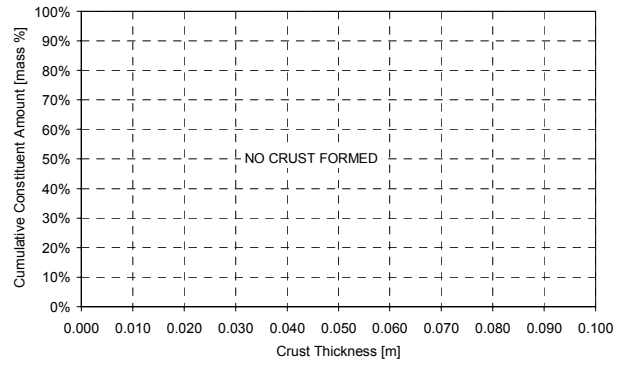
(a)



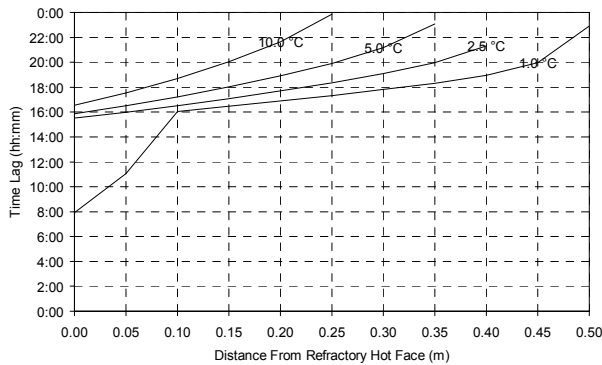
(b)



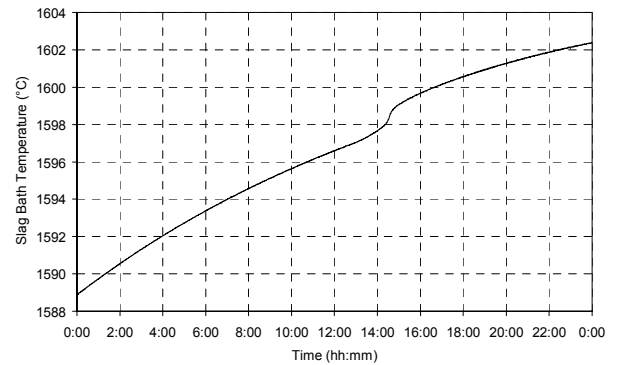
(c)



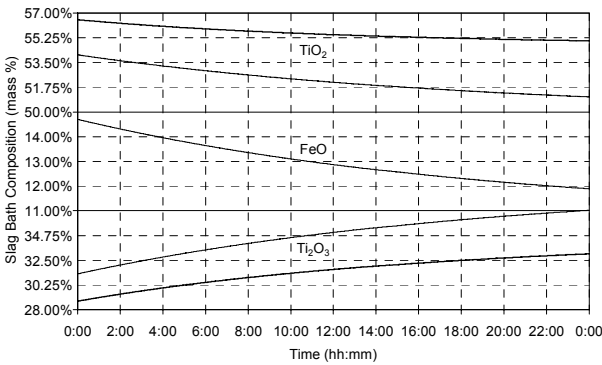
(d)



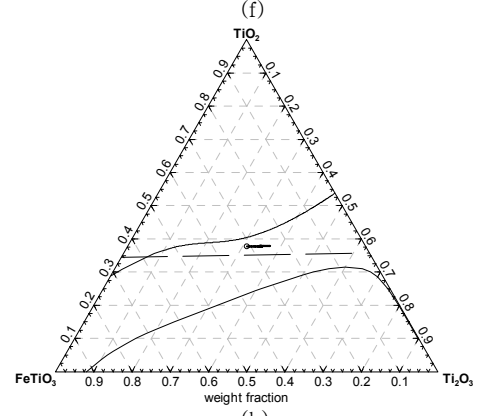
(e)



(f)



(g)



(h)

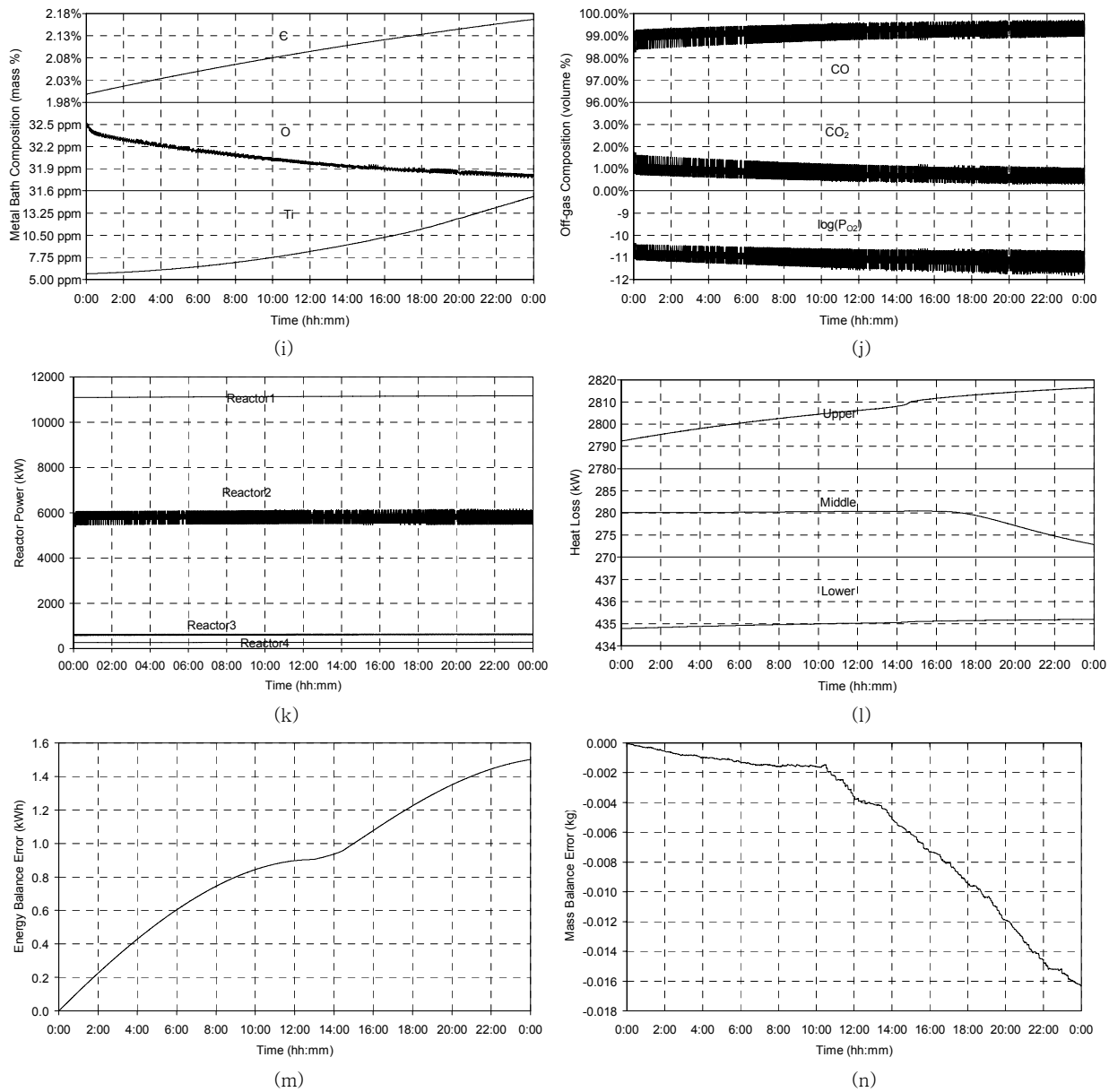
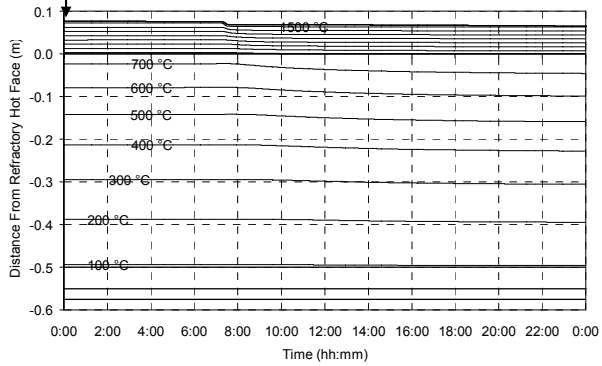


Figure 137 - Experiment 8.17 results.

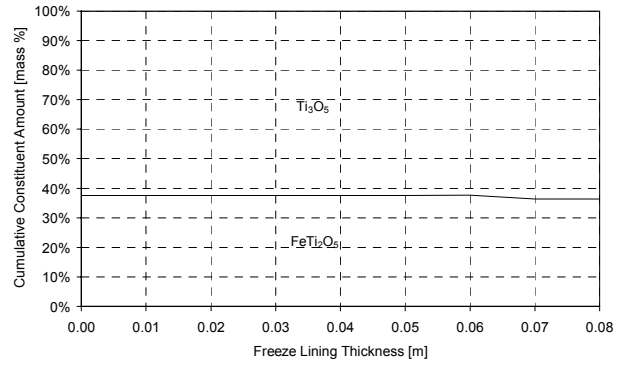


8.3.18 Experiment 8.18

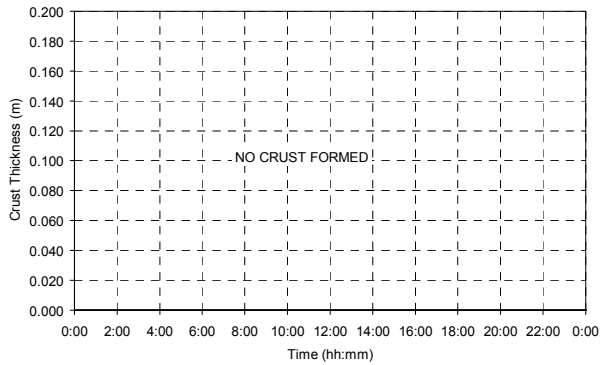
ILMENITE FEED RATE CHANGE	ILMENITE FEED RATE	REDUCTANT FEED RATE CHANGE	REDUCTANT FEED RATE	ELECTRICAL POWER CHANGE	ELECTRICAL POWER
-	20,000 kg/h	-10 kg/ton ilm.	1,500 kg/h	-50 kWh/ton ilm.	20,715 kW



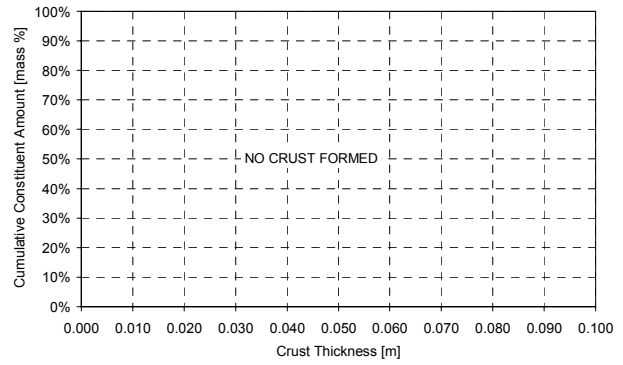
(a)



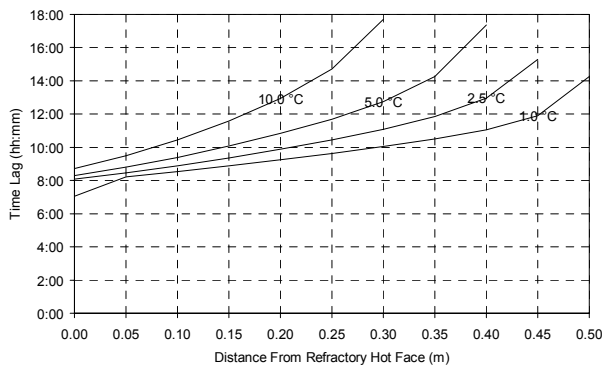
(b)



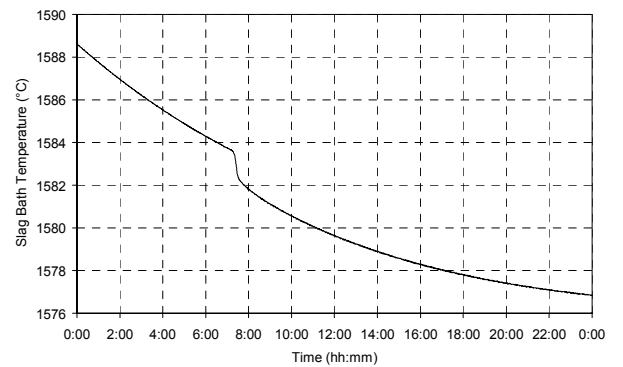
(c)



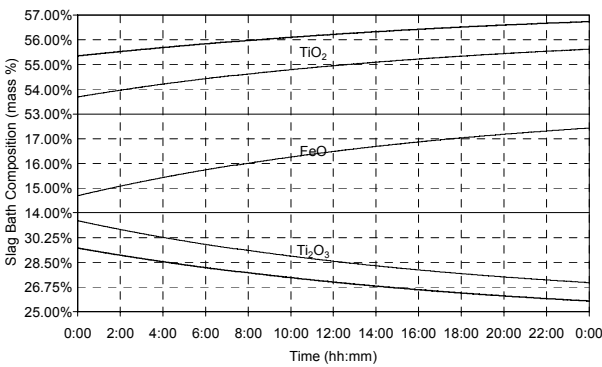
(d)



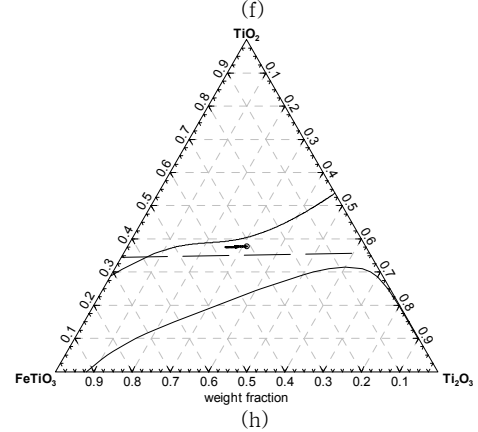
(e)



(f)



(g)



(h)

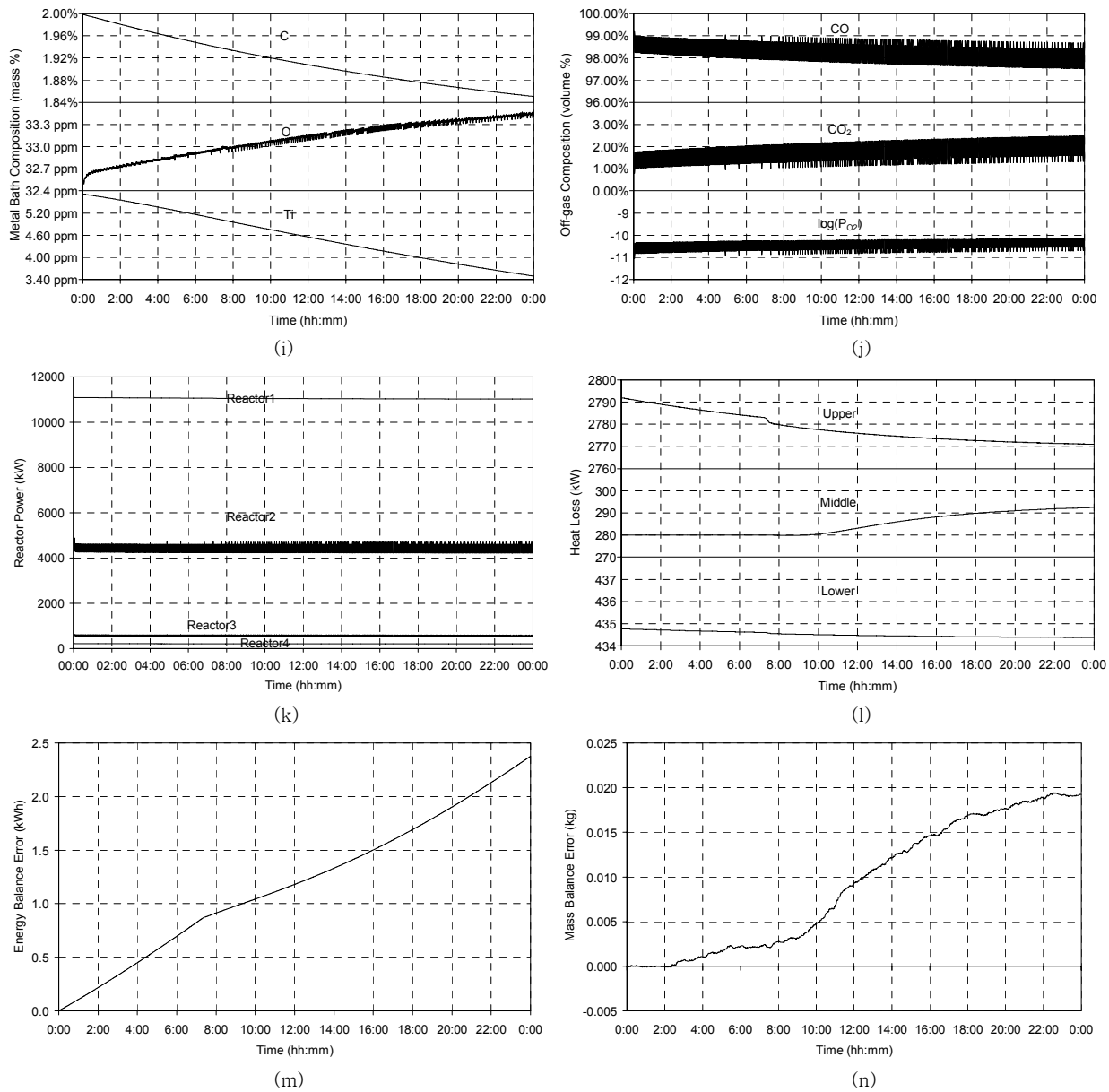
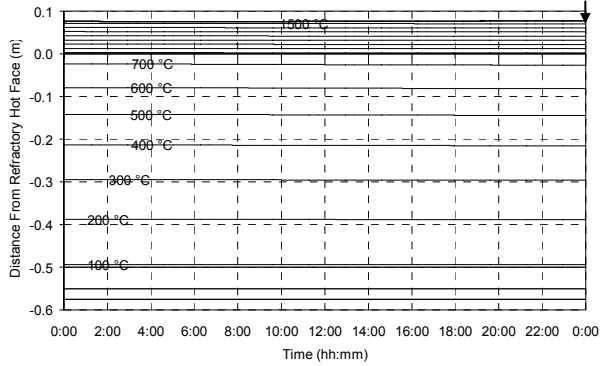


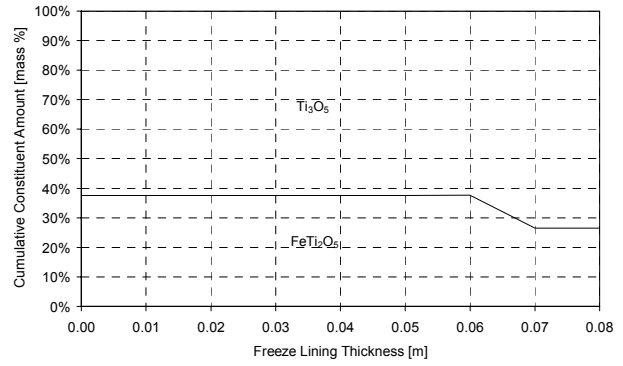
Figure 138 – Experiment 8.18 results.

8.3.19 Experiment 8.19

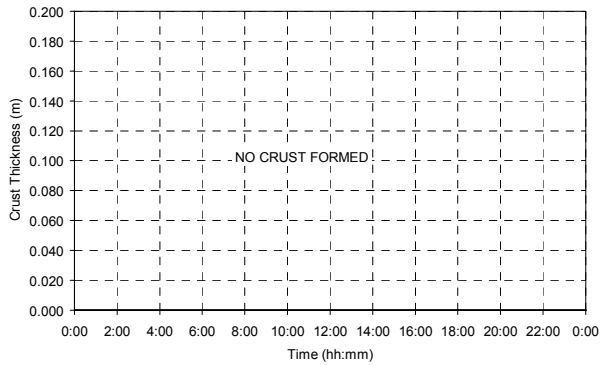
ILMENITE FEED RATE CHANGE	ILMENITE FEED RATE	REDUCTANT FEED RATE CHANGE	REDUCTANT FEED RATE	ELECTRICAL POWER CHANGE	ELECTRICAL POWER
-	20,000 kg/h	+ 10 kg/ton ilm.	1,900 kg/h	+ 52 kWh/ton ilm.	22,755 kW



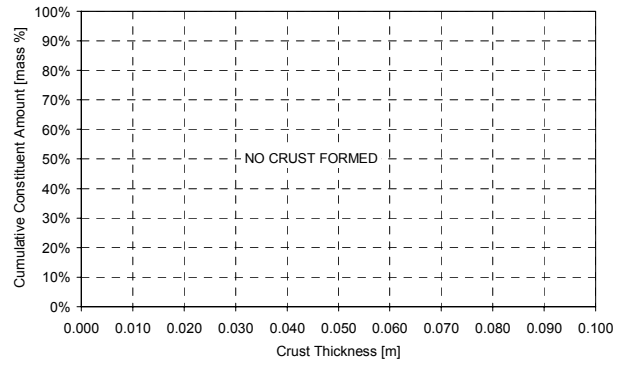
(a)



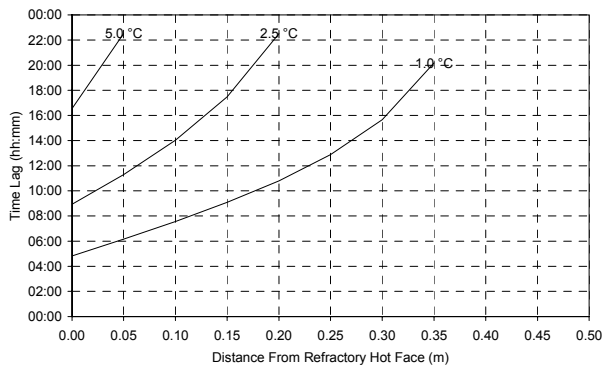
(b)



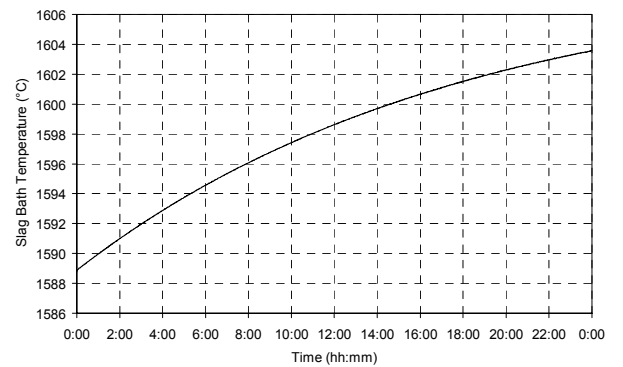
(c)



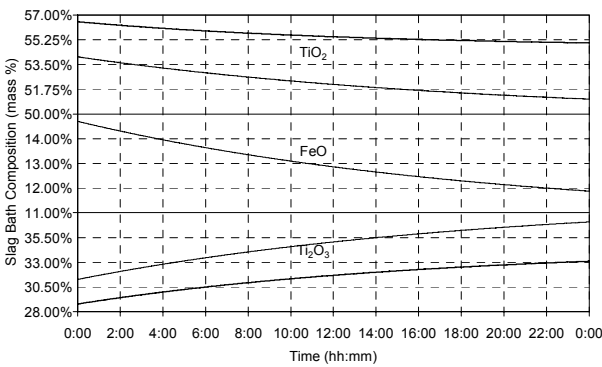
(d)



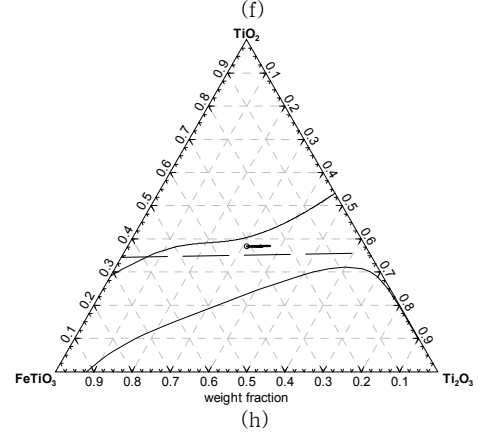
(e)



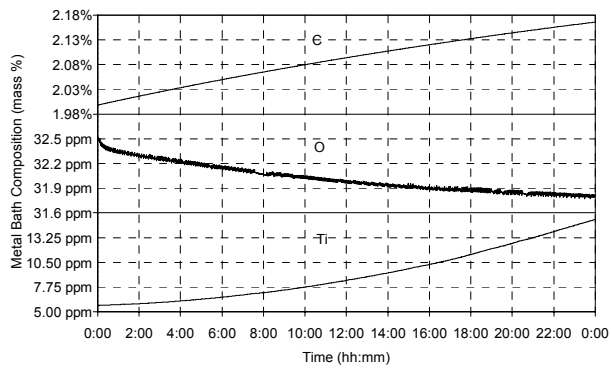
(f)



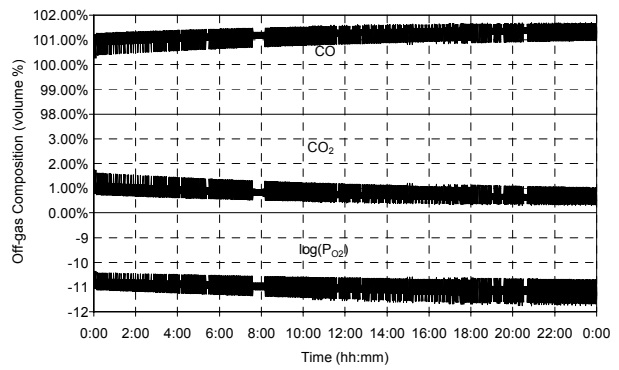
(g)



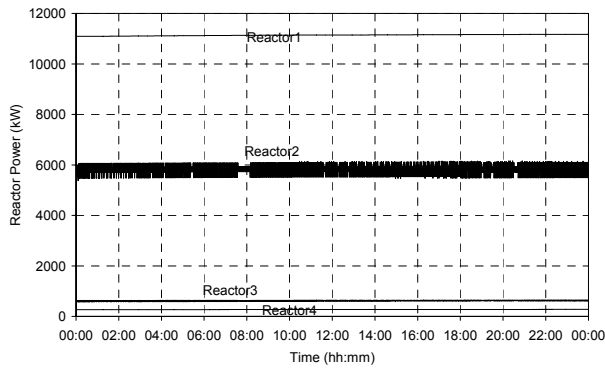
(h)



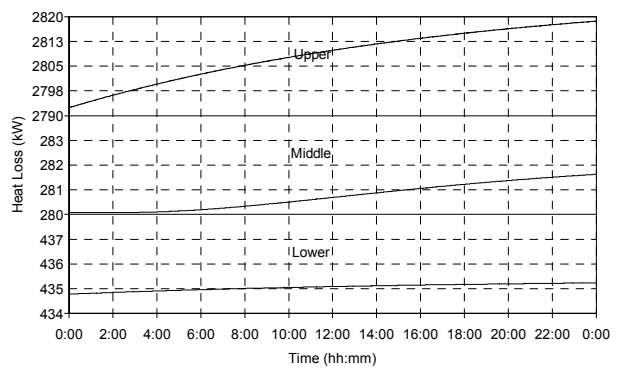
(i)



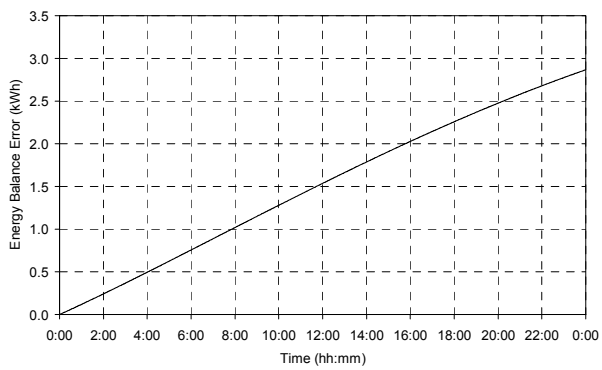
(j)



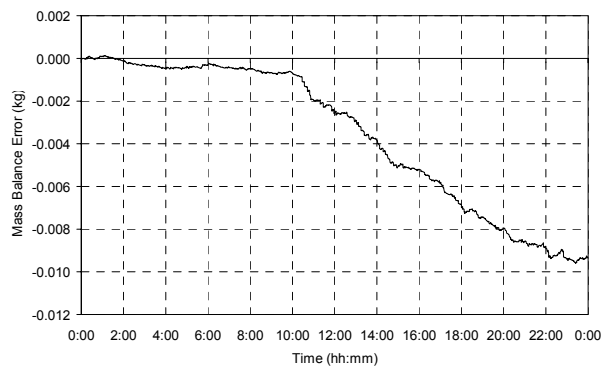
(k)



(l)



(m)

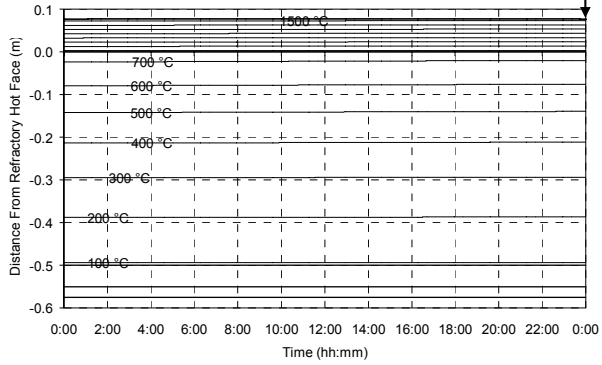


(n)

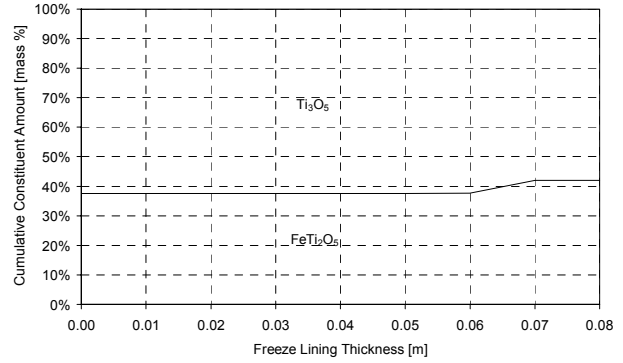
Figure 139 – Experiment 8.19 results.

8.3.20 Experiment 8.20

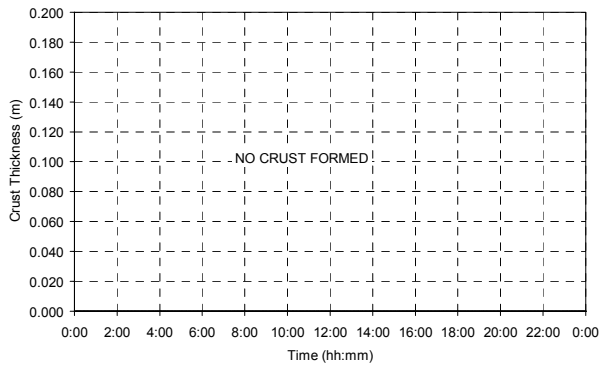
ILMENITE FEED RATE CHANGE	ILMENITE FEED RATE	REDUCTANT FEED RATE CHANGE	REDUCTANT FEED RATE	ELECTRICAL POWER CHANGE	ELECTRICAL POWER
-	20,000 kg/h	-10 kg/ton ilm.	1,500 kg/h	-53 kWh/ton ilm.	20,655 kW



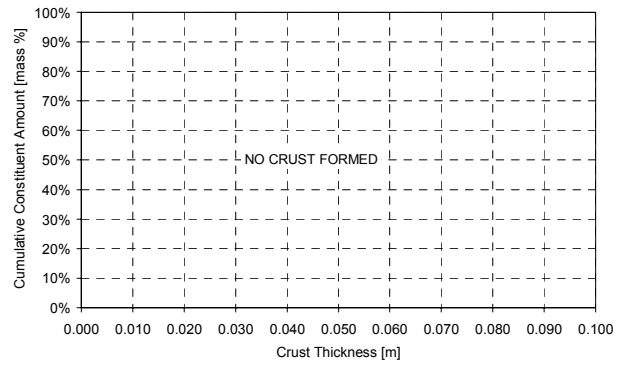
(a)



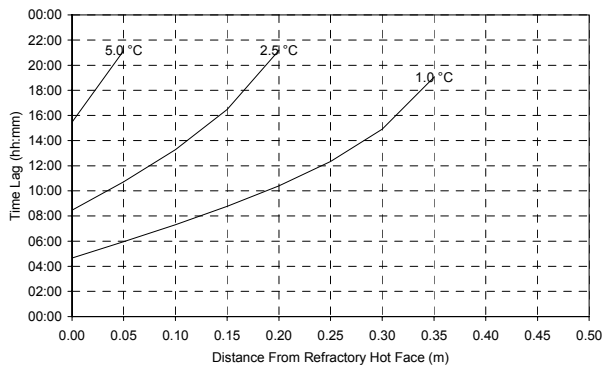
(b)



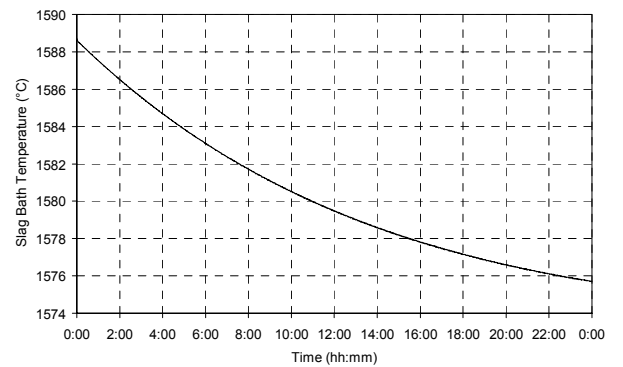
(c)



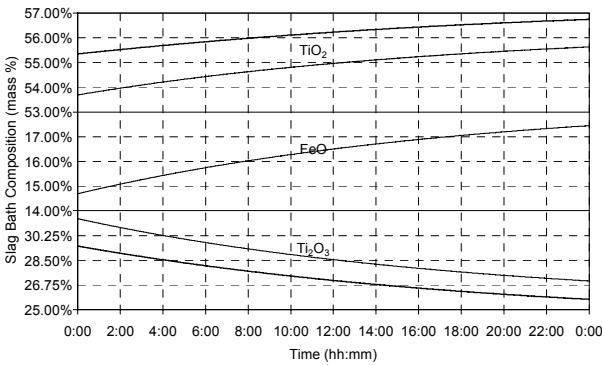
(d)



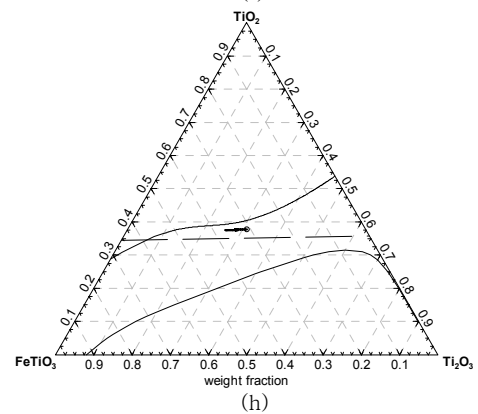
(e)



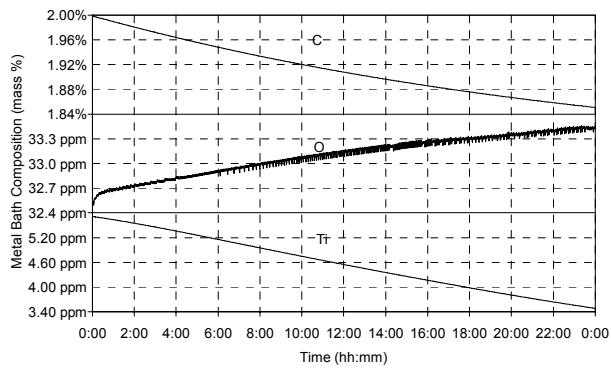
(f)



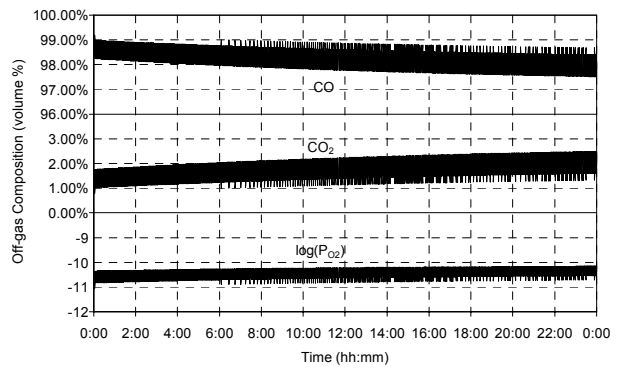
(g)



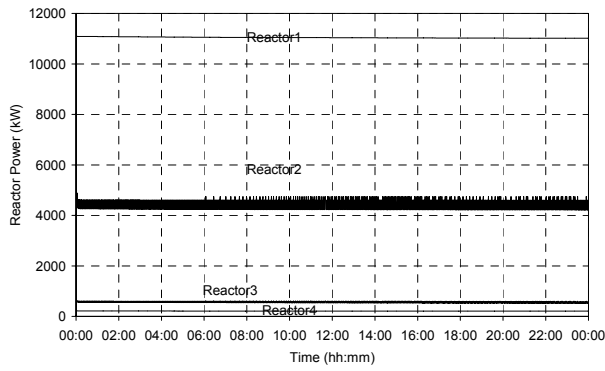
(h)



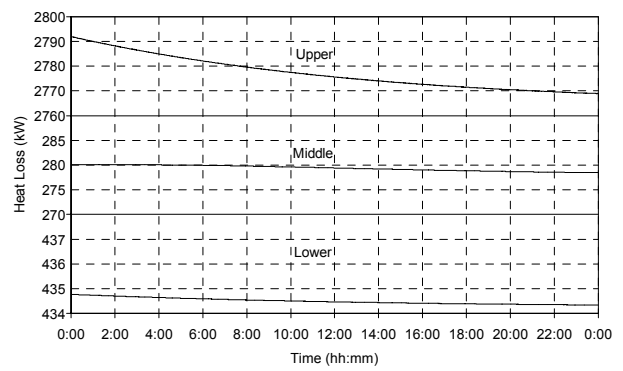
(i)



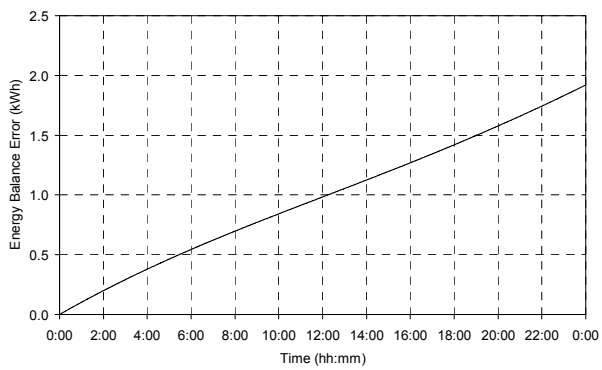
(j)



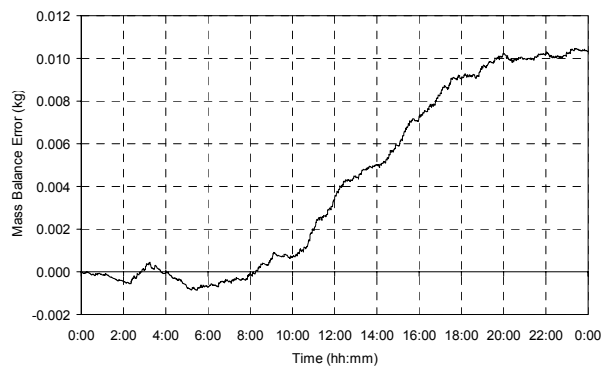
(k)



(l)



(m)



(n)

Figure 140 – Experiment 8.20 results.

## 8.4 DISCUSSION

The experimental results are discussed in the following paragraphs under these headings:

- The impact of severe operational errors
- Independent adjustment of reductant and energy inputs
- Combined adjustment of reductant and energy inputs

## 8.5 THE IMPACT OF SEVERE OPERATIONAL ERRORS

Experiments 8.1 and 8.2 simulated two scenarios in which severe operational errors occurred. Although industrial plants usually have a variety of measures in place to avoid these errors, there is always still the possibility of these or similar errors occurring. For this reason studying the impact of such errors remains relevant.

In the case of experiment 8.1 all feed (ilmenite and reductant) was stopped while the initial electrical power was maintained. This scenario is very similar to those simulated in CHAPTER 6, except that a much more complete process model was used here for conducting the simulation. In the situation described by this experiment, the electrical energy that is normally consumed by heating and melting of ilmenite, and by reduction reactions between slag and reductant suddenly becomes available for heating the slag. The consequences of this situation became clear in the experimental results.

Experiment 8.2 simulated a less severe error. Only the reductant feed was completely stopped and the ilmenite feed and electrical power was maintained. The only heat sinks removed from the system were therefore the reduction reactions between slag and reductant, and dissolution of carbon in the zone beneath the electrode.

### 8.5.1 Freeze Lining Thickness

The freeze lining disappeared completely 19 minutes after all feed was stopped in experiment 8.1. This is comparable to the results achieved in CHAPTER 6, where 10,000 kW of electrical power removed a 102 mm freeze lining in around 20 minutes and a 66 mm freeze lining in 13 minutes. One would expect the freeze lining in experiment 8.1 to melt away faster given the electrical power input of 21,715 kW. The effect of this power input was however reduced by heat losses from the slag bath surface, lower sidewalls and heart. The energy consumed by Reactor2 and Reactor4 in the initial stages of the experiment, and by Reactor3 throughout the experiment further reduced the effective power input. The rate at which the freeze lining disappeared can therefore be understood.

In experiment 8.2 it took 36.5 minutes for the freeze lining to melt away after reductant feed was stopped. The difference of 17.5 minutes compared with experiment 8.1 can be explained by the sustained energy consumption of Reactor1. Because the ilmenite feed rate was maintained, Reactor1 continued consuming in excess of 11,000 kW to heat and melt ilmenite. This reduced the rate at which the freeze lining melted away.

In both cases (experiment 8.1 and 8.2) the freeze lining disappeared at an alarming rate. If an operational error similar to those simulated goes unnoticed for a period longer than the time required for melting away the freeze lining, serious damage to the furnace lining can occur. Another point of concern is that the

freeze lining in an actual furnace does not have a constant thickness around the circumference of the furnace. This creates the possibility that damage may start to occur some time earlier than what is indicated above.

### 8.5.2 Freeze Lining Composition

Because graph (b) shows the composition of the freeze lining as a function of position at the point in time when the freeze lining was at its thickest, and because the freeze lining was at its thickest at the start of both experiments 8.1 and 8.2, no observations could be made from the results of these experiments.

### 8.5.3 Thermal Response of Freeze Lining and Furnace Wall

The thermal response of specifically the furnace wall is important when one considers the use of sidewall thermocouple signals for the purpose of controlling freeze lining thickness. Within the context of the situations simulated in experiments 8.1 and 8.2, it would be valuable if such thermocouple signals provided early warning of the impending damage.

From graph (e) in the experimental results of experiment 8.1 it is evident that a thermocouple capable of detecting and transmitting a 1 °C change in temperature must be installed at a position 5.7 cm away from the refractory hot face if it is to provide a warning within 19 minutes. However, after 19 minutes some damage would already have occurred. Deciding on a safety margin of 5 minutes would then mean that the thermocouple would have to be installed at the hot face of the refractory material. Even then it would only be able to warn 4 minutes before damage sets in.

In the case of experiment 8.2 the thermocouple would have to be installed 11.4 cm from the refractory hot face if its warning is to coincide with refractory damage; and 7.5 cm from the hot face if it is required to warn 5 minutes before.

From graph (a) it is apparent that if a thermocouple is installed 5 cm away from the hot face, it would be reading around 650 °C. The temperature at the hot face is just below 800 °C. At 10 cm the temperature is roughly 560 °C. All of these temperatures are comfortably within the range of type K thermocouples.

Organisations operating ilmenite-smelting furnaces are often conservative when it comes to the depth of insertion of thermocouples in furnace refractory materials. This can be understood because the refractory lining must last for a period of up to 10 years. However, from the results of experiments 8.1 to 8.2 it can be concluded that thermocouples installed at positions further than 5 cm from the refractory hot face would be of little use as warning signals in situations such as those simulated.

### 8.5.4 Slag Bath Temperature

As has been explained in previous chapters, slag bath temperature in an ilmenite-smelting furnace cannot vary independent from liquid slag composition while a freeze lining is present. The slag bath temperature is expected to closely follow the liquidus temperature of the slag. This was demonstrated by the experimental results presented in CHAPTER 6 and CHAPTER 7.

It is evident from graph (f) of experiments 8.1 and 8.2 that the temperature of the liquid slag had risen quite appreciably. The increase was 37 °C for experiment 8.1 and 16 °C for experiment 8.2. What is not evident



from these graphs is the difference between the slag bath temperature and the liquidus temperature of the slag.

Graph (h) of experiment 8.1 shows that only a slight change in slag composition occurred. Given such a small change and an increase of 37 °C in liquid slag temperature, one must conclude that either the liquidus temperature surface is very steep, or that there is an appreciable difference between the slag bath temperature and the liquidus temperature of the slag.

In the case of experiment 8.2 the change in composition is substantially greater, but towards the  $\text{FeTiO}_3$  corner of the graph. One would expect that the liquidus temperature would fall when the composition moves in that direction.

To make interpretation easier, the two (h) graphs were superimposed on the mass fraction version of the liquidus diagram presented in Figure 11.

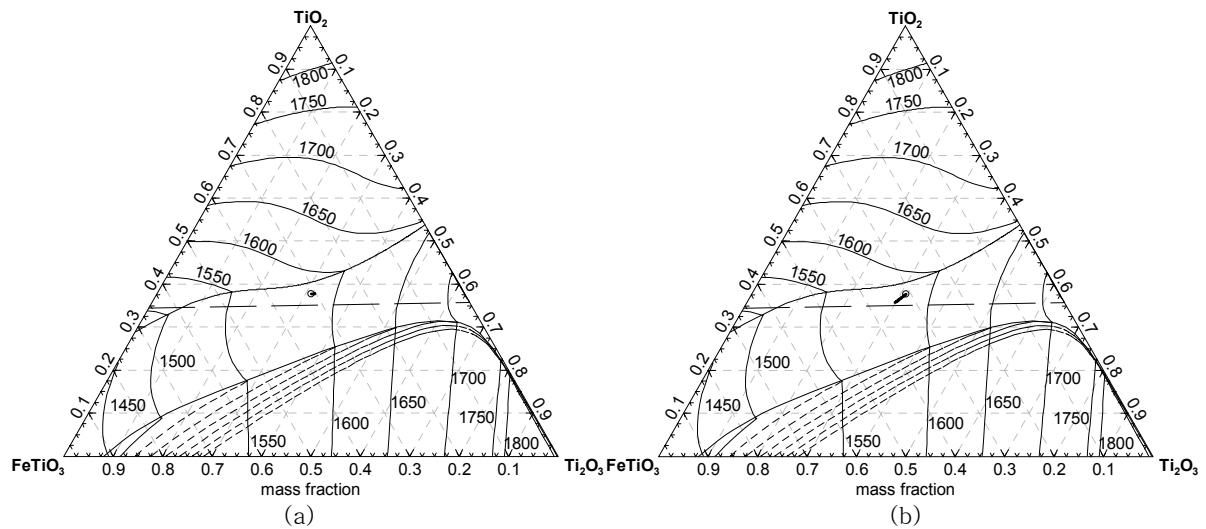


Figure 141 – Graph (h) of experiments 8.1 (a) and 8.2 (b) superimposed on the liquidus diagram.

From Figure 141 it is clear that the slag liquidus temperature in neither experiment went beyond 1600 °C. This means that the flow conditions created in the model by the FreezeLiningFlow and CrustFlow sub-models resulted in a significantly superheated slag bath. Because the model could not be validated on actual plant data, it is uncertain how well the model describes these aspects of the real process. The fact that the model described the freeze lining and crust parts of the process fairly well according to the knowledge and experience of the author about the ilmenite–smelting process, does however lend some confidence to these results. The results are expected to deviate quantitatively from reality, but should display qualitatively what can be expected from an actual process.

### 8.5.5 Slag Bath Composition

The change in liquid slag composition in experiment 8.1 was largely the result of solid slag from the freeze lining entering into the slag bath. Some reduction at the interface between the slag and metal baths also contributed to the change in composition.

A more pronounced change in liquid slag composition occurred during experiment 8.2. The situation in this experiment is comparable (in terms of material inputs) to experiment 7.20. In experiment 8.2 the slag composition also moved towards the  $\text{FeTiO}_3$  corner of graph (h). The direction of the movement seemed to be offset to some degree by the composition of the freeze lining material melted into the bath and, to a lesser degree, reduction taking place at the interface between the slag and metal baths.

### 8.5.6 Metal Bath Composition

The rate of change in carbon content of the metal bath was virtually identical for experiments 8.1 and 8.2. After 10 minutes both had reached 1.99% and after 20 minutes both were at 1.98%. The carbon content dropped further during the second half of experiment 8.2 because of the longer duration.

It is evident from the metal bath O and Ti contents of the two experiments that the oxidation potential in the furnace changed in different directions. During experiment 8.1 the oxygen content of the metal decreased and the Ti content increased with time as a result of reduction reactions between the slag and metal baths removing oxygen from the system.

In the case of experiment 8.2 the trend was in the opposite direction even though the same reduction reactions were active at roughly the same rate, as was evident from the change in carbon content. The reason for the difference is the large quantity of oxygen carried into the furnace with the ilmenite feed.

### 8.5.7 Off-gas Composition

The off-gas composition echoed the observations made from the metal bath composition results. The partial oxygen pressure during experiment 8.2 was clearly higher at  $10^{-10}$  atm compared with that of experiment 8.1 at  $10^{-10.6}$  atm.

### 8.5.8 Reactor Power

The reactor power results shown in graph (k) of experiments 8.1 and 8.2 presented no surprises. Reactor1 power dropped off suddenly during experiment 8.1, but was maintained during experiment 8.2. This is as a result of ilmenite feed being stopped in experiment 8.1.

The power of Reactor2 and Reactor4 diminished during both experiments. This happened because reductant feed was stopped at the start of both experiments. No reductant was therefore available after some time for reaction in these two reactors.

Reactor3 maintained its power in both experiments because contact between the slag and metal baths remained unchanged during both experiments.

### 8.5.9 Heat Losses

Experiment 8.1 and 8.2 furnace heat loss results as shown in graph (l) also behaved as expected. The losses from the lower part of the furnace increased in both cases as a result of an increase in iron temperature. The losses from the middle of the furnace remained virtually constant because of the lag inherent in the heat transfer path through the freeze lining and furnace wall. Similar inertia should have been evident in the lower-furnace heat loss results because conduction also takes place through a

refractory layer. The simplified way in which this heat transfer was modelled however eliminated this lag. The upper-furnace losses rose steadily because of the increase in the temperature of the slag bath.

## 8.6 INDEPENDENT ADJUSTMENT OF REDUCTANT AND ENERGY INPUTS

In experiments 8.3 to 8.10 the suggested 1:5 ratio of reductant input to energy input was deliberately ignored to determine the influence of independent adjustment of these two process inputs. The following four independent adjustments were studied:

- Increase in reductant feed rate (experiments 8.3 and 8.5).
- Decrease in reductant feed rate (experiments 8.4 and 8.6).
- Increase in energy input rate (experiments 8.7 and 8.9).
- Decrease in energy input rate (experiments 8.8 and 8.10).

Experiments 8.5 and 8.10 were run for a period shorter than 24 hours due to software instabilities.

### 8.6.1 Freeze Lining Thickness

The behaviour of the freeze lining during the experiments presented no surprises. In cases where more energy became available (experiments 8.4, 8.6, 8.7 and 8.9), the freeze lining became thinner. During the other four experiments where additional energy was consumed by reduction reactions or simply removed from the electrical power input, the freeze lining became thicker.

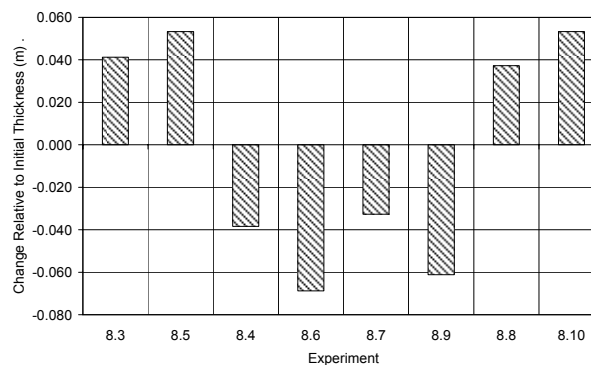


Figure 142 – Chapter 8 subset 2 change in freeze lining thickness.

From the experimental results it is evident that an independent increase in reductant feed rate has, in terms of freeze lining thickness, an influence that is very similar to a decrease in energy input rate given that the ratio between the set points is 1:5. The same similarity was observed between a decrease in reductant feed rate and an increase in energy input rate. This similarity is understandable since an increase in reductant feed rate causes additional energy to be consumed, and a decrease in reductant feed rate causes energy to become available for heating and melting of slag.

### 8.6.2 Freeze Lining Composition

Graph (b) in the result sets could only be used for interpretation in the case of experiments 8.3, 8.5, 8.8 and 8.10 because these were the only experiments that showed an increase in freeze lining thickness.

In all these cases the solidified material consisted of only pseudobrookite and no rutile. After close inspection, it was found that the pseudobrookite  $\text{FeTi}_2\text{O}_5$  content decreased with time during experiments 8.3 and 8.5, and increased in the case of experiments 8.8 and 8.10. These tendencies are not visible in graph (b) because of the scale that was selected. The change in  $\text{FeTi}_2\text{O}_5$  content was dominated by the increase in reduction during experiments 8.3 and 8.5; and by the enrichment of the liquid slag in FeO due to solidification during experiments 8.8 and 8.10.

### 8.6.3 Thermal Response of Freeze Lining and Furnace Wall

The thermal response of the furnace wall as described by graph (e) in each result set varied visibly between the various experiments. The pattern that is present in the data shows that larger set point changes causes quicker response than smaller changes. The response of the wall was also quicker in cases where the freeze lining became thinner compared with cases where the freeze lining grew thicker. Both these observations are consistent with the observations made in paragraph 6.4.2 (page 170).

### 8.6.4 Crust Thickness

Crust formation only occurred during experiments 8.5 and 8.10 (graph (c)). The reason for the crust formation was the relatively large change in energy input rate that resulted from the set point changes applied during these experiments. In both cases the energy input rate was effectively reduced by 200 kW. This reduction in energy input rate firstly caused the freeze lining to grow thicker. This solidification was however not enough to prevent the slag bath temperature from falling below its liquidus. The result was that solid slag was also formed in the Crust conductor module.

The indication of crust formation given by the model may indeed be accurate in that a crust would form in reality. Another possibility is that the solid slag would actually precipitate throughout the slag bath away from the zone close to the arc. Such precipitation would lead to an increase in effective slag viscosity, and an increased probability of slag foaming. Such process instabilities have been known to accompany incorrect set point changes that cause the furnace to become colder and 'close up'.

The volume fraction of solids in the slag bath can be calculated simply by dividing the crust thickness by the slag bath thickness (1 m). The solids content gives an indication of the effective slag viscosity.

### 8.6.5 Crust Composition

The solid slag in the crust consisted of only pseudobrookite and no rutile, similar to the freeze lining. The composition of the pseudobrookite was also very similar to that of the freeze lining. This is to be expected because liquid slag from the slag bath is the source for both the freeze lining and crust.

### 8.6.6 Slag Bath Temperature

Experiments 8.3 and 8.5 showed an initial drop in slag bath temperature, followed by a slow rise. The origin of the initial drop is not clear. The steady rise, however, can be attributed to the changing slag composition and the changing slag liquidus temperature.

The same initial drop in temperature was observed during experiments 8.8 and 8.10. Once again it is not known what the cause of this behaviour is. In these experiments the initial fall in temperature was followed

by a slow decrease in slag bath temperature. This is the result of the slight change in slag bath composition that was caused by slag solidification. In experiment 8.10 the slag bath temperature started increasing slightly once the freeze lining had reached a new stable thickness. This was the result of the slag bath composition starting to change in the opposite direction compared with before.

The slag bath temperature decreased during experiments 8.4 and 8.6 as a result of the decrease in reductant feed rate causing an increase in FeO content. During experiments 8.7 and 8.9 the change was in the opposite direction because of the dominant influence being the introduction of higher melting point material entering into the slag bath from the freeze lining.

### 8.6.7 Slag Bath Composition

Relative changes in slag bath composition for the subset of experiments being discussed here are shown in Figure 143. All changes were calculated as a percentage of the initial composition of each phase constituent.

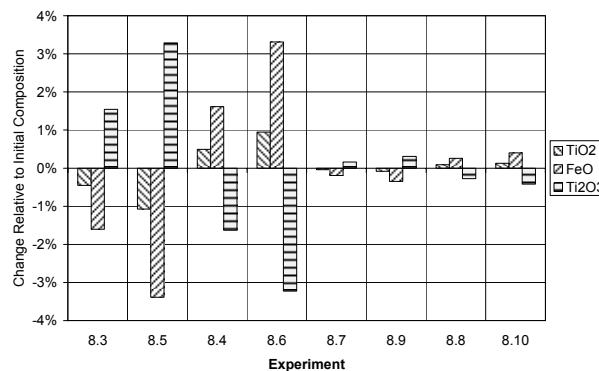


Figure 143 – Slag bath composition change relative to initial composition.

The variations in slag bath composition for the range of experiments were expected. Experiments 8.3 to 8.6 showed an increase in Ti<sub>2</sub>O<sub>3</sub> content and a decrease in FeO and TiO<sub>2</sub> content when the reductant feed rate was increased (experiments 8.3 and 8.5). The opposite was observed when the reductant feed rate was reduced (experiments 8.4 and 8.6).

In the case of experiments 8.7 to 8.10, the only influence on slag bath composition was that of solidification and melting. The FeO and TiO<sub>2</sub> content increased and the Ti<sub>2</sub>O<sub>3</sub> content decreased when the freeze lining became thicker (experiments 8.8 and 8.10). When the freeze lining melted away (experiments 8.7 and 8.9), the change in composition was in the opposite direction.

### 8.6.8 Metal Bath Composition

The reason for the noisy signals in this graph is the approach followed to constrain the slag bath composition close to the M<sub>3</sub>O<sub>5</sub> composition. See paragraphs 5.6.8a and 5.6.8b for details.

Relative changes in slag bath composition for the subset of experiments being discussed here are shown in Figure 144. All changes were calculated as a percentage of the initial composition of each phase

constituent. The results for oxygen in this figure are less accurate, especially for the small changes in composition during experiments 8.7 to 8.10. This is the result of the noise in the oxygen content signal. The change in oxygen content was therefore ignored when interpreting the results of these four experiments.

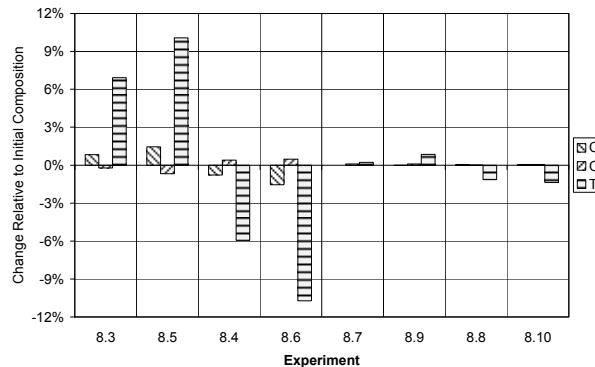


Figure 144 – Metal bath composition change relative to initial composition.

The first four experiments in the subset again did not present any surprises. The increase in reductant feed rate in experiments 8.3 and 8.5 resulted in more reducing conditions in the slag bath. This is evident from the increase in carbon and titanium content, and the reduction in oxygen content for these experiments. The decrease in reductant feed rate in experiments 8.4 and 8.6 had the opposite effect.

The change in composition during experiments 8.7 to 8.10 was expected to be minimal because only the power set point was changed. This was certainly the case for the carbon content. As mentioned before, the oxygen content will not be discussed here. The change in Ti content was also small, but more noticeable than what was expected.

The reason for the increase in Ti content during experiments 8.7 and 8.9 was the composition of the freeze lining that was being melted into the slag bath. This solid slag had a  $Ti_2O_3$  content of roughly 40% and was situated on the stoichiometric  $M_3O_5$  line indicated on graph (h) of the experimental results. This composition is significantly more reduced than the liquid slag in the furnace throughout the duration of the experiment. This resulted in the newly melted slag acting as a ‘reductant’ when entering the slag bath.

The explanation for the decrease in Ti content during experiments 8.8 and 8.10 can be explained similarly. Because the power set point was reduced during these experiments, liquid slag started to solidify. Because solidification tends to enrich the slag bath in  $FeO$  and  $TiO_2$  and reduce the  $Ti_2O_3$  content, the metal bath is gradually exposed to a more oxidised slag bath. This resulted in Ti being oxidised from the metal bath by the slag bath.

### 8.6.9 Off-gas Composition

The reason for the noisy signals in this graph is the approach followed to constrain the slag bath composition close to the  $M_3O_5$  composition. See paragraphs 5.6.8a and 5.6.8b for details.

The off-gas composition results as shown in graph (j) of the experimental results were consistent with expectations. The partial oxygen pressure dropped when the reductant feed rate was increased (experiments 8.3 and 8.5) and increased when the reductant feed rate was decreased (experiments 8.4 and 8.6).

Virtually no change in partial oxygen pressure was observed for experiments 8.7 to 8.10. This is to be expected, because the greatest influence on the off-gas composition comes from Reactor2. This reactor was only subjected to a slight change in slag composition resulting from solidification and melting.

### 8.6.10 Reactor Power

The reason for the noisy signals in this graph is the approach followed to constrain the slag bath composition close to the  $M_3O_5$  composition. See paragraphs 5.6.8a and 5.6.8b for details.

The changes in reactor power relative to the initial steady state for experiments 8.3 to 8.10 are shown in Figure 145. The power values for the various experiments were calculated by taking an average over the duration of the experiment.

For all experiments in the subset, the power of Reactor1 (heating and melting of ilmenite feed) changed only slightly relative to the initial steady state. In the case of experiments 8.3 to 8.6 Reactor1 power was lower than the initial steady state. This was because the slag bath temperature was lower than the initial steady state value for most of the duration of all four of these experiments. In the case of experiments 8.7 to 8.10 Reactor1 power increased when the electrical power set point was increased, and decreased when the electrical power set point was decreased. The reason for this was again the temperature of the slag bath relative to the initial steady state value.

The origin of the relationship between slag temperature and Reactor1 power lies in the fact that this reactor heats up the entering ilmenite to the temperature of the IsoMod1 isothermal module and transforms it to the liquid state. Since the SlagBath mixer module is contained in IsoMod1, it assumes the IsoMod1 temperature. Changes in this temperature influence the enthalpy required to heat up the molten ilmenite, and therefore directly influence Reactor1's power.

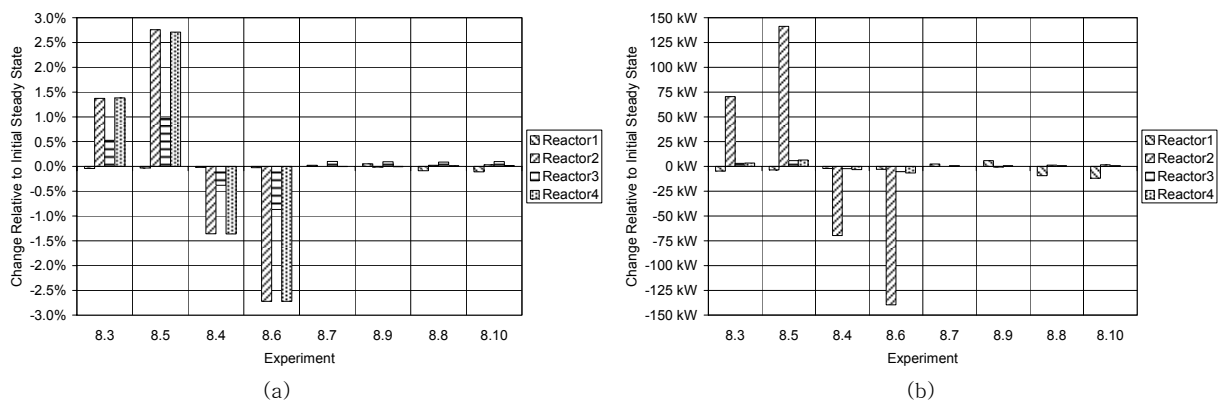


Figure 145 – Changes in reactor power values relative to initial steady state.

In graph (a) the change was calculated as a percentage of the initial steady state value. In graph (b) it was calculated by simply subtracting the kW values.

As expected, Reactor2 (slag–reductant reaction) power increased significantly when the reductant feed rate set point was increased (experiments 8.3 and 8.5) and decreased by roughly the same amount when the reductant feed rate set point was decreased (experiments 8.4 and 8.6). Virtually no change in Reactor2 power was detected when only the electrical power set point was adjusted (experiments 8.7 to 8.10).

Graph (a) of Figure 145 shows Reactor4 (carbon dissolution in metal) power changing by roughly the same percentage as the corresponding Reactor2 power, and in the same direction. This is because both these reactors are directly influenced by the reductant feed rate. The model was configured to dissolve more reductant into the metal bath (Reactor4) when more reductant is fed.

Reactor3 (metal–slag reaction) power increased in cases where the carbon content of the metal bath increased (experiments 8.3 and 8.5), and decreased in cases where the carbon content of the metal bath decreased (experiments 8.4 and 8.6).

### 8.6.11 Heat Losses

Heat loss rate results are shown in graph (l) of the experimental results.

The upper–furnace heat loss rate was a function of the surface temperature of the slag bath. In cases where no crust formed, this temperature was equal to the slag bath temperature. In cases where a crust did form (experiments 8.5 and 8.10), it was equal to the Crust conductor module’s outer temperature.

The middle–furnace heat loss rate was determined by the thickness of the freeze lining. A thinner freeze lining resulted in a higher heat loss rate. This increase however lagged in time behind the thinning of the freeze lining due to the thermal inertia of the furnace wall.

Due to the method used to estimate the lower–furnace heat loss rate, this rate was directly proportional to the temperature of the metal bath.

## 8.7 APPROPRIATELY COMBINED ADJUSTMENT OF REDUCTANT AND ENERGY INPUTS

### 8.7.1 Freeze Lining Thickness

Figure 146 shows the change in freeze lining thickness relative to the initial value for experiments 8.11 to 8.20. The aim of these experiments was to obtain a more accurate value of the required ratio of changes in reductant and energy inputs (to maintain a stable freeze lining). Note that in experiments 8.11 to 8.18 the ratio of 1 kg to 5 kWh was maintained, for increasing sizes of perturbation. From this figure it is evident that the proposed 1:5 ratio of reductant input to energy input does not keep the process in complete balance. Experiments 8.17 and 8.18 show this most clearly. The ratio was therefore adjusted to 1:5.2 for experiment 8.19 and 1:5.3 for experiment 8.20. This caused the freeze lining thickness to remain more constant.



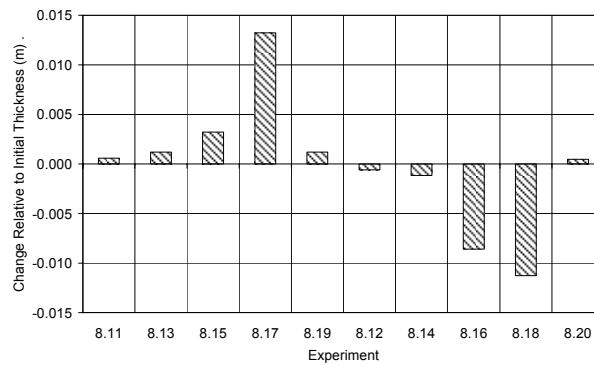


Figure 146 – Chapter 8 subsets 3 and 4 change in freeze lining thickness.

### 8.7.2 Freeze Lining Composition

It is evident from graph (b) of the experimental results that the composition of the freeze lining at the solid-liquid interface was influenced by the change in slag bath composition during the various experiments. During those experiments where the reductant and energy input rates were increased (experiments 8.11, 8.13, 8.15, 8.17 and 8.19), the freeze lining at the interface became richer in  $Ti_3O_5$ . The opposite was evident from the other experiments where the input rates were reduced.

In all cases the freeze lining consisted of only pseudobrookite with no rutile.

### 8.7.3 Thermal Response of Freeze Lining and Furnace Wall

Because the changes made to reductant and energy input rate set points resulted in only slight changes in freeze lining thickness, temperatures in the furnace wall either did not change to any significant degree, or it changed very slowly. This is shown in graph (e) of the experiment result sets.

### 8.7.4 Slag Bath Temperature

The change in slag bath temperature relative to the initial steady state value for the third and fourth experiment subsets are summarised in Figure 147.

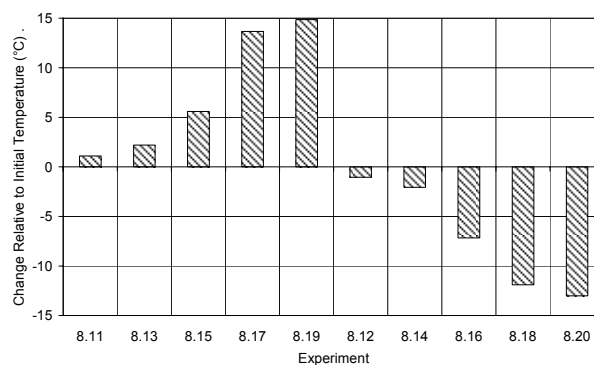


Figure 147 – Chapter 8 subsets 3 and 4 change in slag bath temperature relative to initial steady state.

The tendencies visible in these results were expected. The first five experiments shown in the Figure 147 represent conditions of progressively more reduction. This caused the liquidus temperature of the slag to increase. The opposite was true of the last five experiments in the figure.

### 8.7.5 Slag Bath Composition

Figure 148 shows a summary of the change in slag bath composition for experiments 8.11 to 8.20. The change is expressed as a percentage of the initial content value of each phase constituent.

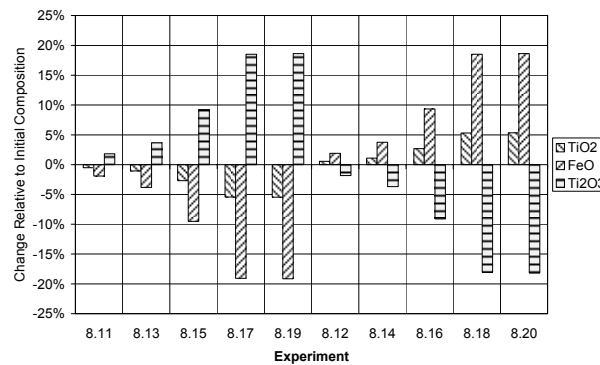


Figure 148 – Chapter 8 subsets 3 and 4 change in slag bath composition relative to initial steady state.

The first five experiments shown in Figure 148 shows an increase in Ti<sub>2</sub>O<sub>3</sub> content and a decrease in TiO<sub>2</sub> and FeO content. This is consistent with the increased reductant and energy feed rate set points associated with these experiments. The last five experiments in this figure show the opposite change in composition. This is the result of the decreased reductant and energy feed rate set points used during these experiments.

In graph (h) of the experimental results it is evident that the direction in which the slag bath composition is changing, is parallel to the stoichiometric M<sub>3</sub>O<sub>5</sub> line. This is a result of the formulation of the Reactor2Flow and Reactor3Flow sub-models. These sub-models were formulated in such a way that the model was able to reproduce the observed compositional invariance of the slag.

### 8.7.6 Metal Bath Composition

Figure 149 summarises the change in metal bath composition of experiments 8.11 to 8.20. The change is again expressed as a percentage of the initial content value of each phase constituent.

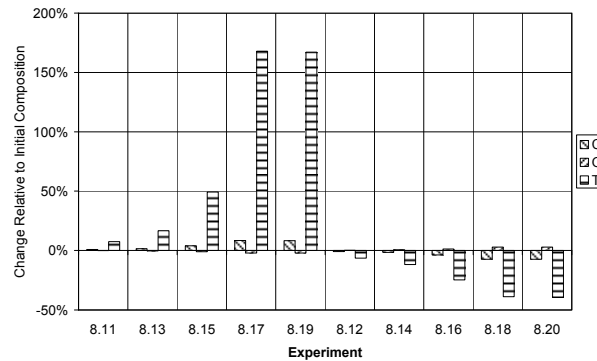


Figure 149 – Chapter 8 subset 3 and 4 change in metal bath composition relative to initial steady state.

The tendencies visible in Figure 149 are as expected. More reducing conditions associated with the first five experiments result in more carbon and titanium and less oxygen in the metal. The opposite was observed from the last five experiments that were executed with progressively less reducing conditions.

### 8.7.7 Off-Gas Composition

The off-gas composition results as presented in graph (j) of the experimental results showed an increase in partial oxygen pressure for experiments in which conditions were adjusted to be less reducing (experiments 8.12, 8.14, 8.16, 8.18 and 8.20). The opposite tendency is evident in the results of the remaining five experiments in which more reducing conditions were used.

### 8.7.8 Reactor Power

Figure 150 summarises the changes in reactor power relative to the initial steady state values. The power values for the various experiments were calculated by taking an average over the duration of the experiment.

The power of Reactor1 changed only slightly due to relatively small changes in slag bath temperature.

The power of Reactor2 increased as the reductant feed rate was increased, and decreased when the reductant feed rate was reduced. Graph (a) shows that the power of Reactor4 changes with the same percentage as Reactor2. This is due to both these reactors being influenced strongly by changes in reductant feed rate.

Reactor3 power increased when the carbon content of the metal bath increased, and decreased when the carbon content of the metal dropped.

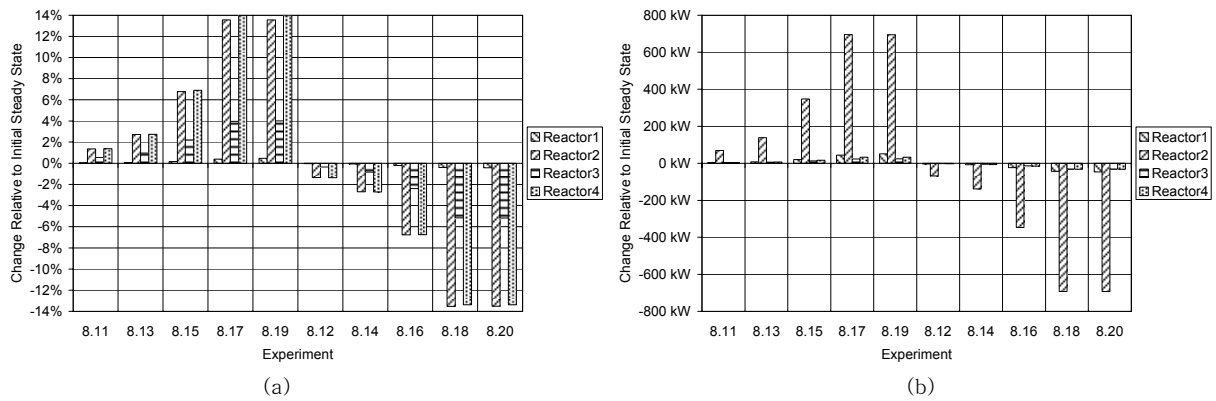


Figure 150 – Chapter 8 subsets 3 and 4 changes in reactor power values relative to initial steady state.

In graph (a) the change was calculated as a percentage of the initial steady state value. In graph (b) it was calculated by simply subtracting the kW values.

### 8.7.9 Heat Losses

The heat losses as shown in graph (l) of the experimental results of experiments 8.11 to 8.20 presented no new insights. The upper-furnace and lower-furnace heat losses were determined by the temperature of the slag bath, and the middle-furnace heat loss by the thickness of the freeze lining.

## CHAPTER 9

## THE DYNAMIC PROCESS RESPONSE TO SOLIDIFICATION AND MELTING OF THE FREEZE LINING AND CRUST

The focus of this chapter is the influence of slag solidification and melting on the slag bath and, of secondary importance, on other parts of the process. A small number of experiments were conducted to specifically study slag solidification and melting in the crust region. The following aspects were considered:

- Freeze lining and crust thickness.
- Temperature distribution through the furnace wall, freeze lining and crust.
- Time lag in temperature response of the refractory brick wall relative to the time when conditions were changed in the slag bath.
- Liquid slag temperature.
- Composition distribution through the freeze lining and crust.
- Liquid slag composition.

In addition to the above list, metal bath composition data, off-gas composition data, heat loss data and reactor power data are also presented to provide a comprehensive set of results for each experiment.

## 9.1 EXPERIMENTAL SETUP

The experimental setup used in this chapter was exactly the same as the setup used in CHAPTER 8. Refer to paragraph 8.1 (page 214) for details. The feed rates of ilmenite and reductant was returned to the values used in CHAPTER 8 after the period of down time. The power set point was set to the values used in CHAPTER 8 plus the additional amount specified to melt away the crust during a specific experiment. The additional power was removed once the entire crust had disappeared.

## 9.2 EXPERIMENTS

The parameters that were varied over the series of experiments include the following:

- Duration for which the furnace was switched off.
- The electrical power applied to melt away the crust.

The furnace was switched off for 30 minutes in experiments 9.1 and 9.2. Once the furnace was switched back on, the power set point was increased to the electrical power input until the crust had been melted away. The same procedure was followed for experiments 9.3 and 9.4, except that the duration of furnace down time was increased to 60 minutes.

EXPERIMENT NO.	DURATION OF DOWN TIME	POWER APPLIED TO MELT AWAY CRUST
9.1	30 minutes	500 kW
9.2	30 minutes	1,000 kW
9.3	60 minutes	500 kW
9.4	60 minutes	1,000 kW

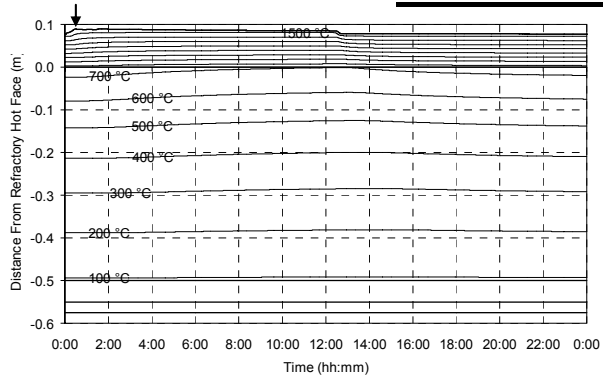
Table 24 – List of experiments conducted for CHAPTER 9.

### 9.3 EXPERIMENTAL RESULTS

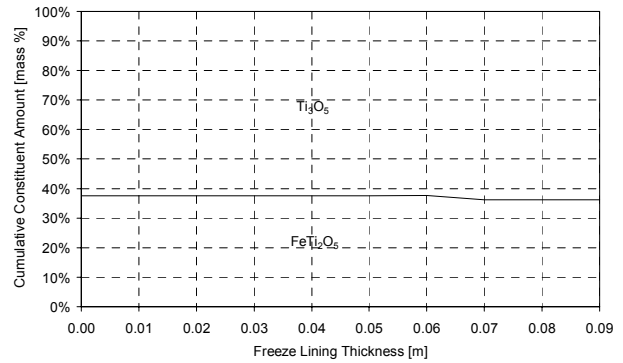
The results of experiments conducted as part of this chapter was presented in exactly the same way as in CHAPTER 8. Refer to paragraph 8.3 (page 216) for details.

9.3.1 Experiment 9.1

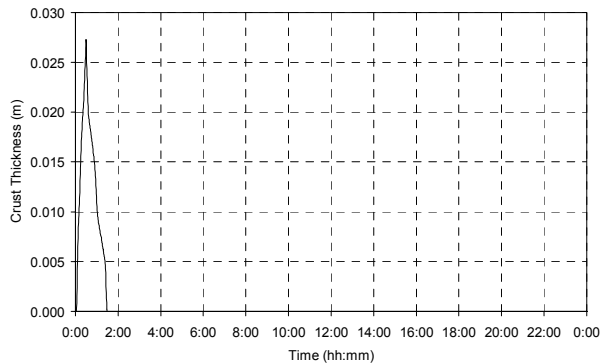
DURATION OF DOWN TIME	POWER APPLIED TO MELT AWAY CRUST
30 minutes	500 kW



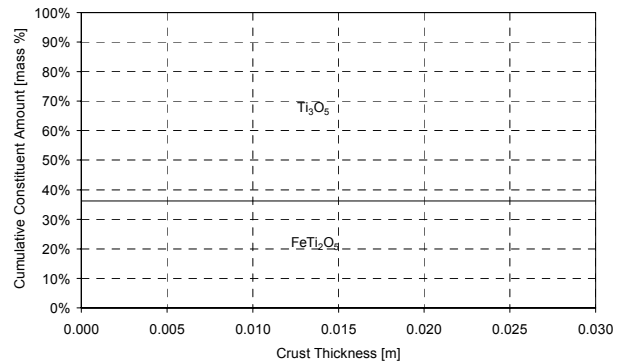
(a)



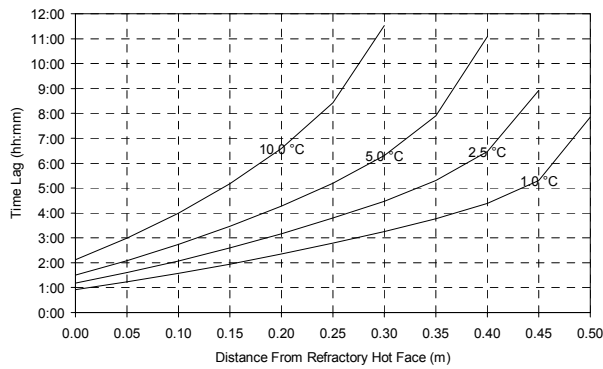
(b)



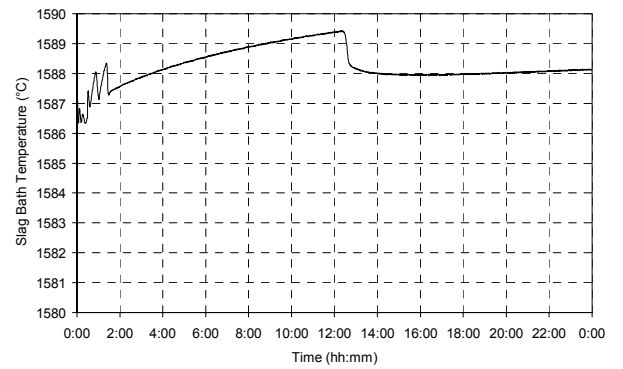
(c)



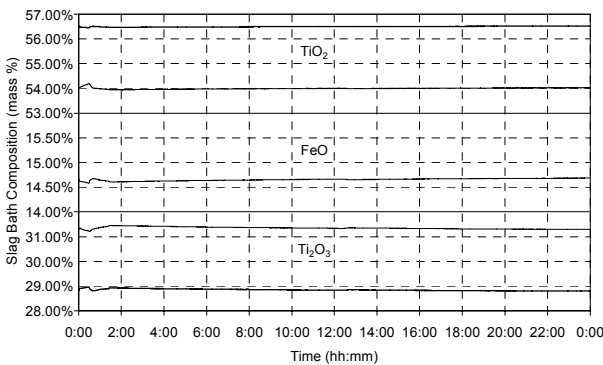
(d)



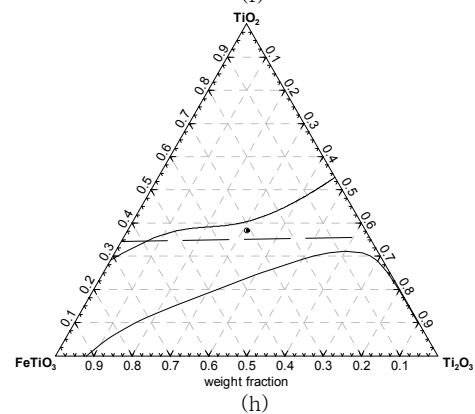
(e)



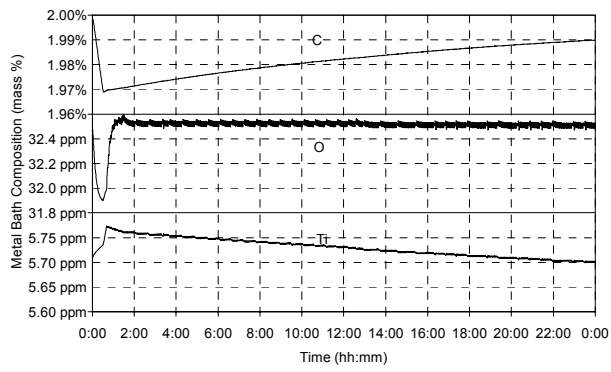
(f)



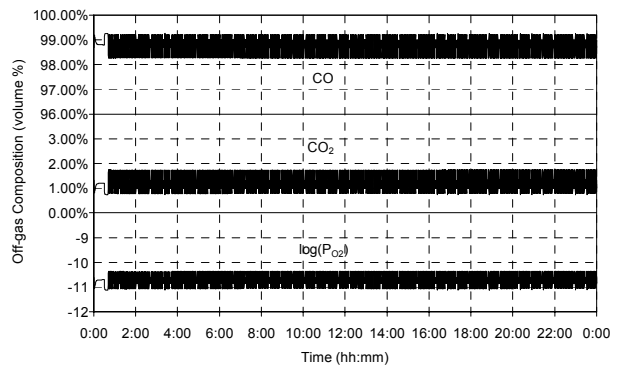
(g)



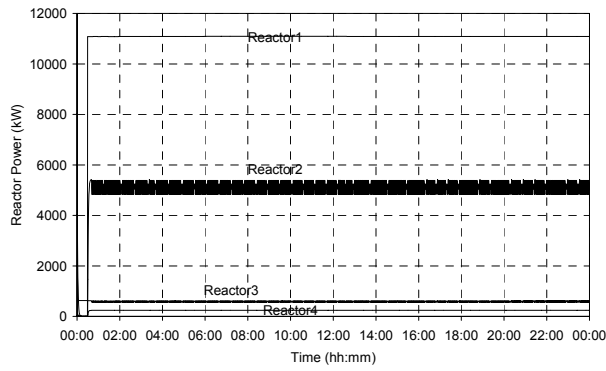
(h)



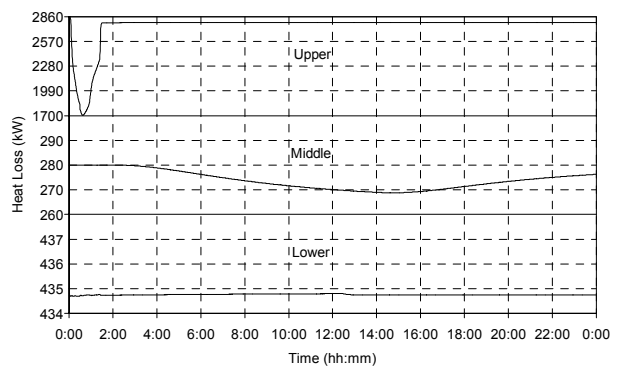
(i)



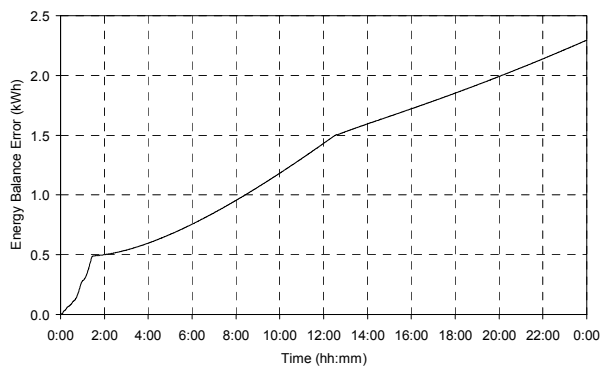
(j)



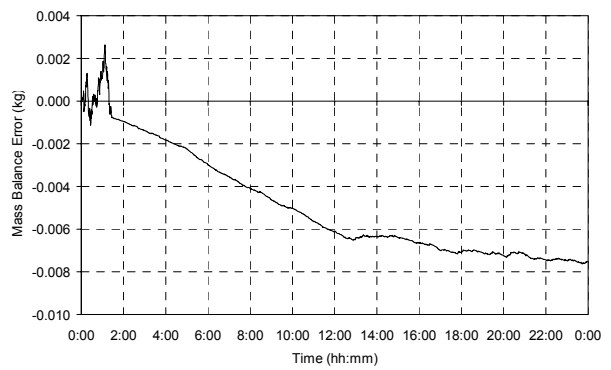
(k)



(l)



(m)



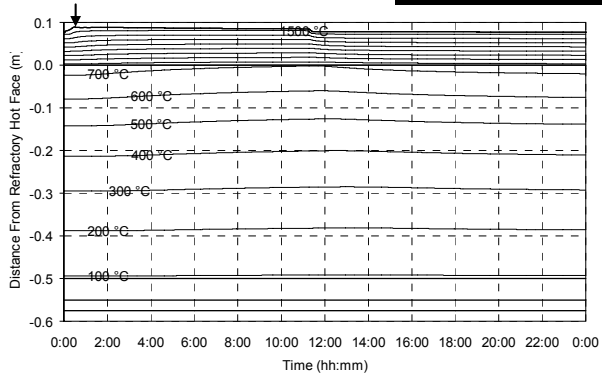
(n)

Figure 151 – Experiment 9.1 results.

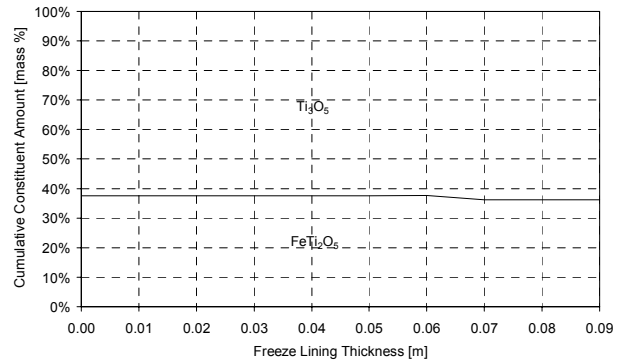


9.3.2 Experiment 9.2

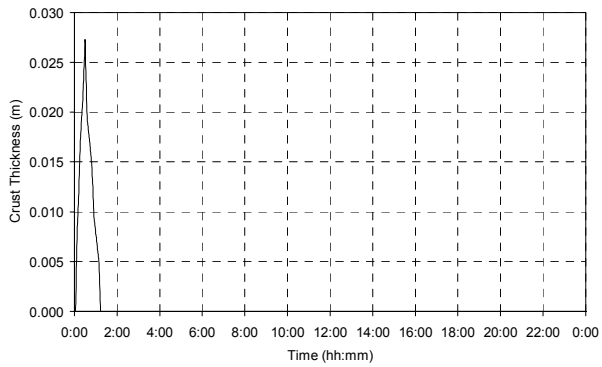
DURATION OF DOWN TIME	POWER APPLIED TO MELT AWAY CRUST
30 minutes	1,000 kW



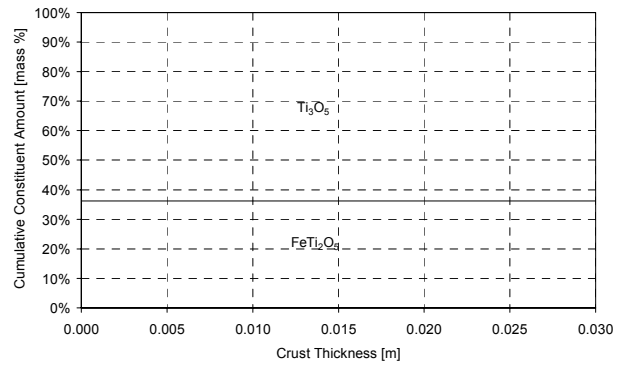
(a)



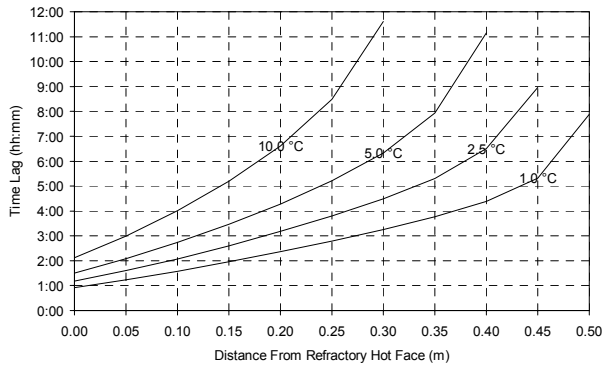
(b)



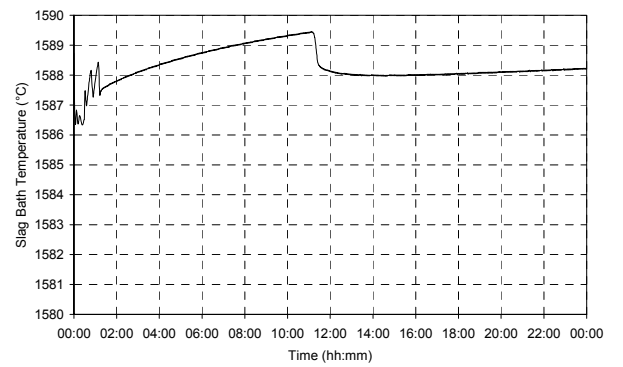
(c)



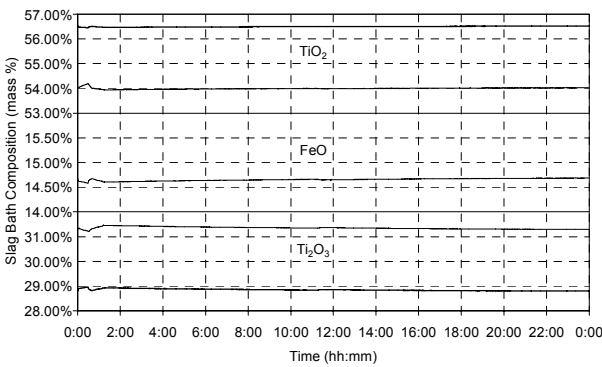
(d)



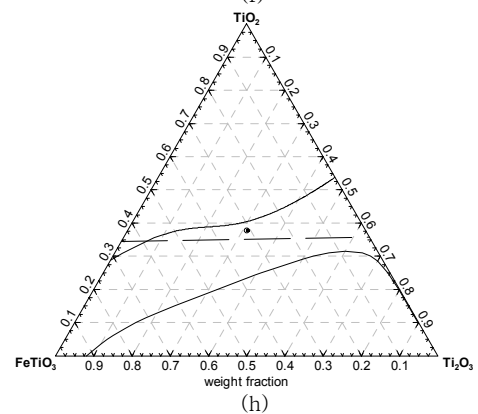
(e)



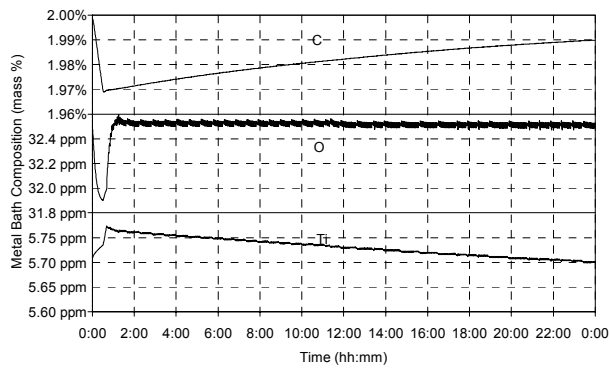
(f)



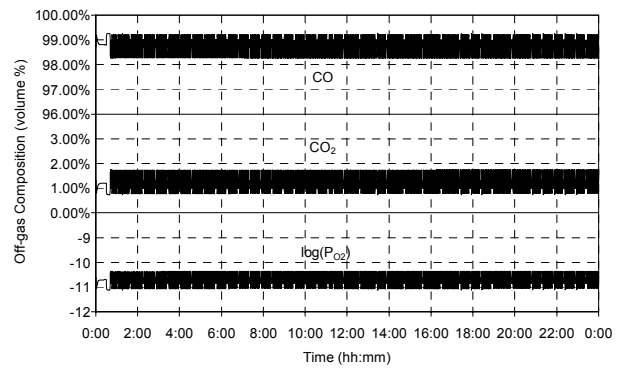
(g)



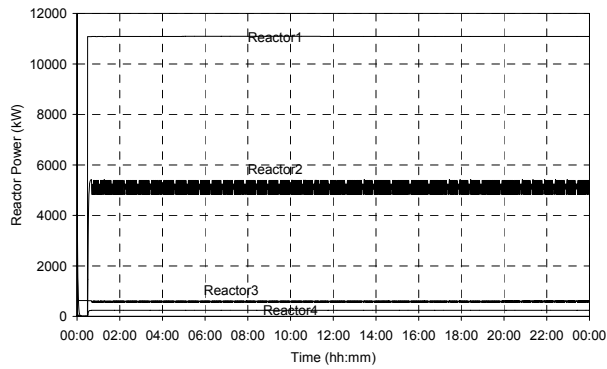
(h)



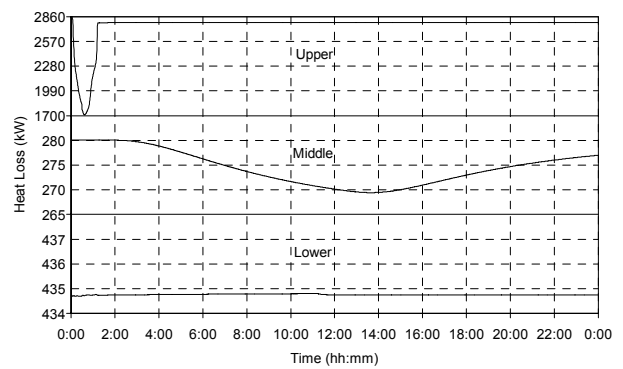
(i)



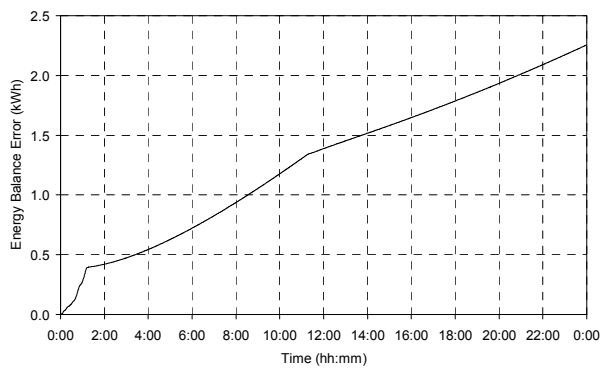
(j)



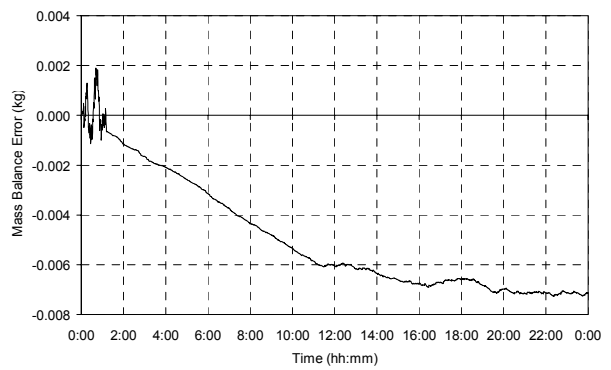
(k)



(l)



(m)

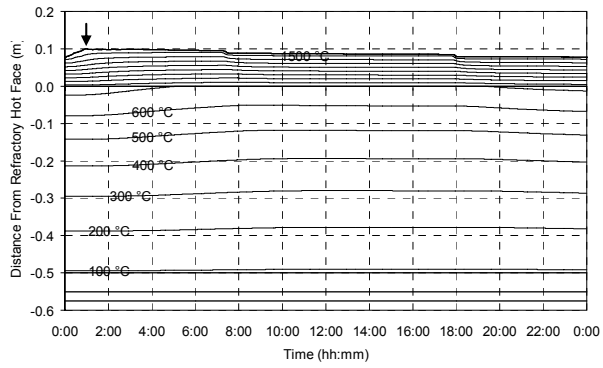


(n)

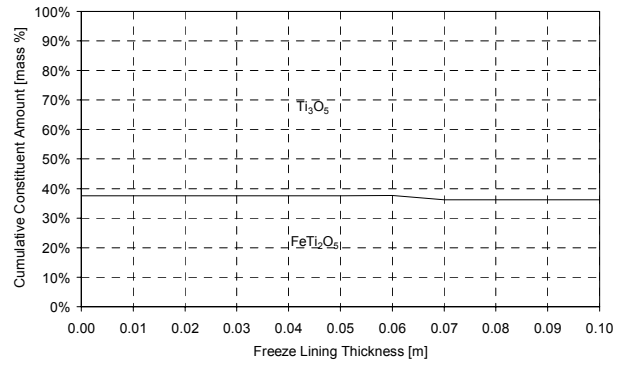
Figure 152 – Experiment 9.2 results.

9.3.3 Experiment 9.3

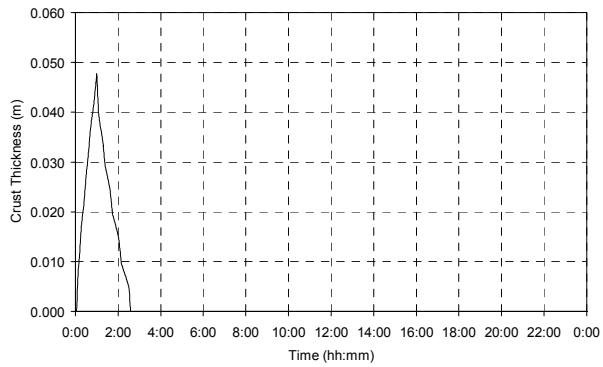
DURATION OF DOWN TIME	POWER APPLIED TO MELT AWAY CRUST
60 minutes	500 kW



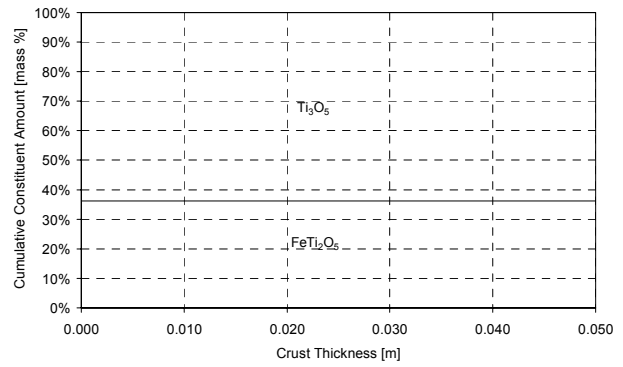
(a)



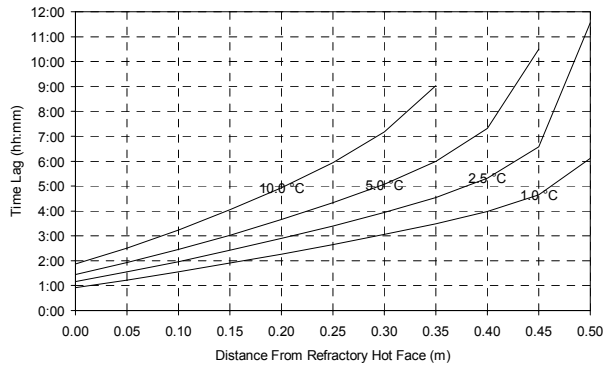
(b)



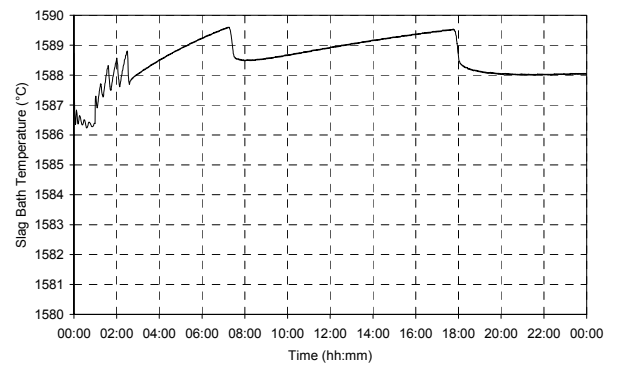
(c)



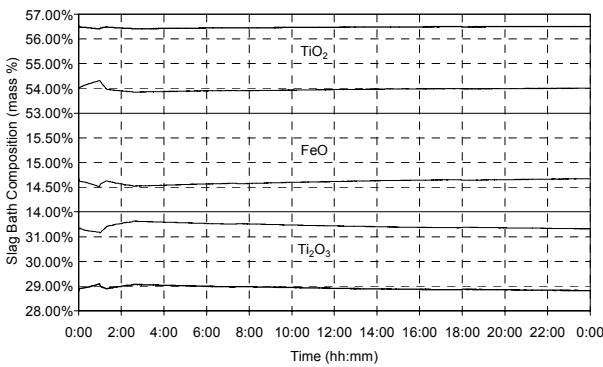
(d)



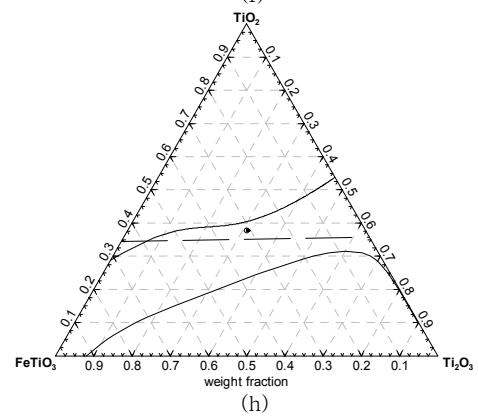
(e)



(f)



(g)



(h)

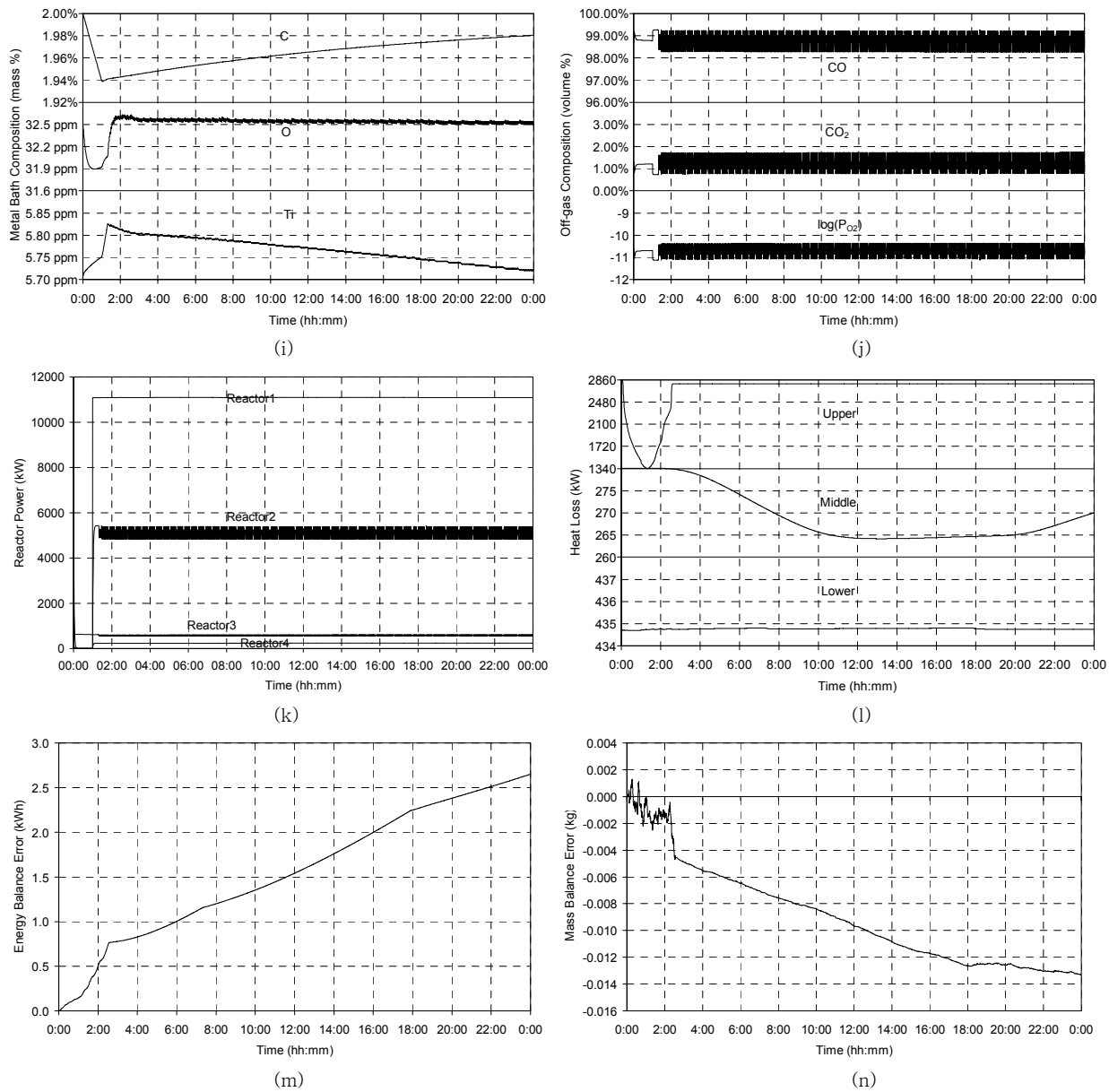
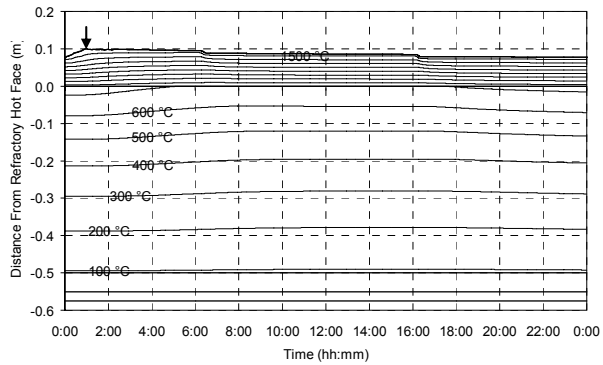


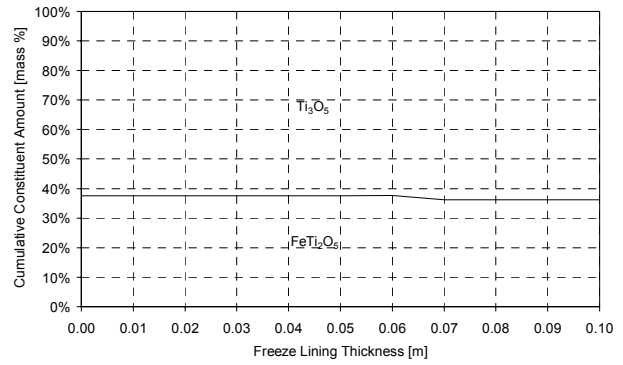
Figure 153 – Experiment 9.3 results.

9.3.4 Experiment 9.4

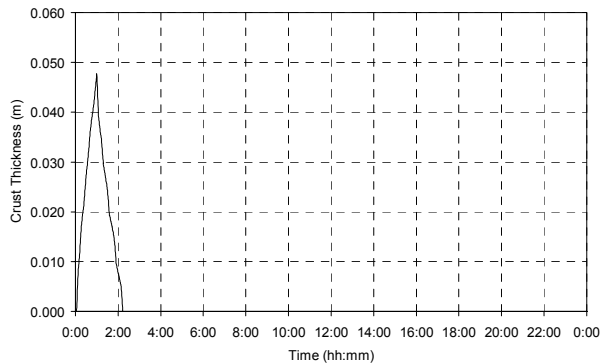
DURATION OF DOWN TIME	POWER APPLIED TO MELT AWAY CRUST
60 minutes	1,000 kW



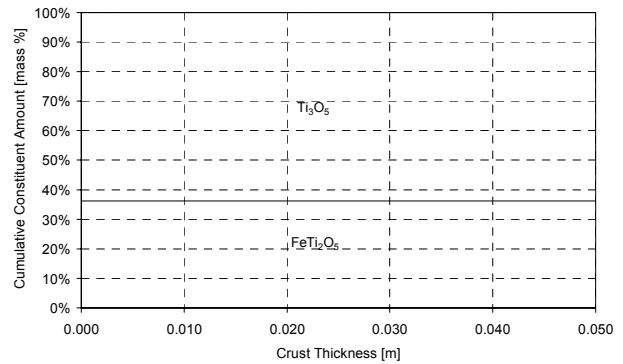
(a)



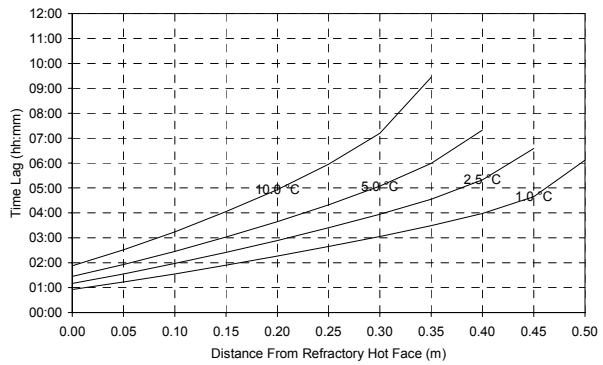
(b)



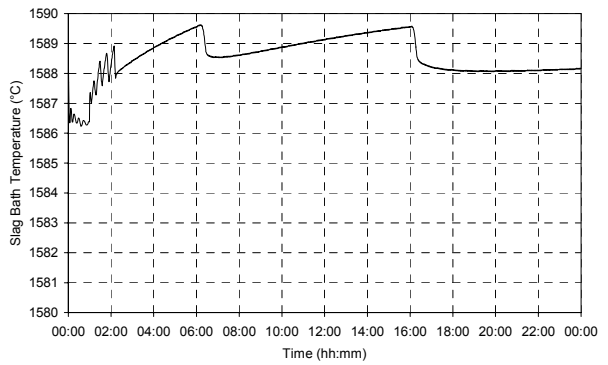
(c)



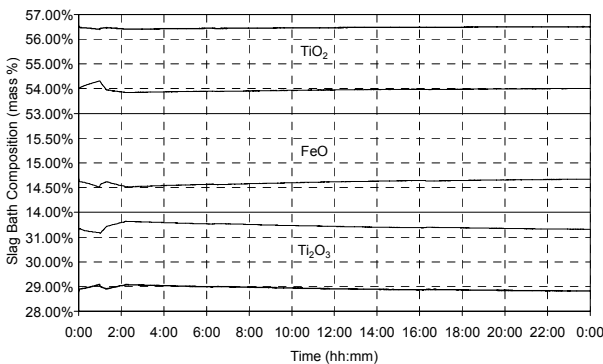
(d)



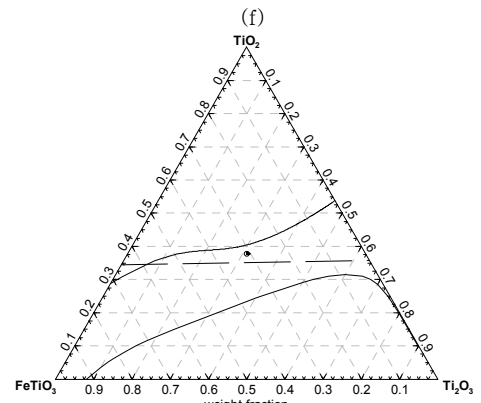
(e)



(f)

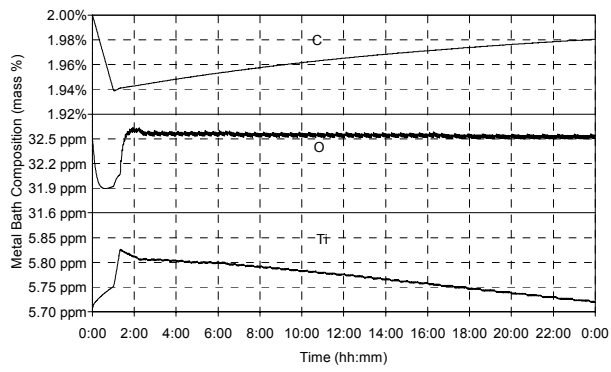


(g)

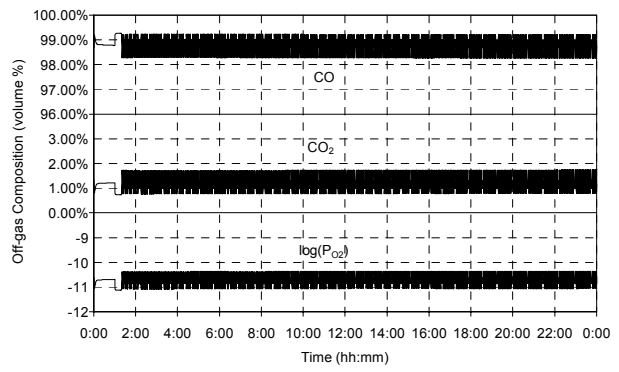


(h)

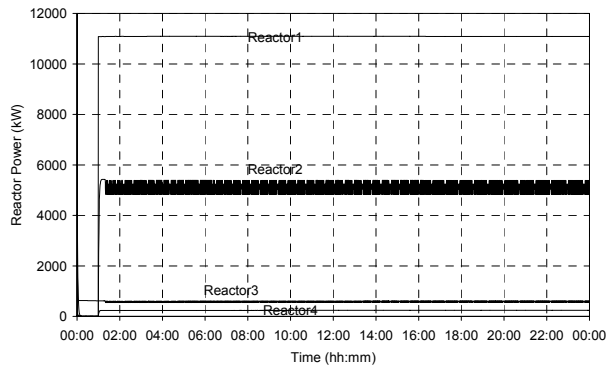




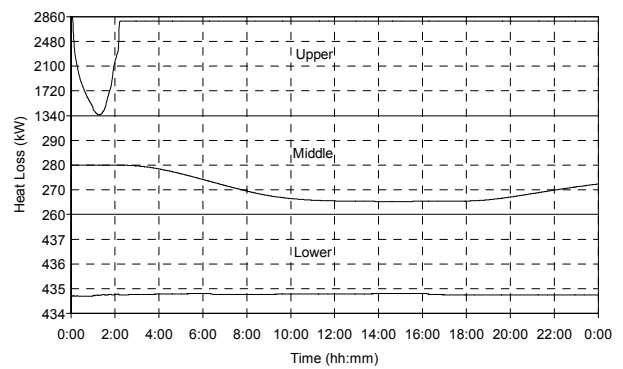
(i)



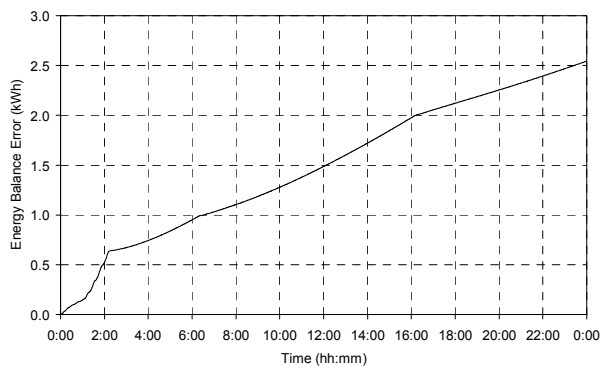
(j)



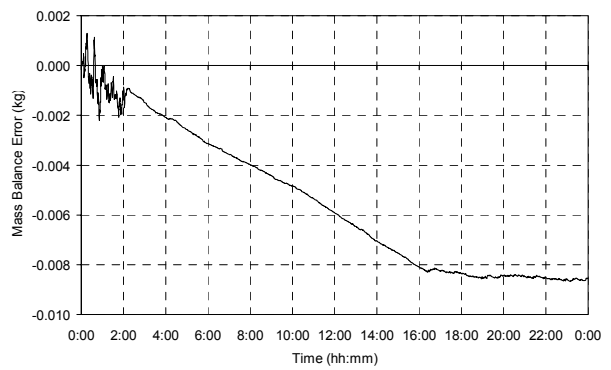
(k)



(l)



(m)



(n)

Figure 154 – Experiment 9.4 results.

## 9.4 DISCUSSION

### 9.4.1 Freeze Lining Thickness

Figure 155 presents the freeze lining thickness vs. time trends of experiments 9.1 to 9.4. This figure clearly shows the influence of the two adjusted variables (downtime duration and electrical power). Longer periods of downtime cause the freeze lining to grow thicker compared to shorter periods.

The higher electrical power (1000 kW) used during experiments 9.2 and 9.4 caused the freeze lining to return to its initial steady state thickness quicker than when the power was set to 500 kW. This was true even though this higher power set point was only employed while a crust was present.

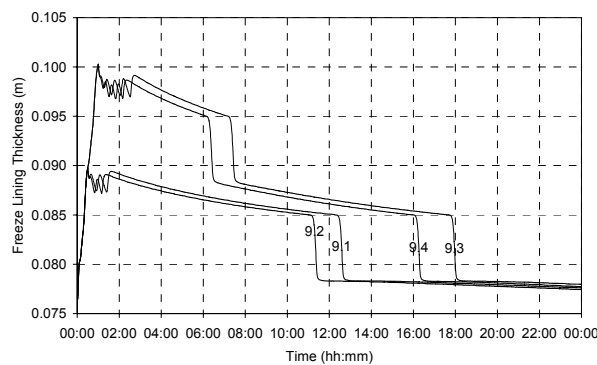


Figure 155 – Influence of downtime duration and electrical power on freeze lining thickness.

The step changes in freeze lining thickness in Figure 155 are the result of transitions from one finite difference node to the next. In reality these step changes will not occur, but the behaviour of an actual freeze lining should display the same tendencies as presented above.

### 9.4.2 Freeze Lining Composition

The freeze lining composition was plotted in graph (b) of the experimental results at its point of maximum thickness. Since this point occurred at the start of the experiment, these graphs do not assist in any form of interpretation. It is however expected that no significant variation in the freeze lining composition would have occurred because there was no great variation in liquid slag composition during any of the experiments. The composition of the freeze lining at its interface with the slag bath would also have been very similar to the crust composition as presented in graph (d).

### 9.4.3 Thermal Response of Freeze Lining and Furnace Wall

Graph (e) in the experimental results once again emphasises the slow thermal response of the furnace lining. A 1 °C change in temperature was only detected at the refractory hot face after 1 hour in all cases. The time required to detect a 1 °C change up to 0.25 m from the refractory hot face was roughly the same for all experiments.

The response during experiments 9.1 and 9.2 was virtually identical, as was the response during experiments 9.3 and 9.4. This indicates that the thermal response during these four experiments was

dominated by the downtime duration. The thermal response during the latter two experiments was in general quicker than the former two experiments. This is due to the larger temperature changes associated with longer downtime.

#### 9.4.4 Crust Thickness

Figure 156 presents a summary of the variation of crust thickness with time for the four experiments conducted as part of this chapter.

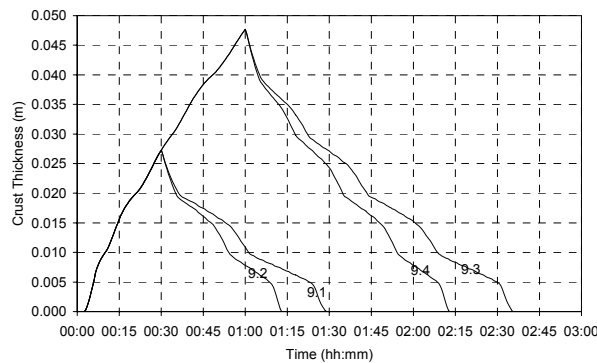


Figure 156 – Chapter 9 summary of crust thickness variation.

The influence of downtime duration is clear. A longer period of down time causes the crust to grow thicker. The rate at which the crust grows thicker however reduces with time. This is a result of a decline in the rate at which heat is extracted from the top of the crust as the crust grows thicker.

The influence of the electrical power set point on the rate at which the crust is melted away is also clear from Figure 156. A higher power input reduces the time required to melt away the crust. A thicker crust, as one would expect, takes longer to melt away.

When comparing experiment 9.1 with 9.2 or experiment 9.3 with 9.4, applying double the amount of extra power did not result in the time required to melt down the crust to reduce by 50%. The reason for this is that the extra power is applied to the entire process and not to the crust alone. Some of the extra power would therefore report as heat losses, some will contribute to melting of the freeze lining, some will melt down the crust, etc.

The volume fraction of solids in the slag bath can be calculated simply by dividing the crust thickness by the slag bath thickness (1 m). The solids content gives an indication of the effective slag viscosity.

#### 9.4.5 Crust Composition

The crusts that formed during the four experiments consisted of only pseudobrookite. No rutile formed. The pseudobrookite was richer in  $Ti_2O_3$  than the slag bath, as would be expected from the solidification behaviour that has been demonstrated in previous chapters.



### 9.4.6 Slag Bath Temperature

The variation of slag bath temperature for the four experiments is presented together in Figure 157. From this figure it is evident that the difference in temperature variation between the four experiments is minimal.

The oscillations of the temperature signal are the result of solidification and melting of crust conductor nodes in the early stages of the experiments (up to around 2 hours), and later due to the solidification and melting of freeze lining conductor nodes.

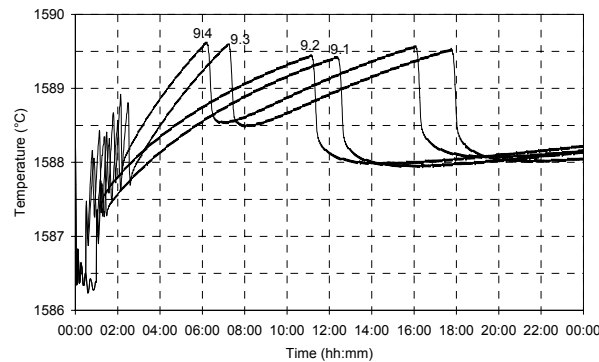


Figure 157 – Chapter 9 summary of variation in slag bath temperature.

### 9.4.7 Slag Bath Composition

The variation in slag bath composition is shown in graphs (g) and (h) of the experimental results. Graph (g) indicates something that had not been observed up to this point. During the period of solidification the slag  $\text{TiO}_2$  content increased and the  $\text{Ti}_2\text{O}_3$  content decreased. This is consistent with observations made in CHAPTER 6. The  $\text{FeO}$  content of the slag, however, decreased during solidification while it increased during experiments presented in CHAPTER 6.

The reason for the drop in  $\text{FeO}$  in the liquid slag can be attributed to reduction taking place at the interface between the slag and metal baths. Reduction reactions at this interface act with solidification to change the slag bath's composition. In the case of  $\text{FeO}$ , the reduction was dominant. In the case of  $\text{TiO}_2$  and  $\text{Ti}_2\text{O}_3$ , solidification was dominant.

## CHAPTER 10

## COMPOSITIONAL INVARIANCE OF HIGH-TITANIA SLAG

This chapter is dedicated to the observed compositional invariance of high-titania slag. The compositional invariance as observed by Pistorius (1999) and others is first discussed. This is followed by a review of the possible causes as reported by Pistorius. Finally, a new mechanism is proposed by which the compositional invariance can be explained.

10.1 THE RELATIONSHIP BETWEEN FeO AND Ti<sub>2</sub>O<sub>3</sub>

Pistorius (1999) identified a relationship between FeO and Ti<sub>2</sub>O<sub>3</sub> in industrial high-titania slags. This relationship was subsequently investigated further (Pistorius, 2002; Pistorius and Coetzee, 2003; Pistorius, 2003; Pistorius, 2004). The relationship is illustrated in Figure 158 and Figure 159.

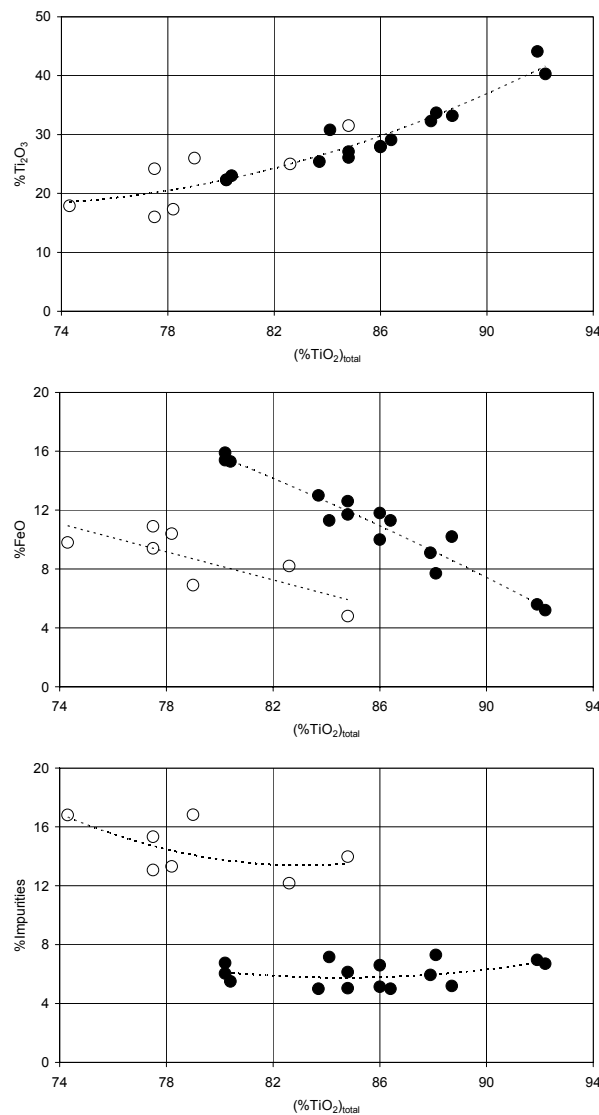


Figure 158 – Compositional relationships in industrial high-titania slags.

Filled circles indicate slags from South African ilmenites and empty circles slags from Canadian ilmenites. The horizontal axis indicates the total Ti content of the slag as TiO<sub>2</sub>.

Recreated from Pistorius (2002).

The data presented in Figure 158 serves as background and highlights the difference between slags produced from South African and Canadian ilmenites. The most important difference between these ore types is the significantly higher alkali earth content of Canadian ilmenites (Pistorius, 2002).

Pistorius (2002) plotted graph (a) of Figure 159 by using the FeO and  $Ti_2O_3$  content as reported in the chemical analyses. He then calculated the Equivalent amounts of FeO and  $Ti_2O_3$  as used in graph (b) by grouping divalent impurities (MgO and MnO) with FeO, and trivalent impurities ( $V_2O_5$ ,  $Cr_2O_3$  and a portion of  $Al_2O_3$ ) with  $Ti_2O_3$ . This was done because it is known that these impurities also occur in the  $M_3O_5$  solid solution.

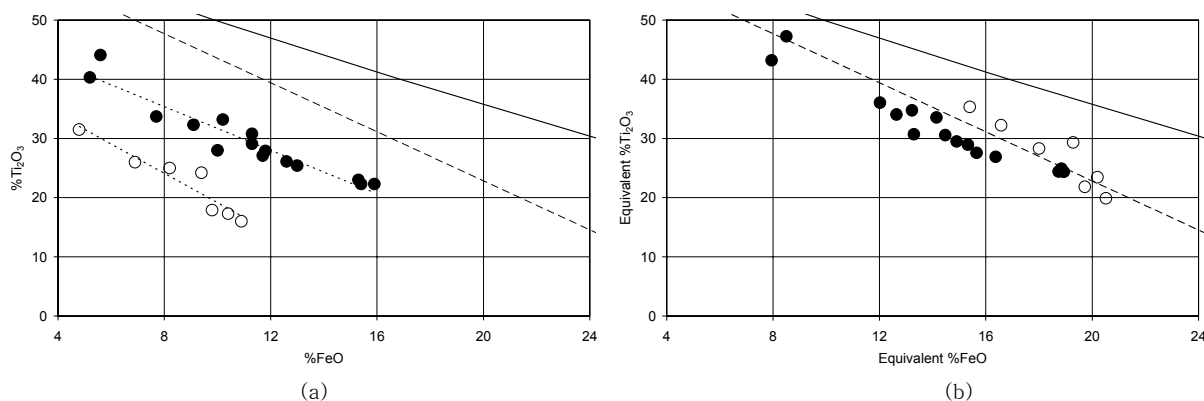


Figure 159 – The relationship between FeO and  $Ti_2O_3$  in industrial high-titania slags.

Filled circles indicate slags from South African ilmenites and empty circles slags from Canadian ilmenites. The dashed line indicates the stoichiometric  $M_3O_5$  composition. The solid line indicates the composition of slag on the slag/(slag +  $Fe^\circ$ ) boundary shown in Figure 14 and represents equilibrium between slag and iron metal. Recreated from Pistorius (2002).

The recalculated  $Ti_2O_3$  vs. FeO presented in graph (b) of Figure 159 most clearly displays the observed compositional invariance of industrial high-titania slags close to the stoichiometric  $M_3O_5$  composition. What is especially noticeable is that slags from both South African and Canadian ilmenites display this relationship.

The reason for the significance of this relationship is the fact that some pigment manufacturers specify a maximum  $Ti_2O_3$  content in slags from their suppliers. Understanding this relationship could therefore assist slag producers to improve control over slag quality. It is of course this relationship that is one of the key issues of the current study.

Pistorius (2002) has considered possible mechanisms that could cause the observed relationship. He broadly identified possible causes as reaction equilibrium, kinetic effects and phase chemistry. These candidates are reviewed again below.

## 10.2 REACTION EQUILIBRIUM AS A POSSIBLE MECHANISM

### 10.2.1 Arguments For

When one considers the observed relationship between FeO and Ti<sub>2</sub>O<sub>3</sub> the most prominent explanation that comes to mind is thermodynamic equilibrium. The reasons are the relatively high temperatures (around 1700 °C) in the smelting furnace and the significant stirring in the slag and metal baths.

The high temperatures make it less likely to find chemical reaction rate controlling steps, and the stirring reduces the probability of finding steps controlled by mass or heat transfer. It would therefore seem that the process should be influenced to a large degree by the drive towards thermodynamic equilibrium.

It is of course known that the slag and metal baths in an ilmenite-smelting furnace are not in thermodynamic equilibrium, and that kinetic effects play a significant role in reactions involving reductant particles. Even when these facts are accepted, it is still argued that thermodynamic equilibrium should have a significant influence on the behaviour of the process. Since there are kinetic barriers between phases that prevent the process from reaching a global equilibrium, one then expects that the influence of the drive towards thermodynamic equilibrium should be visible within a single phase.

The content of different species within a phase should therefore all correlate well with the same dominant factor determining equilibrium in the phase. For example, if measurements of the partial oxygen pressure (P<sub>O<sub>2</sub></sub>) in the slag agree well with a calculated P<sub>O<sub>2</sub></sub> based on the FeO-Fe redox couple, it is expected that a P<sub>O<sub>2</sub></sub> calculated based on the TiO<sub>2</sub>-Ti<sub>2</sub>O<sub>3</sub> redox couple should give the very similar results. (The fact that the opposite was found to be true by Geldenhuis and Pistorius (1999) is deliberately ignored here for the sake of the argument.)

### 10.2.2 Arguments Against

While the above argument in favour thermodynamic equilibrium as a possible mechanism is based on qualitative statements and intuition, the case against it is far more concrete.

The data presented in Figure 159 clearly shows an offset between actual slag compositions and slag compositions in equilibrium with pure iron metal. It is also well known that the slag bath is not in equilibrium with the carbon dissolved in the metal bath. Geldenhuis and Pistorius (1999) further reported a significant difference between the P<sub>O<sub>2</sub></sub> measured and calculated based on the FeO-Fe redox couple, and the P<sub>O<sub>2</sub></sub> calculated based on the TiO<sub>2</sub>-Ti<sub>2</sub>O<sub>3</sub> redox couple.

These observations seem to negate virtually all arguments in favour of thermodynamic equilibrium contributing to the FeO-Ti<sub>2</sub>O<sub>3</sub> relationship.

## 10.3 KINETIC EFFECTS AS A POSSIBLE MECHANISM

### 10.3.1 Arguments For

When Pistorius (1999) identified the FeO-Ti<sub>2</sub>O<sub>3</sub> relationship, he suggested that the relative reaction kinetics of the reduction of FeO to Fe and TiO<sub>2</sub> to Ti<sub>2</sub>O<sub>3</sub> may govern the extent to which the slag compositions deviate from equilibrium.

Very little is known about the kinetics of reduction reactions taking place in an ilmenite-smelting furnace. This results in reaction kinetics remaining a possible mechanism when other options such as thermochemistry that are understood more clearly cannot explain the observed phenomena.

### 10.3.2 Arguments Against

Pistorius (2002) presented three arguments against kinetic effects as a possible mechanism. Firstly he observed that the FeO-Ti<sub>2</sub>O<sub>3</sub> relationship remained remarkably consistent for furnaces with significantly different sizes and stirring patterns. Secondly, the fact that TiO<sub>2</sub> occurs in much higher concentration in the slag compared with FeO, makes it unlikely that mass transfer effects would cause slower reduction rates of TiO<sub>2</sub>. Finally, it is difficult to explain, on the basis of kinetics, why Canadian ilmenites show a consistently lower Ti<sub>2</sub>O<sub>3</sub> content at a specific FeO content.

In general it must be cited again that the high temperatures and strong mixing in the furnace reduce the likelihood of kinetic effects being responsible for the FeO-Ti<sub>2</sub>O<sub>3</sub> relationship.

## 10.4 EUTECTIC GROOVE PHASE EQUILIBRIUM AS A POSSIBLE MECHANISM

### 10.4.1 Arguments For

Pistorius (2002) stated that the FeO-Ti<sub>2</sub>O<sub>3</sub> relationship may be determined by the tendency of the slag to solidify as virtually a single phase (M<sub>3</sub>O<sub>5</sub>). This possibility was further explored and elaborated upon (Pistorius and Coetzee, 2003). The authors argued that the presence of a freeze lining and the resulting influence of the solidification equilibrium between the liquid slag bath and the solid slag of the freeze lining may be the cause of the FeO-Ti<sub>2</sub>O<sub>3</sub> relationship. This was supported by the observation that this relationship was not evident in cases where a freeze lining was absent (Ban and Krüger, 1988).

It was further argued that the eutectic groove that is close to the M<sub>3</sub>O<sub>5</sub> stoichiometric line could serve to constrain the slag composition close to the M<sub>3</sub>O<sub>5</sub> composition. For this to be possible, the liquid slag composition had to be between the eutectic groove and the M<sub>3</sub>O<sub>5</sub> line on the ternary diagram. This has been shown to be true specifically for South African ilmenites (Pistorius, 2002). The argument was strengthened further by the fact that rutile is present in the solidified slag, as would be expected for a slag composition between the M<sub>3</sub>O<sub>5</sub> composition and the eutectic groove. The actual rutile content of the slags was however smaller than what was predicted based on this theory.

### 10.4.2 Arguments Against

The proposed mechanism causing the FeO-Ti<sub>2</sub>O<sub>3</sub> relationship (Pistorius and Coetzee, 2003) was tested by using a simple heat transfer model (Pistorius, 2004). The conclusion from this work was that the phase equilibrium between the freeze lining and liquid slag cannot serve to constrain the liquid slag composition to the eutectic groove.

What would the reason be for this mechanism not being able to produce the observed FeO-Ti<sub>2</sub>O<sub>3</sub> relationship? The most basic explanation is that solidification of slag with a composition between the stoichiometric M<sub>3</sub>O<sub>5</sub> line and the eutectic groove is not able to make a lasting change to the composition of the liquid slag.

The reason is that any change in the composition of the slag bath caused by solidification when the original slag bath composition is situated between the stoichiometric  $M_3O_5$  line and the eutectic groove is only temporary. If such solidification had pushed the composition of the slag bath into the eutectic groove, this means that a significant amount of solid slag must have been produced. If the freeze lining thickness is to remain constant, this solid slag must be melted into the slag bath again. This will cause the exact opposite of the initial compositional change into the eutectic groove. The only way in which such solidification can constrain the slag bath composition close to or on the eutectic groove would be for the solid slag product to be removed from the furnace continuously. This is of course not what happens in reality.

## 10.5 A NEW MECHANISM PROPOSED

This section describes the details of a new mechanism that is suggested to contribute to the observed FeO-Ti<sub>2</sub>O<sub>3</sub> relationship.

### 10.5.1 Requirements

When formulating the mechanism, a clear list of requirements was compiled. These requirements had to be met by the mechanism for it to be considered a feasible explanation of the observed phenomenon, in this case the FeO-Ti<sub>2</sub>O<sub>3</sub> relationship. The following requirements were listed:

- The mechanism must be able to have a sustained influence on the composition of the slag bath.
- The mechanism must be able to adjust the composition of the slag bath towards the stoichiometric  $M_3O_5$  line.

### 10.5.2 Background Information

Available information about all of the most important phenomena relevant to the system and the observed phenomenon was consolidated to serve as background for the formulation of the mechanism. These aspects are summarised below.

#### a. Chemical reaction equilibrium

As has been explained before, the high temperatures and significant stirring in the slag and metal baths create conditions that would favour the drive towards thermodynamic equilibrium. It is therefore expected that the reduction reactions taking place in the furnace would be influenced significantly by such equilibrium. Proof has been provided in Figure 159 that the actual slag compositions do not correspond with the extent of reduction reactions at equilibrium. This is however ignored for the moment to demonstrate the influence of the drive towards equilibrium in isolation.

This influence is shown in Figure 160. This figure was constructed by adding progressively more carbon and adjusting the temperature of the system up to the point where all slag is present in the liquid state. The presence of iron as a reduction product results in the slag composition following the slag/(slag+Fe<sup>o</sup>) phase boundary.

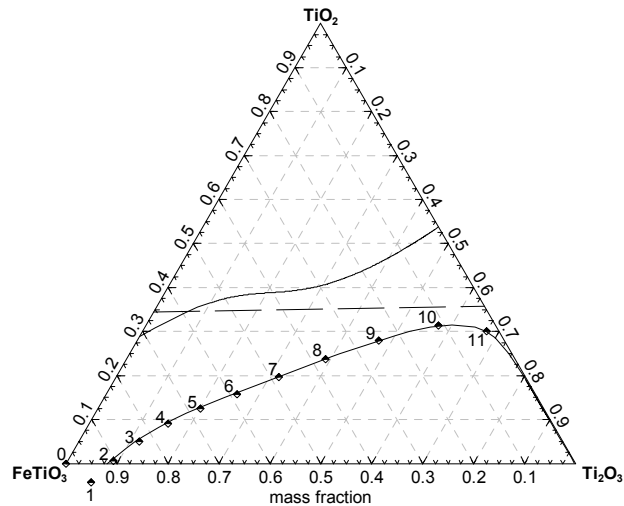


Figure 160 – Slag composition according to reduction reactions at equilibrium.

Numbers next to the symbols indicate the amount of carbon added in kg carbon/100 kg ilmenite.

#### b. Solidification behaviour

The solidification behaviour of the  $\text{FeTiO}_3\text{-TiO}_2\text{-Ti}_2\text{O}_3$  system was discussed and illustrated in paragraph 2.6.2. Liquidus diagrams were provided in Figure 10 and Figure 11, and liquid slag composition trajectories were demonstrated in Figure 14.

Something that can be concluded from the binaries provided in Figure 9, but that is not evident from the liquidus diagrams and the liquid slag composition trajectory diagram, is the influence of solidification on slag composition. For this reason, Figure 161 was constructed.

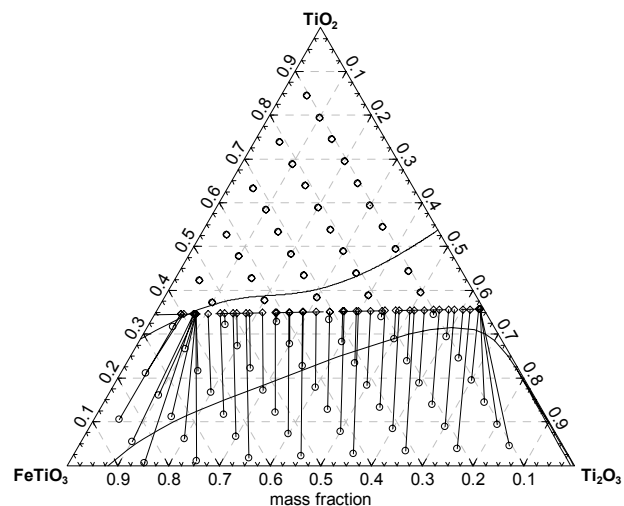


Figure 161 – The influence of solidification on slag composition.

A circle indicates an initial liquid slag composition and a diamond the resulting composition of the slag once it had completely solidified. Paired circles and diamonds are connected with solid lines. In most cases slags were cooled to 1400 °C. Only the three compositions at approximately 85%  $\text{FeTiO}_3$  were cooled to 1300 °C.

From Figure 161 it is interesting to note that all liquid slag compositions above the stoichiometric  $M_3O_5$  line remain unchanged after solidification. In contrast, all liquid slags with composition below this line are altered to a composition exactly on the  $M_3O_5$  line upon complete solidification.

The reason for the contrast in solidification behaviour is that, in the case of compositions above the  $M_3O_5$  line, solidification products only include oxide phases that are collectively view as slag. The entire mass of liquid slag therefore reports as solid slag once solidification is complete. This is not the case for liquid slag with composition below the  $M_3O_5$  line. For these slags, iron metal becomes stable during solidification. Iron is, off course, not seen as slag. The mass of material that is viewed as slag reports to the pseudobrookite (or  $M_3O_5$ ) phase. The change in slag (oxide) composition for slags with original compositions below the  $M_3O_5$  join is caused by the disproportionation reaction ( $Ti_2O_3 + FeO \rightarrow 2TiO_2 + Fe$ ) that occurs during cooling. This reaction hence enriches the slag in  $TiO_2$ , and depletes it of  $FeO$  – giving the composition trajectories that are shown in Figure 161.

#### c. Kinetic effects

Kinetic effects were discussed in 10.3. It is therefore adequate to state that contributions of mass transfer controlled and heat transfer controlled steps to the compositional invariance are improbable due to the significant stirring in both the slag and metal baths. The relatively small size of reductant particles (less than 10 mm diameter) further contributes to high reaction rates. Something that is not known, is the absolute and relative rates at which reduction reactions occur between slag and reductant particles, and between slag and high-carbon metal. One might speculate that the rate at which  $TiO_2$  is reduced to  $Ti_2O_3$ , may differ from the rate at which  $FeO$  is reduced to  $Fe$ .

#### d. Industrial data

The last piece of background information is the knowledge of actual compositions of industrial slags. Compositions of a number of industrial slags have been presented in paragraph 10.1. These same compositions are displayed on the  $TiO_2$ - $FeTiO_3$ - $Ti_2O_3$  ternary diagram in Figure 162. The actual slag  $FeO$  and  $Ti_2O_3$  contents were converted to equivalent contents with the procedure used by Pistorius (2002). It is clear that the compositions of these slags are grouped around the  $M_3O_5$  line. Slags from South African ilmenites tend to have compositions above the  $M_3O_5$  line and slags from Canadian ilmenites below the line.



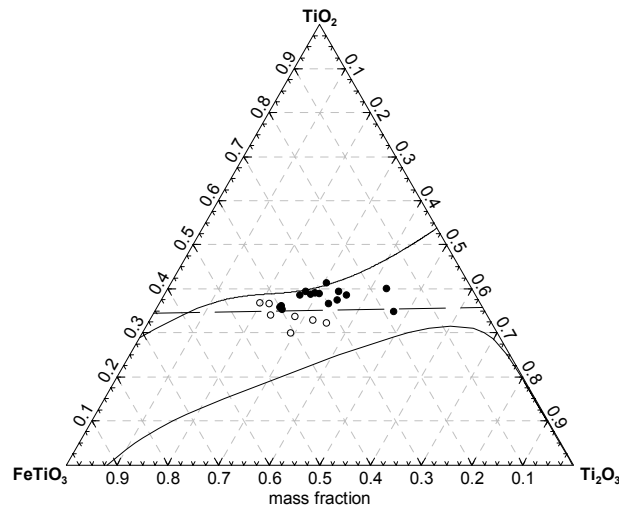


Figure 162 – Ternary view on compositions of industrial slags.

Filled circles represent slag produced from South African ilmenites and empty circles slags from Canadian ilmenites.

### 10.5.3 A Step-by-Step Batch Experiment

The above knowledge about the process was used as the foundation on which the new mechanism was built. The first way of demonstrating the proposed mechanism is by describing a hypothetical step-by-step batch experiment using three of the background information items listed above. These items are knowledge about chemical reaction equilibrium, solidification behaviour and the actual compositions of industrial slags. Because of the uncertainty surrounding kinetic effects, these were not incorporated. All calculations described below were done with FactSage 5.2 and the results of the various steps are shown in Figure 163. The system was allowed to reach equilibrium during each of the steps.

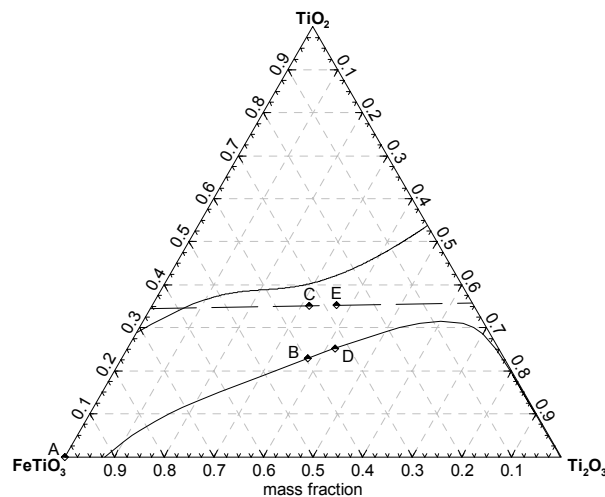


Figure 163 – Composition points resulting from the hypothetical step-by-step batch experiment.

- Step 1:  
Heat 100 g of stoichiometrically pure ilmenite up to its liquidus temperature (1397 °C according to FactSage 5.2). The composition of the system is indicated by point **A** in Figure 163.
- Step 2:  
Add 7.8 g of pure graphite and heat the system to the liquidus temperature of the slag (1582 °C). This produces 61.6 g of slag with a composition indicated by point **B** in Figure 163. This step also produces 27.9 g of liquid iron with a carbon content of 0.11%.
- Step 3:  
Cool the system to the solidus temperature of the slag (1548 °C). The resulting solid slag has a mass of 60.0 g and consists of only pseudobrookite as indicated by point **C** in Figure 163. An additional 1.6 g of metal is produced during solidification.
- Step 4:  
Remove all metal and heat the system to the liquidus temperature of the slag (1587 °C). The slag composition and mass remains unchanged at point **C** in Figure 163 and 60.0 g respectively.
- Step 5:  
Add 0.48 g of carbon and adjust the system temperature to the liquidus temperature of the slag (1598 °C). The slag composition moves to point **D** in Figure 163 and the mass of slag decreases to 59.3 g.  
  
It is interesting to note that a line connecting points **C** and **D** on Figure 163 is parallel to the  $\text{TiO}_2$ - $\text{Ti}_2\text{O}_3$  axis of the diagram. This means that only one reduction reaction, the conversion of  $\text{TiO}_2$  to  $\text{Ti}_2\text{O}_3$ , occurs between these two points. The  $\text{FeO}$  to  $\text{Fe}$  reaction only starts occurring again when the composition of the slag has reached the slag/(slag+  $\text{Fe}^\circ$ ) phase boundary at point **D**.
- Step 6:  
Cool the system down to the solidus temperature of the slag (1562 °C). The slag's composition moves to point **E** in Figure 163 and its mass decreases to 58.0 g. Roughly 1.3 g of metal is produced.
- Step 7:  
Remove all metal and heat the system again to the liquidus temperature of the slag (1600 °C). The slag's composition and mass remain unchanged.

The above description serves to illustrate that a combination of the drive towards chemical reaction equilibrium, slag solidification and slag melting can contribute to constrain the composition of the slag to the stoichiometric  $\text{M}_3\text{O}_5$  line. It does not, however, explain how these phenomena occur and combine in the actual process.

#### 10.5.4 Description

In the case of the real process, a mass of pure ilmenite is not an appropriate starting point for a line of reasoning since this may only be representative of conditions when the furnace is first started up. A more

representative starting point is an established slag bath with a composition in the vicinity of the  $M_3O_5$  line as shown in Figure 162. This starting point is indicated by area **A** in Figure 164.

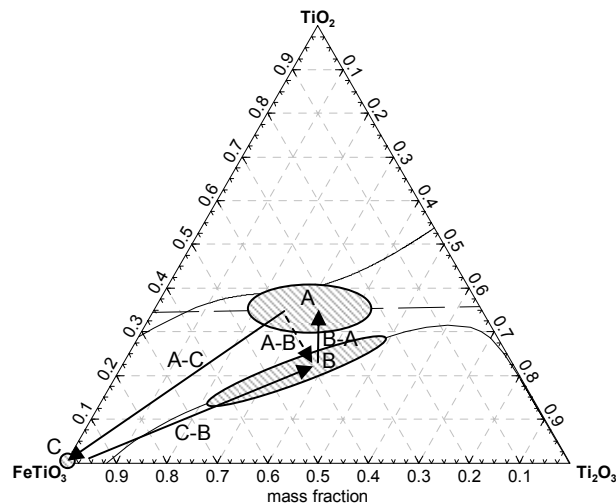


Figure 164 – Illustration of mechanism proposed to cause the observed compositional invariance.

The proposed mechanism explains the observed compositional invariance close to the stoichiometric  $M_3O_5$  line as follows:

- Ilmenite is continuously added to the process. Because of its low melting point (around 1397 °C according to FactSage 5.2), ilmenite is likely to melt quickly and subsequently absorbed into the slag bath. The influence of ilmenite addition on slag bath composition is indicated by composition vector **A-C** in Figure 164.
- Reductant is also fed continuously to the process. Reaction between reductant and liquid slag causes the slag composition to be drawn towards area **B**. This is indicated by composition vector **C-B** in Figure 164. Because vector **A-C** is unlikely to move the slag bath composition to area **C**, vector **C-B** could have been drawn more realistically from a more intermediate point on vector **A-C**.
- The uncertainties associated with vectors **A-C** and **C-B** in terms of extent and direction can be avoided by focusing on the resultant vector **A-B**. This vector shows the combined influence of ilmenite and reductant fed into the furnace on the composition of the slag bath.
- The impinging arc and entering feed material transfer momentum into the slag bath and thereby causes stirring of the slag bath. This stirring continuously causes slag to be circulated to and from the interface between the slag and metal baths.

It is well known and it has been reported (Geldenhuis and Pistorius, 1999) that the slag and metal baths exist at significantly different temperatures. This difference has been reported to be between 38 and 86 °C (Geldenhuis and Pistorius, 1999). Subsequent to this work, Pistorius (1999) even used an assumption that the temperature of the metal bath is 150 °C lower than that of the slag bath.

The fact that such a significant temperature difference exists between the slag and metal baths implies that a temperature gradient must exist at the interface between the two baths. This presents a question: Does the transition from the high temperature of the slag bath to the lower temperature of the metal bath occur in a thermal boundary layer in the slag bath, in a thermal boundary in the metal bath, or in thermal boundary layers on both sides of the interface?

Table 25 shows a comparison of a series of physical properties of molten iron and molten slag. A detailed analysis of these properties and the flow conditions in the furnace is required to provide a final answer to the boundary layer question. However, because the thermal conductivity of slag is estimated to be up to one order of magnitude lower than that of metal, it is proposed that all or most of the temperature transition is located in a liquid slag boundary layer.

SYMBOL	DESCRIPTION	UNITS	MOLTEN IRON	MOLTEN SLAG
Pr	Prandtl number	none	$1.646 \times 10^{-1}$	$2.974 \times 10^1$
$\mu$	Dynamic viscosity	kg/(m.s)	$7.000 \times 10^{-3}$ (Guthrie, 1992)	$3.000 \times 10^{-2}$ (Pistorius and Coetzee, 2003)
$c_p$	Heat capacity	J/(kg.K)	$7.170 \times 10^2$ (Guthrie, 1992)	$9.914 \times 10^2$ (FactSage 5.2)
k	Thermal conductivity	W/(m.K)	$3.050 \times 10^1$ (Guthrie, 1992)	$1.000 \times 10^0$ (Pistorius, 2004)
$\rho$	Density	kg/m <sup>3</sup>	$7.030 \times 10^3$ (Guthrie, 1992)	$3.800 \times 10^3$
$\nu$	Kinematic viscosity	m <sup>2</sup> /s	$9.957 \times 10^{-7}$	$7.895 \times 10^{-6}$
$\alpha$	Thermal diffusivity	m <sup>2</sup> /s	$6.051 \times 10^{-6}$	$2.654 \times 10^{-7}$

Table 25 – Physical properties of molten iron and molten high-titania slag.

Because of the existence of this boundary layer in the slag, the liquid slag circulated to the interface between the slag and metal baths will be cooled. This cooling causes solidification of slag as pseudobrookite and also precipitation of iron metal. The majority of the precipitated metal is taken up into the metal bath. The solidified slag and the remainder of the metal are circulated back into the hotter bulk slag mass. Under the conditions prevalent in the bulk slag, the solidified slag melts and the iron becomes thermodynamically unstable and acts as a reductant converting  $\text{TiO}_2$  to  $\text{Ti}_2\text{O}_3$  and FeO.

The solidification and melting behaviour described above is presented by composition vector **B-A** on Figure 164.

Now it must be confirmed whether the proposed mechanism satisfies the requirements stated earlier. Firstly, it can be said that through this mechanism a sustained influence is exerted on the composition of the slag bath. This is a result of the circulation of slag to and from the interface between the slag and metal baths, and because of the effectively irreversible nature of the action by which iron is removed from the slag phase. It is seen as irreversible because most of the metal is taken up into the metal bath.

Secondly, the mechanism clearly provides a means of adjusting the composition of the slag bath towards the stoichiometric  $\text{M}_3\text{O}_5$  line.

## 10.6 A REFLECTION ON REDUCTION MECHANISMS

From the above proposed mechanism it is possible to gain some important insight into the mechanisms of reduction reactions in the furnace.

### 10.6.1 Reactions in the Bulk Slag and on the Slag Bath Surface

Firstly consider contact between a reductant particle and slag having a composition in area **A** of Figure 164. Such slag may be found on the surface of the slag bath or in the 'body' of the slag bath away from the turbulent zone underneath the electrode. Initially reduction will only involve the conversion of  $\text{TiO}_2$  to  $\text{Ti}_2\text{O}_3$ . The reason for this is that iron metal is not stable under the initial conditions. The composition of the slag in close proximity of the reductant particle must first be changed towards area **B** and the slag/(slag+  $\text{Fe}^\circ$ ) phase boundary where iron metal is able to form. Depending on the rate at which the liquid slag close to the reaction interface with the shrinking reductant particle is being renewed via diffusion and convective mass transfer, the liquid slag in the small system may reach a point of iron metal stability or it may not.

If metal is indeed formed, the produced droplet or droplets must somehow find its way to the metal bath. It is likely that, during this travel, it will come into contact with liquid slag that is representative of the bulk conditions (composition in area **A** and temperature close to the bulk slag temperature) in the slag bath. According to the available thermodynamic data, the carbon in the metal droplet will first react with  $\text{TiO}_2$  to form  $\text{Ti}_2\text{O}_3$  and CO gas. This leaves a virtually pure iron droplet. Under the bulk slag conditions iron is also not stable. It will react with  $\text{TiO}_2$  and  $\text{Ti}_2\text{O}_3$  and FeO will be produced.

It therefore seems that iron produced by reduction reactions between liquid slag and reductant that has to travel through the bulk slag to reach the metal bath, is unlikely to eventually be taken up into the metal bath.

### 10.6.2 Reactions at the Interface between the Slag and Metal Baths

For the portion of the interface area between the slag and metal baths where metal is precipitated as a result of cooling, the tendency of the high-carbon metal to reduce slag will be inhibited for two reasons.

Firstly, the metal at the interface will be enriched in Fe because of the newly precipitated metal and, as a consequence, the carbon content will be lower as a result of the dilution effect. In this way a mass transfer barrier is created that will tend to decrease the rate at which carbon is removed from the metal bath.

Secondly, the slag at the interface will be at least partly solidified. The rate of reaction between liquid metal and solid slag is likely to be lower than reaction between liquid metal and liquid slag.

### 10.6.3 Reactions in the Turbulent Zone underneath the Electrode

The zone underneath the electrode is likely the most uncertain part of the process in terms of prevalent conditions and reaction mechanisms. A number of observations can however be made.

The local slag composition in this zone is likely to be drawn relatively far towards zone **C** in Figure 164 because of the ilmenite entering through the electrode. It is likely that at least some reduction takes place in this zone due to the high temperatures and the presence of reductant particles. It is also likely that,

because of the slag composition, a significant amount of iron metal is formed as a result of the reduction reactions.

Finally, it is likely that, because of the significant presence of both metal droplets and reductant particles and because of the high temperatures, much of the carbon reaching the metal bath is dissolved into metal droplets in this zone.

## CHAPTER 11 CONCLUSION

### 11.1 OBJECTIVES AND APPROACH

The objective of this work was to study and characterise the dynamic behaviour of the freeze lining and slag bath, study and characterise the interactions between freeze lining and slag bath, and to study the compositional invariance of the slag close to the stoichiometric  $M_3O_5$  line and possibly determine the mechanism causing this phenomenon.

The approach used to achieve the objectives focused on mathematical modelling. Process models of the freeze lining and furnace sidewall, of the slag bath crust and of the entire smelting process were constructed. These models were used to study the phenomena of interest by conducting numerous experiments. The experimental results were processed and converted into series of graphs to display the behaviour of the process or of a particular part of the process during the experiments.

### 11.2 CONTRIBUTION OF THIS WORK

#### 11.2.1 Process Models

The process models developed and documented in CHAPTER 3, CHAPTER 4 and CHAPTER 5 do not, strictly speaking, have any value in their own right. Such models only become valuable through their application to the study of specific problems and phenomena as was done in this work. The details on these models presented in this text may however provide a useful starting point for modelling work by other workers.

The models can also be applied to study further issues relevant to ilmenite smelting and, by including the appropriate material property data, to other similar processes. All the models were developed with broader future application in mind.

One aspect that must however be kept in mind is the fact that specific furnace dimensions and material property data were used in the versions of the models presented here. These data items must be replaced with data that is representative of an actual process for the models to be directly applicable to such a process. This fact must also be taken into account when viewing and interpreting experimental results presented in this text.

Given the new insights presented in CHAPTER 10, some of the assumptions made in the formulation of the ISFP model in CHAPTER 5 appear to be critically invalid. The first of these is Assumption 5.1 that assumes the slag bath, metal bath and furnace freeboard to be isothermal. The proposed mechanism behind the observed compositional invariance relies on the slag and metal baths having different temperatures. Such a temperature difference does, of course, occur in reality. The second is Assumption 5.2 that assumes the slag bath to be ideally mixed. The proposed mechanism will cause concentration gradients to form in the slag bath.

The ISFP model should be updated to incorporate the proposed mechanism. This will make the model significantly more representative of the actual process, and it will rid the model of restrictions such as that of the approach used to constrain the liquid slag composition close to the stoichiometric  $M_3O_5$  line.

Another restriction that is worthwhile addressing is the one-dimensional nature of the FLC model. This prevents the model from describing variations in metal and slag bath levels, resulting in a significant limit in the degree to which the model is able to describe the dynamic behaviour of an actual furnace.

Finally the use of actual plant data to adjust the model parameters of the various models can improve greatly the accuracy with which these models describe reality. This will have to be done in co-operation with an organisation operating one or more ilmenite-smelting furnaces.

### 11.2.2 Interactions between Freeze Lining and Slag Bath

The experimental results displaying slag bath and freeze lining behaviour highlighted, and perhaps reconfirmed, the fact that the behaviour and co-existence of, and the interaction between the slag bath and freeze lining are governed by two major influences.

The first is the influence of the phase chemistry of the  $TiO_2$ -FeO- $Ti_2O_3$  system. Solidification and melting result in the formation of phases as predicted by the phase diagram. This is of course expected for the models because of the fact that all of them have a strong thermochemical foundation. The fact that the models were able to produce realistic results perhaps confirms the dominant influence of phase chemistry and the drive towards thermodynamic equilibrium in the actual process. This notion is supported by the fact that the mechanism proposed to cause the observed compositional invariance is also strongly founded on the influence of phase chemistry and the drive towards equilibrium.

The second influence is that of heat transfer. In a situation where more energy is being discharged into the system than can be consumed by reduction reactions and removed via heat loss avenues, the freeze lining will start melting away to increase the rate at which heat can be conducted towards the outer surface of the furnace wall. In an opposite situation the freeze lining will start to grow thicker. The response of the freeze lining is of course not the only effect of such situations. Heat losses through the lower sidewalls and hearth, and from the top of the slag bath will also change, as will the characteristics of reduction reactions taking place (to a limited extent).

The conclusion is therefore that the slag bath and freeze lining behave as expected once one takes cognisance of the thermochemical and heat transfer characteristics of the system.

### 11.2.3 Process Mechanisms

A mechanism that explains the compositional invariance of slag close to the stoichiometric  $M_3O_5$  line was proposed in CHAPTER 10. This mechanism points at the drive towards thermodynamic equilibrium as being a major influence in the process.

This contradicts the speculation in CHAPTER 5 about reaction kinetics and the possibility of it being the cause of the compositional invariance. These speculations are believed to be much further from the truth than the mechanism proposed in CHAPTER 10. Kinetics may indeed account for some yet unexplained



observations, but its influence is likely to be much less determining of general process behaviour compared to the influence of thermochemistry.

As a result of the above-mentioned mechanism, some questions arise about the mechanisms behind other phenomena in the process. The production of iron metal due to contact between liquid slag and reductant on the slag bath surface, and the travel of iron metal droplets from the slag bath surface, through the slag bath and into the metal bath become less probable. These phenomena may in fact occur, but to a limited extent.

There are still some unanswered questions about how the level of carbon in the metal bath is achieved and sustained. Reasoning provided in CHAPTER 10 regarding this issue is intuitively congruent with DC furnace operation, but not necessarily with AC furnace operation. In general, significant uncertainty still exists about reactions and process mechanisms in the turbulent, high-temperature zone underneath the electrode.

#### **11.2.4 The Nature of Thermocouple Signals**

The thermal response of the freeze lining and furnace wall were analysed and included in the result set of virtually each experiment conducted. Of these analyses, the work in CHAPTER 6 probably best characterises the nature of this response.

A significant observation was the asymmetry of the thermal response. Temperatures in the wall respond quicker when the freeze lining becomes thinner than when it grows thicker. This is an important fact to consider when developing an operating strategy or an automatic controller to regulate freeze lining thickness.

Perhaps more striking than the asymmetry of the thermal response was its slowness. This can be seen in Figure 87 (page 171). The sluggish response of these signals leaves one in a 'catch 22' situation regarding the positioning of thermocouples in the furnace sidewalls. By placing a thermocouple too deep, one runs the risk of destroying it when the freeze lining melts away. Conversely, placing it far away from the refractory hot face may prevent one from detecting that the freeze lining is melting away and taking action to prevent damage to the refractory wall. One may decide to view thermocouples as expendable, but repeated removal and installation of thermocouples will also inevitably inflict damage on the refractory wall. Placement of thermocouples in the furnace sidewalls remains a difficult decision to make.

### **11.3 OPPORTUNITIES FOR FUTURE WORK**

The work done in this project provides a platform for future work. Such work can include both improvements to the models presented here, and application of the current and improved versions of the models.

#### **11.3.1 Model Improvements**

The conductor models developed in CHAPTER 3 and CHAPTER 4 can be extended from the current one-dimensional formulation to a two-dimensional one. This will remove the restrictions that especially the FLC model places on the ISFP model. The ISFP model will then be able to describe varying slag and metal levels in the furnace. This will make the model more realistic in that it will be possible to 'operate' it in exactly

the same way that an actual furnace is operated. Such an improvement will also result in the model describing the dynamics of the process significantly better.

The proposed mechanism behind the observed compositional invariance and the additional insights into other mechanisms that were presented in CHAPTER 10 can be incorporated into the ISFP model. This will make the model more representative of the actual process and it will remove restrictions placed on the model by, for example, the method used to constrain the slag composition close to the stoichiometric  $M_3O_5$  line.

The current work incorporated only four constituents ( $TiO_2$ ,  $Ti_2O_3$ ,  $FeO$ , and  $Fe_2O_3$ ) in the liquid slag phase. Of these constituents  $Fe_2O_3$  was never used here. In the liquid metal phase only carbon, oxygen, titanium and titanium oxide solutes were included. Many constituents that occur in reality were therefore omitted here to simplify matters. Such components can be included in the thermochemical data files to better model industrial process and produce modelling results with which operational and process personnel of ilmenite smelters can identify more easily.

The furnace dimensions and material properties of the refractory brick, ramming material and steel shell can be replaced with data of actual furnaces. This will immediately result in an improved representation of such processes. The various parameters of the ISFP model can also be tuned based on data from industrial furnaces. This will further enhance the accuracy with which the model is able to describe these processes.

### 11.3.2 Model Applications

The availability of an accurate process model creates a number of opportunities. In general it provides a 'virtual copy' of the process that one can use and experiment with to study various issues. Without such a model one would either have to resort to experimentation on the actual furnace or a smaller-scale furnace, or to experimentation on laboratory scale. Both these alternatives have benefits and disadvantages. However, they are both likely to be more time-consuming and possibly more expensive than a modelling study.

Firstly, the ISFP model can be applied as a simulation model within a process simulator. Such a simulator can then be used to develop and test a control system for controlling parameters such as freeze lining thickness, slag composition, and slag and metal inventory. This reduces the risks involved with implementing a controller on a furnace, since it has already been tested on an accurate computer-based representation of the process.

Further, the simulator can be used to evaluate the impact of different operating strategies on the process. This can again be done on the actual process also, but at a higher risk of damage and losses in production, and over a longer period of time. Numerous low-risk and relatively quick experiments can be done with a process simulator based on the ISFP model.

The simulator can also be used to evaluate the impact of different thermocouple placements given a specific furnace configuration, feed materials and control strategy. This will enable process engineers to be better informed and more objective when making decisions about the placement of thermocouples in furnace sidewalls.

A process simulator can be used for operator training. The benefits of this are again lower risk of damage and production losses, and a possible saving of time. An operator can be exposed to and tested on a wide range of process conditions and scenarios without running the risk of costly mistakes on an actual furnace.

The models developed here could also be adapted fairly easily for application to AC ilmenite smelting furnaces. The circular geometry should be changed to rectangular in the case of six-in-line AC furnaces. Other than that change, the models could most likely be applied as they are to AC smelting furnaces.

## BIBLIOGRAPHY

- Bale C.W., Chartrand P., Degterov S.A., Eriksson G., Hack K., Ben Mahfoud R., Melançon J., Pelton A.D. and Petersen S. 2002. FactSage thermochemical software and databases. *Calphad*, vol. 26, no. 2, pp. 189–228.
- Bale C.W. and Pelton A.D. 1997. The unified interaction parameter formalism: Thermodynamic consistency and applications. *Metallurgical Transactions A*, vol. 21A, July 1990, pp. 1997 – 2002.
- Ban B.-C. and Krüger J. 1988. Reduzierendes schmelzen von Quilon-ilmenit im gleichstromlichtbogenofen, *Erzmetall*, vol. 41, no. 5, pp. 278–284.
- Brimacombe J.K. 1976. Design of Continuous Casting Machines Based on a Heat-Flow Analysis: State-of-the-Art Review. *Canadian Metallurgical Quarterly*, vol. 15, no. 2, pp. 163 – 176.
- Elstad H., Hildal A., Skaar I.M. and Sorli K. 2003. Monitoring the lining of an ilmenite smelting furnace. *Heavy Minerals Conference 2003*. Cape Town. South Africa Institute of Mining and Metallurgy.
- Eriksson G. 1971. Thermodynamic studies of high temperature equilibria – III. SOLGAS, a computer program for calculating the composition and heat condition of an equilibrium mixture. *Acta Chemica Scandinavica*, vol. 25, pp. 2651 – 2658.
- Eriksson G. 1975. *Chemica Scripta*, vol. 8, p. 100.
- Eriksson G. and Hack K. 1990. ChemSage – A computer program for the calculation of complex chemical equilibria. *Metallurgical Transactions B*, vol. 21B, p. 1013.
- Eriksson G., Pelton A.D., Woermann E. and Ender A. 1996. Measurement and thermodynamic evaluation of phase equilibria in the Fe-Ti-O system. *Berichte der Bunsengesellschaft für Physikalische Chemie*, vol. 100, no. 11, pp. 1839–1849.
- Eriksson G. and Pelton A.D. 1993. Critical evaluation and optimisation of the thermodynamic properties and phase diagrams of the MnO-TiO<sub>2</sub>, MgO-TiO<sub>2</sub>, FeO-TiO<sub>2</sub>, Ti<sub>2</sub>O<sub>3</sub>-TiO<sub>2</sub>, Na<sub>2</sub>O-TiO<sub>2</sub>, and K<sub>2</sub>O-TiO<sub>2</sub> systems, *Metallurgical Transactions B*, vol. 24B, October 1993, pp. 795–805.
- Eriksson G. and Rosen E. 1973. Thermodynamic studies of high temperature equilibria – General equations for the calculation of equilibria in multiphase systems. *Chemica Scripta*, vol. 4, p. 193.
- Flemings M.C. 1997. Chapter 5 – Solidification, in *Advanced physical chemistry for process metallurgy*. Editors N. Sano, W.-K. Lu and P.V. Riboud. Academic Press. pp. 151 – 182.
- Geldenhuis J.M.A. and Pistorius P.C. 1999. The use of commercial oxygen probes during the production of high titania slags. *The Journal of the South African Institute of Mining and Metallurgy*, vol. 99, no. 1, pp. 41–47.
- Gray A. and Pogo D. 1978. Physico-chemical properties of molten titania slags. *Annual volume, Metallurgical Society of the Canadian Institute of Mining and Metallurgy*, Montreal, pp. 97–102.
- GTT Technologies. 1998 *ChemSage Handbook*. Version 4.0.1.


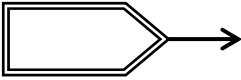



- GTT Technologies. 2001. *ChemApp Programmers Manual*, Edition 3.5.
- Guthrie R.I.L. 1992. *Engineering in process metallurgy*. Oxford University Press, p. 483.
- Handfield G. and Charette G.G. 1971. Viscosity and structure of industrial high TiO<sub>2</sub> slags. *Canadian Metallurgical Quarterly*, vol. 10, no. 3, pp. 235–243.
- Kahn J.A. 1984. Non-rutile feedstocks for the production of titanium. *Journal of Metals*, vol. 36, no. 7, pp. 33–38.
- Nell J. 1999. An overview of phase-chemistry involved in the production of high-titanium slag from ilmenite feedstock. *Heavy Minerals 1999*. R. G. Stimson (ed.). Johannesburg. The South African Institute of Mining and Metallurgy. pp. 137–145.
- Noda T. 1965. Titanium from slag in Japan. *Journal of Metals*, vol. 17, no. 1, pp. 25–32.
- Pauw O.G. 1989. Dynamic simulation of pyrometallurgical processes involving fast reactions at phase boundaries. Ph.D. Thesis, University of Pretoria.
- Pelton A.D. and Blander M. 1986. *Metallurgical Transactions B*, vol. 17B, p. 17.
- Perry R.H. and Green D.W. 1997, Perry's chemical engineers' handbook, 7th Edition, McGraw-Hill International.
- Pesl J. and Eriç R.H. 1999. High-temperature phase relations and thermodynamics in the iron-titanium-oxygen system. *Metallurgical and Materials Transactions B*, vol. 30B, no. 8, pp. 695 – 705.
- Pistorius P.C. 1999. Limits on energy and reductant inputs in the control of ilmenite smelters. *Heavy Minerals 1999*. R. G. Stimson (ed.). Johannesburg. The South African Institute of Mining and Metallurgy. pp. 183–188.
- Pistorius P.C. 2002. The relationship between FeO and Ti<sub>2</sub>O<sub>3</sub> in ilmenite smelter slags. *Scandinavian Journal of Metallurgy*, vol. 31, no. 2, pp. 120–125.
- Pistorius P.C. and Coetzee C. 2003. Physicochemical aspects of titanium slag production and solidification. *Metallurgical and Materials Transactions Series B*, vol. 34B, no. 5, pp. 581 – 588.
- Pistorius P.C. 2003. Fundamentals of freeze lining behaviour in ilmenite smelting. *The Journal of the South African Institute of Mining and Metallurgy*, vol. 103, pp. 509 – 514.
- Pistorius P.C. 2004. Equilibrium interactions between freeze lining and slag in ilmenite smelting. *VII International Conference on Molten Slags Fluxes and Salts*, The South African Institute of Mining and Metallurgy, pp. 237 – 242.
- Pistorius P.C. 2004b. Private communications about work on high-titania slag solidification. University of Pretoria.
- Ramírez-Argáez M.A. 2003. Mathematical modelling of DC electric arc furnace operations. ISSTech 2003 Conference Proceedings.

- Reynolds Q. 2002. Thermal radiation modelling of DC smelting furnace freeboards. *Minerals Engineering*, no. 15, pp. 993 – 1000.
- Rosenqvist T. 1992. Ilmenite Smelting. Transactions of the Technical University of Košice, vol. 2, special issue, pp. 40-46.
- Ruh E. and McDowell J.S. 1962. Thermal conductivity of refractory brick. *Journal of the American Ceramic Society*. vol. 45, no. 4, pp. 189-195.
- Stanaway K.J. 1994. Overview of titanium dioxide feedstocks. *Mining Engineering*, vol. 46, no. 12, pp. 1367-1370.
- Stenkvist S.-E. and Bowman B. 1987. High-power, graphite-cathode DC arc plasma – Properties and practical applications for steelmaking and ferroalloys processing. *Plasma Technology in Metallurgical Processing*, Iron and Steel Society, pp. 103 – 109.
- Thomas B.G. and Brimacombe J.K. 1997. Chapter 8 – Process modeling, in *Advanced physical chemistry for process metallurgy*. Editors N. Sano, W-K. Lu, P.V. Riboud. Academic Press, pp. 253-279.
- Weast R.C. and Astle M.J. 1983. *CRC handbook of chemistry and physics*. 62<sup>nd</sup> Edition, CRC Press, Boca Raton, Florida, p. E-11.


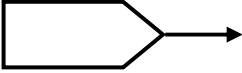



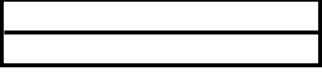

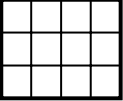
## APPENDIX A – MATERIAL PROPERTIES

MATERIAL	COMPOSITION	DENSITY [kg.m <sup>-3</sup> ]	THERMAL CONDUCTIVITY [kW.m <sup>-1</sup> .°C <sup>-1</sup> ]
Steel (Perry and Green, 1997)	1.2% C, 0.3% Mn	7800	$2.0792 \times 10^{-8} \times T^2 - 4.69295 \times 10^{-5} \times T + 5.6235 \times 10^{-2}$
Graphite Ramming Material (Weast and Astle, 1983)	100% C (solid graphite)	1700	$1.066 \times 10^{-1} \times e^{-0.0011805 \times T}$
Magnesia Brick (Ruh and McDowell, 1962)	93.6% MgO	2787	$1.1511 \times 10^{-2} \times e^{-0.0011304 \times T}$
Solid Slag	Values assumed to be valid for various typical high-TiO <sub>2</sub> slag compositions.	3800	0.001
Liquid Slag	Values assumed to be valid for various typical high-TiO <sub>2</sub> slag compositions.	3800	0.001
Liquid Metal	Dependant on the circumstances modelled.	Not used.	Not used.

## APPENDIX B – MODEL ELEMENT DESCRIPTIONS

NAME	ABBR.	SYMBOL	DESCRIPTION
Energy Flow Stream	EFS		An energy flow stream is used to connect modules with energy output ports and energy input ports. The flow stream receives energy from an output port and passes it to an input port.
Energy Input Module	EIM		An energy input module produces energy. The produced energy is made available at its output port where an energy flow stream receives it.
Energy Output Module	EOM		An energy output module extracts energy. It receives energy at its input port from an energy flow stream.
Energy Fraction Splitter	EXS		An energy fraction splitter is used to split the energy from one energy flow stream into two or more fractions. It makes the fractions available at its output ports where it is received by two or more energy flow streams.
Isothermal Module	ITM		An isothermal module represents a zone in a process that can be approximated as being isothermal. This module contains MMM, MRM, MXS and MPS modules. All the contained MMM modules are given the same temperature.



NAME	ABBR.	SYMBOL	DESCRIPTION
Material Flow Stream	MFS		A material flow stream is used to connect modules with material output ports and material input ports. The flow stream receives material from an output port and passes it to an input port.
Material Input Module	MIM		A material input module produces material. The produced material is made available at its output port where a material flow stream receives it.
Material Output Module	MOM		A material output module extracts material. It receives material at its input port from a material flow stream.
Material Fraction Splitter	MXS		A material fraction splitter is used to split the material from one material flow stream into two or more fractions. It makes the fractions available at its output ports where it is received by two or more material flow streams.
Material Phase Splitter	MPS		A material fraction splitter is used to split multiphase material into single phase material. The number of output ports is equal to the number of phases in the material received at its input port.
Material Reactor Module	MRM		A material reactor module is used to calculate the equilibrium condition of the material received at its input ports. The resulting material is delivered at its output ports as single-phase material.
Material Mixer Module (Ideal Mixer)	MMM		A material mixer module is used to represent a collection of material in a process that can be approximated as being ideally mixed. It can receive material at multiple input ports and deliver material to multiple output ports.
Conductor Module	CDM		A conductor module is used to conduction calculate heat transfer through, for example, a wall. It exchanges liquid material with a mixer module. It models solidification and melting of this liquid.